Handbook of Flexible Organic Electronics

Materials, Manufacturing and Applications

Edited by Stergios Logothetidis

WP
WOODHEAD
PUBLISHING

Handbook of Flexible Organic Electronics

Related titles

High Performance Silicon Imaging
(ISBN 978-0-85709-598-5)

Nitride Semiconductor Light-Emitting Diodes (LEDs)
(ISBN 978-0-85709-507-7)

Chalcogenide Glasses
(ISBN 978-0-85709-345-5)

Handbook of Flexible Organic Electronics

Materials, Manufacturing and Applications

Edited by

Stergios Logothetidis

Notice
No responsibility is assumed by the publisher for any injury and/or damage to persons or
property as a matter of products liability, negligence or otherwise, or from any use or
operation of any methods, products, instructions or ideas contained in the material herein.
Because of rapid advances in the medical sciences, in particular, independent verification
of diagnoses and drug dosages should be made.

For information on all Woodhead Publishing publications
visit our website at http://store.elsevier.com/

Typeset by TNQ Books and Journals
www.tnq.co.in

Printed and bound in the United Kingdom

Working together
to grow libraries in
developing countries

www.elsevier.com • www.bookaid.org

Contents

This page intentionally left blank

List of contributors

A.K. Andreopoulou University of Patras, Greece

M. Barbaro University of Cagliari, Cagliari, Italy

M.J. Beliatis Advanced Technology Institute, University of Surrey, Guildford, UK

A. Bonfiglio University of Cagliari, Cagliari, Italy

B.S. Cook Georgia Tech, Atlanta GA, USA

J.R. Cooper Georgia Tech, Atlanta GA, USA

P. Cosseddu University of Cagliari, Cagliari, Italy

B.W. D'Andrade Exponent, Inc., Washington, DC, USA

P. Delaporte Aix-Marseille University, CNRS, Marseille, France

M. Demelas University of Cagliari, Cagliari, Italy

D. Georgiou Aristotle University of Thessaloniki, Thessaloniki, Greece

S. Grigorian University of Siegen, Siegen, Germany

G. Huebner Institute for Applied Research (IAF), Hochschule der Medien (HdM), Stuttgart, Germany

K.D.G.I. Jayawardena Advanced Technology Institute, University of Surrey, Guildford, UK

J.K. Kallitsis University of Patras, Greece

D. Karnakis Oxford Lasers Ltd, Didcot, UK

A.Z. Kattamis Exponent, Inc., New York, NY, USA

S. Kim Georgia Tech, Atlanta GA, USA

C. Koidis Organic Electronic Technologies P.C. (OET), Thessaloniki, Greece

S. Kourkouli University of Patras, Greece

M. Koyuncu Robert Bosch GmbH, Waiblingen, Germany

M. Krebs VARTA Microbattery GmbH, R&D, Ellwangen, Germany

F.C. Krebs Technical University of Denmark, Roskilde, Denmark

S. Lai University of Cagliari, Cagliari, Italy

A. Laskarakis   Aristotle University of Thessaloniki, Thessaloniki, Greece

Y. Leterrier   Ecole Polytechnique Fédérale de Lausanne (EPFL), Switzerland

S. Logothetidis   Aristotle University of Thessaloniki, Thessaloniki, Greece

A. Loi   University of Cagliari, Cagliari, Italy

E. Lorenz   Robert Bosch GmbH, Waiblingen, Germany

M.F. Mabrook   Bangor University, Bangor, UK

C.A. Mills   Advanced Technology Institute, University of Surrey, Guildford, UK

P.F. Murphy   Exponent, Inc., New York, NY, USA

N. Li Pira   Centro Ricerche Fiat, Strada Torino, Orbassano, TO, Italy

R. Rhodes   Advanced Technology Institute, University of Surrey, Guildford, UK

B. Roth   Technical University of Denmark, Roskilde, Denmark

L.J. Rozanski   Advanced Technology Institute, University of Surrey, Guildford, UK

P.W. Sayers   Bangor University, Bangor, UK

S.R.P. Silva   Advanced Technology Institute, University of Surrey, Guildford, UK

A. Sleiman   Bangor University, Bangor, UK

R.R. Søndergaard   Technical University of Denmark, Roskilde, Denmark

B. Tehrani   Georgia Tech, Atlanta GA, USA

M.M. Tentzeris   Georgia Tech, Atlanta GA, USA

G. Volonakis   Aristotle University of Thessaloniki, Thessaloniki, Greece

Z.G. Wu   Uppsala University, Uppsala, Sweden

I. Zergioti   National Technical University of Athens, Athens, Greece

D.A. Zeze   Durham University, Durham, UK

A. Zimmermann   Robert Bosch GmbH, Waiblingen, Germany

Woodhead Publishing Series in Electronic and Optical Materials

Part One

Properties and materials

This page intentionally left blank

Mechanics of curvature and strain in flexible organic electronic devices

1

Y. Leterrier
Ecole Polytechnique Fédérale de Lausanne (EPFL), Switzerland

1.1 Introduction

The confluence of (soft) organic materials in biology and (hard) inorganic materials in electronics has led during the past several decades to numerous enabling concepts and demonstrations of flexible devices as reviewed by Nathan et al. (2012). Flexible electronics has become a pervasive technology endeavor with a multitude of shape attributes, from single curvature conformal displays and thin film solar cells (Choi, Kim, & Ha, 2008; Crawford, 2005; Lewis, 2006; Pagliaro, Ciriminna, & Palmisano, 2008) to complex curvilinear stretchable devices for biomedical applications (Ko et al., 2009). The extent to which, and the number of times, these multilayer structures can be safely bent or stretched and twisted are essential, but highly challenging design features. In addition to providing basic functions such as electrical conductivity, transparency, or light emission, the selected materials and their structuration into various device architectures must fulfill new criteria to avoid damage during both processing and operational life. Design and process engineers working on the implementation of flexible electronics often lack confidence due to a lack of understanding or a lack of input data for reliable modeling tools. The aim of this Chapter is to introduce basic mechanical concepts and provide key ingredients for rational design of flexible organic electronics. Section 1.2 is devoted to the analysis of stresses and strains and related critical radius of curvature of multilayer structures, with attention paid to relevant material property data and to process-induced internal strains. Section 1.3 and Section 1.4 detail failure mechanics under tensile and compressive loading, respectively, and are illustrated with case studies from the literature. Section 1.5 presents an overview of mechanical test methods available and in development, which are useful to test the limits of multilayer samples and challenge the models described in the two previous sections. Section 1.6 discusses several recent research endeavors relevant to flexible organic electronics including stretchable and foldable devices, roll-to-roll (R2R) processing, and self-repair material strategies. Section 1.7 closes this chapter with a number of final remarks.

1.2   Stress and strain analyses

Figure 1.1 summarizes the main damage events and the state of strain in a compliant
substrate coated on both sides with thin brittle films. Upon bending to some radius of
curvature, the film located on the convex (top) side experiences tensile strain and may
crack and eventually delaminate. The film located on the concave (bottom) side expe-
riences compressive strain and may also delaminate and buckle and possibly crack as
well. Also depicted in Figure 1.1 is the through-thickness strain profile. The neutral
axis is the plane where the strain does not change upon pure bending. As detailed in
the following, the total strain is the sum of an internal strain and a bending strain.
The internal strain is essentially controlled by the fabrication process, and is assumed
in Figure 1.1 to be compressive in the two films and tensile in the substrate. The
bending strain results from the curvature applied during service and is proportional
to the distance from the neutral axis.

1.2.1   Critical radius of curvature

The critical radius of curvature, R_{crit}, is among the key design parameters for flexible
electronics. It is defined as the radius of curvature at which device failure occurs
because of mechanical damage or functional failure (e.g., electrical failure). Failure
in fact occurs at a critical strain, ε_{crit}. Depending on the critical strain level, one
may discriminate various terminologies:

- *flexible electronics*, which comprise films with $\varepsilon_{crit} < 2\%$, are based on substrate materials
  that are thin enough (100 µm) to be safely bent to radius of curvature down to 10 mm,
  but cannot be *stretched.*
- *compliant electronics*, for which $2\% < \varepsilon_{crit} < 10\%$, can be flexed to radius of curvature of
  few mm, allow some in-plane loading, and can be used with thicker substrates.
- *stretchable electronics*, for which $\varepsilon_{crit} > 10\%$, can be conformed to a broad diversity of
  surfaces with two-dimensional curvatures and small radius below a few millimeters.
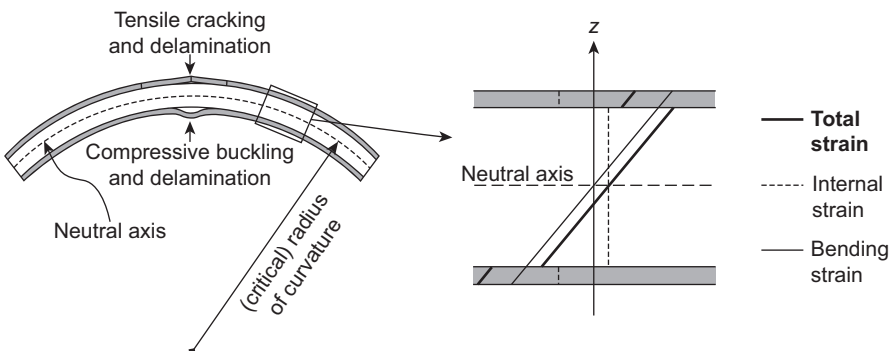
Figure 1.1 Summary sketch of damage events and strain state in a flexed substrate coated
on both sides with thin films. The various terms shown in the figure are discussed in the
chapter.

For stress state in Figure 1.1 and for the elastic case (dissipative processes such as substrate yielding are not considered), R_{crit} is inversely proportional to ε_{crit} and is a function of the multilayer film geometry and mechanical properties. The case of pure bending gives (Suo, Ma, Gleskova, & Wagner, 1999):

$$R_{crit} = \left(\frac{h_f + h_s}{2\varepsilon_{crit}}\right)\left(\frac{1 + 2\eta + \chi\eta^2}{(1 + \eta)(1 + \chi\eta)}\right) \tag{1.1}$$

where h_f and h_s are the film and substrate thicknesses, respectively, $\eta = h_f/h_s$ and $\chi = E_f/E_s$ (E_f and E_s are the Young's moduli of the film and substrate, respectively). Eqn (1.1) simplifies in the case $h_f << h_s$ ($\eta << 1$) and $E_f < \sim 10\,E$ ($\chi < \sim 10$):

$$R_{crit} \approx \frac{h_s}{2\varepsilon_{crit}} \tag{1.2}$$

Figure 1.2 maps the critical radius calculated using Eqn (1.1) versus thickness ratio and Young's modulus ratio. The data were calculated for a critical strain $\varepsilon_{crit} = 0.01$ (a typical value for brittle inorganic layers) and a substrate thickness of 100 μm. The critical radius is found to range from 1 to 15 mm for $0.001 < \eta < 1$ and $0.01 < \chi < 100$, and to be close to 5 mm for cases in which $\eta < 0.01$, as given by Eqn (1.2). For modulus ratio χ higher than several tens, the critical radius rapidly reduces with increasing film thickness, reaching a value as low as 1 mm for a thickness ratio $\eta = 0.1$ and a modulus ratio χ of 100.
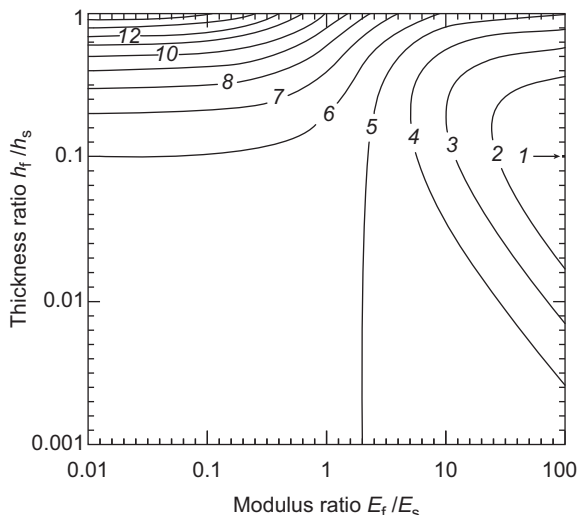
Figure 1.2 Map of critical radius of curvature (solid lines, data in (mm) calculated for a film with a critical strain of 1% on a 100-μm-thick substrate) versus thickness ratio and Young's modulus ratio.

1.2.2   Relevant material properties

The calculation of the critical radius requires knowledge of the critical strain, thickness, and Young's modulus of both film and substrate. Advanced analyses also call for the Poisson's ratio and coefficients of thermal expansion (CTE) and hygroscopic expansion (CHE) of all material constituents (to derive the associated thermal and hygric contributions to the internal strain, see Section 1.2.3). Methods developed to measure these properties are described in Section 1.5, and Table 1.1 compiles experimental data for thin film materials used in organic electronic devices. The Poisson's ratio has a small influence on calculated properties and approximate values are usually sufficient. This is not the case for the CTE and CHE, whose influence on film failure can be considerable.

1.2.3   Intrinsic, thermal, and hygroscopic stresses

Prediction and control of residual stresses is crucial to achieve high-dimensional stability and avoid premature damage in multilayer structures. For both vapor-formed and solution-processed films, residual stresses include intrinsic, thermal, and hygroscopic contributions (Dumont, Tornare, Leterrier, & Månson, 2007; Leterrier, 2003; Ohring, 1992; Spaepen, 2000; Tamulevicius, 1998), as summarized in Table 1.2. Intrinsic stresses are associated with process-induced disorder (tensile or compressive in inorganic films) and a number of shrinkage mechanisms as sketched in Figure 1.3 (generally tensile in organic films). Thermal stresses develop upon cool-down from process temperature or upon temperature variations during service, because material constituents have mismatched thermal expansion coefficients. Thermal stresses are generally compressive in inorganic films and maybe tensile or compressive in organic films when using polymers as substrates. Hygroscopic stresses also develop upon exposure to ambient humidity because of a mismatch in hygroscopic expansion between material constituents. Hygroscopic stresses are generally tensile in inorganic films and can be tensile or compressive in organic films. Additional stresses may develop during postdeposition processes because of further dimensional changes of the polymer substrate, such as upon unloading from R2R manufacturing (Leterrier, Wyser, & Månson, 2001).

Figure 1.4 shows an example of internal stress contributions at 22 °C and 50%RH in silicon nitride films deposited at 200 °C on a polyimide substrate (Dumont et al., 2007). The total internal stress was found to be compressive and to increase in magnitude with increasing film thickness. The intrinsic stress was found to be compressive (approximately -150 MPa) and independent of thickness within experimental scatter. The thermal stress resulting from cooling from 200 °C to 22 °C was also compressive (approximately -500 MPa) and roughly independent of thickness. In contrast, the hygroscopic stress was tensile and comparable in magnitude to the thermal stress. A hygrothermoelastic analysis was enabled to calculate the CTE and CHE of the nitride films (see Section 1.5), using the known values for the PI substrate (CTE of 32×10^{-6} K^{-1} and CHE of approximately 30×10^{-6} (%RH)$^{-1}$ (Dumont et al., 2007; Murray, Hillman, & Pecht, 2004). The CTE of the nitride was found to be close to

Table 1.1 **Compilation of material data relevant for mechanical analyses of organic electronics**

Function	Material	Process method	Typical thickness	Young's modulus 20 °C/100 °C (GPa)	Poisson's ratio (−)	Linear CTE 20 °C/100 °C (×10⁻⁶ K⁻¹)	Linear CHE (×10⁻⁶ (%RH)⁻¹)	Yield or failure strain[a] (%)	References
Substrate	PDMS	Solution cast	1 mm	0.0007/0.0009	0.5	310/310	NA	>100	
	Polyimide foil	Solution cast	10−200 µm	2.5−3.2/2.5−3.2	0.34	20−55/30−55	22	2	
	PES foil	Extrusion	10−200 µm	2.3−2.6/2.3−2.6	0.3	50−60/50−60	28	3	van den Berg, Barink, Giesen, Meinders, and Yakimets (2011)
	PET foil	Extrusion- stretched	10−200 µm	5/3	0.3−0.4	40−50/50−80	5−8	3	
	PEN foil	Extrusion- stretched	10−200 µm	6.5/4.5	0.3−0.4	10−14/20−23	7−8	3	van den Berg et al. (2011)
	Paper[b]	Water slurry + lamination	100 µm	2−6/NA	0.1−0.5	4−16/NA	300−1900	1−5	Caulfield and Gunderson (1988), Schulgasser (1981)
	Steel foil	Cold rolling	100 µm	200/200	0.27−0.31	10−17/10−17	0	0.2	
	Glass foil	Float and fusion	30−600 µm	70/70	0.2	9/9	0	0.1	
Active layer	Pentacene	Solution processed	10−50 nm	1.0−16/NA	0.4	−35−150/NA	NA	>1.5%	Haas et al. (2007), Lipomi, Lee, et al. (2012), Sekitani et al (2005), Tahk et al (2009)
	PEDOT:PPS[c]	Solution processed	10−100 nm	1−2/NA	NA	NA	NA	3−12	Greco et al. (2011), Lang and Dual (2007), Lipomi, Chong, Vosgueritchian, Mei, and Bao (2012)
	P3HT/PCBM[d]	Solution processed	10−100 nm	4.3−6/NA	0.35	NA	NA	2−8	Lipomi, Chong, et al. (2012), Lipomi, Lee, et al. (2012), Tahk et al. (2009)
	Alq3[e]	Vapor deposited	10−100 nm	1−1.7/NA	0.33	NA	NA	NA	Torres, Bakken, Stafford, Li, and Vogt (2010)
	a-Si:H	Vapor deposited	100 nm	125/125	0.25	6/6	NA	0.5	
Diffusion barrier	SiNₓ	Vapor deposited	50−1000 nm	100−150	0.26	10/10	0	0.5−2	
	SiOₓ	Vapor deposited	10−500 nm	80/80	0.2	10−23/10−23	NA	1−4	

Table 1.1 **Continued**

Function	Material	Process method	Typical thickness	Young's modulus 20 °C/100 °C (GPa)	Poisson's ratio (−)	Linear CTE 20 °C/100 °C (×10⁻⁶ K⁻¹)	Linear CHE (×10⁻⁶ (%RH)⁻¹)	Yield or failure strain[a] (%)	References
	Parylene C	Vapor deposited	0.2−100 μm	2.8/NA	0.4	2−35/NA	NA	200	Graz and Lacour (2009), Harder, Yao, He, Shih, and Tai (2002)
	Polymer nanocomposite	Solution processed	1−10 μm	6−10	0.35	30−60/	NA	>5	
Electrode	ITO	Vapor deposited	100−200 nm	115−145	0.3	8/8	NA	1−1.5	Leterrier et al. (2004)
	ZnO	Vapor deposited/solution processed + annealed	0.1−5 μm	117−205/NA	0.3	4−6/NA	NA	0.3	Ong, Zong, Aravind, Choy, and Lu (2003), Yamamoto, Makino, and Yamamoto (2011)
	Ag	Solution processed colloid	1−5 μm	83	0.37	19/20	0	0.2	
	Al	Vapor deposited	100 nm	70	0.35	23.5/23.5	0	3	
	PEDOT-PSS[f]	Solution processed	100 nm	2.3/NA	0.35	NA	0	>20	Lipomi, Lee, et al. (2012), Tahk et al. (2009)
	Graphene	Exfoliation	0.07 nm	1000	0.33	−8/−3	0	13	Zhang and Gu, (2013)
	Graphene oxide	Oxidation of graphite	0.7 nm	208		−67/−67	NA	0.6	Dikin et al. (2007), Su et al. (2012)
	Gold	Vapor deposited	100 nm	69/69	0.42	14.2/14.5	0	1−15	Lacour et al. (2003)
	Carbon nanotubes (CNT)	Chemical vapor deposition	1 nm	1000	0.1−0.55	−1.5	0	16	Zhao and Shi (2011)
	CNT composites	Compounding	1−10 μm	1−10	0.3−0.4	NA	10	>5	Byrne and Gun'ko (2010)

In-plane properties for the polymer substrate foils; NA, not available.
[a]Depends on interfacial adhesion to substrate.
[b]Usually anisotropic.
[c]Poly(3,4-ethylenedioxythiophene):poly(p-phenylene sulfide).
[d]Blend of poly(3-hexylthiophene) (P3HT) with a fullerene derivative of [6,6]-phenyl C61-butyric acid methyl ether (PCBM).
[e]Tris(8-hydroxyquinolinato)aluminum.
[f]Poly(3,4- ethylenedioxythiophene):poly(styrene sulfonate).

Table 1.2 Summary of intrinsic, thermal, and hygroscopic contributions to residual stresses in inorganic and organic films

Stress component	Origin	Inorganic films	Organic films
Intrinsic	Film formation (vapor deposition, solution processing)	− or +	+
Thermal	Difference in CTE between film and substrate and temperature changes	−	− or +
Hygroscopic	Difference in CHE between film and substrate and relative humidity changes	+	− or +

− and + are conventions for compressive and tensile stresses, respectively.

$10^{-5}\,K^{-1}$, i.e., a factor of three times higher than the value for bulk Si_3N_4 $(2.9 \times 10^{-6}\,K^{-1})$. The CHE of the nitride was estimated and found to be close to zero, although with a large uncertainty due to the uncertainty on the CHE of the PI substrate. With these CTE and CHE values, the total stress in the nitride film on the PI substrate, and resulting curvature of the bilayer film, can be calculated for any hygrothermal path.
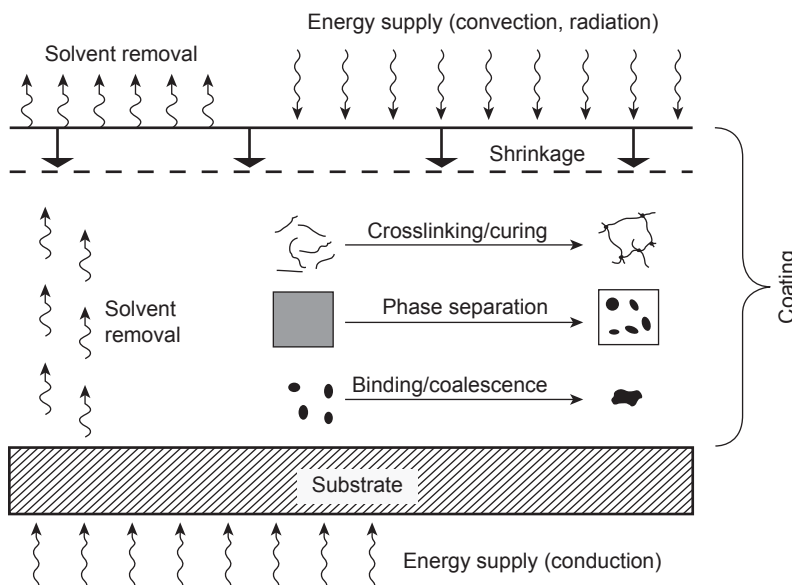
Figure 1.3 Mechanisms contributing to shrinkage during processing of a coating.
Source: Redrawn from Payne (1998).
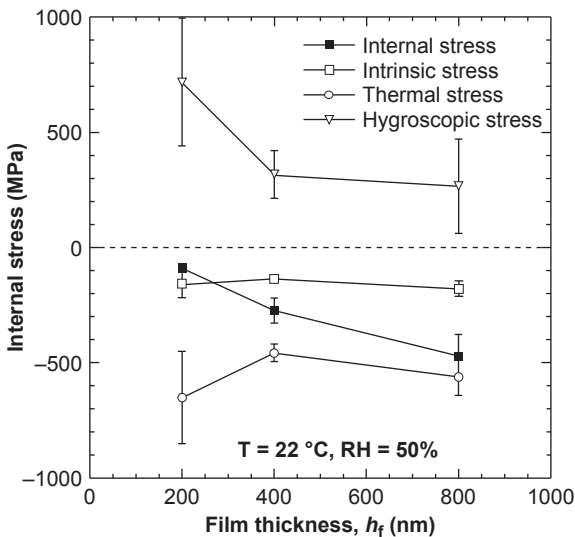
Figure 1.4 Thickness dependence of the total internal stress, intrinsic stress, thermal stress and hygroscopic stress in SiN$_x$ films on a polyimide substrate at 22 °C and 50%RH. *Source*: Reproduced with permission from Dumont et al. (2007).

Internal stresses such as those in Figure 1.4 manifest themselves by curling of the multilayer in the absence of externally applied forces. For thin compliant substrates the multilayer adopts the form of a dome or roll with a single radius of curvature, which can be calculated using classic thermoelastic solutions. For small displacements (large displacements are treated by Masters and Salamon (1993)), the equilibrium radius of curvature R_{eq} of the multilayer is related to the internal strain in individual layers by Townsend, Barnett, and Brunner (1987):

$$\frac{1}{R_{eq}} = \frac{\displaystyle\sum_{k=1}^{N} \overline{E}_k h_k \sum_{i=1}^{N} \overline{E}_i h_i \varepsilon_{k,i} \left(\sum_{j=1}^{k} h_j - h_k/2 \right)}{\begin{aligned}&\frac{1}{12}\sum_{k=1}^{N} \overline{E}_k h_k \sum_{i=1}^{N} \overline{E}_i h_i^3 + \frac{1}{2}\sum_{k=1}^{N} \overline{E}_k h_k \sum_{i=1}^{N} \overline{E}_i h_i \left(h_i - h_k + 2\sum_{j=1}^{k} h_j - 2\sum_{j=1}^{i} h_j \right)\\ &\times \left(\sum_{j=1}^{k} h_j - h_k/2 \right)\end{aligned}}$$

$$(1.3)$$

where $\varepsilon_{k,i} = \varepsilon_{intrinsic,k} - \varepsilon_{intrinsic,i} + (\alpha_k - \alpha_i)\Delta T + (\beta_k - \beta_i)\Delta RH$ is the difference in internal strains between layers i and k. $\Delta T = T - T_0$ is the difference between the actual temperature T and the process temperature T_0 (which would correspond to a stress-free temperature in the case where the intrinsic strains would be zero). $\Delta RH = RH - RH_0$ is

the difference between the actual relative humidity RH and the relative humidity of the process RH_0 (zero in the case of vacuum deposition). The factors $h_{i,k}$, $\varepsilon_{intrinsic,i,k}$, $\alpha_{i,k}$, and $\beta_{i,k}$ represent the thickness, intrinsic strain, and CTE and CHE of layers i,k, respectively.

1.2.4 Stress analysis of multilayer films under bending

The strain (stress) in the multilayer structure under bending is a linear superposition of the internal process-induced strain (stress) and externally applied bending strain (stress). The internal strain ε_i within the multilayer structure is derived from the thermoelastic solution (Eqn (1.3)). The bending strain ε_b is proportional to the distance z from the neutral axis with maximum tensile strain on the top (convex) surface and maximum compressive strain on the bottom (concave) surface as sketched in Figure 1.1:

$$\varepsilon_b = a_0 + a_1 z \tag{1.4}$$

where a_0 and a_1 are constants. The neutral axis is the line within the multilayer structure where the strain does not change upon pure bending. The position z_{NA} of the neutral axis (taking the free surface of the first layer as the origin $z = 0$) is given by:

$$z_{NA} = \frac{\sum\limits_{i=1}^{N} \overline{E}_i h_i \overline{z}_i}{\sum\limits_{i=1}^{N} \overline{E}_i h_i} \tag{1.5}$$

where $\overline{E} = E_i/(1 - \nu_i^2)$ is the plane strain modulus of layer i (E_i and ν_i are its Young's modulus and Poisson's ratio, respectively), $\overline{z}_i$ is the position of the mid-plane of layer i, h_i is the thickness of layer i, and N is the number of layers.

This analysis method is illustrated by application to transparent electrodes developed for organic photovoltaic devices. Figure 1.5 shows the behavior of graphene and indium doped tin oxide (ITO) electrodes on a PET substrate under bending (De Arco et al., 2010). The brittle ITO electrode cracked at a critical bending angle (the corresponding critical radius of curvature was not mentioned in the article), in contrast to the compliant graphene electrode, which survived up to the maximum investigated curvature. The corresponding strain profiles were estimated using the thermoelastic solution (Eqn (1.3)) and data from Table 1.1.

The results are shown in Figure 1.6. The internal strain in the graphene layer was compressive and equal to -0.45%. Upon bending to a radius of curvature of 5 mm, the total strain in graphene became tensile and equal to 0.52%. This value is well below the reported strain to failure of 13% for graphene (Zhang & Gu, 2013). The internal strain in the ITO layer was also compressive and equal to -0.32%. Upon bending to the same radius of curvature of 5 mm, the total strain in ITO became tensile and equal to 0.61%. This value is comparable to the strain at failure of ITO films of similar thickness (Leterrier et al., 2004), hence the cracks in the ITO film shown in Figure 1.5.
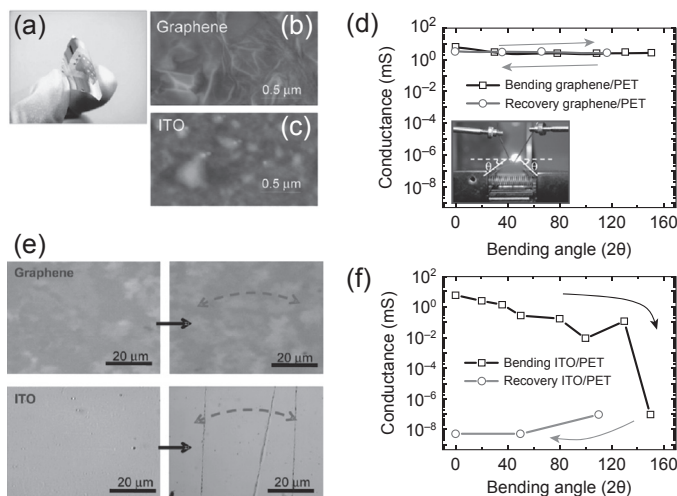
Figure 1.5 (a) Photograph illustrating high flexibility of CVD graphene transferred on a PET flexible substrate. (b,c) AFM images of the surface of CVD graphene and ITO films on PET, respectively. (d,f) Conductance of the CVD graphene and ITO films on PET substrates under bending conditions, respectively. The devices used to monitor the conductance had channel width $(W) = 1$ mm and length $(L) = 1$ mm. (e) Optical images of CVD graphene (top) and ITO (bottom) films on PET before and after being bent at the angles specified in panels b and c. Arrows show the direction of the bending.
Source: Reproduced with permission from De Arco et al. (2010). Copyright (2006) American Chemical Society.

In short, the strain level in both types of transparent electrodes is similar: the markedly different failure behavior essentially comes from the different strain at failure between the two materials. A strategy to avoid cracking of ITO would be to place it at the neutral axis, using an additional layer on the side opposite to the PET substrate, with appropriate thickness and Young's modulus. In the present example, using the same 100 μm thick PET foil as for the substrate (i.e., quasisymmetric PET/ITO/active layer/aluminum/PET structure) would position the ITO top surface of layer a mere 20 nm away from the neutral axis. The addition of this second PET foil would slightly increase the magnitude of the internal compressive strain (-0.36% instead of -0.32% without the second PET foil). At a radius of curvature of 5 mm, the total strain in the ITO layer would remain almost equal to the internal strain of -0.36% (the difference is less than 4×10^{-5}) (i.e., the ITO would not crack).

1.2.5 Failure mechanisms in multilayer films

Figure 1.7 summarizes the main failure mechanisms in a film/substrate structure. Channeling cracks initiate in brittle films on substrates under tensile load and further loading may lead to delamination at the film/substrate interface or failure of the substrate. Compressive loading may lead to buckling failure, also leading to delamination. These different failure events are detailed in the following sections. The reader
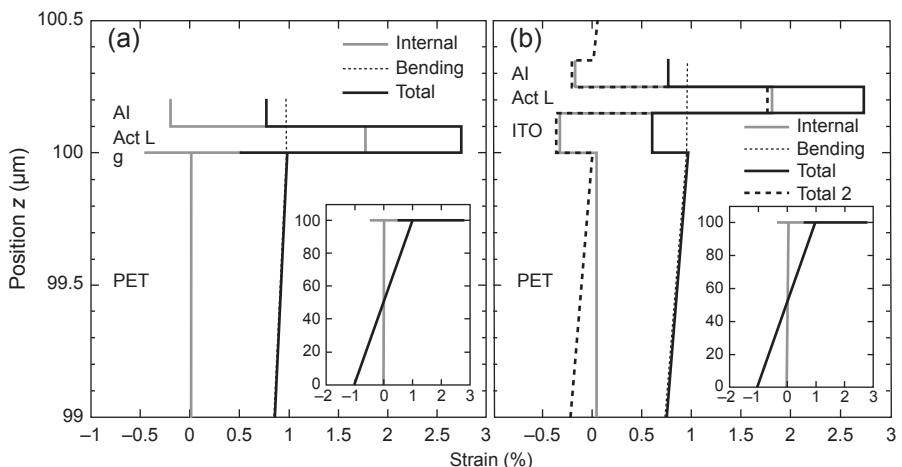
Figure 1.6 Through-thickness strain profiles at 20 °C of thin film organic photovoltaic devices with a 3-nm-thick transparent graphene anode "g" (a) and a 150 nm thick transparent ITO anode "ITO" (b) on a 100-μm-thick PET substrate bent to a radius of curvature of 5 mm. The insets show the strain profiles through the whole thickness of the multilayer structure. The device comprises a 100-nm-thick organic active layer "Act L" and 100-nm-thick aluminum cathode "Al." The Act L and ITO layer include an intrinsic tensile strain of 2% because of cure shrinkage, and an intrinsic compressive strain of −0.3% (Leterrier et al. 2004), respectively. The stress-free temperature (i.e., the processing temperature) was set to 100 °C. The profile of the total strain for a quasisymmetric PET/ITO/Act L/Al/PET structure is shown in (b) ("total 2").

is also referred to the comprehensive fracture mechanics treatment in multilayers by Hutchinson and Suo (1992). A clear and unambiguous analysis of the failure mechanisms of thin films requires the knowledge of (1) the internal stress state of the film and (2) the so-called "locus of failure"—i.e., whether the failure is cohesive (in the
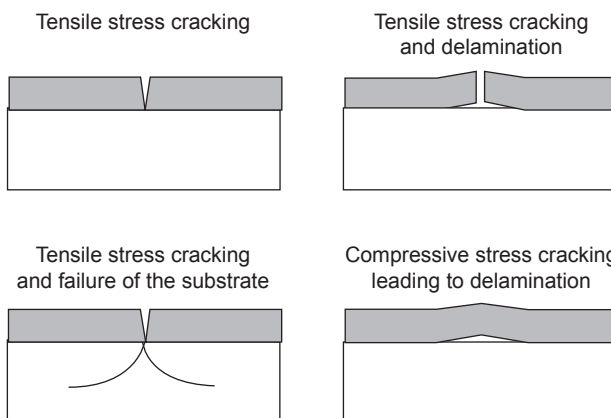
Figure 1.7 Schematic diagram of the main failure mechanisms for a film/substrate system. *Source*: Redrawn from Chalker et al. (1991).

film) or adhesive (at the film/substrate interface). The determination of the locus of failure requires careful examination of damage in the thin film/substrate material, typically under a microscope, and also using an array of advanced characterization tools such as mass spectroscopy (Pitton et al., 1995).

1.3   Failure under tensile stress

1.3.1   *Damage mechanisms: The three stages of tensile failure*

Tensile failure of active layers limits the operational life of flexible organic electronics as shown for instance in the case of solar cells (Awartani et al., 2013). The failure process under tensile loading reveals three damage stages depicted in Figure 1.8 (Wheeler & Osaki, 1990).

Stage I: crack onset and random cracking. Cracks initiate in the film at defect sites and start propagating perpendicular to the loading direction at a critical strain, ε_{crit} (also termed crack onset strain). The interaction between cracks is negligible and the generation of new cracks is governed by the statistical distribution of defects within the film.

Stage II: mid-point cracking. The size of film fragments approaches the critical length for stress transfer. The generation of new cracks diminishes and transverse buckling is observed across fragments due to Poisson's ratio effects.

Stage III: delamination and saturation. No further cracks are generated in this stage and the density of cracks reaches a saturation value, CD_{sat}, related to the so-called critical stress transfer length (Leterrier, Boogh, Andersons, & Månson, 1997). Delamination becomes the dominant failure mechanism.

1.3.2   *Fracture mechanics analysis*

A number of theoretical approaches are available to analyze the tensile failure processes and obtain the cohesive and adhesive properties of films on substrates. The cohesive properties of the film (critical strain, toughness, Weibull modulus) are
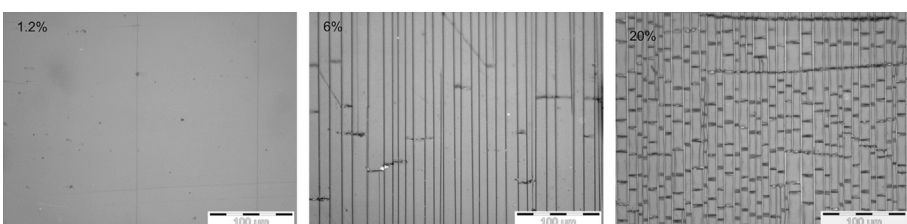
Figure 1.8 Fragmentation of a 140-nm-thick transparent conducting oxide film on a polyethylene terephthalate substrate at 1.2% (stage I with crack initiation at superficial defects), 6% (stage II with initiation of transverse buckling) and 20% strain (stage III with saturation of the failure process). The tensile loading direction was parallel to the scale bar.

derived from the initiation stage I (Hui, Shia, & Berglund, 1999; Kim & Nairn, 2000; Leterrier, Andersons, Pitton, & Månson, 1997, Leterrier, Boogh, et al., 1997; Nairn, 2000; Ochiai, Iwamoto, Nakamura, & Okuda, 2007). The film toughness G_{coh} can be calculated assuming that it is equal to the energy release rate at critical strain (Ambrico & Begley, 2002; Andersons et al., 2008; Beuth, 1992). For a semi-infinite substrate one has:

$$G_{coh} = \frac{\pi}{2} h_f \overline{E}_f \varepsilon_{crit}^2 g\left(\alpha, \beta\right) \tag{1.6}$$

where h_f and $\overline{E}_f = E_f/(1 - v_f^2)$ are the thickness and plane strain modulus of the film (E_f and v_f are the Young's modulus and Poisson's ratio of the film) and $g(\alpha,\beta)$ is a function of the Dundurs parameters α and β (Dundurs, 1969), which describe the elastic mismatch of the layer/substrate system. For substrates of finite thickness, Eqn (1.6) remains accurate when the substrate to film stiffness ratio $\overline{E}_s h_s/\overline{E}_f h_f > 10$, otherwise the approximation devised by Leterrier, Pinyol, Gilliéron, et al. (2010) may be used. In the case of plane strain problems:

$$\alpha = \frac{\overline{E}_f - \overline{E}_s}{\overline{E}_f + \overline{E}_s} \quad \text{and} \quad \beta = \frac{\mu_f\left(1 - 2v_s\right) - \mu_s\left(1 - 2v_f\right)}{2\mu_f\left(1 - v_s\right) + 2\mu_s\left(1 - 2v_f\right)} \tag{1.7}$$

where $\overline{E}_s = E_s/(1 - v_s^2)$ is the plane strain modulus of the substrate (E_s and v_s are the Young's modulus and Poisson's ratio of the substrate), and $\mu_f = E_f/(2 + v_f)$ and $\mu_s = E_s/(2 + v_s)$ are the shear moduli of the film and substrate, respectively. For films with the same properties as their substrate, $\alpha = \beta = 0$. A stiff film on a soft substrate results in $\alpha \to 1$, whereas a soft film on a stiff substrate results in $\alpha \to -1$. The function g is primarily dependent on parameter α, which is therefore more representative of film/substrate elastic contrast than parameter β. For most film/substrate combinations, $0 < \beta < \alpha/4$. Representative values of the two parameters are reported in Table 1.3.

Table 1.3 Dundurs parameters α and β for representative film/substrate combinations

Substrate (Young's modulus (GPa); Poisson's ratio (−))	Film (Young's modulus (GPa); Poisson's ratio (−))	α	β
Steel (200; 0.3)	SiN$_x$ (100; 0.26)	−0.344	−0.124
	Polyimide (3; 0.34)	−0.970	−0.234
Polyimide (3; 0.34)	SiN$_x$ (100; 0.26)	0.939	0.225
	Parylene (2.8; 0.40)	−0.009	0.036

A practical consequence of Eqn (1.6) is that the critical strain for film failure scales with the inverse of square root of film thickness and elastic contrast:

$$\varepsilon_{\text{crit}} = \left(\frac{2G_{\text{coh}}}{\pi h_{\text{f}} \overline{E}_{\text{f}} g(\alpha, \beta)} \right)^{1/2} \tag{1.8}$$

It was, for example, found that the critical strain for silica films on a steel substrate was a factor of almost five times higher than on a polymer substrate (Leterrier, Pinyol, Gilliéron, et al., 2010). This huge difference in critical strain was largely due to the difference in elastic contrast and also to different internal strains. Reducing film thickness, or film/substrate elastic contrast, both lead to an increase in critical strain, hence increasing the admissible curvature of the multilayer device.

Adhesive properties are derived from analysis of the saturation stage III (interfacial shear strength, *IFSS*), and from the development of buckling damage in stage II (interfacial toughness) (Andersons, Tarasovs, & Leterrier, 2009). Several models of the *IFSS* were devised based on elastic (Cox, 1952; Hashin & Shtrikman, 1963; Mendels, Leterrier, & Månson, 1999; Nairn, 1992, 1997), plastic (Agrawal & Raj, 1989; Kelly & Tyson, 1965; Leterrier, Wyser, Månson, & Hilborn, 1994), and elasto-plastic stress transfer analyses (Mcguigan, Briggs, Burlakov, Yanaka, & Tsukahara, 2003; Piggott, 1980). For yielded interfaces, which generally apply when fragmentation proceeds beyond the yield point of the substrate, *IFSS* was found to be proportional to CD_{sat}:

$$IFSS = 1.337\, h_{\text{f}} E_{\text{f}} \varepsilon_{\text{crit}} CD_{\text{sat}} \tag{1.9}$$

Equation (1.9) does not account for the possible statistical nature of film strength see, for example, (Leterrier, Boogh et al., 1997).

The interfacial toughness G_{adh} is obtained from an energy release analysis of the buckling process (Eqn (1.10)) or the edge delamination (Eqn (1.11)) as shown in Figure 1.9:

$$G_{\text{adh}} = \frac{E_{\text{f}} h_{\text{f}} \left(\varepsilon_{\text{buc}}^2 \left(-\nu_{\text{s}} + \frac{\nu_{\text{f}}}{12} \left(\frac{W}{\lambda} \right)^2 \right) \right)}{2} \left(1 + \frac{\left(1 + \frac{\overline{E}_{\text{f}}}{\overline{E}_{\text{s}}} h_{\text{f}} \right)}{b} \right) \tag{1.10}$$

$$G_{\text{adh}} = \frac{E_{\text{f}} h_{\text{f}} \varepsilon_{\text{del}}^2}{24} \left(\frac{W}{\lambda} \right)^4 \tag{1.11}$$

where ε_{buc} and ε_{del} are the onset tensile strains of the buckling and edge delamination events, respectively, W is the width of the buckle or fragment (see Figure 1.9), b is half of the buckle length, and λ is the tensile stress recovery length, related to the *IFSS* and critical strain of the film by $\lambda = 2h_{\text{f}} E_{\text{f}} \varepsilon_{\text{crit}} / IFSS$ (Leterrier et al., 1994).
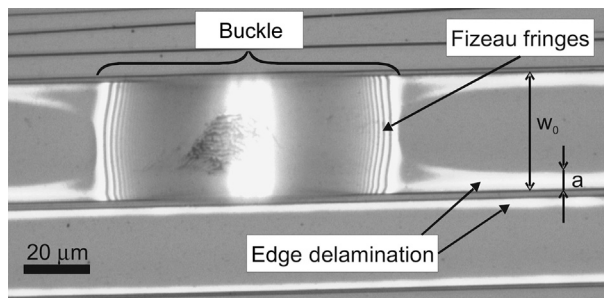
Figure 1.9 Buckle and edge delamination in a fragment of an 800-nm-thick SiN$_x$ gas-barrier film on a polyimide substrate at 8% tensile strain observed under white light microscopy. Fizeau fringes are evident on the edges of the buckles.
Source: Reproduced with permission from Tarasovs, Andersons, and Leterrier (2010).

1.3.3   Role of internal stresses

In the presence of internal stresses, the measured critical strain is a linear combination of an intrinsic failure strain, $\varepsilon_{\text{crit}}^*$ and the internal strain, ε_i ($\varepsilon_{\text{crit}} = \varepsilon_{\text{crit}}^* - \varepsilon_i$). The analysis of internal strains (Sections 1.2.3 and 1.5.2) thus enables determination of the intrinsic failure strain of the film. The knowledge of the various contributions to the actual critical strain of a film on a substrate can be useful to optimize both film composition (and associated intrinsic strain) and processing conditions (and associated internal strain). The *IFSS* obtained from Eqn (1.9) also combines an intrinsic strength, *IFSS** and an internal stress term (Leterrier, 2003):

$$IFSS = IFSS^* - 0.894\, h_{\text{f}} CD_{\text{sat}} \sigma_i \tag{1.12}$$

The factor $0.894\, h_{\text{f}} CD_{\text{sat}}$ results from the yielding condition.

1.4   Failure under compressive stress

1.4.1   Damage mechanisms: Buckling and delamination

Figure 1.10 shows an example of buckling failure of a thin film under compressive loading and resulting adhesive failure at the film—substrate interface. Several morphologies can be observed such as the well-known "telephone-cord" pattern (Moon, Jensen, Hutchinson, Oh, & Evans, 2002) depending on the film thickness, in-plane stress state (uniaxial or biaxial), interfacial toughness, and film toughness. Detailed buckling analysis described next enables one to identify the source of problems and thereby to optimize the processing of the individual layers. For instance, the adhesion quality and influences of processing steps can be quantified using the size of the buckle.
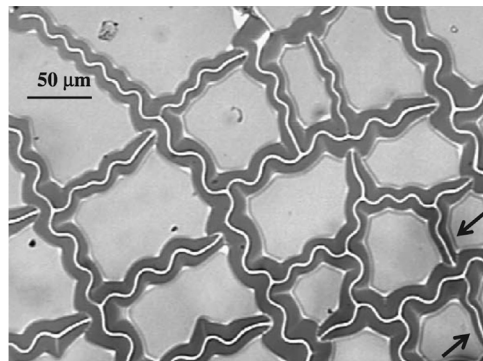
Figure 1.10 Optical micrograph of a telephone-cord buckle network (the arrows indicate small straight buckles).
Source: Reproduced with permission from Abdallah et al. (2006).

1.4.2   Fracture mechanics analysis

The present analysis is limited to straight line-shaped buckles as detailed in the comprehensive treatment of Hutchinson and Suo (1992) and in the study of Cotterell and Chen (2000) focused on compliant substrates (the telephone-cord pattern is analyzed by Giola and Ortiz (1997) and Moon et al. (2002)). The critical buckling strain for a two-sided clamped plate of thickness h under compressive loading is related to the buckle width, W:

$$\varepsilon_{\text{crit}} = \frac{\pi^2}{3}\left(\frac{h}{W}\right)^2 \tag{1.13}$$

The interfacial toughness is obtained from an energy release rate analysis for steady-state tunneling delamination and buckling without cracking, G_{ss} (the case where cracking occurs is also treated by Cotterell and Chen (2000)):

$$G_{\text{ss}} = \frac{\overline{E}_{\text{f}}\varepsilon^2 h_{\text{f}}}{2}\left(1 - \frac{\varepsilon_{\text{crit}}}{\varepsilon}\right)^2 f\left(\Psi; \alpha; \beta\right) \tag{1.14}$$

where ε is the applied compressive strain and $f(\Psi;\alpha;\beta)$ is a function of mode-mixity Ψ and Dundurs parameters. Explicit relations between the adhesion energy and the buckle morphology were developed by Cordill, Fischer, Rammerstorfer, and Dehm (2010).

1.4.3   Role of internal stresses

Similar to the case of tensile failure, the critical strain for onset of buckling failure (Eqn (1.13)) is the sum of an intrinsic critical strain and an internal strain. Large compressive

strains generated during processing combined with insufficient adhesion are often the cause of buckling failure (Evans, Drory, & Hu, 1988; Moon et al., 2002). Further details are given in Bouten, Leterrier, and Slikkerveer (2005). The authors emphasize the importance of increasing interfacial adhesion and decreasing film/substrate elastic contrast to compensate for the presence of internal compressive strains and prevent premature occurrence of buckling failure.

1.5 Mechanical test methods

Conventional mechanical and dilatometry test methods can be used to measure the properties of substrates with thicknesses above a few microns. However, these measurements are highly challenging for films with thickness in the submicron range. Several methods have been developed to measure these properties and the four most important ones are sketched in Figure 1.11 and presented in the following. The key features of these methods are compiled in Table 1.4 and the reader is referred to the abundant information on this subject compiled by Mittal and other researchers in the past decades (Mittal, 1995).

1.5.1 (Nano)indentation

In a nano-indentation experiment, a specimen is indented with a sharp tip, usually in the form of so-called "Berkovich" three-sided diamond pyramid (sharper indents are used for ultrathin films, below 100 nm), while measuring the indentation load and displacement (Chalker, Bull, & Rickerby, 1991; Pharr & Oliver, 1992). The indentation depth is recommended to be less than 10% of the film thickness to minimize substrate influence. The indentation curve sketched in Figure 1.12 consists of a loading and an unloading part. During loading, both elastic and plastic deformation
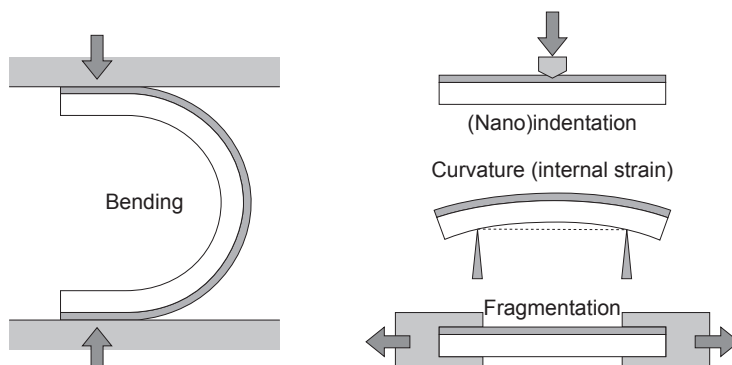
Figure 1.11 The four key techniques used to analyze thin films on substrates.

Table 1.4 Summary of the mechanical test methods for films on substrates

Test	Measured film properties	Advantages	Drawbacks	References

Nano-indentation	Young's modulus
	    Hardness
	    Internal strain
		Extreme force/displacement sensitivity
		    Fast and automated
		    Compatible with *in situ* in AFM and SEM
			Third-body interactions (tip surface)
			    Indirect information on failure mode (not for *in situ*)
				Oliver and Pharr (2004)

Scratch test	Film/substrate adhesion			
X-ray diffraction	Internal strain Elastic constants	High accuracy	Limited to crystalline films	Small and Nix (1992)
Curvature	Internal strain CTE and CHE	Direct measurement on manufactured device	Sensitive to sample geometry	Benabdi and Roche (1997), Leterrier (2003)
Bulge tests	Young's modulus Internal strain	Enables measurement of Young's modulus and internal strain	Sample preparation	Small and Nix (1992)
Tensile testing	Elastic constants	Accurate data modeling	Sample manipulation (thin, low modulus substrates required)	Leterrier, Boogh, et al. (1997)

(Electro-)bending	Critical strain
	  Cohesive properties
		No third-body interaction
		  Tensile and compressive
		  loading
		  Fast and automated
			Indirect information on the
			  failure mode
			  Limited to conductive
			  films (or requires an
			  additional conductive
			  probe layer)
				Bouten et al. (2005)

(Electro-)fragmentation	Critical strain
	  Toughness
	  Film/substrate adhesion
		No third-body interaction
		  Direct observation of
		  failure processes
		  Sensitive to interfacial
		  region
			Time consuming and
			  difficult automation (not
			  for electro-fragmentation)
			  Tensile loading only
			  In situ SEM required for
			  films <50 nm
				Leterrier (2003),
				  Leterrier, Mottet,
				  et al. (2010)

Acoustic and
  heterodyne atomic
  force microscopy
	Elastic constants	High-contrast resolution	Qualitative	Cuberes, Assender,
				  Briggs, and
				  Kolosov (2000)

Scanning local
  acceleration
  microscopy
	Elastic constants	High-contrast resolution	Complex data modeling	Rochat et al. (2004)

Surface acoustic wave
  methods (Brillouin
  scattering)
	Elastic constants	Established optical method	Complex data modeling	Lefeuvre, Kolosov,
				  Every, Briggs, and
				  Tsukahara (2000),
				  Wittkowski et al.
				  (2001)
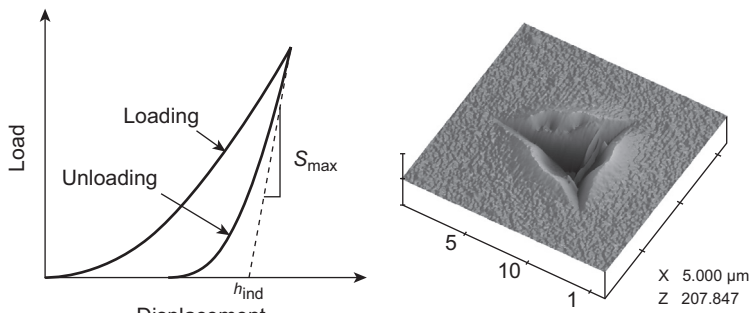
Figure 1.12 Load-displacement curve during an indentation test (left) and AFM of a Berkovitch indentation in an oxide film on a PET substrate (right).

occur, whereas mainly elastic recovery happens during unloading. The elastic modulus E of the indented sample is calculated using the first part of the slope of the unloading curve, S_{max}, through a reduced sample modulus E_r:

$$E_r = 0.179\frac{S_{max}}{h_{ind}} = \left(\frac{1-v_i^2}{E_i} + \frac{1-v^2}{E}\right)^{-1} \tag{1.15}$$

where the factor 0.179 is a constant valid for the Berkovich geometry, and h_{ind} is the indentation depth determined by the intersection between the tangent of the unloading curve at maximum load and the x-axis. Equation (5.1) includes a correction for the elastic constants of the tip (for a diamond indenter the Young's modulus E_i is 1140 GPa and Poisson's ratio v_i is 0.07).

The application of nano-indentation techniques to measure the elastic modulus of films on substrates has led to numerous investigations. Doerner and Nix have proposed the following empirical dependence of the sample modulus, E, on the normalized indentation thickness h_{ind}/h_f, using an adjustable parameter ξ (Doerner & Nix, 1986):

$$\frac{1}{E} = \frac{w}{E_f} + \frac{1-w}{E_s} \quad \text{where} \quad w = 1 - \exp\left\{-\xi\frac{h_f}{h_{ind}}\right\} \tag{1.16}$$

The accuracy of the method is compromised by the presence of "third-body inter-actions" such as indenter-film friction and the occurrence of so-called "piling up." These issues and data processing models were reviewed in detail by Bhushan and Li (2003) and Fischer-Cripps (2006).

1.5.2 Internal stress measurement methods

The two main methods to measure the internal strain in films on substrates (from which the internal stress can be calculated providing that the elastic constants of the film are

known) are X-ray diffraction and bilayer curvature measurements. X-ray diffraction is limited to crystalline materials and provides accurate determination of lattice spacing d. The Bragg equation $\lambda_B = 2d \sin \theta$ (λ_B is the wavelength and θ the scattering angle) enables calculation of the internal strain from the change of lattice spacing and associated change of scattering angle:

$$\varepsilon_i = \frac{\Delta d}{d} = -\cot \theta \, \Delta\theta \tag{1.17}$$

The $\sin^2 \psi$ method, where ψ is the declination angle between the normal to the film surface and the scattering vector, moreover enables measurement of the elasticity coefficients of the film for isotropic materials. In this case, one has:

$$\varepsilon_{\phi\psi} = \frac{1 + \nu_f}{E_f} \sigma_i \sin^2 \psi - \frac{2\nu_f}{E_f} \sigma_i \tag{1.18}$$

where $\varepsilon_{\phi\psi}$ is the strain in the film along directions $\{\phi;\psi\}$ (ϕ represents the in-plane orientation) and σ_i is the in-plane internal stress in the film (see details in (Noyan, Huang, & York, 1995; Withers & Bhadeshia, 2001)).

The bilayer curvature measurements rely on the analysis of the equilibrium curvature of a film/substrate system resulting from the presence of internal strains. The film/substrate system can adopt the shape of a spherical cap (isotropic strain and stiff substrate), a saddle shape, or a roll (compliant substrate) depending on the geometry of the system, the thickness, and elastic properties of the constituents, and on the degree of in-plane anisotropy of the internal strain. In the case of a spherical cap, the in-plane film strain can be calculated using the classic Stoney equation (Stoney, 1909):

$$\varepsilon_i = -\frac{(1 - \nu_f)h_s}{6\eta\chi} \left(\frac{1}{R} - \frac{1}{R_0} \right) \tag{1.19}$$

where R and R_0 are the radii of curvature of the coated and plain substrates, respectively. The "−" sign is a convention (compressive strains are negative and tensile strains are positive). In the latter case of a compliant substrate with a large elastic contrast with the film the following correction to Stoney's equation should be used (Röll, 1976):

$$\varepsilon_i = -\frac{(1 - \nu_f)(1 + \eta(4\chi - 1))h_s}{6(1 - \nu_s)\eta\chi} \left(\frac{1}{R} - \frac{1}{R_0} \right) \tag{1.20}$$

This equation is valid for small deflections (compared with the sample dimensions). Refined models are detailed by Leterrier (2003) and the case of large deflections is treated by Masters and Salamon (1993).

The individual components of the in-plane film strain are identified using the protocol detailed by Dumont et al. (2007). The intrinsic strain is obtained in a first step, from the analysis of the multilayer curvature measured under the conditions prevalent

at the end of the process cycle (e.g., vacuum, temperature). The temperature-dependent thermal strain and humidity-dependent hygroscopic strain are obtained from the change of curvature of the multilayer subjected to iso-hygric temperature jumps and isothermal relative humidity jumps, respectively. This approach combined with modeling tools enabled derivations of the CTE and CHE of thin film materials, using known CTE and CHE of substrate materials (see also Fang and Lo (2000)).

1.5.3 Bending methods

Bending test methods reproduce the loading state of flexed devices under quasistatic or cyclic loading conditions, using template cylinders of known radius (Cairns & Crawford, 2005; Grego, Lewis, Vick, & Temple, 2005), or through loading between two parallel plates as sketched in Figure 1.11 (Abdallah et al., 2006). Bending tests are fast and are thus useful for statistical analyses of critical strain and for rapid screening of a series of materials. However, they are usually limited to conductive films, using electrical measurements as a signature of damage, since a direct observation of the damage state *in situ* in a microscope is hardly feasible.

In the parallel plate geometry, the sample curvature is not constant, with lowest radius of curvature and largest strain ε_{max} in the middle of the bend. For a symmetrical sample with neutral axis at mid thickness:

$$\varepsilon_{max} = C_b h/(L-h) \tag{1.21}$$

where C_b is a geometrical constant equal to 1.198 (Matthewson, Kurkjian, & Gulati, 1986), h is the sample thickness, and L is the distance between the two plates. This loading geometry can also analyze the behavior of compressed layers (i.e., layers located on the concave side of the bent multilayer).

1.5.4 Electro-fragmentation and electro-fatigue

In a fragmentation test, a coated substrate is loaded under uniaxial tension, and the damage state in the film from interfacial stress transfer from the substrate is analyzed as a function of strain. *In situ* tests in an optical or scanning electron microscope are usually used for the detection of cracks. The method is free of third-body interactions and can quantify the cohesive properties (which control critical strain) and the adhesive properties (which control delamination) of films on high-elongation substrates (Leterrier, 2003). The method has been used to analyze a broad range of film/substrate combinations, including inorganic films on polymers (Ben Amor et al., 1998; Leterrier, Andersons, et al., 1997, Leterrier, Boogh, et al., 1997; Rochat et al., 2004; Wojciechowski & Mendolia, 1989), elastomers (Bazhenov, Volynskii, Alexandrov, & Bakeev, 2002) and steel (Plojoux, Leterrier, Månson, & Templier, 2007), and organic films on polymers (Martin, 2003; Nairn & Kim, 1992; Tang, Foran, & Martin, 2001) and PDMS (Twomey, Byrne, Hynes, O'neill, & Dowling, 2009). The fragmentation test is limited to high-elongation substrates (i.e., with a strain to failure several times higher than that of the film).

The critical strain for film failure determined under quasistatic loading (Abdallah et al., 2006; Plojoux et al., 2007) might not be representative of the actual cyclic loading present during operational life. In fact, evidence of slow crack growth was reported for ITO films under fatigue loading at strain levels below the critical strain (Oh, Cho, Cheon, Karim, & Jung, 2007; Pinyol et al., 2008). High cycle fatigue of thin films on polymer substrates has been studied in detail for metallic films (especially Cu and Al) (Eberl et al. 2006; Eve, Huber, Last, & Kraft, 2009; Kraft, Schwaiger, & Wellner, 2001; Lacour, Chan, Wagner, Li, & Suo, 2006; Martynenko, Zhou, Chudnovsky, Li, & Poglitsch, 2002; Park, An, Kim, Huh, & Lee, 2008; Sun et al., 2008; Zhang et al., 2008) and transparent conductive oxide films (Cairns & Crawford, 2005; Lewis, Greco, Chalamala, Vick, & Temple, 2004). Electro-fatigue tests carried out *in situ* in a microscope enabled correlating a macroscopic damage state variable (e.g., electrical resistance) to the actual damage at the microscopic scale, using a combination of electrical measurements and microscopy analyses (Leterrier, Mottet, et al., 2010). Extension of the fragmentation and fatigue methods to dielectric films is possible with a conductive probe layer (Pinyol et al., 2009).

1.5.5 Other methods

Tensile tests have been used to determine the Young's modulus of thin films, from the measured moduli of the substrate and film/substrate multilayer, E, using the classic laminate plate theory (Reddy, 2004):

$$E_\mathrm{f} = \frac{\left(1 - \nu_\mathrm{f}^2\right)}{h_\mathrm{f}} \left(Eh + \frac{E_\mathrm{s} h_\mathrm{s}}{1 - \nu_\mathrm{s}^2} \right) \tag{1.22}$$

Buckling methods have also been used to determine the Young's modulus of thin films, using measured buckle geometry (Hahm, Hwang, Kim, & Khang, 2009; Tahk, Lee, & Khang, 2009). Other specific methods based on various microscopy and acoustic techniques are listed in Table 1.4.

1.6 Toward compliant and stretchable electronics

The previously mentioned mechanical methods and models focus on flexible devices, for which the critical strain $\varepsilon_\mathrm{crit}$ is below 2% (i.e., they cannot be stretched). The emergence of compliant electronics ($2\% < \varepsilon_\mathrm{crit} < 10\%$), stretchable electronics ($\varepsilon_\mathrm{crit} > 10\%$), and *soft machines* (Suo, 2012) stimulates new design approaches, new process methods, and new materials as briefly discussed in the following sections.

1.6.1 Conformal, stretchable, foldable electronic devices

Highly compliant electronic devices have emerged in the past decade following two main approaches, namely designs enabling out-of-plane deformations, and the

development of intrinsically compliant active materials (Lumelsky, Shur, & Wagner, 2001; Rogers, Someya, & Huang, 2010). In the former case, brittle films are processed in the form of wavy patterns, which are able to accommodate tensile strains considerably larger than the intrinsic critical strain of the film. A very effective way to create such patterns is to stretch the substrate during film deposition, resulting in the buckling of the film upon unloading the substrate. The critical strain for gold interconnects could be increased from 1% for freestanding films to more than 15% on prestretched PDMS substrates (Lacour, Wagner, Huang, & Suo, 2003). Similar considerable increase in critical strain was reported for ZnO layers, owing to controlled buckling (Park et al., 2010). A further design opportunity is based on soft interlayers, which very effectively decouple fragile devices "islands" from the underlying substrate (Sun et al., 2009).

The development of compliant active materials (electrodes and semiconducting films) is another strategy to increase critical strain of devices. Examples include semi-transparent metallic mesh electrodes as alternatives to transparent conducting oxides. A Cu nanowire mesh (Kang, Park, Ahn, & Guo, 2010) achieved critical strains higher than those of, for example, ITO (1%) with minimized optical losses, similar to an Ag grid embedded in PEDOT-PSS (Li et al., 2013). Other examples are polymer composites with conducting fillers, which have been exploited for decades, and with high relevance for flexible electronics (e.g., transparent conductors based on graphene (Potts, Dreyer, Bielawski, & Ruoff, 2011)). The relation between critical strain and electronic properties of organic solar cells is addressed in (Awartani et al., 2013), the challenge being that ductility is improved at the expense of the efficiency. The combination of these compliant electronic materials with the basic neutral axis considerations (see Section 1.2.4) would possibly enable foldable, paper-based electronics (Siegel et al., 2010; Suo et al., 1999).

1.6.2   Roll-to-roll processing

A broad diversity of process methods are available to deposit, coat, print, pattern, and etch thin layers on substrates, and all of these are available in R2R form (Nathan et al., 2012). R2R processes are cost-effective methods often required to meet the price target of applications (Izu & Ellison, 2003). Nevertheless, scale-up of the conventional laboratory, small-area batch processes such as spin coating, dip coating, and various vacuum deposition processes to large area applications is not simple. The case of the ubiquitous spin coating is discussed by Krebs et al. (Krebs, 2009), who identify a number of coating and printing methods with high potential for cost-effective production of flexible organic electronics. Additional challenges of R2R processes include overlay accuracy for high-resolution multilayer device architectures (Moonen, Yakimets, & Huskens, 2012) and anisotropic stress state in the deposited films due to uniaxial loading of the substrate foil in the process (Leterrier, Pinyol, Rougier, et al., 2010). These issues, related to the lack of dimensional stability of the flexible polymer foil substrates, can be alleviated to some extent using low-temperature processable materials. R2R processing using soft elastomer substrates may only be possible through the use of a higher modulus flexible carrier to prevent excessive substrate straining.

1.6.3 Self-repair material strategies

Self-healing would be ideal for applications, which are prone to damage, obviously in the case of flexible electronics. Biologically inspired self-healing materials are being actively developed as a *"damage prevention paradigm"* alternative to traditional material engineering and design based on appropriate management of damage (see monograph by Van Der Zwaag, Schmets, and Van Der Zaken (2007) and reviews by Wool (2008), Hager, Greil, Leyens, Van Der Zwaag, and Schubert (2010) and Mauldin and Kessler (2010), the latter with references to several self-healing thin films). Self-healing materials are classified as either autonomic (repair triggered by damage itself) or nonautonomic (repair triggered by an external action such as heat or radiation), or as intrinsic (healing available from the material structure, for instance H-bonded supramolecular networks (Cordier, Tournilhac, Soulie-Ziakovic, & Leibler, 2008) or extrinsic (healing based on additional components such as microcapsules (Kessler, Sottos, & White, 2003) and nanocapsules for thin coatings (Shchukin & Mohwald, 2007). A review of innovative self-healing nanosystems relevant for functional material devices is given by Amendola and Meneghetti (2009). Self-healing encapsulation approaches to improve the lifetime of light emitting diodes are detailed by Lafont, Van Zeijl, and Van Der Zwaag (2012), and self-healing aluminum oxide gate dielectrics in flexible graphene field-effect transistors, in which the damaged oxide is restored automatically through exposure to air or using electrical annealing (Lu, Lin, Yeh, Huang, & Chiu, 2012). Self-healing interconnects based on silver/electrolyte (Ag−Ge−Se) bilayers on flexible polyimide substrates were demonstrated owing to the ability of Ag to electrodeposit in stress-induced cracks (Baliga, Ren, & Kozicki, 2011). A self-healing conductive silver ink circuit containing solvent-filled microcapsules was also demonstrated, in which the circuit material itself was used to autonomously repair scratch damage (Odom et al., 2012).

1.7 Conclusions

Flexible organic devices can be produced using available materials to safely achieve radii of curvature of few cm. Adequate designs should evaluate the critical strain for film or interface failure in the device structure, and great care should be exercised to ensure sufficient adhesion levels between adjacent layers. These basic recommendations imply to determine the internal stress state and a number of material properties. Approaches to identify the intrinsic, thermal, and hygroscopic contributions to the film internal stress are available, and several methods exist to measure properties such as the Young's modulus, CTE, and CHE of thin films.

The analytical models introduced in this chapter are accurate enough to determine the critical radius of curvature for thin flexible devices, for which the critical strain is below $1-2\%$ and R is much greater than the total device thickness h. These models, however, do not address possible changes in the functional properties, such as changes of electrical characteristics of thin film transistors (Bensaid, Boddaert, Benaben, Gwoziecki, & Coppard, 2011; Sekitani et al., 2005) and organic

solar cells (De Arco et al., 2010; Lim et al., 2013). They are also unable to capture mechanical nonlinearities associated with the geometry of actual devices (edge effects, thickness changes, etc.) and also with large displacements ($R < 10\,h$ or $\varepsilon_{\mathrm{crit}} > 2\%$). The case where the radius of curvature becomes smaller than the device dimensions gives rise to complex bifurcation phenomena (Masters & Salamon, 1993). Mechanical models relevant for very large deformations enabled by elastomers derive from classic hyperelastic theories, as used in recent highly flexible and stretchable devices (Fassler & Majidi, 2013; Kwon et al., 2011).

Finally, mechanical models and test methods continuously improve as novel designs, improved fabrication processes, and new materials with increased mechanical stability progress. These joint developments are scientifically self-stimulating, with the formidable challenge to further the understanding of the interplay between interfacial interactions, internal stresses, damage state, mass transport (permeability) and a vast array of optical, electrical, and biological properties in multilayered film structures.

Acknowledgements

References

Abdallah, A. A., Kozodaev, D., Bouten, P. C. P., Den Toonder, J. M. J., Schubert, U. S., & De With, G. (2006). Buckle morphology of compressed inorganic thin layers on a polymer substrate. *Thin Solid Films, 503*(1−2), 167−176.

Agrawal, D. C., & Raj, R. (1989). Measurement of the ultimate shear strength of a metal-ceramic interface. *Acta Metallurgica, 37*(4), 1265.

Ambrico, J. M., & Begley, M. R. (2002). The role of initial flaw size, elastic compliance and plasticity in channel cracking of thin films. *Thin Solid Films, 419*(1−2), 144−153.

Amendola, V., & Meneghetti, M. (2009). Self-healing at the nanoscale. *Nanoscale, 1*(1), 74−88.

Andersons, J., Modniks, J., Leterrier, Y., Tornare, G., Dumont, P., & Månson, J.-A. E. (2008). Evaluation of toughness by finite fracture mechanics from crack onset strain of brittle coatings on polymers. *Theoretical and Applied Fracture Mechanics, 49*, 151−157.

Andersons, J., Tarasovs, S., & Leterrier, Y. (2009). Evaluation of thin film adhesion to compliant substrate by the analysis of progressive buckling in fragmentation test. *Thin Solid Films, 507*, 2007−2011.

Awartani, O., Lemanski, B. I., Ro, H. W., Richter, L. J., Delongchamp, D. M., & O'Connor, B. T. (2013). Correlating stiffness, ductility, and morphology of polymer: fullerene films for solar cell applications. *Advanced Energy Materials, 3*(3), 399−406.

Baliga, S. R., Ren, M., & Kozicki, M. N. (2011). Self-healing interconnects for flexible electronics applications. *Thin Solid Films, 519*(7), 2339−2343.

Bazhenov, S. L., Volynskii, A. L., Alexandrov, V. M., & Bakeev, N. F. (2002). Two mechanisms of the fragmentation of thin coatings on rubber substrates. *Journal of Polymer Science Part B − Polymer Physics, 40*(1), 10−18.

Ben Amor, S., Baud, G., Benmalek, M., Dunlop, H., Frier, R., & Jacquet, M. (1998). Titania coatings on poly(ethylene terephthalate) − adhesion and xps studies. *The Journal of Adhesion, 65*(1−4), 307−329.

Benabdi, M., & Roche, A. A. (1997). Mechanical properties of thin and thick coatings applied to various substrates.1. An elastic analysis of residual stresses within coating materials. *Journal of Adhesion Science and Technology, 11*(2), 281−299.

Bensaid, B., Boddaert, X., Benaben, P., Gwoziecki, R., & Coppard, R. (2011). Reliability of oTFTs on flexible substrate: mechanical stress effect. *European Physical Journal − Applied Physics, 55*(2).

Beuth, J. L. (1992). Cracking of thin bonded films in residual tension. *International Journal of Solids and Structures, 29*(13), 1657−1675.

Bhushan, B., & Li, X. D. (2003). Nanomechanical characterisation of solid surfaces and thin films. *International Materials Reviews, 48*(3), 125−164.

Bouten, P. C. P., Leterrier, Y., & Slikkerveer, P. J. (2005). Mechanics of ITO on plastic substrates for flexible displays. In G. P. Crawford (Ed.), *Flexible flat panel displays*. New-York: Wiley.

Byrne, M. T., & Gun'ko, Y. K. (2010). Recent advances in research on carbon nanotube-polymer composites. *Advanced Materials, 22*(15), 1672−1688.

Cairns, D. R., & Crawford, G. P. (2005). Electromechanical properties of transparent conducting substrates for flexible electronic displays. *Proceedings of IEEE, 93*(8), 1451−1458.

Caulfield, D. F., & Gunderson, D. E. (1988). Paper testing and strength characterised. In: *TAPPI paper preservation symposium, October 19−21, Wahsington, DC* (pp. 31−40). Atlanta, GA: TAPPI Press.

Chalker, P. R., Bull, S. J., & Rickerby, D. S. (1991). A review of the methods for the evaluation of coating-substrate adhesion. *Materials Science and Engineering, A140*, 583−592.

Choi, M. C., Kim, Y., & Ha, C. S. (2008). Polymers for flexible displays: from material selection to device applications. *Progress in Polymer Science, 33*(6), 581−630.

Cordier, P., Tournilhac, F., Soulie-Ziakovic, C., & Leibler, L. (2008). Self-healing and thermoreversible rubber from supramolecular assembly. *Nature, 451*(7181), 977−980.

Cordill, M. J., Fischer, F. D., Rammerstorfer, F. G., & Dehm, G. (2010). Adhesion energies of Cr thin films on polyimide determined from buckling: Experiment and model. *Acta Materialia, 58*(16), 5520−5531.

Cotterell, B., & Chen, Z. (2000). Buckling and cracking of thin films on compliant substrates under compression. *International Journal of Fracture, 104*(2), 169−179.

Cox, H. L. (March 1952). The elasticity and strength of paper and other fibrous materials. *British Journal of Applied Physics, 3*, 72−79.

Crawford, G. P. (2005). *Flexible flat panel displays*. Chichester, England: John Wiley & Sons.

Cuberes, M. T., Assender, H. E., Briggs, G. A. D., & Kolosov, O. V. (2000). Heterodyne force microscopy of PMMA/rubber nanocomposites: nanomapping of viscoelastic response at ultrasonic frequencies. *Journal of Physics D − Applied Physics, 33*(19), 2347−2355.

De Arco, L. G., Zhang, Y., Schlenker, C. W., Ryu, K., Thompson, M. E., & Zhou, C. W. (2010). Continuous, highly flexible, and transparent graphene films by chemical vapor deposition for organic photovoltaics. *ACS Nano, 4*(5), 2865−2873.

Dikin, D. A., Stankovich, S., Zimney, E. J., Piner, R. D., Dommett, G. H. B., Evmenenko, G., et al. (2007). Preparation and characterization of graphene oxide paper. *Nature, 448*(7152), 457−460.

Doerner, M. F., & Nix, W. D. (1986). A method for interpreting the data from depth-sensing indentation instruments. *Journal of Materials Research, 1*, 601−616.

Dumont, P., Tornare, G., Leterrier, Y., & Månson, J.-A. E. (2007). Intrinsic, thermal and hygroscopic residual stresses in thin gas-barrier films on polymer substrates. *Thin Solid Films, 515*(19), 7437−7441.

Dundurs, J. (1969). Edge-bonded dissimilar orthogonal elastic wedges. *Journal of Applied Mechanics, 36*, 650−652.

Eberl, C., Spolenak, R., Kraft, O., Kubat, F., Ruile, W., & Arzt, E. (2006). Damage analysis in Al thin films fatigued at ultrahigh frequencies. *Journal of Applied Physics, 99*, 113501.

Evans, A. G., Drory, M. D., & Hu, M. S. (1988). The cracking and decohesion of thin-films. *Journal of Materials Research, 3*(5), 1043−1049.

Eve, S., Huber, N., Last, A., & Kraft, O. (2009). Fatigue behavior of thin Au and Al films on polycarbonate and polymethylmethacrylate for micro-optical components. *Thin Solid Films, 517*(8), 2702−2707.

Fang, W. L., & Lo, C. Y. (2000). On the thermal expansion coefficients of thin films. *Sensors and Actuators A-Physical, 84*(3), 310−314.

Fassler, A., & Majidi, C. (2013). Soft-matter capacitors and inductors for hyperelastic strain sensing and stretchable electronics. *Smart Materials and Structures, 22*(5), 055023.

Fischer-Cripps, A. C. (2006). Review of analysis and interpretation of nanoindentation test data. *Surface & Coatings Technology, 200*(14−15), 4153−4165.

Giola, G., & Ortiz, M. (1997). Delamination of compressed thin films. In: J. W. Hutchinson, & T. Wu (Eds.), *Advances in applied mechanics* (vol. 33, pp. 531−559).

Graz, I. M., & Lacour, S. P. (2009). Flexible pentacene organic thin film transistor circuits fabricated directly onto elastic silicone membranes. *Applied Physics Letters, 95*(24).

Greco, F., Zucca, A., Taccola, S., Menciassi, A., Fujie, T., Haniuda, H., et al. (2011). Ultra-thin conductive free-standing PEDOT/PSS nanofilms. *Soft Matter, 7*(22), 10642−10650.

Grego, S., Lewis, J., Vick, E., & Temple, D. (2005). Development and evaluation of bend-testing techniques for flexible-display applications. *Journal of the Society for Information Display, 13*(7), 575−581.

Haas, S., Batlogg, B., Besnard, C., Schiltz, M., Kloc, C., & Siegrist, T. (2007). Large uniaxial negative thermal expansion in pentacene due to steric hindrance. *Physical Review B, 76*(20).

Hager, M. D., Greil, P., Leyens, C., Van Der Zwaag, S., & Schubert, U. S. (2010). Self-healing materials. *Advanced Materials, 22*(47), 5424−5430.

Hahm, S. W., Hwang, H. S., Kim, D., & Khang, D. Y. (2009). Buckling-based measurements of mechanical moduli of thin films. *Electronic Materials Letters, 5*(4), 157−168.

Harder, T. A., Yao, T. J., He, Q., Shih, C. Y., & Tai, Y. C. Proc. 15th IEEE International Conference on Micro Electro Mechanical Systems (MEMS 2002), Las Vegas, NV, Jan 20-24, 2002.

Hashin, Z., & Shtrikman, S. (1963). A varational approach to the theory of the elastic behaviour of multiphase materials. *Journal of the Mechanics and Physics of Solids, 11*, 127−140.

Hui, C. Y., Shia, D., & Berglund, L. A. (1999). Estimation of interfacial shear strength: an application of a new statistical theory for single fiber composite test. *Composites Science and Technology, 59*(13), 2037−2046.

Hutchinson, J. W., & Suo, Z. (1992). Mixed-mode cracking in layered materials. *Advances in Applied Mechanics, 29*, 63−191.

Izu, M., & Ellison, T. (2003). Roll-to-roll manufacturing of amorphous silicon alloy solar cells with in situ cell performance diagnostics. *Solar Energy Materials and Solar Cells, 78*(1−4), 613−626.

Kang, M. G., Park, H. J., Ahn, S. H., & Guo, L. J. (2010). Transparent Cu nanowire mesh electrode on flexible substrates fabricated by transfer printing and its application in organic solar cells. *Solar Energy Materials and Solar Cells, 94*(6), 1179−1184.

Kelly, A., & Tyson, W. R. (1965). Tensile properties of fibre-reinforced metals: copper/tungsten and copper/molybdenum. *Journal of the Mechanics and Physics of Solids, 13*, 329−350.

Kessler, M. R., Sottos, N. R., & White, S. R. (2003). Self-healing structural composite materials. *Composites Part A-Applied Science and Manufacturing, 34*(8), 743−753.

Kim, S. R., & Nairn, J. A. (2000). Fracture mechanics analysis of coating/substrate systems part I: analysis of tensile and bending experiments. *Engineering Fracture Mechanics, 65*(5), 573−593.

Ko, H. C., Shin, G., Wang, S. D., Stoykovich, M. P., Lee, J. W., Kim, D. H., et al. (2009). Curvilinear electronics formed using silicon membrane circuits and elastomeric transfer elements. *Small, 5*(23), 2703−2709.

Kraft, O., Schwaiger, R., & Wellner, P. (2001). Fatigue in thin films: lifetime and damage formation. *Materials Science and Engineering A*, (319−321), 919−923.

Krebs, F. C. (2009). Fabrication and processing of polymer solar cells: a review of printing and coating techniques. *Solar Energy Materials and Solar Cells, 93*(4), 394−412.

Kwon, H.-J., Shim, H., Kim, S., Choi, W., Chun, Y., Kee, I., et al. (2011). Mechanically and optically reliable folding structure with a hyperelastic material for seamless foldable displays. *Applied Physics Letters, 98*(15), 151904.

Lacour, S. P., Chan, D., Wagner, S., Li, T., & Suo, Z. G. (2006). Mechanisms of reversible stretchability of thin metal films on elastomeric substrates. *Applied Physics Letters, 88*(8), 204103.

Lacour, S. P., Wagner, S., Huang, Z. Y., & Suo, Z. (2003). Stretchable gold conductors on elastomeric substrates. *Applied Physics Letters, 82*(15), 2404−2406.

Lafont, U., Van Zeijl, H., & Van Der Zwaag, S. (2012). Increasing the reliability of solid state lighting systems via self-healing approaches: a review. *Microelectronics Reliability, 52*(1), 71−89.

Lang, U., & Dual, J. (2007). Mechanical properties of the intrinsically conductive polymer poly(3,4-ethylenedioxythiophene) poly(styrenesulfonate) (PEDOT/PSS). In S. W. Nam, Y. W. Chang, S. B. Lee, & N. J. Kim (Eds.), *Key Engineering Materials. Mechanical Behavior of Materials X*, 345−346, 1189−1192.

Lefeuvre, O., Kolosov, O. V., Every, A. G., Briggs, G. A. D., & Tsukahara, Y. (2000). Elastic measurements of layered nanocomposite materials by Brillouin spectroscopy. *Ultrasonics, 38*(1), 459−465.

Leterrier, Y. (2003). Durability of nanosized gas barrier coatings on polymers. *Progress in Materials Science, 48*, 1−55.

Leterrier, Y., Andersons, J., Pitton, Y., & Månson, J.-A. E. (1997). Adhesion of silicon oxide layers on poly(ethylene terephthalate). II: effect of coating thickness on adhesive and cohesive strengths. *Journal of Polymer Science Part B: Polymer Physics, 35*, 1463−1472.

Leterrier, Y., Boogh, L., Andersons, J., & Månson, J.-A. E. (1997). Adhesion of silicon oxide layers on poly(ethylene terephthalate). I: effect of substrate properties on coating's fragmentation kinetics. *Journal of Polymer Science Part B: Polymer Physics, 35*, 1449−1461.

Leterrier, Y., Médico, L., Demarco, F., Månson, J.-A. E., Betz, U., Escola, M. F., et al. (2004). Mechanical integrity of transparent conductive oxide films for flexible polymer-based displays. *Thin Solid Films, 460*, 156−166.

Leterrier, Y., Mottet, A., Bouquet, N., Gillieron, D., Dumont, P., Pinyol, A., et al. (2010). Mechanical integrity of thin inorganic coatings on polymer substrates under quasi-static, thermal and fatigue loadings. *Thin Solid Films, 519*(5), 1729−1737.

Leterrier, Y., Pinyol, A., Gilliéron, D., Månson, J.-A. E., Timmermans, P. H. M, Bouten, P. C. P, et al. (2010). Mechanical failure analysis of thin film transistor devices on steel and

polyimide substrates for flexible display applications. *Engineering Fracture Mechanics, 77*, 660−670.

Leterrier, Y., Pinyol, A., Rougier, L., Waller, J. H., Månson, J.-A. E., Dumont, P. J. J., et al. (2010). Influences of roll-to-roll process and polymer substrate anisotropies on the tensile failure of thin oxide films. *Thin Solid Films, 518*(23), 6984−6992.

Leterrier, Y., Wyser, Y., & Månson, J.-A. E. (2001). Internal stresses and adhesion of thin silicon oxide coatings on poly(ethylene terephthalate). *Journal of Adhesion Science and Technology, 15*(7), 841−865.

Leterrier, Y., Wyser, Y., Månson, J.-A. E., & Hilborn, J. (1994). A method to measure the adhesion of thin glass coatings on polymer films. *The Journal of Adhesion, 44*, 213−227.

Lewis, J. (2006). Material challenge for flexible organic devices. *Materials Today, 9*(4), 38−45.

Lewis, J., Greco, S., Chalamala, B., Vick, E., & Temple, D. (2004). Highly flexible transparent electrodes for organic light-emitting diode-based displays. *Applied Physics Letters, 85*, 3450−3452.

Li, Y., Mao, L., Gao, Y., Zhang, P., Li, C., Ma, C., et al. (2013). ITO-free photovoltaic cell utilizing a high-resolution silver grid current collecting layer. *Solar Energy Materials and Solar Cells, 113*(0), 85−89.

Lim, K., Jung, S., Kim, J.-K., Kang, J.-W., Kim, J.-H., Choa, S.-H., et al. (2013). Flexible PEDOT: PSS/ITO hybrid transparent conducting electrode for organic photovoltaics. *Solar Energy Materials and Solar Cells, 115*(0), 71−78.

Lipomi, D. J., Chong, H., Vosgueritchian, M., Mei, J. G., & Bao, Z. A. (2012). Toward mechanically robust and intrinsically stretchable organic solar cells: evolution of photovoltaic properties with tensile strain. *Solar Energy Materials and Solar Cells, 107*, 355−365.

Lipomi, D. J., Lee, J. A., Vosgueritchian, M., Tee, B. C. K., Bolander, J. A., & Bao, Z. A. (2012). Electronic properties of transparent conductive films of PEDOT: PSS on stretchable substrates. *Chemistry of Materials, 24*(2), 373−382.

Lu, C. C., Lin, Y. C., Yeh, C. H., Huang, J. C., & Chiu, P. W. (2012). High mobility flexible graphene field-effect transistors with self-healing gate dielectrics. *ACS Nano, 6*(5), 4469−4474.

Lumelsky, V. J., Shur, M. S., & Wagner, S. (2001). Sensitive skin. *IEEE Sensors Journal, 1*(1), 41−51.

Martin, D. C. (2003). Elastica bend testing of the effective interfacial shear strength and critical deformation strains of brittle coatings on ductile substrates. *Progress in Organic Coatings, 48*(2−4), 332−336.

Martynenko, E., Zhou, W., Chudnovsky, A., Li, R. S., & Poglitsch, L. (2002). High cycle fatigue resistance and reliability assessment of flexible printed circuitry. *Journal of Electronic Packaging, 124*(3), 254−259.

Masters, C. B., & Salamon, N. J. (1993). Geometrically nonlinear stress deflection relations for thin-film substrate systems. *International Journal of Engineering Science, 31*(6), 915−925.

Matthewson, M. J., Kurkjian, C. R., & Gulati, S. T. (1986). Strength measurement of optical fibers by bending. *Journal of the American Ceramic Society, 69*(11), 815−821.

Mauldin, T. C., & Kessler, M. R. (2010). Self-healing polymers and composites. *International Materials Reviews, 55*(6), 317−346.

McGuigan, A. P., Briggs, G. A. D., Burlakov, V., Yanaka, M., & Tsukahara, Y. (2003). An elastic-plastic shear lag model for fracture of layered coatings. *Thin Solid Films, 424*(2), 219−223.

Mendels, D.-A., Leterrier, Y., & Månson, J.-A. E. (1999). Stress transfer model for single fibre and platelet composites. *Journal of Composite Materials, 33*(16), 1525−1543.

Mittal, K. L. (1995). *Adhesion measurement of films and coatings*. Utrecht, The Netherlands: VSP.

Moonen, P. F., Yakimets, I., & Huskens, J. (2012). Fabrication of transistors on flexible substrates: from mass-printing to high-resolution alternative lithography strategies. *Advanced Materials, 24*(41), 5526−5541.

Moon, M. W., Jensen, H. M., Hutchinson, J. W., Oh, K. H., & Evans, A. G. (2002). The characterization of telephone cord buckling of compressed thin films on substrates. *Journal of the Mechanics and Physics of Solids, 50*(11), 2355−2377.

Murray, S., Hillman, C., & Pecht, M. (2004). Environmental aging and deadhesion of polyimide dielectric films. *Journal of Electronic Packaging, 126*, 390−397.

Nairn, J. A. (1992). A variational mechanics analysis of the stresses around breaks in embedded fibers. *Mechanics of Materials, 12*, 131−154.

Nairn, J. A. (1997). On the use of shear-lag methods for analysis of stress transfer unidirectional composites. *Mechanics of Materials, 26*(2), 63−80.

Nairn, J. A. (2000). Matrix microcracking in composites. In A. Kelly, & C. Zweben (Eds.), *Comprehensive composite materials: vol. 2. Polymer-matrix composites, Chapter 12* (pp. 403−432). Oxford: Elsevier.

Nairn, J. A., & Kim, S. R. (1992). A fracture-mechanics analysis of multiple cracking in coatings. *Engineering Fracture Mechanics, 42*(1), 195−208.

Nathan, A., Ahnood, A., Cole, M. T., Lee, S., Suzuki, Y., Hiralal, P., et al. (2012). Flexible electronics: the next ubiquitous platform. *Proceedings of the IEEE, 100*, 1486−1517.

Noyan, I. C., Huang, T. C., & York, B. R. (1995). Residual-stress strain analysis in thin-films by X-ray-diffraction. *Critical Reviews in Solid State and Materials Sciences, 20*(2), 125−177.

Ochiai, S., Iwamoto, S., Nakamura, T., & Okuda, H. (2007). Crack spacing distribution in coating layer of galvannealed steel under applied tensile strain. *ISIJ International, 47*(3), 458−465.

Odom, S. A., Chayanupatkul, S., Blaiszik, B. J., Zhao, O., Jackson, A. C., Braun, P. V., et al. (2012). A self-healing conductive ink. *Advanced Materials, 24*(19), 2578−2581.

Oh, J. S., Cho, Y. R., Cheon, K. E., Karim, M. A., & Jung, S. J. (2007). Failure mechanism of patterned ITO electrodes on flexible substrate under static and dynamic mechanical stresses. *Solid State Phenomena*, (124−126), 411−414.

Ohring, M. (1992). *The materials science of thin films*. New-York: Academic Press.

Oliver, W. C., & Pharr, G. M. (2004). Measurement of hardness and elastic modulus by instrumented indentation: advances in understanding and refinements to methodology. *Journal of Materials Research, 19*(1), 3−20.

Ong, C. W., Zong, D. G., Aravind, M., Choy, C. L., & Lu, D. R. (2003). Tensile strength of zinc oxide films measured by a microbridge method. *Journal of Materials Research, 18*(10), 2464−2472.

Pagliaro, M., Ciriminna, R., & Palmisano, G. (2008). Flexible solar cells. *Chemsuschem, 1*(11), 880−891.

Park, J. H., An, J. H., Kim, Y. J., Huh, Y. H., & Lee, H. J. (2008). Tensile and high cycle fatigue test of copper thin film. *Materialwissenschaft und Werkstofftechnik., 39*(2), 187−192.

Park, K., Lee, D. K., Kim, B. S., Jeon, H., Lee, N. E., Whang, D., et al. (2010). Stretchable, transparent zinc oxide thin film transistors. *Advanced Functional Materials, 20*(20), 3577−3582.

Payne, J. A. (1998). *Stress evolution in solidifying coatings (PhD thesis)*. University of Minnesota.

Pharr, G. M., & Oliver, W. C. (July 1992). Measurement of thin film mechanical properties using nanoindentation. *MRS Bulletin*, 28−33.

Piggott, M. R. (1980). *Load bearing fiber composites − Reinforcement processeus*. Elmsford, NY: Pergamon.

Pinyol, A., Meylan, B., Gilliéron, D., Mewani, V., Leterrier, Y., & Månson, J.-A. E. (2009). Electro-fragmentation analysis of dielectric thin films on flexible polymer substrates. *Thin Solid Films, 507*, 2007−2011.

Pinyol, A., Meylan, B., Gilliéron, D., Mottet, A., Mewani, V., Leterrier, Y., et al. (2008). Electro-fragmentation analysis of dielectric thin films on flexible polymer substrates. In V. Buloviæ, S. C.- Sullivan, I. Kymissis, J. Rogers, M. Shtein, & T. Someya (Eds.), *Large-area processing and patterning for active optical and electronic devices* (Materials Research Society Symposium Proceedings vol. 1030e, Warrendale, PA, 2008), 1030-g03-12.

Pitton, Y., Hamm, S. D., Lang, F.-R., Leterrier, Y., Mathieu, H. J., & Månson, J.-A. E. (1995). An adhesion study of SiOx/PET films: a comparison between scratch and fragmentation tests. In: *1st ICAST, Amsterdam, Holland*.

Plojoux, J., Leterrier, Y., Månson, J.-A. E., & Templier, F. (2007). Mechanical integrity analysis of multilayer insulator coatings on flexible steel substrates. *Thin Solid Films, 515*, 6890−6898.

Potts, J. R., Dreyer, D. R., Bielawski, C. W., & Ruoff, R. S. (2011). Graphene-based polymer nanocomposites. *Polymer, 52*(1), 5−25.

Reddy, J. R. (2004). *Mechanics of laminated composite plate and shells: Theory and analysis.* Boca Raton: CRC Press.

Rochat, G., Leterrier, Y., Plummer, C. J. G., Månson, J.-A. E., Szoszkiewicz, R., Kulik, A. J., et al. (2004). Effect of substrate crystalline morphology on adhesion of PECVD thin SiOx coatings on polyamide. *Journal of Applied Physics, 95*(10), 5429−5434.

Rogers, J. A., Someya, T., & Huang, Y. G. (2010). Materials and mechanics for stretchable electronics. *Science, 327*(5973), 1603−1607.

Röll, K. (1976). Analysis of stress and strain distribution in thin films and substrates. *Journal of Applied Physics, 47*, 3224−3229.

Schulgasser, K. (1981). On the in-plane elastic-constants of paper. *Fibre Science & Technology, 15*(4), 257−270.

Sekitani, T., Kato, Y., Iba, S., Shinaoka, H., Someya, T., Sakurai, T., et al. (2005). Bending experiment on pentacene field-effect transistors on plastic films. *Applied Physics Letters, 86*(7), 073511-073511-3.

Shchukin, D. G., & Mohwald, H. (2007). Self-repairing coatings containing active nano-reservoirs. *Small, 3*(6), 926−943.

Siegel, A. C., Phillips, S. T., Dickey, M. D., Lu, N. S., Suo, Z. G., & Whitesides, G. M. (2010). Foldable printed circuit boards on paper substrates. *Advanced Functional Materials, 20*(1), 28−35.

Small, M. K., & Nix, W. D. (1992). Analysis of the accuracy of the bulge test in determining the mechanical properties of thin films. *Journal of Materials Research, 7*(6), 1553−1563.

Spaepen, F. (2000). Interfaces and stresses in thin films. *Acta Materialia, 48*, 31−42.

Stoney, G. G. (1909). The tension of metallic films deposited by electrolysis. *Proceedings of the Royal Society London, a82*, 172−175.

Sun, J. Y., Lu, N. S., Yoon, J., Oh, K. H., Suo, Z. G., & Vlassak, J. J. (2009). Inorganic islands on a highly stretchable polyimide substrate. *Journal of Materials Research, 24*(11), 3338−3342.

Sun, X. J., Wang, C. C., Zhang, J., Liu, G., Zhang, G. J., Ding, X. D., et al. (2008). Thickness dependent fatigue life at microcrack nucleation for metal thin films on flexible substrates. *Journal of Physics D-Applied Physics, 41*(19), 195404.

Suo, Z. G. (2012). Mechanics of stretchable electronics and soft machines. *MRS Bulletin, 37*(3), 218−225.

Suo, Z., Ma, E. Y., Gleskova, H., & Wagner, S. (1999). Mechanics of rollable and foldable film-on-foil electronics. *Applied Physics Letters, 74*(8), 1177−1179.

Su, Y. J., Wei, H., Gao, R. G., Yang, Z., Zhang, J., Zhong, Z. H., et al. (2012). Exceptional negative thermal expansion and viscoelastic properties of graphene oxide paper. *Carbon, 50*(8), 2804−2809.

Tahk, D., Lee, H. H., & Khang, D. Y. (2009). Elastic moduli of organic electronic materials by the buckling method. *Macromolecules, 42*(18), 7079−7083.

Tamulevicius, S. (1998). Stress and strain in the vacuum-deposited thin films. *Vacuum, 51*(2), 127−139.

Tang, H. X., Foran, B., & Martin, D. C. (2001). Quantitative measurement of adhesion between polypropylene blends and paints by tensile mechanical testing. *Polymer Engineering and Science, 41*(3), 440−448.

Tarasovs, S., Andersons, J., & Leterrier, Y. (2010). Estimation of interfacial fracture toughness based on progressive edge delamination of a thin transparent coating on a polymer substrate. *Acta Materialia, 58*(8), 2948−2956.

Torres, J. M., Bakken, N., Stafford, C. M., Li, J. A., & Vogt, B. D. (2010). Thickness dependence of the elastic modulus of tris(8-hydroxyquinolinato)aluminium. *Soft Matter, 6*(22), 5783−5788.

Townsend, P. H., Barnett, D. M., & Brunner, T. A. (1987). Elastic relationships in layered composite media with approximation for the case of thin-films on a thick substrate. *Journal of Applied Physics, 62*(11), 4438−4444.

Twomey, B., Byrne, G., Hynes, A., O'Neill, L., & Dowling, D. (2009). Evaluation of the mechanical behaviour of nanometre-thick coatings deposited using an atmospheric pressure plasma system. *Surface & Coatings Technology, 203*(14), 2021−2029.

van den Berg, D., Barink, M., Giesen, P., Meinders, E., & Yakimets, I. (2011). Hygroscopic and thermal micro deformations of plastic substrates for flexible electronics using digital image correlation. *Polymer Testing, 30*(2), 188−194.

Van Der Zwaag, S., Schmets, A. J. M., & Van Der Zaken, G. (2007). *Self healing materials: An alternative approach to 20 centuries of materials science*. Springer Science+Business Media B.V.

Wheeler, D. R., & Osaki, H. (1990). Intrinsic bond strength of metal-films on polymer substrates - a new method of measurement. *ACS Symposium Series, 440*, 500−512.

Withers, P. J., & Bhadeshia, H. (2001). Overview - residual stress part 1-measurement techniques. *Materials Science and Technology, 17*(4), 355−365.

Wittkowski, T., Jorzick, J., Seitz, H., Schroder, B., Jung, K., & Hillebrands, B. (2001). Elastic properties of indium tin oxide films. *Thin Solid Films, 398*, 465−470.

Wojciechowski, P. H., & Mendolia, M. S. (1989). On the multiple fracture of low-elongation thin films deposited on high-elongation substrates. *Journal of Vacuum Science and Technology, A7*(3), 1282.

Wool, R. P. (2008). Self-healing materials: a review. *Soft Matter, 4*(3), 400−418.

Yamamoto, N., Makino, H., & Yamamoto, T. (2011). Young's modulus and coefficient of linear thermal expansion of ZnO conductive and transparent ultra-thin films. *Advances in Materials Science and Engineering*, 136217. http://dx.doi.org/10.1155/2011/136127.

Zhang, Y. Y., & Gu, Y. T. (2013). Mechanical properties of graphene: effects of layer number, temperature and isotope. *Computational Materials Science, 71*, 197−200.

Zhang, G. P., Sun, K. H., Zhang, B., Gong, J., Sun, C., & Wang, Z. G. (2008). Tensile and fatigue strength of ultrathin copper films. *Materials Science Engineering A*, (483−484), 387−390.

Zhao, P., & Shi, G. (2011). Study of poisson ratios of single-walled carbon nanotubes based on an improved molecular structural mechanics model. *CMC-Computers Materials & Continua, 22*(2), 147−168.

Appendix: Nomenclature

a_0, a_1 Constants in strain profile Eqn (1.4).

b Half of buckle length

CD, CD_{sat} Crack density, crack density at saturation

CHE, CHE_f, CHE_s Coefficients of hygroscopic expansion, of film, of substrate

CTE, CTE_f, CTE_s Coefficients of thermal expansion, of film, of substrate

d lattice spacing

E, E_f, E_s Young's moduli of multilayer, of film, of substrate

$\overline{E}_f, \overline{E}_c$ Plane strain moduli of film, of substrate

$g(\alpha;\beta)$ Normalized energy release rate

G_{coh}, G_{adh} Film toughness, interfacial toughness

G_{ss} Steady-state energy release rate

h, h_f, h_s Thicknesses of multilayer, of film, of substrate

$IFSS, IFSS*$ Interfacial shear strength, intrinsic IFSS

k Variable

N Number of layers in a multilayer

R_0, R Radii of curvature of substrate, of coated substrate

R_{crit} Critical radius of curvature

R_{eq} Equilibrium radius of curvature

w x^{ξ} Weighing and adjustable factors in nano-indentation tests

W Buckle width

α, β Dundurs parameters

χ Film-to-substrate Young's modulus ratio

ε Strain

ε_{crit}, COS Critical failure strain, crack-onset strain

ε_{crit}^* Intrinsic crack-onset strain

ε_i Film internal strain

ν, ν_f, ν_s Poisson's ratio of multilayer, of film, of substrate

η Film-to-substrate thickness ratio

λ_B Iensile stress recovery length

ψ Mode mixity

μ_f, μ_s Shear modulus of film, of substrate

σ_i In-plane internal film stress

$\sigma_{in}, \sigma_{th}, \sigma_{hy}$ Intrinsic, thermal, hygroscopic contributions to film stress

θ, ψ, ϕ Scattering vector, declination angle, in-plane orientation (X-ray scattering)

Structural and electronic properties of fullerene-based organic materials: density functional theory-based calculations

2

G. Volonakis, S. Logothetidis
Aristotle University of Thessaloniki, Thessaloniki, Greece

2.1 Introduction

Organic electronics (OE) is one of the most rapidly growing technological fields with many applications already available in the global markets. Some of the main advantages compared with the traditional silicon-based technology are (1) the low-cost required for OE device fabrication using compatible roll-to-roll production lines, (2) the ease of processing and ability to tailor the properties of the related organic materials, and finally (3) the key features of OE devices such as flexibility resulting from the use of suitable substrates and the comparatively low energy consumption. However, the current performance and lifetimes of OE devices is significantly lower than the ones of traditional electronic devices. The possibility of improvements though, remains quite large. To achieve higher quality and better performing OE materials, a profound knowledge of the complex physical and chemical properties is required. To reach such a solid understanding and therefore achieve the desired optimization, a lot of work still has to be done by experimentalists and theoreticians in deep complementarity. In this chapter, we will present recent results on the structural details and the electronic properties of prototype organic semiconductors by using first-principles (ab-initio) calculations based on the density functional theory (DFT). Specifically, we will focus on the structural details, impurity-related effects, and finally the electronic properties of two prototype electron-accepting materials of OE, the C_{60} fullerenes, and their derivative $PC_{60}BM$.

In more detail, the first part of the chapter includes a brief overview of the theoretical background, the current limitations and possible ways to overcome them. Next we focus on the description of the structural conformations organic crystals may form, and in addition we present results for the atomic-scale details of the crystals along continuous structural transformations paths. In the last part of the chapter, we address another crucial factor for the optimization of OE devices, that is the presence of impurities inside the molecular crystals of organic semiconductors. Such defects are known to degrade the devices performance and lifetimes. We present first-principles based

results to find the stability and energetics of prototype impurities inside the semicon-
ductors and reveal the effects on the materials properties. Finally we conclude and
discuss some future trends regarding the use of DFT-based computations for the study
of OE materials.

2.2 Theoretical background

2.2.1 DFT fundamentals

The calculation of the ground-state energy and properties of a system of interacting
ions and electrons requires the solution of the many-body Schrödinger equation
given by:

$$\mathcal{H}\Psi\left(\overrightarrow{\mathbf{R}}_I; \overrightarrow{\mathbf{r}}_i\right) = E\Psi\left(\overrightarrow{\mathbf{R}}_I; \overrightarrow{\mathbf{r}}_i\right), \tag{2.1}$$

where Ψ is the many-body wave function, $\overrightarrow{\mathbf{R}}_I$ the position of ions, $\overrightarrow{\mathbf{r}}_i$ variables that
describe the electrons, E the energy of the system, and $\mathcal{H}$ the hamiltonian of the system
(Kaxiras, 2003). In the Born-Oppenheimer approximation, the hamiltonian of the
system can be written as follows:

$$\begin{aligned}
\mathcal{H} = &-\sum_i \frac{\hbar^2}{2m_e}\nabla^2_{\overrightarrow{\mathbf{r}}_i} - \sum_{iI} \frac{Z_I e^2}{\left|\overrightarrow{\mathbf{R}}_I - \overrightarrow{\mathbf{r}}_i\right|} \\
&+ \frac{1}{2}\sum_{ij(i\neq j)} \frac{e^2}{\left|\overrightarrow{\mathbf{r}}_i - \overrightarrow{\mathbf{r}}_j\right|} + \frac{1}{2}\sum_{IJ(I\neq J)} \frac{Z_I Z_J e^2}{\left|\overrightarrow{\mathbf{R}}_I - \overrightarrow{\mathbf{R}}_J\right|}.
\end{aligned} \tag{2.2}$$

The first term describes the kinetic energy of electrons, the second the Coulomb
interactions of electrons with ions, the third the electron—electron interactions, and
finally the last term describes the ionic interactions. Unfortunately, the solution of
Eqn (2.1) is impossible because of the nature of electrons, as described in the third
term of Eqn (2.2). Different methods have been formulated to get approximate solu-
tions to the Schrödinger equation. In the context of mean field theories, the simplest
one is the so-called Hartree approximation. Furthermore, to incorporate the fermionic
nature of electrons, the wavefunction should be antisymmetrized; such approximation
has been widely applied and is known as Hartree-Fock.

A different way to solve the many-body Schrödinger equation (Eqn (2.1)) is the
application of DFT. Hohenberg, Kohn and Sham developed DFT in a series of articles
in the mid-1960s (Hohenberg & Kohn, 1964; Kohn & Sham, 1965). Since then, it has
been the most successful and popular method to study the ground state of many elec-
tron systems. Its success is strongly supported by the huge number of published
research articles including results based on DFT. In the following section, we will
briefly overview the basic ideas behind the theory.

The main concept of the DFT is that instead of dealing with Eqn (2.1) and consequently with the many-body wavefunction $\Psi(\vec{\mathbf{R}}_I; \vec{\mathbf{r}}_i)$, one could deal with a different formulation that involves the total density of electrons $n(\vec{\mathbf{r}})$. The first step toward modern DFT was made in 1964 when Kohn and Hohenberg (Hohenberg & Kohn, 1964) proved that there is a one-to-one correspondence between the electron density $n(\vec{\mathbf{r}})$ and an external potential $V(\vec{\mathbf{r}})$. In 1965, Kohn and Sham (Kohn & Sham, 1965) showed that the problem of many interacting electrons in an external potential could be mapped exactly to a set of noninteracting electrons in an effective external potential. This led to the self-consistent, single-particle equations known as the Kohn−Sham equations for single-particle orbitals φ_i:

$$\left[-\frac{\hbar^2}{2m_e}\nabla^2 + V^{\mathrm{eff}}\left(\vec{\mathbf{r}}, n(\vec{\mathbf{r}})\right) \right]\varphi_i(\vec{\mathbf{r}}) \; = \; \varepsilon_i\varphi_i(\vec{\mathbf{r}}),$$
(2.3)

where the effective potential $V^{\mathrm{eff}}\left(\vec{\mathbf{r}}, n(\vec{\mathbf{r}})\right)$ is given by:

$$V^{\mathrm{eff}}\left(\vec{\mathbf{r}}, n(\vec{\mathbf{r}})\right) \; = \; V(\vec{\mathbf{r}}) + e^2 \int \frac{n(\vec{\mathbf{r}}')}{|\vec{\mathbf{r}} - \vec{\mathbf{r}}'|}\mathrm{d}\vec{\mathbf{r}}' + \frac{\delta E_{\mathrm{XC}}[n(\vec{\mathbf{r}})]}{\delta n(\vec{\mathbf{r}})}.$$
(2.4)

In Eqn (2.4), the first term $V(\vec{\mathbf{r}})$ is the external (ionic) potential, the second term is the Coulomb interactions resulting from the rest electrons, and the last term corresponds to the exchange and correlation effects of electrons. Currently, the proper description of the last term of Eqn (2.4) remains the main challenge for further development of modern electronic structure calculations. Probably the two most common exchange/correlation functionals used are the local density approximation (LDA) and the generalized gradient approximation (GGA). Within the LDA, the exchange/correlation potential depends locally on the electronic density (i.e. on the value of the density on a specific site). Though the LDA is quite a simple approximation, it is successful in the description of various materials properties. Efforts to improve the LDA functionals lead to the construction of the GGA, within which the exchange/correlation potential depends on the value of the density at a site and in addition on its gradient.

2.2.2 Limits and extents

Some important limitations of the modern DFT functionals are the so-called "band gap problem" and the neglect of weak van der Waals (vdW) interactions. These limitations are specifically crucial for the application of the DFT on organic semiconductors. In particular, although the proper incorporation of vdW interactions may be insignificant for inorganic solids, for organic materials, vdW are critical. This happens because organic materials form molecular crystals, where molecules arrange periodically creating well-ordered three-dimensional structures. In such structures, the interactions between neighbouring molecules are mostly vdW type; therefore, omitting them may lead to significant failures of the approach.

Regarding the band gap problem, the exact reasons for its origin are still under debate. Several approaches are known to address the problem and find band gaps significantly larger, and in better agreement with the measured values. In this chapter, we will show some results applying to one of these approaches, namely the use of hybrid functionals (Becke, 1993). Hybrid functionals admix a standard local density functional to a certain amount of Fock exchange. Specifically, the PBE0 (Perdew, Ernzerhof, & Burke, 1996) functional that will be applied in the chapter, is defined as a mix of exchange (E_X^{PBE}) and correlation parts (E_C^{PBE}) of the PBE density functional with 25% of Fock exchange (E_X^{HF}), and is given by:

$$E_{XC}^{PBE0} = \frac{1}{4}E_X^{HF} + \frac{3}{4}E_X^{PBE} + E_C^{PBE}. \tag{2.5}$$

To properly incorporate the vdW interactions in a DFT functional, different approaches are actually being developed (Dion, Rydberg, Schröder, Langreth, & Lundqvist, 2004; Wu, Vargas, Nayak, Lotrich, & Scoles, 2001). One of the most popular to date is the so-called DFT-D method. In DFT-D, a semiempirical dispersion potential is added to the conventional Kohn−Sham DFT energy:

$$E_{DFT-D} = E_{KS-DFT} + E_{DISP.} \tag{2.6}$$

Specifically, in the DFT-D2 method (Grimme, 2006) that will be applied on organic crystals at the following parts of this chapter, the dispersion energy E_{DISP} is defined as:

$$E_{DISP} = -\frac{s_6}{2} \sum_{i=1}^{N} \sum_{j=1}^{N} \sum_{L} \frac{C_6^{i,j}}{\left|\overrightarrow{\mathbf{r}}^{i,0} - \overrightarrow{\mathbf{r}}^{j,L}\right|^6} f\left(\overrightarrow{\mathbf{r}}^{i,0} - \overrightarrow{\mathbf{r}}^{j,L}\right), \tag{5.7}$$

where N is the number of atoms in the system, s_6 is a global scaling factor that depends on the DFT functional used, $C_6^{i,j}$ is the semiempirical factor of the dispersion that depends on the atom type, $L = (l_1, l_2, l_3)$ are the translations along the lattice vectors of the unit cell, $\overrightarrow{\mathbf{r}}^{i,L}$ is the position of atom i after the translation L, and finally $f(r^{i,j})$ is the damping function given by:

$$f(r^{i,j}) = \frac{1}{1 + e^{-d\left(\overrightarrow{r}^{i,j}/R_o^{i,j}-1\right)}}. \tag{2.8}$$

Default values for the semiempirical coefficient $C_6^{i,j}$ and the vdW radii $R_o^{i,j}$ can be found in the work of Grimme (2006). This approach has previously been successfully employed for the investigation of properties of fullerenes and other organic electronics materials (Tsetseris, 2014; Tsetseris & Pantelides, 2005; Volonakis, Tsetseris, & Logothetidis, 2012; Volonakis, Tsetseris, & Logothetidis, 2013a, 2013b).

2.3 Structural transformations of fullerenes based on DFT calculations

2.3.1 Structural details and insights by DFT

C_{60} fullerenes are known to form well-defined molecular crystals called fullerites. Experimental studies have shown that in ambient conditions fullerites adopt a close-packed face-centred cubic (FCC) lattice (Iwasa et al., 1994). A schematic representation of such conformation is depicted in Figure 2.1(a), where the C_{60} molecules are forming the FCC lattice, similar to what atoms do in conventional crystals. The intermolecular interactions in such structures are mostly weak vdW and, as mentioned previously, are crucial for the proper description of these systems. As a benchmark study for the application of DFT on fullerites, one can calculate the total energy of the FCC crystal for different volumes. Figure 2.1(b) shows a comparison of DFT with an LDA functional (DFT-LDA) and the DFT-D2 method described in Section 2.2.2. The DFT-LDA approach underestimates the equilibrium volume of the structure by almost 4% (682 $Å^3$) compared with the experimental values of 708−711 $Å^3$ (David, Ibberson, Dennis, Hare, & Prassides, 1992; Iwasa et al., 1994; Núñez-Reguiro, Marques, Hodeau, Béthoux, & Perroux, 1995). Inclusion of the weak vdW interactions using the DFT-D2 significantly improves the description and the calculated equilibrium volume is found 703 $Å^3$ (see Figure 2.1(b)). This value is less than 1% smaller than the available experimental data. These volume values correspond to FCC lattice constants of 13.99 and 14.11 Å calculated with the DFT-LDA and DFT-D2 approaches, respectively.
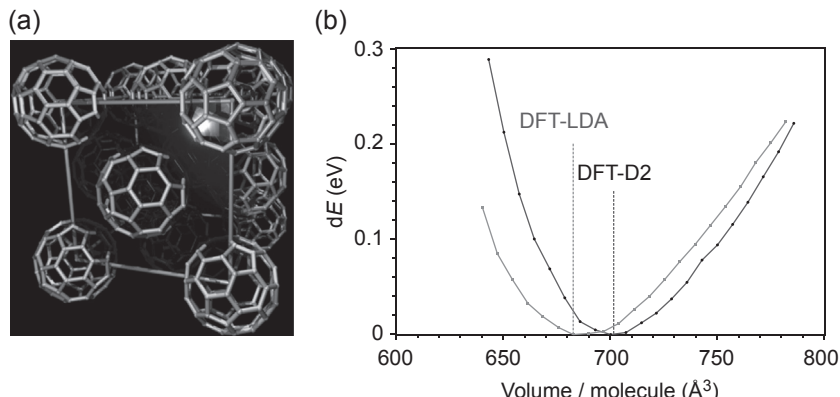
Figure 2.1 (a) Schematic representation of the face-centred cubic (FCC) lattice formed by C_{60} molecules. *(Source: Adapted from Terrones & Terrones (2003); © IOP Publishing. Reproduced by permission of IOP Publishing. All rights reserved.).* (b) Total energy of the FCC conformations for different volumes calculated with DFT-LDA approach and the DFT-D2 method to include the vdW interactions.

One of the most important derivatives of fullerenes is [6,6]-phenyl C-61-butyric acid methyl ester ($PC_{60}BM$). The addition of the functional group to the C_{60} molecule increases the solubility and thus the ease of process of fullerenes. Such enhancement made $PC_{60}BM$ one of the most successful electron acceptor materials in organic electronics devices. However, in contrast to the case of C_{60} fullerenes, the exact structure of the molecular crystals formed by $PC_{60}BM$ is not clear. To resolve this issue, DFT calculations have been employed to investigate the atomic-scale details of the crystal structures adopted by $PC_{60}BM$'s molecules. It has been shown that between the close-packed cubic structures the energetically favourable one is the simple cubic (SC) (Nápoles-Duarte, Reyes-Reyes, Ricardo-Chavez, Garibay-Alonso, & López-Sandoval, 2008; Volonakis et al., 2013a). As shown in Figure 2.2(a), based on DFT-LDA calculations, the binding energy (i.e. the absolute difference between the energy per molecule of the cubic crystals and the energy of an isolated $PC_{60}BM$ molecule) of the SC structure is smaller than the others. In particular, the calculated binding energy (E_b) of the body-centred cubic (BCC) conformation is found less than 0.1 eV higher. On the other hand, the FCC crystal conformation has a significantly larger E_b
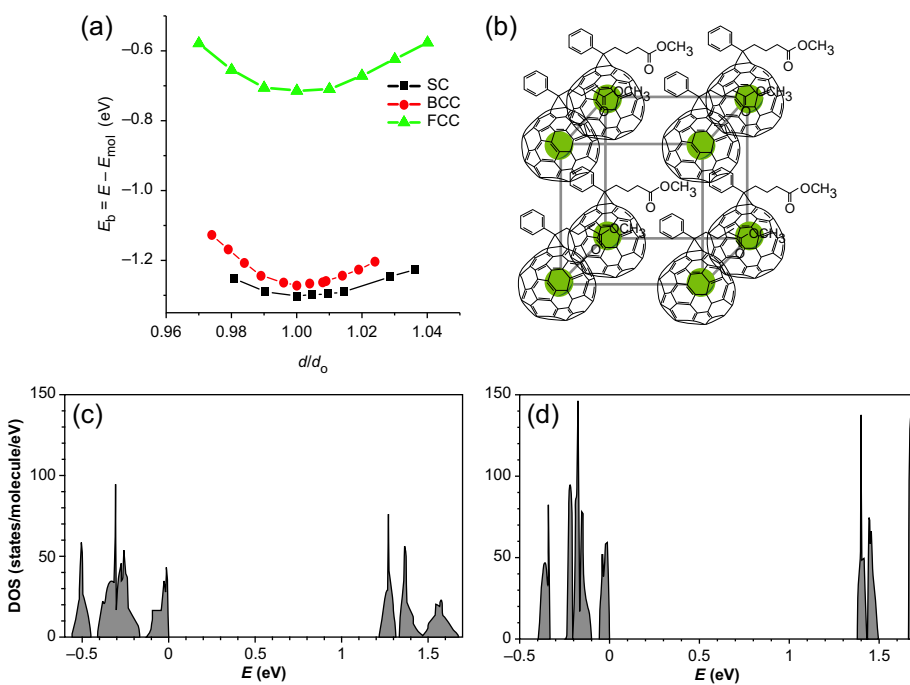
Figure 2.2 (a) Dependence of the molecular binding energy E_b on the fullerene to fullerene distance d in a $PC_{60}BM$ crystal. d_o is the calculated d at the equilibrium configuration. (b) Schematic representation of the simple cubic (SC) lattice formed by $PC_{60}BM$ molecules. Electronic density of states (DOS) for (c) the SC PCBM crystal structure and (d) body-centred-cubic PCBM crystal structure. Zero energy is set at the top of the valence band. *Source*: (a), (c), and (d) are adapted from Volonakis et al. (2012).

(more than 0.6 eV) and thus is the less favourable configuration (Volonakis et al., 2012). This is a remarkable difference with C_{60} fullerenes that are known to form FCC crystals at room temperature.

Having calculated the stability of the different cubic structures $PC_{60}BM$ molecules may form; the electronic properties for the stable structures have been probed. Figure 2.2(c) and (d) depicts the electronic density of states for the two most stable cubic lattices. It is clear that the presence of the functional group lead not only to the formation of different possible stable lattice structures, but also to significant effects on the electronic properties. The electronic band gaps E_g based on a DFT-LDA approach are 1.22 and 1.38 eV for the SC (Figure 2.2(c)) and BCC (Figure 2.2(d)) configurations, respectively. The corresponding E_g for the FCC lattice, not shown here, has been calculated at 1.40 eV (Volonakis et al., 2012). As explained in Section 2.2.2 of this chapter, due to well-known DFT limitations, these values are significantly underestimated compared with the experimental (~ 2.4 eV) (Yoo, Kum, & Cho, 2011). The use of a hybrid functional approach like the PBE0 (Perdew et al., 1996) further improves the value for the E_g. For example, the electronic band gap for the room temperature stable fullerene FCC crystals is 2.3 eV (Lof, van Veenendaal, Koopmans, Jonkman, & Sawatzky, 1992), whereas based on DFT, it has been calculated at 1.1 and 2.2 eV using LDA and PBE0 functionals, respectively (Volonakis et al., 2013a).

2.3.2 Continuous transformations

Polymorphism (i.e. the ability for the molecules of a system to arrange in different crystal structures) may significantly affect the performance of organic semiconducting materials in OE devices. Polymorphism appears in organic semiconductors because of the weak intermolecular vdW bonding and has been associated with important effects on the electronic properties of the semiconductors. Thus, understanding the atomic-scale mechanisms that underlie polymorphism and in particular, the identification of new possible stable polymorphs, is critical for the further development and optimization of organic molecular crystals related with OE devices.

Continuous transformations between different crystal lattices of inorganic crystals, such as Fe, have attracted much interest over the past few years (Friák, Šob, & Vitek, 2001; Kraft, Marcus, Methfessel, & Scheffler, 1993; Šob, Friák, Legut, Fiala, & Vitek, 2004; Šob, Wang, & Vitek, 1997; Tsetseris, 2005). Usually there are two continuous transformation paths considered (1) the tetragonal (also called "Bain transformation") and (2) the trigonal transformation. These two paths connect, in a continuous way, the cubic crystal conformations through a series of body-centred tetragonal (BCT) and trigonal lattices, respectively. Recently, these continuous transformations paths have been used to explore the polymorphism of fullerenes' (Volonakis et al., 2013a) and $PC_{60}BM$'s (Volonakis et al., 2012) molecular crystals that are known to form cubic lattices, as already discussed. In what follows, we present in more detail selective results and discuss some of the most important findings on the transformation paths of solid C_{60} and $PC_{60}BM$.

Along both tetragonal and trigonal transformation paths different structures are described by different c/a ratio. Especially for the tetragonal path the c vector is

parallel to the [001] direction and the *a* vector is parallel to the [100] direction of the BCC structure as shown in the schematic presented in Figure 2.3(a). In this way, the BCC and FCC structures are now special cases of the BCT lattice with *c*/*a* ratios equal to 1 and $\sqrt{2}$, respectively. To further clarify, in Figure 2.3(a), the tetragonal cell for the FCC case ($c/a = \sqrt{2}$) is marked by the thick solid line. For the trigonal path, *c* is now a vector parallel to the [111] direction (Figure 2.3(b)) and vector *a* is perpendicular to *c*. This way, the BCC, SC, and FCC lattices are considered special cases of a trigonal lattice with different *c*/*a* ratio of 1, 2, and 4, respectively. Figure 2.3(b) illustrates a schematic of the FCC lattice (conventional lattice is shown by the dotted line) as described by a rhombohedral cell (thick solid line), with $c_{rh} = \sqrt{3}c/2$ and $a_{rh} = \sqrt{2}a$. Finally, having defined the *c*/*a* ratio for both studied paths, one can create a two-dimensional (2D) grid of structures by varying the *c*/*a* ratio and the volume. For each of these structures (that are connected along the path), it is possible to calculate the cohesive energies (E_{coh}) and produce the contour plot as the ones presented in Figure 2.4.

Based on this procedure, Figure 2.4(a) presents the E_{coh} variation along the tetragonal path for the molecular crystal of C_{60}. Structure I ($c/a = \sqrt{2}$) corresponds to the room temperature stable FCC phase discussed in the previous part of the chapter. Along the path, the different maxima of E_{coh} (marked by the white dots) correspond to different stable structures that C_{60} may form (i.e. polymorphs). The maxima close to the $c/a = 0.75$ (structure 1D) and the $c/a = 1.65$ region (structure 2D-T), are known polymer phases of fullerites. In these structures, the neighbouring C_{60} molecules are covalently bonded through $[2 + 2]$ cycloadditions to each other along the one or two directions forming the so-called one-dimensional (1D) and 2D tetragonal polymers, respectively. For the 1D polymer phase, the constants of the tetragonal lattice are $a = 12.2$ Å and $c = 9.1$ Å. The length of the vector *c*, which corresponds to the distance between the covalently bonded fullerenes, is in excellent agreement with available experimental
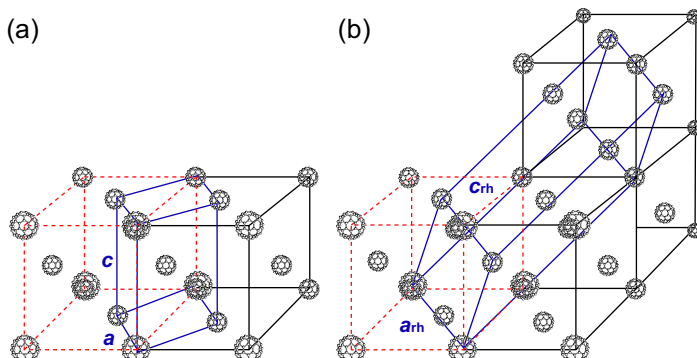
Figure 2.3 Schematic of (a) the body-centred tetragonal (thick solid lines) and (b) rhombohedral cell (thick solid lines) that describe a face-centred-cubic (FCC) lattice. The dotted lines indicate the conventional FCC cell. (C_{60} molecules are shown out of scale.)
Source: Adapted from Volonakis et al. (2013a); © IOP Publishing. Reproduced by permission of IOP Publishing. All rights reserved.
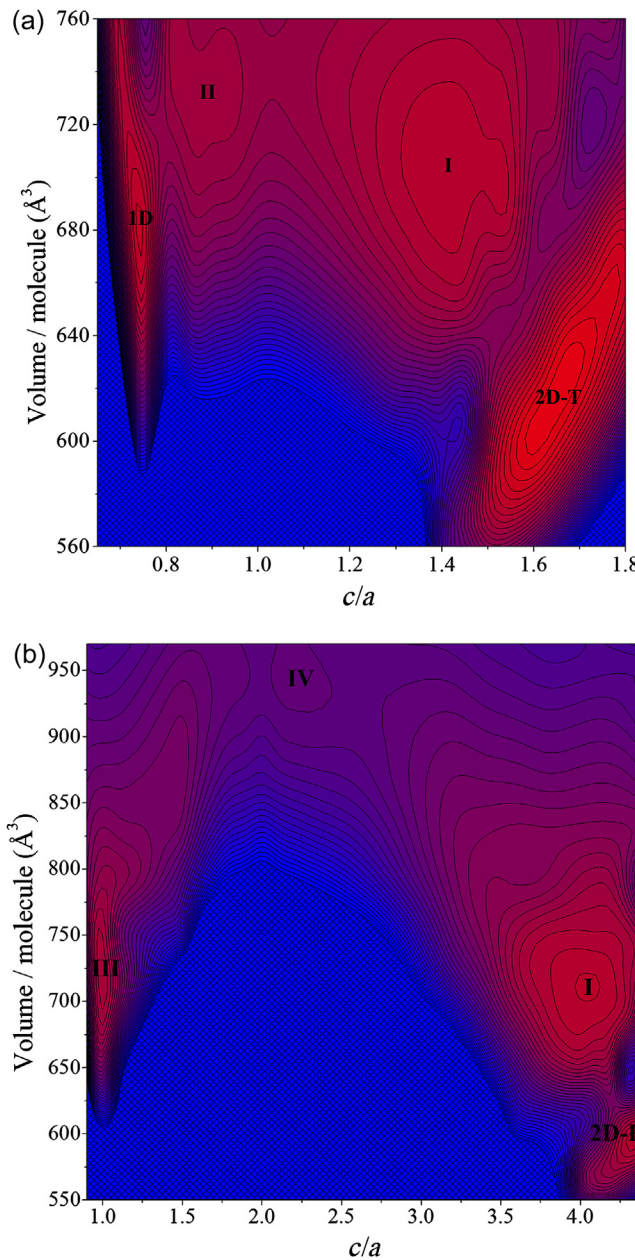
Figure 2.4 Contour plot of E_{coh} along (a) the tetragonal and (b) the trigonal continuous path. Lighter (red) regions correspond to preferable structures (with higher E_{coh}), while darker (blue) regions are less favourable. BCC and FCC lattices correspond to $c/a = 1$ and $c/a = \sqrt{2}$ (dashed lines), respectively. White dots represent maxima of the E_{coh}, crossed regions have negative E_{coh}, and the interval between lines is 0.05 eV. Labels I, II, 1D, and 2D-T refer to corresponding stable structures. Can be seen in Plate I (see colour section between pages 224 and 225).
Source: Adapted from Volonakis et al. (2013a); © IOP Publishing. Reproduced by permission of IOP Publishing. All rights reserved.

data (9.1−9.3 Å) (Agafonov et al., 1997; Davydov et al., 2000; Iwasa et al., 1994; Moret, Launois, Persson, & Sundqvist, 1997; Núñez-Reguiro et al., 1995; Papoular et al., 2008). For the 2D-T polymer phase, the lattice constants are calculated $a = 9.1$ Å and $c = 14.6$ Å, again very close to the reported experimental values ($a = 9.0−9.1$ Å, $c = 14.9−15.0$ Å) (Davydov et al., 2000; Lepoittevin, Alvarez-Murga, Marques, Mezouar, & Hodeau, 2013; Núñez-Reguiro et al., 1995). The last E_{coh} maximum in Figure 2.4(a), which is also the least energetically favoured one, is a C_{60} polymorph with no intermolecular covalent bonds and a tetragonal lattice close to the BCC region ($c/a = 0.9$).

Similar to the tetragonal path, the variation of the E_{coh} along the trigonal path is shown in Figure 2.4(b). Structure I corresponds to the FCC room temperature lattice. At the BCC limit ($c/a = 1$), a new polymorph (structure III) is reported with similar structural features with the structure II of the tetragonal path. In addition, another stable polymorph, but with significantly smaller E_{coh}, is located close to the SC region (structure IV) with a $c/a = 2.2$. The last stable conformation (structure 2D-R), found along the path of Figure 2.4(b), corresponds to another polymer phase of C_{60} with a trigonal (rhombohedral) lattice. This is a 2D polymer phase, where the neighbouring molecules are bonded through [2 + 2] cycloadditions along the plane that is perpendicular to the [111] direction. The E_{coh} of the 2D-R structure is found lower than the other 2D polymer (structure 2D-T), in agreement with experimental data (Okada and Saito; 1999; Pérez-Terrazas, Romero, & Terrones, 2008) and the dimensions of the rhombohedral cell are $a = 9.21$ Å and $c = 24.8$ Å, again close to previous reports (Chen, Yamanaka, Sako, Inoue, & Yasukawa, 2002; Davydov et al., 2000; Iwasa et al., 1994; Lepoittevin et al., 2013; Núñez-Reguiro et al., 1995). In Table 2.1 the structural details of all stable conformations along both the tetragonal and trigonal path are summarized.

Table 2.1 **Structural details of the stable configurations along the tetragonal and trigonal continuous transformation paths**

Structure label	Crystal lattice type	*c/a* ratio	*V* (Å³)	E_{coh} (eV)
I	FCC	2	703	1.55
II	BCT	0.9	728	1.37
III	BCC	1	710	1.43
IV	Trigonal	2.2	960	0.91
1D	BCT	0.75	680	1.6
2D-T	BCT	1.6	607	1.82
2D-R	Trigonal	4.4	605	1.43

V in Å³, the volume per molecule of the structure; E_{coh} in eV, molecular cohesive energy.

In another work (Volonakis et al., 2012), the trigonal and tetragonal transformations were studied for the molecular crystal of the fullerene derivative PC$_{60}$BM. As discussed in a previous section of this chapter, PC$_{60}$BM molecular crystals can attain different cubic lattices and, based on DFT calculations, it has been shown that the SC and BCC lattices are strongly energetically favoured. Furthermore, the crucial role of the functional group to the stability of the formed molecular crystals has been discussed. Having that in mind, it becomes intriguing to study the continuous paths that interconnect these lattices. The investigation of the tetragonal and trigonal paths of PC$_{60}$BM has revealed additional atomic-scale details between these structures and further exposed the key role of the position of the tail to the crystal formation.

In more detail, the contour plot of Figure 2.5(a) depicts the variation of E_{coh} along the tetragonal transformation path. The sole maximum at the $c/a = 1$ represents the stable BCC conformation discussed previously. What is particularly interesting is that upon applying the same transformation path to a PC$_{60}$BM configuration with another positioning of the functional group (e.g. the FCC lattice configuration), the contour plot for the variation of the Ecoh is significantly different, as shown in Figure 2.5(b). In particular, two different maxima are found, one with the FCC lattice and another close to the BCC region ($c/a = 1.1$), but at larger volumes than the BCC structure found along the path in Figure 2.5(a). These differences have been attributed to the various possible orientations of the fullerene cages and the different positioning of the functional group. Similar results have also been found for the case of the trigonal transformation paths, where again the existence of different paths has been shown (Volonakis et al., 2012). Along these paths, new stable BCT and trigonal PC$_{60}$BM polymorphs have been identified and their structural details are summarized in Table 2.2.

2.4 Prototype impurities in fullerene crystals and electronic effects

One of the most crucial factors for further development and improvement of organic electronic materials is their reliability. OE devices are usually required to operate under ambient atmosphere and at the same time are very sensible to the external conditions. One of the main reasons that organic crystals exhibit such sensitivity is the weak vdW intermolecular bonding of the organic molecules inside the crystals that allows free space for the accommodation of extrinsic defects, such as water and oxygen molecules. These extrinsic impurities are known to degrade the devices' performance and lifetimes (Grossiord, Kroon, Andriessen, & Blom, 2012; Schafferhans, Baumann, Wagenpfahl, Deibel, & Dyakonov, 2010; Seeman et al., 2009; Sirringhaus, 2009) and thus the devices are now required to be protected by barriers, as extensively discussed in Chapter 20.

First-principles-based calculations can be a powerful tool to investigate the effects that impurities have on the physical properties of organic materials (Tsetseris & Pantelides, 2007, 2008, 2009, 2011). In the following section of this chapter, we will reveal the atomic-scale effects of impurities on the structural details and the
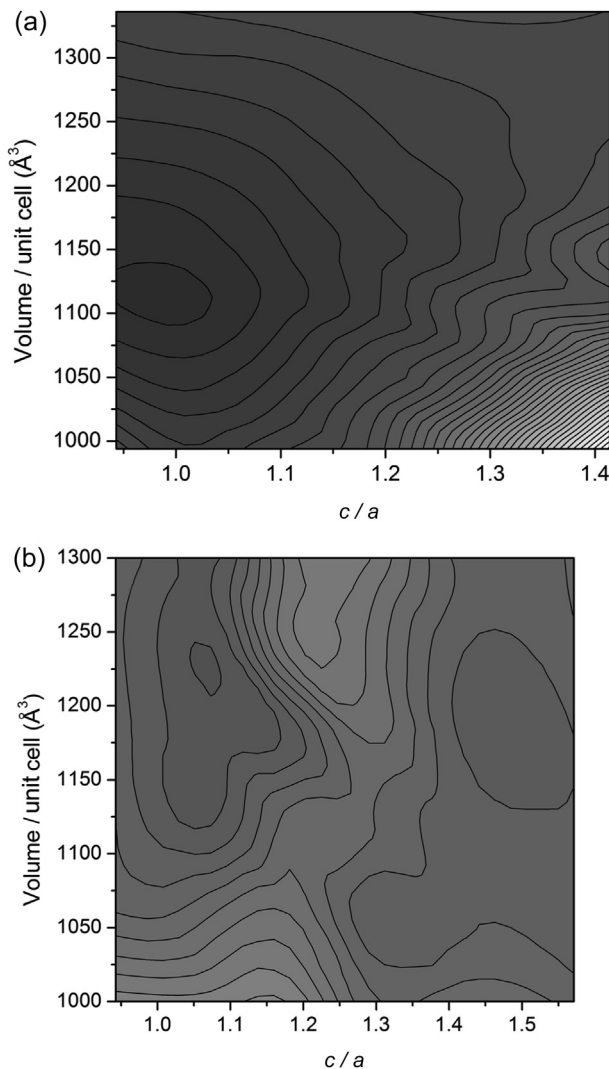
Figure 2.5 E_{coh} variation along two tetragonal transformation paths of $PC_{60}BM$. The energy difference between successive contours is 0.05 eV. $c/a = 1$ and $c/a = \sqrt{2}$ correspond to the body-centred and face-centred cubic structures, respectively. (Darker regions correspond to larger binding energies and thus enhanced crystal stability.)
Source: Adapted from Volonakis et al. (2012).

electronic properties of fullerene-based organic semiconducting crystals. In particular, we discuss the effects of impurities on the molecular crystals of C_{60} and its derivative $PC_{60}BM$, probably the two most widely used and successful acceptors for OE devices. Thus, the interaction of these materials with prototype impurity-related molecules is crucial for the understanding of the atomic-scale mechanisms that underlie the degradation process of OE devices.

Table 2.2 Structural details of the stable configurations along the tetragonal and trigonal continuous transformation paths

Crystal lattice type	c/a ratio	V (Å^3)	E_{coh} (eV)
BCT	1.1	1240	0.81
BCT	1.5	1180	0.73
Trigonal	0.9	1070	1.36
Trigonal	1.7	1050	1.49
Trigonal	0.8	1035	1.51
Trigonal	1.7	1015	1.61

V in Å^3, the volume per molecule of the structure; E_{coh} in eV, molecular cohesive energy.

2.4.1 Structural details and stability of impurities

DFT-based calculations have been employed to probe the structural details of the attachment of oxygen and water on both isolated C_{60} and $PC_{60}BM$ molecules and also on their molecular crystals. Results show different possible distinct stable configurations that can be attained upon the interaction of the impurities with the organic molecules.

In particular, for the adsorption of oxygen on molecular C_{60}, it has been shown that atomic O prefers to adsorb forming an epoxy group over a 6-6 bond of the fullerene (i.e. a bond on the fullerene that connects two hexagons) (Tsetseris & Pantelides, 2010, 2011). Adsorption over the 6−5 bond has also been found stable, and the energy barrier of the pathway between theses two structures has been calculated at 54 kcal/mol (Sohn, Kim, & Lee, 2010). Such a high barrier leaves open the possibility of isolating the $C_{60}O$ structures with the O adsorbed over a 6−5 bond, in accordance with experimental observations (Weisman, Heymann, & Bachilo, 2001). Similar to C_{60} molecules, when atomic oxygen attacks a $PC_{60}BM$ molecule (Reese et al., 2010), it was found that the 6−6 bond is again the favourable point for O to attach. Such attachment has a direct impact on the energy levels of $PC_{60}BM$ as discussed in the next section. We should note here that it has been found that both the stability and the structural details of the reported $C_{60}O$ isomers are sensible as a choice of the basis set and the electron correlation description (Sohn et al., 2010).

More recently, DFT-based calculations have been used to probe the effects of impurities on the crystalline conformations attained by C_{60} fullerenes (Tsetseris & Pantelides, 2010) and their $PC_{60}BM$ derivative (Volonakis et al., 2013b). Regarding fullerites, at first the stability and the structural details for the adsorption of O_2 and H_2O in C_{60} crystal conformations have been investigated. It has been shown that oxygen may at first occupy either tetrahedral or octahedral crystalline voids, but always retaining its triplet state. Further annealing could lead to the dissociation of O_2 and the chemical attachment either on the fullerene cage or even allow oxygen

to form bridge-like structures between neighbouring C_{60} molecules. In other words, using a first-principles approach, the complete sequence of interactions, starting from the insertion of oxygen molecules inside the crystal configuration up to the dissociation of O_2 has been probed. In that same work (Tsetseris & Pantelides, 2010), the identified defective configurations have been associated with different electronic properties.

Following on, we present in detail more recent results on the crystalline structure of $PC_{60}BM$. The stability of the structures is assessed through the E_b, defined as the energy difference between the energy of the defective system and the energy of the pristine crystal and an isolated impurity. Similar to C_{60}, it was shown that if oxygen and water molecules are incorporated inside the crystal of PC_{60} BM, numerous stable structures might be formed. Specifically, an oxygen atom can physically adsorb intact inside the molecular crystal retaining its spin polarization, as shown in Figure 2.6(a). The energy gain for such configuration based on the DFT-D method is found at 0.15 eV per adsorbed molecule.

An increase of the temperature can lead to the chemical bonding of the water molecule on top of the fullerene cage of $PC_{60}BM$ as shown in Figure 2.6(b). Specifically, the oxygen molecule is now chemisorbed over a 6−6 bond (i.e. a bond that connects two adjacent hexagons of the fullerene) on the C_{60} part of $PC_{60}BM$. The E_b for such arrangement is found to be higher by just 0.05 eV compared with the E_b of the physisorbed configuration of Figure 2.6(a). Further temperature increase may lead to the formation of chemisorbed atomic O impurity species. Two possible configurations have been reported and are depicted in Figure 2.7(a) and (b). These structures are associated with the formation of epoxy pairs over a 6−6 and a 6−5 bond of the C_{60} part, respectively. These are found to be very stable and have large E_b values of 1.2 for the formation of a pair of epoxies
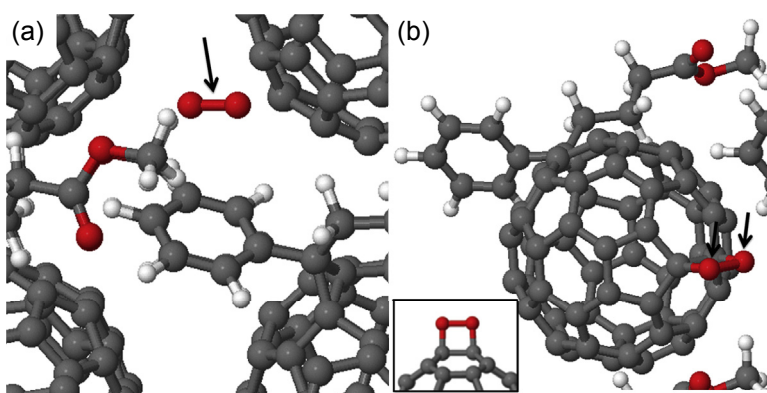
Figure 2.6 (a) Intercalated oxygen molecule (marked by the arrow) between $PC_{60}BM$. (b) Defective $PC_{60}BM$ configuration with oxygen molecules (marked by the arrows) chemisorbed over a so-called 6-6 bond of the fullerene moiety. C atoms, grey; O atoms, dark grey; H atoms, white spheres.
Source: Adapted from Volonakis et al. (2013b).
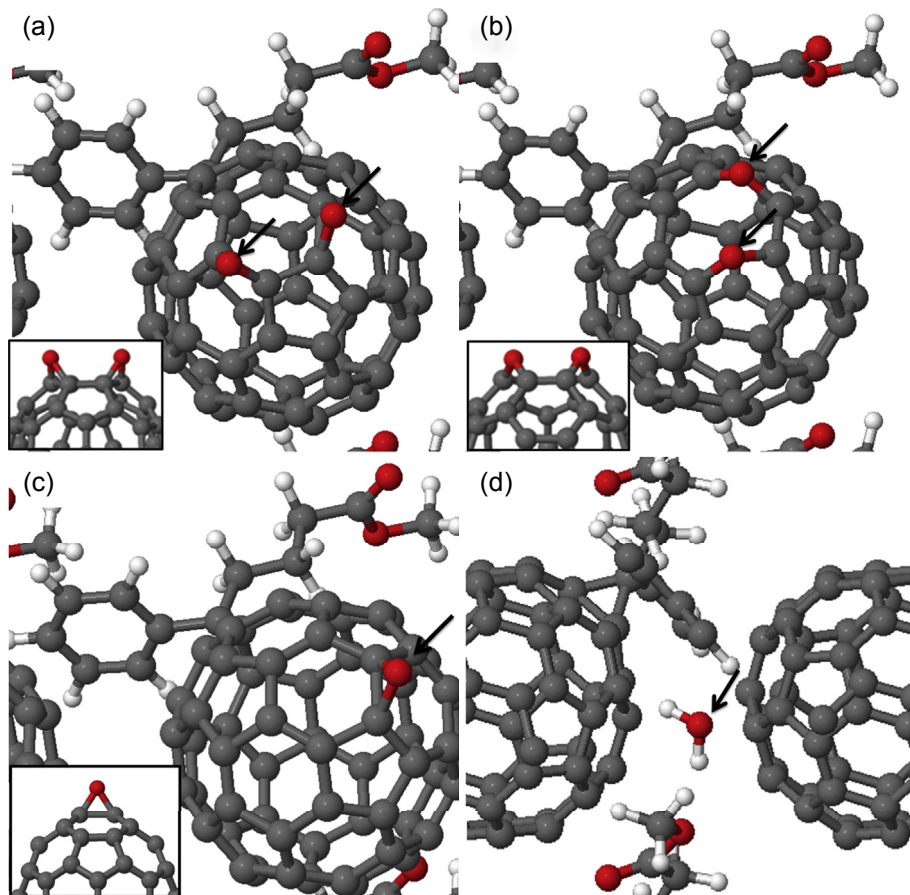
Figure 2.7 Defective $PC_{60}BM$ configurations with two oxygen atoms (marked by the arrows) adsorbed on top of neighbouring (a) 6−6 and (b) 6−5 bonds of the fullerene cage. (c) Atomic oxygen configuration within a $PC_{60}BM$ crystal: an epoxy group (marked by the arrow) on a 6−6 carbon−carbon bond. (d) An H_2O molecule (marked by the arrow) physisorbed within a $PC_{60}BM$ crystalline void. C atoms, grey; O atoms, dark grey; H atoms, white spheres. *Source*: Adapted from Volonakis et al. (2013b).

over the 6−6 bond and 1.5 eV for the epoxies over the 6−5 bond. Furthermore, by removing a single oxygen atom, the possibility of the presence of a single impurity has been taken into account. A small energy gain of 0.4 eV has been found in the conformation shown in Figure 2.7(c) compared with the structure in Figure 2.7(a). In other words, a single O-impurity over a 6−6 bond is favoured compared with a pair of such impurities.

Finally, water molecules are found to stably physisorb intact between neighbouring $PC_{60}BM$ molecules, as shown in Figure 2.7(d). This structure is associated with an E_b of 0.5 eV, a value significantly higher than the one related to the intact

physisorbtion of molecular O_2. Such enhanced stability has been explained by the presence of a hydrogen bond between the water molecule and the dangling O of the $PC_{60}BM$'s functional group. The distance between the O and the water's H is 1.93 Å.

2.4.2   Effects of impurities on the electronic properties

In the previous section, we discussed DFT results on the stability of impurity-related defective crystal structures of fullerene-based organic materials. What is even more interesting for the OE devices is to associate the stable conformations that may form during exposure to ambient conditions with possible modifications of the electronic properties.

To reveal possible effects resulting from the presence of impurities, the plot in Figure 2.8 shows the electronic density of states (DOS) of the pristine $PC_{60}BM$ molecular crystal (shaded area) compared with the electronic DOS of the defective configuration depicted in Figure 2.6(a), where an intact O_2 molecule stands between the $PC_{60}BM$ molecules. The arrows mark a pair of new states that appears close to the middle of the electronic band gap of $PC_{60}BM$. Such levels may act as deep-charge carrier traps or even promote charge recombination and concomitantly are expected to be detrimental for the performance of the material in OE devices. The presence of deep traps in $PC_{60}BM$ has also been reported by different experimental observations (Schafferhans et al., 2010).

The formation of the very stable structures shown in Figure 2.7 (a) and (b) has been associated with different effects than molecular O_2 on the electronic properties. As can
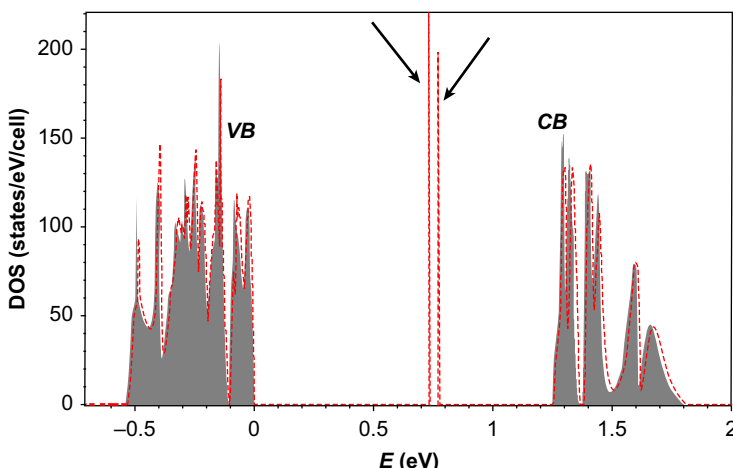
Figure 2.8 Density of states (DOS) plot of the pristine $PC_{60}BM$ molecular crystal (shaded area) and of the impurity-related configuration of Figure 2.6(a) (dotted line). VB, valence band; CB, conduction band.
Source: Adapted from Volonakis et al. (2013b).
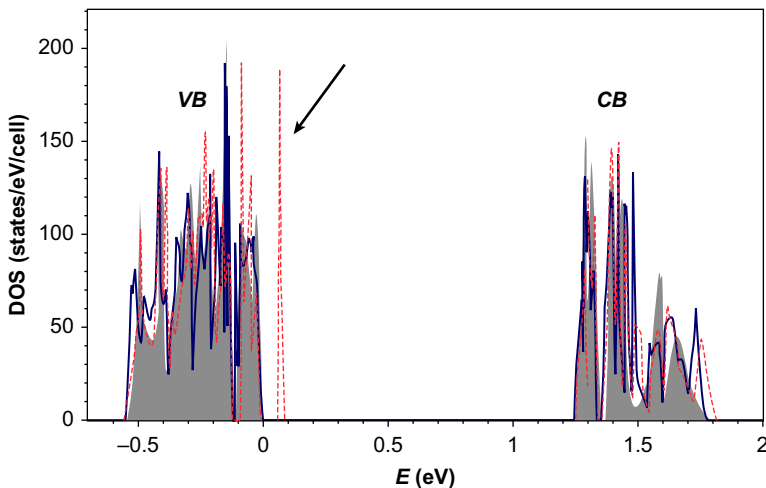
Figure 2.9 Density of states (DOS) plot of the pristine $PC_{60}BM$ molecular crystal (shaded area), of the impurity-related configuration of Figure 2.7(a) (solid line), and of the impurity-related configuration of Figure 2.7(b) (dotted line). VB, valence band; CB, conduction band. *Source*: Adapted from Volonakis et al. (2013b).

be seen by the DOS plot (solid line) in Figure 2.9 , the formation of epoxies on top of the 6−6 bonds of the C_{60} part has minimal effects close to the Fermi level of $PC_{60}BM$. On the other hand, a new state (dotted line) close to the valence band is formed when epoxies are attached on the 6−5 bonds shown in Figure 2.7(b). Such acceptor-like state will facilitate trapping of the charge carriers of the organic semiconductor decreasing its performance.

2.5 Summary and future trends

Over the past few years, modern computational approaches based on the DFT have emerged as a powerful tool to probe the structural and electronic properties of organic electronic materials. In this chapter, we have briefly reviewed the fundamentals of the DFT and described some of its current limitations that closely relate with the description of organic semiconductors. One notable issue with DFT-based calculations in organic semiconductors is the lack of proper description of the long-range, weak vdW forces that dominate the intermolecular interactions of the molecular crystals. To overcome this, we discussed a popular method, known as DFT-D, which is the addition of a semiempirical dispersion potential to the conventional Kohn−Sham energy.

Next, in the main part of the chapter, we presented selective computational results for the calculation of the atomic-scale details of the structural and electronic properties of fullerenes and their $PC_{60}BM$ derivative. At first, the stability of the known crystal lattices that the organic molecules form has been calculated and found to be close to available experimental data. Next, because polymorphism is important for OE materials, we presented in short, recent studies showing the continuous transformation

paths between the different known polymorphs of the C_{60} and $PC_{60}BM$ molecular crystals. The use of these transformation paths is well established for the case of inorganic materials, but is very new for probing polymorphs of molecular crystals.

Another topic discussed in this chapter is the use of theoretical DFT-based approaches to investigate the interactions between prototype impurity molecules (namely, oxygen and water) with fullerene molecules and their crystalline structures. We presented results that identify the structural details of the defective conformations that can be attained upon the interaction of oxygen species with the isolated molecules and furthermore when impurities are introduced inside the molecular crystals. The stability of these structures has been found, and the most energetically stable and thus favourable configurations are presented. Finally, for all these stable defective structures, the modifications of the electronic properties introduced by the presence of the impurities have been calculated. In this way, the theoretical calculations have been successfully used to associate specific defective configurations with distinct effects on the semiconductor's electronic properties, providing a way to better understand the exact mechanisms that underlie the deterioration of the performance of fullerene-based materials.

First-principles quantum-mechanical calculations based on the DFT have been successfully employed to address many different key issues of the OE materials. The continuing increase of available computational power together with the ongoing development and optimization of the employed methods and codes will enable further application of DFT-based theoretical approaches on even more complex and demanding questions regarding OE semiconducting materials that still remain unresolved.

References

Agafonov, V., Davydov, V. A., Kashevarova, L. S., Rakhmanina, A. V., Kahn-Harari, A., Dubois, P., et al. (1997). 'Low-pressure' orthorhombic phase formed from pressure-treated C_{60}. *Chemical Physics Letters, 267*, 193−198.

Becke, A. D. (1993). Density-functional thermochemistry. III. The role of exact exchange. *Journal of Chemical Physics, 98*, 5648−5652.

Chen, X., Yamanaka, S., Sako, K., Inoue, Y., & Yasukawa, M. (2002). First single-crystal X-ray structural refinement of the rhombohedral C_{60} polymer. *Chemical Physics Letters, 356*, 291−297.

David, W. I. F., Ibberson, R. M., Dennis, T. J. S., Hare, J. P., & Prassides, K. (1992). Structural phase transitions in the fullerene C_{60}. *Europhysics Letters, 18*, 219−225.

Davydov, V. A., Kashevarova, L. S., Rakhmanina, A. V., Senyavin, V. M., Céolin, R., Szwarc, H., et al. (2000). Spectroscopic study of pressure-polymerized phases of C_{60}. *Physical Review B, 61*, 11936.

Dion, M., Rydberg, H., Schröder, E., Langreth, D. C., & Lundqvist, B. I. (2004). Van der Waals density functional for general geometries. *Physical Review Letters, 92*, 246401.

Friák, M., Šob, M., & Vitek, V. (2001). Ab initio calculation of phase boundaries in iron along the bcc-fcc transformation path and magnetism of iron overlayers. *Physical Review B, 63*, 052405.

Grimme, S. (2006). Semiempirical GGA-type density functional constructed with a long-range dispersion correction. *Journal of Computational Chemistry, 27*, 1787−1799.

Grossiord, N., Kroon, J. M., Andriessen, R., & Blom, P. W. M. (2012). Degradation mechanisms in organic photovoltaic devices. *Organic Electronics, 13*, 432−456.

Hohenberg, P., & Kohn, W. (1964). Inhomogeneous electron gas. *Physical Review B, 136*, 864.

Iwasa, Y., Arima, T., Fleming, R. M., Siegrist, T., Zhou, O., Haddon, R. C., et al. (1994). New phases of C_{60} synthesized at high pressure. *Science, 264*, 1570.

Kaxiras, E. (2003). *Atomic and electronic structure of solids*. Cambridge: Cambridge University Press.

Kohn, W., & Sham, L. J. (1965). Self-consistent equations including exchange and correlation effects. *Physical Review A, 140*, 1133.

Kraft, T., Marcus, P. M., Methfessel, M., & Scheffler, M. (1993). Elastic constants of Cu and the instability of its bcc structure. *Physical Review B, 48*, 5886.

Lepoittevin, C., Alvarez-Murga, M., Marques, L., Mezouar, M., & Hodeau, J. L. (2013). Structural characterization of corrugated anisotropic graphene-based carbons obtained from the collapse of 2D C_{60} polymers. *Carbon, 52*, 278−287.

Lof, R. W., van Veenendaal, M. A., Koopmans, B., Jonkman, H. T., & Sawatzky, G. A. (1992). Band gap, excitons, and Coulomb interaction in solid C_{60}. *Physics Review Letters, 68*, 3924.

Moret, R., Launois, P., Persson, P.-A., & Sundqvist, B. (1997). First X-ray diffraction analysis of pressure polymerized C_{60} single crystals. *Europhysics Letters, 40*, 55−60.

Nápoles-Duarte, J. M., Reyes-Reyes, M., Ricardo-Chavez, J. L., Garibay-Alonso, R., & López-Sandoval, R. (2008). Effect of packing on the cohesive and electronic properties of methanofullerene crystals. *Physical Review B, 78*, 035425.

Núñez-Reguiro, M., Marques, N., Hodeau, J.-L., Béthoux, O., & Perroux, M. (1995). Polymerized fullerite structures. *Physics Review Letters, 74*, 278.

Okada, S., & Saito, S. (1999). Electronic structure and energetics of pressure-induced two-dimensional C_{60} polymers. *Physical Review B, 59*, 1930.

Papoular, R. J., Toby, B. H., Davydov, V. A., Rakhmanina, A. V., Dzyabchenko, A., Allouchi, H., et al. (2008). Single-crystal and synchrotron X-ray powder diffraction study of the one-dimensional orthorhombic polymer phase of C_{60}. *Chemical Physics Letters, 460*, 93−99.

Perdew, J., Ernzerhof, M., & Burke, K. (1996). Rationale for mixing exact exchange with density functional approximations. *Journal of Chemical Physics, 105*, 9982.

Pérez-Terrazas, J. E., Romero, A. H., & Terrones, M. (2008). Effects of novel and stable intermolecular connections in the mechanical and electronic properties of C_{60} polymerized structures. *Chemical Physics Letters, 458*, 128−133.

Reese, M. O., Nardes, A. M., Rupert, B. L., Larsen, R. E., Olson, D. C., Lloyd, M. T., et al. (2010). Photoinduced degradation of polymer and polymer−fullerene active layers: experiment and theory. *Advanced Functional Materials, 20*, 3476−3483.

Schafferhans, J., Baumann, A., Wagenpfahl, A., Deibel, C., & Dyakonov, V. (2010). Oxygen doping of P3HT: PCBM blends: Influence on trap states, charge carrier mobility and solar cell performance. *Organic Electronics, 11*, 1693−1700.

Seemann, A., Egelhaaf, H. J., Brabec, J., & Hauch, J. A. (2009). Influence of oxygen on semi-transparent organic solar cells with gas permeable electrodes. *Organic Electronics, 10*, 1424−1428.

Sirringhaus, H. (2009). Reliability of organic field-effect transistors. *Advanced Materials, 21*, 3859−3873.

Šob, M., Friák, M., Legut, D., Fiala, J., & Vitek, V. (2004). The role of ab initio electronic structure calculations in studies of the strength of materials. *Materials Science and Engineering A, 387*, 148−157.

Šob, M., Wang, L. G., & Vitek, V. (1997). Local stability of higher-energy phases in metallic materials and its relation to the structure of extended defects. *Computational Materials Science, 8*, 100−106.

Sohn, W. Y., Kim, T. W., & Lee, J. S. (2010). Structure and energetics of $C_{60}O$: a theoretical study. *Journal of Physical Chemistry A, 114*, 1939.

Terrones, H., & Terrones, M. (2003). Curved nanostructured materials. *New Journal of Physics, 5*, 126.

Tsetseris, L. (2005). Noncollinear magnetism of iron along the tetragonal Bain transformation. *Physical Review B, 72*, 012411.

Tsetseris, L. (2014). Functionalization of nanographenes: metallic and insulating hexabenzocoronene derivatives. *Journal of Physical Chemistry C, 118*, 1347−1352.

Tsetseris, L., & Pantelides, S. T. (2005). Atomic-scale mechanisms of selective adsorption and dimerization of pentacene on Si surfaces. *Applied Physics Letters, 87*, 233109.

Tsetseris, L., & Pantelides, S. T. (2007). Intercalation of oxygen and water molecules in pentacene crystals: first-principles calculations. *Physical Review B, 75*, 153202.

Tsetseris, L., & Pantelides, S. T. (2008). Large impurity effects in rubrene crystals: first-principles calculations. *Physical Review B, 78*, 115205.

Tsetseris, L., & Pantelides, S. T. (2009). Modification of the electronic properties of rubrene crystals by water and oxygen-related species. *Organic Electronics, 10*, 333.

Tsetseris, L., & Pantelides, S. T. (2010). Oxygen and water-related impurities in C_{60} crystals: a density-functional theory study. *Physical Review B, 82*, 045201.

Tsetseris, L., & Pantelides, S. T. (2011). Intermolecular bridges and carrier traps in defective C_{60}. *Physical Review B, 84*, 195202.

Volonakis, G., Tsetseris, L., & Logothetidis, S. (2012). Continuous transformation paths for the molecular crystals of the PCBM fullerene derivative. *Synthetic Metals, 162*, 2421−2427.

Volonakis, G., Tsetseris, L., & Logothetidis, S. (2013a). Continuous transformations of C_{60} crystals: polymorphs, polymers, and the ideal strength of fullerites. *Journal of Physics: Condensed Matter, 25*, 435303.

Volonakis, G., Tsetseris, L., & Logothetidis, S. (2013b). Impurity-related degradation in a prototype organic photovoltaic material: a first-principles study. *Organic Electronics, 14*, 1242−1248.

Weisman, R. B., Heymann, D., & Bachilo, S. M. (2001). Synthesis and characterization of the "missing" oxide of C_{60}: [5,6]-Open $C_{60}O$. *Journal of the American Chemical Society, 123*, 9720.

Wu, X., Vargas, M. C., Nayak, S., Lotrich, V., & Scoles, G. (2001). Towards extending the applicability of density functional theory to weakly bound systems. *Journal of Chemical Physics, 115*, 8748.

Yoo, S. H., Kum, J. M., & Cho, S. O. (2011). Tuning the electronic band structure of PCBM by electron irradiation. *Nanoscale Research Letters, 6*, 545.

Hybrid and nanocomposite materials for flexible organic electronics applications

3

S.R.P. Silva, M.J. Beliatis, K.D.G.I. Jayawardena, C.A. Mills, R. Rhodes, L.J. Rozanski
Advanced Technology Institute, University of Surrey, Guildford, UK

3.1 Introduction

Hybrid and nanocomposite materials can truly be considered advanced functional materials. Composed of more than one material, either chemically attached to one another or physically held in close proximity (Sanchez, Julian, Belleville, & Popall, 2005), they can be designed to produce different properties (permeability, electrical conduction, optical absorption, etc.) from their parent bulk materials. This ability to design a material's properties, controllable at the nanoscale, is driving the development of novel materials that are attractive for a variety of engineering disciplines. Organic electronics is one area that is benefiting significantly from the development of hybrid and nanocomposite materials, which can be integrated into all of the component layers of a device's architecture. These new materials have the potential to enhance the conductivity of the formed layers and improve durability as well as air/thermal stability, while retaining inherent flexibility for future flexible electronic devices.

Areas of organic electronics in which hybrid/composite materials are particularly beneficial are within inorganic hybrid solar cells (Greenham, Peng, & Alivisatos, 1996; Han et al., 2012, 2013; Huynh, Dittmer, & Alivisatos, 2002) and similar hybrid organic light-emitting diodes (Sessolo & Bolink, 2011; Vaynzof, Kabra, Brenner, Sirringhaus, & Friend, 2012). Here, solid-state inorganic semiconductors are replaced by a semiconducting polymer matrix incorporating inorganic nanoparticles (NPs). Compared with conventional inorganic semiconductor materials (i.e., silicon), which require energy-intensive production techniques, this new hybrid organic electronics technology can be developed at lower temperatures and processed from solution, dramatically reducing both energy and emission costs arising from production (Saunders & Turner, 2008). In this chapter, we will review the materials used in such hybrid and nanocomposite devices, concentrating on materials applicable to flexible organic electronic applications, and highlight the advantages and limitations of their use.

3.1.1 Definitions

A nanomaterial can be defined as being a material possessing at least one dimension that is less than 100 nm in length (Saunders & Turner, 2008). The interest in such nanoscale materials, and in particular NPs, is underpinned by the remarkable optical,
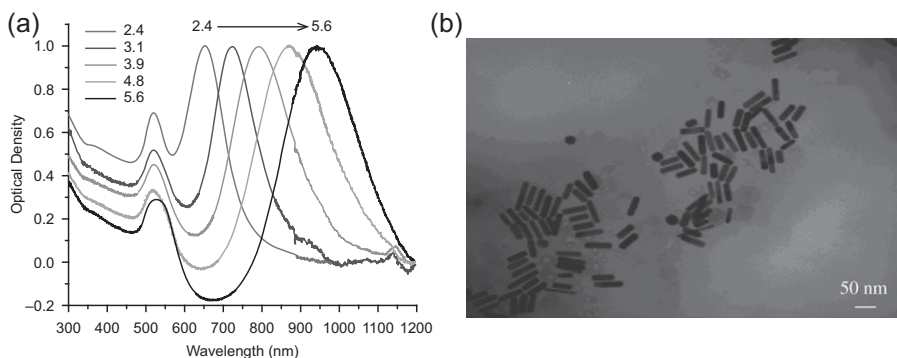
Figure 3.1 (a) Surface plasmon absorption spectra of gold nanorods of different aspect ratios, showing the sensitivity of the strong longitudinal band to the aspect ratios of the nanorods. (b) Transmission electron microscopy image of nanorods of an aspect ratio of 3.9.
Source: Reprinted with permission from Huang, X., El-Sayed, I. H., Qian, W., & El-Sayed, M. A. (2006). *Journal of American Chemical Society* 128, 2115−2120. Copyright (2006) American Chemical Society.

electrical, and physical properties gained by the material as the size or aspect ratio changes (Figure 3.1). These characteristic properties depend on the size and shape of the NP and can be tuned during synthesis by changing the processing conditions. The unique characteristics of NPs arise as the result of a phenomenon called size quantization, which occurs at nanometer dimensions (Weller, 1993).

The simplified structure of conventional inorganic semiconducting materials usually involves a crystalline lattice consisting of atoms of a single element or elements with the same valency (Bar Lev, 1993). The valence electrons of these atoms form the covalent bonds between the atoms that make up the lattice. In an intrinsic semiconductor, the valence electrons are tightly bound in the covalent bonds but thermal vibrations in the lattice can cause electrons to escape from their neighboring atoms to form conducting species (holes and electrons). Typically, however, the concentration of charge carriers is small, and it is necessary to modify the chemical structure of an intrinsic semiconductor to increase the number of mobile charge carriers significantly. Replacement of some atoms in the crystal lattice of the semiconductor with atoms of elements with higher (or lower) valency achieves this. This doping of the intrinsic semiconductor leads to the formation of an extrinsic semiconductor in which free charge carriers dominate its properties. When produced over large areas, these inorganic semiconducting materials are crystalline in nature and brittle, requiring energy-intensive processing methods such as high temperature and vacuum to achieve large-area crystal growth. Conversely, nanometric inorganic semiconductors can be produced using much milder processing conditions.

In contrast, the electrical properties of polymeric semiconductors are best explained by considering the earliest identified and simplest of semiconducting polymers, trans-polyactylene (Figure 3.2) (Skotheim, Elsenbamer, & Reynolds, 1998). This unsaturated polymer consists of C−H groups with alternating single and double bonds to
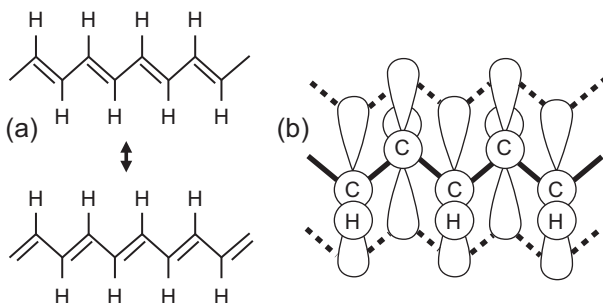
Figure 3.2 (a) Kekulé-type structures showing energetically identical conformers and (b) orbital structure showing the π-bonding orbitals of a section of trans-polyacetylene (C = carbon, H = hydrogen, solid lines = σ-bond, white dumbbell = π-orbital, dashed lines = π-bond).

their neighbors by overlapping σ- and π-orbitals, respectively. This conjugated system is interchangeable across the carbon atoms forming the polymer backbone, producing conformations of the polymer with identical energies. The discrete bonding model is actually a simplification in that the bonds between carbon atoms are hybrids rather than discrete bonds. The sp^2 hybrid orbitals on the carbon atoms involved in the π-bonding overlap with their neighbors to form a continuous system through which electrons can travel. Hence, polymers of this type are said to be quasi-metallic.

3.1.2 Historical overview

The word *nanocomposite* first became established in the scientific literature in the early 1990s (Scopus (http://www.scopus.com/home.url) search term: nanocomposite, July 1, 2013). Currently approximately 7000 journal articles (2010, 2011) use the term per year. Of these, 2400 articles (35%) mention the term *organic*, and of these approximately 500 mention the term *electronic*. The term *hybrid* has a longer history; it was first established in the 1960s and is currently mentioned in over 35,000 articles. Of these, 5000 also mention the term *organic*, and of these 1500 mention *electronic*. Whereas the first hybrid materials can be traced back to antiquity in the form of ancient paints, the modern technological equivalent, also in the paints industry, originated in the 1950s (Arkles, 2001).

3.1.3 Nanomaterials

Inorganic nanostructures typically used in hybrid and composite materials for flexible electronics applications invariably contain some electrically conducting character. Examples of such materials include carbon nanostructures, metal NPs, and transition metal oxides.

Carbon nanostructures used in hybrid and composite systems are based on carbon allotropes; the simplest of these is graphene. Graphene is a two-dimensional structure consisting of carbon atoms arranged in an sp^2-bonded hexagonal structure (Novoselov

et al., 2004). The advantages of using graphene in organic electronic devices include high carrier mobility ($\sim 2.6 \times 10^5$ cm^2/Vs) (Mayorov et al., 2011), high stability in air, and, for optoelectronic systems, an optical transmission approaching 97% at 550 nm for single layers (Tan et al., 2012).

Another commonly used carbon allotrope, carbon nanotubes (CNTs), consist of tubes of graphene (Iijima, 1991). These are classified depending on the number of coaxial tubes forming the CNT. For single-walled (SWCNT), double-walled (DWCNT), or multi-walled (MWCNT) (Saito, Dresselhaus, & Dresselhaus, 1998) CNTs, the properties of an individual CNT depend on the chirality of the tube. SWCNTs are further classified as being metallic or low band-gap semiconductors depending on their structure. MWCNTs, on the other hand, are metallic in nature because of the range of chiralities. The properties of MWCNTs have been more extensively defined, but SWCNTs are more complex owing to the difficulty in controlling chirality during growth. Recent developments have led to the production of hybrid CNT−polymer systems (Dabera et al., 2012; Nish, Hwang, Doig, & Nicholas, 2007), which has in turn allowed nanotubes with specific chiral properties to be isolated (Hersam, 2008).

Wide band-gap metal oxides are another class of material system that has recently attracted significant attention for use in organic electronics (Han et al., 2012, 2013). Metal oxides such as those based on titanium (TiO_2 or TiO_x), zinc (ZnO), molybdenum (MoO_3), vanadium (V_2O_5), nickel (NiO_3), and tungsten (WO_3) have typically been used in interfacial layers (Gilot, Barbu, Wienk, & Janssen, 2007; Han et al., 2009; Kim et al., 2006; Li, Chu, Shrotriya, Huang, & Yang, 2006; Park et al., 2010; Sun et al., 2011). Not only do the Fermi levels of these materials allow favorable electron or hole extraction, they are also known to be effective moisture and oxygen scavengers (Cho, Lee, & Heeger, 2009) and some even absorb damaging ultraviolet rays (Yang et al., 2010), resulting in prolonged lifetimes for organic electronic devices. High transparency in the visible region of the electromagnetic spectrum for thin films of these metal oxides makes them appealing as interfacial layers in organic electronics, but with their wide band gaps, some have been effectively used as part of the active layer. For example, ZnO NPs have been used as acceptor materials in organic solar cells (Han et al., 2013) and as emitters in organic light-emitting diodes (Periyayya, Kang, Ryu, & Hong, 2011; Son et al., 2012), which allows them to function within different layers of the organic electronic devices. Alternatively, TiO_x, created through the sol-gel process as both an electron transport layer and an optical spacer (to shift the light intensity maximum within the active layer), has been used to produce organic photovoltaics (OPVs) with nearly 100% internal quantum efficiencies (Park et al., 2009).

Metal nanostructures can similarly be used in organic electronic devices for increased light absorption, extraction, or enhanced charge transport. Gold (Au) and silver (Ag) have been widely investigated for improving organic optoelectronic device performance through proven electrical conduction, forming a new generation of transparent conductors (Hu, Wu, & Cui, 2011). These NPs display plasmonic effects (Ebbesen, Lezec, Ghaemi, Thio, & Wolff, 1998; Maier et al., 2003) and scatter light in the visible region of the electromagnetic spectrum (Beliatis et al., 2013).

3.2   Production methods

3.2.1   Processing

Metals such as Au have work functions that are exemplary for transport of electrical current within a device. However, incorporation of thin metal films into the device is not always practicable owing to high cost and/or blocking of light transmission. Therefore, there is interest in using metal grids or, more recently, metal NPs (NP) instead because these can be applied over large areas and onto flexible substrates. Metal NPs can be formed through a variety of methods including chemical synthesis (Grzelczak, Pérez-Juste, Mulvaney, & Liz-Marzán, 2008), thermal annealing (Ramesh, Porel, & Radhakrishnan, 2009), E-beam lithography (Kim et al., 2012), and laser annealing (Beliatis, Henley, & Silva, 2011), among others. Each of these different production techniques has benefits and limitations. Solution-processed metal NPs have well-controlled sizes but they can have dispersion and film quality limitations, and produce hazardous waste (Grzelczak et al., 2008). Thermal technologies, on the other hand, produce a variety of NP sizes but can be used to create NPs *in situ* (Beliatis et al., 2011) from pure metal films, although these methods require costly high temperatures and vacuum processing, which add complexity.

Typically, lithographic techniques do not normally translate to large areas, and therefore there has been much interest in using lasers for NP formation. There is a need to carefully match the desired metal NP size for use in organic electronics, depending on whether the need is for using localized surface plasmon resonances (LSPR), which can increase the light absorption cross-section for thin films (Bohren & Huffman, 1983) or for a physical scattering of light into or out of the device (Pillai, Catchpole, Trupke, & Green, 2007). LSPR tend to dominate in small NPs (between 2 and 20 nm in diameter), whereas scattering effects dominate in the larger NPs (over 50 nm in diameter). However, care is needed when attempting to incorporate metal NPs into a thin film device because they can cause electrical short circuits.

The initial use of transition metal oxides (TMOs) in organic electronics was through evaporation of thin layers, but as the need for flexible, large-area films increased, interest shifted toward using solution-processable NPs of TMOs. Different methods for forming high-quality TMO NP layers through solution methods include spin casting, printing, and spraying. Of these, the creation of TMO NPs follows two main techniques: formation using solution-processed methods, drying the end product NPs, and then dispersing them to form a colloidal solution; and doctor blading of TMO NPs *in situ* on a substrate from a precursor solution that is then annealed. Early dispersions of the colloidal TMO NPs required polymer or surfactant buffers to prevent agglomeration, which hindered their electrical function (Meyer, Khalandovsky, Görrn, & Kahn, 2011). Harsh plasma treatments could remove these insulating materials from the films, but the damaging effects were detrimental to most organic materials. Films made from the colloidal dispersions are of poor quality with high-surface roughness (Liu, Shao, Guo, Zhao, & Xie, 2010; Stubhan et al., 2012). However, TMO NPs grown *in situ* from sol-gel films produced smooth, well-formed thin films matching their evaporated counterparts in effectiveness (Chen, Chen, &

Chuang, 2011; Girotto, Voroshazi, Cheyns, Heremans, & Rand, 2011; Manders et al., 2013; You et al., 2012; Zilberberg et al., 2011). Nevertheless, problems remain with the sol-gel method; some films require temperatures up to 250 °C to form the NPs (Girotto et al., 2011; Zilberberg et al., 2011). To counter this problem, novel low-temperature synthesis approaches have been developed, using temperature ranges compatible with organic electronic materials (Jasieniak, Seifter, Jo, Mates, & Heeger, 2012; Xie et al., 2013).

Carbon nanotubes are mainly produced by three methods: (1) electric arc discharge, (2) laser ablation, and (3) chemical vapor deposition (CVD). Arc discharge produces both SWCNTs and MWCNTs with few defects, but requires considerable purification to remove carbonaceous byproducts. Conversely, laser ablation methods can produce both types of CNTs at a much higher purity than arc discharge ($\sim$90%), and with careful modification of the laser and catalyst can form predominately SWCNTs (Scott, Arepalli, Nikolaev, & Smalley, 2001). Chemical vapor deposition (CVD) growth allows for large quantities with high purity, which can also be grown where desired on a substrate (Boskovic, Stolojan, Khan, Haq, & Silva, 2002; Miller, Hatton, Chen, & Silva, 2007; Teo et al., 2001). Alternatively, CVD growth can be modified using photothermal methods to drastically decrease the growth temperature, allowing new types of substrates to be used (Chen, Jensen, Stolojan, & Silva, 2011; Shang, Tan, Stolojan, Papakonstantinou, & Silva, 2010).

The addition of CNTs to polymer solutions for incorporation in thin films can also be problematic because of their propensity to aggregate in solution or films. This creates rough and uneven surfaces, which can create electrical shorts within thin-film organic electronic devices. With a view to alleviating this problem, a principle issue in the work reported by Kymakis and Amaratunga (2002) was the dispersion technique. In it, carbon nanotubes were tip sonicated in solvent before adding the polymer. Although tip sonication leads to separation of nanotubes, which usually form bundles during growth, it is not known to be an efficient technique for separating individual nanotubes, because they will revert to a bundled state if further processing or additives such as surfactants are not used (Nismy, Adikaari, & Silva, 2010). Thus, various groups took the approach of modifying the CNTs themselves to enhance dispersion within a solution (Zhang et al., 2003). These chemically functionalized MWCNTs can be better dispersed in solution, but they can also then be combined with organic small molecules or polymers within the nanocomposite films. The use of functionalized MWCNTs to achieve better dispersion in a rr-poly(3-hexylthiophene) (P3HT) matrix was first reported by Pradhan, Batabyal, and Pal (2006). Although an improvement in the extracted photocurrent from a polymer solar cell was observed, unlike in the work reported by Kymakis and Amaratunga, Pradhan et al. attributed the improved charge extraction to the CNT's hole transport nature. Others have used the CNTs in low concentrations as active contributors to the optoelectronic device, as a separate charge acceptor in OPV (Nismy, Jayawardena, Adikaari, & Silva, 2011), or to enhance the brightness of OLEDs (Abdulbaki, Tangonan, Advincula, Randall Lee, & Krishnamoorti, 2012). The CNTs in these instances acted as high-mobility charge pathways or bridging sites for better percolation in the polymer phase (when used

with PC$_{61}$BM as an acceptor), or both. The success of integrating CNTs into polymeric materials paved the way for the development of active composites and hybrid materials.

Of more recent note, graphene has also found its way into organic electronic devices in the form of solution-processed graphene oxide (GO). Whereas graphene itself can be mechanically exfoliated from graphite (which does not produce even, large-area films) or grown under high-temperature/pressure conditions (CVD) similar to CNTs (producing higher-quality, flexible thin films but at higher cost (Tan et al., 2012)), there has been great interest in using it in a similar fashion as CNTs for organic electronics. Similar to the CNTs, graphite can be chemically functionalized and exfoliated to produce single or few layer sheets of water-soluble GO. This is most commonly achieved through the Hummer's method, in which the inexpensive graphite powder is oxidized using a mixture of sulfuric acid, sodium nitrate, and potassium permanganate, and then individual or a few layers of flakes of oxidized graphene are sloughed off via sonication (Hummers & Offeman, 1958). Because of the ability to tune its work function (Dreyer, Park, Bielawski, & Ruoff, 2010), GO can be used in organic electronics to inject or extract holes (Li, Tu, Lin, Chen, & Chhowalla, 2010) and can be reduced to enhance the conductivity of the final film (Yun et al., 2011). Graphene oxide can also undergo further chemical modification (Liu et al., 2012), lowering its work function from 4.7 to 4.0 eV to facilitate electron injection and extraction between the active layers of the organic electronic device and its external electronics.

3.2.2 Composite material production

The simplest method for forming inorganic−organic composite materials is to disperse the already formed inorganic NPs into an organic matrix, either by mixing the soluble NPs into a solvated polymer or organic host and then forming a film from the composite solution, or by applying the NPs separately to a surface and coating them with the organic layer. This has been achieved for thin interfacial layers and as part of the active layer in organic electronic devices. One example of enhancing the properties of an existing (semi) conducting polymer material is the introduction of metal NPs coated with surfactants into a matrix of poly(3,4-ethylenedioxythiophene) poly(styrene sulfonate) (PEDOT:PSS); a widely used solution-processable hole transport layer (HTL). The incorporation of metal NPs (Au or Ag) in PEDOT:PSS-containing polymer solar cells has produced improvements in power conversion efficiency (PCE) in combination with active layers of rr-P3HT: PC$_{61}$BM (Beliatis et al., 2013; Chen et al., 2009; Kim, Kang, Guo, & Kim, 2008; Lee, Park, Kim, Lee, & Cho, 2009; Morfa, Rowlen, Reilly, Romero, & Van De Lagemaat, 2008), MEH-PPV (Qiao et al., 2011), PCDTBT: PC$_{71}$BM (Baek et al., 2013), and PTB7:PC$_{71}$BM (Baek et al., 2013). Incorporation of both Ag and Au NPs into PEDOT:PSS OPV containing PTB7:PC$_{71}$BM resulted in a PCE of 8.67% (Lu, Luo, Xu, & Yu, 2012), the highest reported so far for photovoltaics incorporating metal NPs. Such a result demonstrates the importance of incorporating such nanostructures in polymer composites for OPVs.

The use of CNTs incorporated into a conjugated polymer matrix for polymer solar cells was originally proposed by Ago, Petritsch, Shaffer, Windle, and Friend (1999)

and is a concept that has been revived (Dissanayake & Zhong, 2010; Hatton, Blanchard, Stolojan, Miller, & Silva, 2007; Miller et al., 2007; Scharber et al., 2006). After the initial reports on MWCNTs as a hole acceptor, the next generation of polymer/CNT composites was developed with the aim of using nanotubes as an electron transport material, in which SWCNTs were used in conjunction with poly(3-octylthiophene) (P3OT) (Kymakis & Amaratunga, 2002) in place of the widely used fullerene derivatives. The observed PCE increase was attributed to the enhanced exciton dissociation at the polymer−nanotube interface.

Transition metal oxide NPs have also been used in this manner to form composite films, with the use of hybrid ZnO-reduced GO (rGO) nanoparticles used as part of the active layer within an OLED to produce white light (Son et al., 2012) and mixed with an electron-transporting small organic molecule host, a lithium quinolate complex (Liq), to produce a stable, high-efficiency interfacial layer (Chiba et al., 2012). Zinc nanowires used as an acceptor instead of PCBM provided PCEs up to 0.4%: their wide band-gap nature makes them appealing as acceptor materials (Abdulalmohsin & Cui, 2012). A secondary method for forming inorganic−organic composite layers is to grow inorganic nanomaterials *in situ* from precursors that have been previously mixed with the organic material. This has been completed successfully for ZnO NPs grown slowly within the active P3HT polymer matrix as it dries in a humid environment, followed by a low-temperature annealing step to produce devices with 1.22% PCE (Han et al., 2013).

3.2.3 Hybrid NP synthesis

Sanchez et al. (2005) have detailed some chemical synthesis routes for the fabrication of hybrid NPs using methods such as self-assembly, sol-gel, hydrothermal growth, and host−guest chemistry (Figure 3.3). We have covered sol-gel and hydrothermal
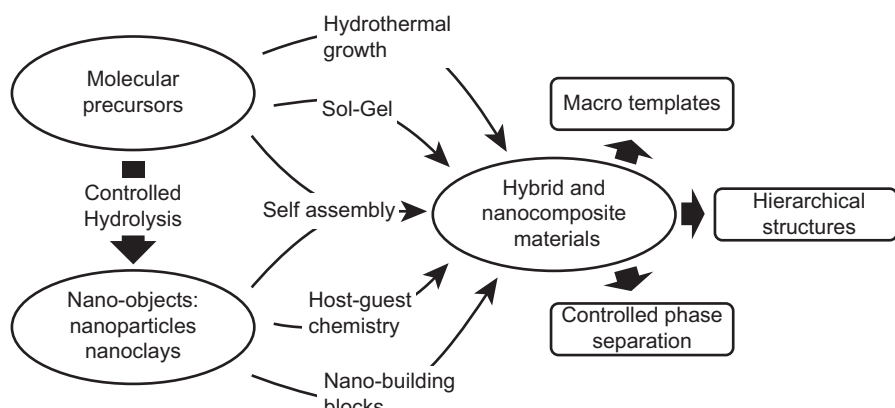

Figure 3.3 Scheme of the main chemical routes for the synthesis of organic−inorganic hybrids. *Source*: Sanchez et al. (2005).

methods for the NP synthesis in section 3.2.1; here, we will focus on the techniques used to form organic−inorganic hybrids, or the inorganic hybrids used in organic electronics. One common method is that of self-assembly, which has been used for a variety of materials. For example, self-assembly occurs during the noncovalent functionalization of CNTs, although self-assembly of solubilized CNTs that have undergone covalent functionalization also occurs to some degree when mixed into an organic host. These functionalization methods are more common because they facilitate smooth, well-dispersed CNT films without inhibiting conductivity. Covalent functionalization occurs through chemical modification of the CNT sidewall, either through acid treatments that introduce hydroxyl and carboxyl groups or through the direct attachment of small molecule or polymer chains via further chemical modification (frequently using amine groups to bond with the oxidized defects that have been created through acid treatment) (Banerjee, Hemraj-Benny, & Wong, 2005).

Metal NPs have been attached to carbon nanotubes in an attempt to combine their positive traits, such as the flexibility and strength of the CNT with the plasmonic and scattering effects of the metal NP. This is achieved through organic attachment groups allowing attachment directly to the NP or through an organic covering monolayer (Satishkumar, Vogl, Govindaraj, & Rao, 1996), although they have also been attached through noncovalent means: by hydrophobic interactions or hydrogen bonding of the organic surface passivation of the metal NPs or by growing the metal NPs from precursors through reduction or thermal methods (Georgakilas et al., 2007). While creating water-soluble CNTs, covalent functionalization damages the nanotube sidewalls, which can decrease conductivity in the final film. Noncovalent functionalization, in which small molecules or polymers adhere to the sidewall through Van der Waals forces or π−π stacking, leaves the CNTs undamaged although soluble in common solvents. This has been demonstrated for the spontaneous wrapping of CNTs by a conjugated polymer, P3HT (Dabera et al., 2012), and by a similar π−π stacking and spontaneous self-assembly of phthalocyanine small molecules onto MWCNTs (Hatton et al., 2007), in both cases creating a true organic−inorganic hybrid material in which the CNT acts either as an acceptor or donor.

As soluble flakes of GO are essentially unzipped carbon nanotubes, they can be functionalized in the same manner as the CNTs. Spontaneous assembly of phthalocyanine molecules on GO in solution produced a stable hybrid with a demonstrated photoresponse, which shows that the GO can act as a charge collector from the organic material (Zhang, Feng, Tang, & Feng, 2010). In addition, GO can be used as part of inorganic−inorganic hybrids, which can then be combined with organic materials to produce further hybrid layers. Graphene oxide has been reduced in a solution-thermal process with ZnO precursors to form a novel, stable ZnO NP hybrid wrapped with a single layer of reduced GO, which is used as part of the emitting layer in OLEDs (Son et al., 2012). A similar but simpler technique was developed using prefabricated NPs of ZnO or TiO_2/TiO_x, which are combined in solution with GO and hydrothermally reduced. This was then used as an effective electron transport layer in OPV (Jayawardena, Prabhath, Dabera, & Silva, 2013).

Nanoparticles, in particular metal NPs, often require some sort of functionalization, usually a ligand coating to retain solution solubility and prevent aggregation.

Ligands made from surfactants will spontaneously coat the formed NPs in solution, whereas more specific ligands (such as those with thiol end groups) will preferentially order and bond to the metallic surface. These ligands tend to have solubilizing end groups, which are frequently long alkyl chains (Kamat, 2002). Although when combined with organic materials, metal NPs can frequently act as trapping sites, quenching charge transport/light emission from the organic material (Xue et al., 2011), even with capping ligands, it is possible to prevent this with inorganic/nonconducting insulator caps on metal NPs in a core shell configuration (Brown et al., 2010). Further organic—inorganic hybrids have been functionalized with organic dyes through spontaneous self-assembly, demonstrating successful charge transfer between the dye and the NPs (Liu, Sanyasi Rao, & Nunzi, 2011).

3.3   Properties

3.3.1   Electrical conduction

Organic materials with the requisite potential for conduction (hybrid atomic orbitals on carbon allowing the overlap of π—bonds and the formation of highest occupied molecular orbital and lowest unoccupied molecular orbital states with a small enough band-gap for charge carrier promotion) can now be designed by paying attention to the requirements for energy-level matching to contact electronics and environmental stability (Bernius, Inbasekaran, O'brien, & Wu, 2000; Mcgehee & Heeger, 2000). However, the nature of charge carriers in semiconducting polymers is more complex than for inorganic semiconductors because any alteration in the electronic structure of the atoms in the polymer may cause a change in the structural configuration of the polymer around that atom. As a result, excitations such as the production of electrons and holes can cause chain distortions to occur in the surrounding polymer, leading to the formation of solitons, polarons, and bipolarons (Mcgehee, Miller, Moses, & Heeger, 1999). These lattice distortions and Coulomb interactions should be included in any description of the structure of conjugated polymers. The nanometric inorganic component is then designed with processing requirements and complementary properties in mind. Electrical conduction in nanocomposite materials depends on the conduction pathways through the active materials and any barriers to conduction at the interfaces between materials and electrical contacts or within the materials themselves.

Typically, conduction mechanisms in bulk semiconductor materials can be described based on the limiting conduction pathway, either through the bulk of the semiconductor (Frenkel, 1938; Lampert, 1956; Rakhmanova & Conwell, 2000) or at the electrode interfaces (Fowler & Nordheim, 1928; Parker, 1994). These conduction mechanisms can be analyzed using direct current or small-scale alternating current techniques allied to spectroscopic data elucidating the energy levels occurring in the organic materials (Taylor, 2006).

In photovoltaics, the photogeneration of free carriers (in inorganic Si or GaAs, for example) or excitons (in organics, which are dissociated to form free carriers) can

be undertaken in semiconducting materials when exposed to photons with energies exceeding their optical band-gap (Adikaari, Dissanayake, & Silva, 2010). SWCNTs are inorganics known to be an exception to this rule, because they generate excitons upon photoexcitation owing to their one-dimensional nature. Once separated, these charges can be swept through a device via a built-in field and extracted at electrical contacts. Carbon-based allotropes have excellent energy-level matching to organic semiconductors and electrodes, and display high thermal, oxidative, and chemical stability. The ability to functionalize carbons with a plethora of moieties allows the work function and affinities of carbon-based materials to be tuned for either electron or hole transport or injection. Similar to CNTs, graphene is another material system that has primarily been used as a hole transport layer in its oxidized form. When oxidized, graphene (or GO) is known to be water soluble with a lower work function compared with pristine graphene, which makes it better for hole injection and extraction.

This ability to tune energy levels through chemical modification also allows the carbon materials to function for electron injection (of which there are fewer materials available) instead of hole injection. MWCNTs can have their outer walls nitrogen doped, lowering their work function from 4.6 eV for the pristine nanotubes to 4.4 eV (Lee et al., 2011) (conversely, boron can be added to make CNTs more p-type). This lowered work function makes them suitable for electron injection into a device, and unlike the more common electron transport materials, they do not degrade with exposure to water or oxygen. In a similar fashion, GO can have its acid groups esterified (Liu et al., 2012), lowering its work function by 0.7 eV.

The widespread use of MWCNTs in place of SWCNTs is generally a result of the uniformity of their electronic properties. Whereas pristine MWCNTs have a work function of $\sim$4.8 eV (Dissanayake & Zhong, 2010), photoelectron spectroscopic and Kelvin probe measurements revealed a work function of 5.1 eV for functionalized MWCNTs (Hatton et al., 2009; Miller, Hatton, & Silva, 2006). Tuning of the work function is likely to facilitate selective charge transport through the nanotubes. Much like silicon, CNTs have been found to be doped p- or n-type through the incorporation of group III or V elements into defect sites created in the tube. In this regard, boron and nitrogen doping has been reported (Lee et al., 2011) because of the ease with which such elements can be incorporated into the nanotube structure. Going one step further, Lee et al. (2013) Indium Phosphide (InP) quantum dots attached to CNTs, in which the InP:CNTs, much like in the work of Nismy et al. (2011), are used to improve exciton dissociation and charge transfer (in this case, electrons) into the nanotubes.

Work on incorporation of carbon nanotubes has been expanded into low band-gap polymers (Lu et al., 2013). MWCNTs incorporated into organic photovoltaic active layers led to an improvement in PCE attributed to increased light coupling, exciton dissociation, and charge transport as a result of incorporation of nanotubes into the active layer.

3.3.2 Support organics

Support organic materials can be separated into two main areas: small organic molecules and organic polymers. Small organic molecules have production advantages, with less

variation in their structural conformation than polymers. They can be evaporated or solubilized, allowing particularly uniform thin films to be produced, and they tend to be more environmentally stable than their polymer counterparts. One example of a common small molecule used in organic light-emitting diodes is tris(8-hydroxyquinolinato) aluminum (AlQ_3), a coordination complex of aluminum bidentate bonded to three 8-hydroxyquinoline ligands. Various substituents can be added to the quinoline rings to affect its luminescence properties (Montes, Pohl, Shinar, & Anzenbacher, 2006).

Organic polymers, by comparison, are highly flexible when it comes to chemical modification. The addition of solubilizing moieties impart solubility, and it is possible to design block copolymers that produce order spontaneously within a thin film to improve charge separation or recombination. For example, PEDOT:PSS is a conductive polymer mixture composed of two constituents: a conjugated polymer, PEDOT and a polyelectrolyte, PSS. Whereas PEDOT itself exhibits many favorable characteristics, including exceptional conductivities ($\sim$300 S/cm), high environmental stability (Kvarnström et al., 1999), and almost total transparency within the visual spectrum, it remains insoluble in industrial solvents unless mixed with PSS (Groenendaal, Jonas, Freitag, Pielartzik, & Reynolds, 2000). As a composite, PEDOT:PSS has found extensive use within the field of organic electronics, most notably as an HTL in OPVs (Brabec, Dyakonov, & Scherf) and OLEDs (Kim et al., 2002), but also as electrodes in capacitors and dye-sensitized solar cells (Hong, Xu, Lu, Li, & Shi, 2008).

Despite these favorable characteristics, PEDOT:PSS has a number of drawbacks. First, it is known that common PEDOT:PSS solutions are highly acidic and at temperatures above 100 °C, can potentially solubilize ITO (Wong et al., 2002). This can result in indium contamination of the interface layer, and even a small amount may affect the work function of the material and impede the function of the device (Girtan & Rusu, 2010). This contamination effect is exacerbated when the device is exposed to air, owing to the highly hygroscopic nature of PSS and the resultant formation of aqueous acidic solutions (in the form of H_3O^+ ions) that can serve to transport indium throughout the HTL layer (De Jong, Van Ijzendoorn, & De Voigt, 2000). The formation of hydronium ions will also result in the degradation of organic components within the photoactive layer, which are frequently sensitive to moisture and oxidative attack (Sutherland et al., 1996). The combination of all these effects is a negative impact on device stability, and research is currently underway to discover materials that can replace PEDOT:PSS without sharing its detrimental qualities (Yun et al., 2011).

3.4 Limitations

3.4.1 Electrical

As with any novel field of work, the incorporation of NPs in a polymer system can appear to produce contradictory literature results. For example, Wang et al. (2011) suggested that metallic NPs produce an improvement in carrier extraction in OPV, supported by a drop in series resistance and improved short circuit current density. On

the other hand, Xue et al. (2011) claimed improvement in mobility owing to metal NPs but a loss in carrier extraction as a result of the metal NPs acting as charge trapping sites. This confusion is compounded by the magnitude of possible combinations of materials and device architectures using hybrid materials and nanocomposites. Future experimentation and examination of the electrical properties will elucidate the specific conduction mechanisms occurring, which are likely to be influenced by their environment and processing.

Carbon allotropes have their own problems. One important property of carbon nanotubes, whether SWCNT or MWCNT, is the unique electrical property that results in ballistic charge transport (Saito et al., 1998). Unfortunately, charge transport in CNT networks is often impaired by junction barriers (Javey, Guo, Wang, Lundstrom, & Dai, 2003) that lead to mobility of less than 1 cm^2/Vs. However, the mobility achievable by CNT networks remains sufficient to improve organic electronics because of the low mobility found in polymer semiconductors (typically less than 10^{-3} cm^2/VS) (He et al., 2011). Despite widespread use of carbon nanotubes within organic semiconductors, there is debate on the part of the scientific community regarding the role of the carbon nanotubes (Jayawardena, Rozanski, et al., 2013). Certain groups claim nanotubes to be a hole transporter (Ago et al., 1999; Berson, De Bettignies, Bailly, Guillerez, & Jousselme, 2007; Nismy et al., 2011); others claim that nanotubes are an electron transporter (Schuettfort, Nish, & Nicholas, 2009; Kymakis & Amaratunga, 2002, 2005; Saito, 1998).

Likewise, the outstanding electrical properties of graphene have only been reported for micromechanically cleaved graphene samples, with large-area graphene produced through CVD displaying poorer charge transport properties (Tan et al., 2011, 2012). Another disadvantage of CVD-deposited graphene has been the requirement for etching of the copper foil used for graphene growth and subsequent transfer techniques. The latter results in organic residues (Park et al., 2012) on the graphene sheet, which significantly affect its transport properties (Tan et al., 2011). As a result, attempts at graphene synthesis focused on preparation of graphene solutions (Wu et al., 2009) that can be printed (Torrisi et al., 2012) or deposited on substrates using methods compatible with roll-to-roll processes.

3.4.2 Physical

Careful control of morphology during NP synthesis and processing conditions during film preparation is required to prevent separation of the polymer and NP phases (Saunders & Turner, 2008). For example, prepared CNTs tend to aggregate in bundles and do not easily disperse unless they are treated with surfactant (decreasing film conductivity) (Jo, Jung, Lee, & Jo, 2010) or functionalized with soluble small molecules or polymers through covalent (Hatton et al., 2009) and noncovalent techniques (Dabera et al., 2012; Hatton et al., 2007). Similarly, the most common route to make GO is through the Hummer's method, in which inexpensive graphite powder is oxidized using a mixture of sulfuric acid, sodium nitrate, and potassium permanganate, from which individual or few layers of flakes of oxidized graphene are exfoliated via sonication (Hummers & Offeman, 1958). Similar to covalent functionalization

of CNTs, this oxidation process disrupts the conductivity of graphene, making it more insulating.

In a similar fashion, it has often been necessary to use a solubilizing ligand to prevent aggregation of NPs within a solvent. However, the requirement for this ligand can cause problems itself. In particular, long ligand molecules (such as oleic acid) can create a layer surrounding the NP, inhibiting the properties of the NP, such as electrical conductivity or surface area effects. One solution is to exchange long ligands with smaller molecules that can then be evaporated from the final film (Saunders & Turner, 2008). This can assist in allowing the properties of the NP to be accessed, but the use of shorter ligands can reduce the effect of steric stabilization, resulting in aggregation either in dispersion or during solvent evaporation (Saunders & Turner, 2008). Investigations into the effect of the ligand upon charge transfer (Pientka et al., 2004) showed that the use of shorter ligands such as pyridine can result in enhanced charge transfer. An additional problem is that the ligands used are frequently incompatible with the chosen polymer (Balazs, Emrick, & Russell, 2006), resulting in phase separation and the formation of large NP or polymer domains. As a result, it has been necessary to develop more compatible ligands or directly link the NP to the polymer to produce a hybrid material (Liu, Tanaka, Sivula, Alivisatos, & Fréchet, 2004).

The effect of solvents and heat treatment upon the final film morphology also needs to be considered, with rearrangement of the components in the material giving a more amorphous or crystalline phase. This can be particularly important for organic optoelectronic applications (Huynh, Dittmer, Libby, Whiting, & Alivisatos, 2003). It has been noted that NP/polymer blends are inherently immiscible and during spin coating will undergo phase separation and form extensive, aggregated domains (Saunders & Turner, 2008). Different groups have attempted to improve the interactions between the organic and inorganic phases, using, for example, precursors (Beek, Slooff, Wienk, Kroon, & Janssen, 2005) or ligand or polymer functionalization (Liu et al., 2004). One solution is to pre-prepare the inorganic layer by producing, for example, vertically aligned nanorods (Takanezawa, Hirota, Wei, Tajima, & Hashimoto, 2007) or hyperbranched semiconducting nanocrystals (Gur, Fromer, Chen, Kanaras, & Alivisatos, 2007) before integrating the conjugated polymer. However, incorporation of polymers into a nanostructured inorganic layer has proved difficult owing to the highly hydrophobic nature of the NP layer (Saunders & Turner, 2008).

3.5 Electronics applications

3.5.1 Materials

Hybrid and nanocomposite materials can be used for a number of materials applications within flexible organic electronics devices. We have shown that these materials can be used within the active layers in devices for organic electronics and optoelectronics. The organic component of these hybrid systems, the semiconducting polymers, provides numerous advantages over conventional bulk inorganic semiconductors such as silicon. Compared with silicon, conjugated polymers are cheap to produce and are

soluble in organic solvents, which allows for films to be cast from solution by processes such as spin coating (Rhodes et al., 2010), inkjet printing (Sirringhaus et al., 2000), and screen printing (Pschenitzka & Sturm, 1999), and because conjugated polymers can be used to manufacture flexible films, it is also possible to employ large-scale roll-to-roll manufacturing processes (Coakley & Mcgehee, 2004; Koidis, Logothetidis, Ioakeimidis, Laskarakis, & Kapnopoulos, 2013; Logothetidis, 2008), increasing production rates. Unlike the extremely high temperatures required for the extraction and refinement of electronics-grade silicon (Horie et al., 2008), all of these processes can potentially be performed at room temperature and under ambient conditions.

As stated previously, the nanomaterial incorporated in the organic layer introduces its own desirable properties. For example, the high transparency and electron conductivity of the fullerenes ensured that they received particular attention for use in organic electronics, and OPVs in particular (Delgado, Bouit, Filippone, Herranz, & Martín, 2010; Spanggaard & Krebs, 2004). For example, the use of PCBM (Figure 3.4) (Hummelen et al., 1995; Yu, Gao, Hummelen, Wudl, & Heeger, 1995) in a polymer/fullerene PV cell is currently the most widely studied form of polymer-nanomaterial photovoltaic cell (Hoppe & Sariciftci, 2008).

3.5.2 Applications

Various examples of flexible electronics applications in which hybrid and nanocomposite materials may be used have been referred to earlier in this chapter, and reviews of further application examples can be found later in this book or in the literature, e.g., (Merhari, 2009; Nalwa, 2003; Sanchez et al., 2005). Typically, for organic electronics, hybrid and nanocomposite materials are used as sensor materials, coatings and barriers, optical and optoelectronics devices, batteries, and ionic conductors such as proton exchange materials. Typically, electrical switching components such as field effect transistors have been studied using hybrid and composite materials, but other organic electrical components, such as capacitors and memory elements, can also be developed. Other more exotic applications, such as piezoelectric composites, have also
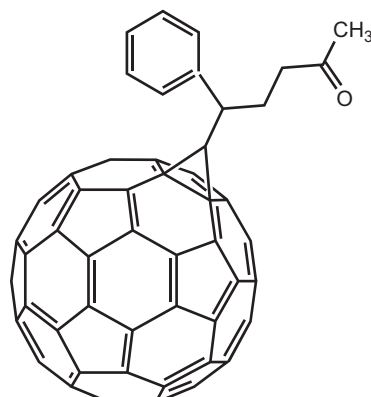

Figure 3.4 Chemical structural of [6,6]-phenyl C61 butyric acid methyl ester (PCBM).

been developed (Wang, 2012), which illustrates that hybrid and nanocomposite materials can be used throughout the energy generation and usage cycle.

However, it is in optoelectronics where hybrid and nanocomposite materials have perhaps found their strongest niche. Within optoelectronic devices such as OPVs and light-emitting diodes, for example, the hybrid/composite materials can be used in a variety of areas within the device architecture, from the active photoemitter/photoabsorber to the electrical transport and blocking layers, to encapsulation and barrier coatings, and even to the electrical contacts (as long as the added nanomaterial does not quench the generated excitons or emitted light).

Photovoltaic cells are constructed from either inorganic semiconducting materials, such as silicon (Chapin, Fuller, & Pearson, 1954) or germanium (Isomura et al., 2002), and so forth, or organics such as P3HT (Padinger, Rittberger, & Sariciftci, 2003) or poly(triarylamine) (Madec, Morrison, Rabjohns, Turner, & Yeates, 2010), etc. As we have discussed, hybrid devices use both in concert, blending inorganic NPs into a semiconducting polymer matrix (Huynh et al., 2002). The polymer−NP hybrid solar cell, for example, is based on the bulk heterojunction concept developed for organic devices, and involves the juxtaposition of inorganic NPs with a semiconducting polymer to form a photoactive layer (Saunders & Turner, 2008). The use of different NPs enables the use of different *n*- or *p*-type semiconductors (which can be further chemically modified) to optimize the device to maximize efficiency (Günes & Sariciftci, 2008). Indeed, photovoltaics is an area in which a defined technology progression can be seen leading to the current use of hybrid and nanocomposite materials. The development of OPVs integrating hybrid/nanocomposite materials points to the next generation of this technology (Figure 3.5) in which control of the material properties at the nanoscale has a marked effect on the efficiency of the final device (Jayawardena, Rozanski, et al., 2013).

The first generation (1G) of photovoltaics was originally defined for inorganic materials as high-cost/high-efficiency, mainly thick crystalline (typically silicon) films. Low-cost/low-efficiency, second-generation (2G) photovoltaics are based on the use of thin-film technology, in which cost reduction occurs through a saving in the bulk material cost, but with a consequently lower performance. The key factor that worked in favor for 2G photovoltaic cells was the cost per watt delivery, but the need for extended surface areas to compensate for the lower efficiency is an issue. Third-generation (3G) solar cells include nanocrystalline films, active quantum dot photovoltaics, tandem or stacked multilayers of inorganics, or novel device concepts such as hot carrier cells (Green, 2001), in which the aim is to obtain higher performance than their 2G counterparts, at lower cost. The currently modest success of 3G cells suggests that significant improvements in device performances are still required if this technology is to be competitive with previous generations in terms of cost per watt. As a consequence, the fourth generation (4G) of photovoltaics technology combines the low cost and flexibility of organic thin films with the stability of novel inorganic nanostructures, with the aim of improving the optoelectronic properties (Jayawardena, Rozanski, et al., 2013). These new device architectures, incorporating novel hybrid and nanocomposite materials, will pave the way towards the performance levels necessary for next-generation photovoltaic solar cells to rival those of their analogous inorganic systems.
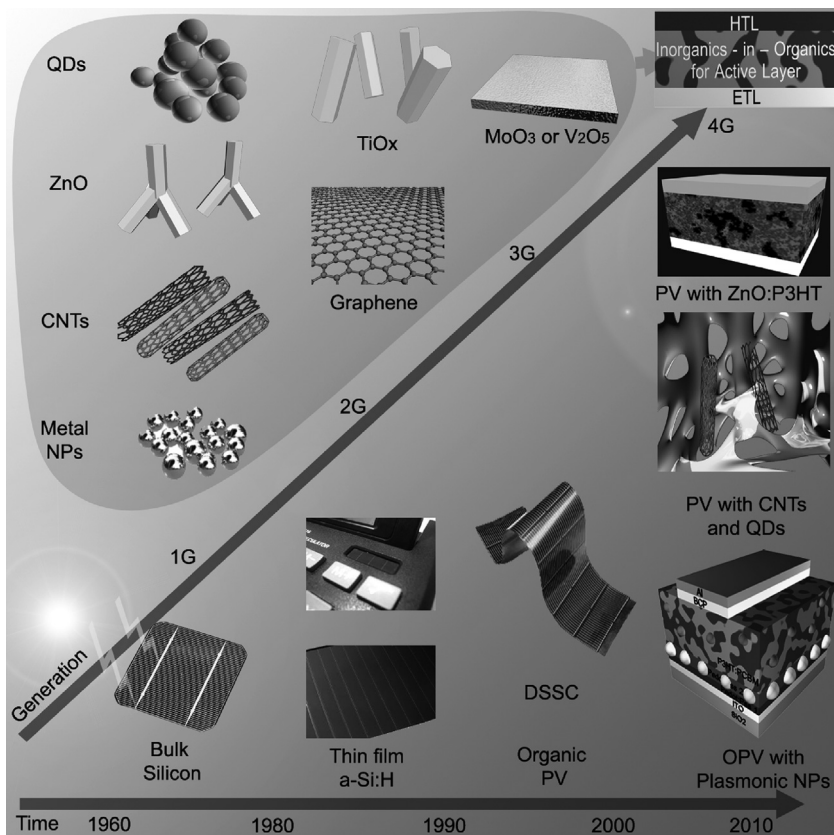
Figure 3.5 Timeline of the development of photovoltaic devices, from first-generation (1G) bulk silicon to fourth-generation (4G) flexible, hybrid/nanocomposite devices. Examples of associated nanomaterial components, integrated into the 4G devices, are also illustrated. *Source*: Jayawardena, Rozanski, et al. (2013) – Reproduced by permission of The Royal Society of Chemistry.

3.6   Future trends

Organic electronics has benefited from the development of hybrid and nanocomposite materials: a family of truly "advanced materials" designed and built at the nanoscale. These materials will lead the way in reducing the cost of future generations of flexible electronics and provide a myriad of properties to enhance the performance of existing organic electronic devices, and/or add value to them, as well as provide a basis for the production of future, novel electronics technologies. The production of hybrid and nanocomposite systems has already had a marked effect in improving the previous generation of organic-only semiconductor devices, but a number of hurdles need to be overcome before these hybrid/nanocomposite systems display performances rivaling their established solid-state inorganic counterpart devices. However, because

of the potentially wide range of available organic semiconductors (both small molecule and polymeric) and NP types (carbon allotrope, metal oxides, etc.), there is immense scope for the future of flexible organic electronics.

3.7   Sources of further information and advice

The two-volume *Handbook of Organic-Inorganic Hybrid Materials and Nanocomposites* (Nalwa, 2003) covers many aspects of organic−inorganic hybrid material and nanocomposite production and characterization, including topics on molecular building blocks; synthetic production routes; sol-gel chemistry; ultrathin film processing; fibers; xerogels; spectroscopic characterization; mechanical, thermal, electronic, optical, catalytic, and biological properties; organic−inorganic interfaces; and commercial applications. A more up-to-date focus on applications of these materials can also be found in *Hybrid Nanocomposites for Nanotechnology* (Merhari, 2009), with different examples of magnetic and electrical, optical, and biomedical applications.

Acknowledgements

References

Abdulalmohsin, S., & Cui, J. (2012). Graphene-enriched P3HT and porphyrin-modified ZnO nanowire arrays for hybrid solar cell applications. *The Journal of Physical Chemistry C, 116*, 9433−9438. http://dx.doi.org/10.1021/jp301881s.

Abdulbaki, M. K., Tangonan, A., Advincula, R. C., Randall Lee, T., & Krishnamoorti, R. (2012). Properties of single-walled carbon nanotube-based poly (phenylene vinylene) electroluminescent nanocomposites. *Journal of Polymer Science Part B: Polymer Physics, 50*, 272−279. http://dx.doi.org/10.1002/polb.23007.

Adikaari, A. A. D. T., Dissanayake, D. M. N. M., & Silva, S. R. P. (2010). Organic & inorganic solar cells: recent developments and outlook. *Selected Topics in Quantum Electronics, IEEE Journal of, 16*, 1595−1606. http://dx.doi.org/10.1109/JSTQE.2010.2040464.

Ago, H., Petritsch, K., Shaffer, M. S., Windle, A. H., & Friend, R. H. (1999). Composites of carbon nanotubes and conjugated polymers for photovoltaic devices. *Advanced Materials (Weinheim, Germany), 11*, 1281−1285. http://dx.doi.org/10.1002/(SICI)1521-4095(199910)11:15<1281::AID-ADMA1281>3.0.CO;2−6.

Arkles, B. (2001). Commercial applications of sol-gel-derived hybrid materials. *MRS Bulletin, 26*, 402−408. http://dx.doi.org/10.1557/mrs2001.94.

Baek, S.-W., Noh, J., Lee, C.-H., Kim, B., Seo, M.-K., & Lee, J.-Y. (2013). Plasmonic Forward Scattering Effect in Organic Solar Cells: A Powerful Optical Engineering Method. *Scientific Report, 3*. http://dx.doi.org/10.1038/srep01726.

Balazs, A. C., Emrick, T., & Russell, T. P. (2006). Nanoparticle polymer composites: where two small worlds meet. *Science, 314*, 1107−1110. http://dx.doi.org/10.1126/science.1130557.

Banerjee, S., Hemraj-Benny, T., & Wong, S. S. (2005). Covalent surface chemistry of single-walled carbon nanotubes. *Advanced Materials (Weinheim, Germany), 17*, 17−29. http://dx.doi.org/10.1002/adma.200401340.

Bar Lev, A. (1993). *Semiconductors and electronic devices*. United Kingdom: Prentice Hall Intrenational Ltd.

Beek, W. J., Slooff, L. H., Wienk, M. M., Kroon, J. M., & Janssen, R. A. (2005). Hybrid solar cells using a zinc oxide precursor and a conjugated polymer. *Advanced Functional Materials, 15*, 1703−1707. http://dx.doi.org/10.1002/adfm.200500201.

Beliatis, M. J., Henley, S., Han, S., Gandhi, K., Adikaari, D., Stratakis, E., et al. (2013). Organic solar cells with plasmonic layers formed by laser nanofabrication. *Physical Chemistry Chemical Physics, 15*, 8237−8244. http://dx.doi.org/10.1039/C3CP51334C.

Beliatis, M. J., Henley, S. J., & Silva, S. R. P. (2011). Engineering the plasmon resonance of large area bimetallic nanoparticle films by laser nanostructuring for chemical sensors. *Optics Letters, 36*, 1362−1364. http://dx.doi.org/10.1364/OL.36.001362.

Bernius, M. T., Inbasekaran, M., O'Brien, J., & Wu, W. (2000). Progress with light-emitting polymers. *Advanced Materials (Weinheim, Germany), 12*, 1737−1750. http://dx.doi.org/10.1002/1521-4095(200012)12:23<1737::AID-ADMA1737>3.0.CO;2-N.

Berson, S., De Bettignies, R., Bailly, S., Guillerez, S., & Jousselme, B. (2007). Elaboration of P3HT/CNT/PCBM composites for organic photovoltaic cells. *Advanced Functional Materials, 17*, 3363−3370. http://dx.doi.org/10.1002/adfm.200700438.

Bohren, C. F., & Huffman, D. R. (1983). *Absorption and scattering of light by small particles*. New York: Wiley-Interscience.

Boskovic, B. O., Stolojan, V., Khan, R. U., Haq, S., & Silva, S. R. P. (2002). Large-area synthesis of carbon nanofibres at room temperature. *Nature Materials, 1*, 165−168. http://dx.doi.org/10.1038/nmat755.

Brabec, C., Dyakonov, V., & Scherf, U. *Organic photovoltaics − materials, device physics, and manufacturing technologies*. John Wiley & Sons.

Brown, M. D., Suteewong, T., Kumar, R. S. S., D'innocenzo, V., Petrozza, A., Lee, M. M., et al. (2010). Plasmonic dye-sensitized solar cells using core−shell metal−insulator nanoparticles. *Nano Letters, 11*, 438−445. http://dx.doi.org/10.1021/nl1031106.

Chapin, D., Fuller, C., & Pearson, G. (1954). A new silicon p-n junction photocell for converting solar radiation into electrical power. *Journal of Applied Physics, 25*, 676−677. http://dx.doi.org/10.1063/1.1721711.

Chen, C.-P., Chen, Y.-D., & Chuang, S.-C. (2011). High-performance and highly durable inverted organic photovoltaics embedding solution-processable vanadium oxides as an interfacial hole-transporting layer. *Advanced Materials (Weinheim, Germany), 23*, 3859−3863. http://dx.doi.org/10.1002/adma.201102142.

Chen, F.-C., Wu, J.-L., Lee, C.-L., Hong, Y., Kuo, C.-H., & Huang, M. H. (2009). Plasmonic-enhanced polymer photovoltaic devices incorporating solution-processable metal nanoparticles. *Applied Physics Letters, 95*, 013305. http://dx.doi.org/10.1063/1.3174914.

Chen, G. Y., Jensen, B., Stolojan, V., & Silva, S. R. P. (2011). Growth of carbon nanotubes at temperatures compatible with integrated circuit technologies. *Carbon, 49*, 280−285. http://dx.doi.org/10.1016/j.carbon.2010.09.021.

Chiba, T., Pu, Y.-J., Hirasawa, M., Masuhara, A., Sasabe, H., & Kido, J. (2012). Solution-processed inorganic−organic hybrid electron injection layer for polymer light-emitting devices. *ACS Applied Materials & Interfaces, 4*, 6104−6108. http://dx.doi.org/10.1021/am301732m.

Cho, S., Lee, K., & Heeger, A. J. (2009). Extended lifetime of organic field-effect transistors encapsulated with titanium sub-oxide as an 'active' passivation/barrier layer. *Advanced Materials (Weinheim, Germany), 21*, 1941−1944. http://dx.doi.org/10.1002/adma.200803013.

Coakley, K. M., & Mcgehee, M. D. (2004). Conjugated polymer photovoltaic cells. *Chemistry of Materials, 16*, 4533−4542. http://dx.doi.org/10.1021/cm049654n.

Dabera, G. D. M., Jayawardena, K. I., Prabhath, M. R., Yahya, I., Tan, Y. Y., Nismy, N. A., et al. (2012). Hybrid carbon nanotube networks as efficient hole extraction layers for organic photovoltaics. *ACS Nano, 7*, 556−565. http://dx.doi.org/10.1021/nn304705t.

De Jong, M. P., Van Ijzendoorn, L. J., & De Voigt, M. J. A. (2000). Stability of the interface between indium-tin-oxide and poly(3,4-ethylenedioxythiophene)/poly(styrenesulfonate) in polymer light-emitting diodes. *Applied Physics Letters, 77*, 2255−2257. http://dx.doi.org/10.1063/1.1315344.

Delgado, J. L., Bouit, P.-A., Filippone, S., Herranz, M.Á., & Martín, N. (2010). Organic photovoltaics: a chemical approach. *Chemical Communications (Cambridge, United Kingdom), 46*, 4853−4865.

Dissanayake, N. M., & Zhong, Z. (2010). Unexpected hole transfer leads to high efficiency single-walled carbon nanotube hybrid photovoltaic. *Nano Letters, 11*, 286−290. http://dx.doi.org/10.1021/nl103879b.

Dreyer, D. R., Park, S., Bielawski, C. W., & Ruoff, R. S. (2010). The chemistry of graphene oxide. *Chemical Society Reviews, 39*, 228−240. http://dx.doi.org/10.1039/B917103G.

Ebbesen, T. W., Lezec, H., Ghaemi, H., Thio, T., & Wolff, P. (1998). Extraordinary optical transmission through sub-wavelength hole arrays. *Nature, 391*, 667−669. http://dx.doi.org/10.1038/35570.

Fowler, R. H., & Nordheim, L. (1928). Electron emission in intense electric fields. *Proceedings of the Royal Society of London. Series A, Containing Papers of a Mathematical and Physical Character, 119*, 173−181. http://dx.doi.org/10.1098/rspa.1928.0091.

Frenkel, J. (1938). On pre-breakdown phenomena in insulators and electronic semi-conductors. *Physics Review, 54*, 647−648. http://dx.doi.org/10.1103/PhysRev.54.647.

Georgakilas, V., Gournis, D., Tzitzios, V., Pasquato, L., Guldi, D. M., & Prato, M. (2007). Decorating carbon nanotubes with metal or semiconductor nanoparticles. *Journal of Materials Chemistry, 17*, 2679−2694. http://dx.doi.org/10.1039/B700857K.

Gilot, J., Barbu, I., Wienk, M. M., & Janssen, R. A. (2007). The use of ZnO as optical spacer in polymer solar cells: theoretical and experimental study. *Applied Physics Letters, 91*, 113520. http://dx.doi.org/10.1063/1.2784961.

Girotto, C., Voroshazi, E., Cheyns, D., Heremans, P., & Rand, B. P. (2011). Solution-processed MoO_3 thin films as a hole-injection layer for organic solar cells. *ACS Applied Materials & Interfaces, 3*, 3244−3247. http://dx.doi.org/10.1021/am200729k.

Girtan, M., & Rusu, M. (2010). Role of ITO and PEDOT: PSS in stability/degradation of polymer:fullerene bulk heterojunctions solar cells. *Solar Energy Materials and Solar Cells, 94*, 446−450. http://dx.doi.org/10.1016/j.solmat.2009.10.026.

Green, M. A. (2001). Third generation photovoltaics: Ultra-high conversion efficiency at low cost. *Progress in Photovoltaics: Research and Applications, 9*, 123−135. http://dx.doi.org/10.1002/pip.360.

Greenham, N. C., Peng, X., & Alivisatos, A. P. (1996). Charge separation and transport in conjugated-polymer/semiconductor-nanocrystal composites studied by photoluminescence quenching and photoconductivity. *Physical Review B, 54*, 17628. http://dx.doi.org/10.1103/PhysRevB.54.17628.

Groenendaal, L., Jonas, F., Freitag, D., Pielartzik, H., & Reynolds, J. R. (2000). Poly (3, 4-ethylenedioxythiophene) and its derivatives: past, present, and future. *Advanced Materials, 12*, 481−494. http://dx.doi.org/10.1002/(SICI)1521-4095(200004)12:7<481::AID-ADMA481>3.0.CO;2-C.

Grzelczak, M., Pérez-Juste, J., Mulvaney, P., & Liz-Marzán, L. M. (2008). Shape control in gold nanoparticle synthesis. *Chemical Society Reviews, 37*, 1783−1791. http://dx.doi.org/10.1039/B711490G.

Günes, S., & Sariciftci, N. S. (2008). Hybrid solar cells. *Inorganica Chimica Acta, 361*, 581−588. http://dx.doi.org/10.1016/j.ica.2007.06.042.

Gur, I., Fromer, N. A., Chen, C.-P., Kanaras, A. G., & Alivisatos, A. P. (2007). Hybrid solar cells with prescribed nanoscale morphologies based on hyperbranched semiconductor nanocrystals. *Nano Letters, 7*, 409−414. http://dx.doi.org/10.1021/nl062660t.

Han, S., Shin, W. S., Seo, M., Gupta, D., Moon, S. J., & Yoo, S. (2009). Improving performance of organic solar cells using amorphous tungsten oxides as an interfacial buffer layer on transparent anodes. *Organic Electronics, 10*, 791−797. http://dx.doi.org/10.1016/j.orgel.2009.03.016.

Han, S. J., Adikaari, A., Jayawardena, K., Nismy, N., Kim, Y. H., Kim, J. W., et al. (2013). Band alignment effects at the metal electrode interface of poly (3-hexylthiophene): zinc oxide hybrid photovoltaics. *Applied Physics Letters, 102*, 081607. http://dx.doi.org/10.1063/1.4794402.

Han, T.-H., Lee, Y., Choi, M.-R., Woo, S.-H., Bae, S.-H., Hong, B. H., et al. (2012). Extremely efficient flexible organic light-emitting diodes with modified graphene anode. *Nature Photonics, 6*, 105−110. http://dx.doi.org/10.1038/nphoton.2011.318.

Hatton, R. A., Blanchard, N., Tan, L. W., Latini, G., Cacialli, F., & Silva, S. R. P. (2009). Oxidised carbon nanotubes as solution processable, high work function hole-extraction layers for organic solar cells. *Organic Electronics, 10*, 388−395. http://dx.doi.org/10.1016/j.orgel.2008.12.013.

Hatton, R. A., Blanchard, N. P., Stolojan, V., Miller, A. J., & Silva, S. R. P. (2007). Nanostructured copper phthalocyanine-sensitized multiwall carbon nanotube films. *Langmuir, 23*, 6424−6430. http://dx.doi.org/10.1021/la070156d.

He, Z., Zhong, C., Huang, X., Wong, W. Y., Wu, H., Chen, L., et al. (2011). Simultaneous enhancement of open-circuit voltage, short-circuit current density, and fill factor in polymer solar cells. *Advanced Materials, 23*, 4636−4643. http://dx.doi.org/10.1002/adma.201103006.

Hersam, M. C. (2008). Progress towards monodisperse single-walled carbon nanotubes. *Nature Nanotechnology, 3*, 387−394. http://dx.doi.org/10.1038/nnano.2008.135.

Hong, W., Xu, Y., Lu, G., Li, C., & Shi, G. (2008). Transparent graphene/PEDOT−PSS composite films as counter electrodes of dye-sensitized solar cells. *Electrochemistry Communications, 10*, 1555−1558. http://dx.doi.org/10.1016/j.elecom.2008.08.007.

Hoppe, H., & Sariciftci, N. (2008). *Polymer solar cells in photoresponsive polymers*. Heidelberg: Springer Berlin.

Horie, M., Luo, Y., Morrison, J. J., Majewski, L. A., Song, A., Saunders, B. R., & Turner, M. L. (2008). Triarylamine polymers by microwave-assisted polycondensation for use in organic field-effect transistors. *Journal of Materials Chemistry, 18*, 5230−5236. http://dx.doi.org/10.1039/B808840C.

Hu, L., Wu, H., & Cui, Y. (2011). Metal nanogrids, nanowires, and nanofibers for transparent electrodes. *MRS Bulletin, 36*, 760−765. http://dx.doi.org/10.1557/mrs.2011.234.

Hummelen, J. C., Knight, B. W., Lepeq, F., Wudl, F., Yao, J., & Wilkins, C. L. (1995). Preparation and characterization of fulleroid and methanofullerene derivatives. *The Journal of Organic Chemistry, 60*, 532−538. http://dx.doi.org/10.1021/jo00108a012.

Hummers, W. S., Jr, & Offeman, R. E. (1958). Preparation of graphitic oxide. *Journal of the American Chemical Society, 80*, 1339. http://dx.doi.org/10.1021/ja01539a017.

Huynh, W. U., Dittmer, J. J., & Alivisatos, A. P. (2002). Hybrid nanorod-polymer solar cells. *Science, 295*, 2425−2427. http://dx.doi.org/10.1126/science.1069156.

Huynh, W. U., Dittmer, J. J., Libby, W. C., Whiting, G. L., & Alivisatos, A. P. (2003). Controlling the morphology of nanocrystal−polymer composites for solar cells. *Advanced Functional Materials, 13*, 73−79. http://dx.doi.org/10.1002/adfm.200390009.

Iijima, S. (1991). Helical microtubules of graphitic carbon. *Nature, 354*, 56−58.

Isomura, M., Nakahata, K., Shima, M., Taira, S., Wakisaka, K., Tanaka, M., & Kiyama, S. (2002). Microcrystalline silicon−germanium solar cells for multi-junction structures. *Solar Energy Materials and Solar Cells, 74*, 519−524. http://dx.doi.org/10.1016/S0927-0248(02)00069-7.

Jasieniak, J. J., Seifter, J., Jo, J., Mates, T., & Heeger, A. J. (2012). A solution-processed MoOx anode interlayer for use within organic photovoltaic devices. *Advanced Functional Materials, 22*, 2594−2605. http://dx.doi.org/10.1002/adfm.201102622.

Javey, A., Guo, J., Wang, Q., Lundstrom, M., & Dai, H. (2003). Ballistic carbon nanotube field-effect transistors. *Nature, 424*, 654−657. http://dx.doi.org/10.1038/nature01797.

Jayawardena, K. D. G. I., Prabhath, M. R., Dabera, G. D., & Silva, S. R. P. (2013). Solution processed reduced graphene oxide/metal oxide hybrid electron transport layers for highly efficient polymer solar cells. *Journal of Materials Chemistry A, 1*, 9922−9927. http://dx.doi.org/10.1039/C3TA11822C.

Jayawardena, K. D. G. I., Rozanski, L. J., Mills, C. A., Beliatis, M. J., Nismy, N. A., & Silva, S. R. P. (2013). 'Inorganics-in-organics': recent developments and outlook for 4G polymer solar cells. *Nanoscale, 5*, 8411−8427. http://dx.doi.org/10.1039/C3NR02733C.

Jo, J. W., Jung, J. W., Lee, J. U., & Jo, W. H. (2010). Fabrication of highly conductive and transparent thin films from single-walled carbon nanotubes using a new non-ionic surfactant via spin coating. *ACS Nano, 4*, 5382−5388. http://dx.doi.org/10.1021/nn1009837.

Kamat, P. V. (2002). Photophysical, photochemical and photocatalytic aspects of metal nanoparticles. *The Journal of Physical Chemistry B, 106*, 7729−7744. http://dx.doi.org/10.1021/jp0209289.

Kim, J. Y., Kim, S. H., Lee, H. H., Lee, K., Ma, W., Gong, X., & Heeger, A. J. (2006). New architecture for high-efficiency polymer photovoltaic cells using solution-based titanium oxide as an optical spacer. *Advanced Materials (Weinheim, Germany), 18*, 572−576. http://dx.doi.org/10.1002/adma.200501825.

Kim, M. S., Kang, M. G., Guo, L. J., & Kim, J. (2008). Choice of electrode geometry for accurate measurement of organic photovoltaic cell performance. *Applied Physics Letters, 92*, 133301. http://dx.doi.org/10.1063/1.2895058.

Kim, R. S., Zhu, J., Park, J. H., Li, L., Yu, Z., Shen, H., et al. (2012). E-beam deposited Ag-nanoparticles plasmonic organic solar cell and its absorption enhancement analysis using FDTD-based cylindrical nano-particle optical model. *Optics Express, 20*, 12649−12657. http://dx.doi.org/10.1364/OE.20.012649.

Kim, W. H., Makinen, A. J., Nikolov, N., Shashidhar, R., Kim, H., & Kafafi, Z. H. (2002). Molecular organic light-emitting diodes using highly conducting polymers as anodes. *Applied Physics Letters, 80*, 3844−3846. http://dx.doi.org/10.1063/1.1480100.

Koidis, C., Logothetidis, S., Ioakeimidis, A., Laskarakis, A., & Kapnopoulos, C. (2013). Key factors to improve the efficiency of roll-to-roll printed organic photovoltaics. *Organic Electronics, 14*, 1744−1748. http://dx.doi.org/10.1016/j.orgel.2013.04.015.

Kvarnström, C., Neugebauer, H., Blomquist, S., Ahonen, H. J., Kankare, J., Ivaska, A., & Sariciftci, N. S. (1999). In situ ftir spectroelectrochemical characterization of poly(3,4-ethylenedioxythiophene) films. *Synthetic Metals, 101*, 66. http://dx.doi.org/10.1016/S0379-6779(98)01133-3.

Kymakis, E., & Amaratunga, G. (2002). Single-wall carbon nanotube/conjugated polymer photovoltaic devices. *Applied Physics Letters, 80*, 112−114. http://dx.doi.org/10.1063/1.1428416.

Kymakis, E., & Amaratunga, G. A. (2005). Carbon nanotubes as electron acceptors in polymeric photovoltaics. *Reviews on Advanced Materials Science, 10*, 300−305.

Lampert, M. A. (1956). Simplified theory of space-charge-limited currents in an insulator with traps. *Physical Review, 103*, 1648−1656. http://dx.doi.org/10.1103/PhysRev.103.1648.

Lee, J. H., Park, J. H., Kim, J. S., Lee, D. Y., & Cho, K. (2009). High efficiency polymer solar cells with wet deposited plasmonic gold nanodots. *Organic Electronics, 10*, 416−420. http://dx.doi.org/10.1016/j.orgel.2009.01.004.

Lee, J. M., Kwon, B.-H., Park, H. I., Kim, H., Kim, M. G., Park, J. S., et al. (2013). Exciton dissociation and charge-transport enhancement in organic solar cells with quantum-dot/N-doped CNT hybrid nanomaterials. *Advanced Materials (Weinheim, Germany), 25*, 2011−2017. http://dx.doi.org/10.1002/adma.201204454.

Lee, J. M., Park, J. S., Lee, S. H., Kim, H., Yoo, S., & Kim, S. O. (2011). Selective Electron- or Hole-Transport Enhancement in Bulk-Heterojunction Organic Solar Cells with N- or B-Doped Carbon Nanotubes. *Advanced Materials (Weinheim, Germany), 23*, 629−633. http://dx.doi.org/10.1002/adma.201003296.

Li, G., Chu, C.-W., Shrotriya, V., Huang, J., & Yang, Y. (2006). Efficient inverted polymer solar cells. *Applied Physics Letters, 88*, 253503. http://dx.doi.org/10.1063/1.2212270.

Li, S.-S., Tu, K.-H., Lin, C.-C., Chen, C.-W., & Chhowalla, M. (2010). Solution-processable graphene oxide as an efficient hole transport layer in polymer solar cells. *ACS Nano, 4*, 3169−3174. http://dx.doi.org/10.1021/nn100551j.

Liu, F., Sanyasi Rao, B., & Nunzi, J.-M. (2011). A dye functionalized silver−silica core−shell nanoparticle organic light emitting diode. *Organic Electronics, 12*, 1279−1284. http://dx.doi.org/10.1016/j.orgel.2011.04.013.

Liu, F., Shao, S., Guo, X., Zhao, Y., & Xie, Z. (2010). Efficient polymer photovoltaic cells using solution-processed MoO3 as anode buffer layer. *Solar Energy Materials and Solar Cells, 94*, 842−845. http://dx.doi.org/10.1016/j.solmat.2010.01.004.

Liu, J., Tanaka, T., Sivula, K., Alivisatos, A. P., & Fréchet, J. M. (2004). Employing end-functional polythiophene to control the morphology of nanocrystal-polymer composites in hybrid solar cells. *Journal of the American Chemical Society, 126*, 6550−6551. http://dx.doi.org/10.1021/ja0489184.

Liu, J., Xue, Y., Gao, Y., Yu, D., Durstock, M., & Dai, L. (2012). Hole and electron extraction layers based on graphene oxide derivatives for high-performance bulk heterojunction solar cells. *Advanced Materials (Weinheim, Germany), 24*, 2228−2233. http://dx.doi.org/10.1002/adma.201104945.

Logothetidis, S. (2008). Flexible organic electronic devices: materials, process and applications. *Materials Science and Engineering: B, 152*, 96−104. http://dx.doi.org/10.1016/j.mseb.2008.06.009.

Lu, L., Luo, Z., Xu, T., & Yu, L. (2012). Cooperative plasmonic effect of Ag and Au nanoparticles on enhancing performance of polymer solar cells. *Nano Letters, 13*, 59−64. http://dx.doi.org/10.1021/nl3034398.

Lu, L., Xu, T., Chen, W., Lee, J. M., Luo, Z., Jung, I. H., et al. (2013). The role of n-doped multiwall carbon nanotubes in achieving highly efficient polymer bulk heterojunction solar cells. *Nano Letters, 13*, 2365−2369. http://dx.doi.org/10.1021/nl304533j.

Madec, M.-B., Morrison, J. J., Rabjohns, M., Turner, M. L., & Yeates, S. G. (2010). Effect of poly (triarylamine) molar mass distribution on organic field effect transistor behaviour. *Organic Electronics, 11*, 686−691. http://dx.doi.org/10.1016/j.orgel.2009.12.015.

Maier, S. A., Kik, P. G., Atwater, H. A., Meltzer, S., Harel, E., Koel, B. E., & Requicha, A. A. (2003). Local detection of electromagnetic energy transport below the diffraction limit in metal nanoparticle plasmon waveguides. *Nature Materials, 2*, 229−232. http://dx.doi.org/10.1038/nmat852.

Manders, J. R., Tsang, S.-W., Hartel, M. J., Lai, T.-H., Chen, S., Amb, C. M., et al. (2013). Solution-processed nickel oxide hole transport layers in high efficiency polymer photovoltaic cells. *Advanced Functional Materials, 23*, 2993−3001. http://dx.doi.org/10.1002/adfm.201202269.

Mayorov, A. S., Gorbachev, R. V., Morozov, S. V., Britnell, L., Jalil, R., Ponomarenko, L. A., et al. (2011). Micrometer-scale ballistic transport in encapsulated graphene at room temperature. *Nano Letters, 11*, 2396−2399. http://dx.doi.org/10.1021/nl200758b.

Mcgehee, M. D., & Heeger, A. J. (2000). Semiconducting (conjugated) polymers as materials for solid-state lasers. *Advanced Materials (Weinheim, Germany), 12*, 1655−1668. http://dx.doi.org/10.1002/1521-4095(200011)12:22<1655::AID-ADMA1655>3.0.CO;2−2.

Mcgehee, M. D., Miller, E. K., Moses, D., & Heeger, A. J. (1999). *Advances in synthetic metals: Twenty years of progress in science and technology*. Amsterdam: Elsevier Science.

Merhari, L. M. (2009). *Hybrid nanocomposites for nanotechnology: Electronic, optical, magnetic and biomedical applications*. New York: Springer.

Meyer, J., Khalandovsky, R., Görrn, P., & Kahn, A. (2011). MoO3 Films spin-coated from a nanoparticle suspension for efficient hole-injection in organic electronics. *Advanced Materials (Weinheim, Germany), 23*, 70−73. http://dx.doi.org/10.1002/adma.201003065.

Miller, A. J., Hatton, R. A., Chen, G., & Silva, S. R. P. (2007). Carbon nanotubes grown on InO: Sn glass as large area electrodes for organic photovoltaics. *Applied Physics Letters, 90*, 023105. http://dx.doi.org/10.1063/1.2431437.

Miller, A. J., Hatton, R. A., & Silva, S. R. P. (2006). Interpenetrating multiwall carbon nanotube electrodes for organic solar cells. *Applied Physics Letters, 89*, 133117. http://dx.doi.org/10.1063/1.2431437.

Montes, V. A., Pohl, R., Shinar, J., & Anzenbacher, P. (2006). Effective Manipulation of the Electronic Effects and Its Influence on the Emission of 5-Substituted Tris (8-quinolinolate) Aluminum (III) Complexes. *Chemistry-A European Journal, 12*, 4523−4535. http://dx.doi.org/10.1002/chem.200501403.

Morfa, A. J., Rowlen, K. L., Reilly, T. H., Romero, M. J., & Van De Lagemaat, J. (2008). Plasmon-enhanced solar energy conversion in organic bulk heterojunction photovoltaics. *Applied Physics Letters, 92*, 013504. http://dx.doi.org/10.1063/1.2823578.

Nalwa, H. S. (2003). *Handbook of organic-inorganic hybrid materials and nanocomposites*. American Scientific Publishers.

Nish, A., Hwang, J.-Y., Doig, J., & Nicholas, R. J. (2007). Highly selective dispersion of single-walled carbon nanotubes using aromatic polymers. *Nature Nanotechnology, 2*, 640−646. doi:10.1038/nnano.2007.290.

Nismy, N., Adikaari, A., & Silva, S. (2010). Functionalized multiwall carbon nanotubes incorporated polymer/fullerene hybrid photovoltaics. *Applied Physics Letters, 97*, 033105. http://dx.doi.org/10.1063/1.3464970.

Nismy, N. A., Jayawardena, K., Adikaari, A., & Silva, S. R. P. (2011). Photoluminescence quenching in carbon nanotube-polymer/fullerene films: carbon nanotubes as exciton dissociation centres in organic photovoltaics. *Advanced Materials (Weinheim, Germany), 23*, 3796−3800. http://dx.doi.org/10.1002/adma.201101549.

Novoselov, K. S., Geim, A. K., Morozov, S., Jiang, D., Zhang, Y., Dubonos, S., et al. (2004). Electric field effect in atomically thin carbon films. *Science, 306*, 666−669. http://dx.doi.org/10.1126/science.1102896.

Padinger, F., Rittberger, R. S., & Sariciftci, N. S. (2003). Effects of postproduction treatment on plastic solar cells. *Advanced Functional Materials, 13*, 85−88. http://dx.doi.org/10.1002/adfm.200390011.

Park, H., Chang, S., Jean, J., Cheng, J. J., Araujo, P. T., Wang, M., et al. (2012). Graphene Cathode-Based ZnO Nanowire Hybrid Solar Cells. *Nano Letters, 13*, 233−239. http://dx.doi.org/10.1021/nl303920b.

Park, S. H., Roy, A., Beaupré, S., Cho, S., Coates, N., Moon, J. S., et al. (2009). Bulk heterojunction solar cells with internal quantum efficiency approaching 100%. *Nature Photonics, 3*, 297−302. http://dx.doi.org/10.1038/nphoton.2009.69.

Park, S. Y., Jeong, W. I., Kim, D. G., Kim, J. K., Lim, D. C., Kim, J. H., et al. (2010). Large-area organic solar cells with metal subelectrode on indium tin oxide anode. *Applied Physics Letters, 96*, 173301. http://dx.doi.org/10.1063/1.3419925.

Parker, I. D. (1994). Carrier tunneling and device characteristics in polymer light-emitting diodes. *Journal of Applied Physics, 75*, 1656. http://dx.doi.org/10.1063/1.356350.

Periyayya, U., Kang, J. H., Ryu, J. H., & Hong, C.-H. (2011). Synthesis and improved luminescence properties of OLED/ZnO hybrid materials. *Vacuum, 86*, 254−260. http://dx.doi.org/10.1016/j.vacuum.2011.06.016.

Pientka, M., Dyakonov, V., Meissner, D., Rogach, A., Talapin, D., Weller, H., et al. (2004). Photoinduced charge transfer in composites of conjugated polymers and semiconductor nanocrystals. *Nanotechnology, 15*, 163. http://dx.doi.org/10.1088/0957-4484/15/1/032.

Pillai, S., Catchpole, K., Trupke, T., & Green, M. (2007). Surface plasmon enhanced silicon solar cells. *Journal of Applied Physics, 101*, 093105. http://dx.doi.org/10.1063/1.2734885.

Pradhan, B., Batabyal, S. K., & Pal, A. J. (2006). Functionalized carbon nanotubes in donor/acceptor-type photovoltaic devices. *Applied Physics Letters, 88*, 093106. http://dx.doi.org/10.1063/1.2179372.

Pschenitzka, F., & Sturm, J. (1999). Three-color organic light-emitting diodes patterned by masked dye diffusion. *Applied Physics Letters, 74*, 1913−1915. http://dx.doi.org/10.1063/1.123711.

Qiao, L., Wang, D., Zuo, L., Ye, Y., Qian, J., Chen, H., & He, S. (2011). Localized surface plasmon resonance enhanced organic solar cell with gold nanospheres. *Applied Energy, 88*, 848−852. http://dx.doi.org/10.1016/j.apenergy.2010.09.021.

Rakhmanova, S., & Conwell, E. (2000). Electric-field dependence of mobility in conjugated polymer films. *Applied Physics Letters, 76*, 3822−3824. http://dx.doi.org/10.1063/1.126793.

Ramesh, G., Porel, S., & Radhakrishnan, T. (2009). Polymer thin films embedded with in situ grown metal nanoparticles. *Chemical Society Reviews, 38*, 2646−2656. http://dx.doi.org/10.1039/B815242J.

Rhodes, R., Horie, M., Chen, H., Wang, Z., Turner, M., & Saunders, B. (2010). Aggregation of zinc oxide nanoparticles: from non-aqueous dispersions to composites used as photoactive layers in hybrid solar cells. *Journal of Colloid and Interface Science, 344*, 261−271. http://dx.doi.org/10.1016/j.jcis.2009.12.062.

Saito, R., Dresselhaus, G., & Dresselhaus, M. S. (1998). *Physical properties of carbon nano-tubes*. London: Imperial College Press.

Sanchez, C., Julian, B., Belleville, P., & Popall, M. (2005). Applications of hybrid organic−inorganic nanocomposites. *Journal of Materials Chemistry, 15*, 3559−3592. http://dx.doi.org/10.1039/B509097K.

Satishkumar, B., Vogl, E. M., Govindaraj, A., & Rao, C. (1996). The decoration of carbon nanotubes by metal nanoparticles. *Journal of Physics D-Applied Physics, 29*, 3173−3176. http://dx.doi.org/10.1088/0022-3727/29/12/037.

Saunders, B. R., & Turner, M. L. (2008). Nanoparticle−polymer photovoltaic cells. *Advances in Colloid and Interface Science, 138*, 1−23. http://dx.doi.org/10.1016/j.cis.2007.09.001.

Scharber, M. C., Mühlbacher, D., Koppe, M., Denk, P., Waldauf, C., Heeger, A. J., & Brabec, C. J. (2006). Design rules for donors in bulk-heterojunction solar cells—Towards 10% energy-conversion efficiency. *Advanced Materials (Weinheim, Germany), 18*, 789−794. http://dx.doi.org/10.1002/adma.200501717.

Schuettfort, T., Nish, A., & Nicholas, R. J. (2009). Observation of a type II heterojunction in a highly ordered polymer − carbon nanotube nanohybrid structure. *Nano Letters, 9*, 3871−3876. http://dx.doi.org/10.1021/nl902081t.

Scott, C. D., Arepalli, S., Nikolaev, P., & Smalley, R. E. (2001). Growth mechanisms for single-wall carbon nanotubes in a laser-ablation process. *Applied Physics A, 72*, 573−580. http://dx.doi.org/10.1007/s003390100761.

Sessolo, M., & Bolink, H. J. (2011). Hybrid Organic−Inorganic Light-Emitting Diodes. *Advanced Materials (Weinheim, Germany), 23*, 1829−1845. http://dx.doi.org/10.1002/adma.201004324.

Shang, N., Tan, Y., Stolojan, V., Papakonstantinou, P., & Silva, S. (2010). High-rate low-temperature growth of vertically aligned carbon nanotubes. *Nanotechnology, 21*, 505604. http://dx.doi.org/10.1088/0957-4484/21/50/505604.

Sirringhaus, H., Kawase, T., Friend, R., Shimoda, T., Inbasekaran, M., Wu, W., & Woo, E. (2000). High-resolution inkjet printing of all-polymer transistor circuits. *Science, 290*, 2123−2126. http://dx.doi.org/10.1126/science.290.5499.2123.

Skotheim, T. A., Elsenbamer, R. L., & Reynolds, J. R. (1998). *Handbook of conducting polymers* (2nd ed.). New York: Marcel Dekker Inc.

Son, D. I., Kwon, B. W., Park, D. H., Seo, W.-S., Yi, Y., Angadi, B., et al. (2012). Emissive ZnO-graphene quantum dots for white-light-emitting diodes. *Nature Nanotechnology, 7*, 465−471. http://dx.doi.org/10.1038/nnano.2012.71.

Spanggaard, H., & Krebs, F. C. (2004). A brief history of the development of organic and polymeric photovoltaics. *Solar Energy Materials and Solar Cells, 83*, 125−146. http://dx.doi.org/10.1016/j.solmat.2004.02.021.

Stubhan, T., Litzov, I., Li, N., Wang, H., Krantz, J., Machui, F., et al. (2012). Low-temperature solution-processed metal oxide buffer layers fulfilling large area production requirements. SPIE organic photonics+ electronics. *International Society for Optics and Photonics*, 84770J. http://dx.doi.org/10.1117/12.945866.

Sun, Y., Takacs, C. J., Cowan, S. R., Seo, J. H., Gong, X., Roy, A., et al. (2011). Efficient, air-stable bulk heterojunction polymer solar cells using MoOx as the anode interfacial layer. *Advanced Materials (Weinheim, Germany), 23*, 2226−2230. http://dx.doi.org/10.1002/adma.201100038.

Sutherland, D. G. J., Carlisle, J. A., Elliker, P., Fox, G., Hagler, T. W., Jimenez, I., et al. (1996). Photo-oxidation of electroluminescent polymers studied by core-level photoabsorption spectroscopy. *Applied Physics Letters, 68*, 2046−2048. http://dx.doi.org/10.1063/1.116298.

Takanezawa, K., Hirota, K., Wei, Q.-S., Tajima, K., & Hashimoto, K. (2007). Efficient charge collection with ZnO nanorod array in hybrid photovoltaic devices. *The Journal of Physical Chemistry C, 111*, 7218−7223. http://dx.doi.org/10.1021/jp071418n.

Tan, Y., Jayawardena, K., Adikaari, A., Tan, L., Anguita, J., Henley, S., et al. (2012). Photo-thermal chemical vapor deposition growth of graphene. *Carbon, 50*, 668−673. http://dx.doi.org/10.1016/j.carbon.2011.09.025.

Tan, Y., Tan, L., Jayawardena, K., Anguita, J., Carey, J., & Silva, S. (2011). Field effect in chemical vapour deposited graphene incorporating a polymeric gate dielectric. *Synthetic Metals, 161*, 2249−2252. http://dx.doi.org/10.1016/j.synthmet.2011.08.029.

Taylor, D. (2006). Space charges and traps in polymer electronics. *Dielectrics and Electrical Insulation, IEEE Transactions on, 13*, 1063−1073. http://dx.doi.org/10.1109/TDEI.2006.247833.

Teo, K., Chhowalla, M., Amaratunga, G., Milne, W., Hasko, D., Pirio, G., et al. (2001). Uniform patterned growth of carbon nanotubes without surface carbon. *Applied Physics Letters, 79*, 1534−1536. http://dx.doi.org/10.1063/1.1400085.

Torrisi, F., Hasan, T., Wu, W., Sun, Z., Lombardo, A., Kulmala, T. S., et al. (2012). Inkjet-printed graphene electronics. *ACS Nano, 6*, 2992−3006. http://dx.doi.org/10.1021/nn2044609.

Vaynzof, Y., Kabra, D., Brenner, T. J., Sirringhaus, H., & Friend, R. H. (2012). Recent advances in hybrid optoelectronics. *Israel Journal of Chemistry, 52*, 496−517. http://dx.doi.org/10.1002/ijch.201100108.

Wang, D. H., Park, K. H., Seo, J. H., Seifter, J., Jeon, J. H., Kim, J. K., et al. (2011). Enhanced power conversion efficiency in PCDTBT/PC70BM bulk heterojunction photovoltaic devices with embedded silver nanoparticle clusters. *Advanced Energy Materials, 1*, 766−770. http://dx.doi.org/10.1002/aenm.201100347.

Wang, Z. L. (2012). Progress in piezotronics and piezo-phototronics. *Advanced Materials (Weinheim, Germany), 24*, 4632−4646. http://dx.doi.org/10.1002/adma.201104365.

Weller, H. (1993). Colloidal semiconductor Q-particles: chemistry in the transition region between solid state and molecules. *Angewandte Chemie International Edition in English, 32*, 41−53. http://dx.doi.org/10.1002/anie.199300411.

Wong, K. W., Yip, H. L., Luo, Y., Wong, K. Y., Lau, W. M., Low, K. H., et al. (2002). Blocking reactions between indium-tin oxide and poly (3,4-ethylene dioxythiophene):poly(styrene sulphonate) with a self-assembly monolayer. *Applied Physics Letters, 80*, 2788−2790. http://dx.doi.org/10.1063/1.1469220.

Wu, J., Agrawal, M., Becerril, H. A., Bao, Z., Liu, Z., Chen, Y., & Peumans, P. (2009). Organic light-emitting diodes on solution-processed graphene transparent electrodes. *ACS Nano, 4*, 43−48. http://dx.doi.org/10.1021/nn900728d.

Xie, F., Choy, W. C. H., Wang, C., Li, X., Zhang, S., & Hou, J. (2013). Low-temperature solution-processed hydrogen molybdenum and vanadium bronzes for an efficient hole-transport layer in organic electronics. *Advanced Materials (Weinheim, Germany), 25*, 2051−2055. http://dx.doi.org/10.1002/adma.201204425.

Xue, M., Li, L., De Villers, B. J. T., Shen, H., Zhu, J., Yu, Z., et al. (2011). Charge-carrier dynamics in hybrid plasmonic organic solar cells with Ag nanoparticles. *Applied Physics Letters, 98*, 253302. http://dx.doi.org/10.1063/1.3601742.

Yang, T., Cai, W., Qin, D., Wang, E., Lan, L., Gong, X., et al. (2010). Solution-processed zinc oxide thin film as a buffer layer for polymer solar cells with an inverted device structure. *The Journal of Physical Chemistry C, 114*, 6849−6853. http://dx.doi.org/10.1021/jp1003984.

You, J., Chen, C. C., Dou, L., Murase, S., Duan, H. S., Hawks, S., et al. (2012). Metal Oxide Nanoparticles as an Electron-Transport Layer in High-Performance and Stable Inverted Polymer Solar Cells. *Advanced Materials (Weinheim, Germany), 24*, 5267−5272. http://dx.doi.org/10.1002/adma.201201958.

Yu, G., Gao, J., Hummelen, J., Wudl, F., & Heeger, A. (1995). Polymer photovoltaic cells: enhanced efficiencies via a network of internal donor-acceptor heterojunctions. *Science-AAAS-Weekly Paper Edition, 270*, 1789−1790. http://dx.doi.org/10.1126/science.270.5243.1789.

Yun, J. M., Yeo, J. S., Kim, J., Jeong, H. G., Kim, D. Y., Noh, Y. J., et al. (2011). Solution-Processable Reduced Graphene Oxide as a Novel Alternative to PEDOT: PSS Hole Transport Layers for Highly Efficient and Stable Polymer Solar Cells. *Advanced Materials (Weinheim, Germany), 23*, 4923−4928. http://dx.doi.org/10.1002/adma.201102207.

Zhang, J., Zou, H., Qing, Q., Yang, Y., Li, Q., Liu, Z., et al. (2003). Effect of chemical oxidation on the structure of single-walled carbon nanotubes. *The Journal of Physical Chemistry B, 107*, 3712−3718. http://dx.doi.org/10.1021/jp027500u.

Zhang, X., Feng, Y., Tang, S., & Feng, W. (2010). Preparation of a graphene oxide−phthalocyanine hybrid through strong $\pi-\pi$ interactions. *Carbon, 48*, 211−216. http://dx.doi.org/10.1016/j.carbon.2009.09.007.

Zilberberg, K., Trost, S., Meyer, J., Kahn, A., Behrendt, A., Lützenkirchen-Hecht, D., Frahm, R., & Riedl, T. (2011). Inverted organic solar cells with sol−gel processed high work-function vanadium oxide hole-extraction layers. *Advanced Functional Materials, 21*, 4776−4783. http://dx.doi.org/10.1002/adfm.201101402.

Organic polymeric semiconductor materials for applications in photovoltaic cells

4

J.K. Kallitsis, S. Kourkouli, A.K. Andreopoulou
University of Patras, Greece

4.1   Introduction

The photogenerated charge formation in organic materials was discovered by Heeger and Sariciftci in 1995 (Sariciftci, Smilowitz, Heeger, & Wudl, 1992; Yu, Gao, Hummelen, Wundl, & Heeger, 1995) using blends of poly(1,4-phenylene vinylene) (PPV) and fullerene derivatives. This discovery made possible after the initial observation of the inherent properties of organic materials in photovoltaics by Tang (1986) and the discovery of the electroluminescence by the group of Friend in Cambridge (Burroughes et al., 1990). Since then, a large amount of the scientific effort has been devoted to improve the performance and the stability of the newly generated photovoltaic cells based on the concept of bulk heterojunction (BHJ) in polymer-based systems (Bian, Zhu, Tang, Tang, & Zhang, 2012; Chen & Cao, 2009; Chochos, Tagmatarchis, & Gregoriou, 2013; Chu et al., 2011; Guo, Baumgarten, & Müllen, 2013; He, Zhong, et al., 2012; Li, Zhu, & Yang, 2012; Peet, Heeger, & Bazan, 2009; Su, Lan, & Wie, 2012; Zhao & Zhan, 2011; Zhou, Zuo, et al., 2013).

The active layer of a typical organic photovoltaic cell is composed of a polymeric semiconductor, as the electron donor, blended with a fullerene derivative, as the electron acceptor. The known semiconducting conjugated polymers PPV and poly(3-hexyl thiophene) (P3HT) were initially used as the electron donors, that after light absorption generate excitons which are dissociated to provide electrons to a neighboring electron accepting phase.

The correct matching of the energy levels of the electron donor and the electron acceptor, the efficient light absorption, and the required morphology of a nanophase-separated system with bicontinuous structures were, and still are, the crucial parameters that determine the final photovoltaic efficiency.

The synthesis of new materials aiming to improve the energy efficiency of photovoltaic devices is a primary research area of focus of the scientific community. Attempts in this direction are to either replace the commonly used polymeric materials that act as electron donors, and those that act as electron acceptors, or to improve the performance of the overall system with methodologies that will drastically contribute to the optimization of device's performance, reaching values higher than 8% (He, Zhong, et al., 2012) (Figure 4.1).

HOMO = Highest occupied molecular orbital
LUMO = Lowest unoccupied molecular orbital
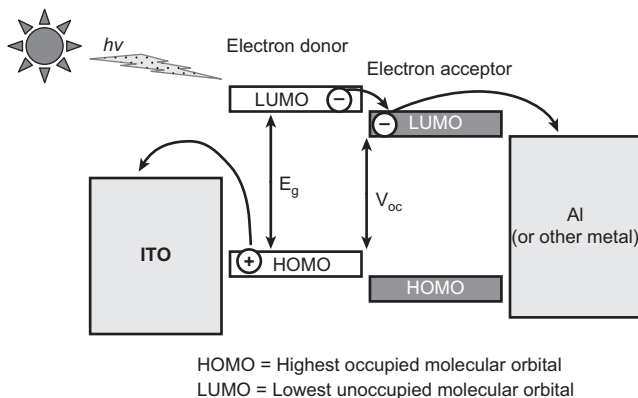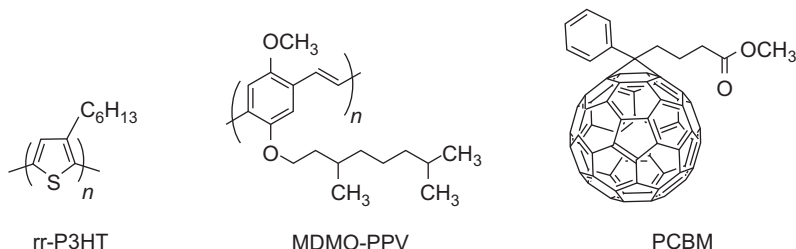
Figure 4.1 Schematic of energy levels and charge transfer process in an Organic Photovoltaic (OPV) device.

Indeed, in recent years, there has been an impressive improvement on the device performance mainly from the development of a large number of more efficient polymeric electron donors. Another route employed is to control and stabilize the morphology of the system through the use of copolymers with electron donor and electron acceptor units and hybrid materials modified with carbon nanostructures. These new hybrid materials are expected to have improved properties, controlled energy levels, and to contribute to the better mixing of the photoactive electron donor and acceptor materials improving thus, the morphology and hence the efficiency of the photovoltaic device.

4.2 Polymeric electron donors for bulk-heterojunction photovoltaic solar cells

The most studied polymer electron donors for organic photovoltaics are the regioregular poly(3-hexylthiophene) (*rr*-P3HT) and PPVs, such as poly[2-methoxy-5-(3,7-dimethyloctyloxy)-1,4-phenylene-vinylene] (MDMO-PPV), Scheme 4.1. P3HT in combination with the electron acceptor PCBM ([6,6]-phenyl-C61-butyric acid methyl ester) has dominated in the studies for organic photovoltaics affording efficiencies near 5%. However, the need to achieve higher yields has led the research community to work toward the synthesis of new polymeric donors with more suitable characteristics for photovoltaics.

Below, a brief description of the basic appropriate characteristics of an electron donor for photovoltaic systems is presented. The electron donor (*p*-type semiconductor) in a photovoltaic device is the responsible material for the absorption of solar light. The maximum of the electromagnetic radiation of the visible spectrum is near infrared (700−900 nm) and thus the maximum of the electron donors' absorption should be located in that region. However, most polymers' band gap is about

Scheme 4.1 Electron donors regioregular poly(3-hexylthiophene) (*rr*-P3HT), poly[2-methoxy-5-(3,7-dimethyloctyloxy)-1,4-phenylene-vinylene] (MDMO-PPV), and the electron acceptor PCBM ([6,6]-phenyl-C61-butyric acid methyl ester), initially studied in OPVs.
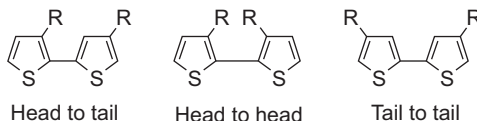
$E_g = 2$ eV, which means that they absorb only a small part of the incoming light, about 30%. Based on the emission spectrum of the sun, it is calculated that the band gap of the optimal polymeric donor should be approximately 1.5 eV.

The way to create low-band-gap materials is based mainly on the intermolecular charge transfer achieved by alternating electron-rich (donor) and electron-deficient (acceptors) units along the same polymeric backbone. Alternating donor—acceptor polymers (D—A) give the opportunity to researchers to produce materials with controlled energy levels (preferably high-lying higher occupied molecular orbital (HOMO) and low-lying lower unoccupied molecular orbital (LUMO)) and also to minimize the bond length alternation along the π-conjugated backbone. Essential characteristics of the electron donor are also good hole mobility and the capacity to create, in combination with the electron acceptor, a stable film on the device, which will lead to the appropriate morphology.

4.2.1 Thiophene containing conjugated polymers

The thiophene ring is the most widely used building blocks for the construction of conjugated polymers mainly because of its high environmental stability. Thiophene chemistry has been well developed for a long time, allowing tuning of the electronic properties in a wide range through versatile structural variations. The polymers containing thiophene moieties present interesting electronic, optical, and redox properties, unique self-assembling abilities on solid surfaces and in bulk. The high polarizability of sulfur atoms in thiophenes leads also to a stabilization of the conjugated chains and to excellent charge carrier transport, which are crucial for optoelectronic applications (Mishra, Ma, & Bäuerle, 2009). Thiophene-containing polymers exhibit hole transport characteristics and have been applied as *p*-type semiconductors for Organic field effect transistors (OFETs) and OPV.

The early research on unsubstituted polythiophenes in the 1980s was carried out for field-effect transistor (FET) applications, showing mobilities of only 10^{-5} cm^2/V s (Tsumura, Koezuka, & Ando, 1986). To improve their solubility and film-forming properties, a variety of side chains was introduced onto the polythiophene backbone, leading to a large number of polythiophene derivatives. P3HT

Head to tail   Head to head   Tail to tail
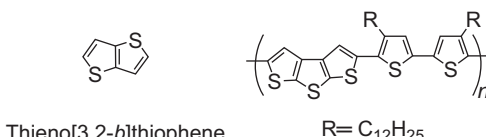
Scheme 4.2 Possible couplings of two 3-substituted thiophene monomers linked at their 2- and 5-positions: 2.5′ or head−tail (HT), 2.2′ or head−head (HH), 5.5′ or tail−tail (TT).

is a key polymeric material applied in OFETs and OPV. The regioregularity of P3HT plays an important role in the molecular arrangement and subsequent device performances (Sirringhaus et al., 1999). Regioregular P3HT (*head-to-tail coupling*, see Scheme 4.2) exhibits mobilities from 0.05 to 0.2 cm^2/V s by adopting an edge-on orientation (Chang et al., 2004; Sirringhaus et al., 1999). The performance of P3HT in OPV is also constantly enhanced by various optimization strategies, and record power conversion efficiencies (PCEs) of 6.5% has been achieved when using proper electron acceptors (Zhao, He, & Li, 2010). The selenophene-based polymers were initially developed as alternatives to polythiophenes for OPV applications; however, studies found that these kind of polymers showed generally ambipolar charge transport (Chen et al., 2010).

Polymers with 3,4-disubstituted thiophenes rings showed PCEs in polymer: fullerene BHJ solar cells closed to 4.2% (Ko et al., 2011). Further studies on these polymers in comparison with P3HT demonstrated that the degree of polymer backbone twisting induced by 3,4-disubstituents increased the ionization potential and enhanced the V_{oc} (open-circuit voltage ($J = 0$)) while retaining the I_{sc} (current density at short-circuit ($V = 0$)). This molecular design provides a simple method to tune the degree of backbone twisting in polymer backbones for the optimization of organic electronic devices (Osaka, Akita, Koganezawa, & Takimiya, 2012).

Other thienoacenes with further extended conjugation have also been incorporated into polythiophene backbones to develop *p*-type semiconductors, Scheme 4.3. Particularly, trithienoacene polymers with alkyl chains only at the thiophene rings, Scheme 4.3, exhibited an excellent hole mobility of 0.3 cm^2/V s with a very high current on/off ratio (Li et al., 2008).

Thieno[3,2-*b*]thiophene   R= C$_{12}$H$_{25}$

Scheme 4.3 Examples of thienoacenes consisting of fused thiophene rings.

4.2.2 *Alternating donor−acceptor copolymers*

As mentioned previously, the key requirements for high-efficiency conjugated polymer donors are the broad absorption and a narrower energy band gap (E_g), lower lying
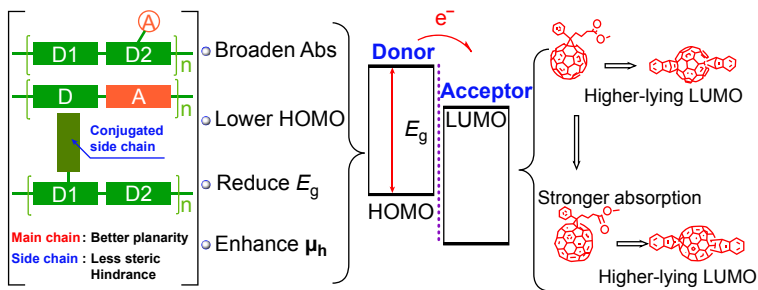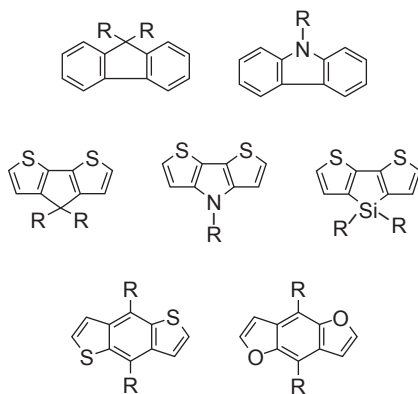
Figure 4.2 Schematic illustration of basic requirements of electron donors for OPVs. Reprinted with permission from Li (2012). Copyright 2012 American Chemical Society.

HOMO level, and higher hole mobility (Kularatne, Magurudeniya, Sista, Biewer, & Stefan, 2013). The strategies to meet these requirements are:

- Alternating D−A copolymerization for narrower E_g and lower-lying HOMO,
- Substitution with electron-withdrawing groups for lower-lying HOMO,
- Two-dimensional conjugation for broad absorption and higher hole mobility.

Moreover, better main chain planarity and less side chain steric hindrance could strengthen π-π stacking and increase hole mobility. These concepts are schematically summarized in the following section (Li, 2012) (Figure 4.2).

Typical groups, which are used as electron donors in D−A systems, are thiophene, carbazole, fluorene, and their heterocyclic derivatives, Scheme 4.4 (Bian et al., 2012).

Scheme 4.4 Typical groups used as electron donors in donor acceptor systems (e.g., fluorene, carbazole, and their heterocyclic derivatives with thiophene).
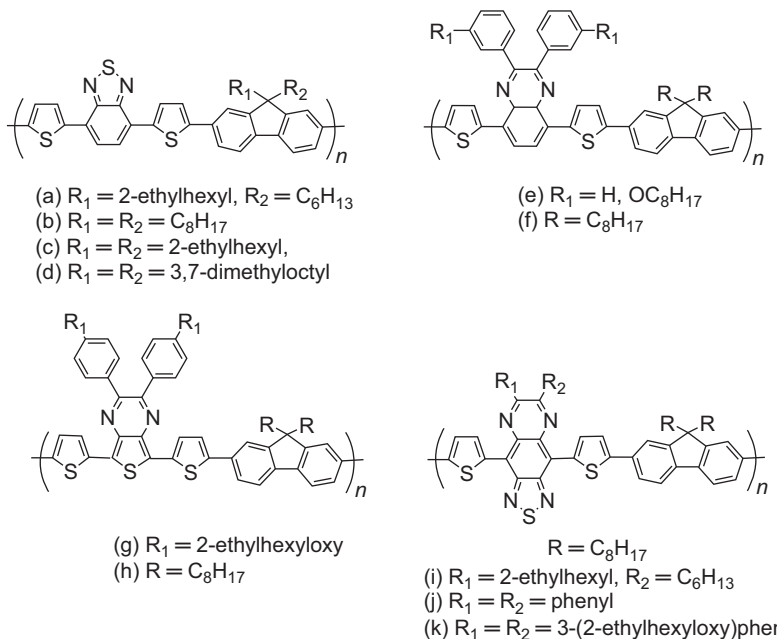
4.2.2.1 Fluorene-based D−A copolymers

Fluorene and its derivatives have been extensively investigated for their application in OLEDs because of their rigid planar molecular structure, excellent hole-transporting properties, good solubility, and exceptional chemical stability (Scherf & List,

2002) and (Tang et al., 2007). Together with their low HOMO levels, polyfluorenes (PFs) are expected to reach higher V_{oc} and J_{sc} values in their devices. All these expectations make fluorene unit a promising electron-donating moiety in the donor polymer design. The feasibility of dialkylation at 9-position and selective bromination at the 2,7-positions allow the desired molecular transformation to achieve good solubility, in the first case, and extended conjugation via aromatic ring cross-coupling reactions.

Fluorene-based homopolymers and copolymers containing electron-donating moieties are generally not suitable for solar conversion purposes because of their weak absorption of visible light. However, the alternating copolymer of fluorene and electron-rich bithiophene (Tang et al., 2007) gave a moderate efficiency because of the high hole mobility of this polymer and well-defined nanoscale segregation morphology in the active layer (Tang, Chellappan, Liu, Chen, & Ke, 2009).

By incorporating the electron-deficient benzothiazole (BT) unit into the polymer backbone, polyfluorenes exhibited reduced LUMO levels and narrower band gaps that allowed fine-tuning of the emission over the entire visible region (Herguth, Jiang, Liu, & Jen, 2002). Along this line, Andersson and coworkers (Svensson et al., 2003) demonstrated the first breakthrough in the design of D−A PFs, in which electro-accepting 4,7-dithien-2-yl-2,1,3-benzothiadiazole (DTBT) was used to reduce the band gap of (a) in Scheme 4.5, structures (a)−(d). They have synthesized a series of copolymers thereof, known as alternating polyfluorene copolymers.

(a) $R_1 = $ 2-ethylhexyl, $R_2 = C_6H_{13}$
(b) $R_1 = R_2 = C_8H_{17}$
(c) $R_1 = R_2 = $ 2-ethylhexyl,
(d) $R_1 = R_2 = $ 3,7-dimethyloctyl

(e) $R_1 = $ H, OC_8H_{17}
(f) $R = C_8H_{17}$

(g) $R_1 = $ 2-ethylhexyloxy
(h) $R = C_8H_{17}$

$R = C_8H_{17}$
(i) $R_1 = $ 2-ethylhexyl, $R_2 = C_6H_{13}$
(j) $R_1 = R_2 = $ phenyl
(k) $R_1 = R_2 = $ 3-(2-ethylhexyloxy)phenyl

Scheme 4.5 Alternating polyfluorene copolymers incorporating the electron-deficient benzo-thiazole (BT) unit.
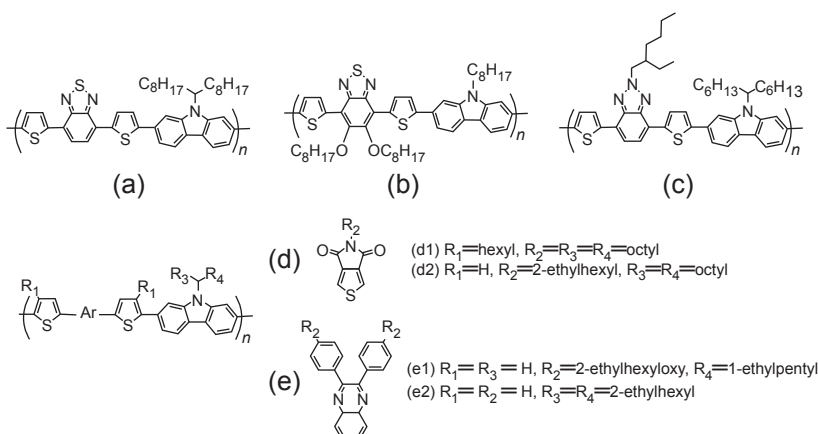
By varying the side chains in the 9-position of fluorene for solubility improvement, a series of PFs, (c)−(d) were developed by Cao and coworkers (Allard et al., 2010; Zhou et al., 2004).

Also a number of D−A fluorene based copolymers have been synthesized by replacing the 2,1,3-benzothiadiazole with various heterocyclic acceptor units such as quinoxalines and pyrazine structures (e)−(h) in Scheme 4.5. In all cases, fluorene D−A copolymers have been synthesized by Suzuki cross-coupling polymerization.

By using an even stronger acceptor such as [1,2,5] thiadiazolo[3,4-g]quinoxaline structures (i)−(k) in Scheme 4.5, D−A copolymers with increased HOMO level and reduced band gap were obtained. However, these polymers exhibited very poor efficiencies with PCBM because the energy difference between the LUMO of the D−A copolymers (−3.9 eV) and the LUMO of PCBM (−3.8 eV) was too low for an efficient charge transfer (Dennler, Scharber, & Brabec, 2009).

4.2.2.2 2,7-carbazole D−A polymers

Carbazole is structurally similar to fluorine, and its derivatives have been widely used as electron donors. Carbazole-based polymers present excellent thermal, photochemical, and air stability because of their deep-lying HOMO levels, high-electron-mobility, and a tendency to form charge-transfer complexes (Blouin et al., 2008). However, their limited solubility is due to the strong interchain interactions and their planar polymer backbone conformation. The latter causes problems during copolymer dissolution in organic solvents and device fabrication, resulting in lower PCEs. A variety of carbazole alternating D−A copolymers have been synthesized using Suzuki cross-coupling polymerization, among which a few selected D−A copolymers, shown in Scheme 4.6.

Scheme 4.6 Alternating D−A copolymers based on carbazole.

A very important contribution on the synthesis of alternating D−A copolymers based on carbazole with improved absorption and good yields in the photovoltaic devices were performed by Leclerc and his group.

More specifically, poly[N-9′-heptadecanyl-2,7-carbazole-alt-5,5-(4′,7′-di-2-thienyl-2′,1′,3′-benzothiadiazole)] polymer (a) in Scheme 4.6, known as PCDTBT, was reported for the first time by Leclerc (Beaupré & Leclerc, 2013; Chu et al., 2011). Since then, the preparation of this polymer has been optimized and 2,7-dibromocarbazole is now prepared in high yield using two simple steps from commercially available 4,4-dibromobiphenyl. Although poly(N-alkyl-2,7-carbazole) derivatives generally exhibit poor solubility and low molecular weights, the use of a 9-heptadecanyl side chain on the nitrogen atom of the carbazole unit was a major breakthrough for soluble and high molecular weight poly(2,7-carbazole) derivatives. The PCDTBT polymer (a), is prepared using the widely used Suzuki cross-coupling polymerization (Mishra et al., 2009; Tsumura et al., 1986).

The copolymer (a) had a deep-lying HOMO of −5.5 eV, a low-lying LUMO of −3.60 eV, and a band gap of 1.88 eV(Beaupré & Leclerc, 2013) Heeger et al. optimized the conditions for its device fabrication, by adding a titanium oxide as an optical spacer and a hole blocking layer sandwiched between the active layer and the aluminum layer; by increasing the blend ratio to (a): $PC_{71}BM = 1:4$; and by changing the solvent from chloroform to dichlorobenzene. These optimized conditions resulted in an increase of PCE to 6.2% ($J_{SC} = 11.9$ mA/cm^2, $V_{oc} = 0.88$ V, FF = 0.66) (Park, Roy, et al., 2009).
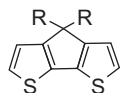
More recently, Cao reported a higher PCE of 8.37% for D−A polymer (a), by incorporating an alcohol/water soluble poly[(9,9-bis(3-(N,N-dimethylamino)propyl)-2,7-fluorene)-alt-2,7-(9,9-dioctylfluorene) as a cathode interlayer in a BHJ solar cell with $PC_{71}BM$ (He, Zhong, et al., 2012).

Zhang et al. synthesized D−A polymer (b), Scheme 4.6, with an electron donating alkoxy group attached to the acceptor moiety that increased the HOMO by 0.2 eV when compared with the polymer (a) (Qin et al., 2009). Polymer (b) exhibited an initial PCE of 2.75% ($J_{SC} = 8.0$ mA/cm^2, $V_{oc} = 0.74$ V, FF = 0.55), which was increased to 5.4% upon addition of 1,8-diiodooctane (DIO) additive ($J_{SC} = 9.6$ mA/cm^2, $V_{oc} = 0.81$ V, FF = 0.69) (Qin et al., 2009).

Other D−A copolymers of carbazole have been synthesized by Suzuki cross-coupling polymerization by varying the acceptor units, as shown in Scheme 4.6 structures (c)−(e) (Kularatne et al., 2013).
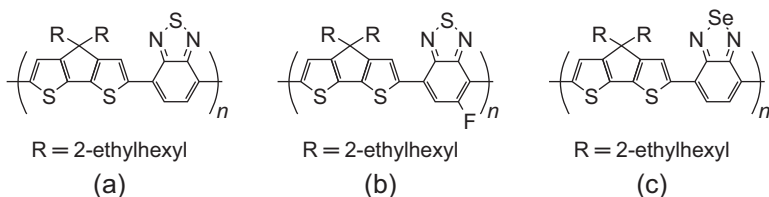
4.2.2.3 D-A polymers of bridged bithiophenes

The fused thiophene analogs can produce alternating D−A copolymers with high planarity. The thiophene analog of fluorene is the cyclopenta[2,1-b:3,4-b′]dithiophene (CPDT), Scheme 4.7, which is obtained by fusing two thiophene rings. CPDT is much more electron rich than fluorene and hence has a stronger orbital mixing with the acceptor units. The CPDT is a versatile building block for a variety of functional conjugated polymers, because the 4-carbon of the CPDT can be functionalized with a wide range of substituents enabling the fine tuning of the electronic properties of the resulting copolymers (Hou et al., 2008).

Cyclopenta[2,1-*b*:3,4-*b'*]dithiophene

Scheme 4.7 Cyclopenta[2,1-*b*:3,4-*b'*]dithiophene (CPDT).

R = 2-ethylhexyl

(a)

R = 2-ethylhexyl

(b)

R = 2-ethylhexyl

(c)

Scheme 4.8 Cyclopenta[2,1-*b*:3,4-*b'*]dithiophene D−A copolymer incorporating the 2,1,3-benzothiadiazole or 2,1,3-benzoselenodithiophene acceptor units.
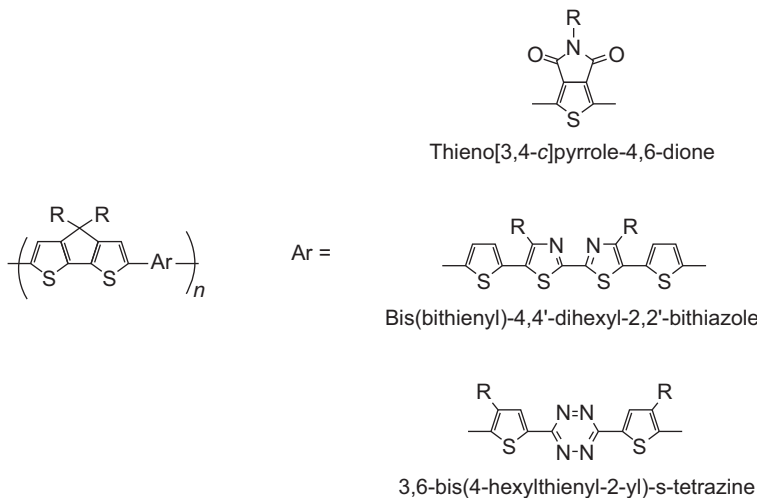
In 2005, Brabec et al. synthesized the first cyclopenta[2,1-*b*:3,4-*b'*]dithiophene D−A copolymer, structure (a) in Scheme 4.8, by Stille cross-coupling polymerization resulting in a copolymer with a HOMO of −5.30 eV and a band gap of 1.40 eV, which exhibited a PCE of 3.5% (Muhlbacher et al., 2006). However, because of the unfavorable phase separation of the polymer-fullerene blend, low PCEs were obtained for this polymer (Moule et al., 2008). Bazan et al. further optimized the device performances of the same copolymer with $PC_{71}BM$ and with a processing additive 1,8-octanedithiol and obtained a PCE of 5.5% with a J_{SC} of 16.2 mA/cm^2 (Peet et al., 2007). One factor for the improvement of this PCE is that the alkane dithiols influence the physical interactions between the polymer chains and/or between polymer and fullerene phases (Peet et al., 2007).

Neher et al. further improved the PCE of CPDT-2,1,3-benzothiadiazole D-A polymer to 6.16% by attaching a fluorine atom to the 2,1,3-benzothiadiazole acceptor unit (b) (Albrecht et al., 2012). Yang et al. synthesized a CPDT-2,1,3-benzoselenodithiophene D-A polymer (c) which had a HOMO of 0.08 eV lower than that of (a) (Hou et al., 2008).
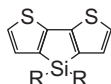
A variety of CPDT D−A polymers have also been synthesized by replacing the 2,1,3-benzothiadiazole acceptor, influencing thus the HOMO and the LUMO energy levels and the optical band gaps. Thieno[3,4-*c*]pyrrole-4,6-dione, bis(bithienyl)-4,4'-dihexyl-2,2'-bithiazole, and 3,6-bis(4-hexylthienyl-2-yl)-*s*-tetrazine acceptors, Scheme 4.9, have been used to generate CPDT D−A polymers that showed better performances in BHJ solar cells with PCEs of 3% (Kularatne et al., 2013).

Another fused-ring thiophene donor building block that attracted much attention in the past few years is dithieno[3,2-*b*:2',3'-*d*]silole D−A polymers (DTS), in which the C atom at the 4-position has been replaced with a silicon atom, Scheme 4.10.

DTS D−A polymers have lower LUMO levels and have shown better performances in optoelectronic devices when compared with CPDT analogues. The changes in the electronic properties are due to the effective orbital mixing allowing for a low-lying

Thieno[3,4-*c*]pyrrole-4,6-dione

Ar =

Bis(bithienyl)-4,4'-dihexyl-2,2'-bithiazole

3,6-bis(4-hexylthienyl-2-yl)-s-tetrazine

Scheme 4.9 Examples of CPDT D−A polymers using different accepting units.
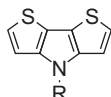
Scheme 4.10 The dithieno[3,2-*b*:2′,3′-*d*]silole fused thiophene unit.

LUMO and a low band gap (Kim, Fei, James, Heeney, & Kim, 2012). Moreover, the introduction of silicon stabilizes the diene HOMO when compared with the carbon counterpart, enhancing the ambient stability of the silole polymers (Huo, Chen, Hou, Chen, & Yang, 2009). A variety of DTS D−A copolymers with different acceptor units have been synthesized by Stille or Suzuki cross-coupling polymerizations.

Another class of structurally related analogues of CPDT is dithieno[3,2-*b*:2′,3′-*d*] pyrrole (DTP), in which a nitrogen atom is inserted at the 4-position, Scheme 4.11.

As discussed earlier, the atom of the 4-position of CPDT plays a pivotal role in the electronic properties of the resulting polymer. In the case of nitrogen and due to its stronger electron donating ability, the HOMO of the polymer is increased and the band gap is reduced. However, because of the higher HOMO level, DTP D−A polymers are not stable in air and can be easily oxidized (Zhang, Guo, et al., 2009). DTP D−A copolymers with various acceptor units have been synthesized by Stille cross-coupling polymerization.

**Scheme 4.11** The dithieno[3,2-*b*:2′,3′-*d*]pyrrole (DTP) unit.

4.2.2.4   Benzo[1,2-b:4,5-b′]dithiophene donor-A polymers
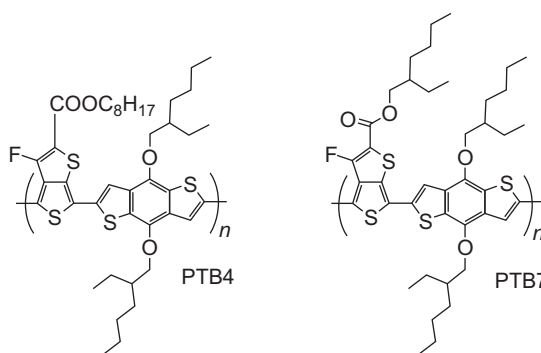
Benzo[1,2-*b*:4,5-*b*′]dithiophene (BDT), Scheme 4.12, is one of the most used donor building block for the synthesis of semiconducting polymers used in OFETs and BHJ solar cells (Liang, Feng, et al., 2009; Liang et al., 2010; Liang, Wu, et al., 2009; Sista et al., 2010; Sista et al., 2011; Son et al., 2011).

Benzo[1,2-*b*:4,5-*b*']dithiophene   Thieno[3,4-*b*]thiophene

Scheme 4.12 The benzo[1,2-*b*: 4,5-*b*′]dithiophene and thieno [3,4-*b*]thiophene building blocks.

    The BDT building block offers two advantages: the fused BDT allows the incorporation of substituents on the central benzene core while maintaining the planarity of the two thiophene units, and the symmetric nature of the BDT monomer eliminates the need of controlling regioregularity during the polymerization (Sista et al., 2010). Moreover, because of the large planar conjugated structure of the BDT unit, the polymer can easily form $\pi-\pi$ stacks, which renders high charge carrier mobility. A series of novel semiconducting polymers based on alternating ester substituted thieno[3,4-*b*] thiophene and benzodithiophene units, Scheme 4.12, exhibit a synergistic combination of properties that lead to an excellent photovoltaic effect (Liang, Wu, et al., 2009). The stabilization of quinoidal structure from thieno-[3,4-*b*]thiophene results in a low band gap of the polymer of about 1.6 eV, showing efficient absorption around the region with the highest photon flux of the solar spectrum (about 700 nm). The rigid backbone results in a good hole mobility of the polymer, and the side chains on the ester and benzodithiophene enable good solubility in organic solution and suitable miscibility with the acceptor. The introduction of fluorine into the thieno[3,4-*b*]thiophene provides the polymer with a relatively low-lying HOMO energy level, which offers enhanced V_{oc}. The polymer chain was found to be stacked on the substrate in the face-down conformation that favors charge transport. All these advantages of thieno
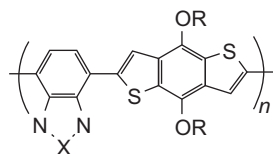

Scheme 4.13 Alternating D−A polymers PTB based on thieno[3,4-*b*] thiophene and benzodithiophene.

[3,4-*b*]thiophene and benzodithiophene polymers (PTBs), Scheme 4.13, enabled their application in BHJ polymer/fullerene solar cells and a PCE up to 6.1% has been achieved from PTB4/PC61BM prototype devices (Son et al., 2011).

After an extensive structural optimization a new polymer from the PTB family, PTB7, shown in Scheme 4.13, was developed which exhibited an excellent photovoltaic effect. A PCE of about 7.4% has been achieved from PTB7/PC71BM solar cell devices. The branched side chains in ester and benzodithiophene render the polymer's good solubility in organic solvents.

Hou et al. first introduced the BDT-conjugated polymers, by copolymerizing alkoxy-substituted BDT with electron-rich and electron-deficient aromatic units, as for example with benzo[2,1,3]thiadiazole or benzo[2,1,3]selenadiazole acceptors units, Scheme 4.14 (Hou et al., 2008).
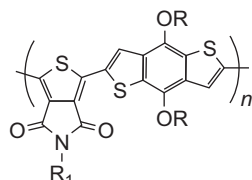
N-alkylthienopyrroledione has also used as an acceptor for the synthesis of BDT D−A copolymers, Scheme 4.15 structures (a)−(e). Leclerc et al. synthesized polymer (a), which showed an initial PCE of 5.5% (Zou et al., 2010). Frechet et al. further optimized the device performance by using DIO additive and increased the PCE to 6.8% (Piliego et al., 2010).

X = S, Se
R = $C_{12}H_{25}$
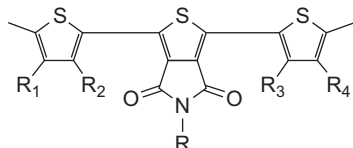
Scheme 4.14 Benzodithiophene based polymers with benzo[2,1,3]thiadiazole or benzo[2,1,3] selenadiazole acceptors units.

(a) R1 = octyl, R = 2-ethylhexyl
(b) R1 = 2-octyldodecyl, R = dodecyl
(c) R1 = 2-octyldodecyl, R = 2-ethylhexyl
(d) R1 = R = 2-ethylhexyl
(e) R1 = 3,7-dimethyloctyl, R = 2-ethylhexyl
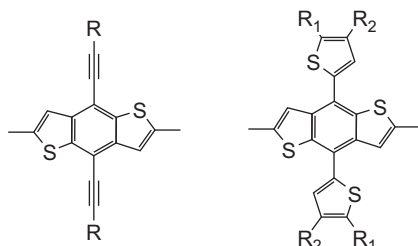
Scheme 4.15 *N*-alkylthienopyrroledione bearing BDT-conjugated polymers.

Several groups synthesized BDT D−A copolymers with thienopyrroledione as the acceptor unit and thiophene or substituted thiophene as the bridging conjugated moiety (Scheme 4.16) to BDT. The efficiencies did not improve with the additional conjugation along the polymer backbone and the highest reported PCE was 3.9% (Najari et al., 2011).

Scheme 4.16 Thienopyrroledione acceptor unit employed in several BDT-conjugated polymers.

The choice of the substituents attached to the 4 and 8 positions of the BDT moiety play a crucial role in controlling the solubility, molecular weight, optical, and electronic properties of conjugated polymers. Phenylethynyl, triisopropylsilylethnyl, alkylthienyl, and alkylbithienyl substituents, Scheme 4.17, were attached on the BDT and used as donors to generate D−A BDT copolymers (Kularatne et al., 2013).
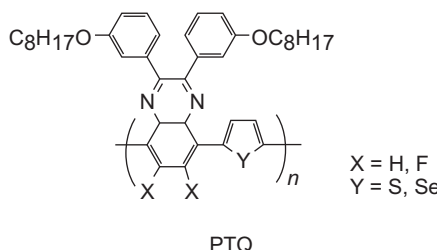
Scheme 4.17 Structures of ethnyl- or alkylthienyl- substituted benzodithiophene.

4.2.2.5 Quinoxaline bearing D−A copolymers

A promising conjugated polymer consisting of alternating thiophene and quinoxaline units (TQ1) has been designed and synthesized, which has a high photovoltaic efficiency of 6−7% combined with an efficient synthesis (Huo et al., 2008; Lai, Chueh, Chen, Wu, & Chen, 2009; Wang et al., 2010; Wang et al., 2013; Yamamoto et al., 2003; Zhuang et al., 2013). Having a simple, high-yielding synthetic route that will reduce materials' cost is of critical importance for the commercialization of polymer solar cells (PSCs). To further explore possibilities of improving the photovoltaic performance, modifications in chemical structures to push the efficiency toward the theoretical limit in single junction photovoltaic cells, achieving both a high short-circuit current density (J_{SC}) and a high V_{oc} is crucial, along with a high fill factor (FF). Both J_{SC} and V_{oc} are limited by the band gap of the active material and alignment of the HOMO and the LUMO levels

with respect to the acceptor material used in the D—A heterojunction. The PCE is not monotonically correlated to either the band gap of the donor material or the LUMO level offset of the donor to the acceptor, but both of them need to be optimized independently (Zhuang et al., 2013).

Along these lines is an easily synthesized D—A type of low-band-gap polymer based on thiophene and quinoxaline named poly[2,3-bis-(3-octyloxyphenyl) quinoxaline-5,8-diyl-alt-thiophene-2,5-diyl] (PTQ, X=H, Y=S), Scheme 4.18, was reported for application in polymer solar cells.
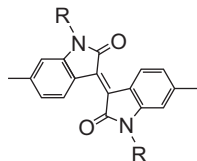
Scheme 4.18 Poly[2,3-bis-(3-octyloxyphenyl) quinoxaline-5,8-diyl-alt-thiophene-2,5-diyl] D—A polymer.

This polymer structure and its optical properties have previously been disclosed by Yamamoto et al (Yamamoto et al., 2003). Several similar polymers with different side chains were synthesized with low molecular weights, showing poor photovoltaic performance (Huo et al., 2008; Lai et al., 2009). After optimization of the synthesis of TQ1 and study of its optical, electrochemical, and photovoltaic properties, it was found that the polymer shows promising photophysical properties with a broad absorption spectrum and an optical band gap of 1.70 eV, meanwhile the HOMO and LUMO levels are located in suitable positions matching with those of PCBMs and keeping a high V_{oc} of about 0.9 V. Based on the excellent photophysical and electrochemical properties, a PCE of 6% was achieved by simply processed devices, which demonstrates TQ1 to be a particularly promising candidate for high-efficiency polymer solar cells (Wang et al., 2010).

Moreover, the side chain architecture of alternating copolymers based on thiophene and quinoxaline (TQ) was found to strongly influence the solubility and photovoltaic performance. TQ polymers with different linear or branched alkyloxy-phenyl side chains on the quinoxaline unit were compared showing that attaching the linear alkyloxy side-chain segment at the *meta-* instead of the *para-* position of the phenyl ring reduces the planarity of the backbone but the delocalization across the backbone is not affected. The reduced tendency for aggregation of TQ polymers with linear *meta-*alkyloxy-phenyl persists in the solid state. As a result, it is possible to avoid the decrease in charge-transfer state energy that is observed for bulk-heterojunction blends of more ordered TQ polymers and fullerenes. The associated gain in open-circuit voltage of disordered TQ:fullerene solar cells, accompanied by a higher short-circuit current density, leads to a higher power conversion efficiency overall (Wang et al., 2013).

4.2.2.6   Isoindigo bearing D—A copolymers
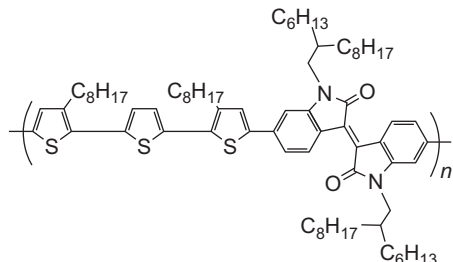
Isoindigo, Scheme 4.19, is a structural isomer of the famous pigment indigo and has been developed as an electron acceptor for designing D—A polymers (Stalder, Mei, & Reynolds, 2010).
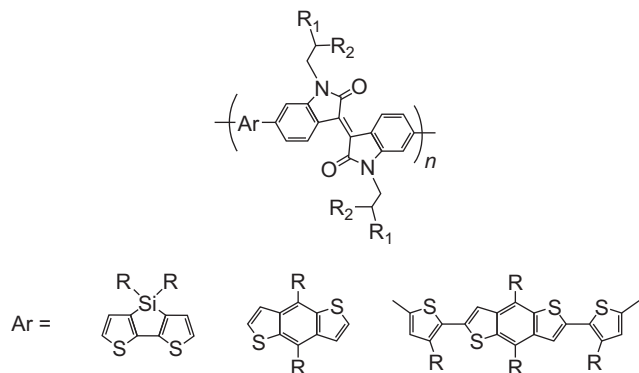

Scheme 4.19 Chemical structure of the isoindigo moiety.

Its homopolymer presented an *n*-type character, capable of serving as an acceptor material to fabricate all-PSCs. When blended with P3HT it yielded a PCE of 0.5% (Stalder et al., 2011). After copolymerization with donor units, many containing D—A polymers were synthesized for OFET and PSC devices. For the application in solar cells, the polymer bearing terthiophene as donating groups, Scheme 4.20, afforded a PCE of 6.3% when blended with PC71BM, which is a record reported for isoindigo polymers (Wang, Ma, et al., 2011).

Other donor units were also combined, Scheme 4.21, which exhibited acceptable PCEs higher than 4% (Ma et al., 2012; Stalder, Grand, Subbiah, So, & Reynolds, 2012).
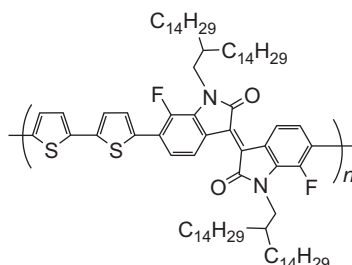

Scheme 4.20 A terthiophene-isoindigo alternating D—A copolymer.

Scheme 4.21 Examples of isoindigo-based copolymers.

Isoindigo was structurally modified to design new acceptors. Fluorination of the isoindigo unit gave a new acceptor, which was expected to lower the LUMO level of the corresponding polymer and increase the electron mobility. As a result, the LUMO level of polymer shown in Scheme 4.22 was reported to be lower than that of the polymer without fluorine. FET devices applying this polymer and fabricated under ambient conditions provided improved electron mobility of 0.43 cm^2/V s by comparison with the nonfluorinated polymer, whereas maintaining high hole mobility up to 1.85 cm^2/V s (Lei et al., 2012).

Scheme 4.22 Fluorinated isoindigo-based copolymer with bithiophene as the donating unit.

4.3 Fullerene and polymeric-based electron acceptors for bulk heterojunction photovoltaic solar cells

Many polymeric donors with suitable band gaps have been developed; however, their photovoltaic performances are still around 10%, mainly due to the irrelative high energy levels compared with that of PCBM, which reduced the device's V_{oc}, and hence their PCE.
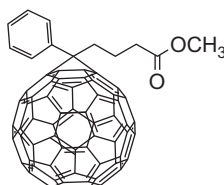
The basic requirements of materials with an electron acceptor character (*n*-type semiconductors) in photovoltaic devices are good electron mobilities for the successful collection of electrons in the cathode, good electrochemical properties, and suitable energy level values, particularly the LUMO level.

Finding the appropriate value of the LUMO level of the electron acceptor is a complex process since it affects many factors that contribute to the final performance of the device. The LUMO level of the electron acceptor must be high enough so as to achieve a higher V_{oc}, but not higher than the LUMO level of the electron donor, to permit the electron transition from the electron donor to the electron acceptor. Otherwise, the electron will return to the HOMO of the electron donor without contributing to the photovoltaic effect. The effectiveness of this transition is also affected, by the band gap between the LUMO level of the donor and the LUMO level of the acceptor.

Other important parameters that influence the ability of the electron acceptor to be used in photovoltaic devices are solubility in organic solvents, good film-forming properties, and to present a compatible surface energy with that of the electron donor.

4.3.1 Fullerene-based electron acceptors

The predominant electron acceptors, which have resulted in high efficiencies in organic photovoltaic devices together with P3HT, as the electron donor, are the fullerene derivatives PC60BM and PC70BM, Scheme 4.23. For this reason, much research interest has been focused in recent years on the synthesis of more fullerene derivatives.

PCBM

[6,6]-phenyl-C61-butyric acid methyl ester

Scheme 4.23 The electron acceptor PC60BM, [6,6]-phenyl-C61-butyric acid methyl ester.

The study of polymer solar cells began by the groups of Sariciftci and Heeger (Sariciftci et al., 1992; Yu et al., 1995) using poly((1-methoxy)-4-(2-ethylhexyloxy)-p-phenylenevinylene) as the electron donor and C60 as the electron acceptor. However, the final efficiency of photovoltaic devices was quite low. Thereafter, Hummelen, Wudl, and their research teams developed a soluble derivative of fullerene the [6,6] phenyl-C61-butyric acid methyl ester known as PC60BM or PCBM (Hummelen et al., 1995). Using PC60BM, in the active layer of the photovoltaic devices, a disadvantage of weaker absorption in the visible region (400−800 nm) because of the high symmetry of C60 appeared. This problem has been overcome by the development of PC70BM, which shows much stronger absorbance in the ultraviolet−Vis spectrum at 200−700 nm, and particularly in the visible region compared with PC60BM (Wienk et al., 2003) (Figure 4.3).

In the attempt to optimize the efficiency of photovoltaic cells, several new derivatives of fullerene have been synthesized to present the above characteristics and even better properties than PC60BM and PC70BM (He & Li, 2011). Following is a classification of several fullerene derivatives according to their structure.

Several research teams (Chen, Yao, & Chen, 2012; Drees et al., 2005; Wang, He, et al., 2011; Zhao, He, Xu, et al., 2010; Zheng et al., 2004) found significant solubility improvements by changing either the length of the butyl chain or the end methyl ester group of PCBM but without altering the aromatic part. As an example, four C60 derivatives were reported, (a)−(d) (see Scheme 4.24) by changing the methyl end group with butyl, octyl, dodecyl, and cetyl groups for further improving the solubility of PC60BM (Zheng et al., 2004). The morphology of the materials is strongly affected increasing their electron mobility. The efficiency of the new systems did not improve, showing yields even lower than the known system PCBM-P3HT in BHJ devices. Also,
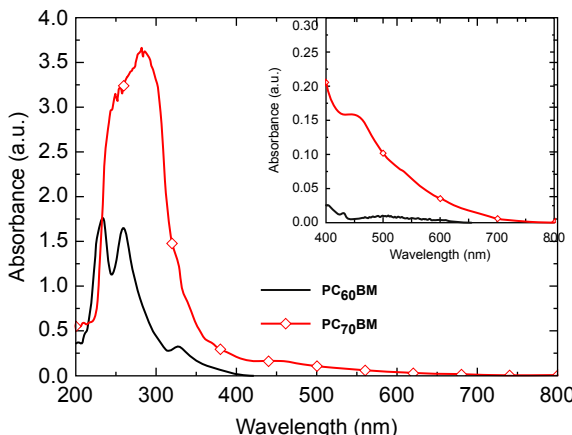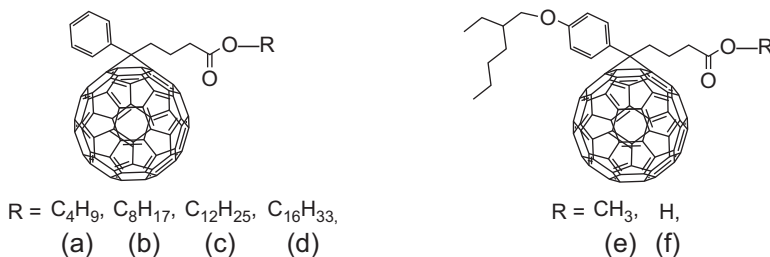
Figure 4.3 Absorption spectra of PC60BM and PC70BM in THF solutions (10^{-5} mol/L), the inset shows the enlarged absorption spectra in the visible region (He & Li, 2011).
Reproduced from He and Li (2011) with permission of The Royal Society of Chemistry (RSC) on behalf of the Centre National de la Recherche Scientifique (CNRS) and the RSC; http://dx.doi.org/10.1039/C0CP01178A.

Scheme 4.24 Derivatives of PC60BM having different alkyl ester groups or alkoxyl substituted phenyl ring.
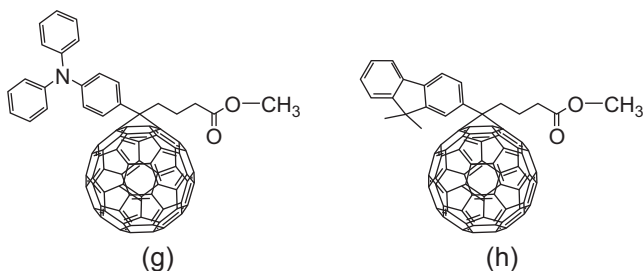
minor changes were observed in the energy levels and the electrochemical properties of those new fullerene derivatives.

Similarly, derivatives of PCBM have been synthesized by modifying the aromatic part (Kooistra et al., 2007; Yang et al., 2008; Zhang, Yip, et al., 2009). This category was created by adding new groups in the phenyl ring, by replacing the phenyl ring with other cyclic groups such as thiophene and fluorene, or with aliphatic groups, with or without simultaneous modification of the existing aliphatic part.

As an example other C60 derivatives were synthesized, (e) and (f) (see Scheme 4.24), by adding an alkoxyl substituent on the phenyl ring and changing the methyl end group with a hydrogen atom in (f) (Yang et al., 2008).

Hummelen et al. also studied alkoxyl substituents onto the phenyl ring of PC60BM. They also found that the alkoxyl substituent can raise the LUMO energy

level and the V_{oc} effectively (Kooistra et al., 2007). Several PC60BM-like C60 derivatives were also synthesized, by changing the butyl middle chain in the side chain of PC60BM to propyl, pentyl, hexyl, and heptyl chains for investigating the effect of the alkyl middle chain length on the photovoltaic properties of the C60 derivatives (Zhao, He, Xu, et al., 2010). PC60BM with a bulky triphenylamine (g) or 9,9-dimethylfluorene (h) were also synthesized, Scheme 4.25, aiming at suppressing the crystallization of the resulting materials for higher stability inside the PSCs (Zhang, Yip, et al., 2009).

(g)   (h)

Scheme 4.25 Triphenylamine and 9,9-dimethylfluorene derivatives of PC60BM.

Working in this direction, research groups introduced nitrogen and silicon (Morvillo & Bobeico, 2008; Park, Yang, et al., 2009; Yang, Cho, et al., 2009), among the aromatic and the aliphatic moieties. Most of those molecules presented increased LUMO levels and higher thermal stability, but still without improved efficiencies of the final photovoltaic device.

As mentioned previously, controlling the LUMO level is a crucial factor for the properties of the electron acceptor. Large differences between the HOMO level of the donor and the LUMO level of the acceptor lead to the improvement of V_{oc} value, and thus the increase of the final efficiency of the photovoltaic device.

Many non-PCBM fullerene acceptors with higher energy levels reported so far have shown better performance in P3HT-based OPV systems (He, Chen, et al., 2010; He, Shao, Xiao, Smith, & Hong, 2013; He, You, et al., 2012); however, their performance in low-band-gap polymer systems are poor. Despite some efforts on novel fullerene acceptors in OPV, there is still room for further improving the photovoltaic performance of low-band-gap polymer donor materials. Thus, research effort focus on the design of novel fullerene acceptor materials with higher LUMO levels, which are suitable for the application in low-band-gap polymer single layer. To up-shift the LUMO level of a fullerene molecule, several approaches are available. The first is adding more substitutes on the fullerene core to obtain fullerene multiadduct thus reducing the number of double bonds and resulting in the destruction of the conjugation of the fullerene molecule. As a result, the LUMO level would be increased. However, these fullerene multiadducts will have much lower electron mobilities, which will impact the device's J_{sc}. The second approach is using endohedral fullerene as starting material to replace fullerene when synthesizing fullerene

derivatives. However, the solubilities of endohedral fullerene derivatives in common organic solvents are much worse than that of fullerene derivatives. Using long-chain substitutes can address the solubility problem, but it will also decrease their electron mobility at the same time. In addition, the synthesis of endohedral fullerenes is tedious, which results in much higher costs in obtaining the final products as compared to acceptors with C60 or C70 as the starting materials. The third approach is using a metal fullerene complex. These complexes also have higher energy levels than C70 because of the interaction between fullerene and metal moieties. However, they are typically thermally unstable, which presents challenges in common device optimization processes, such as thermal annealing.

An example to overcome these problems was the synthesis of a C70 mono adduct that showed relatively good performance (6.00%PCE with low-band-gap polymer PBDTTT-C) (He, You, et al., 2012). Furthermore and to balance the LUMO level, solubility, and electron mobility of fullerene acceptors, a fullerene acceptor (ICBM) based on C70 was designed. The electron-donating property of the propylidene segment helped to shift the LUMO level further up, whereas the ester group enhance its miscibility with donor materials as compared with C70 derivatives with alkyl chain substitutes. The photovoltaic devices based on ICBM or PC70BM as acceptors, and P3HT or PTB7 as donors showed PCEs 5.00% and 6.67%, respectively. This was the first time a high LUMO level acceptor showed better performance than PC70BM in both P3HT and a low-band-gap polymer donor system.
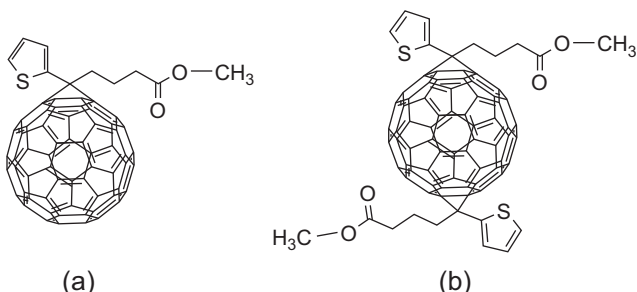
Several other methods have been proposed to raise the LUMO level (Garcia-Belmonte et al., 2010; Kooistra et al., 2007; Matsuo, 2012; Rondeau-Gagne, Lafleur-Lambert, Soldera, & Morin, 2011) for the reduction of p-electrons in the fullerene, by modifying the structure of the fullerene with several groups, and particularly by the introduction of substituents which act as electron donors. Based on this methodology, several research groups have developed a variety of fullerene derivatives (Cates et al., 2009; Choi et al., 2010; Lin, Li, & Zhan, 2012). In many cases, the LUMO level was increased by consequently increasing the value of V_{oc}, but the value of PCE was equal or lower than the yield of the known system P3HT-PCBM. This was mainly because the LUMO level of the acceptor did not reach the appropriate value to facilitate the transition of the electron from the LUMO of the donor to the LUMO of the acceptor.

As mentioned previously, another interesting group of fullerene derivatives are endohedral fullerenes. Trimetallic nitride endohedral fullerenes were discovered in 1999 by Stevenson and his group (Stevenson et al., 1999). Theoretical and experimental studies have shown that the LUMO level of this fullerene category is much higher than that of the "empty" fullerene (Cardona, Elliott, & Echegoyen, 2006; Farrington et al., 2012; Liu et al., 2012; Ross et al., 2009). Ross et al. (2009) recently synthesized a series of soluble derivatives Lu3N@C80, which resulted in raising the LUMO level and in combination with the electron donor P3HT in OPVs they presented a PCE of 4.2%.

The fullerene bisadducts and multiadducts, which are also discussed previously, possess an up-shifted LUMO energy level, and their respective PSCs showed higher open-circuit voltages. In the synthesis of PC60BM, the products also includes
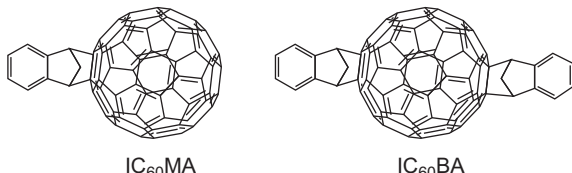
the PC60BM-bisadduct (bisPC60BM), the PC60BM-trisadduct (trisPC60BM), the PC60BM-tetraadduct, and altogether higher-adducts (Lenes et al., 2008; Lenes et al., 2009). The influence of the PC70BM bisadducts to the photovoltaic properties was investigated using poly(2,5-bis(3-hexadecylthiophen-2-yl)thieno [3,2-*b*]thiophene) (pBTTT) as the donor and the fullerene derivatives as acceptor (Cates et al., 2009).

A series of the thienyl-substituted methano-fullerenes, including ThC60BM (a), ThC60BM-bisadduct (b), ThC60BM-triadduct, and ThC60BM-tetra adduct (see Scheme 4.26), aiming at improving the miscibility of the polymer donor and the fullerene acceptor and increasing the V_{oc} of the PSCs (Choi et al., 2010). They also studied the photovoltaic properties of the PSCs with P3HT as donor and the C60 derivatives as acceptor. Lenes et al. also studied the photovoltaic performance of bisThC60BM (b) and bisThC70BM, their results indicate that the two bisadducts show higher V_{oc} than their respective mono adducts ThC60BM (a) and ThC70BM, similar to the trend of the devices based on bisPC60BM and PC60BM.

(a)   (b)

Scheme 4.26 Mono- and bisadducts of thienyl-substituted methano-fullerenes C60.

For improving the photovoltaic performance of the PSCs based on P3HT, the most efficient derivatives up to now are the indene-C60 bisadduct (IC60BA) and the indene-C70 bisadduct (IC70BA). Scheme 4.27 shows the bis and mono indene-C60 adducts (He, Chen, et al., 2010; He, Zhao, et al., 2010; Zhao, He, & Li, 2010). These derivatives have shown significant improvements of the V_{oc} while giving good PCE values as reported for indene-C60 bisadduct (ICBA). The cells based on P3HT as donor and ICBA as acceptor showed a high V_{oc} of 0.84 V and


IC$_{60}$MA   IC$_{60}$BA
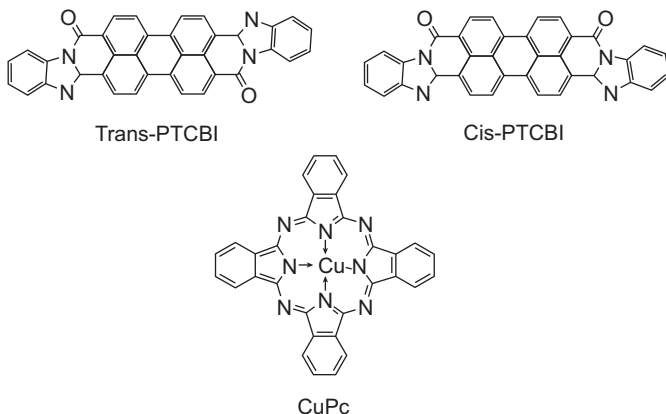
Scheme 4.27 The indene-C60 mono adduct (ICMA) and bisadduct (ICBA).

a PCE value of 5.44% (He, Chen, et al., 2010). After device optimization of BHJ PSCs based on P3HT as donor and ICBA as acceptor, the optimized cells with the P3HT:ICBA weight ratio of 1:1, solvent annealing and prethermal annealing at 150 °C for 10 minutes, exhibits a high PCE of 6.48% with V_{oc} of 0.84 V, I_{sc} of 10.61 mA/cm^2, and FF of 72.7%, under the illumination of AM 1.5G, 100 mW/cm^2 (He, Zhao, et al., 2010; Zhao, He, & Li, 2010).

4.3.2   Non-fullerene organic electron acceptors

The first heterojunction OSC reported by Tang was using organic small molecules like 3,4,9,10-perylenetetracarboxylic *bis*-benzimidazole (PTCBI) (50 nm) as the acceptor and copper phthalocyanine (CuPc) (30 nm) as the donor, Scheme 4.28 (He, Zhao, et al., 2010).

Trans-PTCBI   Cis-PTCBI

CuPc

Scheme 4.28 Examples of organic small molecular electron acceptors used in OPVs.

Since then, considerable scientific effort has been devoted to the understanding of the behavior of small organic molecules in organic photovoltaics (Hudhomme, 2013). Among the different molecules, perylene-3,4:9,10-bis(dicarboximide) (PBI) derivatives are considered as the best n-type organic semiconductors available to date (Huang, Barlow, & Marder, 2011; Würthner, 2004). Because of their unique optical, redox, and stability properties and charge-carrier mobilities, PBI dyes provide significant prospects for application in photovoltaic devices (Schmidt-Mende et al., 2001).
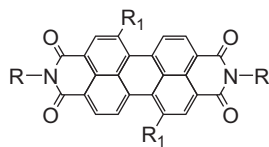
An interesting work was carried out on ethylpropyl-substituted PBI at the imide periphery (a) which was blended with a variety of donor polymers, Scheme 4.29.

Interesting results were also reported with the device using the 1,7-bis(4-*tert*-butylphenoxy)-bay substituted PBI derivative containing pyrene moieties at the imide positions (b), Scheme 4.29. This pyrene-PBI-pyrene triad acceptor was blended with a phenylenevinylene based oligomer acting as the donor.
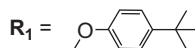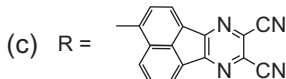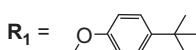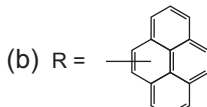
Small molecular acceptors combining the highly electron-deficient 2-vinyl-4,5-dicyanoimidazole moiety named Vinazene and benzothiadiazole were

developed as processable oligomers for photovoltaics applications, (c) in Scheme 4.29 (Woo, Holcombe, Unruh, Sellinger, & Frechet, 2010). These oligomers displayed a wide range of optical and electronic properties thanks to the modification of the central aromatic moiety. Best results were described by blending this bis-vinazene−benzothiadiazole oligomer with an octylphenyl-substituted polythiophene giving a device for which recorded a PCE of 1.4%.

Another approach introduced the concept of aromaticity gain as a driving force to reach efficient small molecule acceptors represented by the use of a 9,9′-bifluorenylidene (99′BF) polycycle scaffold (Brunetti, Gong, Tong, Heeger, & Wudl, 2010).

(a)   R = ethylpropyl R_1 = H

(b) R =

R_1 =

(c) R =

R_1 =

Scheme 4.29 Examples of perylene-3,4:9,10-bis(dicarboximide) (PBI) derivatives reported as n-type organic semiconductors.

4.3.3 Polymer-based electron acceptors

To improve the light absorption of photovoltaic cells, an optional approach is the introduction of a conjugated polymer acceptor to form all-polymer BHJ. However, and because of severe phase separation between two different conjugated polymers, the development of a conjugated polymer acceptor with enhanced light absorption and electron accepting and transporting properties, similar to those of PCBM, is a real challenge (Zhao & Zhan, 2011). To date, employment of conjugated polymer acceptors in polymer solar cells has been met with limited success. The basic requirements for an ideal polymeric acceptor include:

- good solubility and film-forming properties;
- strong and broad bandwidth absorption;

- high electron mobility;
- suitable HOMO/LUMO energy levels relative to the *p*-type electron donor;
- high purity and high molecular weight.

Representative examples of electron accepting and transporting polymers used in PSCs are presented in the following section. Most polymer acceptors are derivatives of poly(perylenediimide)s (PDI) and cyano-substituted poly(*p*-phenylene vinylene)s.

Conjugated polymers with deep LUMO levels are potential candidates as electron acceptors. These are generally realized through the use of electron-withdrawing groups, either as side-chain substituents or as main-chain units of D−A polymers. An advantage of using polymers as electron-accepting materials instead of fullerene derivatives is their higher chemical structure versatility. Moreover, the mechanism of structure formation on the mesoscale is less complex, than in blends with small molecules, and thus relatively pure phases can be achieved. In particular, the fast diffusion of fullerene derivatives within conjugated polymers does not take place in all-polymer systems. In addition, it was shown that in the case of P3HT and poly((1-methoxy)-4-(2-ethylhexyloxy)-*p*-phenylenevinylene) combinations a minimum structure size was found at the critical blend ratio, as calculated from the simple Flory−Huggins theory. Similar to polymer-fullerene systems, the morphology formation in all-polymer systems is a self-assembly process and is influenced by external parameters (Ruderer et al., 2013).

Among the various electron accepting groups, the cyano group has been commonly used as a side chain substituent (Chochos et al., 2007; Gupta, Kabra, Kolishetti, Ramakrishnan, & Narayan, 2007; Halls et al., 1995; Holcombe, Woo, Kavulak, Thompson, & Frechet, 2009; Kietzke, Hoerhold, & Neher, 2005). For example, the electron donating polythiophene derivative was combined either with the electron accepting cyano-substituted poly(*p*-phenylene vinylene) (MEH-cyano-PPV) showing an efficiency of 1.9%, or with the known electron accepting ladder-type poly(benzimidazobenzophenanthroline), which afforded a similar efficiency of 1.5% (Alam & Jenekhe, 2004).

To further improve the photovoltaic efficiency, researchers started to employ n-type polymers with excellent absorption properties and high LUMO energy levels as acceptors to replace fullerene derivatives. For instance, polymers with broad absorption (300−850 nm) and high electron mobility (1.3×10^{-2} cm^2/V s), like poly(perylenediimide-alt-dithienothiophene), are polymer acceptor candidates for all PSCs. The structure diversity of the polymer donors and of the acceptors makes it easy to tune their energy levels and their absorptions, thus optimizing the final PSC's efficiency.

However, and despite the exciting advantages of all-PSCs, the highest PCEs achieved are just above 3%. The low photocurrent and the low fill factor are mostly responsible for these unsatisfactory performances. These two factors are related to the poor exciton dissociation at the D−A interface and low carrier mobility.

Perylene diimides (Zhan et al., 2007; Zhou et al., 2011) like a PDI-based acceptor polymer in combination with polythiophene derivatives have produced BHJ solar cells with a PCE of 2.23%. Naphthalene diimide (Fabiano et al., 2011; Moore et al., 2011;
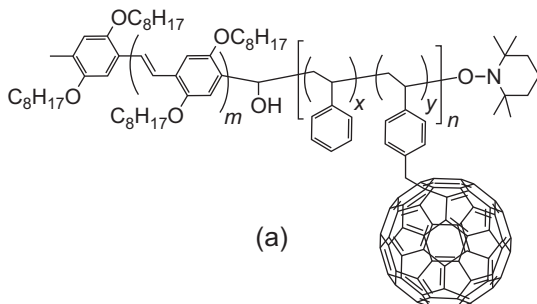
Holcombe et al., 2011) units have also been used as acceptor units in deep-LUMO D−A polymers. Among the different acceptor polymers in BHJ solar cells, a benzothiadiazole-fluorene copolymer has one of the highest PCE reported to date, at 2.7%. In a more recent report, all-polymer solar cells with a 3.3% PCE were presented by a novel polymer/polymer blend system comprising a new NDI-selenophene copolymer acceptor and a thiazolothiazole-dithienosilole copolymer donor (Earmme, Hwang, Murari, Subramaniyan, & Jenecke, 2013).

In 2009, Facchetti and coworkers reported a novel n-type polymer, P(NDI2OD-T2) (also known as Polyera ActivInk N2200), that exhibited a large electron field-effect mobility (Yan et al., 2009). A series of publications followed, shedding light on the injection and transport of charges, energetic disorder, and film morphology or texture. The polymer was further applied as the electron-accepting component in OSCs, though with rather low power-conversion efficiencies (Fabiano et al., 2011; Holcombe et al., 2011; Steyrleuthner et al., 2012; Yan et al., 2009; Yan et al., 2012; Zhan et al., 2007; Zhou et al., 2011). Lately, a careful selection of processing solvents to tune optimal active layer morphology in a D−A copolymer blend [PTB7:P(NDI2OD-T2)] yields bulk heterojunction microstructures with intra-domain percolative pathways and enhanced charge transport that resulted in microstructures afford all-polymer solar cells with power conversion efficiencies as high as 2.7% (Zhou, Lin, et al., 2014).

4.4   Hybrid structures of polymer, copolymer semiconductors with carbon nanostructures

As was discussed previously, the morphology of the active layer as well as its stability are two key factors in the design and development of efficient organic photovoltaics. Thus, the use of well-known concepts for nanophase separation and compatibility of the block copolymers were also used to create hybrid structures based on electron D−A block architectures. Additionally, and since the semiconducting conjugated polymeric electron donors are resembling the conformation and behavior of rigid-rod polymers, the attachment of the fullerene derivatives on a flexible polymeric block was an ideal approach to control morphology. Indeed such synthetic approaches led to phase separation motives that were observed in rod-coil phase separation morphologies.
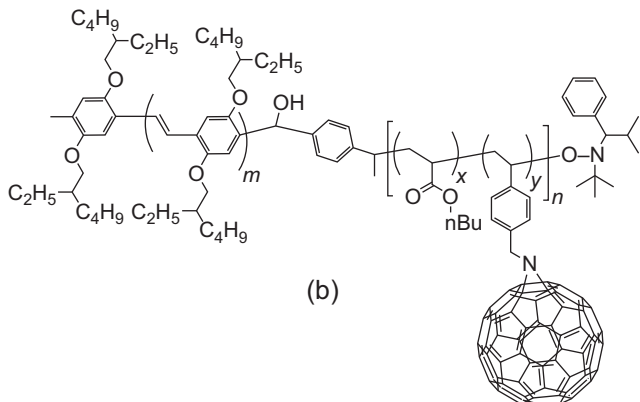
Initially functionalized PPVs and PHTs were used as the donor blocks and fullerene was covalently attached on flexible polymeric blocks like polystyrene using controlled radical polymerization techniques as the synthetic strategy. The first D−A copolymer with good electronic properties was synthesized by the group of Hadziioannou (de Boer et al., 2001), wherein the rod conjugated polymer PPV (electron donor) was used as macroinitiator for the polymerization NMRP (nitroxide-mediated radical polymerization) of two coil polymers (polystyrene, polychlorostyrene). Then the synthesized copolymer was modified with fullerene molecules (ATRA, atom transfer radical addition) obtaining thus, electron accepting properties, structure (a), Scheme 4.30.

(a)
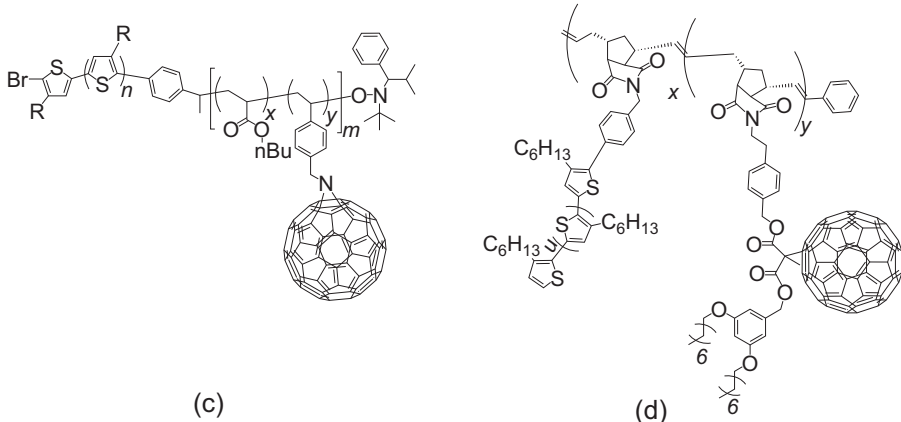
Scheme 4.30 Structure of the first electron D−A rigid-flexible block copolymer having a PPV rigid block and polystyrene based flexible coil functionalized with fullerene units.

This structure was modified several times in the years to follow in order to improve the synthetic route and deal with the various problems encountered (Barrau et al., 2008; van der Veen, de Boer, Stalmach, van de Wetering, & Hadziioannou, 2004). After examination of the C60 effect on the final electronic properties of the macromolecules, it was found that the electron mobility was increased, although still below the electron mobility of net PCBM. Also even though C60 was immobilized onto the coil copolymeric block, crystallinity problems were still observed. Nevertheless, that the hybrid copolymer gave a better performance than the polymers themselves in blend reinforces the idea of using conjugated rod-coil hybrid copolymers in photovoltaic devices. Another representative structure of a hybrid copolymer consisting of PPV and C60 is presented as structure (b) in Scheme 4.31 (Barrau et al., 2008).

Thereafter, and as a solution to the previous problem of C60 crystallinity, the replacement of PPV by other more suitable polymers, which would permit better control of generating aggregates of the final material, was examined. Most research groups (Dante, Yang, Walker, Wudl, & Nguyen, 2010; Li, Xu, Yang, & Yang, 2010; Richard

(b)

Scheme 4.31 A fullerene-grafted rod−coil block copolymer having an alkoxy-substituted PPV rigid block and poly(n-butyl acrylate)-poly(chloromethyl styrene) flexible coils. The chloromethyl styrene groups were used for the incorporation of the fullerene moieties.
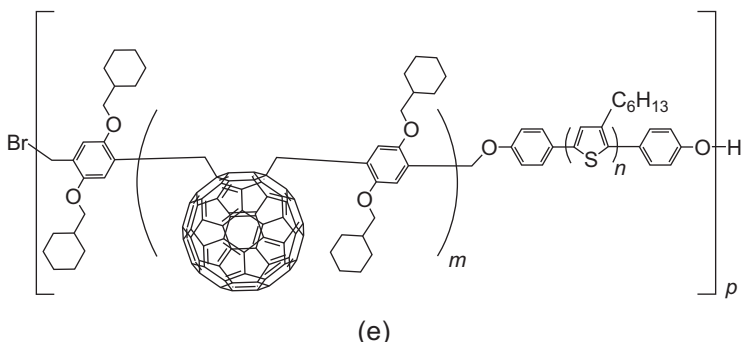
Scheme 4.32 Examples of poly(3-alkylthiophene) based hybrid copolymers.
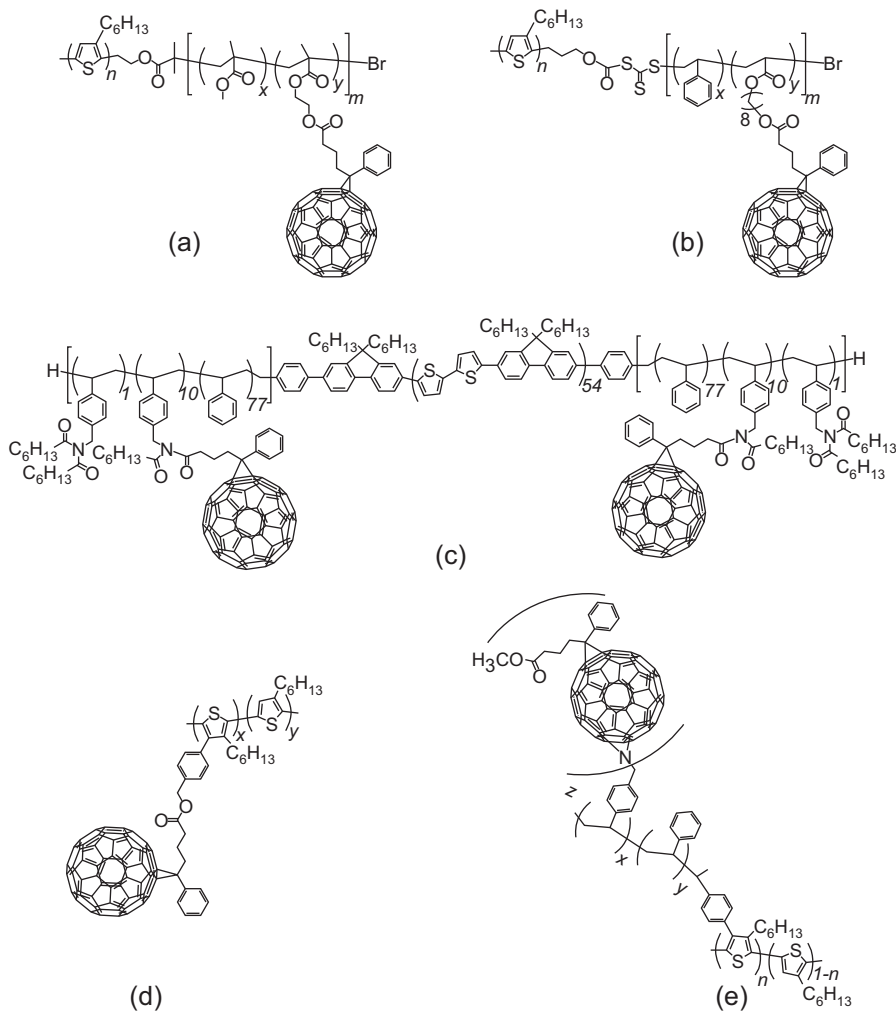
et al., 2008; Sivula, Ball, Watanabe, & Fréchet, 2006) synthesized hybrid copolymers similar to the above structure using poly (3-alkylthiophene) as the rod chain, structures (c), (d) in Scheme 4.32. The characterization of the new hybrid materials showed that the appropriate characteristics for their use in photovoltaic devices were obtained, and that the morphology of the active layer was significantly improved, but no great difference in the performance of the device was observed.

A different approach in the synthesis of hybrid polythiophene-C60 copolymer proposed the insertion of fullerene between the coil polymer chain, structure (e) Scheme 4.33, in an effort to control the orientation of the molecule to the electrodes when it is introduced in the blend and therefore the final morphology of the active layer (Hiorns et al., 2010).

To improve the morphology and increase the performance of the device, some research groups focused on the development of hybrid copolymers bearing

Scheme 4.33 A hybrid polythiophene-C60 copolymer with the insertion of fullerene moieties between the coil polymer chain.
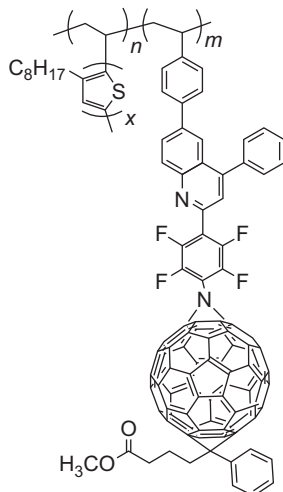
Scheme 4.34 Examples of various reported architectures of P3AT hybrid copolymers with PC60BM.

immobilized units of PCBM (Bicciocchi, Chen, Rizzardo, & Ghiggino, 2013; Gholamkhass & Holdcroft, 2010; Jea Uk, Jae Woong, Todd, Thomas, & Won Ho, 2010; Lee, Cirpan, Emrick, Russell, & Jo, 2009; Lee, Jung, Emrick, Russell, & Jo, 2010; Yang, Cho, et al., 2009; Yang, Lee, et al., 2009), which is the dominant electron acceptor in BHJ devices, showing much better properties than C60. As is shown in Scheme 4.34 structures (a)−(e), hybrid copolymers were synthesized by creating initiators at the end group of poly(thiophene)s or by modifying the side chains of the polythiophene ring in the 4 position.

Another interesting approach was the synthesis of polythiophene–co-poly(4-vinylpyridine) copolymers because P4VP is known to associate non covalently with PCBM (Sary et al., 2010), based on the fact that each molecule of PCBM can form noncovalent bonds with up to six molecules of 4-vinyl pyridine (4VP) (Laiho et al., 2006).

Most recently, a direct coupling of fullerenes onto semiconducting copolymers bearing electron-accepting poly(vinylphenyl perfluorophenyl-quinoline) blocks and electron-donating regioregular poly(3-alkyl thiophene) blocks has been demonstrated, Scheme 4.35. Through this route, one of the fluorine atoms of the perfluorophenyl ring is transformed to an azide that undergoes [3 + 2]-cycloaddition onto the fullerene's surface, producing 1,6-azo bridged carbon nanostructure–organic semiconducting hybrids (Kakogianni, Kourkouli, Andreopoulou, & Kallitsis, 2014).

Scheme 4.35 rr-Poly(3-octyl thiophene)-co-[poly(perfluorphenyl-quinoline)-PCBM] hybrids.

4.5 Conclusions

In conclusion, the progress above described the synthesis of new polymeric electron donors, based on the understanding of the influence of different structural parameters on the materials absorption, HOMO-LUMO levels, and charge mobility. This progress resulted in an impressive increase of the efficiency in organic solar cells up to 8% in quite a short period. Further optimization of the device architecture also contributed in the increase of efficiencies up to 10%, a value that is considered as a prerequisite for the commercialization of the OPV technology. Efforts on the materials synthesis optimization are currently under way to give cost-efficient solutions for the materials preparation that will enable large scale development of plastic solar cells through roll-to-roll techniques.

References

Alam, M. M., & Jenekhe, S. A. (2004). *Chemistry of Materials, 16*, 4647−4656.

Albrecht, S., Janietz, S., Schindler, W., Frisch, J., Kurpiers, J., Kniepert, J., et al. (2012). *Journal of the American Chemical Society, 134*, 14932−14944.

Allard, N., Aich, R. B., Gendron, D., Boudreault, P. L. T., Tessier, C., Alem, S., et al. (2010). *Macromolecules, 43*, 2328−2333.

Barrau, S., Heiser, T., Richard, F., Brochon, C., Ngov, C., van de Wetering, K., et al. (2008). *Macromolecules, 41*, 2701−2710.

Beaupré, S., & Leclerc, M. (2013). *Journal of Materials Chemistry A, 1*, 11097−11105.

Bian, L., Zhu, E., Tang, J., Tang, W., & Zhang, F. (2012). *Progress in Polymer Science, 37*, 1292−1331.

Bicciocchi, E., Chen, M., Rizzardo, E., & Ghiggino, K. P. (2013). *Polymer Chemistry, 4*, 53−56.

Blouin, N., Michaud, A., Gendron, D., Wakim, S., Blair, E., Neagu-Plesu, R., et al. (2008). *Journal of the American Chemical Society, 130*, 732−742.

de Boer, B., Stalmach, U., van Hutten, P. F., Melzer, C., Krasnikov, V. V., & Hadziioannou, G. (2001). *Polymer, 42*, 9097−9109.

Brunetti, F. G., Gong, X., Tong, M., Heeger, A. J., & Wudl, F. (2010). *Angewandte Chemie International Edition, 49*, 532−536.

Burroughes, J. H., Bradley, D. D. C., Brown, A. R., Marks, R. N., Mackay, K., Friend, R. H., et al. (1990). *Nature, 347*, 539−541.

Cardona, C. M., Elliott, B., & Echegoyen, L. (2006). *Journal of the American Chemical Society, 128*, 6480−6485.

Cates, C. N., Gysel, R., Beiley, Z., Miller, C. E., Toney, M. F., Heeney, M., et al. (2009). *Nano Letters, 9*, 4153−4157.

Chang, J. F., Sun, B. Q., Breiby, D. W., Nielsen, M. M., Solling, T. I., Giles, M., et al. (2004). *Chemistry of Materials, 16*, 4772−4776.

Chen, J., & Cao, Y. (2009). *Accounts of Chemical Research, 42*, 1709−1718.

Chen, Z. Y., Lemke, H., Albert-Seifried, S., Caironi, M., Nielsen, M. M., Heeney, M., et al. (2010). *Advanced Materials, 22*, 2371−2375.

Chen, L., Yao, K., & Chen, Y. (2012). *Journal of Materials Chemistry, 22*, 18768−18771.

Chochos, C. L., Economopoulos, S. P., Deimede, V., Gregoriou, V. G., Lloyd, M. T., Malliaras, G. G., et al. (2007). *The Journal of Physical Chemistry C, 111*, 10732−10740.

Chochos, C. L., Tagmatarchis, N., & Gregoriou, V. G. (2013). *RSC Advances, 3*, 7160−7181.

Choi, J. H., Son, K. I., Kim, T., Kim, K., Ohkubo, K., & Fukuzumi, S. (2010). *Journal of Materials Chemistry, 20*, 475−482.

Chu, T. Y., Lu, J., Beaupré, S., Zhang, Y., Pouliot, J.-R., Wakim, S., et al. (2011). *Journal of the American Chemical Society, 133*, 4250−4253.

Dante, M., Yang, C., Walker, B., Wudl, F., & Nguyen, T.-Q. (2010). *Advanced Materials, 22*, 1835−1839.

Dennler, G., Scharber, M. C., & Brabec, C. J. (2009). *Advanced Materials, 21*, 1323−1338.

Drees, M., Hoppe, H., Winder, C., Neugebauer, H., Sariciftci, N. S., Schwinger, W., et al. (2005). *Journal of Materials Chemistry, 15*, 5158−5163.

Earmme, T., Hwang, Y.-J., Murari, N. M., Subramaniyan, S., & Jenecke, S. A. (2013). *Journal of the American Chemical Society, 135*, 14960−14963.

Fabiano, S., Chen, Z., Vahedi, S., Facchetti, A., Pignataro, B., & Loi, M. A. (2011). *Journal of Materials Chemistry, 21*, 5891−5896.

Farrington, B. J., Jevric, M., Rance, G. A., Ardavan, A., Khlobystov, A. N., Briggs, G. A. D., et al. (2012). *Angewandte Chemie International Edition, 51*, 3587−3590.

Garcia-Belmonte, G., Boix, P. P., Bisquert, J., Lenes, M., Bolink, H. J., La Rosa, A., et al. (2010). *The Journal of Physical Chemistry Letters, 1*, 2566−2571.

Gholamkhass, B., & Holdcroft, S. (2010). *Chemistry of Materials, 22*, 5371−5376.

Guo, X., Baumgarten, M., & Müllen, K. (2013). *Progress in Polymer Science, 38*, 1832−1908.

Gupta, D., Kabra, D., Kolishetti, N., Ramakrishnan, S., & Narayan, K. S. (2007). *Advanced Functional Materials, 17*, 226−232.

Halls, J. J. M., Walsh, C. A., Greenham, N. C., Marseglia, E. A., Friend, R. H., Moratti, S. C., et al. (1995). *Nature, 376*, 498−500.

He, Y. J., Chen, H. Y., Hou, J. H., & Li, Y. F. (2010). *Journal of the American Chemical Society, 132*, 5532, 5532.

He, Y. J., Chen, H.-Y. M., Hou, J. H., & Li, Y. F. (2010). *Journal of the American Chemical Society, 132*, 1377−1382.

He, Y., & Li, Y. (2011). *Physical Chemistry Chemical Physics, 13*, 1970−1983.

Herguth, P., Jiang, X., Liu, M. S., & Jen, A. K. Y. (2002). *Macromolecules, 35*, 6094−6100.

He, Y., Shao, M., Xiao, K., Smith, S. C., & Hong, K. (2013). *Solar Energy Materials and Solar Cells, 118*, 171−178.

He, Y. J., You, J. B., Dou, L. T., Chen, C.-C., Richard, E., Cha, K., et al. (2012). *Chemical Communications, 48*, 7616−7618.

He, Y. J., Zhao, G. J., Peng, B., & Li, Y. F. (2010). *Advanced Functional Materials, 20*, 3383−3389.

He, Z., Zhong, C., Su, S., Xu, M., Wu, H., & Cao, Y. (2012). *Nature Photonics, 6*, 591−595.

Hiorns, R. C., Cloutet, E., Ibarboure, E., Khoukh, A., Bejbouji, H., Vignau, L., et al. (2010). *Macromolecules, 43*, 6033−6044.

Holcombe, T. W., Norton, J. E., Rivnay, J., Woo, C. H., Goris, L., Piliego, C., et al. (2011). *Journal of the American Chemical Society, 133*, 12106−12114.

Holcombe, T. W., Woo, C. H., Kavulak, D. F. J., Thompson, B. C., & Frechet, J. M. J. (2009). *Journal of the American Chemical Society, 131*, 14160−14161.

Hou, J., Park, M.-H., Zhang, S., Yao, Y., Chen, L.-M., Li, J.-H., et al. (2008). *Macromolecules, 41*, 6012−6018.

Huang, C., Barlow, S., & Marder, S. R. (2011). *Journal of Organic Chemistry, 76*, 2386−2407.

Hudhomme, P. (2013). *EPJ Photovoltaics, 4*(40401), p1−p11.

Hummelen, J. C., Knight, B. W., LePeq, F., Wudl, F., Yao, J., & Wilkins, C. L. (1995). *Journal of Organic Chemistry, 60*, 532−538.

Huo, L., Chen, H.-Y., Hou, J., Chen, T. L., & Yang, Y. (2009). *Chemical Communications*, 5570−5572.

Huo, L., Tan, Z. A., Wang, X., Zhou, Y., Han, M., & Li, Y. (2008). *Journal of Polymer Science Part A: Polymer Chemistry, 46*, 4038−4049.

Jea Uk, L., Jae Woong, J., Todd, E., Thomas, P. R., & Won Ho, J. (2010). *Nanotechnology, 21*, 105201.

Kakogianni, S., Kourkouli, S. N., Andreopoulou, A. K., & Kallitsis, J. K. (2014). *Journal of Materials Chemistry A, 2*, 8110−8117.

Kietzke, T., Hoerhold, H.-H., & Neher, D. (2005). *Chemistry of Materials, 17*, 6532−6537.

Kim, J. S., Fei, Z., James, D. T., Heeney, M., & Kim, J.-S. (2012). *Journal of Materials Chemistry, 22*, 9975−9982.

Kooistra, F. B., Knol, J., Kastenberg, F., Popescu, L. M., Verhees, W. J. H., Kroon, J. M., et al. (2007). *Organic Letters, 9*, 551−554.

Ko, S. W., Verploegen, E., Hong, S., Mondal, R., Hoke, E. T., Toney, M. F., et al. (2011). *Journal of the American Chemical Society, 133*, 16722−16725.

Kularatne, R. S., Magurudeniya, H. D., Sista, P., Biewer, M. C., & Stefan, M. C. (2013). *Journal of Polymer Science Part A: Polymer Chemistry, 51*, 743−768.

Lai, M. H., Chueh, C. C., Chen, W. C., Wu, J. L., & Chen, F. C. (2009). *Journal of Polymer Science Part A: Polymer Chemistry, 47*, 973−985.

Laiho, A., Ras, R. H. A., Valkama, S., Ruokolainen, J., Österbacka, R., & Ikkala, O. (2006). *Macromolecules, 39*, 7648−7653.

Lee, J. U., Cirpan, A., Emrick, T., Russell, T. P., & Jo, W. H. (2009). *Journal of Materials Chemistry, 19*, 1483−1489.

Lee, J. U., Jung, J. W., Emrick, T., Russell, T. P., & Jo, W. H. (2010). *Journal of Materials Chemistry, 20*, 3287−3294.

Lei, T., Dou, J. H., Ma, Z. J., Yao, C. H., Liu, C. J., Wang, J. Y., et al. (2012). *Journal of the American Chemical Society, 134*, 20025−20028.

Lenes, M., Shelton, S. W., Sieval, A. B., Kronholm, D. F., Hummelen, J. C., & Blom, P. W. M. (2009). *Advanced Functional Materials, 19*, 3002−3007.

Lenes, M., Wetzelaer, G. J. A. H., Kooist, F. B., Veenstra, S. J., Hummelen, J. C., & Blom, P. W. M. (2008). *Advanced Materials, 20*, 2116−2119.

Li, Y. (2012). *Accounts of Chemical Research, 45*, 723−733.

Liang, Y., Feng, D., Wu, Y., Tsai, S.-T., Li, G., Ray, C., et al. (2009). *Journal of the American Chemical Society, 131*, 7792−7799.

Liang, Y., Wu, Y., Feng, D., Tsai, S.-T., Son, H.-J., Li, G., et al. (2009). *Journal of the American Chemical Society, 131*, 56−57.

Liang, Y., Xu, Z., Xia, J., Tsai, S.-T., Wu, Y., Li, G., et al. (2010). *Advanced Materials, 22*, E135−E138.

Lin, Y., Li, Y., & Zhan, X. (2012). *Chemical Society Reviews, 41*, 4245−4272.

Li, J., Qin, F., Li, C. M., Bao, Q. L., Chan-Park, M. B., Zhang, W., et al. (2008). *Chemistry of Materials, 20*, 2057−2059.

Liu, G., Khlobystov, A. N., Charalambidis, G., Coutsolelos, A. G., Briggs, G. A. D., & Porfyrakis, K. (2012). *Journal of the American Chemical Society, 134*, 1938−1941.

Li, M., Xu, P., Yang, J., & Yang, S. (2010). *Journal of Materials Chemistry, 20*, 3953−3960.

Li, G., Zhu, R., & Yang, Y. (2012). *Nature Photonics, 6*, 153−161.

Matsuo, Y. (2012). *Chemical Letters, 41*, 754−759.

Ma, Z. F., Wang, E. G., Jarvid, M. E., Henriksson, P., Inganäs, O., Zhang, F. L., et al. (2012). *Journal of Materials Chemistry, 22*, 2306−2314.

Mishra, A., Ma, C.-Q., & Bäuerle, P. (2009). *Chemical Reviews, 109*, 1141−1176.

Moore, J. R., Albert-Seifried, S., Rao, A., Massip, S., Watts, B., Morgan, D. J., et al. (2011). *Advanced Energy Materials, 1*, 230−240.

Morvillo, P., & Bobeico, E. (2008). *Physica Status Solidi (RRL) − Rapid Research Letters, 2*, 260−262.

Moule, A. J., Tsami, A., Bünnagel, T. W., Forster, M., Kronenberg, N. M., Scharber, M., et al. (2008). *Chemistry of Materials, 20*, 4045−4050.

Muhlbacher, D., Scharber, M., Morana, M., Zhu, Z., Waller, D., Gaudiana, R., et al. (2006). *Advanced Materials, 18*, 2884−2889.

Najari, A., Beaupre, S., Berrouard, P., Zou, Y., Pouliot, J.-R., Lepage-Perusse, C., et al. (2011). *Advanced Functional Materials, 21*, 718−728.

Osaka, I., Akita, M., Koganezawa, T., & Takimiya, K. (2012). *Chemistry of Materials, 24*, 1235−1243.

Park, S. H., Roy, A., Beaupre, S., Cho, S., Coates, N., Moon, J. S., et al. (2009). *Nature Photonics, 3*, 297−302.

Park, S. H., Yang, C., Cowan, S., Lee, J. K., Wudl, F., Lee, K., et al. (2009). *Journal of Materials Chemistry, 19*, 5624−5628.

Peet, J., Heeger, A. J., & Bazan, G. C. (2009). *Accounts of Chemical Research, 42*, 1700−1708.

Peet, J., Kim, J. Y., Coates, N. E., Ma, W. L., Moses, D., Heeger, A. J., et al. (2007). *Nature Materials, 6*, 497−500.

Piliego, C., Holcombe, T. W., Douglas, J. D., Woo, C. H., Beaujuge, P. M., & Frechet, J. M. J. (2010). *Journal of the American Chemical Society, 132*, 7595−7597.

Qin, R., Li, W., Li, C., Du, C., Veit, C., Schleiermacher, H.-F., et al. (2009). *Journal of the American Chemical Society, 131*, 14612−14613.

Richard, F., Brochon, C., Leclerc, N., Eckhardt, D., Heiser, T., & Hadziioannou, G. (2008). *Macromolecules Rapid Communications, 29*, 885−891.

Rondeau-Gagne, S., Lafleur-Lambert, A., Soldera, A., & Morin, J.-F. (2011). *New Journal of Chemistry, 35*, 942−947.

Ross, R. B., Cardona, C. M., Guldi, D. M., Sankaranarayanan, S. G., Reese, M. O., Kopidakis, N., et al. (2009). *Nature Materials, 8*, 208−212.

Ruderer, M. A., Wang, C., Schaible, E., Hexemer, A., Xu, T., & Müller-Buschbaum, P. (2013). *Macromolecules, 46*, 4491−4501.

Sariciftci, N. S., Smilowitz, L., Heeger, A. J., & Wudl, F. (1992). *Science, 258*, 1474−1476.

Sary, N., Richard, F., Brochon, C., Leclerc, N., Lévêque, P., Audinot, J.-N., et al. (2010). *Advanced Materials, 22*, 763−768.

Scherf, U., & List, E. J. W. (2002). *Advanced Materials, 14*, 477−487.

Schmidt-Mende, L., Fechtenkötter, A., Müllen, K., Moons, E., Friend, R. H., & MacKenzie, J. D. (2001). *Science, 293*, 1119−1122.

Sirringhaus, H., Brown, P. J., Friend, R. H., Nielsen, M. M., Bechgaard, K., Langeveld-Voss, B. M. W., et al. (1999). *Nature, 401*, 685−688.

Sista, P., Nguyen, H., Murphy, J. W., Hao, J., Dei, D. K., Palaniappan, K., et al. (2010). *Macromolecules, 43*, 8063−8070.

Sista, P., Xue, B., Wilson, M., Holmes, N., Kularatne, R. S., Nguyen, H., et al. (2011). *Macromolecules, 45*, 772−780.

Sivula, K., Ball, Z. T., Watanabe, N., & Fréchet, J. M. J. (2006). *Advanced Materials, 18*, 206−210.

Son, H. J., Wang, W., Xu, T., Liang, Y., Wu, Y., Li, G., et al. (2011). *Journal of the American Chemical Society, 133*, 1885−1894.

Stalder, R., Grand, C., Subbiah, J., So, F., & Reynolds, J. R. (2012). *Polymer Chemistry, 3*, 89−92.

Stalder, R., Mei, J. G., & Reynolds, J. R. (2010). *Macromolecules, 43*, 8348−8352.

Stalder, R., Mei, J. G., Subbiah, J., Grand, C., Estrada, L. A., So, F., et al. (2011). *Macromolecules, 44*, 6303−6310.

Stevenson, S., Rice, G., Glass, T., Harich, K., Cromer, F., Jordan, M. R., et al. (1999). *Nature, 401*, 55−57.

Steyrleuthner, R., Schubert, M., Howard, I., Klaumünzer, B., Schilling, K., Chen, Z., et al. (2012). *Journal of the American Chemical Society, 134*, 18303−18317.

Su, Y. W., Lan, S. C., & Wie, K. H. (2012). *Mater Today, 15*, 554−562.

Svensson, M., Zhang, F. L., Veenstra, S. C., Verhees, W. J. H., Hummelen, J. C., Kroon, J. M., et al. (2003). *Advanced Materials, 15*, 988−991.

Tang, C. W. (1986). *Applied Physics Letters, 48*, 183−185.

Tang, W. H., Chellappan, V., Liu, M. H., Chen, Z. K., & Ke, L. (2009). *ACS Applied Materials and Interfaces, 1*, 1467−1473.

Tang, W. H., Ke, L., Tan, L., Lin, T. T., Kietzke, T., & Chen, Z. K. (2007). *Macromolecules, 40*, 6164−6171.

Tsumura, A., Koezuka, H., & Ando, T. (1986). *Applied Physics Letters, 49*, 1210−1212.

van der Veen, M. H., de Boer, B., Stalmach, U., van de Wetering, K. I., & Hadziioannou, G. (2004). *Macromolecules, 37*, 3673−3684.

Wang, E., Bergqvist, J., Vandewal, K., Ma, Z., Hou, L., Lundin, A., et al. (2013). *Advanced Energy Materials, 3*, 806−814.

Wang, H., He, Y., Li, Y., & Su, H. (2011). *The Journal Physical Chemistry A, 116*, 255−262.

Wang, E., Hou, L., Wang, Z., Hellström, S., Zhang, F., Inganäs, O., et al. (2010). *Advanced Materials, 22*, 5240−5244.

Wang, E. G., Ma, Z. F., Zhang, Z., Vandewal, K., Henriksson, P., Inganäs, O., et al. (2011). *Journal of the American Chemical Society, 133*, 14244−14247.

Wienk, M. M., Kroon, M. J., Verhees, W. J. H., Knol, J., Hummelen, J. C., Hal, P. A. V., et al. (2003). *Angewandte Chemie International Edition, 42*, 3371−3374.

Woo, C. H., Holcombe, T. W., Unruh, D. A., Sellinger, A., & Frechet, J. M. J. (2010). *Chemistry of Materials, 22*, 1673−1679.

Würthner, F. (2004). *Chemical Communications, 14*, 1564−1579.

Yamamoto, T., Lee, B. L., Kokubo, H., Kishida, H. K., Hirota, K., Wakabayashi, T., et al. (2003). *Macromolecular Rapid Communications, 24*, 440−443.

Yan, H., Chen, Z. H., Zheng, Y., Newman, C., Quinn, J. R., Dotz, F., et al. (2009). *Nature, 457*, 679−686.

Yan, H., Collins, B. A., Gann, E., Wang, C., Ade, H., & McNeill, C. R. (2012). *ACS Nano, 6*, 677−688.

Yang, C., Cho, S., Heeger, A. J., & Wudl, F. (2009). *Angewandte Chemie International Edition, 48*, 1592−1595.

Yang, C., Kim, J. Y., Cho, S., Lee, J. K., Heeger, A. J., & Wudl, F. (2008). *Journal of the American Chemical Society, 130*(20), 6444−6450.

Yang, C., Lee, J. K., Heeger, A. J., & Wudl, F. (2009). *Journal of Materials Chemistry, 19*, 5416−5423.

Yu, G., Gao, J., Hummelen, J., Wundl, F., & Heeger, A. (1995). *Science, 270*, 1789−1791.

Zhang, S., Guo, Y., Fan, H., Liu, Y., Chen, H.-Y., Yang, G., et al. (2009). *Journal of Polymer Science Part A: Polymer Chemistry, 47*, 5498−5508.

Zhang, Y., Yip, H.-L., Acton, O., Hau, S. K., Huang, F., & Jen, A. K. Y. (2009). *Chemistry of Materials, 21*, 2598−2600.

Zhan, X., Tan, Z., Domercq, B., An, Z., Zhang, X., Barlow, S., et al. (2007). *Journal of the American Chemical Society, 129*, 7246−7247.

Zhao, G. J., He, Y. J., & Li, Y. F. (2010). *Advanced Materials, 22*, 4355−4358.

Zhao, G., He, Y., Xu, Z., Hou, J., Zhang, M., Min, J., et al. (2010). *Advanced Functional Materials, 20*, 1480−1487.

Zhao, X., & Zhan, X. (2011). *Chemical Society Reviews, 40*, 3728−3743.

Zheng, L., Zhou, Q., Deng, X., Yuan, M., Yu, G., & Cao, Y. (2004). *The Journal of Physical Chemistry B, 108*, 11921−11926.

Zhou, E., Cong, J., Wei, Q., Tajima, K., Yang, C., & Hashimoto, K. (2011). *Angewandte Chemie International Edition, 50*, 2799−2803.

Zhou, Q. M., Hou, Q., Zheng, L. P., Deng, X. Y., Yu, G., & Cao, Y. (2004). *Applied Physical Letters, 84*, 1653−1655.

Zhou, N., Lin, H., Lou, S. J., Yu, X., Guo, P., Manley, E. F., et al. (2014). *Advanced Energy Materials, 4*, 1−8.

Zhou, J., Zuo, Y., Wan, X., Long, G., Zhang, Q., Ni, W., et al. (2013). *Journal of the American Chemical Society, 135*, 8484−8487.

Zhuang, W., Zhenbc, H., Kroona, R., Tangb, Z., Hellströma, S., Houb, L., et al. (2013). *Journal of Material Chemistry A, 1*, 13422−13425.

Zou, Y., Najari, A., Berrouard, P., Beaupre, S., Reda, A. B., Tao, Y., et al. (2010). *Journal of the American Chemical Society, 132*, 5330−5331.

This page intentionally left blank

Part Two

Technologies

This page intentionally left blank

High-barrier films for flexible organic electronic devices

5

D. Georgiou, S. Logothetidis
Aristotle University of Thessaloniki, Thessaloniki, Greece

5.1 Introduction

There is currently a rapidly growing research effort regarding the development and optimization of organic, inorganic, and hybrid nanomaterials and processes for the manufacturing of organic electronic devices onto flexible polymeric substrates (flexible organic electronics (OEs)) (Georgiou et al., 2008a). These offer substantial advantages, such as being lightweight, thin, robust, comfortable, rollable and compatible with large-scale manufacturing processes, and offer the possibility for low-cost, roll-to-roll processing in high volumes (Kim et al., 2005) (Logothetidis, 2008) (Kopola et al., 2011).

Encapsulation of the active layers of OEs with flexible polymeric substrates represents one of the major challenges for flexible OEs to reveal their full potential (Charton et al., 2006). Protection of the device's functional layers (such as electrodes, organic semiconductors, and conductors) against atmospheric gas molecules (H_2O and O_2) has an important role in the functionality and stability of these devices (for example, flexible displays as organic light-emitting diodes (OLEDs), electrochromic displays, lighting, and so forth, and flexible organic photovoltaic cells (OPVs)) (Laskarakis et al., 2009a). Permeation of these molecules into the device's structure corrodes the device's active layers and reduces the overall performance and lifetime of the device, prohibiting its market implementation (Singh et al., 2007) (Chen et al., 2007) (Amberg-Schwab et al., 2006). In more detail, organic semiconductors used, e.g., in OPVs, are unstable and exposure to air and moisture can lead to their degradation by oxygen atoms to form linkages with vinyl groups with consequent disruption of coupling and the creation of carbonyl groups. Studies show that during the exposure of photovoltaic devices to light and air, the active layer thickness increased and the values of the refractive index and the absorption coefficient also increased (Dennler et al., 2006).

Therefore, the use of high-barrier films for highly sensitive materials is necessary to increase the stability and lifetime of flexible electronic devices and allow their large-scale production.

5.2 Encapsulation of flexible OEs

5.2.1 Requirements

The main values for determining permeability are the oxygen transmission rate (OTR) and the water vapor transmission rate (WVTR) (Amberg-Schwab, 2005). The
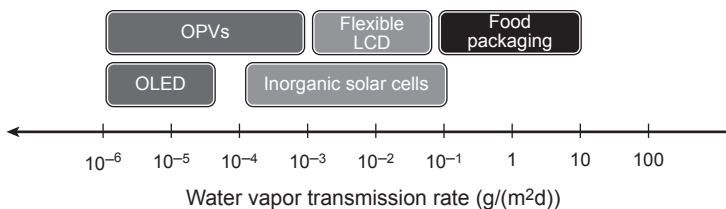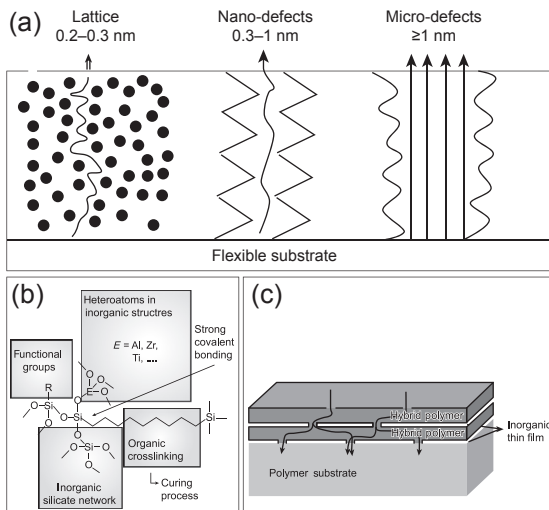
Figure 5.1 Barrier performance requirements for various applications including organic electronics.

requirements for gas protection depend on the specific application (Figure 5.1) (Liao et al., 2010). For example, sensitive food products can be protected with a single polymer film coated with one inorganic layer, achieving permeation values of WVTR of 10^{-1} g/m^{2}d and OTR of 10^{-2} cm^3/m^{2}d bar. Flexible electronic devices such as OLED displays and OPVs require a more complex layer stack as a permeation barrier to achieve ultralow permeation values of 10^{-5} g/m^2 d (WVTR) and 10^{-5} cm^3/m^{2}d bar (OTR) (Park et al., 2011) (Charton et al., 2006).

5.2.2   Materials

Some conventional encapsulation solutions involve (Logothetidis et al., 2010):

- Metal foils for applications that do not require transparency. Metal sheets have good mechanical properties, are low-cost to produce, and have excellent thermal conductivity and barrier performance. Although this method is effective, it can be used only for applications that do not require transparency. Moreover, metal foils exhibit high surface roughness and different thermal expansion coefficients compared with other materials used in OEs (Logothetidis et al., 2010).
- Glass: To be flexible, the thickness of the glass should be less than 100 µm and its mechanical properties are not desirable. Moreover, its implementation in roll-to-roll processes increases the cost because a high-purity process is required (Logothetidis et al., 2010).
- Inorganic thin films of metal oxides such as silicon oxide and aluminum oxide deposited onto a polymeric substrate. This technology reduces the O_2 and H_2O permeation rates just by two to three orders of magnitude from the permeation rate values of uncoated plastic substrate (Logothetidis et al., 2010) (Haas et al., 1999). This is because the barrier response of the inorganic coatings is defined by their lattice disorder, which results from the deposition process. This disorder has the form of macro- and nanodefects (pinholes and microcracks) that are formed during the growth process of inorganic thin films by physical vapor deposition methods such as sputtering and evaporation. These defects (Figure 5.2(a)) provide easy pathways for moisture and oxygen permeation and limit the barrier performance of the inorganic film—polymer substrate system (Haas et al., 1999) (Hedenqvist et al., 2003) (Amberg-Schwab et al., 2000) (Yanaka, 2001). Promising single-layer encapsulation films have also been achieved using inorganic thin films such as Al$_2$O$_3$ deposited by atomic layer deposition (ALD) (Park et al., 2005) (Potscavage et al., 2007). The ALD deposited films are desirable because of their high density, low number of defects, and ability to conform to coat surfaces at relatively low temperatures (Park et al., 2005). The main disadvantage of this technique is the mechanical stability of the barrier materials (Ghosh et al., 2005).

Figure 5.2 (a) Proposed gas transport pathways through the inorganic barrier layer. (b) Structural elements of a hybrid polymer. (c) Alternating inorganic and hybrid polymer layers deposited onto a flexible polymeric substrate.

- Multilayer films are widely used when high-barrier performance is required. These materials usually consist of alternating organic and inorganic multilayers (Weaver et al., 2002) (Lewis & Weaver, 2004). Main disadvantages of this technology are the roughness and the defects of the inorganic layers (Chiang et al., 2006) (Chen et al., 2007) (Chwang et al., 2003). To achieve the desired properties, the creation of multilayer structures with five alternating layers of organic/inorganic films (technology Vitex) has been proposed that add to the production cost although the structures achieve barrier performance to 10^{-6} g/m^2/day. Other multilayer structures consist of ultraviolet (UV)-curable epoxy hybrid materials with MgO or structures of SiN$_x$ and SiO$_x$ with parylene or poly(methyl methacrylate). Finally, a study suggested replacing the organic layer with nanoparticles, but this technology is still at an early stage (Ho Jung et al., 2011).
- Hybrid polymers have attracted interest lately for their use as barrier materials (Figure 5.2(b)). These are inorganic-organic nanocomposites that can be synthesized by sol-gel processes at relatively low temperatures. The combination of hybrid polymers and inorganic layers could overcome the previously mentioned drawbacks, leading to a significant improvement in the barrier properties of the whole material structure. This is the result of the synergetic effect of confining permeation to the defect zones of the inorganic layer and forming chemical bonds between the hybrid polymer and the inorganic layer (Figure 5.2(c)). This technology appears to be the most promising, because the materials are produced by large-scale roll-to-roll processes and show the required stability and barrier performance (Amberg-Schwab, 2011).

5.2.3 Technologies

Development of desirable encapsulation technologies is essential for improving the lifetime and reliability of OEs (Aziz et al., 1998) (Kolosov et al., 2001). A number of approaches to encapsulation (Figure 5.3) have been developed, including use of thin-film coatings, metal lids, and glass, and sealing devices between two glass
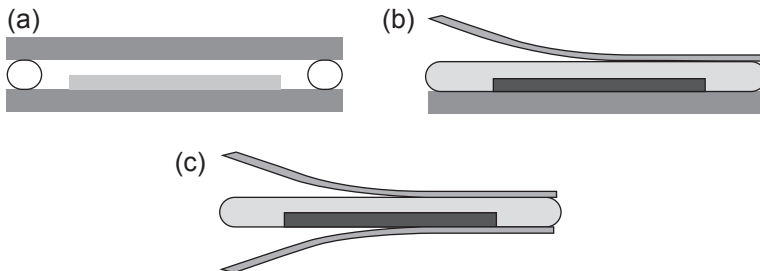
Figure 5.3 Encapsulation technologies for organic electronics (a) glass−glass encapsulation (b) glass−foil encapsulation (c) foil−foil encapsulation.

substrates (Burrows et al., 1994) (Weaver et al., 2002). However, these rigid materials are not amenable for use in flexible OEs. Several flexible encapsulation approaches have been developed including encapsulation of the device by laminating a glass or metal substrate with a barrier foil, but with this technology the device is not fully flexible. Another promising technology for the encapsulation of OEs is foil-to-foil encapsulation. With this technology, the device is processed on a barrier foil followed by lamination of a second barrier foil. A disadvantage of this technique is side diffusion of the gasses through the adhesive (Lewis & Weaver, 2004).

Of the various approaches to encapsulation, foil-to-foil technology has attracted the most attention owing to its light weight, transparency, and high level of mechanical flexibility. Most of the research in developing encapsulation materials for OEs has focused on their barrier performance, but other critical aspects must be considered in developing this technology; for instance, the encapsulation process must be compatible with OEs. For active layers and substrates with low glass-transition temperatures and thermal stability, the processing temperatures at which the barrier layers can be deposited are limited. This inevitably requires the inorganic layers that exist in encapsulation to be deposited at low temperatures for device compatibility when deposited directly on the device. Thus, the development and integration of high-barrier encapsulation films with OEs remain a challenging (Lewis & Weaver, 2004).

5.3 Permeability mechanisms through barrier materials

The basic function of barrier films is to limit the exposure of OEs to water vapor and oxygen. This is done by controlling the permeation rate through barrier films. A gradient of the chemical potential such as pressure and concentration is the driving force for permeation. Formally, permeation is described as a two-step process combining absorption of a substance into a solid followed by diffusion of the substance (Hanika et al., 2003). Therefore, in the case of a homogeneous film at steady state, permeability P is equal to the product of solubility coefficient S and diffusion coefficient D (Roberts et al., 2002):

$$P = D \cdot S \tag{5.1}$$

The diffusion and solubility coefficients are related to the intrinsic properties of the materials; the permeation rate of barrier materials is reported as g/m^2day at a given temperature and relative humidity in the case of water vapor permeation and as cm^3/m^2day at a given temperature and pressure in the case of gas permeation (Langowski, 2008).

This process can be described using the first law of diffusion of Fick and Henry's law (Figure 5.4(a)). Based on the above, flux J is proportional to the concentration as:

$$J = -D\nabla(c) \tag{5.2}$$

where c is the concentration. Based on Henry's law, which relates the concentration to the partial pressure based on the equation $c = S \cdot \Delta P$, the concentration in Eqn (5.2) can be replaced using the solubility coefficient and partial pressure. In the case of steady state, flux J is equal to:

$$J = \frac{DS(P_o - P_i)}{L} \tag{5.3}$$

In the case of multilayer barrier structures, the diffusion of water vapor and oxygen through multilayer films is an important issue to be addressed. The equation for the total permeability coefficient P_T of a multilayer barrier structure with n barrier layers with a thickness L_n and permeability coefficient P_n as shown in Figure 5.4(b) is:

$$\frac{1}{P_T} = \frac{L_{Total}}{\frac{L_1}{P_1} + \frac{L_2}{P_2} + \frac{L_3}{P_3} + \cdots + \frac{L_n}{P_n}} \tag{5.4}$$

where L_{Total} is the total thickness of the multilayer barrier structure. This total permeability coefficient of the multilayer barrier structure is derived assuming a constant flux through all barrier layers under steady-state conditions (Langowski, 2008).
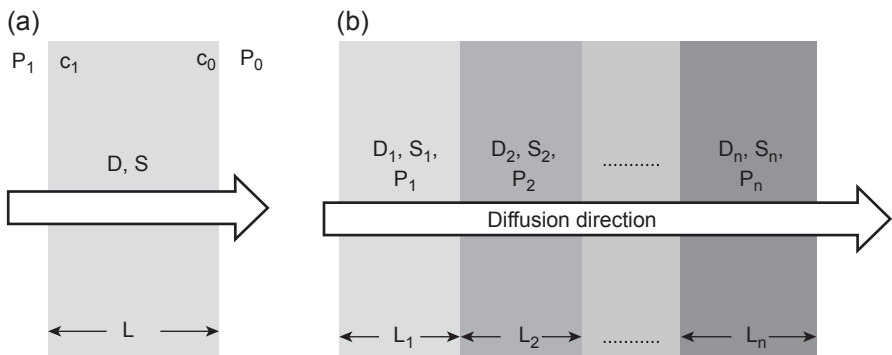
Figure 5.4 Permeation of gases or vapors through a single layer (a) and multilayer barrier materials (b).

5.4   Permeation measurement techniques

The development of high-barrier materials creates the need to develop suitable techniques for measuring gas permeability through these materials (Graff et al., 2005).

The main techniques for evaluating barrier response include the following:

- Coulometric measurement methods
- The calcium (Ca) test (optical and electrical)
- The tritium test, which offers high sensitivity but requires radioactive elements.

The operating principle of these techniques is based on detection of the permeate gas or changes caused by oxygen or water in some materials. With coulometric methods, a dry chamber is separated from a wet chamber of known temperature and humidity by the tested barrier material. The dry chamber and wet chamber make up a diffusion cell in which the test barrier material is sealed. Water vapor diffusing through the film mixes with the gas in the dry chamber and is carried to a coulometric sensor that measures the water vapor permeate. The amplitude of the electrical signal produced by the test film is then compared with the signal produced by measuring a calibration film of known WVTR. This information is then used to calculate the rate at which moisture is transmitted through the material being tested.

Typically, these systems are useful for analyzing most single-layer and some multi-layer films but are not sensitive enough to detect the ultralow permeation rates of advanced encapsulation materials, because they have a lower limit on the order of 10^{-4} g/m^2/day.

The Ca test (Figure 5.5) is a widely known method for measuring ultralow permeation rate barrier films. Calcium is a conducting and opaque metal that becomes nonconducting and transparent after oxidation. It rapidly oxidizes in air owing to the highly negative Gibbs free energy of formation of Ca oxides, which makes it sensitive for detecting the presence of oxygen and water vapor. Because the oxide is a dielectric and transparent, it is possible to monitor the consumption of Ca by measuring the change in electrical conductance (electrical Ca test) or in an optical transparency (optical Ca test). Hence, the measurement of Ca conductance or
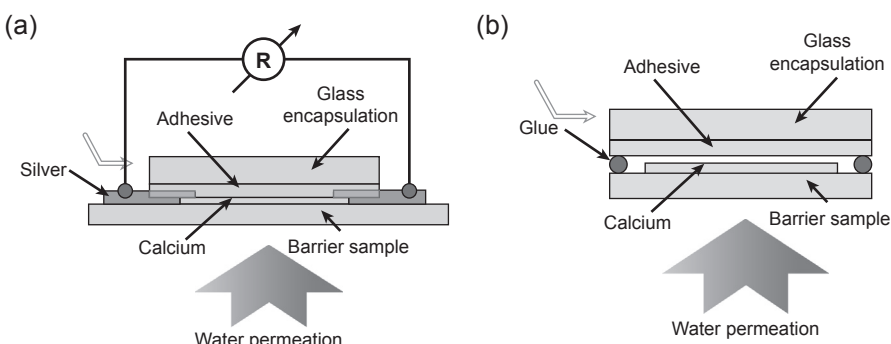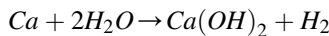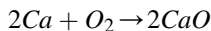
Figure 5.5 Electrical (a) and optical (b) calcium test for measurement of gas permeability through barrier materials.

transparency changes provides an indirect method to determine the oxidation and corrosion rates of Ca (Pichler, 1997) (Schubert et al., 2011). The chemical reaction of Ca in air is as follows:

$$2Ca + O_2 \rightarrow 2CaO$$

$$Ca + 2H_2O \rightarrow Ca(OH)_2 + H_2$$

Because a visual change is observed, the Ca test can distinguish between bulk and defect-based permeation; however, it does not discriminate between oxygen and water permeation.

5.5 Advances in high-barrier materials

5.5.1 Inorganic barrier materials

Materials commonly used as inorganic barrier films are silicon oxide (SiO_x), aluminum oxide (AlO_x), silicon nitride (SiN), and titanium oxide (TiO_2) (Seino et al., 2002). The barrier response of inorganic thin films is affected by many factors such as the type of material, deposition rate, film thickness, growth mechanism, substrate, substrate roughness, film morphology, and deposition technique as well as the deposition temperature and pressure (Garcia-Ayuso et al., 1996) (Henry et al., 1999).

The barrier properties are affected by the thickness of the inorganic thin film (Benmalek & Dunlop, 1995). An increase in thickness of the oxide induces a decrease in permeability that is connected to the microstructure of the film (Deng, 2000). Also, thickness is another critical value that the barrier properties exhibits a minimum for a specific thickness value (Leterrier, 2003). For SiO_x films on Polyethylene terephthalate (PET) substrate the critical value of the thickness is $70-140$ nm. The effect the thickness exhibits on permeability is associated with the nucleation stage and growth mechanism of oxide (Erlat et al., 2000). Another important factor that affects the barrier properties of inorganic films is the growth mechanism. Studies have shown that a uniform nucleation stage induces growth of uniform film without defects and with improved barrier properties (Erlat et al., 2000).

To investigate the influence of the substrate's chemical structure and roughness on the growth mechanisms and barrier properties of inorganic thin films, SiO_x was deposited onto two different substrates (PET Melinex 401 flexible polymeric substrate with a thickness of 50 μm and a hybrid barrier layer deposited onto PET). The surface roughness of PET and hybrid PET showed different values of roughness and peak-to-peak distance. The surface roughness (peak-to-peak distance) of PET and hybrid PET was 1.18 nm (14 nm) and 0.26 nm (2.82 nm), respectively. These values of surface roughness show that depositing hybrid material onto polymer leads to a smooth polymeric surface (Haas et al., 1999). *In situ* and real-time spectroscopic ellipsometry (SE) was used to monitor SiO_x barrier thin films deposited by an electron beam evaporation technique (Georgiou et al., 2008b). Analysis of real-time SE measurements in the visible−far-UV (Vis-fUV) energy range revealed information about the optical properties, deposition rate, and growth mechanism and how they are affected by the substrate's surface.

Parametrization of the optical and electronic properties of SiO_x thin films was performed by modeling the measured pseudodielectric function $<\varepsilon(\omega)>$ during SiO_x deposition. The $<\varepsilon(\omega)>$ was analyzed by use of the Tauc-Lorentz (TL) dispersion model, which uses a combination of the Tauc joint density of states and the quantum mechanical Lorentz oscillator model (Jellison & Modine, 1996) (Leterrier, 2003). The geometrical structure used for analysis includes a three-phase model: air/SiO_x/substrate. Figure 5.6 shows the evolution of the imaginary part $<\varepsilon_2(\omega)>$ of the measured pseudodielectric function $<\varepsilon(\omega)>$ as measured during deposition of the SiO_x thin film with stoichiometry $x = 1.7$, onto a PET polymeric substrate. The $<\varepsilon_2(\omega)>$ measured in the 3- to 6.5-eV spectral region simultaneously on 32 different wavelengths. Analysis of individual $<\varepsilon(\omega)>$ spectra was performed with this theoretical model and proved the time dependence of the SiO_x film thickness and its optical properties.

Figure 5.7 shows the evolution of thickness of the SiO_x films with stoichiometry $x = 1.7$ deposited onto PET and hybrid PET substrates; the inset graph focuses on the first 100 s of deposition. Figure 5.7 shows that the deposition rate of the SiO_x thin film onto the hybrid PET substrate is higher than in the case of SiO_x/PET. This may be because of the inorganic network of the hybrid layer that favors the deposition of SiO_x film onto its surface. Figure 5.7 suggests that evolution of the SiO_x film thickness can be separated into three stages, according to the growth mechanisms taking place:

Stage I: At this stage, there is an abrupt increase in apparent thickness, attributed mostly to surface modification by SiO_x (charged and neutral) particles. This modification includes changing surface chemical bonding and incorporating the particles into the polymeric surface, initially causing the formation of a composite material constituting a PET with an SiO_x overlayer (Georgiou et al., 2008a).

Stage II: A nanocrystallite SiO_x layer with a low deposition rate is formed on this composite material.
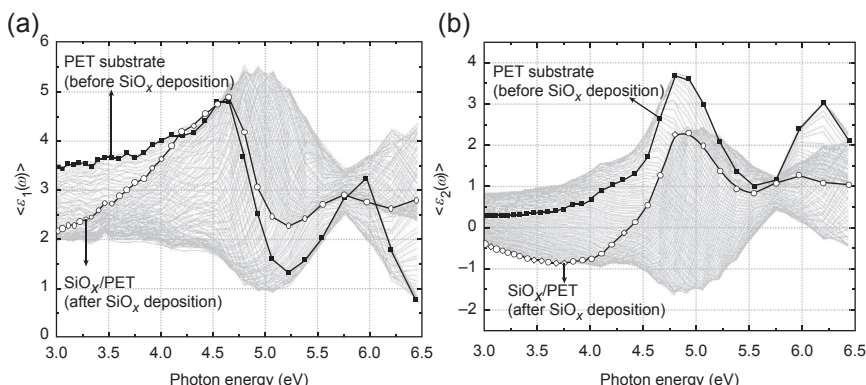
Figure 5.6 Real-time measured real $<\varepsilon_1(\omega)>$ (a) and imaginary $<\varepsilon_2(\omega)>$ parts of the pseudodielectric function in the visible−far-UV (Vis-fUV) spectral region during deposition of SiO_x ($x \rightarrow 1.7$) thin film onto PET substrate.
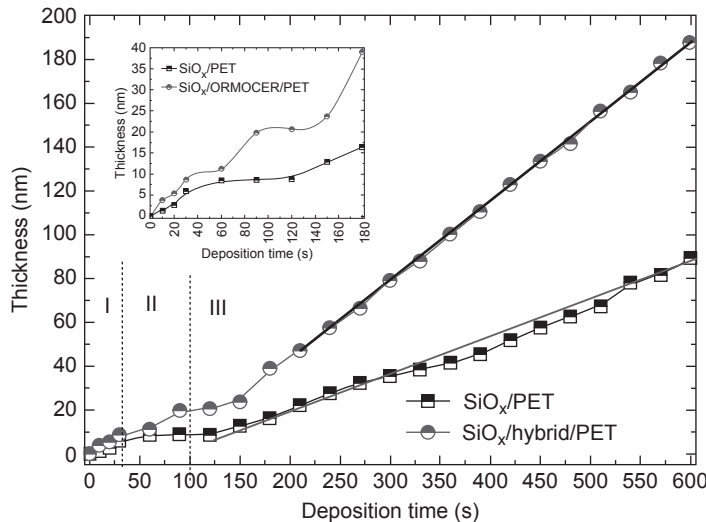
Figure 5.7 Time evolution of SiO_x ($x \rightarrow 1.7$) film thickness deposited onto PET, and hybrid PET substrates. The dashed line indicates different stages of growth mechanism.

Stage III: Layer-by-layer growth of SiO_x material starts until the end of the deposition in the case of the hybrid PET substrates. However, in the case of PET substrate, SiO_x growth is governed by an island-growth mechanism.

To enhance the information deduced from the evolution of SiO_x film thickness with time, the derivative of the thickness as a function of the deposition time was calculated. Study of the deposition rate provided information about the growth mechanism of SiO_x films on different substrates and how they are affected by the chemical structure and surface properties of the substrates. The three growth stages are significantly pronounced in Figure 5.8. More specifically, in the early stages of growth, the abrupt increase in the deposition rate up to 0.45 nm/s for SiO_x/hybrid PET at $t = 40$ s and to 0.24 nm/s for SiO_x/PET at $t = 30$ is attributed mostly to surface modification and the formation of a separate cluster with a size that increases until the first ~ 40 s for SiO_x/hybrid PET and SiO_x/PET (stage I).

After stage I, the reduction in the deposition rate indicates that the coalescence stage in which the initial growth of the SiO_x clusters has taken place (stage II). At the end of stage II, at $t \sim 90$ s, stage III is where growth of the SiO_x film takes place because it is also affected by the chemical structure and surface properties of the substrate. In the case of SiO_x/PET, the deposition rate at higher deposition times ($t > 120$ s) follows an oscillating behavior. Oscillation of the deposition rate is characteristic of island-type growth and defines the distinct growth stages (Dennler et al., 2001). This behavior is repeated, as indicated by the oscillating deposition rate. Study of the deposition rate of SiO_x/hybrid PET indicates that this deposition is governed by a layer-by-layer growth mechanism. In the case of the hybrid PET for time >160 s, the SiO_x film thickness increases linearly with time and the deposition rate is almost stable, resulting in homogeneous layer deposition.
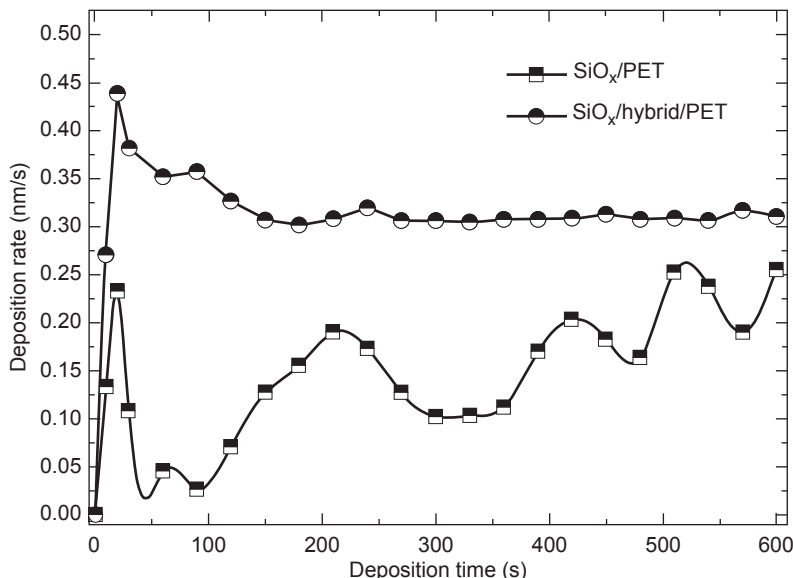
Figure 5.8 Time evolution of SiO_x ($x \rightarrow 1.7$) deposition rate deposited onto PET and hybrid PET substrates.

Table 5.1 summarizes the best-fit parameters of the $<\varepsilon(\omega)>$ analysis as well as the barrier properties of the barrier materials. Table 5.1 shows that the different growth mechanisms affect the refractive index of the SiO_x film, which was determined to have higher values in the case of SiO_x/hybrid PET (layer-by-layer growth) than SiO_x/PEN ($n = 1.87$) SiO_x/PET (island-type growth). Moreover, the growth of inorganic thin film onto the polymeric substrate significantly improves the barrier properties. This is because the permeation of gas molecules takes place only through defect sites in the inorganic barrier film. Finally, growth of the inorganic barrier film onto a substrate with low roughness (hybrid PET) induces the development of an inorganic barrier film with a lower number of defects and improved barrier response.

Table 5.1 Optical and barrier properties of SiO_x barrier films deposited onto different substrates

	Thickness/ SiO_x (nm)	ω_g/ SiO_x (eV)	ω_0/ SiO_x (eV)	n/ SiO_x	OTR (cm^3/ d m^2 bar) 23°C/50% Relative Humidity	WVTR (gr/d m^2) 23°C/85% Relative Humidity
PET	—	—	—	—	23	3
Hybrid/PET	—	—	—	—	15.7	2.39
SiO_x/PET	89.3	3.16	9.11	1.39	0.9	0.7
SiO_x/Hybrid/PET	187.5	3.28	9.18	1.43	0.1	0.2

5.5.2 Hybrid barrier materials

Inorganic barrier films exhibit high permeation rates in defects that increase the O_2 and water permeation rates. The most obvious solution for the encapsulation of flexible OEs is to use multilayer structures that consist of an inorganic layer and a hybrid (inorganic−organic) polymer (Singh et al., 2007) (Logothetidis, 2005). Use of a multilayer structure consisting of an inorganic nanolayer with a hybrid polymer layer leads to improvement in barrier response owing to the confinement of permeation to the defect zones of the inorganic layer and the formation of chemical bonds between the hybrid polymer and the inorganic layer with good adhesion (Amberg-Schwab et al., 2006). The new class of hybrid (inorganic−organic) nanocomposite barrier materials includes silicate-based materials, also known as ORMOCER (Haas et al., 1999) (Amberg-Schwab et al., 2000). These are synthesized by organic crosslinking of polycondensed alkoxysilanes (sol−gel processing), which offers tremendous flexibility in polymer synthesis by variations in catalyst, temperature, and alkoxysilane scaffold (Charton et al., 2006). This flexibility enables the adjustment of ORMOCER1s to particular application parameters. Synthesis of inorganic−organic hybrid polymers is carried out by poly-condensation (sol−gel chemistry), followed by organic crosslinking reactions. These materials combine the key properties of constituents such as high transparency, hardness, chemical and thermal stability (glass-like), low processing temperatures, functionalization, toughness (polymer-like), and flexibility (silicone-like) (Houbertz et al., 2003) (Haas & Rose, 2003).

Figure 5.9 shows improvement in barrier performance of the encapsulation material. This consists of a sequence of alternating inorganic (e.g., SiO_x, or AlO_x) and hybrid polymer bilayers that are deposited on top of the PET flexible polymeric substrate. This combination of hybrid polymer and inorganic layer leads to a significant improvement in the barrier properties of the whole material structure. This can be attributed to the synergetic effect of confinement of the permeation to the defect zones of the inorganic layer and formation of chemical bonds between the hybrid polymer and the inorganic layer. Also, the use of alternating inorganic−hybrid layers provides a tortuous path (synergetic barrier effect): The probability of an atmospheric gas molecule penetrating the entire multilayer structure is significantly reduced when complex paths have to be followed, minimizing overall gas permeation (Kelley et al., 2004) (Haas & Rose, 2003).
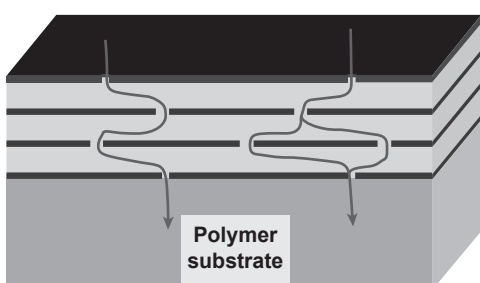
Figure 5.9 Alternating inorganic and hybrid polymer layers deposited onto a flexible polymeric substrate.

The barrier response and optical properties of hybrid barrier materials are affected by the percentage of solid content (Georgiou et al., 2009). The optical and barrier properties of three alcohol-based hybrid polymer samples, F33, F38, and F48, were investigated. These samples were synthesized with different amounts (percentage) of solid content, indicated by the number (F33 has 33% solid content). Moreover, the F38 and F48 samples are thermally curable materials whereas the F33 was cured by UV radiation. After the hybrid polymer synthesis and curing process, the hybrid polymer lacquers were deposited by a spiral applicator onto SiO_x films that had previously been deposited by electron beam evaporation onto PET substrate. The optical properties of the hybrid polymer samples were studied by SE covering the Vis−fUV spectral region (1.5−6.5 eV).

To extract quantitative results from analysis of the optical response of hybrid polymers, we must treat these as composite materials consisting of organic and inorganic components. The measured dielectric function $<\varepsilon(\omega)>$ in the Vis−fUV spectral region was analyzed using a four-phase geometrical model consisting of a hybrid polymer layer (with thickness d) on top of an inorganic nanolayer grown on a PET (bulk) substrate. For the ambient medium we used air in which $\varepsilon_1(\omega) = 1$ and $\varepsilon_2(\omega) = 0$ for all energy values ω. Figure 5.10 shows the theoretical model for analysis of the measured $<\varepsilon(\omega)>$ spectra from the barrier material systems studied.

To take into account the optical response of the intermediate SiO_x layer deposited onto the PET substrate, we measured and modeled an SiO_x/PET sample and used the results (layer thickness and bulk dielectric function $<\varepsilon(\omega)>$) from this analysis for parameterization of the measured $<\varepsilon(\omega)>$ from the complete multilayer hybrid/SiO_x/PET layer stack. To analyze the optical response of the hybrid polymers with various solid contents, we assumed a composite material consisting of organic and inorganic parts. This was performed using the Bruggeman effective medium approximation (BEMA), described in the following equation:

$$f \frac{1 - \tilde{\varepsilon}_{eff}}{1 + 2\tilde{\varepsilon}_{eff}} + (1 - f) \frac{\tilde{\varepsilon} - \tilde{\varepsilon}_{eff}}{\tilde{\varepsilon} + 2\tilde{\varepsilon}_{eff}} = 0 \tag{5.5}$$

where $\tilde{\varepsilon}$ is the bulk dielectric function of the hybrid polymer and f is the volume fraction parameter (Azzam & Bashara, 1977).

Analysis of $<\varepsilon(\omega)>$ revealed that the volume fraction of the inorganic component increases with an increase in solid content, from 4.44% (F33) to 5.49 (F38), and finally
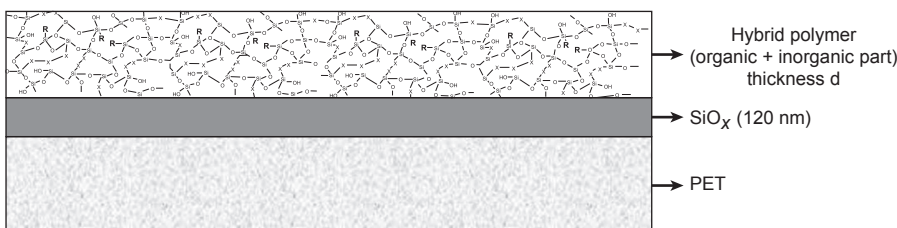
Figure 5.10 Theoretical model used to analyze $<\varepsilon(\omega)>$ for hybrid−SiO_x−PET samples.

to 6.28 (F48). On the other hand, the optical response of the inorganic component remains stable, as shown by the calculated parameters of the TL model. The fundamental energy gap ω_g is determined to be 2.47 eV whereas the Penn gap is $\omega_0 = 6.15$ eV. These values indicate that the stoichiometry of the inorganic component of the hybrid polymers remains constant and is close to unity because the ω_0 is correlated to the stoichiometry x of the SiO_x component and the reference value of ω_0 for SiO_2 is 10.78 eV, whereas the value ω_0 for SiO is 5.7 eV (Gravalidis et al., 2004).

The best-fit parameters concerning the organic part of the different hybrid polymers from the analysis of $<\varepsilon(\omega)>$ are summarized in Table 5.2. These include the fundamental and Penn gap values, ω_g and ω_0, respectively, as well as the refractive index n of the hybrid polymer materials, calculated in energy $\omega = 0$ eV and the volume fraction of the inorganic component. Table 5.2 includes measured gas permeation values of the thin hybrid polymer samples, which have shown the best barrier response (Georgiou et al., 2009).

From Table 5.2 it is clear that the solid content of the hybrid polymer affects both its optical transparency and the maximum optical absorption of the interband electron transition, ω_0. The hybrid polymer F33 is characterized by a vg value of 2.41, whereas this value increases for the hybrid polymers F38 and F48 to 5.52 and 6.46 eV, respectively (Georgiou et al., 2009).

These findings lead to the conclusion that UV curing during the synthesis process results in hybrid polymers of low optical transparency, whereas the thermal curing process leads to hybrid polymers of higher optical transparency. The amount of the solid content also seems to affect optical transparency, because the two thermally cured hybrid polymers, F38 and F48, have slightly different values for fundamental energy gap ω_0. In addition, the maximum electronic absorption energy ω_0 increases from 6.83 eV (F33) to 8.16 eV (F48). Figure 5.11 shows the real and the imaginary parts of the calculated bulk dielectric function of the hybrid polymers that describe

Table 5.2 Best-fit parameters from an analysis of measured $<\varepsilon(\omega)>$ hybrid polymers and measured barrier values in terms of water vapor transmission rate (WVTR) and oxygen transmission rate (OTR)

Sample	ω_g (eV)	ω_0 (eV)	n (ω = 0 eV)	Volume fraction of inorganic component (%)	WVTR (gr/d m^2) 23°C/ 85% Relative Humidity	OTR (cm^3/ d m^2 bar) 23°C/ 50% Relative Humidity
F33	2.41 ± 0.09	6.83 ± 0.1	1.577	4.44 ± 0.09	0.015	0.004
F38	5.52 ± 0.09	7.36 ± 0.11	1.516	5.49 ± 0.1	0.05	0.01
F48	6.46 ± 0.11	8.19 ± 0.45	1.494	6.28 ± 0.3	0.1	0.05
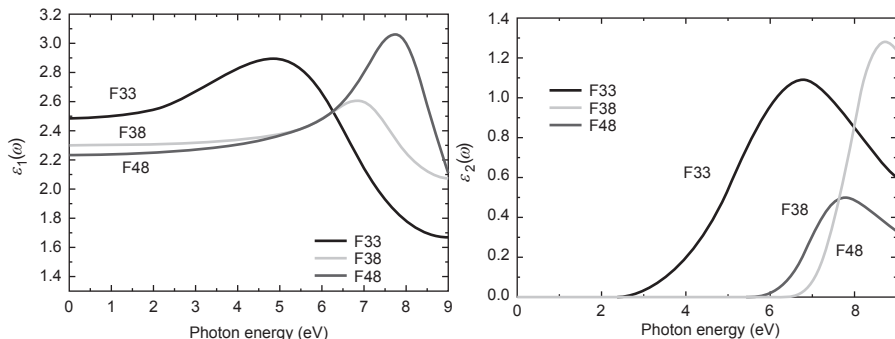
Figure 5.11 Calculated dielectric function $\varepsilon(\omega) = \varepsilon_1(\omega) + i\varepsilon_2(\omega)$ of hybrid polymers based on the best-fit parameter deduced from the analysis of measured $<\varepsilon(\omega)>$.

the optical response of the hybrid polymer materials. The $\varepsilon(\omega)$ is calculated from 0 to 9 eV and includes only the optical response in the visible and UV spectral regions (electronic transitions), but it does not take into account the optical absorptions of the hybrid polymers at higher energies ($\omega > 9$ eV).

Finally, from an analysis of the measured $<\varepsilon(\omega)>$, the refractive index n of the hybrid polymers was calculated and the increase in solid content in the hybrid polymers is associated with a reduction in the refractive index n values from 1.58 (F33) to 1.49 (F48). This reduction in the refractive index could be associated with a lower density of the hybrid polymer, which can lead to a less cohesive inorganic−organic bonding network and to a poor barrier response, as shown in Figure 5.12.
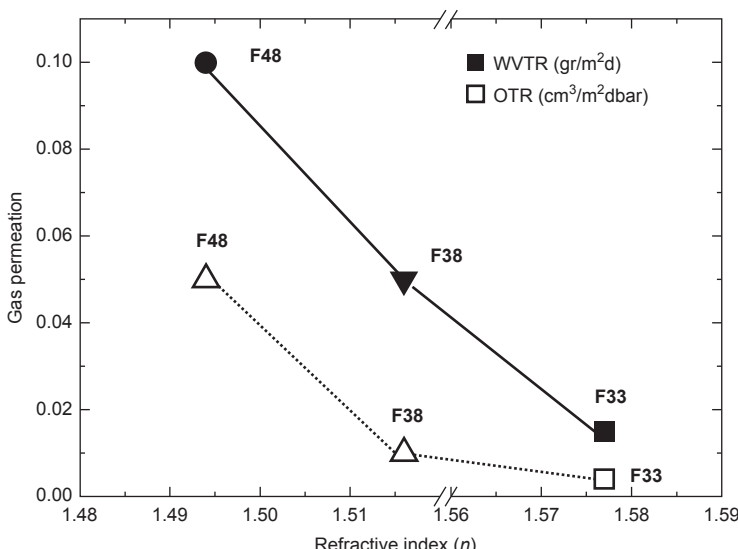
Figure 5.12 Correlation between estimated values of refractive index of hybrid polymers and measured values of water vapor transmission rate (WVTR) and oxygen transmission rate (OTR).

This can be attributed to the formation of a more cohesive inorganic−organic network in the hybrid polymer structure and close to the interface with the SiO_x interlayer, because of the use of a smaller amount of solid content and the use of UV radiation during the curing treatment of the hybrid polymers (F33 sample). This cohesive network is correlated with increased adhesion between the hybrid polymer and the SiO_x interlayer as a result of bonding, with the Si−OH groups of the SiO_x reducing the remaining microporosity of SiO_x.

From this, it could be concluded that one of the main factors that affects the barrier response of hybrid polymers is crosslinking between the inorganic and the organic components, as well as its adhesion on the substrate. One promising approach in this direction is the inclusion of SiO_2 nanoparticles (SiO_2-NP) during the synthesis process of the hybrid polymers, with the final aims of enhancing inorganic−organic crosslinking and achieving a more cohesive bonding network between the organic and inorganic components (Laskarakis et al., 2009).

To increase the covalent bonds and result in a more cohesive inorganic−organic network, which is expected to further improve barrier properties, different contents (1−30%) of SiO_2-NP 60 nm in size have been included inside hybrid polymer F38 during the synthesis process.

To analyze the optical response of the hybrid polymer with embedded SiO_2-NP, we assume a composite material that consists of an organic part (organic component of the hybrid polymer) and an inorganic part that includes both the inorganic component of the hybrid polymer and the embedded SiO_2-NP. Modeling of the optical response of the hybrid polymer was performed by the BEMA to calculate the volume fraction of each constituent as well (Azzam & Bashara, 1977).

Table 5.3 shows the calculated values of the fundamental band gap ω_g, maximum absorption energy ω_0, refractive index n, and measured WVTR and OTR values.

Table 5.3 Best-fit parameters from an analysis of measured $<\varepsilon(\omega)>$ of the hybrid polymers including SiO_2-NPs and measured barrier values in terms of water vapor transmission rate (WVTR) and oxygen transmission rate (OTR)

% SiO_2	ω_g (eV)	ω_0 (eV)	n ($\omega = 0$ eV)	WVTR (gr/d m^2) 23°C/85% Relative Humidity	OTR (cm^3/ d m^2 bar) 23°C/50% Relative Humidity
0	5.52	7.36	1.516	0.05	0.01
1	5.55	7.35	1.522	0.001	0.0004
5	5.59	7.32	1.483	0.005	0.0009
10	5.68	7.14	1.472	0.007	0.007
20	5.89	7.13	1.442	0.006	0.006
30	5.79	7.11	1.420	0.01	—

As can be seen in Table 5.3, the hybrid polymers with the best barrier response are those that include 1% of SiO_2-NP in their structure; they are characterized by values of band gap $\omega_g = 5.55$ eV and maximum absorption energy $\omega_0 = 7.35$ eV. Also, the barrier response of these hybrid polymers is $OTR = 0.0004$ cm^3/m^2 d bar and $WVTR = 0.001$ g/m^2 d (Logothetidis et al., 2010).

Moreover, from the values of calculated refractive index $n(\omega = 0)$ with SiO_2-NP in the hybrid, it is clear that an increase in the amount of SiO_2-NP in the hybrid polymers leads to a reduction in refractive index $n(\omega = 0)$ values that can be correlated to a reduction in the film's density. Consideration of the measured barrier response of these materials (Table 5.3) leads to the conclusion that the hybrid polymers with a lower refractive index (that can be correlated to lower density) are characterized by higher gas molecule permeation values (poorer barrier performance) than hybrid polymers with higher refractive index values (that can be correlated to higher density) (Laskarakis & Logothetidis, 2006).

From the results, is it clear that the inclusion of inorganic SiO_2-NPs with low concentration ($\sim 1\%$) in the hybrid polymer structure also improves barrier properties. However, although the inclusion of SiO_2-NP in the hybrid materials was originally intended to provide a more cohesive organic–inorganic network, the increase in the SiO_2-NP content results in a reduction in the materials refractive index (lower density). This has been justified by representative barrier measurements showing that materials with a higher amount of SiO_2-NP have poorer barrier performance (Logothetidis et al., 2010).

5.6   Conclusions

Successful encapsulation of flexible OEs is a main challenge that must be overcome to achieve their large scale-production and commercialization. In this chapter, *in situ* and real-time SE were applied in the study of the growth mechanism of inorganic barrier materials (SiO_x) on different flexible substrates. Their barrier properties were also measured to evaluate the quality of the barrier films and investigate factors affecting the barrier response. Results showed that the growth mechanism and the barrier response of the inorganic thin films were affected by the chemical structure of the substrates and the nanotopography. Concerning the hybrid barrier materials, the effect of the chemical composition and the addition of nanoparticles to the optical and barrier properties were studied. Regarding the chemical composition of the hybrid barrier materials, results showed that the amount of solid content affected their properties. As a consequence, the hybrid barrier material–inorganic barrier material–flexible substrate selected for development of the barrier system is SiO_x as an inorganic barrier material combined with a hybrid barrier material with a lower solid content (F33 or F38). Furthermore, study of the addition of silicon dioxide nanoparticles (SiO_2-NPs) showed that adding a low range of SiO_2-NPs (1–5%) to the hybrid barrier material F38 induced improvement of the barrier response. Overall, the results show that the value of the refractive index of the barrier material, which is related to the material's density, is the factor for evaluating barrier properties because in all cases the higher values of the refractive index lead to improvement of the barrier properties.

Acknowledgements

References

Amberg-Schwab, S. (2005). Inorganic-organic polymers with barrier properties against water vapor, oxygen and migrating monomers. In S. Sakka (Ed.), *Hanbook of sol−gel science* (pp. 455−478). Norwell: Kluwer Academic Publishers.

Amberg-Schwab, S., Katschorek, H., Weber, U., Hoffmann, M., & Burger, A. (2000). Barrier properties of inorganic−organic polymers: influence of starting compounds, curing conditions and storage-scaling-up to industrial application. *Journal of Sol−gel Science and Technology, 19*, 125−129.

Amberg-Schwab, S., Weber, U., Burger, A., Nique, S., & Xalter, R. (2006). Development of passive and active barrier coatings on the basis of inorganic−organic polymers. *Monatshefte für Chemie, 137*(5), 657−666.

Aziz, H., Popovic, Z., Xie, S., Hor, A.-M., Hu, N.-X., Tripp, C., & Xu, G. (1998). Humidity-induced crystallization of tris (8-hydroxyquinoline) aluminum layers in organic light-emitting devices. *Applied Physics Letters, 72*(7), 756.

Azzam, R. M. A., & Bashara, N. M. (1977). *Ellipsometry and polarized light*. Amsterdam: North Holland.

Benmalek, M., & Dunlop, H. M. (1995). Inorganic coatings on polymers. *Surface and Coatings Technology, 76*, 821−826.

Burrows, P. E., Bulovic, V., Forrest, S. R., Sapochak, L. S., McCarty, D. M., & Thompson, M. E. (1994). Reliability and degradation of organic light emitting devices. *Applied Physics Letters, 65*, 2922.

Charton, C., Schiller, N., Fahland, M., Holländer, A., Wedel, A., & Noller, K. (2006). Development of high barrier films on flexible polymer substrates. *Thin Solid Films, 502*, 99−103.

Chen, T. N., Wuu, D. S., Wu, C. C., Chiang, C. C., Chen, Y. P., & Horng, R. H. (2007). Improvements of permeation barrier coatings using encapsulated parylene interlayers for flexible electronic applications. *Plasma Processes and Polymers, 4*, 180−185.

Chiang, C. C., Wuu, D. S., Lin, H. B., Chen, Y. P., Chen, T. N., Lin, Y. C., et al. (2006). Deposition and permeation properties of SiN$_x$/parylene multilayers on polymeric substrates. *Surface and Coatings Technology, 200*, 5843−5848.

Chwang, A. B., Rothman, M. A., Mao, S. Y., Hewitt, R. H., Weaver, M. S., Silvernail, et al. (2003). Thin film encapsulated flexible organic electroluminescent displays. *Applied Physics Letters, 83*, 413−415.

Deng, C.-S. (2000). Nucleation and growth of gas barrier aluminium oxide on surfaces of poly(ethylene terephthalate) and polypropylene: effects of the polymer surface properties. *Journal of Polymer Science: Part B: Polymer Physics, 38*, 3151−3162.

Dennler, G., Houdayer, A., Latrèche, M., Séguid, Y., & Wertheimer, M. R. (2001). Studies of the earliest stages of plasma-enhanced chemical vapor deposition of SiO_2 on polymeric substrates. *Thin Solid Films, 382*, 1−3.

Dennler, G., Lungenschmied, C., Neugebauer, H., Sariciftci, N. S., Latrèche, M., & Czeremuszkin, G. (2006). A new encapsulation solution for flexible organic solar cells. *Thin Solid Films, 511−512*, 349−353.

Erlat, A. G., Wang, B. C., & Spontak, R. J. (2000). Morphology and gas barrier properties of thin SiO_x coatings on polycarbonate: correlations with plasma-enhanced chemical vapor deposition conditions. *Journal of Materials Research, 15*(3), 704−717.

Garcia-Ayuso, G., Vázquez, L., & Martínez-Duart, J. M. (1996). Atomic force microscopy (AFM) morphological surface characterization of transparent gas barrier coatings on plastic films. *Surface and Coatings Technology, 80*, 203−206.

Georgiou, D., Laskarakis, A., Logothetidis, S., Amberg-Scwhab, S., Weber, U., Schmidt, et al. (2009). Optical properties of hybrid polymers as barrier materials. *Applied Surface Science, 255*, 8023−8029.

Georgiou, D., Laskarakis, A., Koidis, C., Goktsis, N., & Logothetidis, S. (2008a). Growth mechanisms of silicon oxide nano-layers grown onto polymeric substrates for flexible electronics applications. *Physica Status Solidi C, 5*(10), 3387−3391.

Georgiou, D., Logothetidis, S., Koidis, C., & Laskarakis, A. (2008b). In-situ and real-time monitoring of high barrier layers growth onto polymeric substrates. *Physica Status Solidi C, 5*(5), 1300−1303.

Ghosh, A. P., Gerenser, L. J., Jarman, C. M., & Fornalik, L. E. (2005). Thin-film encapsulation of organic light-emitting devices. *Applied Physics Letters, 86*, 223503.

Graff, G. L., Burrows, P. E., Williford, R. E., & Praino, R. F. (2005). Barrier layer technology for flexible displays. In G. P. Crawford (Ed.), *Flexible flat panel displays* (pp. 57−75). England: John Wiley & Sons Ltd.

Gravalidis, C., Gioti, M., Laskarakis, A., & Logothetidis, S. (2004). Real-time monitoring of silicon oxide deposition processes. *Surface and Coatings Technology, 180−181*, 655−658.

Haas, K., Amberg-Schwab, S., Rose, K., & Schottner, G. (1999). Functionalized coatings based on inorganic−organic polymers (ORMOCER®s) and their combination with vapor deposited inorganic thin films. *Surface and Coatings Technology, 111*, 72−79.

Haas, K.-H., & Rose, K. (2003). Hybrid Inorganic/Organic polymers with nanoscale building blocks: precursors, processing, properties and applications. *Reviews on Advanced Materials Science, 5*, 47−52.

Hanika, M., Langowski, H.-C., Moosheimer, U., & Peukert, W. (2003). Inorganic layers on polymeric films − influence of defects and morphology on barrier properties. *Chemical Engineering & Technology, 26*(5), 605−614.

Hedenqvist, S., & Johansson, K. S. (2003). Barrier properties of SiO_x-coated polymers: multilayer modelling and effects of mechanical folding. *Surface and Coatings Technology, 172*, 7−12.

Henry, B. M., Dinelli, F., Zhao, K. Y., Grovenor, C. R. M., Kolosov, O., Briggs, G. A. D., et al. (1999). A microstructural study of transparent metal oxide gas barrier films. *Thin Solid Films, 355−356*, 500−505.

Ho Jung, K., Bae, J.-Y., Park, S. J., Yoo, S., & Bae, B.-S. (2011). High performance organic-inorganic hybrid barrier coating for encapsulation of OLEDs. *Journal of Materials Chemistry, 21*, 1977−1983.

Houbertz, R., Domann, C., Cronauer, C., Schmitt, A., Martin, H., Park, J.-U., et al. (2003). Inorganic−organic hybrid materials for application in optical devices. *Thin Solid Films, 442*, 194−200.

Jellison, G. E., & Modine, F. A., Jr. (1996). Parameterization of the optical functions of amorphous materials in the interband region. *Applied Physics Letters, 69*(3), 371.

Kelley, T. W., Baude, P. F., Gerlach, C., Ender, D. E., Muyres, D., Haase, M. A., et al. (2004). Recent progress in organic electronics: materials, devices, and processes. *Chemistry of Materials, 16*(23), 4413−4422.

Kim, T. W., Yan, M., Erlat, A. G., McConnelee, P. A., Pellow, M., Deluca, J., et al. (2005). Transparent hybrid inorganic/organic barrier coatings for plastic organic light-emitting diode substrates. *Journal of Vacuum Science & Technology A, 23*(4), 971.

Kolosov, D., English, D. S., Bulovic, V., Barbara, P. F., Forrest, S. R., & Thompson, M. E. (2001). Direct observation of structural changes in organic light emitting devices during degradation. *Journal of Applied Physics, 90*(7), 3242.

Kopola, P., Aernouts, T., Sliz, R., Guillerez, S., Ylikunnari, M., Cheyns, D., et al. (2011). Gravure printed flexible organic photovoltaic modules. *Solar Energy Materials and Solar Cells, 95*, 1344−1347.

Langowski, H. C. (2008). Permeation of gases and condensable substances through monolayer and multilayer structures. In O. Piringer, & A. Banert (Eds.), *Plastic packaging interactions with food and pharmaceuticals* (pp. 297−349). Weinheim: Wiley-VCH Verlag GmbH & Co. KGaA.

Laskarakis, A., Logothetidis, S., Georgiou, D., Amberg-Schwab, S., & Weber, U. (2009a). On the influence of silicon oxide nanoparticles on the optical and surface properties of hybrid (inorganic−organic) barrier materials. *Thin Solid Films, 517*, 6275−6279.

Laskarakis, A., Georgiou, D., Logothetidis, S., Amberg-Schwab, S., & Weber, U. (2009b). Study of the optical response of hybrid polymers with embedded inorganic nanoparticles for encapsulation of flexible organic electronics. *Materials Chemistry and Physics, 115*, 269−274.

Laskarakis, A., & Logothetidis, S. (2006). On the optical anisotropy of poly(ethylene terephthalate) and poly(ethylene naphthalate) polymeric films by spectroscopic ellipsometry from visible-far ultraviolet to infrared spectral regions. *Journal of Applied Physics, 99*, 066101.

Leterrier, Y. (2003). Durability of nanosized oxygen-barrier coatings on polymers. *Progress in Materials Science, 48*(1), 1−55.

Lewis, J. S., & Weaver, M. S. (2004). Thin-film permeation-barrier technology for flexible organic light-emitting devices. *IEEE Journal of Selected Topics in Quantum Electronics, 10*, 45−57.

Liao, K.-S., Yambem, S. D., Haldar, A., Alley, N. J., & Curran, S. A. (2010). Designs and architectures for the next generation of organic solar cells. *Energies, 3*(6), 1212−1250.

Logothetidis, S. (2005). Polymeric substrates and encapsulation for flexible electronics: bonding structure, surface modification and functional nanolayer growth. *Reviews on Advanced Materials Science, 10*(5), 387−397.

Logothetidis, S. (2008). Flexible organic electronic devices: Materials, process and applications. *Materials Science and Engineering B-Advanced Functional Solid-State Materials, 152*(1-3), 96−104.

Logothetidis, S., Laskarakis, A., Georgiou, D., Amberg-Schwab, S., Weber, U., Noller, K., et al. (2010). Ultra high barrier materials for encapsulation of flexible organic electronics. *The European Physical Journal Applied Physics, 51*, 33203.

Park, S.-H. K., Oh, J., Hwang, C.-S., Lee, J.-I., Yang, Y. S., & Chu, H. Y. (2005). Ultrathin film encapsulation of an OLED by ALD. *Electrochemical and Solid-state Letters, 8*(2), H21−H23.

Park, J.-S., Chae, H., Kyoon Chung, H., & Lee, S. I. (2011). Thin film encapsulation for flexible AM-OLED: a review. *Semiconductor Science and Technology, 26*(3), 034001.

Pichler, K. (1997). Conjugated polymer electroluminescence: technical aspects from basic devices to commercial products. *Philosophical Transactions of the Royal Society A, A355*, 829−842.

Potscavage, W. J., Yoo, S., Domercq, B., & Kippelen, B. (2007). Encapsulation of pentacene/C60 organic solar cells with Al_2O_3 deposited by atomic layer deposition. *Applied Physics Letters, 90*(25), 253511.

Roberts, A. P., Henry, B. M., Sutton, A. P., Grovenor, C. R. M., Briggs, G. A. D., Miyamoto, T., et al. (2002). Gas permeation in silicon-oxide/polymer (SiO_x/PET) barrier films: role of the oxide lattice, nano-defects and macro-defects. *Journal of Membrane Science, 208*, 75−88.

Schubert, S., Klumbies, H., Müller-Meskamp, L., & Leo, K. (2011). Electrical calcium test for moisture barrier evaluation for organic devices. *Review of Scientific Instruments, 82*, 094101.

Seino, T., & Sato, T. (2002). Aluminum oxide films deposited in low pressure conditions by reactive pulsed dc magnetron sputtering. *Journal of Vacuum Science & Technology A, 20*(3), 634−637.

Singh, B., Bouchet, J., Rochat, G., Leterrier, Y., Månson, J.-A. E., & Fayet, P. (2007). Ultra-thin hybrid organic/inorganic gas barrier coatings on polymers. *Surface and Coatings Technology, 201*(16−17), 7107−7114.

Weaver, M. S., Michalski, L. A., Rajan, K., Rothman, M. A., Silvernail, J. A., Brown, J. J., et al. (2002). Organic light-emitting devices with extended operating lifetimes on plastic substrates. *Applied Physics Letters, 81*, 2929.

Yanaka, M. (2001). How cracks in SiO_x-coated polyester films affect gas permeation. *Thin Solid Films, 397*(1−2), 176−185.

Advanced interconnection technologies for flexible organic electronic systems

6

M. Koyuncu, E. Lorenz, A. Zimmermann
Robert Bosch GmbH, Waiblingen, Germany

6.1   Introduction

Future electronic systems must provide technological responses to the ever-increasing prominence of electronic devices in daily life. The smartphone era and social networking over the Internet has resulted in a society with a much different sense of communication and interaction. Hand held devices like smartphones are currently the main interfaces between device owners and networks, but a clear trend is the connectivity of everyday objects equipped with sensors, to each other and users, over a network. Two important aspects for the future of electronic devices can be derived from this trend: enhanced integration into/onto objects and increased functional density. The latter is well described by Figure 6.1, which shows the future trend for electronic systems (ITRS).

While the *y*-axis represents the continued scaling of the transistor density, functional diversification depicted by the *x*-axis represents the 'More-than-Moore' concept and is expected to play a stronger role in future systems. These are nondigital functionalities (RF communication, power control, passive components, sensors, actuators) and do not necessarily scale according to Moore's Law. This, in combination with increased processing capability, is expected to give the technological response to future needs.

While digital processing takes place in a System-on-Chip, energy harvesting or storage, passives and the interaction with the environment take place through sensors/actuators in a System-in-Package (SiP). 'More-Moore' governs processing of data, whereas More-than-Moore is more relevant for SiP, where the interaction with the environment or the user is concerned (More-than-Moore). The challenge therefore lies in the heterogeneous integration of the digital and nondigital functions within a system. The term integration comprises two components, mechanical integrity and electrical connectivity. While the latter ensures signal transfer through electrical interconnections, mechanical integrity forms the basis for reliability and integration of the electronic system into its physical surrounding.

Foil-based systems offer a suitable platform for this purpose, reaching a very high level of packaging density with (ultra-)thin components and the additional advantage of mechanical flexibility. The flexible nature of these systems can be engineered to meet the needs of specific applications, which may mean being bendable, conformably
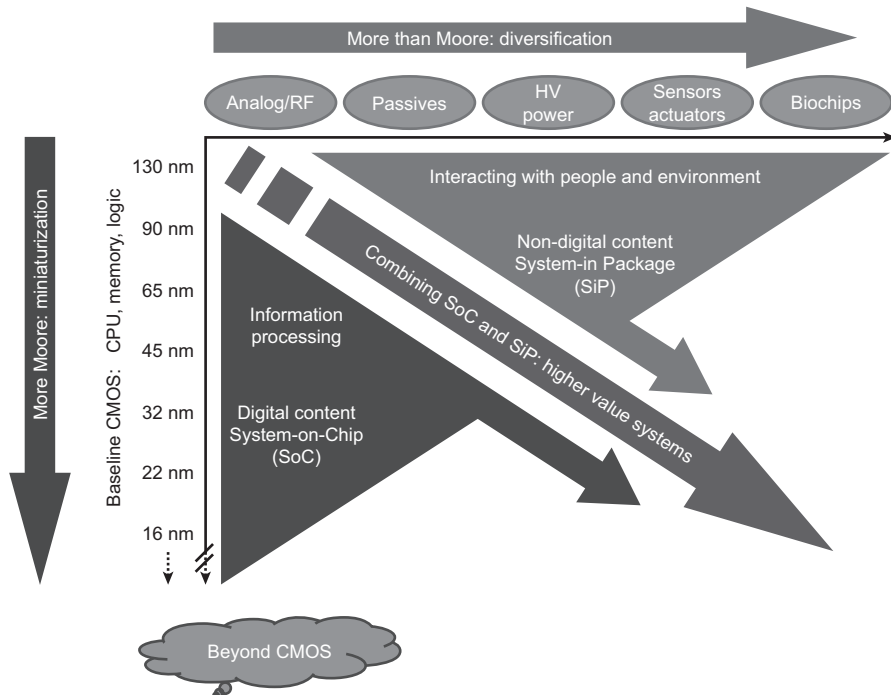
Figure 6.1 Moore's Law and more.
Source: Ref. ITRS.

shaped, elastic, stretchable or a combination of these. Another advantage of foil-based systems is their manufacturability — as they are compatible with cost-effective manufacturing technologies (e.g. roll-to-roll manufacturing), components such as antennas and passives can be implemented into the manufacturing process of the foil (homogeneous integration).

The flexibility aspect does not only refer to the foil (serving as substrate), but also implies compatibility of the components as well as mechanical and electrical inter-connections. Electronics based on the conventional printed circuit board (PCB) is the precursor of this technology, and has been engineered to a high reliability level for challenging applications. The technology is mostly based on metallic interconnec-tions (i.e. soldering technology), for which there are well-defined surface mount and pin-in-hole processes defined by industrywide standards as well as technical specifi-cations from entities such as the International Electrotechnical Commission (IEC), the JEDEC Solid State Technology Association and the Japan Electronics and Infor-mation Technology Industries Association. Packaged surface-mounted devices (SMD) have been successfully integrated onto polyimide (PI) foils, in which the advantages of flexibility can compensate for the high cost of PI foil that is compatible with the soldering process. Foil-based technology with integrated circuits (ICs) and auxiliary electronics integrated directly onto/into PI, as well as more cost-effective

foils (polyethylene naphthalate (PEN), polyethylene terephthalate (PET)), including (ultra-)thin organic/inorganic components however, is still in its infancy. As a result, foil-based technologies will make enormous increases in packaging density possible, and offer decisive advantages compared to traditional PCB for certain applications.

This chapter focuses on interconnection technologies for foil-based flexible systems and refers to System-in-Foil for the rest of this chapter. It will not address the already existing solutions like flexible displays, for which the reader is referred to comprehensive reviews elsewhere (Cheng & Wagner, 2009; Nathan et al., 2012).

6.2 Materials and processes

A System-in-Foil is a composite structure comprising substrates, components and electrical interconnections that are mechanically and electrically networked to each other. Components of very different sizes and mechanical properties, as well as interconnections in minuscule dimensions, have to be joined in a series of process steps that must be well designed, taking critical parameters such as thermal endurance of components and materials, mechanical robustness and process tolerances into account. The following subsections will survey the materials involved and techniques to analyse this process chain, and serve as a guide for applications that can profit from the advantages of this technology.

6.2.1 Substrates and components

Various substrate technologies can be used for flexible electronics. These include PI, (heat stabilized) PEN, PET and LCP (liquid-crystal polymer), and are reviewed by MacDonald et al. (2007). Components compatible with this technology differ from conventional counterparts, particularly in terms of packaging and thickness, for which possible classifications are suggested in Table 6.1. Based on the manufacturing environment of the components and the foils, integration technologies are of two classifications. Heterogeneous integration refers to a component-manufacturing environment that differs significantly from that of the foil and requires mechanical and electrical integration with at least one processing step (e.g. ICs). Homogeneous integration refers to the case in which the component emerges during substrate foil production, such as the manufacturing environment of a lithographically-produced antenna structure. Process examples and detailed information on materials are provided in Table 6.2.

This classification discussion is undertaken to support the development of a systematic approach for integration technologies (mechanical and electrical) and is akin to the classification of conventional components based on lead frames such as small-outline IC and quad-flat no-leads; or substrates such as ball grid array and land grid array. The substrate of the component plays the most important role in this classification. For components like ICs, the substrate and the functional material are both silicon: the circuit components (ICs) are accommodated within the

Table 6.1 **Classification of components for a System-in-Foil**[1]

Component type	Component examples	Integration technique	Process example	Materials for integration	Typical process parameters
IC	Bare die	Heterogeneous	Flip chip, embedding, jetted contacts	ACA, NCA, ICA, conductive ink	*NCA-flip chip:* $T = 150-220\ °C$ $F = 30-150$ g/bump *ACA-flip chip:* $T \sim 180-220\ °C$ $F = 10-75$ g/bump
Foil component	Sensors, photovoltaic modules, batteries *or* foils with a combination of already integrated components	Heterogeneous	Lamination, jetted contacts, thermode	ICA, ACA/ACF, PSA/NCA	*ACF (pre-bonding/ bonding):* $T \sim 100\ °C\ /\ > 170\ °C$ $P = 1$ MPa / 2 MPa
Passives	Inductors, capacitors, resistors	Homogeneous/ Heterogeneous	Lithography, screen printing	ICA, thick film technology	Curing of *ICA* (epoxy-based) room temperature to 150 °C; 24 h–3 min, trimming
Discretes	SMD	Heterogeneous	Pick and place	Conductive ink/ ICA for SMT	Sintering of *Conductive Ink* 170–200 °C/15min

[1]ACA, anisotropic conductive adhesive; ACF, anisotropic conductive film; NCA, nonconductive adhesive; ICA, isotropic conductive adhesive; ICP, isotropic conductive paste; PSA, pressure-sensitive adhesive; PI, polyimide; PET, polyethylene terephthalate; PEN, polyethylene naphthalate; LCP, liquid-crystal polymer; SMT, surface-mount technology.

Table 6.2 **Typical materials used in mechanical and electrical integration to form a System-in-Foil**

Material	Polymer matrix	Metal fillers	Characteristic	Some material properties
ICA/ICP	Various systems based on epoxy, silicone, thermoplastic materials	Typically Ag, Ni, or Cu flakes	Filler volume significantly higher than percolation threshold (15−25% volume fraction) Conducts in x-, y- and z-direction	E(RT) = 1−7 GPa Tg = −50−300 °C CTE1 = 20−90 ppm/K CTE2 = 100−250 ppm/K Bulk Resistivity: $10^{-4}\,\Omega$ cm
ACA/ACF	Thermosetting epoxy resin	Typically Ag, Ni, Sn/ Pb particles or Ni/ Au coated polymere spheres	Filler volume below percolation threshold Conducts only in z-direction	E(RT) = <1−9 GPa Tg = 80−180 °C CTE1 = 20−90 ppm/K CTE2 = 100−2000 ppm/K Resistivity (z-direction) = $10^{-4}\,\Omega$ cm
NCA	Acrylate, thermoplastic polyurethane	None	Contains non-conductive fillers (e.g. SiO2)	E(RT) = <1−9 GPa Tg = −30−200 °C CTE1 = 50−100 ppm/K CTE2 = 100−300 ppm/K Bulk Resistivity: 10^{8} MΩ cm

ACA, anisotropic conductive adhesive; ACF, anisotropic conductive film; NCA, nonconductive adhesive; ICA, isotropic conductive adhesive; ICP, isotropic conductive paste.
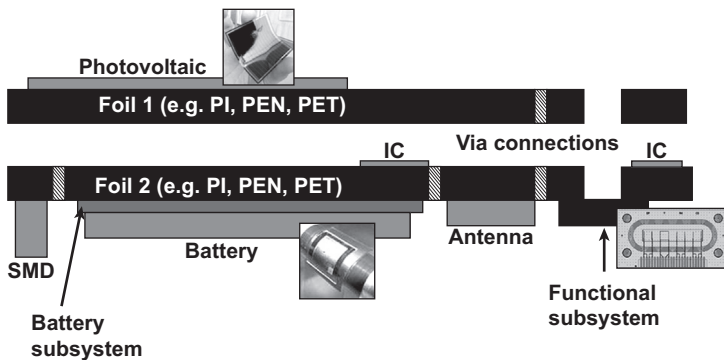
Figure 6.2 Schematic representation of a System-in-Foil comprising various components and subsystems. Component pictures courtesy of CEA-Leti, STMICROELECTRONICS, Fraunhofer-EMFT.

first few microns, while the rest of the material serves as the substrate. In contrast to the conventional active components, the silicon is not housed (e.g. by a moulding compound), but is integrated onto the foil as bare die. Foil components, on the other hand, are those where the functional material is applied on an organic/inorganic (e.g. polymer/glass) substrate that accommodates the terminals for signal I/O. Another example of a foil component is a substrate on which components of either type have previously been mounted. These fulfil a given functionality, representing a module or a subsystem, with internal and external data communication capability. They offer the advantage of being tested separately and are included in the process as a 'known good subsystem'.

Passives include capacitors, inductors and resistors, the integration of which can be either homogeneous or heterogeneous depending on the available technologies. Discrete SMD components are those whose packaged form and thickness cannot be modified to achieve flexibility, such as quartz timers and large capacitors, yet they must be integrated into the System-in-Foil for complete functionality. A schematic view of a System-in-Foil is shown in Figure 6.2. Two large-size foils with circuitry, the so-called system foils, form the backbone of the system, accommodating various components and providing electrical connectivity for the whole system. The components and the foils are integrated through mechanical and electrical interconnections: a modular structure is evident in which the backbone consists of energy, processing and communication capabilities; functionality is defined by a functional subsystem.

6.2.2 Integration technologies

Integration technologies both on a subsystem and system level require a thorough consideration of several factors. The process sequences for the whole system must be aligned with each other, and consider both materials and process conditions such as processing temperature and temperature duration. The techniques and these considerations are discussed in the following sections.

6.2.2.1 Integration of ICs

There are numerous approaches reported in the literature for integration of silicon dies having conventional thickness, as well as thin/ultrathin dies onto/into foils. The subject of this chapter will be the latter, of which the fabrication is reviewed by Burghartz (2011). The residual stress in the silicon can also play a role in the selection of the integration technology, which spans the range from precise placement and mounting to self-assembly techniques with acceptable accuracy, compensated by adaptive interconnection formations (Kuran & Tichem, 2013) − a summary of these techniques is given in Table 6.3. They differ principally in the orientation of the chip with respect to the substrate surface: mechanical mounting with active side up, followed by forming of electrical interconnections, versus mounting in flip chip configuration to form the electrical connection, followed by an optional strengthening of the mechanical interface. A common goal of all techniques is the reliable integration of chips with high throughput for applications from health care and disposable electronics to document safety, biomedicine and other fields.

A thin/ultrathin package based on PI substrate technology is the UTCP (ultrathin chip package) (Angelopoulos & Kaiser, 2011). A chip of approximately 20 µm thickness is embedded between two PI layers, resulting in a flexible package of 60 µm thickness suitable for second-level assembly on a PCB or foil. The process involves the deposition of PI on a rigid carrier, placement of chip with the active side up followed by the deposition of the next PI layer to embed the chip. Vias on the bond pad of the chip are opened by laser drilling, a process compatible with small bond pad sizes. TiW/Cu metallization from the top PI layer to pads is done with a lithography step followed by the release of the package from the rigid carrier. The peak temperature during the process exceeds 300 °C for the curing of the base PI layer.

Integration of ICs onto foils, such as PI and PET substrates, has also been investigated extensively to produce low-cost embedded circuitry for various applications. A variety of processes, some of them readily available and well developed, have potential to form interconnections with the chips positioned active side up. Substrate materials, as well as the bond pad pitch and size, are primary factors for the selection of the integration process and materials. Screen printing, as a well-known and readily available method for printing circuitry onto foils, is limited in terms of resolution. With recent advances in ink-jet technology such as aerosol jetting, the resolution has significantly improved to a level that this technology can produce interconnections onto chips (Figure 6.3). On the other hand, the increased resolution is more expensive, thus rendering the process economically less feasible for generating conductive traces. An optimized combination of the different processes along the production line can overcome the technological and economical limitations.

Another approach is patterning a groove for the chip and circuitry on the foil using a laser process, with subsequent filling with conductive paste through screen printing (Dietzel et al., 2011). The maximum process temperature and duration along the process chain determine the substrate material of choice (or vice versa), which is one of the most important cost factors. Conventional materials used for

Table 6.3 Integration techniques for thin/ultrathin ICs

Integration technique	Process	Characteristic	Chip contact	Surface compatibility	Active side	References
Self-assembly	• Fluidic self assembly via programmable surfaces • Self assembly via magnetization of bumps	• Mechanical and electrical connection can be one step • Rather coarse pitch	Galvanic-, stud-bumps or UBM	Noble/nonnoble	Up or down	Teh et al. (2004), Bock, Scherbaum, Yacoub-George, Landesberger (2008)
Flip chip (NCA)	• Die bonder applying heat and pressure at the same time	• Mechanical and electrical connection in one step • Min. achievable pitch $\geq 50\ \mu m$	Galvanic- or stud-bumps	Noble/nonnoble	Down	Li et al. (2010), Kim and Kim (2013), Caers and de Vries (2003)
Flip chip (ACA)	• Die bonder applying heat and pressure at the same time	• Ultra fine pitch achievable ($\leq 50\ \mu m$) • Mechanical and electrical connection in one step • Curing and sufficient pressure are crucial for the electrical connection.	Galvanic-, stud-bumps or UBM	Noble/nonnoble	Down	Li et al. (2010a, 2010b)

Flip chip (ICA)	• Deposition of ICA onto the contact areas • Dipcoating of bumps	• Pitch is limited either by the resolution of the dispensing process or due to the minimum possible clearance between the pads on chip and substrate	Galvanic- or stud-bumps	Noble/nonnoble	Down	Li, Lu, Wong (2010c)
Jetted contacts	• Mechanical integration with NCA/PSA • Aerosol jet for electrical connection	• Chip mounting and electrical connection in two different steps • Pitch limited by resolution of jet-process (<100 μm)	UBM[1]	Noble	Up	Stoukatch et al. (2012), King and Renn
Chip-in-Flex	• Embedding chip between foils; i.e. LCP, PI • Flip chip process • Microvia process	• Pitch limited due to accuracy of laser-drilling • 23 − process steps: Integration, embedding, electrical connection (microvia) • Mechanical Protection	Galvanic-, stud-bumps or UBM[1]	Noble/nonnoble	Up or down	Wolf et al. (2014)

[1]UBM, Under bump metallization bump.
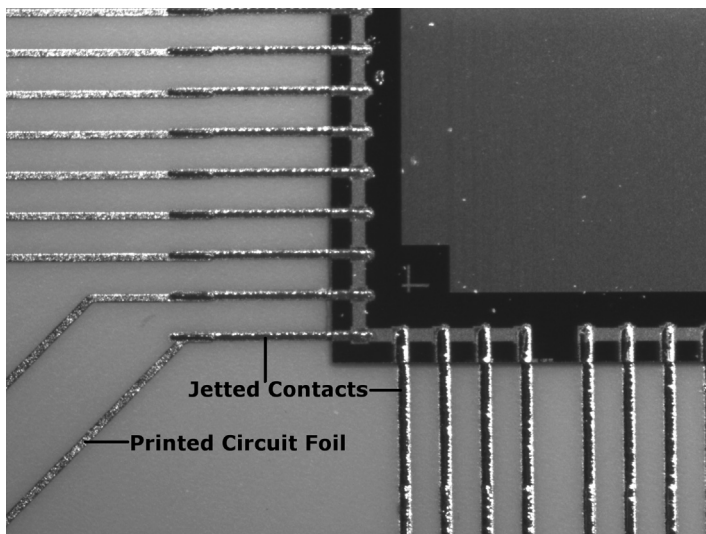
Figure 6.3 Chip with Aerosol Jet-printed conductive tracks (300 μm pitch).

interconnections also represent a significant share of the cost, as they contain high amounts of silver, and the size of the filler particles has to be in the submicron range for high-resolution printing. Compatibility of these materials with nonnoble metalliza-tion is also an important aspect. There are various approaches from major material sup-pliers for damping the impact of silver price fluctuations on materials costs, as well as compatibility with nonnoble metallization. The use of these materials may provide a cost-effective solution based on the reliability requirements of the application.

Another technique to embed thin/ultrathin chips into foils is based on chip technol-ogy (Kugler, Koyuncu, Zimmermann, & Kostelnik, 2011). The chip is laminated be-tween two LCP foils, the top foil having a bare copper surface, and is laser drilled to expose the bond pads on the chip. In a subsequent galvanic process, the bond pads are connected to the blank copper, which is then structured (Ultimum) as shown in Figure 6.4. The seed/catalyst in the formulation of the top foil ensures copper deposi-tion on the sidewalls of the holes during electrochemical plating. Vias in the foils connect the circuitry on both foils in the same process.

Flip chip technique is a common integration process with various material options. In this case, the electrical contacts are established during the mounting of the chip onto the foil. The process can be based on adhesives, soldering or thermocompression technologies.

Nonconductive adhesive (NCA), anisotropic conductive adhesive (ACA) and isotropic conductive adhesive (ICA) are among the most common adhesive processes. NCA is applied in paste or film form on the substrate or wafer level using conventional dispensing, screen/jet printing or lamination. The process involves simultaneous appli-cation of pressure and temperature by the die bonder, and the applied pressure ensures contact between pillars/bumps on the bond pads of the chip (Figure 6.5(a)) and the
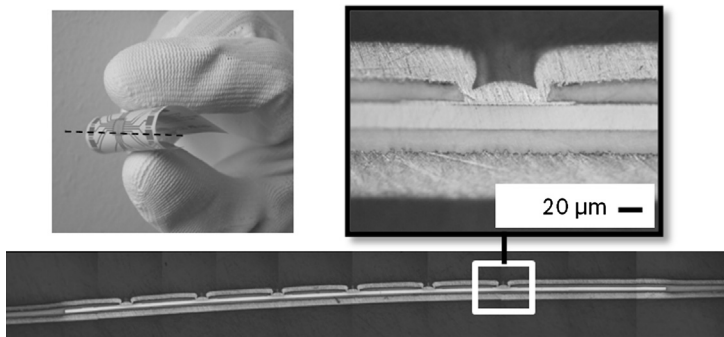
Figure 6.4 An ultrathin chip embedded in liquid-crystal polymer (LCP) foils. Courtesy of Würth Elektronik GmbH Co. & KG.

pads on the foil (Figure 6.5(b)). Applied heat, usually supplied by the die bonder or ultraviolet radiation applied through the substrate, cures the adhesive during the chip assembly process. The cure shrinkage of the NCA provides mechanical integrity of the assembly, maintaining electrical connectivity by compressive force that reaches resistance values comparable to soldered contacts.
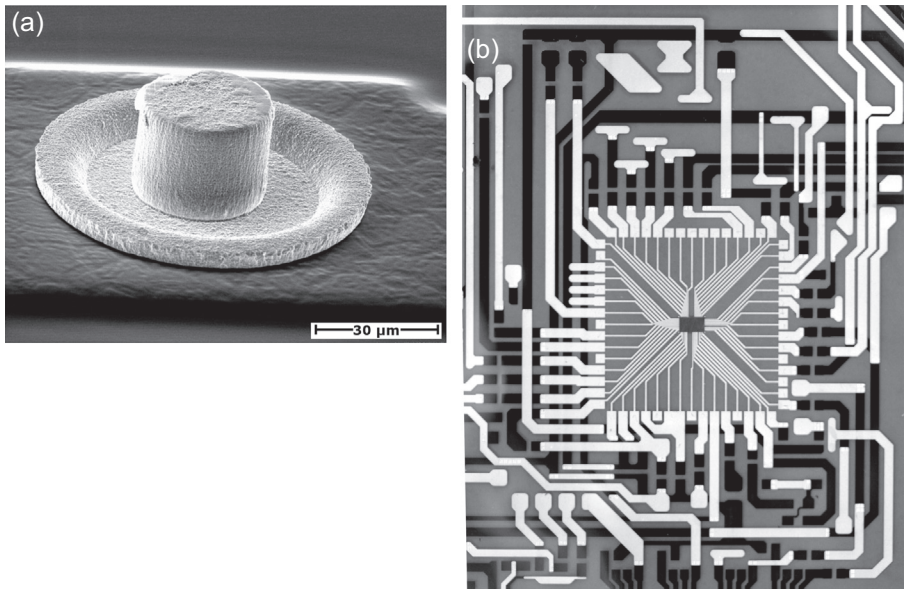
Figure 6.5 (a) Scanning electron microscope (SEM) image of a galvanic Au-pillar; and (b) photograph of a microcontroller fan-out on a 50 μm thick system foil with 10 μm thick Cu traces.

Process speed has to be aligned with the reaction kinetics of the NCA. The geometry of the tool and the applied force are critical to obtaining a connection without damaging the thin/ultrathin die and compensating for bump height tolerances, especially if the bond pad distribution on the die is not symmetrical; ductile materials for bumps (e.g. Au) are therefore more suitable for the process. The cure shrinkage of the NCA during processing has to tolerate the elastic deformation in the system and possible expansion of the adhesive due to moisture uptake in the field. Extensive care has to be taken to prevent NCA contact with the tool, especially in the case of very small die sizes. The temperature and duration of this process offer high throughput based on materials that cure within seconds (snap-cure) at moderate temperatures, allowing the use of less costly substrates. Materials and processes are reviewed by Li, Lu, and Wong (2010). Comparative process and reliability data for NCAs in paste and film forms are provided by Chiang (Chiang, Chan, Ralph, & Holland, 2006).

ACA is applied by similar methods as those used for NCA, either onto substrates or the wafer, with the foil form being more common. ACA contains a low-volume fraction of conductive particles (below percolation threshold) dispersed in a thermosetting (epoxy) or thermoplastic matrix to provide electrical conductivity only in the direction of applied force (i.e. z-direction) (Gilleo, 1995; Li, Moon, & Wong, 2005; Li & Wong, 2006). Conductive particles are metallic or metal-coated polymer fillers; Au, Ag, Cu or Ni particles offer different properties in terms of reliability and cost. Au offers the advantage of being inert and highly conductive, but its advantages need to compensate for its high cost. Cu, despite being cost-effective, has long-term stability problems due to oxidation, while Ni suffers similar problems under temperature and humidity loading. As a result, Ag offers a compromise in terms of cost and chemical stability and is a common filler material for ACAs.

Polymer particles coated with Ag or Ni/Au are also used as a low-cost alternative and have found wide application in cases where Ni coating is prone to the aforementioned long-term reliability problems. To soften the matrix and form a conductive bridge between the opposing electrodes, special equipment applies pressure and a defined temperature ramp with a thermode. A dwell at the processing temperature allows curing of the epoxy (see Table 6.3). Several parameters, such as the thermal mass of the whole system, pressure level and distribution, surface topography and matrix properties, play a role in forming a reliable interconnection. The process is well suited for fine-pitch applications due to lack of inplane conductivity, whereas the matrix with chemical shrinkage provides mechanical stability. The technology can also be used for providing contacts between foil components and system foils.

6.2.2.2 Integration of foil components

Foil components for a System-in-Foil can be sensors, batteries or structured foils with integrated components forming modules or subsystems (Figure 6.2). Subsystems are testable modular parts with previously integrated components that increase the yield of the complete process and enable a modular system.

Depending on the (relative) size of the foils, as well as the I/O structure on foil components and system foils, mechanical and electrical integration might involve disparate
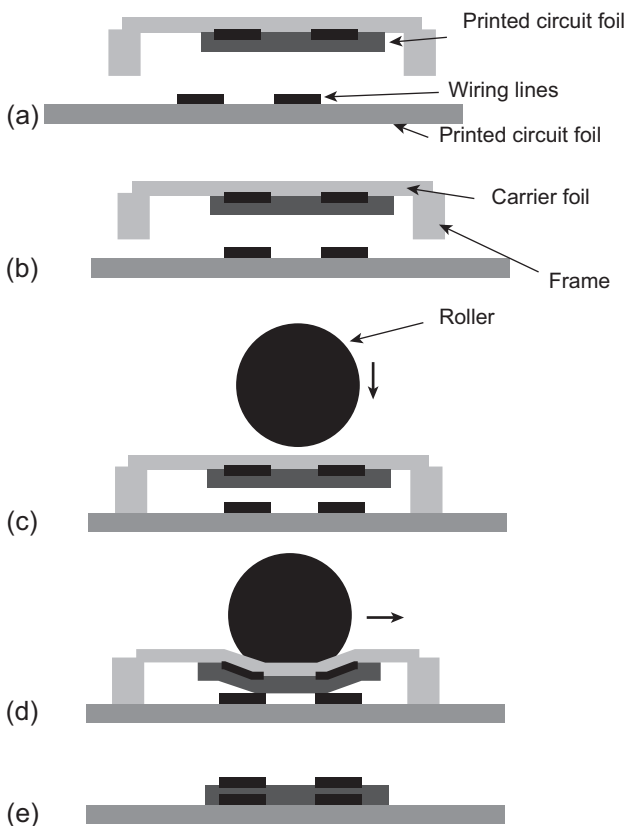
Figure 6.6 Workflow for foil-to-foil interconnection using a foil chuck and an optical vision system. (a) Loading of the carrier foil; (b) alignment in x, y, φ direction, and movement of the printed-circuit foil; (c) settling of frame and roller; (d) lamination by lateral roller motion; and (e) aligned foil laminate.

processing steps, typically requiring a mechanical integration step to precede the formation of electrical interconnections. Tolerances in the mechanical integration step will influence the subsequent process. Lamination using an adhesive foil such as pressure-sensitive adhesive (PSA) is an intuitive method to mechanically join two foils. The process has to have enough accuracy to align the pads on both foils and account for the tolerances of the next step. It should also be compatible with the already integrated components on the involved foils and still provide robust mechanical integrity.

Such a process is described in Figure 6.6 (German Patent No, 2012). One foil is placed onto a vacuum chuck, whereas the other, backed with PSA, is attached to a carrier foil. The two foils are aligned using an x-/y-axis system with rotational capability. A vision system checks the alignment on the fiducial markings on different locations in an iterative manner, relying on optical transparency of the foils. If the transparency of
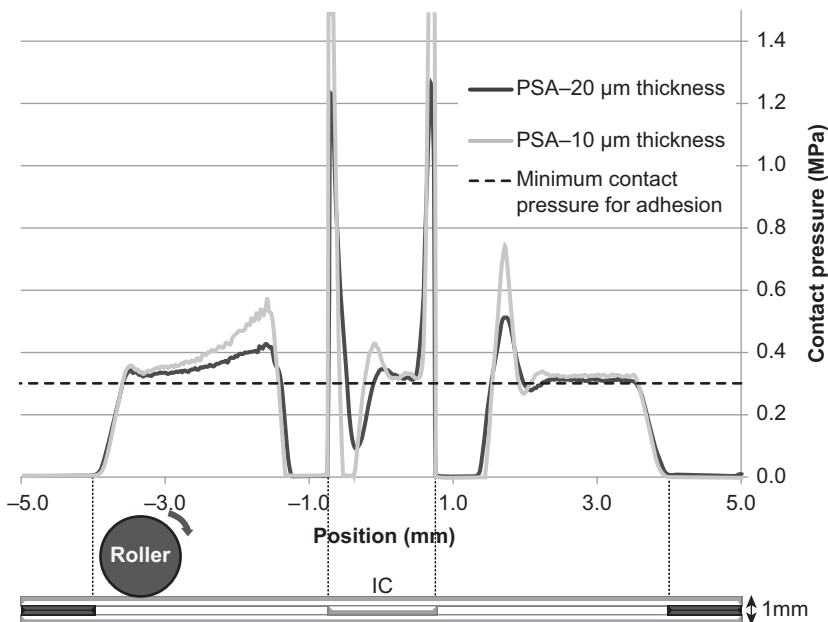
Figure 6.7 Stress distribution in pressure-sensitive adhesive (PSA) for the process step shown in Figure 6.5d calculated for 10 and 20 μm pressure-sensitive adhesive (PSA) thickness and an IC thickness of 25 μm at a roller force of 15 N.

either foil is too low, e.g. in the case of PI, alignment-holes are drilled into the foil to guide alignment. Once the alignment is reached, the foils are laminated using a roller to minimize trapped air between the two foils.

After assembly, the laminated foils are released from the carrier foil. Compliant materials on the roller ensure a reliable process for the existing components on the foils. The simulation of the rolling step in Figure 6.6(d) is shown in Figure 6.7, where two PI foils of 50 μm foils are joined. Stress distribution on the PSA is a function of the distance to the chip and the rigid frames of the carrier foil. The pressure drops in the immediate vicinity of the chip and stress singularities at the edges are evident. In-homogeneous stress distribution on the chip is due to roller speed, causing wave propagation on the top foil. In the regions adjacent to the frame, the stress in the top foil is reduced to almost zero. The simulation shows the potential failure sources in the joined structure and helps process optimization without costly iterations involving physical analysis.

This mechanical integration step is followed by the formation of electrical inter-connections which can be in the form of via-filling from the top to the bottom foil, or deposition of ICA onto pads on both foils to form bridges in case of unequal foil sizes. Plating processes common in PCB manufacturing, or flexible foils for traditional surface-mount technology, are not always suitable due to the commonly used components and adhesives. Normally curing of the ICA up to 150 °C is necessary,
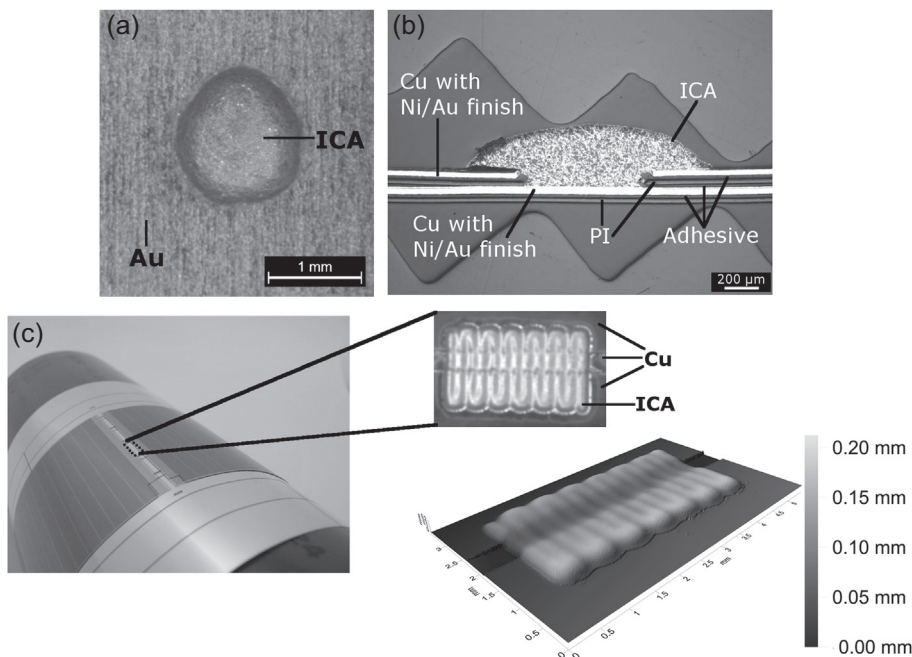
Figure 6.8 Electrical interconnections formed by jetted isotropic conductive adhesive (ICA) between a foil component and the system foil. (a) Top; (b) cross-sectional view of a via-filling; and (c) top view of mounted flexible PV cells (left) and microscopic view & 3-D topography of an isotropic conductive adhesive (ICA) bridge.

which is an important factor for material selection and process flow design. Temperature endurance and excursions of the existing components should be taken into account. Although curing equipment with focused light/laser source for localized heat application or materials that cure at room temperature do exist at a laboratory scale, the industrialization aspect (e.g. processing time) has to be considered as well.

Options for the deposition process of ICA include screen/stencil printing as well as contactless processes such as dispensing or jetting, where the latter has higher potential to protect existing components and ensure sound via-filling or bridge formation; Figure 6.8(b) shows a cross-sectional view of such interconnections. Filled vias are shown in Figure 6.8(a), whereas a bridge formed by jetting of ICA between two foil components, simultaneously providing electrical interconnection to the system foil, is shown in Figure 6.8(c). The topography of the ICA reflects the jet head movement and the topography on the foil. One of the potential problems for vias is trapped air; its effect on the reliability is yet to be clarified. The processes have to be optimized to achieve (application specific) acceptable reliability with the least amount of material and highest throughput.

Although anisotropic conductive films can also be used to integrate two foils, their use in areas without electrical pads (i.e. for the sole purpose of mechanical integration) is too expensive. However, partial application on the pads where the principal mechanical integration is done with a PSA can be advantageous to establish electrical contacts with localized heating using a thermode.

6.2.2.3   Process flow

The process flow to obtain a System-in-Foil has to be designed carefully, since it involves a number of different component technologies in terms of materials, process temperatures and equipment. Components may have disparate geometrical and mechanical properties as well as different endurance characteristics for process temperatures, time and excursions. The order in which components are integrated onto the system foils and the system foils to each other depends on machine capability and optimization of electrical-testing sequences.

Parallel processing and modularizing of process flow can provide considerable advantages in terms of throughput and yield, while integration of components sensitive to temperature should occur further down in the process chain to minimize exposure to increased temperatures. Homogeneous integration of passive components should be utilized wherever possible, and where such integration is not possible (e.g. quartz timers), the layout and process chain have to be adapted accordingly. Mounting all similar SMD components on only one side of the foil as the last processing step can definitely ease the mounting process, although it does require a final curing step.

6.3   Reliability

The reliability of the System-in-Foil technology still has to be proven — as in conventional electronic packaging, reliability is governed by the mismatch of thermal, mechanical and chemical properties of the involved components, substrates and interconnections. Research on main failure mechanisms is limited, disclosure of which will enhance further optimization of materials, processes and design. Reliability requirements for the system are predominantly defined by the application. Certain tests such as temperature cycling and temperature/humidity storage are common for consumer and automotive electronics, and the conditions are well defined in industrywide standards, e.g. AEC-Q100. An overview of research on the reliability of materials and processes is given in this section, and aspects of mechanical flexibility are also addressed.

6.3.1   Hygrothermal and thermal stress

For all adhesive types, mechanical properties as well as the adhesion of polymers are strong functions of temperature and moisture, especially above the glass transition temperature (Jagt, 1998). Since a conductive adhesive joint does not form a metallurgical joint like solder materials do, but rather forms a nonpermanent pressure contact,

the contact pressure provided by the polymer matrix is crucial for joint reliability: any environmental influence which decreases the contact pressure increases the contact resistance. The polymer matrix undergoes viscoelastic relaxation and creep deformation under thermal stress. Moisture ingress causes swelling of the matrix and also reduces the bulk mechanical and the adhesion strength (Caers, de Vries, Zhao, & Wong, 2003; Frisk, Lahokallio, Mostofizadeh, Kiilunen, & Saarinen, 2012; Li & Wong, 2006). Teh et al. (2004) report the effect of moisture on flip chip packages on FR4. Swelling of the NCA leads to bowing of the assembly, causing tension in the central region of the die and compression at the edges. This results in delamination between NCA and the die, spreading from the centre to the edges, enhanced by the loss of adhesion strength. The results are supported by numerical analysis.

For high-temperature storage and temperature cycling tests, the CTE mismatch in the assembly is the most critical parameter, resulting in high stress in the assembly that might lead to interfacial delamination. In the case of a flip chip assembly with ACA, a combination of low CTE and high modulus will reduce the thermally induced shear strain (Li, Lu, &Wong, 2010b). For ICAs, moisture ingress and the resulting swelling of the polymer matrix may lead to a loss in contact pressure between the particles resulting in a higher constriction resistance (Holm, 1967). Additionally, moisture-induced delamination at the interfaces results in increased contact resistance (Frisk et al., 2012). Moisture and thermal stress can induce cracks mostly at the adhesive interfaces and accelerate crack propagation in the bulk. Once cracks are induced, they propagate along the interface or through the bulk, leading in the worst case to an open circuit (Liu et al., 2011). The sensibility to moisture and temperature of the conductive joint is strongly influenced by the degree of curing. As an example, incomplete curing results in a strong increase of resistance under moisture loading due to higher moisture uptake (Liu et al., 2011; Teh et al., 2004).

Besides ageing the polymer matrix, moisture also affects metallic parts of the joint, such as bumps, conductive tracks or conductive particles in ICA/ACA − this can lead to an increase in contact resistance, such as that of a flip chip package (Caers et al., 2003). The effect of moisture gets even more pronounced due to galvanic corrosion and oxidation if nonnoble metallization is involved. If noble and nonnoble materials are combined in a joint (e.g. a silver-filled epoxy and a Ni substrate metallization), the combination acts as an electrochemical cell triggering galvanic corrosion. In this process, the nonnoble metal acts as the anode, becomes oxidized and forms metal ions (M^+). The noble metal acts as cathode and forms hydroxide (OH^-) together with the free electrons and oxygen and water from the environment. This hydroxide reacts to form a layer of metal hydroxide or metal oxide at the interface (Frisk et al., 2012; Liu et al., 2011; Lu, Tong, & Wong, 1999). If silver is used in a humid environment, electromigration can also occur (Li & Wong, 2006).

Substrate material and metallization also play an important role on the reliability of electrical interconnections formed by adhesives. For a reliable joint, the adhesive must simultaneously form a bond to the polymer substrate and the existing metallization, e.g. PI, PEN, PET, Ag, Cu, Au, etc. The bond strength
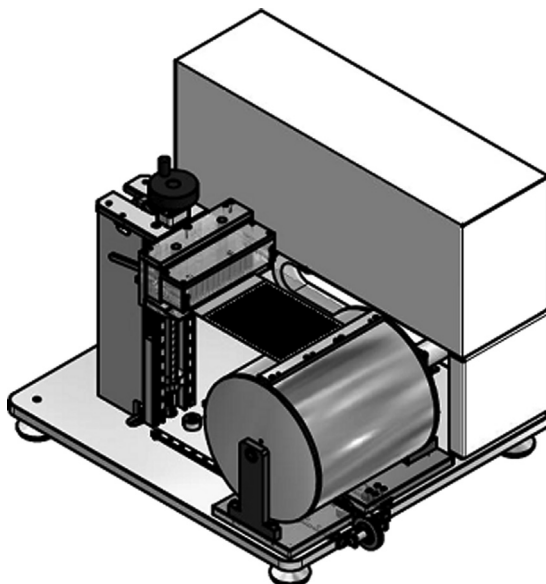
Figure 6.9 Schematic of a bending test device for a System-in-Foil.

can be influenced by the material combination, the surface roughness and/or the substrate pretreatment; e.g. heating, wet chemical cleaning, plasma treatment, silane treatment or mechanical surface treatments such as grit blasting (Gomatam & Sancaktar, 2005).

6.3.2   Reliability under bending stress

Su et al. and Constable et al. investigated the behaviour of electrically conductive adhesives under bending. In a four-point bending setup and a micromechanical tester they observed that the relative movement of metallic filler particles leads to wearing out of the contact area, causing an increase in constriction resistance (Constable, Kache, Teichmann, Muhle, & Gaynes, 1999; Su & Qu, 2008). Mo et al. investigated the influence of shear stress on the electrical properties of an ICA joint (Mo et al., 2002). The increase in the resistance of the joint in shear stress and low-cycle fatigue tests was explained by the initiation of microcracks as well as abrasion of the contact surface between the filler particles diminishing the effective contact area and resulting in a larger relative movement between filler particles.

The mechanical flexibility of a System-in-Foil depends not only on the behaviour of materials, but also on that of the components under mechanical bending. A bending test device combined with electrical measurements (Figure 6.9) (Project Interflex) can monitor the change in electrical resistance during bending (Project Interflex). The components are integrated onto a foil with a test circuit. One end of the foil is fixed and contacted by the measurement pins while the other end with the assembled
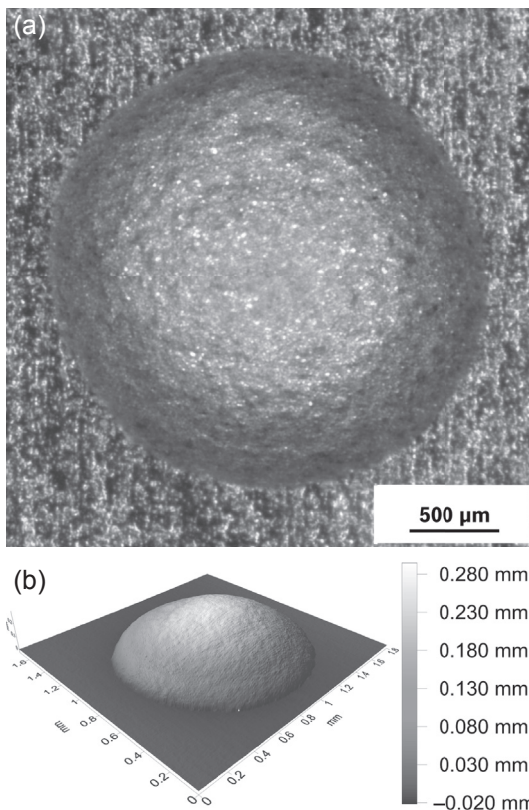
Figure 6.10 Views of boltlike via-filling. (a) Microscopic image; and (b) 3-D topography measured by white-light profilometry.

component is rolled onto a drum. The synchronized rotation and horizontal movement of the drum towards the measurement pins avoids stretching of the foil while enabling real time electrical resistance measurements (Figure 6.10). The bending radius is defined by that of the drum and can be varied between 10 and 100 mm.

To study the reliability of ICAs as interconnection material for the 3-D integration of foils and foil-components, a test layout is designed and fabricated with printed circuit foils which are laminated to each other and have a mechanically drilled blind-hole via on one side, which is filled with ICA to provide the electrical contact between the top and the bottom foil.

The diameter and the depth of blind-hole vias are 750 μm and 100 μm, respectively. The jetted via-fillings have a boltlike shape with an average diameter of 1.3 mm and average height of 230 μm; Figure 6.10 shows a typical via-filling. Figure 6.11 shows the change in resistance, measured with the four-point probe method, with nine different via-fillings as a function of bending cycle. The initial resistance varies between 60 and 120 mOhm in the flat state. Values occurring in the flat state are more reliable than those that occur in the bent state, due to cracks that develop in the conducting tracks (compare Figures 6.12(a) and (c)). The resistance change of Via-3 is shown on a smaller scale in
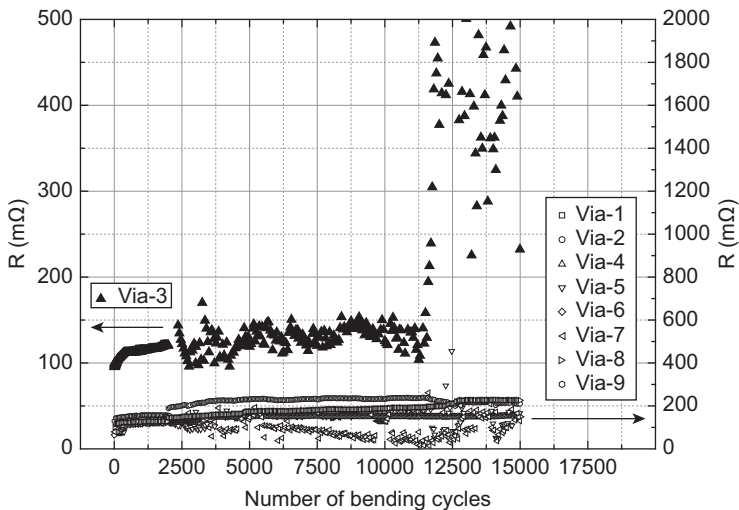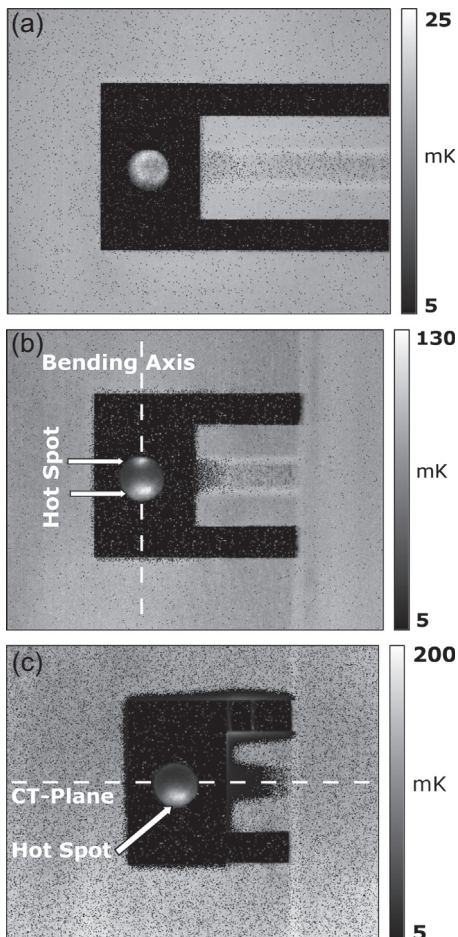
Figure 6.11 Electrical resistance change of nine different via-fillings as a function of number of bending cycles.

Figure 6.11 for brevity, and discussed in more detail, together with lock-in thermography (LIT) images. In this method, the sample is excited periodically by a current and a synchronized measurement of the temperature rise due to joule heating is carried out using an infrared camera. A lock-in amplifier is used to increase the signal-to-noise ratio for a better spatial resolution of temperature. Figure 6.12 shows the LIT images at different stages during the experiment.

In the initial state, a homogenous temperature distribution within the via-filling (Figure 6.12(a)) is observed with a maximum relative temperature increase of 25 mK. After 2000 bending cycles, during which electrical resistance increases by 30%, an inhomogeneous temperature distribution becomes obvious (Figure 6.12(b)). Two localized hot spots emerge (with a temperature rise of 130 mK), while the rest of the via-filling remains cold, indicating a localized current flow. The hot spots are located along the bending axis as shown by the inset, pointing to lower mechanical stresses in these areas. With continued bending, the resistance values begin to increase at a stable rate until an abrupt increase in excess of approximately 11,500 cycles, denoting unstable contact behaviour. A LIT image at 15,000 bending cycles (Figure 6.12(c)) shows a single remaining contact spot. Further analysis with computer tomography along the plane intersecting the hot spot (Figure 6.13) indicates that the rest of the via-filling has delaminated from the metal surface on the top foil.

In addition to the substrates and interconnections, the components also have to withstand the bending stress and maintain their characteristics. For example, foil-based batteries also have to provide full capacity under bending (Figure 6.14). Bending is especially challenging for ICs because silicon is used as a base material, and it is rather brittle and only behaves flexibly when thinned down to 50 μm or less (Endler et al., 2012). Due

Figure 6.12 Lock-in thermography images of Via-3 at different stages. (a) Initial state; (b) after 2000 bending cycles; and (c) after 15,000 bending cycles.

to the different processing steps in the fabrication of thin chips, such as grinding, polishing, etching, sawing and cutting, silicon is under high residual stress. This stress can lead to failure while bending because of induced microcracks within the chip. A detailed analysis and simulation of the mechanical reliability of thin chips under uniaxial bending stress can be found in the literature (Hoang, Endler, & Harendt, 2011; Schoenfelder, Bagdahn, & Petzold, 2011). An example of a bent 20 μm thick Si-Chip placed on a PI substrate is shown in Figure 6.15.

6.3.3 Finite element method (FEM) simulation of flip chip on polyimide

To better understand the NCA-flip chip process and the failure mechanisms, finite element analysis (FEA) is a powerful method. Stresses due to bending stress
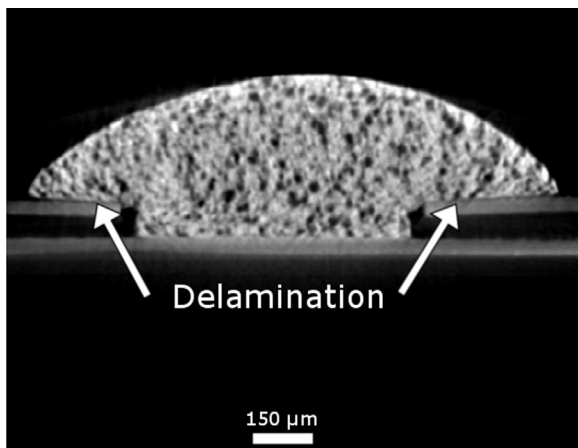
Figure 6.13 Computer tomography image of Via-3 after 15,000 bending cycles.

(40 mm diameter) and temperature cycling (−40 through +150 °C) are simulated and compared (Seventh Framework Programme).

Compressive stress develops in the bumps due to the curing shrinkage of the NCA exerting contact pressure between the pads. This pressure is necessary to establish the electrical contact between the chip and substrate, and therefore should not decrease during bending or temperature cycling. The simulation shows that the stress in the bumps due to the flip chip process is much higher than any additional stress which occurs due to bending or temperature cycling.

A potentially critical aspect for bump reliability is that the bumps slide on the pads because there is no metallurgical bonding. For the bending test, sliding is

Figure 6.14 Foil-based thin-film battery (10×10 mm^2) bent to 6.5 mm bending radius.
Source: Ref. Seventh Framework Programme.
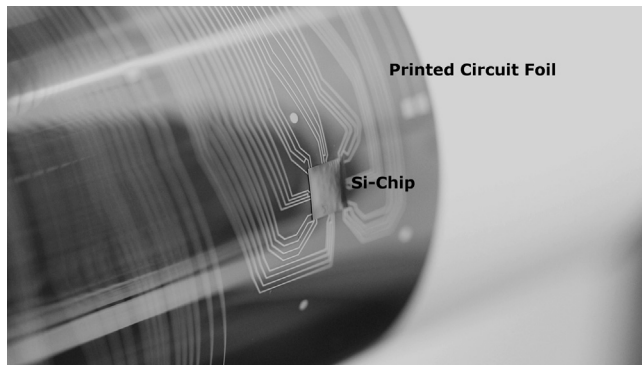
Figure 6.15 20 µm thick Si-chip (5×5 mm^2) mounted on a 50 µm polyimide (PI) printed circuit foil in a nonconductive adhesive (NCA) flip chip process and bent to 30 mm bending radius.

caused by different mechanics, namely the respective bending properties of die and substrate. Since the chip is much stiffer than the substrate, it cannot be bent as easily as the foil, and therefore the contact pressure between the bumps and the pads decrease. During temperature cycling, the bumps can slide on the pads due to softening and hardening of the NCA, which reduces and increases the contact pressure periodically. Those effects are not critical for contact resistance if they occur once, but contacts may wear out if cyclic tests are carried out. In both cases, another critical parameter is the warpage of the die along the bump, which causes the risk of die fracture. Figure 6.16 shows a comparison of the FEA for bending and temperature cycling. It can be obviously seen, that in both analyses the main stress occurs in the bump row with 4.5 MPa for thermal cycling and 3.75 MPa for bending. In the case of the bending analysis, it is clearly visible that only the bump row parallel to the bending axis is affected, while for temperature cycling nearly all bumps are affected in the same way.

6.4 Summary and future trends

Foil-based systems with thin/ultrathin components such as sensors, power harvesting and storage, in addition to ICs and antennas, provide superior packaging and functional density. The resulting System-in-Foil with the additional advantage of mechanical flexibility will offer the possibility of integration of intelligence and connectivity into everyday objects contributing to decentralization of data collection and processing. Not only components, but electrical interconnections as well, should be able to withstand and not limit the flexible nature of the system. The mechanical and electrical integration of a variety of components with different geometrical and physical properties into one system requires the combination of a number of materials and processes in a well-designed process flow.

(a)

(b)
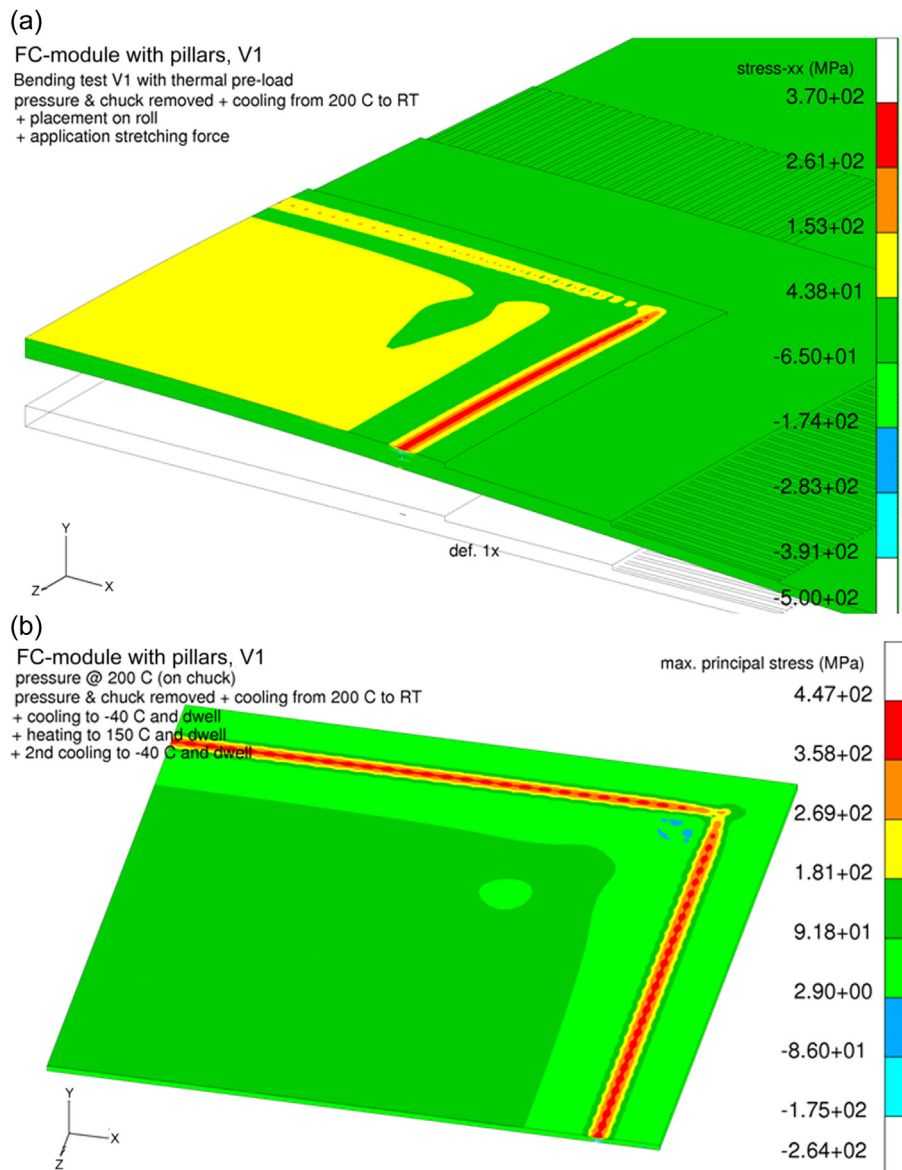
Figure 6.16 (a) Finite element analysis (FEA) of a flip chip module mounted on polyimide (PI) and bent to 20 mm bending radius; (b) FEA of the same flip chip module after processing at 240 °C and temperature cycled between −40 °C and 150 °C. Can be seen in Plate II (see colour section between pages 224 and 225).

While integration relies on available polymer materials, handling of thin/ultra-thin components plays a key role. The processes differ from the conventional soldering technology, particularly in terms of process temperature, which can be realized well below 150 °C. The technology can be related to printed electronics in terms of used materials and technologies. Although an industrywide standard for processes and reliability testing does not exist for these technologies, a standardization effort within the IEC has recently been initiated under TC-119. This is an important step in defining mainstream technologies and a supply chain providing technical solutions for new applications, providing conformable systems with a highly functional density.

Acknowledgements

References

AEC-Q100. http://www.aecouncil.com/AECDocuments.html Accessed 30.05.14.

Angelopoulos, E. A., & Kaiser, A. (2011). Epitaxial growth and selective etching techniques. In J. Burghartz (Ed.), *Ultra-thin chip technology and applications* (pp. 53−60). New York, NY: Springer New York.

Bock, K., Scherbaum, S., Yacoub-George, E., & Landesberger, C. (2008). Selective one-step plasma patterning process for fluidic self-assembly of silicon chips. In *Electronic components and technology conference, 2008. IEEE 58th* (pp. 1099−1104).

Burghartz, J. (Ed.). (2011). *Ultra-thin chip technology and applications*. New York, NY: Springer New York.

Caers, J. F., de Vries, J., Zhao, X., & Wong, E. (2003). Some characteristics of anisotropic conductive and non-conductive adhesive flip chip on flex interconnections. *Journal of Semiconductor Technology and Science, 3*, 122−131.

Cheng, I.-C., & Wagner, S. (2009). Overview of flexible electronics technology. In W. S. Wong, & A. Salleo (Eds.), *Electronic materials: science & technology* (vol. 11, pp. 1−28). US: Boston, MA: Springer.

Chiang, W. K., Chan, Y. C., Ralph, B., & Holland, A. (2006). Processability and reliability of nonconductive adhesives (NCAs) in fine-pitch chip-on-flex applications. *Journal of Electronic Materials, 35*(3), 443−452.

Constable, J., Kache, T., Teichmann, H., Muhle, S., & Gaynes, M. (1999). Continuous electrical resistance monitoring, pull strength, and fatigue life of isotropically conductive adhesive joints. *Components and Packaging Technologies, IEEE Transactions on, 22*(2), 191−199.

Dietzel, A., Brand, J., Vanfleteren, J., Christiaens, W., Bosman, E., & Baets, J. (2011). System-in-Foil technology. In J. Burghartz (Ed.), *Ultra-thin chip technology and applications* (pp. 141−157). New York, NY: Springer New York.

Endler, S., Angelopoulos, E. A., Ferwana, S., Harendt, C., Hassan, M.-U., & Burghartz, J. N. (2012). Ultradünne chips in flexibler elektronik. *PLUS, 5*, 1142−1148.

Frisk, L., Lahokallio, S., Mostofizadeh, M., Kiilunen, J., & Saarinen, K. (2012). Reliability of isotropic electrically conductive adhesives under condensing humidity testing. In *Electronics packaging technology conference (EPTC), 2012 IEEE 14th* (pp. 174−179).

German Patent No. DE102011004383A1. (2012).

Gilleo, K. (1995). Assembly with conductive adhesives. *Soldering & Surface Mount Technology, 7*(1), 12−17.

Gomatam, R. R., & Sancaktar, E. (2005). Effects of various adherend surface treatments on fatigue behavior of joints bonded with a silver-filled electronically conductive adhesive. *Journal of Adhesion Science and Technology, 19*(8), 659−678.

Hoang, T., Endler, S., & Harendt, C. (2011). Structure impaired mechanical stability of ultra-thin chips. In J. Burghartz (Ed.), *Ultra-thin chip technology and applications* (pp. 219−232). New York, NY: Springer New York.

Holm, R. (1967). *Electric contact*. New York, NY, USA: Springer Verlag. pp. 232−265.

International Technology Roadmap for Semiconductors. Update − Overview. www.itrs.net Accessed 30.05.14.

Jagt, J. (1998). Reliability of electrically conductive adhesive joints for surface mount applications: a summary of the state of the art. *Components, Packaging, and Manufacturing Technology, Part A, IEEE Transactions on, 21*(2), 215−225.

Kim, S.-C., & Kim, Y.-H. (2013). Review paper: flip chip bonding with anisotropic conductive film (ACF) and nonconductive adhesive (NCA). *Current Applied Physics, 13*, S14−S25.

King, B., Renn, M. Aerosoljet® direct write printing for mil-aero electronic applications. http://www.optomec.com/whitepapers/ Accessed 30.03.14.

Klosterman, D., Li, L., & Morris, J. (1998). Materials characterization, conduction development, and curing effects on reliability of isotropically conductive adhesives. *Components, Packaging, and Manufacturing Technology, Part A, IEEE Transactions on, 21*(1), 23−31.

Kugler, A., Koyuncu, M., Zimmermann, A., & Kostelnik, J. (2011). Chip embedding in laminates. In J. Burghartz (Ed.), *Ultra-thin chip technology and applications* (pp. 159−165). New York, NY: Springer New York.

Kuran, E. E., & Tichem, M. (2013). Magnetic self-assembly of ultra-thin chips to polymer foils. *Automation Science and Engineering, IEEE Transactions on, 10*(3), 536−544.

Li, Y., Moon, K.-S., & Wong, C. P. (2005). Electronics without Lead. *Science, 308*(5727), 1419−1420.

Li, Y., Lu, D., & Wong, C. P. (2010a). Non-conductive Adhesives/Films (NCA/NCF). In D. Lu, C. Wong, & Yi (Eds.), *Electrical conductive adhesives with nanotechnologies* (1st ed.). (pp. 279−301). s.l: Springer-Verlag.

Li, Y., Lu, D., & Wong, C. P. (2010b). Anisotropically conductive Adhesives/Films (ACA/ACF). In D. Lu, C. Wong, & Yi (Eds.), *Electrical conductive adhesives with nanotechnologies* (1st ed.). (pp. 227−278). s.l: Springer-Verlag.

Li, Y., Lu, D., & Wong, C. P. (2010c). Isotropically conductive adhesives (ICAs). In D. Lu, C. Wong, & Yi (Eds.), *Electrical conductive adhesives with nanotechnologies* (1st ed.). (pp. 121−125). Springer-Verlag.

Li, Y., & Wong, C. (2006). Recent advances of conductive adhesives as a lead-free alternative in electronic packaging: materials, processing, reliability and applications. *Materials Science and Engineering: R: Reports, 51*(1−3), 1−35.

Liu, J., Salmela, O., Särkkä, J., Morris, J. E., Tegehall, P.-E., & Andersson, C. (2011). Conductive adhesive joint reliability. In J. Liu, O. Salmela, J. Sarkka, J. E. Morris, P.-E. Tegehall, & C. Andersson (Eds.), *Reliability of microtechnology: Interconnects,*

devices and systems (1st ed.). (pp. 71−98). New York, NY: Springer Science+Business Media LLC.

Lu, D., Tong, Q., & Wong, C. (1999). Mechanisms underlying the unstable contact resistance of conductive adhesives. *Electronics Packaging Manufacturing, IEEE Transactions on, 22*(3), 228−232.

MacDonald, W. A., Looney, M. K., MacKerron, D., Eveson, R., Adam, R., Hashimoto, K., et al. (2007). Latest advances in substrates for flexible electronics. *Journal of the Society for Information Display, 15*(12), 1075.

Mo, Z., Wang, X., Wang, T., Li, S., Lai, Z., & Liu, J. (2002). Electrical characterization of isotropic conductive adhesive under mechanical loading. *Journal of Electronic Materials, 31*(9), 916−920.

Nathan, A., Ahnood, A., Cole, M. T., Sungsik, L., Suzuki, Y., Hiralal, P., et al. (2012). Flexible electronics: the next ubiquitous platform. *Proceedings of the IEEE, 100*, 1486−1517 (Special Centennial Issue).

Project Interflex, Seventh Framework Programme, European Comission, Contract No. 247710. www.project-interflex.eu (accessed 30.05.14).

Project Pronto Ultimum, Microtec Südwest Cluster,Federal Ministry of Education and Research, Contract No. 16SV5134. http://www.pronto-ultimum.de/ (accessed May 30, 2014).

Schoenfelder, S., Bagdahn, J., & Petzold, M. (2011). Mechanical characterisation and modelling of thin chips. In J. Burghartz (Ed.), *Ultra-thin chip technology and applications* (pp. 195−218). New York, NY: Springer New York.

Stoukatch, S., Laurent, P., Dricot, S., Axisa, F., Seronveaux, L., Vandormael, D., et al. (2012). Evaluation of aerosol jet printing (AJP) technology for electronic packaging and inter-connect technique. In *Electronic system-integration technology conference (ESTC), 2012 4th* (pp. 1−5). IEEE.

Su, B., & Qu, J. (2008). Fatigue behavior of electrically conductive adhesives. *Journal of Adhesion Science and Technology, 22*(8−9), 927−946.

Teh, L., Anto, E., Wong, C., Mhaisalkar, S., Wong, E., Teo, P., et al. (2004). Development and reliability of non-conductive adhesive flip-chip packages. *Thin Solid Films, 462−463*, 446−453.

More-than-Moore: White paper. www.itrs.net Accessed 30.05.14.

Wolf, J., Berschauer, K., Kugler, A., Lorenz, E., Gneiting, T., Harendt, C., & Yu, Z. (2014). In ECWC13; VDE Verlag (Ed.), *Ultra-thin silicon chips in flexible microsystems*. Berlin − Offenbach: VDE VERLAG.

Yim, M. J., & Paik, K. W. (2006). Recent advances on anisotropic conductive adhesives (ACAs) for flat panel displays and semiconductor packaging applications. *International Journal of Adhesion and Adhesives, 26*(5), 304−313.

This page intentionally left blank

Roll-to-roll printing and coating techniques for manufacturing large-area flexible organic electronics

7

B. Roth, R.R. Søndergaard, F.C. Krebs
Technical University of Denmark, Roskilde, Denmark

7.1   Introduction

The need for electronics that can be processed at low cost and very high speeds has created the potential for new technologies based on organic materials to emerge, as they can be developed using solution processing. Organic photovoltaics (OPVs), organic thin film transistors (OTFTs), organic light-emitting diodes (OLEDs) and electrochromic devices (ECs) are all examples of such technologies. Most of them have now reached a maturity stage at the laboratory level, where upscaling and faster processing becomes the next development phase. In that context, roll-to-roll (R2R) processing on flexible substrates has always been the final goal for such upscaling, as it represents the ultimate combination of fast processing and cheap substrates. So far, only a few examples of actual transfer to R2R processing have been carried out, and this chapter aims at introducing some of the different R2R printing and coating techniques that have so far been employed for the preparation of organic electronics.

   Going from small glass substrates to large-area R2R processing is not as straightforward as one would think. Some of the most common techniques used in the preparation of organic electronics on a laboratory scale, such as spin-coating and metal evaporation, are not compatible with high-throughput R2R production. R2R metal evaporation can be carried out in principle, but it requires a vacuum, which is time-consuming and comes with a high cost that does not comply with the philosophy of low-cost technologies. Consequently, silver is presently the only real candidate for metal electrode deposition by R2R, as silver inks are uniquely available commercially in forms that can be both coated and printed. Another issue that needs consideration in the long term upscaling process is the environmental impact of production of large volumes. In that respect the solvents generally used for processing of small-scale electronics constitutes a serious problem in the transfer, as they are generally toxic, carcinogenic or otherwise harmful. It is of course possible to perform R2R processing from such solvents. However, when envisaging for example the OPV technology in relation to energy production and the sheer volumes of solvents needed for such, it is evident that only water or other benign solvents can be used.

Doing otherwise will simply be too expensive if precautions has to be taken towards ensuring a healthy working environment and avoiding damage to the surrounding ecosystems.

Such changes in processing methods, materials and processing solvents evidently have their consequences and transfer to large area basically requires re-optimization of every parameter taken into account in preparation of a device — parameters that took years to refine in the laboratory. Compared to small-scale devices, little focus has been put on actual large-scale processing of organic electronics, and experience with, and understanding of, R2R processing in this context is limited to very few people — especially when processing at high speeds. A clear indication of the difficulty of such a transfer is observed from the current status of large-area OPV technology, probably the most mature of the technologies mentioned in this chapter with respect to R2R progress: among all the high-performing low-band-gap polymers that have proven their worth in small-scale devices, only a tiny fraction have outperformed the old P3HT polymer when it comes to larger areas - but it is not for lack of trying.

Because organic electronics can be processed from solution, there are a number of existing R2R methods suitable for processing them on a larger scale. Roughly two kinds of deposition methods have proven useful in the preparation of organic electronics, noncontact coating techniques and contact printing techniques (except for ink-jet printing). Printing allows two-dimensional patterning, whereas coating at best allows for one-dimensional patterning and is mostly used for layer deposition over large areas.

The following chapter is a nonexhaustive review of roll-to-roll deposition techniques that are of interest for high-throughput, cheap preparation of flexible electronics. The chapter will also include references to R2R-compatible reports on organic electronics in order to broaden the perspective.

7.2 Printing techniques

Roll-to-roll printing techniques are all contact methods, with the exception of ink-jet printing where the name may be misleading, as it is not a 'true' printing technique. Generally, printing techniques involve a pattern transfer from a solid carrier onto a substrate by physical contact resulting in a two-dimensional motif.

7.2.1 Screen printing

In screen printing the ink is pushed through the open area of an otherwise solid mesh with the help of a squeegee. high-viscosity inks with thixotropic (shear thinning) properties are required for this kind of printing, as low-viscosity inks will simply run through the screen by gravity. The printed pattern is defined by the screen's open area and thickness as well as ink viscosity. The wet-layer thickness is therefore usually high ($10-500$ µm). Two existing screen-printing methods are suitable for R2R: flatbed screen printing and rotary screen printing. Illustrations of the two techniques are shown in Figure 7.1 and Figure 7.2.

Flat bed screen printing
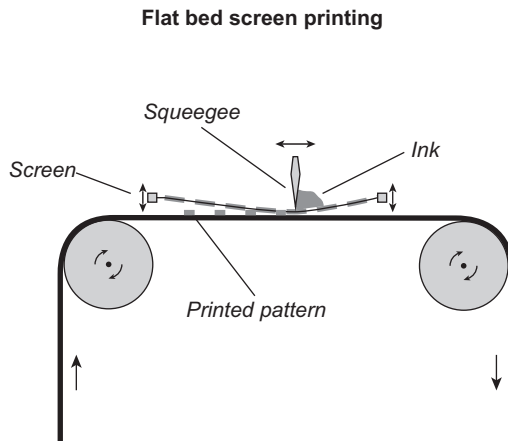
Figure 7.1 Illustration of the flatbed screen-printing principle.

Rotary screen printing
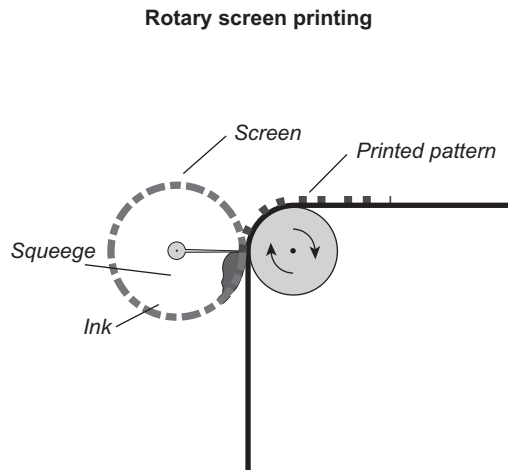
Figure 7.2 Illustration of the rotary screen-printing principle.

Albeit flatbed screen printing is a stepwise process, it has been successfully adapted to R2R. First, the mesh is pressed into contact with the web. Then a squeegee is swept across the screen, forcing the ink through the mesh's open area and transferring the printing pattern on to the substrate. Finally, the screen is raised and the web is moved forward — and so on. This method allows the printing on large areas up to 10 m². However, the ink is left in contact with the ambient and factors such as solvent evaporation can affect the printing process.

In the case of rotary screen printing, the screen is bent into a cylinder shape. This cylinder is rotating at the same rate as the web, making rotary screen printing a fully R2R process that allows speeds over 100 m/min opposed to 0−35 m/min for flatbed screen printing. The ink is situated inside the cylinder and is therefore less exposed to the surroundings. The squeegee (also inside the screen) is placed in a stationary

position and forces the ink through the mesh as the screen rotates, resulting in a continuous printing of the pattern at each cylinder rotation.

Although rotary screen printing gives better edge definition/resolution, the screen is significantly more expensive than the flatbed analogue and more difficult to clean because of its limited access. Setting up and starting a multilayer screen print process is also more challenging in the rotary case, but more reliable once running, making rotary screen printing more suitable for large-scale processes. Flatbed screen printing, on the other hand, is the go-to technique for small-scale lab experiments.

For OPVs, screen printing has so far mainly been used to print electrodes (Amb et al., 2012; Angmo, Hösel, & Krebs, 2012; Bundgaard, Hagemann, Manceau, Jørgensen, & Krebs, 2010; Dam & Krebs, 2012; Galagan, Rubingh, et al., 2011; Helgesen et al., 2012; Krebs, Fyenbo, & Jørgensen, 2010; Krebs et al., 2011; Krebs, Gevorgyan, & Alstrup, 2009; Krebs, Tromholt, & Jørgensen, 2010; Manceau, Angmo, Jørgensen, & Krebs, 2011; Yu et al., 2012) because it gives a thick silver layer ensuring high conductivity (Figure 7.3 shows an example of flatbed-screen-printed silver back electrodes). Some cases where PEDOT:PSS (Espinosa et al., 2013; Hösel, Søndergaard, Jørgensen, & Krebs, 2013; Krebs, 2009; Krebs, Jørgensen, et al., 2009; Sommer-Larsen, Jørgensen, Søndergaard, Hösel, & Krebs, 2013) (see rotary screen printing of PEDOT:PSS in Figure 7.4) and/or the active layer (Krebs, Jørgensen, et al., 2009; Zhang, Chae, & Cho, 2009) were printed using screen printing, have also been reported.

Screen printing has also been used to print electrodes for OLEDs and OTFTs. Ryu et al. have prepared an active matrix organic light-emitting diode (AMOLED) using screen printing (Ryu, Kim, Jeong, & Song, 2013). In the AMOLED, they prepared the OTFT's silver gate electrodes, as well as the scan bus lines of the panel, by screen printing silver nanoparticle ink on the full surface of the device followed by photolithography and etching to obtain the desired pattern.

The technology has also been used to print the emitting layer in OLEDs. Lee et al. screen-printed a green-emitting layer (Lee, Choi, Chae, Chung, & Cho, 2008) based on

Figure 7.3 Flatbed screen-printing of silver top electrodes: The squeegee is sweeping across the screen. The printed electrodes can be observed in the lower left part of the picture.
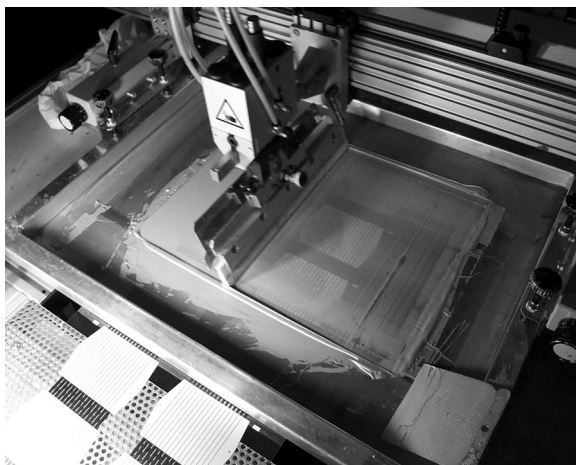
Figure 7.4 Rotary screen-printing of PEDOT:PSS, the printing pattern is visible on the screen (top of the picture).

Ir(ppy)$_3$ (a widely used green emitter) mixed with poly(N-vinyl carbazole) (PVK) as polymer host, 2-(4-biphenylyl)-5-(4-*tert*-butylphenyl)-1,3,4-oxadiazole (PBD) as electron-transporting materials and N,N-Di(naphthalene-1-yl)-N,N-diphenyl-benzidine (α-NPD) as hole-transporting material. The screen-printed layers on indium tin oxide (ITO) glass substrate are shown in Figure 7.5.

Finally, Verilhac et al. have screen-printed a polytriarylamine as the P-channel semiconductor of OTFTs (Verilhac et al., 2010).

7.2.2 Flexoprinting

In flexoprinting, the contact and transfer of the ink is made between a soft printing-plate cylinder and the substrate. The cylinder is usually made of rubber or a photo-polymer, where the printing pattern stands in relief like a stamp (an example of a

Figure 7.5 Photograph showing the screen-printed green-emissive layer (the bright square – colours are not shown) on patterned ITO substrate for OLED preparation.
Reproduced from Lee et al. (2008) with the permission from Elsevier.
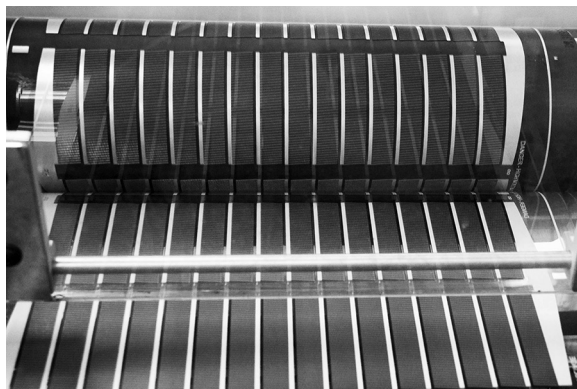
Figure 7.6 The printing cylinder with the relief carrying the ink (in this case a silver paste) during printing. The final printed pattern on the web can be observed in the bottom part of the picture.

patterned printing plate cylinder can be seen in the upper part of the picture in Figure 7.6). The cylinder shape ensures R2R compatibility. A ceramic anilox cylinder provides the inking of the printing cylinder through micro cavities embedded in its surface. The printed-layer thickness is directly linked to the volume of the cavities in the anilox roll in a process where ink is transferred through simple surface tension forces when the printing plate and the anilox are touching. The anilox cylinder itself is often supplied with ink by a fountain roller partially dipped in an ink bath. A doctor blade is used to doff off any excess ink on the anilox roll ensuring that only the cavities are filled with ink. It is also possible to use a chambered-doctor-blade system to avoid solvent evaporation. The process is illustrated in Figure 7.7.

Flexoprinting is quite new to the field of organic electronics, and only a few examples have been reported (Hübler et al., 2011; Krebs, Fyenbo, et al., 2010; Søndergaard, Hösel, Jørgensen, & Krebs, 2013; Yu et al., 2012). Søndergaard et al. have made ITO-free ECs by using flexoprinting to print a hexagonal silver grid on a flexible
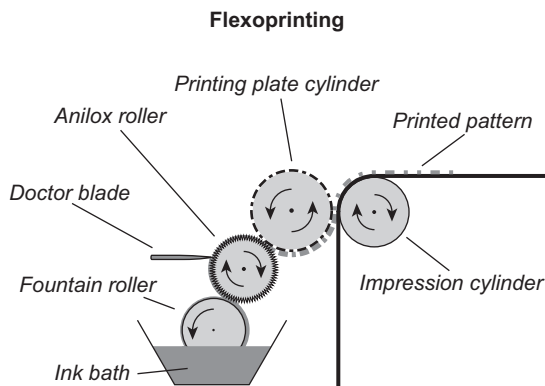
Flexoprinting

Figure 7.7 Illustration of the flexoprinting principle.

substrate (Søndergaard et al., 2013) and flexoprinted fine silver grids (<50 μm) has also proven suitable for replacement of ITO in OPVs (Yu et al., 2012). For OPVs, flexo-printing has furthermore been used to print PEDOT:PSS (Hübler et al., 2011) as well as to deposit a wetting agent on the active layer (Krebs, Fyenbo, et al., 2010) and for OTFTs it has been used to print an insulator and the gates (Huebler et al., 2007).

7.2.3   Gravure printing

Gravure printing is a widely used processing method often used to print large volumes of magazines and catalogues. Opposed to flexoprinting, the ink in gravure printing is transferred from carved micro cavities and not from a relief. These cavities, embedded in the printing cylinder, form the printing pattern. A second softer impression cylinder pushes the web against the primary printing cylinder and the ink is transferred from the cavities to the web through matching surface energies of the ink and substrate. The printing cylinder is partially immersed in an ink bath and similar to the anilox in flexo-printing a doctor blade is used to remove any excess ink from the printing cylinder leaving ink only in the cavities (operating principle is shown in Figure 7.8). As for flexoprinting it is also possible to use a chambered doctor blade. Gravure printing is highly dependent of ink viscosity, substrate speeds as well as the pressure applied by the impression roller and great care is therefore required in the choosing of process-ing conditions and ink formulation. However, the process is suitable for low-viscosity ink and high printing rates up to 15 m/s can be achieved.

Gravure printing has been used on several occasions to prepare OTFTs. Hambsch et al. printed 50.000 transistors using only gravure printing with a yield of 75% (Hambsch et al., 2010). Other reports include printing of the semiconductor layer of OTFTs (Huebler et al., 2007; Verilhac et al., 2010; Voigt et al., 2010; Vornbrock, Sung, Kang, Kitsomboonloha, & Subramanian, 2010), as well as silver gate electrodes (Voigt et al., 2010; Vornbrock et al., 2010) and insulators (Huebler et al., 2007; Voigt et al., 2010; Vornbrock et al., 2010). Use of gravure printing for OLEDs was also re-ported recently by Kopola, Tuomikoski, Suhonen, and Maaninen (2009) who prepared 30 cm^2 OLEDs on glass substrates using gravure to process both PEDOT:PSS and a
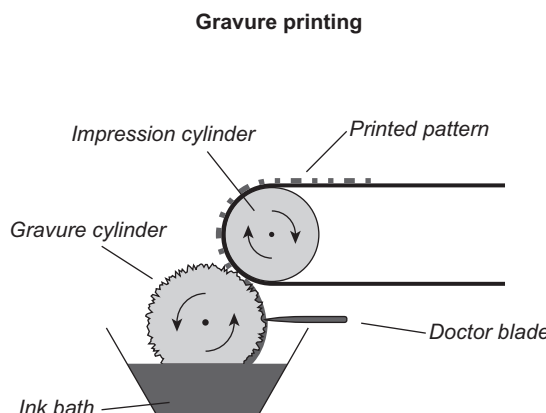
Gravure printing

Figure 7.8 Illustration of the gravure-printing principle.

Figure 7.9 Gravure-printed large-area OLED (active area 30 cm^2) with two printed organic layers (PEDOT and a blue-emitting layer — colour does not show).
Reproduced from Kopola et al. (2009) with the permission from Elsevier.

blue-emitting layer. In the final device (see Figure 7.9), these were sandwiched between ITO and a metallic cathode.

Until now, only a few cases employing gravure printing to prepare OPVs have been reported. Kopola et al. have on two occasions used gravure printing to prepare regular architecture devices. A desktop gravure printability tester (single sheets, not R2R) was used to deposit PEDOT:PSS and P3HT:PCBM for single cells (PCE: 2.8%, 0.19 cm^2) (Kopola et al., 2010) and the same printer was used for processing small modules of five cells in series (PCE: 1.9%, 9.6 cm^2) (Kopola et al., 2011). Other noteworthy examples are the printing of an OPV on paper reported by Hübler et al. (2011) and the use of an industrial gravure printer for OPV preparation by Yang et al. (2013). In the latter case, the top silver electrode was evaporated, whereas the hole-transporting layer (PEDOT:PSS), the electron-transporting layer (ZnO) and the active layer (P3HT: PCBM) were all printed with the gravure printer using ITO-coated polyethylene terephthalate (PET) as substrate. The modules composed of five cells in series (45 cm^2) yielded a PCE in the range 0.22−0.86%.

7.2.4   Ink-jet printing

As stated previously, contrary to traditional printing techniques, ink-jet printing does not transfer the printing pattern through contact. Ink-jet printing is a fully digital nonimpact method. The two-dimensional pattern is based on a pixelated drawing where each pixel is either left blank or receives an ink drop, and in special cases it is possible to work in 3D by printing multiple layers.

Ink-jet printing is advantageous because it is easy to change the printing pattern by computer, and no physical adjustment of the printing apparatus is required. Furthermore, as it is a noncontact technique it can be used to print on sensitive substrates or 3D structures. The main drawback lies within the ink formulation (density, surface tension, viscosity, boiling point, etc.), which needs to be adjusted to fit a number of parameters including nozzle size, printing surface and materials — such parameters make it more difficult to formulate an ink with only benign solvents. However, Lange, Schindler, Wegener, Fostiropoulos, and Janietz (2013) used ink jets to print a blend of

poly[9,9-dioctylfluorenyl-2,7-dyil-co-10,12-bis(thiophen-2-y)-3,6-dioxooctyl-11-thia-9,13-diaza-cyclopenta[b]triphenylene] (PFDTBTP) and PCBM as active layer in a solar cell using only nonchlorinated solvents.

Two kinds of ink-jet printing are commonly used: drop-on-demand and continuous.

In continuous ink-jet printing, a continuous jet of droplets is formed and is then electrostatically deviated to print on the desired pixels. Because only one nozzle is required, this type of ink-jet printing is very fast. However, the printing area is limited.

Three types of drop-on-demand ink-jet printing are generally available: piezoelectric, thermal and electrostatic. Piezoelectric ink-jet printing (illustrated in Figure 7.10) is the most commonly used, as it is suitable for the printing of most materials. A piezoelectric element is placed in the channel on top of the nozzle, and when a voltage is applied to this element it expands and ejects a droplet through the nozzle. Thermal ink-jet printing requires one of the ink compounds to have a low boiling point and the ejection of a droplet is carried out by momentarily heating the ink inside the nozzle. For electrostatic ink-jet printing, an electrostatic field is applied between the nozzle and an electrode drawing the free charges contained in the ink to the surface. Droplets are formed when the electrostatic forces exceed the surface tension. In order to comply with this technology the ink needs to be charged.

Commercially available ink-jet printers allow resolutions up to 600 DPI and speeds up to 75 m/min.

Ink-jet printing of silver gates and source/drain in OTFTs has been reported on several occasions (Chung, Kim, Kwon, Lee, & Hong, 2011; Lee, Lim, Park, Kim, & Kim, 2013; Tobjörk, Kaihovirta, Mäkelä, Pettersson, & Österbacka, 2008; Vornbrock et al., 2010), as has the printing of PEDOT:PSS as gate (Tobjörk et al., 2008). Chung et al. (2011) have shown that ink-jet printing is a promising technology

Ink-jet printing

Ink supply

Piezoelectric element

Printed pattern
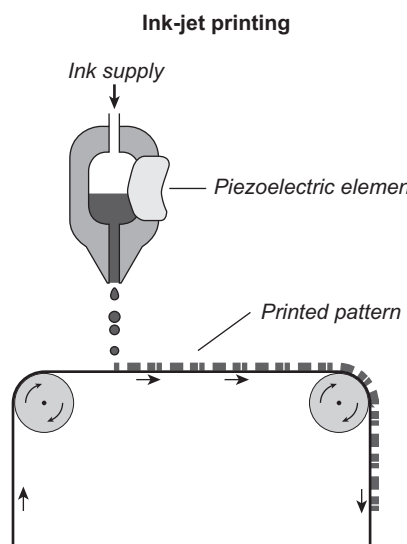
Figure 7.10 Schematic illustration of piezo-based drop-on-demand ink-jet printing.

for OTFT preparation, by making a fully ink-jet-printed inverter on a flexible polyarylate substrate. This inverter is made of two *p*-type OTFTs with silver gate, source/drain electrodes, poly-4-vinylphenol (PVP) as gate-dielectric layer and 6,13-bis (triisopropylsilylethynyl) (TIPS) pentacene as active semiconductor layer. The OTFTs yielded a mobility of 10.02 cm^2/(V·s), an on/off ratio of 10^4 and a threshold voltage of −1.2 V.

For OPVs, ink-jet printing has mostly been used to prepare small-scale devices on glass (0.03−1 cm^2) as well as to deposit PEDOT:PSS (Eom et al., 2009), P3HT: PCBM (Aernouts, Aleksandrov, Girotto, Genoe, & Poortmans, 2008; Hoth, Choulis, Schilinsky, & Brabec, 2007; Hoth, Schilinsky, Choulis, & Brabec, 2008) or both (Eom et al., 2010; Lange et al., 2010). In true R2R processing of OPVs, ink jets have also been used to deposit patterned silver front grid lines (Yu et al., 2012) as shown in Figure 7.11.

For OLEDs, ink jets have also been used to print the emissive layer (Kwon et al., 2012; Teichler et al., 2013), and recently Gorter et al. (2013) prepared small-molecule OLEDs on ITO-coated glass substrate (30 × 30 mm^2) using ink jets to print the emissive layer (Tris-(8-hydroxyquinoline)aluminium) (Alq3)), the hole-injection layer (PEDOT:PSS) and the hole transport layer (α-NPD).

7.2.5   Spray coating

Similar to ink-jet printing, spray coating is also a noncontact technique where the layer is deposited through a spurt of ink droplets. However, in this case the spray is random and there is no digital control of the deposited pattern. Spray coating is consequently by definition a zero-dimensional coating method. Masking can be used to deposit a two-dimensional pattern, but the edge definition is low, and recovery of the ink deposited on the mask can be tricky. Another option is to use a laser after spray coating to etch the desired pattern.

Figure 7.11 Example of a R2R ink-jet-printed silver grid.
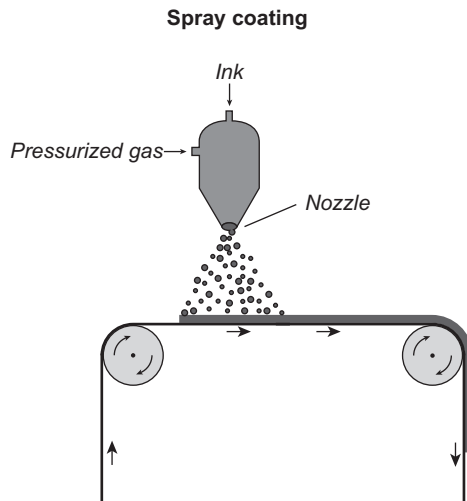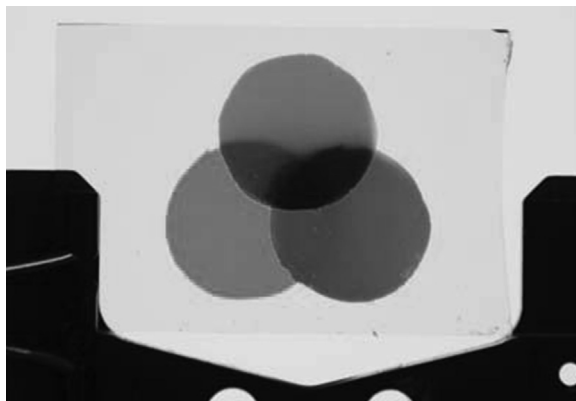
Spray coating

Figure 7.12 Illustration of spray coating.

In most spray coating apparatus the ink is atomized with a pressurized gas such as nitrogen (Yu et al., 2010) (this principle is illustrated in Figure 7.12), but ultrasonication (Steirer et al., 2009) with a directed carried gas, or electrospraying (Kim et al., 2012), is also possible. The droplet size is related to the ink viscosity, surface tension, density as well as the gas pressure and the nozzle shape. The droplets kinetic energy influence how they will spread upon impact on the substrate, and the deposited layer quality depends on numerous factors such as the length between the nozzle and the web's surface, coating speed, how many layers are coated, ink and surface energy of the ink and of the substrate.

Although spray coating is a fully R2R-compatible technique, it has not been used much because of the risk of contamination of the equipment by the ink mist. However, small lab-scale roll coaters have been developed (Dam & Krebs, 2012) and used successfully to spray-coat polymeric layers in ECs (Jensen, Dam, Reynolds, Dyer, & Krebs, 2012). Several reports using spray coating for the processing of ECs with a large range of colours can be found (Amb, Beaujuge, & Reynolds, 2010; Beaujuge et al., 2012; Beaujuge, Ellinger, & Reynolds, 2008; Mortimer, Graham, Grenier, & Reynolds, 2009; Reeves et al., 2004), but all are limited to small ITO-coated glass substrates (Figure 7.13). The use of spray coating to prepare small-scale OPVs has been reported for the active layer (Chen et al., 2010; Girotto, Rand, Genoe, & Heremans, 2009; Park et al., 2011), silver back electrodes (Girotto, Rand, Steudel, Genoe, & Heremans, 2009; Hau, Yip, Leong, & Jen, 2009), hole-transport layer and active layer (Girotto, Moia, Rand, & Heremans, 2011; Kang et al., 2012) and electron-transport, active and hole-transport layers (Lewis, Lafalce, Toglia, & Jiang, 2011). Some of the prepared OPVs yield similar performances to spin-coated devices, demonstrating the potential of this technique (Kang et al., 2012). The use of spray coating for OLED preparation is so far limited. One noticeable application was replacement of ITO as

Figure 7.13 Thin films of blue, red, and yellow polymers (colours do not show) ECs spray-cast onto ITO slides through circular shadow masks. Reproduced from Amb, Kerszulis, Thompson, Dyer, and Reynolds (2011) with permission from The Royal Society of Chemistry.

anode in a flexible OLEDs by a double-layer graphene/PEDOT:PSS where the PEDOT:PSS was spray coated (Wu, Li, Wu, & Guo, 2014).

7.3 Coating techniques

Coating techniques are generally noncontact techniques and are in most cases limited to deposition of a homogenous layer following the web length. Accordingly most coating techniques are one-dimensional. However, compared to printing techniques the layer thickness can in most cases be tightly controlled. Coating methods are also suitable for a broad range of viscosities and are less sensible with respect to surface wetting, as the ink is 'poured' onto the substrate compared to the surface-energy-dependent transfer involved in many printing techniques. Briefly, coating is achieved through a meniscus standing between the coating head and the substrate that is continuously fed with ink as the web moves.

7.3.1 *Knife coating*

Knife coating as a R2R technique is similar to doctor-blading on a laboratory scale. The layer is deposited at a stationary knife, in front of which an ink reservoir is continuously supplying the meniscus standing between the web and the blade, as shown in Figure 7.14. The web movement ensures the layer deposition as it passes the knife. The wet thickness is related to the gap size between the knife and the substrate and to some extent also to the web speed. As a rule of thumb the wet thickness is roughly half the gap size. Knife coating is suitable for deposition of homogeneous layers on large areas and can be carried out at high speed (>10 m/min). For OPVs, deposition of ZnO as a hole-blocking layer (Krebs, 2009), and PEDOT:PSS as an electron-blocking layer (Hoth et al., 2009) and active layer (Wengeler, Schmidt-Hansberg, Peters, Scharfer, & Schabel, 2011) have been reported. Knife coating has also been used on a small scale (4×4 cm^2) to coat organic layers (hole-transport
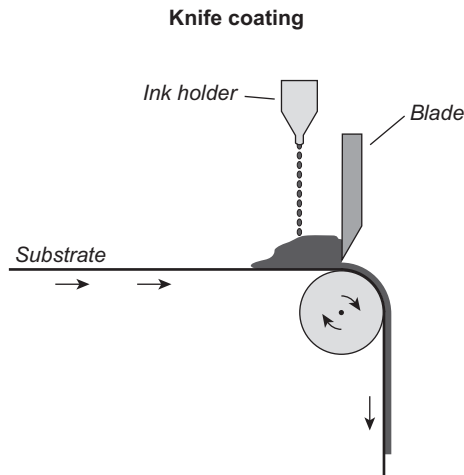
Knife coating

Figure 7.14 Illustration of Knife coating operating principle.

layer, emissive layer, electron-transport layer) in OLEDs (Chang et al., 2012). Chen et al. developed a multilayer blade-coating method that can be used for both polymers and small-molecule OLEDs (Chen et al., 2011) (see Figure 7.15).

7.3.2   Slot-die coating

In slot-die coating, the ink is pumped through a slot inside the coating head mounted close to the web. After formation of a meniscus, which is maintained by continuous pumping, the moving substrate leads to the deposition of a homogeneous layer along the web (illustrated in Figure 7.16). When fitted with a meniscus guide the coating
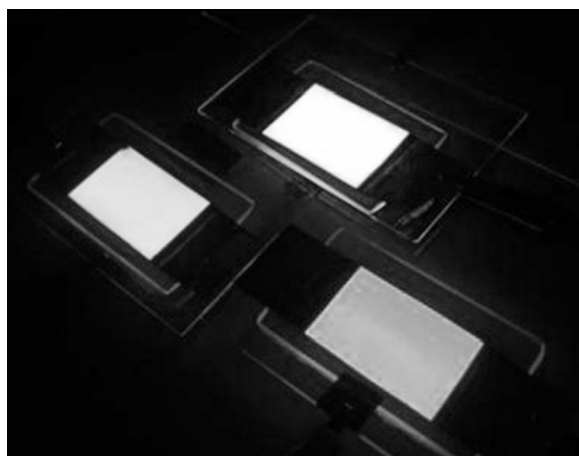
Figure 7.15 Large-area OLED made by the blade-only method. The active area is $2 \times 3 \text{ cm}^2$. Reproduced from Chen et al. (2011) with permission from AIP Publishing LLC.
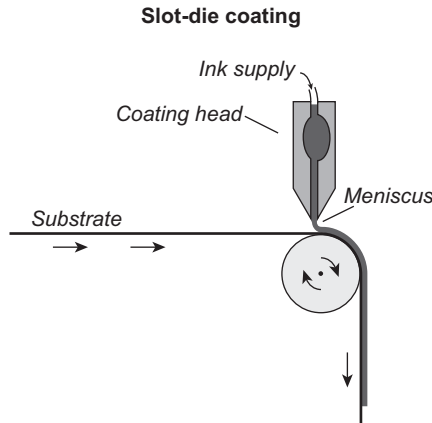
Slot-die coating

Figure 7.16 Illustration of slot-die coating.

head allows deposition of stripes. It is possible to regulate the wet-layer thickness precisely, as this is defined directly by the pumping rate, the web speed and the width of the coat. Slot-die coating is a powerful technique that allows for the simultaneous deposition of tightly grouped homogeneous stripes at speeds up to 100 m/min.

Wu, Kerk, and Wong (2013) used slot-die to coat an aqueous solution of PEDOT: PSS and silver nanowires on PET substrates, as a substitute for ITO as a transparent electrode. Within ECs, slot-die coating has also been used to deposit the active-polymer layer and the counter-polymer layer in ITO- and vacuum-free ECs (Søndergaard et al., 2013). As for OPVs, slot-die coating is by far the most widely used R2R processing technique and it has been used on numerous occasions to deposit hole-blocking layers, active layers and electron-blocking layers (Amb et al., 2012; Angmo et al., 2012; Blankenburg, Schultheis, Schache, Sensfuss, & Schrödner, 2009; Bundgaard et al., 2010; Dam & Krebs, 2012; Galagan, Vries, et al., 2011; Helgesen et al., 2012; Krebs, 2009; Krebs, Fyenbo, et al., 2010; Krebs et al., 2011; Krebs, Gevorgyan, et al., 2009; Krebs, Tromholt, et al., 2010; Larsen-Olsen, Machui, et al., 2012; Manceau et al., 2011; Søndergaard, Manceau, Jørgensen, & Krebs, 2012; Wengeler et al., 2011; Yu et al., 2012; Zimmermann, Schleiermacher, Niggemann, & Würfel, 2011). Similarly to knife coating, slot-die coating has been used to prepare OLEDs mainly through deposition of PEDOT:PSS, the emissive layer (see Figure 7.17) (Youn, Jeon, Shin, & Yang, 2012) and ZnO (Sandström, Dam, Krebs, & Edman, 2012).

7.4 Specialist coating techniques

7.4.1 Brush painting

As a layer-forming process, brush painting is probably the oldest; it is also one of the toughest to model, as brush painting is a blend of multiple techniques. The brush is soaked in the ink, which is then retained in the brush hairs by surface tension.
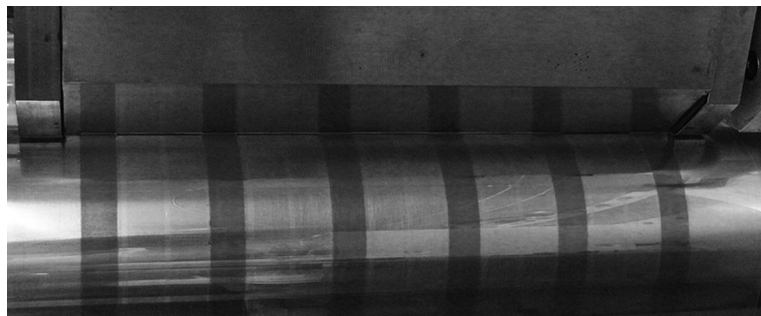
Figure 7.17 Slot die coating of the emissive layer 'Super Yellow' on a flexible ITO substrate for OLEDs.

When the brush is put in contact with the substrate a meniscus is formed, and the subsequent brushing movement pulls the ink from the brush and on to the web. Depending on the brush size, two-dimensional patterning is possible.

Only a few examples of brush painting have been published within organic electronics. For small-scale OPVs, one or more layers have been reported deposited by this technique (Heo, Lee, Song, Ku, & Moon, 2011; Kim, Na, Jo, Tae, & Kim, 2007; Kim, Na, Kang, & Kim, 2010), and recently Lee, Shin, Noh, Na, and Kim (2013) prepared an electrode that is an interesting alternative to ITO by brush painting on a flexible substrate (in this case, PET). Once integrated in OPV devices, this electrode made of PEDOT:PSS and silver nanowires yields efficiencies similar to devices with ITO. The use of brush painting on a R2R scale is fully conceivable, but so far no attempts have been reported.

7.4.2   Double slot-die coating

Double slot-die coating is a recent evolution in R2R processing of organic electronics and so far has only been used in the preparation of OPVs. During this particular process, two inks are deposited at the same time with a single coating head (see Figure 7.18) reducing production time as well as cost. Ideally the technique should allow for coating of numerous layers in one step. However, the deposition of just two layers at the same time has proven quite challenging. Recently, Larsen-Olsen et al. used this technique in order to coat an aqueous suspension of P3HT:PCBM and PEDOT:PSS simultaneously at a rate of 1 m/min (Larsen-Olsen, Andreasen, et al., 2012).

7.4.3   Differentially pumped slot-die coating

This technique was developed by Alstrup, Jørgensen, Medford, and Krebs (2010) as a fast and easy way to investigate acceptor/donor ratio in the active layer of an organic solar cell. The two compounds are pumped simultaneously into the coating head (where they are mixed), but with dissimilar pumping rates (see Figure 7.19). By varying the

Double slot-die coating
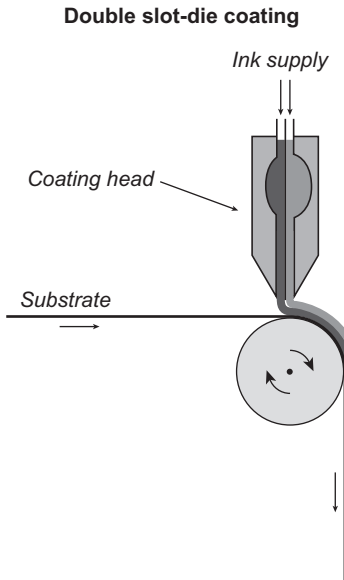
Figure 7.18 Illustration of double slot-die coating.

Differientialy pumped slot die
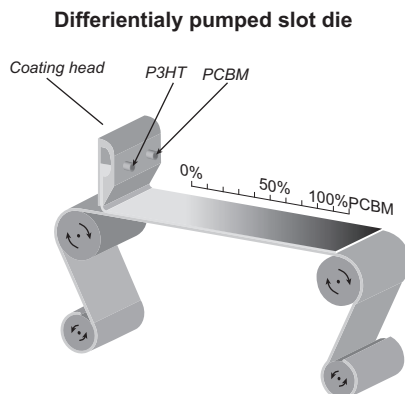
Figure 7.19 Differentially pumped slot-die coating. Screening P3HT:PCBM ratio from 0 : 1 to 1 : 0.

relative pumping rates gradually, while maintaining a constant combined pumping rate, a film with a gradient composition is produced. Subsequent analysis of device performance along this gradient allows determining the optimal ratio of a specific pair of donor and acceptor materials. This method is a powerful tool in OPV research that reduces the time for donor/acceptor ratio screening from days/weeks to a matter of hours (Amb et al., 2012; Bundgaard et al., 2010; Søndergaard et al., 2012). Although the method is developed for OPVs, in principle it should be directly transferrable to any other two-component system where an optimized ratio is desired.

7.5   Encapsulation techniques

Protection of the finished device from the surrounding environment is often needed when organic materials and especially conducting polymers are involved. Roll-to-roll encapsulation has so far only been applied to organic solar cells and the following section is thus exclusively about solar cell encapsulation. Though the principles described are general, they might serve as fruitful inspiration for other organic electronic technologies.

Once a solar cell is processed onto the substrate encapsulation is required. Lamination is performed mainly to ensure device stability over time, but it also protects the sensitive device stack from mechanical stress. The lamination principle basically consists of joining a second foil, called a laminate, with the one on which the cells have been deposited. In order to ensure chemical stability of the device, a barrier foil is normally used to ensure minimum permeability of oxygen and water. The foil carrying the devices can be laminated on both sides to improve the stability.

7.5.1   Cold lamination

Cold lamination is carried out with a pressure sensitive adhesive. This adhesive is put onto the laminate with the help of a liner, which is removed (Krebs, Tromholt, et al., 2010) right before the laminate is put into contact with the substrate carrying the devices. The two foils meet in a nip where they are pressed together between two rolls in order to ensure good adhesion as shown in Figure 7.20. This lamination process is simple and fast (>20 m/min). The principal issue is that a relatively thick adhesive layer (around 50 μm or more) is needed compared to adhesives used in different lamination processes. Handling the sticky laminate can also prove challenging. A comparative OPV stability study performed by Hösel et al. (2013) analysed the different lamination

Lamination

Laminate

Nip

Solar cell stack

Substrate
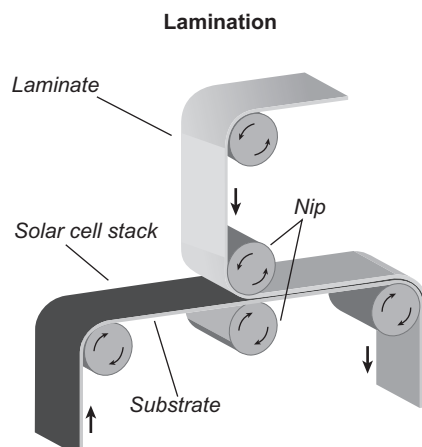
Figure 7.20 Illustration of Cold and Hot lamination. The laminate holds the adhesive. Nip rolls can be heated for hot lamination.

techniques described in this section. The study showed that for cold lamination the active layer experiences bleaching around the edges when laminated on only one side. Long-term stability requires lamination on both sides.

7.5.2   Hot lamination

Hot lamination is a process similar to cold lamination (see Figure 7.20). However, in this case the adhesive can be handled on the laminate surface without a liner and because this adhesive is heat activated handling the laminate is much easier. The laminate is joined with the substrate carrying solar cells as the foils are pressed together between two heated rolls. This causes the adhesive to melt momentarily and upon cooling it forms a tight seal. Figure 7.21 shows the hot lamination of OPV modules. Besides being easier to handle this lamination process also allows use of thinner adhesive layers (down to 20 µm). Stability-wise, only slight bleaching is observed around the edges of the active layer when single laminated by hot-melt (Hösel et al., 2013).

7.5.3   UV lamination

In UV lamination the adhesive is UV sensitive. The UV curable adhesive is added to the laminate foil and after joining with the OPV carrying substrate in a nib the combined foils are exposed to UV light, ensuring the formation of a tight seal (Figure 7.22). Stability wise no bleaching is observed making UV-curable resin the best fit for single lamination (Hösel et al., 2013). This lamination technique is by far the more complex, as it requires an extra step to deposit the UV adhesive onto the laminate. This deposition is usually done through flexoprinting. Although complicated the technique allows for precise tuning of the adhesive thickness (1−100 µm).

Figure 7.21 Hot lamination of organic solar cells modules.
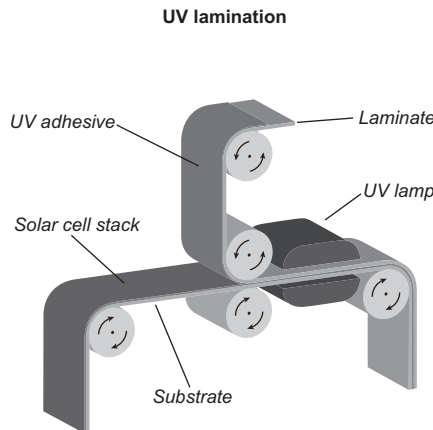
UV lamination

Figure 7.22 Illustration of UV lamination. The UV reactive adhesive is applied on the laminate by flexoprinting.

7.6 Applications

The ultimate goal of preparation by R2R processing is of course to have a product that can be integrated and commercialized.

As previously mentioned, OPV is probably the most mature technology with respect to R2R processing, but so far the commercialisation process has not really shown its potential. The Konarka solar bag, which allows the user to recharge small devices such as mobile phones, is the only real product so far. Several noncommercial demonstrations of integrating the technology have been reported though. One of the earliest examples is the 'solar hat' that can be used to power a small radio. More than 2000 130 cm^2 modules were produced for this campaign using only screen printing (Krebs, Jørgensen, et al., 2009). Another example was carried out as part of the 'Lighting Africa Project', where solar cell modules (20 × 25 cm^2) were used to charge a small reading light equipped with a rechargeable battery (Krebs, Nielsen, Fyenbo, Wadstrøm, & Pedersen, 2010). The same concept was later used to make 10,000 credit card sized OE-A flashlight demonstrators (Krebs et al., 2011). Recently, Espinosa et al. prepared small laser pointers similar in size to the OE-A flashlight to show the current progresses in OPV technology. These laser pointers use ITO-free OPV modules to charge a lithium-ion polymer battery (Espinosa et al., 2013). Although OPVs have been greatly studied, only a few examples have been publicly available (most of them are listed above). As a platform for researchers as well as a means to educate the public on 'what is an organic solar cell', Krebs, Hösel, et al. (2013) prepared tens of thousands of 'freeOPV' modules available for free to anyone who asks. These entirely R2R-processed modules are ITO-free and yield a PCE in the range of 1.5−2% (10.0 × 14.2 cm^2).

All of the examples above are good illustrations of OPV technology's potential, but in order to prosper as a renewable energy source, the OPV technology needs to be connected to the electrical grid. By introducing the infinity concept where interconnected

single cells are R2R processed continuously along the web Sommer-Larsen et al. showed that in order to effectively integrate R2R processed OPV the whole solar cell roll needs to be handled uncut (Sommer-Larsen et al., 2013), as the cutting and wiring of small discrete units is time- and cost-consuming. Using the uncut roll of solar cells is quite challenging because it does not allow for reconfiguration of the cells after R2R coating. The thin film structure of OPVs makes them unable to carry high current, meaning that all the cells along the roll must be connected in series. Such configuration delivers much higher voltages (around 10 kV for a roll of 0.305 × 100 m) than typical silicon modules and is much less sensible to individual cell performances than the silicon analogue. Pushing the use of the uncut OPV roll further, Krebs, Espinosa, Hösel, Søndergaard, and Jørgensen (2013) constructed a 1000 m^2 solar park. This solar park is connected to the electrical grid and consists of four tilted wood platforms (100 m long and 2.5 m high) that can be fitted with six rows of one-foot-wide foils (see Figure 7.23). The solar cells employed are based on the infinity process described earlier (Sommer-Larsen et al., 2013). As of now infinity stretches up to 1.5−2.2 km long have been prepared constituting over 300,000 single cells connected in series. To be efficiently used, these rolls are only cut once and then laid onto the platform. Krebs et al. developed a simple process to install and remove the foil at the same time at a rate over 100 m/min. At this rate with the current technology it is possible to install over 200 W$_{peak}$ per minute, far beyond the rate of other solar cell technologies.

Albeit not as mature as OPVs in R2R development, OLEDs are present in many commercial products. Lamps were the first commercially available products to use OLEDs and nowadays a large range of colours are available. OLEDs have also been used for displays in MP3 players, digital cameras, smartphones and TVs. However, none of these OLEDs devices reportedly have been prepared by R2R processing.

Similarly, EC technology has yielded several interesting applications spreading from light control, switching between clear and frosted glass, small EC displays that can be used for postcards and even a moisture sensor that lets you know when to water your plants − but again, none of these reports the use of R2R processing.

Figure 7.23 Solar park based on OPV, 250-square-metre wood panel with six solar-cell foils and an active area of 88 square metres.

Figure 7.24 Photograph of printed paper loudspeaker demonstrating its flexibility. Reproduced from Hübler et al. (2012) with permission from Elsevier.

Of the more surprising but notable applications, the printing of loudspeakers on paper by Hübler et al. should be mentioned (Hübler et al., 2012). These speakers, shown in Figure 7.24, were made by sandwiching the active piezoelectric layer between two PEDOT:PSS layers that act as electrodes and yield a sound pressure up to 80 dB.

7.7   Future trends

Roll-to-roll processing certainly has a bright future for fast and low-cost large-area organic electronics production. However, several challenges lie ahead for most of the technologies that are at the verge of transferring from the laboratory to the larger R2R processing scale. Many of the methodologies have to be adapted to new R2R-compatible processing methods, which is often not a straightforward process. Other challenges, such as finding functionally reliable substitutes for ITO as the transparent electrode on flexible substrates, will be crucial to keeping costs down. On the technical level, the registration used to align the multilayer structures during processing must still be improved — especially at high speeds. Particularly, OTFT and high-resolution OLEDs require precise multilayer structures.

In the long run environmental factors also have to be considered and development of new materials that can be processed from benign solvents will be required. In a large-scale production the toxic solvents currently used simply have too many complications and hazards with respect to both the working environment and the surrounding ecosystems and using such will affect the cost negatively. Life cycle and financial analyses of R2R-processed large-area organic electronics are powerful tools to guide the research

toward large-scale production. Such analysis have so far mostly been applied in relation to OPVs (Azzopardi et al., 2011; Espinosa, García-Valverde, & Krebs, 2011; Espinosa, García-Valverde, Urbina, & Krebs, 2011; Espinosa, García-Valverde, et al., 2012; García-Valverde, Cherni, & Urbina, 2010; Kalowekamo & Baker, 2009; Nielsen, Cruickshank, Foged, Thorsen, & Krebs, 2010; Powell, Bender, & Lawryshyn, 2009), and recent studies on OPV production have shown that if avoiding scarce elements and vacuum steps, and if using only solar heat and solar energy during processing, energy payback times can be brought down to a few days (Espinosa, Hösel, Angmo, & Krebs, 2012). The use of such tools will be essential to the success of all the technologies described in this chapter in order to navigate around the pitfalls that can negatively affect the insurance of fast production of low-cost organic electronics.

References

Aernouts, T., Aleksandrov, T., Girotto, C., Genoe, J., & Poortmans, J. (2008). Polymer based organic solar cells using ink-jet printed active layers. *Applied Physics Letter, 92*, 033306.

Alstrup, J., Jørgensen, M., Medford, A. J., & Krebs, F. C. (2010). Ultra fast and parsimonious materials screening for polymer solar cells using differentially pumped slot-die coating. *ACS Applied Materials and Interfaces, 2*, 2819−2827.

Amb, C. M., Beaujuge, P. M., & Reynolds, J. R. (2010). Spray-Processable Blue-to-Highly transmissive switching polymer Electrochromes via the Donor−Acceptor approach. *Advanced Materials, 22*, 724−728.

Amb, C. M., Craig, M. R., Koldemir, U., Subbiah, J., Choudhury, K. R., Gevorgyan, S. A., et al. (2012). Aesthetically pleasing conjugated polymer: fullerene blends for blue-green solar cells via roll-to-roll processing. *ACS Applied Materials & Interfaces, 4*, 1847−1853.

Amb, C. M., Kerszulis, J. A., Thompson, E. J., Dyer, A. L., & Reynolds, J. R. (2011). Propylenedioxythiophene (ProDOT)−phenylene copolymers allow a yellow-to-transmissive electrochrome. *Polymer Chemistry, 2*, 812.

Angmo, D., Hösel, M., & Krebs, F. C. (2012). All solution processing of ITO-free organic solar cell modules directly on barrier foil. *Solar Energy Materials and Solar Cells, 107*, 329−336.

Azzopardi, B., Emmott, C. J. M., Urbina, A., Krebs, F. C., Mutale, J., & Nelson, J. (2011). Economic assessment of solar electricity production from organic-based photovoltaic modules in a domestic environment. *Energy and Environmental Science, 4*, 3741.

Beaujuge, P. M., Ellinger, S., & Reynolds, J. R. (2008). Spray processable green to highly transmissive electrochromics via chemically polymerizable donor−acceptor heterocyclic pentamers. *Advanced Materials, 20*, 2772−2776.

Beaujuge, P. M., Vasilyeva, S. V., Liu, D. Y., Ellinger, S., McCarley, T. D., & Reynolds, J. R. (2012). Structure-performance correlations in spray-processable green dioxythiophene-benzothiadiazole donor−acceptor polymer Electrochromes. *Chemistry of Materials, 24*, 255−268.

Blankenburg, L., Schultheis, K., Schache, H., Sensfuss, S., & Schrödner, M. (2009). Reel-to-reel wet coating as an efficient up-scaling technique for the production of bulk-heterojunction polymer solar cells. *Solar Energy Materials and Solar Cells, 93*, 476−483.

Bundgaard, E., Hagemann, O., Manceau, M., Jørgensen, M., & Krebs, F. C. (2010). Low band gap polymers for roll-to-roll coated polymer solar cells. *Macromolecules, 43*, 8115−8120.

Chang, Y.-F., Chiu, Y.-C., Yeh, H.-C., Chang, H.-W., Chen, C.-Y., Meng, H.-F., et al. (2012). Unmodified small-molecule organic light-emitting diodes by blade coating. *Organic Electronics, 13*, 2149−2155.

Chen, C.-Y., Chang, H.-W., Chang, Y.-F., Chang, B.-J., Lin, Y.-S., Jian, P.-S., et al. (2011). Continuous blade coating for multi-layer large-area organic light-emitting diode and solar cell. *Journal of Applied Physics, 110*, 094501.

Chen, L., Hong, Z., Kwan, W., Lu, C.-H., Lai, Y., Lei, B., et al. (2010). Multi-source/component spray coating for polymer solar cells. *ACS Nano, 4*, 4744−4752.

Chung, S., Kim, S. O., Kwon, S.-K., Lee, C., & Hong, Y. (2011). All-inkjet-printed organic thin-film transistor inverter on flexible plastic substrate. *IEEE Electron Device Letters, 32*, 1134−1136.

Dam, H. F., & Krebs, F. C. (2012). Simple roll coater with variable coating and temperature control for printed polymer solar cells. *Solar Energy Materials and Solar Cells, 97*, 191−196.

Eom, S., Park, H., Mujawar, S. H., Yoon, S., Kim, S.-S., Na, S.-I., et al. (2010). High efficiency polymer solar cells via sequential inkjet-printing of PEDOT: PSS and P3HT: PCBM inks with additives. *Organic Electronics, 11*, 1516−1522.

Eom, S. H., Senthilarasu, S., Uthirakumar, P., Yoon, S. C., Lim, J., Lee, C., et al. (2009). Polymer solar cells based on inkjet-printed PEDOT: PSS layer. *Organic Electronics, 10*, 536−542.

Espinosa, N., García-Valverde, R., & Krebs, F. C. (2011). Life-cycle analysis of product integrated polymer solar cells. *Energy & Environmental Science, 4*, 1547.

Espinosa, N., García-Valverde, R., Urbina, A., & Krebs, F. C. (2011). A life cycle analysis of polymer solar cell modules prepared using roll-to-roll methods under ambient conditions. *Solar Energy Materials and Solar Cells, 95*, 1293−1302.

Espinosa, N., García-Valverde, R., Urbina, A., Lenzmann, F., Manceau, M., Angmo, D., et al. (2012). Life cycle assessment of ITO-free flexible polymer solar cells prepared by roll-to-roll coating and printing. *Solar Energy Materials and Solar Cells, 97*, 3−13.

Espinosa, N., Hösel, M., Angmo, D., & Krebs, F. C. (2012). Solar cells with one-day energy payback for the factories of the future. *Energy & Environmental Science, 5*, 5117.

Espinosa, N., Lenzmann, F. O., Ryley, S., Angmo, D., Hösel, M., Søndergaard, R. R., et al. (2013). OPV for mobile applications: an evaluation of roll-to-roll processed indium and silver free polymer solar cells through analysis of life cycle, cost and layer quality using inline optical and functional inspection tools. *Journal of Materials Chemistry A, 1*, 7037.

Galagan, Y., Rubingh, J. J., Andriessen, R., Fan, C.-C., Blom, P. W. M., Veenstra, S. C., et al. (2011). ITO-free flexible organic solar cells with printed current collecting grids. *Solar Energy Materials and Solar Cells, 95*, 1339−1343.

Galagan, Y., Vries, I. G. de, Langen, A. P., Andriessen, R., Verhees, W. J. H., Veenstra, S. C., et al. (2011). Technology development for roll-to-roll production of organic photovoltaics. *Chemical Engineering and Processing: Process Intensification, 50*, 454−461.

García-Valverde, R., Cherni, J. A., & Urbina, A. (2010). Life cycle analysis of organic photovoltaic technologies. *Progress in Photovoltaics: Research and Application, 18*, 535−558.

Girotto, C., Moia, D., Rand, B., & Heremans, P. (2011). High-performance organic solar cells with spray-coated hole-transport and active layers. *Advanced Functional Materials, 21*, 64−72.

Girotto, C., Rand, B., Genoe, J., & Heremans, P. (2009). Exploring spray coating as a deposition technique for the fabrication of solution-processed solar cells. *Solar Energy Materials and Solar Cells, 93*, 454−458.

Girotto, C., Rand, B., Steudel, S., Genoe, J., & Heremans, P. (2009). Nanoparticle-based, spray-coated silver top contacts for efficient polymer solar cells. *Organic Electronics, 10*, 735−740.

Gorter, H., Coenen, M. J. J., Slaats, M. W. L., Ren, M., Lu, W., Kuijpers, C. J., et al. (2013). Toward inkjet printing of small molecule organic light emitting diodes. *Thin Solid Films, 532*, 11−15.

Hambsch, M., Reuter, K., Stanel, M., Schmidt, G., Kempa, H., Fügmann, U., et al. (2010). Uniformity of fully gravure printed organic field-effect transistors. *Materials Science and Engineering: B, 170*, 93−98.

Hau, S. K., Yip, H.-L., Leong, K., & Jen, A. K.-Y. (2009). Spraycoating of silver nanoparticle electrodes for inverted polymer solar cells. *Organic Electronics, 10*, 719−723.

Helgesen, M., Carlé, J. E., Andreasen, B., Hösel, M., Norrman, K., Søndergaard, R. R., et al. (2012). Rapid flash annealing of thermally reactive copolymers in a roll-to-roll process for polymer solar cells. *Polymer Chemistry, 3*, 2649−2655.

Heo, S., Lee, J., Song, H., Ku, J., & Moon, D. (2011). Patternable brush painting process for fabrication of flexible polymer solar cells. *Solar Energy Materials and Solar Cells, 95*, 3041−3046.

Hösel, M., Søndergaard, R. R., Jørgensen, M., & Krebs, F. C. (2013). Comparison of UV-Curing, hotmelt, and pressure sensitive adhesive as roll-to-roll encapsulation methods for polymer solar cells. *Advanced Engineering Materials, 15*, 1068−1075.

Hoth, C., Choulis, S., Schilinsky, P., & Brabec, C. J. (2007). High photovoltaic performance of inkjet printed polymer: fullerene blends. *Advanced Materials, 19*, 3973−3978.

Hoth, C., Schilinsky, P., Choulis, S., & Brabec, C. J. (2008). Printing highly efficient organic solar cells. *Nano Letters, 8*(9), 2806−2813.

Hoth, C., Steim, R., Schilinsky, P., Choulis, S. A., Tedde, S. F., Hayden, O., et al. (2009). Topographical and morphological aspects of spray coated organic photovoltaics. *Organic Electronics, 10*, 587−593.

Hübler, A. C., Bellmann, M., Schmidt, G. C., Zimmermann, S., Gerlach, A., & Haentjes, C. (2012). Fully mass printed loudspeakers on paper. *Organic Electronics, 13*, 2290−2295.

Hübler, A. C., Trnovec, B., Zillger, T., Ali, M., Wetzold, N., Mingebach, M., et al. (2011). Printed paper photovoltaic cells. *Advanced Energy Materials, 1*, 1018−1022.

Huebler, A. C., Doetz, F., Kempa, H., Katz, H. E., Bartzsch, M., Brandt, N., et al. (2007). Ring oscillator fabricated completely by means of mass-printing technologies. *Organic Electronics, 8*, 480−486.

Jensen, J., Dam, H. F., Reynolds, J. R., Dyer, A. L., & Krebs, F. C. (2012). Manufacture and demonstration of organic photovoltaic-powered electrochromic displays using roll coating methods and printable electrolytes. *Journal of Polymer Science Part B: Polymer Physics, 50*, 536−545.

Kalowekamo, J., & Baker, E. (2009). Estimating the manufacturing cost of purely organic solar cells. *Solar Energy, 83*, 1224−1231.

Kang, J., Kang, Y., Jung, S., Song, M., Kim, D.-G., Kim, C.-S., et al. (2012). Fully spray-coated inverted organic solar cells. *Solar Energy Materials and Solar Cells, 103*, 76−79.

Kim, Y., Lee, J., Kang, H., Kim, G., Kim, N., & Lee, K. (2012). Controlled electro-spray deposition of highly conductive PEDOT: PSS films. *Solar Energy Materials and Solar Cells, 98*, 39−45.

Kim, S., Na, S.-I., Jo, J., Tae, G., & Kim, D.-Y. (2007). Efficient polymer solar cells fabricated by simple brush painting. *Advanced Materials, 19*, 4410−4415.

Kim, S., Na, S., Kang, S., & Kim, D. (2010). Annealing-free fabrication of P3HT: PCBM solar cells via simple brush painting. *Solar Energy Materials and Solar Cells, 94*, 171−175.

Kopola, P., Aernouts, T., Guillerez, S., Jin, H., Tuomikoski, M., Maaninen, A., et al. (2010). High efficient plastic solar cells fabricated with a high-throughput gravure printing method. *Solar Energy Materials and Solar Cells, 94*, 1673−1680.

Kopola, P., Aernouts, T., Sliz, R., Guillerez, S., Ylikunnari, M., Cheyns, D., et al. (2011). Gravure printed flexible organic photovoltaic modules. *Solar Energy Materials and Solar Cells, 95*, 1344−1347.

Kopola, P., Tuomikoski, M., Suhonen, R., & Maaninen, A. (2009). Gravure printed organic light emitting diodes for lighting applications. *Thin Solid Films, 517*, 5757−5762.

Krebs, F. C. (2009). Polymer solar cell modules prepared using roll-to-roll methods: knife-over-edge coating, slot-die coating and screen printing. *Solar Energy Materials and Solar Cells, 93*, 465−475.

Krebs, F. C., Espinosa, N., Hösel, M., Søndergaard, R. R., & Jørgensen, M. (2013). Rise to power − OPV-based solar Parks. *Advanced Materials, 26*, 29−39.

Krebs, F. C., Fyenbo, J., & Jørgensen, M. (2010). Product integration of compact roll-to-roll processed polymer solar cell modules: methods and manufacture using flexographic printing, slot-die coating and rotary. *Journal of Materials Chemistry, 20*, 8994.

Krebs, F. C., Fyenbo, J., Tanenbaum, D. M., Gevorgyan, S. A., Andriessen, R., Remoortere, B. van, et al. (2011). The OE-A OPV demonstrator anno domini 2011. *Energy & Environmental Science, 4*, 4116−4123.

Krebs, F. C., Gevorgyan, S. A., & Alstrup, J. (2009). A roll-to-roll process to flexible polymer solar cells: model studies, manufacture and operational stability studies. *Journal of Materials Chemistry, 19*, 5442.

Krebs, F. C., Hösel, M., Corazza, M., Roth, B., Madsen, M. V., Gevorgyan, S. A., et al. (2013). Freely available OPV—the fast way to progress. *Energy Technology, 1*, 378−381.

Krebs, F. C., Jørgensen, M., Norrman, K., Hagemann, O., Alstrup, J., Nielsen, T. D., et al. (2009). A complete process for production of flexible large area polymer solar cells entirely using screen printing—first public demonstration. *Solar Energy Materials and Solar Cells, 93*, 422−441.

Krebs, F. C., Nielsen, T. D., Fyenbo, J., Wadstrøm, M., & Pedersen, M. S. (2010). Manufacture, integration and demonstration of polymer solar cells in a lamp for the "Lighting Africa" initiative. *Energy & Environmental Science, 3*, 512.

Krebs, F. C., Tromholt, T., & Jørgensen, M. (2010). Upscaling of polymer solar cell fabrication using full roll-to-roll processing. *Nanoscale, 2*, 873−886.

Kwon, J., Eom, S. H., Moon, B. S., Shin, J., Kim, K.-S., Lee, S.-H., et al. (2012). Studies on printing inks containing poly [2-methoxy-5-(2-ethylhexyl-oxyl)-1,4-phenylenevinylene] as an emissive material for the fabrication of polymer light-emitting diodes by inkjet printing. *Bulletin of the Korean Chemical Society, 33*, 464−468.

Lange, A., Schindler, W., Wegener, M., Fostiropoulos, K., & Janietz, S. (2013). Inkjet printed solar cell active layers prepared from chlorine-free solvent systems. *Solar Energy Materials and Solar Cells, 109*, 104−110.

Lange, A., Wegener, M., Boeffel, C., Fischer, B., Wedel, A., & Neher, D. (2010). A new approach to the solvent system for inkjet-printed P3HT: PCBM solar cells and its use in devices with printed passive and active layers. *Solar Energy Materials and Solar Cells, 94*, 1816−1821.

Larsen-Olsen, T. T., Andreasen, B., Andersen, T. R., Böttiger, A. P. L., Bundgaard, E., Norrman, K., et al. (2012). Simultaneous multilayer formation of the polymer solar cell stack using roll-to-roll double slot-die coating from water. *Solar Energy Materials and Solar Cells, 97*, 22−27.

Larsen-Olsen, T. T., Machui, F., Lechene, B., Berny, S., Angmo, D., Søndergaard, R. R., et al. (2012). Round-robin studies as a method for testing and validating high-efficiency ITO-free polymer solar cells based on roll-to-roll-coated highly conductive and transparent flexible substrates. *Advanced Energy Materials, 2*, 1091−1094.

Lee, D.-H., Choi, J. S., Chae, H., Chung, C.-H., & Cho, S. M. (2008). Highly efficient phosphorescent polymer OLEDs fabricated by screen printing. *Displays, 29*, 436−439.

Lee, D.-H., Lim, K.-T., Park, E.-K., Kim, J.-M., & Kim, Y.-S. (2013). Optimized ink-jet printing condition for stable and reproducible performance of organic thin film transistor. *Microelectronic Engineering, 111*, 242−246.

Lee, J.-H., Shin, H.-S., Noh, Y.-J., Na, S.-I., & Kim, H.-K. (2013). Brush painting of transparent PEDOT/Ag nanowire/PEDOT multilayer electrodes for flexible organic solar cells. *Solar Energy Materials and Solar Cells, 114*, 15−23.

Lewis, J. E., Lafalce, E., Toglia, P., & Jiang, X. (2011). Over 30% transparency large area inverted organic solar array by spray. *Solar Energy Materials and Solar Cells, 95*, 2816−2822.

Manceau, M., Angmo, D., Jørgensen, M., & Krebs, F. C. (2011). ITO-free flexible polymer solar cells: from small model devices to roll-to-roll processed large modules. *Organic Electronics, 12*, 566−574.

Mortimer, R. J., Graham, K. R., Grenier, C. R. G., & Reynolds, J. R. (2009). Influence of the film thickness and morphology on the colorimetric properties of spray-coated electrochromic disubstituted 3,4-propylenedioxythiophene polymers. *ACS Applied Materials & Interfaces, 1*, 2269−2276.

Nielsen, T. D., Cruickshank, C., Foged, S., Thorsen, J., & Krebs, F. C. (2010). Business, market and intellectual property analysis of polymer solar cells. *Solar Energy Materials and Solar Cells, 94*, 1553−1571.

Park, S.-Y., Kang, Y.-J., Lee, S., Kim, D.-G., Kim, J.-K., Kim, J. H., et al. (2011). Spray-coated organic solar cells with large-area of 12.25 cm^2. *Solar Energy Materials and Solar Cells, 95*, 852−855.

Powell, C., Bender, T., & Lawryshyn, Y. (2009). A model to determine financial indicators for organic solar cells. *Solar Energy, 83*, 1977−1984.

Reeves, B. D., Grenier, C. R. G., Argun, A. A., Cirpan, A., McCarley, T. D., & Reynolds, J. R. (2004). Spray coatable electrochromic dioxythiophene polymers with high coloration efficiencies. *Macromolecules, 37*, 7559−7569.

Ryu, G. S., Kim, J. S., Jeong, S. H., & Song, C. K. (2013). A printed OTFT-backplane for AMOLED display. *Organic Electronics, 14*, 1218−1224.

Sandström, A., Dam, H. F., Krebs, F. C., & Edman, L. (2012). Ambient fabrication of flexible and large-area organic light-emitting devices using slot-die coating. *Nature Communications, 3*, 1002.

Sommer-Larsen, P., Jørgensen, M., Søndergaard, R. R., Hösel, M., & Krebs, F. C. (2013). It is all in the pattern-high-efficiency power extraction from polymer solar cells through high-voltage serial connection. *Energy Technology, 1*, 15−19.

Søndergaard, R. R., Hösel, M., Jørgensen, M., & Krebs, F. C. (2013). Fast printing of thin, large area, ITO free electrochromics on flexible barrier foil. *Journal of Polymer Science Part B: Polymer Physics, 51*, 132−136.

Søndergaard, R. R., Manceau, M., Jørgensen, M., & Krebs, F. C. (2012). New low-bandgap materials with good stabilities and efficiencies comparable to P3HT in R2R-coated solar cells. *Advanced Energy Materials, 2*, 415−418.

Steirer, K. X., Reese, M. O., Rupert, B. L., Kopidakis, N., Olson, D. C., Collins, R. T., et al. (2009). Ultrasonic spray deposition for production of organic solar cells. *Solar Energy Materials and Solar Cells, 93*, 447−453.

Teichler, A., Shu, Z., Wild, A., Bader, C., Nowotny, J., Kirchner, G., et al. (2013). Inkjet printing of chemically tailored light-emitting polymers. *European Polymer Journal, 49*, 2186−2195.

Tobjörk, D., Kaihovirta, N. J., Mäkelä, T., Pettersson, F. S., & Österbacka, R. (2008). All-printed low-voltage organic transistors. *Organic Electronics, 9*, 931−935.

Verilhac, J.-M., Benwadih, M., Seiler, A.-L., Jacob, S., Bory, C., Bablet, J., et al. (2010). Step toward robust and reliable amorphous polymer field-effect transistors and logic functions made by the use of roll to roll compatible printing processes. *Organic Electronics, 11*, 456−462.

Voigt, M. M., Guite, A., Chung, D.-Y., Khan, R. U. A., Campbell, A. J., Bradley, D. D. C., et al. (2010). Polymer field-effect transistors fabricated by the sequential gravure printing of polythiophene, two insulator layers, and a metal ink gate. *Advanced Functional Materials, 20*, 239−246.

Vornbrock, A. de la F., Sung, D., Kang, H., Kitsomboonloha, R., & Subramanian, V. (2010). Fully gravure and ink-jet printed high speed pBTTT organic thin film transistors. *Organic Electronics, 11*, 2037−2044.

Wengeler, L., Schmidt-Hansberg, B., Peters, K., Scharfer, P., & Schabel, W. (2011). Investigations on knife and slot die coating and processing of polymer nanoparticle films for hybrid polymer solar cells. *Chemical Engineering and Processing: Process Intensification, 50*, 478−482.

Wu, L. Y. L., Kerk, W. T., & Wong, C. C. (2013). Transparent conductive film by large area roll-to-roll processing. *Thin Solid Films, 544*, 427−432.

Wu, X., Li, F., Wu, W., & Guo, T. (2014). Flexible organic light emitting diodes based on double-layered graphene/PEDOT: PSS conductive film formed by spray-coating. *Vacuum, 101*, 53−56.

Yang, J., Vak, D., Clark, N., Subbiah, J., Wong, W. W. H., Jones, D. J., et al. (2013). Organic photovoltaic modules fabricated by an industrial gravure printing proofer. *Solar Energy Materials and Solar Cells, 109*, 47−55.

Youn, H., Jeon, K., Shin, S., & Yang, M. (2012). All-solution blade−slit coated polymer light-emitting diodes. *Organic Electronics, 13*, 1470−1478.

Yu, J.-S., Kim, I., Kim, J.-S., Jo, J., Larsen-Olsen, T. T., Søndergaard, R. R., et al. (2012). Silver front electrode grids for ITO-free all printed polymer solar cells with embedded and raised topographies, prepared by thermal imprint, flexographic and inkjet roll-to-roll processes. *Nanoscale, 4*, 6032−6040.

Yu, B., Vak, D., Jo, J., Na, S., Kim, S.-S., Kim, M.-K., et al. (2010). Factors to be considered in bulk heterojunction polymer solar cells fabricated by the spray process. *IEEE Journal of Selected Topics in Quantum Electronics, 16*, 1838−1846.

Zhang, B., Chae, H., & Cho, S. M. (2009). Screen-printed polymer: fullerene bulk-heterojunction solar cells. *Japanese Journal of Applied Physics, 48*, 020208.

Zimmermann, B., Schleiermacher, H.-F., Niggemann, M., & Würfel, U. (2011). ITO-free flexible inverted organic solar cell modules with high fill factor prepared by slot die coating. *Solar Energy Materials and Solar Cells, 95*, 1587−1589.

This page intentionally left blank

Integrated printing for 2D/3D flexible organic electronic devices

8

B.S. Cook, B. Tehrani, J.R. Cooper, S. Kim, M.M. Tentzeris
Georgia Tech, Atlanta GA, USA

8.1 Introduction

Ever since the advent of the printing press in the early 1400s in Mainz, Germany, printing has been an unequaled method of reproduction for manuscripts and artwork. The printing process, developed by a hand of entrepreneuring inventors including Gutenberg, Fust, and Schoeffer, in 1450 was a tightly guarded secret because it was the first technological development that enabled the comparatively cheap and rapid multiplication of manuscripts, which at the time were in high demand and commanded steep prices (Hamilton, 1918). For nearly a decade, the process remained closely guarded within the printing guilds of Mainz until the sack of the city in 1462. After the sack of the city, the members of the printing guilds dispersed and took the knowledge of the printing process with them. As the knowledge disseminated, printing took off like wildfire across Europe, which enabled a new age of accessibility to knowledge and the literary arts (Hamilton, 1918; Society for Promoting Christian Knowledge, 1855).

Just as the first printing press revolutionized the reproduction of manuscripts and books over half of a millennium ago by drastically cutting costs and increasing production capacity, modern day inkjet printers are revolutionizing electronics fabrication by allowing for faster, cheaper, more flexible, and more accessible methods to pattern and package electronic circuits and systems.

Current methods of patterning electronics are typically subtractive, which require the selective removal of material from a bulk sheet to leave the desired pattern (Wiederrecht, 2009). This selective removal, or etching, requires expensive masks, which define the pattern to be etched, and harsh chemicals to remove the unwanted material. The masking and etching steps must then be repeated for each layer of patterned material that is deposited. This methodology makes subtractive processing time-intensive, and it creates a large amount of material and chemical waste. However, inkjet printing has the innate advantage of being a noncontact and additive fabrication and patterning process, meaning that the materials that are patterned to form the electronics systems are directly deposited in the desired pattern in a layer-by-layer fashion (Wiederrecht, 2009). This additive technique decreases fabrication time, eliminates the need for expensive masks, and minimizes the material and chemical waste produced from the fabrication process.

The initial electronics applications targeted by inkjet printing are large-area, low-frequency electronics that benefit from reel-to-reel and roll-to-roll manufacturing. These technologies have been adapted from the newsprint industry. These applications

include low-cost and disposable printed radiofrequency (RF) identification tags for
asset tracking (Inkjet-Flex, 2013; Orecchini, Alimenti, Palazzari, Rida, & Tentzeris,
2011; Yang, Rida, Vyas, & Tentzeris, 2007), printed electrodes for solar cells and flex-
ible screens (Angmo, Larsen-Olsen, Jrgensen, Snder-gaard, & Krebs, 2013; Angmo,
Sweelssen, Andriessen, Galagan, & Krebs, 2013; Kim, Na, & Kim, 2012; Optomec,
2013), flexible single-layer printed circuit boards (PCBs) (Abowd, Kawahara, Hodges,
& Cook, 2013; Inkjet-Flex, 2013; Yang, Zhang, Staiculescu, Wong, & Tentzeris,
2009), and printed sensors and sensor arrays for large-area and wearable electronics
(T-Ink, 2013; Yang et al., 2009). However, just as the integrated circuit industry
that was started by Jack Kilby in 1958 advanced from low-frequency, large-area cir-
cuits, to modern day nanoscale compact processes operating in the terahertz regime
(Saxena, 2009), inkjet printing, which is currently in its beginning stages, is seeing
a push to reach higher frequencies, smaller and more compact vertically integrated
stack-ups, and cheaper and faster production.

8.2   Fundamentals of inkjet printing

Inkjet printing is conceptually a relatively simple process. An ink is loaded into a
reservoir that feeds a nozzle. This nozzle is moved horizontally over a substrate,
and an actuator is used to eject a drop of ink from the nozzle. The ink droplet
then hits and adsorbs to the surface of the substrate as seen in Figure 8.1. By deter-
mining when drops are ejected as the nozzle passes over the substrate, patterned
features are created.

However, although the theory of operation is simple, the details that go into making
a successful and reliable process for inkjet-printed multilayer RF electronics, or any
inkjet printing process for that matter, are quite complex.
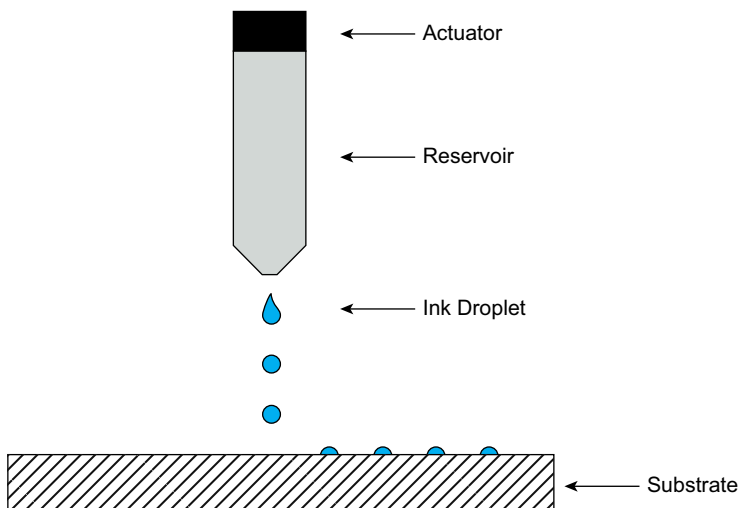
Figure 8.1 Mapping of physical properties of an ink to jet-ability and drop formation.

Key factors that must be tuned to create a successful printing process for RF electronics include

- Nozzle type and characteristics (piezo, thermal, electrostatic, acoustic, actuation, waveform)
- Ink formulation (material loading, viscosity, surface tension, carrier fluid)
- Substrate or top-layer surface properties (roughness, free surface energy, ink chemical compatibility)
- Post-print curing (annealing pressure and temperature, ultraviolet (UV) exposure, laser annealing)

8.2.1 Inkjet printing modalities

There are two distinct modes of inkjet printing, as displayed in Figure 8.2: (1) continuous, which is used in industrial and mass-production environments, and (2) drop-on-demand (DOD), which is used in small-volume and prototyping environments (Magdassi, 2010; Wiederrecht, 2009).

8.2.1.1 DOD inkjet printing

DOD printing, shown in Figure 8.2(a), is the most common printing modality used today in consumer and small-volume printers because of its simplicity. In DOD printing, the printer nozzle is passed over the substrate, and an actuator ejects a droplet wherever patterned material is required. This method works very well for small-volume and prototype environments and is more flexible on the variety of inks it can jet. However, DOD printing suffers from transient effects upon actuator startup and the increased risk of nozzle clogging.

8.2.1.2 Continuous inkjet printing

For industrial environments where quality and cost are a crucial factor, continuous inkjet printing, shown in Figure 8.2(b), minimizes transient and clogging issues. Continuous inkjet printing continuously fires the actuator at a fixed frequency to eject ink droplets. To perform patterning, a "catcher," which is a plate situated below the nozzle, actuates into and out of the path of the droplets, only allowing the droplets to pass when pattern material is required.
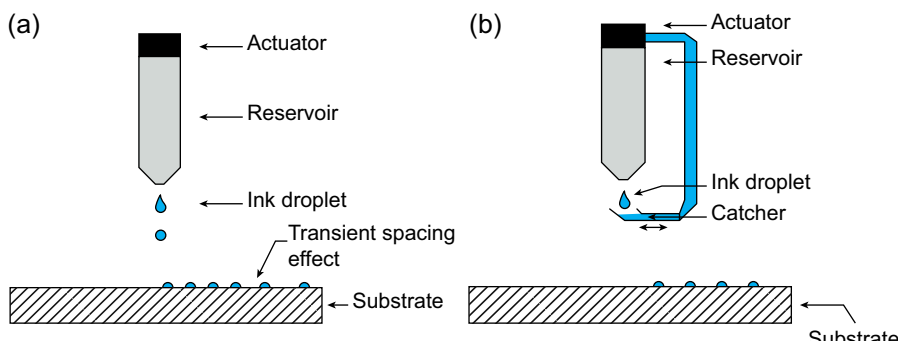
Figure 8.2 Printing modalities: (a) drop-on-demand (DOD) and (b) continuous.

8.2.2   Actuators and inkjet printer nozzles

There are several actuator types that control the type of ink and feature sizes obtainable in the process. These include thermal, piezo, electrodynamic, and acoustic actuators, which are shown in Figure 8.3 (Choi et al., 2011; Hamazaki & Morita, 2009; Magdassi, 2010; Wiederrecht, 2009).

8.2.2.1   Thermal

Thermal actuators are the most common of the inkjet printing actuators and are well known for being the actuator of choice for consumer photoprinters because they are cheap and work with a wide range of inks. Thermal actuators work by triggering a heating element, which is within or near the ink reservoir, which causes a rapid volume expansion within the ink. This volume expansion increases the pressure in the cavity, causing a drop to be ejected. Thermal inkjet nozzles are the cheapest and the most reliable, but they eject larger drops than the other actuators, which are in the range of 80−100 pL (Wiederrecht, 2009).
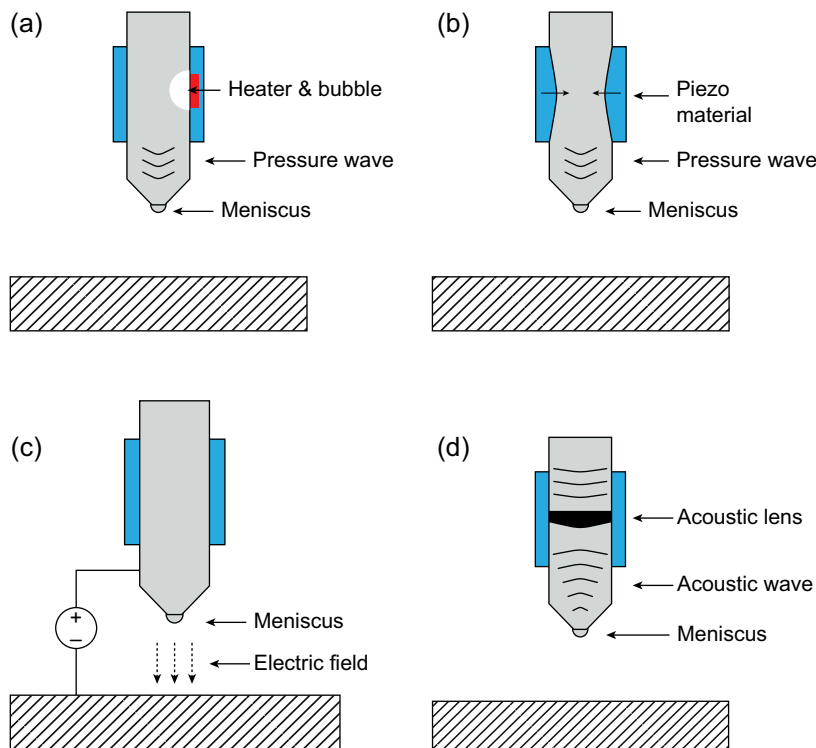
Figure 8.3 Inkjet actuation modalities: (a) thermal, (b) piezo, (c) electrodynamic, and (d) acoustic.

8.2.2.2 Piezo

Piezo actuators are another commonly used type of actuator because they work with a wide variety of inks and produce much smaller droplets than thermal actuated inkjet nozzles. Piezo actuators work by placing a piezo material around or inside of the ink reservoir, which is triggered to contract and expand, causing a buildup of pressure and then vacuum within the chamber allowing precise control on the formation of the drop.

8.2.2.3 Electrodynamic

Electrodynamic actuation of print nozzles is a method used when extremely fine feature sizes are required with the caveat that the ink contains free ions. To eject a drop, a voltage is applied between the nozzle and a conductive base on which the substrate rests as shown in Figure 8.3(c). This voltage creates an electric field that causes the ions in the ink to accumulate near the meniscus at the opening of the nozzle thus deforming the meniscus into a cone. When the voltage is removed, the meniscus reforms, ejecting a drop in the process. Electrodynamic actuation can produce drops with volumes below 1 fL, which is much lower than other actuation methods (Choi et al., 2011; Wiederrecht, 2009).

8.2.2.4 Acoustic

Acoustic actuated inkjet nozzles have the advantage of large nozzle openings to prevent clogging while still producing small feature sizes. To eject a droplet, an ultrasonic acoustic wave is focused onto the meniscus using a lens. This concentration of acoustic energy causes a transient surface force that overcomes the surface tension of the meniscus for a short period of time allowing a drop to escape. By controlling the focal point of the lens, variable volume drops can be obtained in the 50-fL range (Hamazaki & Morita, 2009).

8.2.3 Ink formulation

The typical formulation of an electronic ink is shown in Table 8.1. First, a liquid solvent is chosen that can dissolve/disperse the deposition material. This solvent must

Table 8.1 **Typical composition of an electronic ink**

Component	Purpose
Solvent (50−80%)	Primary solvent and carrier fluid
Co-solvent (5−50%)	Increase boiling point, modify surface tension
Deposition material (0.5−40%)	Key component, material that forms the final film
Surfactant (0−2%)	Modify surface tension, improve wetting characteristics
Others (1%)	Dispersants, pH buffers, defoamers

have an adequate viscosity (η) and surface tension (γ) for the nozzle type used in the printer. The chosen solvent must have a high enough boiling point as to mitigate drying at the nozzle/air interface when not jetting but low enough to be evaporated through mild heating. If these conditions cannot be met by using a single solvent, then a co-solvent may be added that is miscible in the primary solvent and dissolves the deposition material to modify the viscosity, surface tension, and boiling point/vapor pressure of the mixture (Magdassi, 2010; Tekin, Gans, & Schubert, 2004). Surfactants and other additives such as dispersants and pH buffers may also be added when solvent systems alone cannot meet these conditions (Magdassi, 2010).

8.2.4   *Jetting and drop formation for piezo-based inkjet nozzles*

After an ink has been formulated to meet the specifications of a selected DOD printer nozzle, adjusting the droplet formation, velocity, and volume is dependent on the nozzle temperature and the jetting waveform that is applied to the piezo actuator. When the jetting waveform is correctly configured, the drop formation will appear as seen in Figure 8.4. However, in a case in which the ink is not within the specifications of the printer, or the waveform and nozzle temperature are not configured correctly, no jetting or satellite droplets can occur, as shown in Figure 8.5.

8.2.5   *Substrate wetting*

Once an ink and its jetting waveform have been tuned for the specified printer nozzle, the properties of the substrate onto which the ink will be deposited must be considered to ensure proper wetting and feature formation. The critical parameters to consider for the substrate are the free surface energy (γ_{total}), which is related to the contact angle of the droplet on the substrate (θ_c), and the surface roughness. When a drop of liquid comes into contact with the substrate, surface forces are experienced at the solid−liquid boundary γ_{SL}, the solid−air boundary γ_{SV}, and the liquid−air boundary γ_{LV} as shown in Figure 8.6. These forces are determined by the surface tension of the ink, γ_L, and the surface energy of the substrate, γ_S.
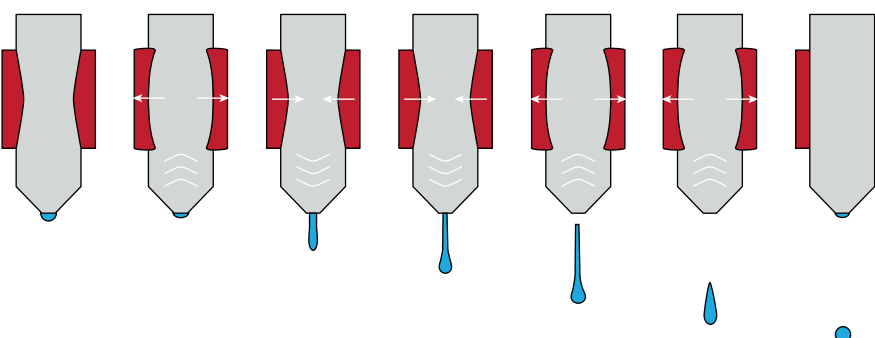
Figure 8.4 Droplet progression for a standard piezo drop-on-demand (DOD) print nozzle waveform.
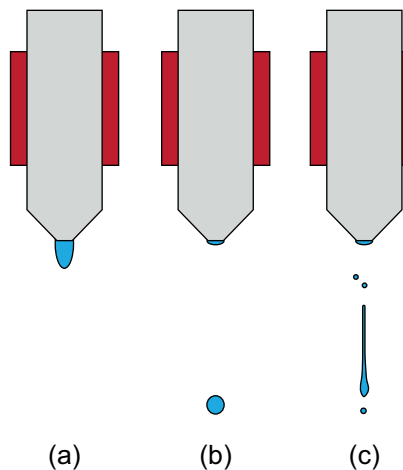
Figure 8.5 Drops in which there is (a) no jetting, (b) ideal jetting, and (c) satellite droplets.
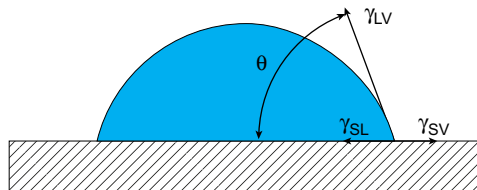
Figure 8.6 Surface tension and contact angle of a droplet on a substrate.

The interaction of these three forces determines the contact angle of the droplet on the substrate, as shown in Eqns 8.1 and 8.2 (Attension, 2014). The contact angle is directly related the wettability of the substrate.

$$\cos(\theta) = \frac{\gamma_S - \gamma_{SL}}{\gamma_L} \tag{8.1}$$

$$\gamma_{SL} = \gamma_L + \gamma_S - 2\sqrt{\gamma_L \gamma_S} \tag{8.2}$$

By understanding the surface energy of the substrate and the surface tension of the fluid, the wetting behavior of the ink can be determined. When the surface energy of the substrate is much lower than the surface tension of the ink ($\gamma_S < \gamma_L$), poor wetting will occur and the ink will ball on the surface. As γ_S increases with respect to γ_L, the contact angle decreases until the critical surface tension γ_C is reached and the ink completely wets the substrate, producing a uniform film. Several methods can be used to change the surface energy of the substrate, including UV ozone, plasma, and chemical treatments.

8.3   Electronic inks

8.3.1   Conductive inks

8.3.1.1   Solution-based conducting inks

Conductive inks were initially formulated by dissolving conducting polymers such as PEDOT:PSS or conducting elements such as carbon into a solvent that would yield films with low conductivities of 10^2 S/m (Kawase, Sirringhaus, Friend, & Shimoda, 2001; Newman & Turner, 1992). However, these low-conductivity solution-based inks are not feasible to use for high-efficiency printed electronics.

8.3.1.2   Nanoparticle-based conducting inks

Some of the first highly conductive inks that have been able to be processed at low enough temperatures for polymer and organic substrates are metallic silver nanoparticle dispersions that reach conductivities in excess of 10^7 (S/m) with curing temperatures below 250 °C (Szczecha, Megaridisa, Gamotaaand, & Zhanga, 2000). Nanoscale particles exhibit a unique property in that the melting point decreases drastically with miniaturization as shown in Eqn. (8.3), in which T_0 is the bulk melting temperature, σ is related to the thermal conductivity of the metal, and r is the radius of the particle.

$$T_m(r) \ = \ T_0\Big(1 - \frac{\sigma}{r}\Big) \tag{8.3}$$

Using this property, recent works have demonstrated conductivities of silver nanoparticle ink on the order of 1.2×10^7 (S/m), 5 times lower than bulk silver, through the creation of smaller nanoparticles (30−50 nm) and using special curing techniques (Cook & Shamim, 2012). Nanoparticle inks typically have to be composed of noble metals (e.g., silver, gold) to mitigate oxidation upon curing.

8.3.1.3   Catalyst-based conducting inks

Metals such as copper cannot be easily deposited using nanoparticles because of oxidation during sintering. However, copper is preferable in many applications because it is much cheaper than silver and has a higher bulk conductivity.

To overcome the obstacle of depositing non-noble metals, catalyst-based inks have been developed that deposit a catalyst for the metal to be deposited. The substrate is then placed in a plating bath that coats the catalyst with a bulk metallization. This process allows for depositing films equivalent in conductivity to those deposited using noble metallic nanoparticles at a large cost reduction. The solution-based patterning also avoids nozzle-clogging problems and costs associated with noble metal particle-based inks (Cook, Fang, et al., 2013).

8.3.2   Dielectric inks

Creating vertically integrated structures using inkjet printing requires the printing of dielectric layers. Most research has focused on producing thin-film printed dielectrics

for printed transistor gates. These dielectrics are typically soluble organic polymers with relative permittivities (ε_r) of 3−5, loss tangents (tan δ) in the range of 0.02−0.05, and are approximately 100−500 nm thick when printed (Soltman & Subramanian, 2007). Higher permittivity precursor-based ceramics can also be printed with relative permittivities on the order of 1000 and thicknesses up to 400 nm (Kaydanova et al., 2007; Nikfalazar et al., 2013). However, these higher permittivity inks require sintering at temperatures in excess of 1000 °C, which is too high for most flexible and large-area applications.

In practical electronic fabrication, dielectric materials are deposited onto a host substrate with a desired thickness, referred to as a thin or thick dielectric film. Thick-film deposition is typically used when large three-dimensional features are desired (e.g., with multilayer antennas and various micro-electro-mechanical system devices; Cook, Tehrani, Cooper, & Tentzeris, 2013). Thin-film deposition is advantageous in the fabrication of capacitors, in which dielectric thickness is inversely proportional to capacitance, and RF device miniaturization, in which the width of a microstrip line is linearly proportional to the dielectric thickness for a given impedance. The current state of inkjet printing uses two polymer-based inks for thick and thin dielectric film deposition.

8.3.2.1 Thin dielectrics

For applications in which thin transistor gates, or high-capacitance structures, are required, thin-film dielectrics are preferred. Thin-film dielectric inks are typically formulated by a longer-chain soluble polymer, such as poly(4-vinylphenol) (PVP), which can be dissolved in a low weight percentage to create a high-viscosity solution. With optimal droplet spacing, PVP films can be deposited with a thickness below 500 nm per layer as shown in Figure 8.7.

8.3.2.2 Thick dielectrics

Recent advances in ink development have allowed for the deposition of dielectric layers that are in the range of 10−200 μm thick for applications in three-dimensional electronic
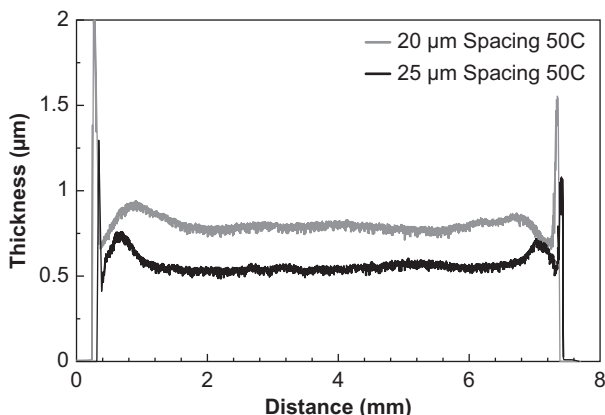
Figure 8.7 Film thickness of printed thin-film dielectric inks versus drop spacing.
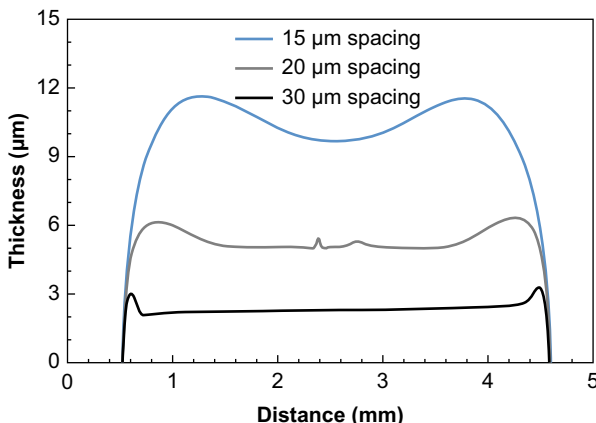
Figure 8.8 Film thickness of printed thick-film dielectric inks versus drop spacing.

structure development (Cook, Tehrani, et al., 2013; Cook, Cooper, & Tentzeris, 2013). These thick-layer dielectric inks are formulated by short chain soluble polymers, such as SU-8, which can be dissolved in a high weight percentage while maintaining a low solution viscosity. With the optimal droplet spacing, SU-8 films can be deposited with a thickness of 10−12 μm per layer as shown in Figure 8.8.

8.3.3 Carbon nanomaterials

Although conducting and insulating inks form the key foundations of an electronics printing process, semiconducting inks are required to make active components and sensors. Research has recently produced inks that can deposit carbon nanotubes and graphene platelets that exhibit semiconducting and sensing properties that are far superior to printed semiconductors such as pentacene (Li et al., 2013; Lee et al., 2012).

8.4 Vertically integrated inkjet-printed electronic passive components

To develop fully printed systems, the basic building blocks, including discrete components (capacitors, inductors, resistors), active devices (transistors, diodes), and high-frequency components (antennas, transmission lines, filters), need to be in place. Therefore, before venturing into complex, integrated circuits, the development of these devices must first be covered.

In the following section, the fabrication of capacitors, inductors, interlayer vias, and millimeter-wave antennas using inkjet printing is covered. All four devices demonstrate the purely additive nature of inkjet printing in a multilayer, or vertically integrated, construction.

8.4.1 Inkjet-printed capacitors

Metal-insulator-metal (MIM) capacitors, shown in Figure 8.9, are a basic building block of electronic systems and allow for high capacitance with little real estate.

(a)

1. Clean and UVO Substrate   2. Pattern Bottom Plate (M1)

3. Pattern Dielectric   4. Pattern Top Plate (M2)

(b)

1 mm
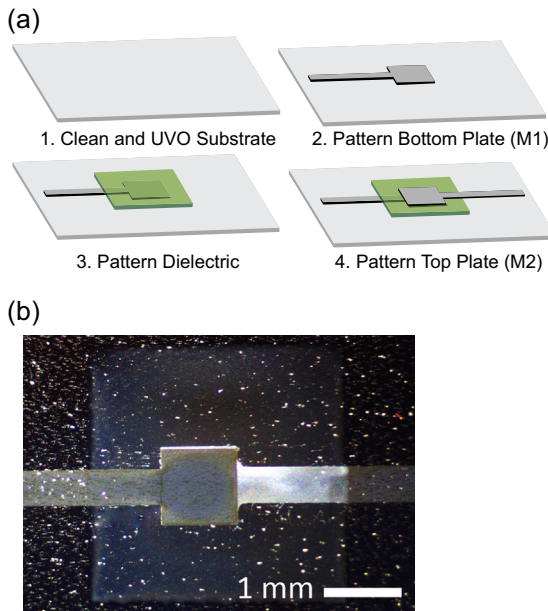
Figure 8.9 (a) Process for fabricating MIM capacitors and (b) inkjet-printed MIM capacitor.

Capacitors are important for energy storage, signal filtering, and high-frequency tuning applications. To fabricate MIM capacitors using inkjet printing, a simple three-layer deposition process is followed in which the bottom plate is first deposited, followed by the dielectric, and finally the top plate. Figure 8.9 shows inkjet-printed MIM capacitors that operate up to 3 GHz.

Figure 8.10 shows a performance comparison of MIM capacitors fabricated with thick- and thin-film printed dielectrics. Although both capacitors have a plate area of 2.25 mm^2, the thin-film dielectric yields a much higher capacitance per unit area as expected.

8.4.2 Inkjet-printed inductors

Spiral inductors are another commonly used component in electronic systems. Inductors are important for signal filtering, for high-frequency resonators and tuning, and for magnetic coupling of signals. To fabricate inductors using inkjet printing, a simple three-layer printing approach is taken, as shown in Figure 8.11. First, the bottom spiral is printed. To connect the inside of the spiral to the second terminal, a dielectric spacer is patterned with two via holes and a bridging conductor is printed.

One of the biggest limitations in the past has been the Q of the conductors, which was low because of the low conductivity of previous conductive inks and the inability to print thick dielectric spacers for the overpass bridge. However, with recent advancements, high Q values of over 20 have been able to be achieved for large inductance values up to 25 nH (Cook et al., 2014). Figure 8.12 shows the measured inductance
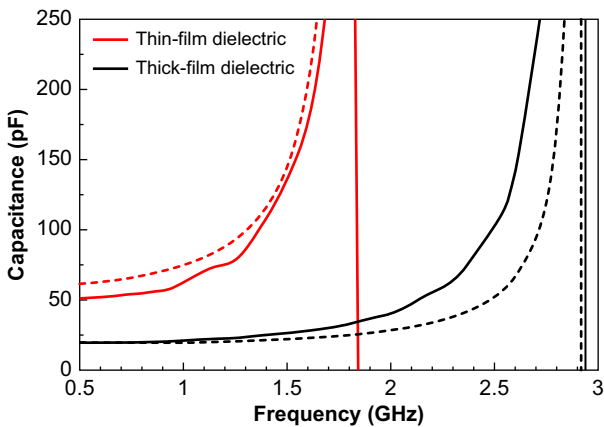
Figure 8.10 Measured capacitance versus frequency of thin- and thick-film dielectric capacitors.
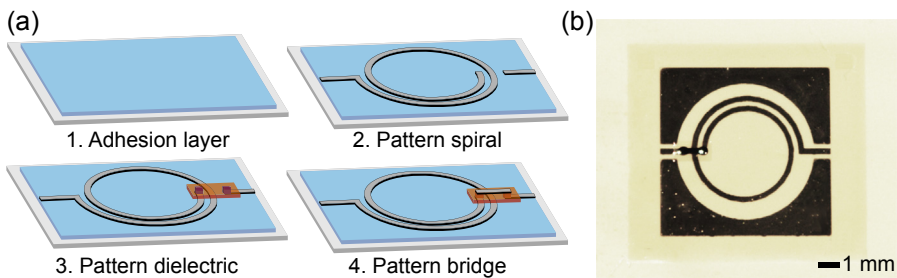
Figure 8.11 (a) Process for fabricating spiral inductors, and (b) inkjet-printed spiral inductor.
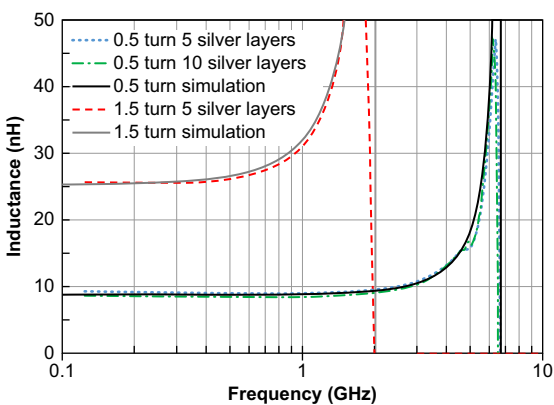
Figure 8.12 Measured inductance versus frequency of the spiral inductors.
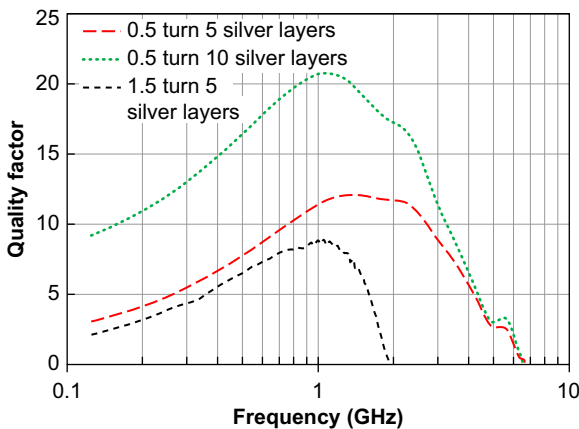
Figure 8.13 Measured Q versus frequency of the spiral inductors.

over frequency for printed 0.5- and 1.5-turn spiral inductors. The printed inductors have very stable performance and operate up to 7 GHz. Figure 8.13 shows the measured quality factor of the printed inductors, which reaches up to over 20, nearing that of conventional discrete inductors.

8.4.3 Inkjet-printed vias

Many electronic designs require an electric connection between two conducting layers separated by a dielectric material, such as the interlayer connections required for the inductors in the previous section. These through-layer connections are often referred to as vias. In typical PCB fabrication, electronic vias are created by physically punching or drilling conductive holes into a host substrate, bridging a connection between top and bottom conductive plating. With inkjet printing, a nonsubtractive processes of interconnect fabrication is desired to remain consistent with its additive nature of processing.

Inkjet-printed vias are realized through selective patterning, in which a hole is left in a dielectric pattern to allow for interconnection between two metallic layers through the printed dielectric film. Figure 8.14 shows a cross section of an inkjet-printed via in a printed SU-8 dielectric thick film (Tehrani, Bito, Benjamin, Cook, & Tentzeris, 2014).

The sidewalls of inkjet-printed dielectric films exhibit a sloped profile in contrast to an ideal vertical shape. One technique used to increase the slope of dielectric sidewalls is to use multiple print-cure-print sessions; however, this method increases the production time for an electronic print. Optimized methods of curing and surface pretreatment have the potential to further increase the profile of printed dielectrics to that of an ideal film. Although not ideal in profile uniformity, measurements have shown that the performance of inkjet-printed vias deviates negligibly from ideal at DC operation with resistances of less than 0.01 (Tehrani et al., 2014).

A second method of making vias using inkjet printing when the substrate is already present is the stepped through-hole method. When not additively building a substrate,
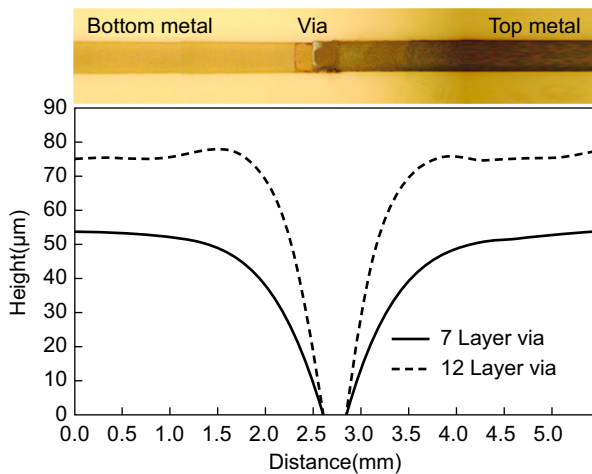
Figure 8.14 Additive fabrication of through-layer vias with different printed dielectric thicknesses.

a hole can be drilled through the substrate, which can then be printed over with a conductive ink to form a through-substrate via connection. However, because the layers deposited by conductive inks are typically on the order of 1 μm thick per layer, and substrates are typically 50 μm or thicker, the ink is not able to coat the vertical side walls of the drilled through hole. To accommodate the thin ink layers, a stepped through hole can be laser milled as shown in Figure 8.15. The stepped profile allows for low-resistance connections through thick substrates that have thicknesses greater than 1 mm.

8.4.4   Inkjet-printed antennas

Some of the hottest areas in inkjet-printed antennas are large-area printed antennas for conformal body-area networks, foldable/portable antennas for space deployment, and conformal antenna arrays for automotive radar applications. Recently, using multilayer printing techniques, high-performance antennas that operate into the millimeter-wave
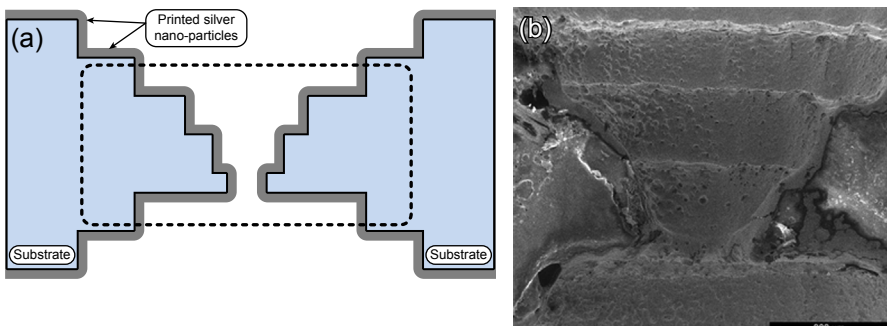
Figure 8.15 (a) Process for fabricating through-substrate vias and (b) through-substrate via SEM.
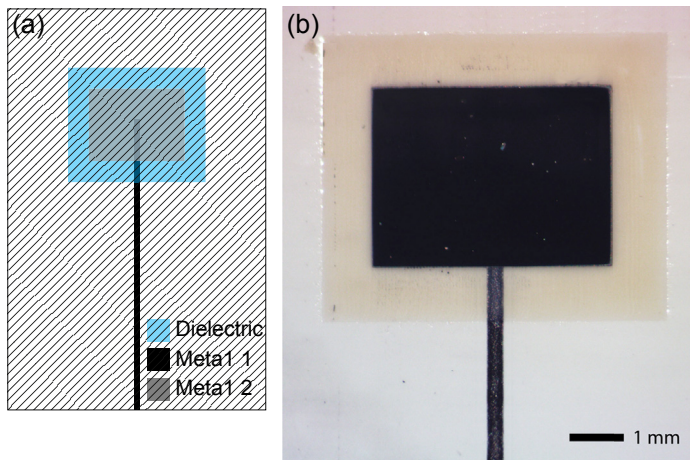
Figure 8.16 (a) Design of the proximity-fed patch antenna and (b) fabricated proximity-fed antenna.

regime have become achievable. The first millimeter-wave vertically integrated antennas are shown in Figure 8.16. The coupled patches in this instance are designed for the 24.5-GHz ISM band. The topology consists of a printed transmission line, a 40-μm printed dielectric spacer, and a printed patch radiating element.

Typically, multiple laminates would have to be used for designs such as this; however, with the ability to print thick dielectrics, the dielectric for the patch can be printed only where needed, saving large amounts of material.

The fabrication process is a three-step process in which the microstrip transmission line is first printed using a silver nanoparticle ink. The thick-layer dielectric is then deposited and cured. The final step consists of printing the patch on top of the dielectric spacer and heat-curing the structure. The measured return loss of the fabricated antenna is shown in Figure 8.17. It can be seen that the inkjet-printed antenna resonates
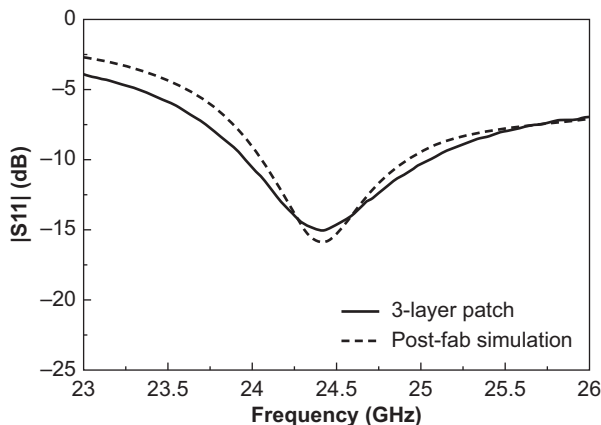
Figure 8.17 Return loss of the printed millimeter-wave antennas.
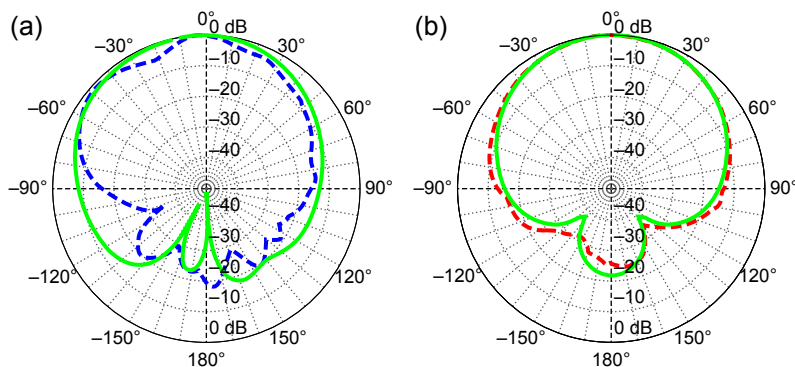
Figure 8.18 (a) E-plane radiation pattern and (b) H-plane radiation pattern.

at 24.5 GHz and matches well with simulations. The fact that the antenna matches so well with the simulation means that printing technology is becoming extremely reliable and that the current multilayer processes are now at a stage in which they are characterized and repeatable.

The measured radiation patterns, which are compared with simulation in Figure 8.18, show a well-matched experimental result that has a high directivity in the broadside direction.

8.5   Conclusions

Over the past decade, inkjet-based electronics fabrication has come a long way and has demonstrated major advantages for low-cost, flexible, and postprocessing applications. Looking past individual printed components is the realization of fully printed systems and modules. As printing technology advances, fully printed systems that are realized from the ground up are becoming visible and include power storage, computation, and human interface, which will be able to greatly reduce the cost and production difficulty of future electronic systems.

References

Abowd, G., Kawahara, Y., Hodges, S., & Cook, B. S. (2013). Instant inkjet circuits: lab-based inkjet printing to support rapid prototyping of ubi-comp devices. In *UbiComp*.

Angmo, D., Larsen-Olsen, T. T., Jrgensen, M., Snder-gaard, R. R., & Krebs, F. C. (2013). Roll-to-roll inkjet printing and photonic sintering of electrodes for ITO free polymer solar cell modules and facile product integration. *Advanced Energy Materials, 3*(2), 172−175.

Angmo, D., Sweelssen, J., Andriessen, R., Galagan, Y., & Krebs, F. C. (2013). Inkjet printing of back electrodes for inverted polymer solar cells. *Advanced Energy Materials, 3*(9), 1230−1237.

Attension. (2014). *Surface free energy − background, calculation and examples by using contact angle measurements*. Technical report. Attension.

Choi, K.-H., Rahman, K., Muhammad, N. M., Khan, Ar-shad, Kwon, Ki-R., Doh, Y.-H., & Kim, H.-C. (2011). Electrohydrodynamic Inkjet − Micro Pattern Fabrication for Printed Electronics Applications. In B. Cui (Editor), *Recent advances in nanofabrication techniques and applications* (pp. 547−568). InTech.

Cook, B. S., Cooper, J. R., & Tentzeris, M. M. (2013). Multi-layer rf capacitors on exible substrates utilizing inkjet printed dielectric polymers. *Microwave and Wireless Components Letters, IEEE, 23*(7), 353−355.

Cook, B. S., Fang, Y., Kim, S., Le, T., Goodwin, B., Sandhage, K. H., & Tentzeris, M. M. (2013). Inkjet catalyst printing and electroless copper deposition for low-cost patterned microwave passive devices on paper. *Electronic Materials Letters, 9*(5), 669−676.

Cook, B. S., Mariotti, C., Revier, D., Cooper, J. R., Aluigi, L., & Tentzeris, M. M. (2014). Inkjet-printed, vertically-integrated, high-performance inductors and transformers on flexible LCP substrate. In *International Microwave symposium* (pp. 1−3).

Cook, B. S., & Shamim, A. (2012). Inkjet printing of novel wideband and high gain antennas on low-cost paper substrate. *IEEE Transactions on Antennas and Propagation, 60*(9), 4148−4156.

Cook, B. S., Tehrani, B., Cooper, J., & Tentzeris, E. (2013). Multi-layer inkjet printing of millimeter-wave proximity-fed patch arrays on exible substrates. *IEEE Antennas and Wireless Propagation Letters.*

Hamazaki, T., & Morita, N. (2009). Ejection characteristics and drop modulation of acoustic inkjet printing using Fresnel lens. *Journal of Fluid Science and Technology, 2*, 25−36.

Hamilton, F. W. (1918). *History of printing (part 1)*. MacCalla & Co.

Inkjet-Flex. (2013). *Applications − RFID antennas*. http://www.inkjetex.com/.

Kawase, T., Sirringhaus, H., Friend, R. H., & Shimoda, T. (2001). Inkjet printed via-hole interconnections and resistors for all-polymer transistor circuits. *Advanced Materials, 21*, 1601−1605.

Kaydanova, T., Miedaner, A., Perkins, J. D., Curtis, C., Alleman, J. L., & Ginley, D. S. (2007). Direct-write inkjet printing for fabrication of barium strontium titanate-based tunable circuits. *Thin Solid Films, 515*(78), 3820−3824.

Kim, J., Na, S.-I., & Kim, H.-K. (2012). Inkjet printing of transparent inznsno conducting electrodes from nano-particle ink for printable organic photovoltaics. *Solar Energy Materials and Solar Cells, 98*(0), 424−432.

Lee, C. W., Raman Pillai, S. K., Luan, X., Wang, Y., Ming Li, C., & Chan-Park, M. B. (2012). High-performance inkjet printed carbon nanotube thin film transistors with high-k HfO_2 dielectric on plastic substrate. *Small, 8*(19), 2941−2947.

Li, J., Ye, F., Vaziri, S., Muhammed, M., Lemme, M. C., & Stling, M. (2013). Efficient inkjet printing of graphene. *Advanced Materials, 25*(29), 3985−3992.

Magdassi, S. (2010). *The chemistry of inkjet inks*. World Scientific Publishing Company. Incorporated.

Newman, J., & Turner, A. (1992). Ink-jet printing for the fabrication of amperometric glucose biosensors. *Analytrca Chumca Acta, 262*, 13−17.

Nikfalazar, M., Sazegar, M., Friederich, A., Kohler, C., Zheng, Y., Wiens, A., & Jakoby, R. (2013). Inkjet printed bst thick-films for x-band phase shifter and phased array applications. In *2013 International workshop on antenna technology (iWAT)* (pp. 1−4).

Optomec. (2013). *Optomec − Solar cell platform*. http://www.optomec.com.

Orecchini, G., Alimenti, F., Palazzari, V., Rida, A., & Tentzeris, M. M. (2011). Design and fabrication of ultra-low cost radio frequency identification antennas and tags exploiting paper substrates and inkjet printing technology. *IET Microwaves Antennas & Propagation, 5*, 993−1001.

Saxena, A. N. (2009). *Invention of integrated circuits: Untold important facts*. World Scientific.

Society for Promoting Christian Knowledge. (1855). *The history of printing*. W. Clowes and Sons.

Soltman, D., & Subramanian, V. (2007). *Inkjet-printed line morphologies and temperature control of the coffee ring effect*. American Chemical Society. pp. 1−8.

Szczecha, J. B., Megaridisa, C. M., Gamotaaand, D. R., & Zhanga, J. (2000). Manufacture of microelectronic circuitry by drop-on-demand dispensing of nano-particle liquid suspensions. *MRS Proceedings, 624*, 23−28.

Tehrani, B., Bito, J., Cook, B. S., & Tentzeris, M. M. (2014). Fully inkjet-printed multilayer microstrip and t-resonator structures for the rf characterization of printable materials and interconnects. In *2014 IEEE MTT-S International Microwave Symposium Digest (IMS)*.

Tekin, E., Gans, B.-J. de, & Schubert, U. S. (2004). Ink-jet printing of polymers - from single dots to thin film libraries. *Journal of Materials Chemistry, 14*, 2627−2632.

T-Ink. (2013). *T-Ink's conductive and sensing inks for consumer and wearable electronics*. http://www.t-ink.com/.

Wiederrecht, G. (2009). *Handbook of nanofabrication*. Elsevier.

Yang, L., Rida, A., Vyas, R., & Tentzeris, M. M. (2007). RFID tag and RF structures on a paper substrate using inkjet-printing technology. *IEEE Transactions on Microwave Theory and Techniques, 55*.

Yang, L., Zhang, R., Staiculescu, D., Wong, C. P., & Tentzeris, M. M. (2009). A novel conformal RFID-enabled module utilizing inkjet-printed antennas and carbon nanotubes for gas-detection applications. *IEEE Antennas and Wireless Propagation Letters, 8*, 653−656.

In situ characterization of organic electronic materials using X-ray techniques

9

S. Grigorian
University of Siegen, Siegen, Germany

9.1   Introduction

It is believed that organic electronics is a low-cost and environmentally friendly alternative to silicon-based technology and will be achievable within the near future (Bao & Locklin, 2007; Klauk, 2006). Despite current progress in the understanding of organic device functionality, complete understanding of fabrication protocol is a complex task. Considerable effort by numerous groups has been placed on understanding the complex structural properties of the conjugated organic systems and blends (Brinkmann & Rannou, 2009; Kim, 2006b; Kline et al., 2005; Prosa, Winokur, Moulton, Smith, & Heeger, 1992; Salleo, Kline, DeLongchamp, & Chabinyc, 2010). Although there have been intentions to influence the final functionality of organic devices, the main approach is based on trial-and-error protocol. Here, in most cases, structural and device properties are measured separately and correlated afterward (Kim et al., 2005; Sirringhaus et al., 1999; Zen et al., 2006). The disadvantage of such correlation is that reaching the final enhanced device is rather a long trial-and-error process. Hence, there has been an increasing interest in the development of *in situ* characterization techniques. One of the widely used approaches to enhance structural properties is postfabrication annealing of organic films (Karagiannidis et al., 2011; Kim, 2006a; Werzer, Matoy, Strohriegl, & Resel, 2007). A time-resolved annealing can be considered as a prototyping tool for such *in situ* characterization techniques as demonstrated on poly(3-hexylthiophene) (P3HT) (Joshi et al., 2009). P3HT is one of the widely used conjugated polymers for organic field effect transistor (OFET), rather than its blend with phenyl-C61-butyric acid methyl ester (PCBM) for solar cell applications (Padinger, Rittberger, & Sariciftci, 2003) because of their relatively high device efficiency and stability (Hauch et al., 2008; Reyes-Reyes, Kim, & Carroll, 2005). Stability of a working device has been recently addressed by *in situ* X-ray and atomic force microscopy measurements under an applied electric field (Grigorian et al., 2011). These investigations revealed a well-pronounced lateral expansion and significant softening of postfabricated P3HT prototype devices. *In situ* structural characterization of the crystallization process of P3HT:PCBM blend was elaborately investigated in (Sanyal et al., 2011; Schmidt-Hansberg, Klein, Sanyal, Buss, & de Medeiros, 2012). Observed structural changes of P3HT:PCBM blends during thermal annealing confirmed that the

concentration of the PCBM acting as a plasticizer and affected the crystallization of the P3HT (Lilliu et al., 2011).

9.2 Grazing incidence X-ray diffraction

Grazing incidence X-ray diffraction (GIXD) technique is widely used for thin film investigations in which striking X-ray incident angle enables depth-resolve studies (Dosch, 1992). Increasing incident angle, α_i one can probe a top surface, subsurface, or an entire film at the angles higher than the critical angle, α_{cf} of the total external reflection of the film. A typical diffraction pattern measured at BL9 beamline, DELTA of drop cast P3HT film (in this review, high-molecular-weight P3HT is considered as that which has been described in Joshi et al. (2009)) probed by the striking X-rays at $\alpha_i > \alpha_{cf}$ is shown in Figure 9.1. Grey and black axes are directed parallel and perpendicular to the film surface normal probing so-called out-of-plane and in-plane GIXD geometries, respectively (see Figure 9.1). Most intense (h00) series with domination of the ellipsoidally shaped (100) reflex are mainly distributed along out-of-plane direction. The (h00) peaks shown by line profile (gray) in Figure 9.1 are correlated to interplanar distances of the hexyl side chains. In contrast, a less intense (020) peak related to the π-π stacking is mainly observable along in-plane direction (black line profile, Figure 9.1). Such diffraction pattern with π-π stacking parallel to the film surface corresponds to the preferential edge-on orientation shown by inset to Figure 9.1. Here polymer backbones are parallel to [001], side chains onward [001], and π-π stacking along [010] directions,
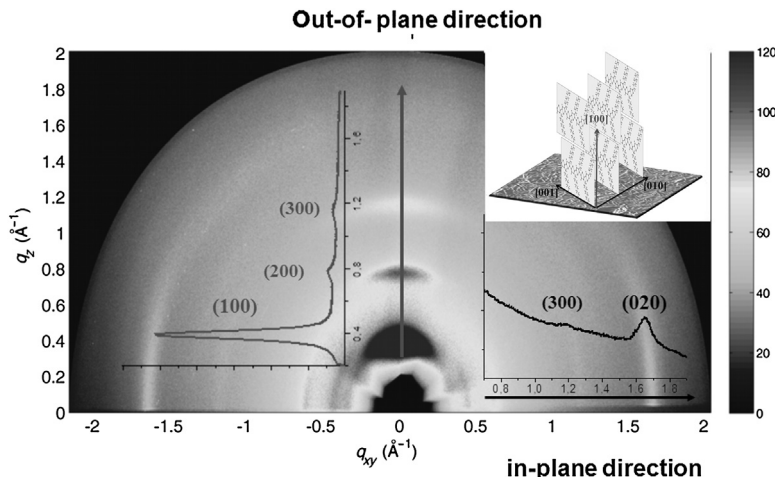
Figure 9.1 A typical 2D P3HT diffraction pattern with a series of the (h00) and the (020) peaks; inset illustrates edge-on orientation.

correspondingly. Such geometry is favourable for high performance of OFETs (Bao & Locklin, 2007; Sirringhaus et al., 1999).

9.3 Temperature-dependent studies

Postcast annealing is a typical approach to improve thin film morphology. Typically morphologies of the films cast by fast proceeding protocols are not in equilibrium and annealing is a necessary technological step to enhance structural properties as well as device performance. Increase of the structural order and expansion of P3HT film were analyzed in Werzer, Matoy, Strohriegl, and Resel (2007). Annealing of P3HT thin films improves their OFET performance two-fold (Zen et al., 2004). Similarly for P3HT:PCBM spin cast films, thermal treatment strongly influences on the nanomechanical properties and the structure (Karagiannidis, Kassavetis, Pitsalidis, & Logothetidis, 2011). Moreover, annealing promotes initial anisotropy as it has been demonstrated for dip-coated P3HT films (Ali, Pietsch, & Grigorian, 2013). Temperature-resolved enhancement of the structural properties in the vicinity of the (100) out-of-plane peak is shown in Figure 9.2. Before each measurement at the chosen temperature, thin P3HT film was thermally stabilized for 15 min. A clear trend of the thermal expansion up to 10% for 220 °C upon annealing is clearly visible (gray out-of-plane profile, Figure 9.2). Additionally, about a two-fold increase of intensity can be achieved after annealing (gray versus black curve with the round symbols, Figure 9.2). However, as it was shown for spin cast P3HT films using a similar annealing protocol, the structural enhancement does not necessary improve OFET performance (Joshi et al., 2009). Therefore, it is a highly demanding approach enabling direct monitoring of both the structural and electrical properties.
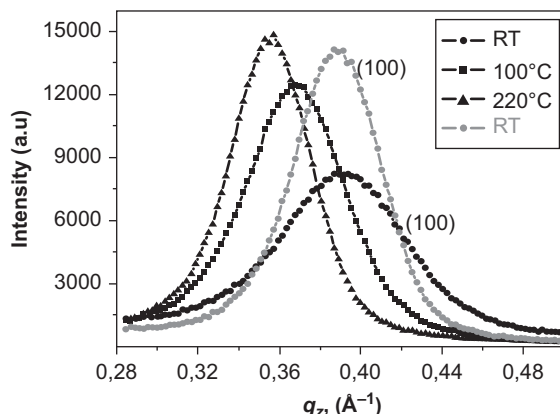
Figure 9.2 The (100) *in situ* annealing profiles of the thin P3HT film measured along the out-of-plane direction.

9.4 *In situ* X-ray studies

Conventionally, the morphology and structure of organic conjugated systems has been studied separately from their device performance (Sirringhaus et al., 1999; Kim et al., 2005; Zen et al., 2006). Recently, a direct correlation between structural and electrical properties of P3HT solidification from a chloroform solution was successfully accomplished using a custom-made chamber with motorized syringe for controlled solution deposition and operating under inert atmosphere (Grodd, Pietsch, & Grigorian, 2012).

A particular advantage in using large area detectors for *in situ* studies is to monitor extended range in reciprocal space with all essential features of diffracted pattern (see Figure 9.1). However, readout time for such detectors (e.g., MAR image plate detector) might be rather long in order to observe all peculiarities of the fast solidification processes. An alternative approach is to measure using fast counting detectors which are free of dark current and readout noise, and to zoom in on particular areas of interest. Typically the most intense signal from conjugated polythiophene films can be detected along out-of-plane direction. Our further consideration will be focused on this direction, and *in situ* studies will be demonstrated on thiophene-based polymer and oligomer systems. X-ray studies were conducted at BL 9, DELTA synchrotron at the energy of 13 keV using a fast counting and noise free Pilatus 100 K detector. Because of its small area, the position of detector was optimized to measure the highly intense (100) P3HT peak. Time-resolved development of the (100) peak of P3HT in *p*-xylene solution under ambient conditions is shown in Figure 9.3. Using a specially designed chamber with a motorized syringe, a controlled amount of P3HT solution was deposited. This chamber permits lateral movements of the substrate with electrically connected gold electrodes allowing an exact adjustment of the deposition area. For the current studies, three droplets of 100 µl in total were deposited in the middle of a 1-mm channel. X-ray measurements were performed at the incident angle of $0.1°$ ($\alpha_i > \alpha_{cf}$) and smaller than the critical angle of the substrate ($0.14°$). Time-resolved seven snapshots of solidification process starting from an initial liquid state (snapshot at 65 s) toward a final solid film (snapshot at 5000 s) are shown in Figure 9.3. The duration of each snapshot was chosen to be 1 s and two-dimensional (2D) patterns confirm a monotone increase of intensity with solidification of film. Interestingly, each of the measured 2D patterns can be addressed to the corresponding current response of the system. Electrical response of conductive channel was measured at the fixed voltage of 10 V applied to the gold electrodes. The current level at initial liquid stage is ultimately low in the range of nA. Similarly, a one magnitude lower current level was measured for the pure *p*-xylene and toluene solvents. For a direct structure and electrical response correlation, 2D snapshots were integrated over the most intense rectangular area ($\Delta q_z = 0.035$ Å^{-1} and $\Delta q_{x,y} = 0.075$ Å^{-1} along out-of- and in-plane directions, respectively). Integrated (100) intensity (black curve) and current (gray curve) profiles are shown in Figure 9.3. The initial liquid stage is characterized by the low level of the both intensity and current. With solidification, we detect a different manner of increase of a current and diffracted signal. For the integrated intensity (black curve, Figure 9.3) over a long time scale, a monotone linear increase until the saturation plateau for the final solid film is observed. In contrast, a current increase is
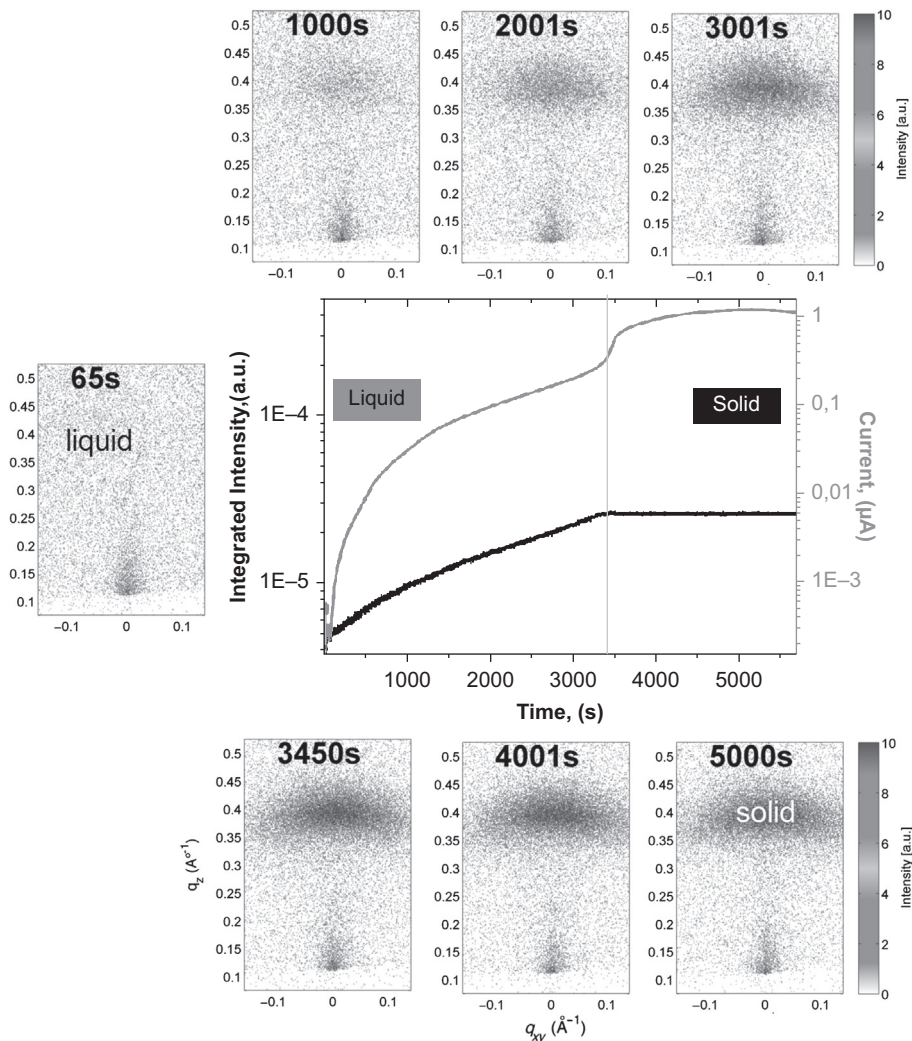
Figure 9.3 Time-resolved correlation of the structural and electrical properties for P3HT film: 2D patterns are single snapshots of the different stages of solidification, the black and gray line profiles show the integrated signal of the most intense structural peak and electrical response of the system, respectively.

more complex (gray curve, Figure 9.3) and can be separated into different stages: initial strong enhancement until 1000 s, then similar to the structure nearly linear increase to 3450 s, and afterwards, a strong nonlinear increase during the next 100 s until 3550 s followed by the final saturation level. For the sake of simplicity, the solidification process is schematically separated on liquid/wet and solid/dry stages by the gray vertical line in Figure 9.3.

To show a general applicability of the described direct correlation approach, the next example is demonstrated on a conjugated thiophene-based oligomer system, namely, α-substituted quinquethiophene (5T) synthesized by Kumada reaction as described elsewhere (Ponomarenko & Kirchmeyer, 2003). From a huge variety of the oligomer family, hex-5T-hex oligomer is chosen for comparison because of similarity to P3HT main ingredients, namely, being composed from the same thiophene rings (five in a total) and hexyl side chain ending groups (two in a total). Comparable to other oligothiophenes, a main feature of the crystal structure is the herringbone packing of the molecules precisely determined for α-substituted quaterthiophene thin films (Moret et al., 2005).

Because hex-5T-hex reduced solubility for time-resolved studies, 0.3 mg/mL 5T solution in toluene was used. Similar to P3HT, three droplets in a total amount of about 100 μm were deposited in the middle of a 1-mm channel. Herein we focus on the most intense structural signal, which is similar to P3HT and is mainly distributed along an out-of-plane direction. The maximum of intensity in centred at $q_z = 0.19$ Å^{-1}, which corresponds with the whole length of hex-5T-hex oligomer (33 Å). Figure 9.4 demonstrates a direct monitoring of the structural development and electrical response of 5T oligomer system during the solidification process. Six 2D snapshots have been chosen schematically to illustrate the essential stages of the structural development from initial solution to final solid state. Interestingly, in the solid-phase diffraction patterns a second peak is revealed at the higher q-values (bottom 2D patterns, Figure 9.4). This second peak is an influence on the scattering pattern of thin film because of the total substrate reflection and refraction at the grazing X-ray geometry (Breiby, Bunk, Andreasen, Lemked, & Nielsen, 2008). For X-ray−integrated intensity later, only the first, most intense peak will be taken into account.

The second deposition was done at 820 s and the liquid phase is illustrated at 901 s in the upper-left snapshot in Figure 9.4. Already in the rather short time of 60 s, one can see a weak intensity peak at $q_z = 0.19$ Å^{-1} position. This peak develops faster within the next 20 s, shown in the snapshot at 981 s. Afterwards, structural development is rather slow with overall further monotone increase of intensity. Interestingly, there is a weak hump at the moment 1100 s followed by final solidification of the film (similar 2D patterns at 1101 s and 1121 s, in Figure 9.4). Line profiles in Figure 9.4 demonstrate a direct correlation between structure (black curve) and current (gray curve) correlation. Because of the rather highly intense hex-5T-hex spot a rectangular area ($\Delta q_z = 0.005$ Å^{-1} and $\Delta q_{x,y} = 0.075$ Å^{-1} along out-of- and in-plane directions, respectively) was chosen for integration. In contrast to the P3HT example of initial deposition on the bare testbed, for hex-5T-hex it is demonstrated a second deposition process. Therefore, for both the current and structure, initial constant level is observed. Upon deposition of solution, these initial films are rapidly dissolved causing reduction of the scattered intensity and decrease of the electrical response. Two gray vertical lines schematically separate liquid and solid regions. Having, generally, similar structural and electrical features in the first solid phase and, afterwards, in the main part of the liquid phase, one can see a dramatic difference in the final part of the liquid phase and followed the solid phase. We detect a pronounced delay of about 120 s between maxima of the structure and electrical response. Despite this delay there are similar
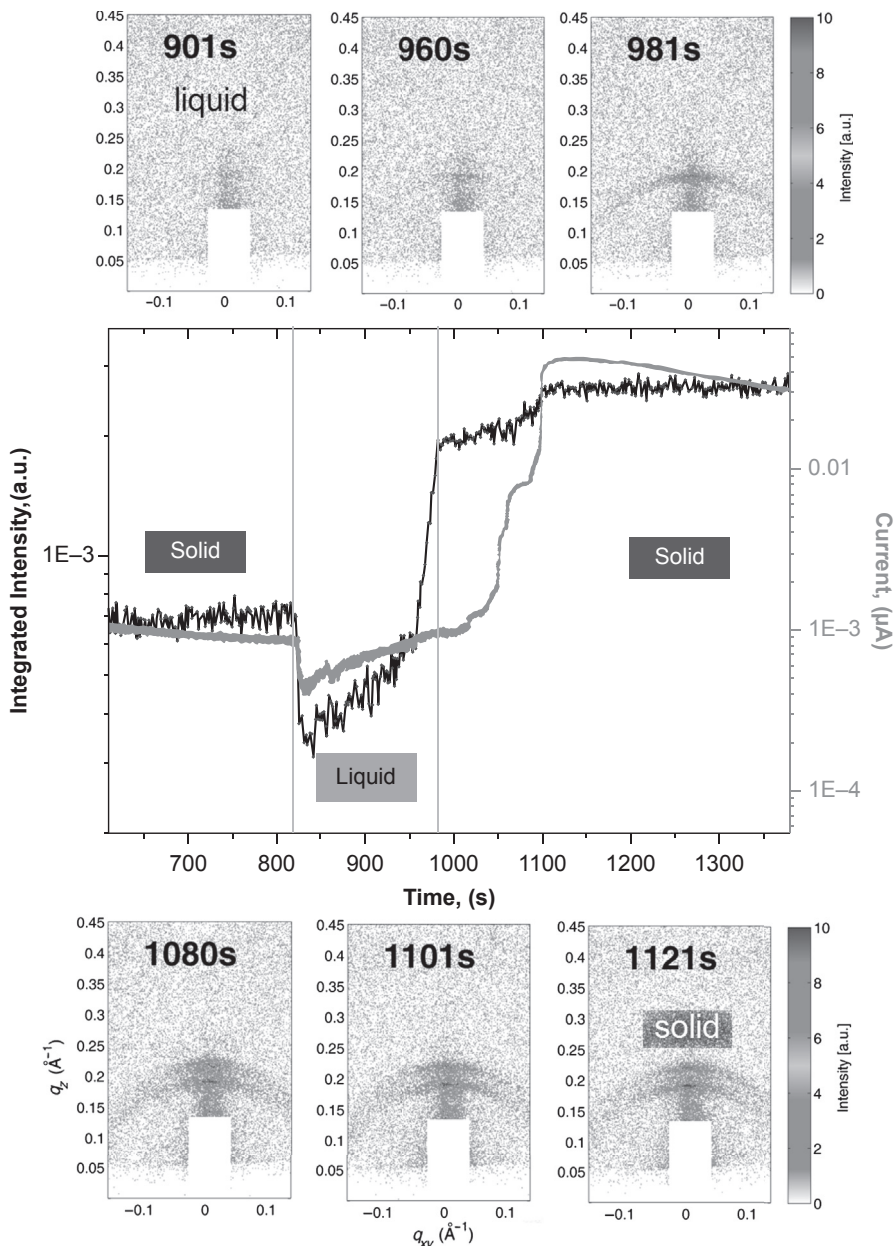
Figure 9.4 Time-resolved correlation of the structural and electrical properties for hex-5T-hex film: 2D patterns are single snapshots of the different stages of solidification, the black and gray line profiles show the integrated signal of the most intense structural peak and electrical response of the system, respectively.

features of the rapid improvement within 20—50 s of both the structure and the current (see Figure 9.4). Interestingly, at the last stage of solidification, a nearly simultaneous final increase of current and structure is observed at the 1101 s, followed by plateaux of intensity and saturation for the current (black and gray curves in Figure 9.4, respectively) afterwards.

9.5   Conclusions

Combined *in situ* GIXD and electrical studies demonstrate a unique opportunity of direct monitoring of the structural and electrical enhancement of the conducting organic systems. These measurements allow reconstructing a complete history of film fabrication enabling direct control of the particular properties of organic devices. Polymer and oligomer networks composed from the same ingredients (thiophene rings and hexyl side chains) show complex solidification behavior. In both cases, we detected a pronounced delay between the maximum conductivity and the highest level of X-ray intensity. Despite this delay, oligomer systems show similar features of the structural transitions and electrical response in which enhancement of the structural and electrical properties is caused by a growth of the crystalline domains. The 5T oligomers are highly crystalline and the saturation in the final stage of solidification process is dominated by formation of the hard grain boundaries. For P3HT polymer, being semicrystalline with domination of amorphous matrix nonlinear current response is observed with monotone structural enhancement, indicating that overall the interconnecting network play a key role for charge transport. *In situ* studies enable a direct correlation of the structural and electrical properties and opens the possibility for a rational design strategy of future devices for organic electronics.

Acknowledgements

References

Ali, K., Pietsch, U., & Grigorian, S. (2013). Enhancement of field-effect mobility due to structural ordering in poly(3-hexylthiophene) films by the dip-coating technique. *Journal of Applied Crystallography, 46*, 908—911.

Bao, Z., & Locklin, J. (Eds.). (2007). *Organic field-effect transistors*. Boca Raton, FL: CRC Press.

Breiby, D. W., Bunk, O., Andreasen, J. W., Lemked, H. T., & Nielsen, M. M. (2008). Simulating X-ray diffraction of textured films. *Journal of Applied Crystallography, 41*, 262−271.

Brinkmann, M., & Rannou, P. (2009). Molecular weight dependence of chain packing and semicrystalline structure in oriented films of regioregular poly(3-hexylthiophene) revealed by high-resolution transmission electron microscopy. *Macromolecules, 42*, 1125−1130.

Dosch, H. (1992). Critical phenomena at surfaces and Interfaces: evanescent X-ray and neutron scattering. In G. Hohler (Ed.), *Springer tracts in modern physics* (Vol. 126). Berlin: Springer-Verlag.

Grigorian, S., Tranchida, D., Ksenzov, D., Schäfers, F., Schönherr, H., & Pietsch, U. (2011). Structural and morphological changes of P3HT films in the planar geometry of an OFET device under an applied electric field. *European Polymer Journal, 47*, 2189−2196.

Grodd, L., Pietsch, U., & Grigorian, S. (2012). Direct correlation between electric and structural properties during solidification of poly(3-hexylthiophene) drop cast films. *Macromolecular Rapid Communications, 33*, 1765−1769.

Hauch, J. A., Schilinsky, P., Choulis, S. A., Childers, R., Biele, M., & Brabec, C. J. (2008). Flexible organic P3HT: PCBM bulk-heterojunction modules with more than 1 year outdoor lifetime. *Solar Energy Materials and Solar Cells, 92*, 727−731.

Joshi, S., Pingel, P., Grigorian, S., Panzner, T., Pietsch, U., Neher, D., et al. (2009). Bimodal temperature behavior of structure and mobility in high molecular weight P3HT thin films. *Macromolecules, 42*, 4651−4660.

Karagiannidis, P. G., Kassavetis, S., Pitsalidis, C., & Logothetidis, S. (2011). Thermal annealing effect on the nanomechanical properties and structure of P3HT: PCBM thin films. *Thin Solid Films, 519*, 4105−4109.

Kim, Y., Cook, S., Tuladhar, M. S., Choulis, S. A., Nelson, J., Durrant, J. R., et al. (2006a). A strong regioregularity effect in self-organizing conjugated polymer films and high-efficiency polythiophene: fullerene solar cells. *Nature Materials, 5*, 197−203.

Kim, D. H., Jang, Y., Park, Y. D., & Cho, K. (2006b). Layered molecular ordering of self-organized poly(3-hexylthiophene) thin films on hydrophobized surfaces. *Macromolecules, 39*, 5843−5847.

Kim, D. H., Park, Y. D., Jang, Y., Yang, H., Kim, Y. H., Han, J. I., et al. (2005). Enhancement of field-effect mobility due to surface-mediated molecular ordering in regioregular polythiophene thin film transistors. *Advanced Functional Materials, 15*, 77−82.

Klauk, H. (Ed.). (2006). *Organic electronics − materials*. Weinheim: Manufacturing and Applications Wiley-VCH.

Kline, R. J., McGehee, M. D., Kadnikova, E. N., Liu, J., Frechet, J. M. J., & Toney, M. F. (2005). Dependence of regioregular poly(3-hexylthiophene) film morphology and field-effect mobility on molecular weight. *Macromolecules, 38*, 3312−3319.

Lilliu, S., Agostinelli, T., Pires, E., Hampton, M., Nelson, J., & Macdonald, J. E. (2011). Dynamics of crystallization and Disorder during annealing of P3HT/PCBM bulk Heterojunctions. *Macromolecules, 44*, 2725−2734.

Moret, M., Campione, M., Borghesi, A., Miozzo, L., Sassella, A., Trabattoni, S., et al. (2005). Structural characterisation of single crystals and thin films of a,v-dihexylquaterthiophene. *Journal of Materials Chemistry, 15*, 2444−2449.

Padinger, F., Rittberger, R. S., & Sariciftci, N. S. (2003). Effects of postproduction treatment on plastic solar cells. *Advanced Functional Materials, 13*, 85−88.

Ponomarenko, S., & Kirchmeyer, S. (2003). Synthesis and thermal behaviour of α,α'-didecyloligothiophenes. *Journal of Materials Chemistry, 13*(2), 197−202.

Prosa, T., Winokur, M., Moulton, J., Smith, P., & Heeger, A. (1992). X-ray structural studies of poly (3-alkylthiophenes): an example of an inverse comb. *Macromolecules, 25*, 4364−4372.

Reyes Reyes, M., Kim, K., & Carroll, D. L. (2005). "High-efficiency photovoltaic devices based on annealed poly(3-hexylthiophene) and 1-(3-methoxycarbonyl)-propyl-1- phenyl- blends. *Applied Physics Letters, 87*, 08350−08353.

Salleo, A., Kline, R. J., DeLongchamp, D. M., & Chabinyc, M. L. (2010). Microstructural characterization and charge transport in thin films of conjugated polymers. *Advanced Materials, 22*, 3812−3838.

Sanyal, M., Schmidt-Hansberg, B., Klein, M. F. G., Colsmann, A., Munuera, C., Vorobiev, A., et al. (2011). In situ X-Ray study of drying-temperature influence on the structural evolution of bulk-heterojunction polymer-fullerene solar cells processed by doctor-blading. *Advanced Energy Materials, 1*, 363−367.

Schmidt-Hansberg, B., Klein, M. F. G., Sanyal, M., Buss, F., de Medeiros, G. Q. G., et al. (2012). Structure formation in low-bandgap polymer: fullerene solar cell blends in the course of solvent evaporation. *Macromolecules, 45*, 7948−7955.

Sirringhaus, H., Brown, P. J., Friend, R. H., Nielsen, M. M., Bechgaard, K., Langeveld-Voss, B. M. W., et al. (1999). Two-dimensional charge transport in self-organized, high-mobility conjugated polymers. *Nature, 401*, 685−688.

Werzer, O., Matoy, K., Strohriegl, P., & Resel, R. (2007). Temperature treatment of semi-conducting polymers: an X-ray reflectivity study. *Thin Solid Films, 515*, 5601−5605.

Zen, A., Pflaum, J., Hirschmann, S., Zhuang, W., Jaiser, F., Asawapirom, U., et al. (2004). Effect of molecular weight and annealing of poly(3-hexylthiophene)s on the performance of organic field-effect transistors. *Advanced Functional Materials, 14*, 757−764.

Zen, A., Saphiannikova, M., Neher, D., Grenzer, J., Grigorian, S., Pietsch, U., et al. (2006). Effect of molecular weight on the structure and crystallinity of poly(3-hexylthiophene). *Macromolecules, 39*, 2162−2171.

In-line monitoring and quality control of flexible organic electronic materials

A. Laskarakis, S. Logothetidis
Aristotle University of Thessaloniki, Thessaloniki, Greece

10.1 Introduction

In recent years, there has been a tremendous effort in the science and technology of organic-based electronic devices fabricated to either glass or flexible polymer substrates, such as polyethylene terephthalate (PET) or polyethylene naphthalate (PEN). This effort led to the rapidly emerging sector of organic electronics (OE), which is expected to revolutionize several aspects of our lives (Cavallini, Facchini, Massi, & Biscarini, 2004; Kopola et al., 2011; Krebs, 2009a; Laskarakis & Logothetidis, 2007; de Leeuw & Cantatore, 2008; Logothetidis & Laskarakis, 2009a). The main novel applications of organic electronics have expanded beyond conventional silicon and include organic photovoltaic cells (OPVs), organic light emitting diodes (OLEDs) for display and lighting, organic thin film transistors (OTFTs), thin film batteries, organic chemical and biological sensors, to name but a few (Cavallini et al., 2004; Kopola et al., 2011; Krebs, 2009a; Kumar & Chand, 2011; de Leeuw & Cantatore, 2008). In addition, OE devices are expected to appear in several industrial and consumer sectors, that include informatics, automotives, architecture, building construction, health care, security, textiles and wearable electronics, by entirely new design concepts since the flexible OE devices can be adapted to follow complex surface shapes (Cavallini et al., 2004; Kopola et al., 2011; Krebs, 2009a; de Leeuw & Cantatore, 2008; White Paper OE-A Roadmap, 2011).

The OE devices offer an attractive balance between cost and performance, complemented by versatility and functionality. These benefits originate from the deposition of organic semiconducting materials by solution-based methods onto flexible polymer substrates, the mechanical flexibility of the device, the ability to be rolled when the device is not used, and the lightweight and conformable design. These advantages make these devices most attractive for large-scale as well as for mobile applications.

Each OE device consists of a multilayer stack that includes thin films of organic semiconductors (small molecules, polymers) with sufficient electrical conductivity, transparent electrodes for charge transport, encapsulation materials for the protection of the sensitive device materials from atmospheric gas permeation, and finally the substrates, onto which the device is fabricated, such as flexible polymer sheets

(PET, PEN) and glass substrates (Laskarakis & Logothetidis, 2006; Laskarakis & Logothetidis, 2007; Laskarakis, Logothetidis, Kassavetis, & Papaioannou, 2008). The performance, efficiency, and lifetime of these devices are defined by the physical (optical, electrical, structural, mechanical) properties and the nanoscale morphology of the above materials. These should meet specific and advanced requirements, such as high optical transparency, sufficient electrical conductivity, structural stability, ultra-low atmospheric gas permeability, film−substrate adhesion, etc.

In addition, the fabrication methods of OEs presently employed mainly in laboratory or pilot-scale facilities include the spin-coating or drop-casting methods. These methods offer the advantages of low-cost fabrication and allow the demonstration of very good device performance (Azarova et al., 2010; Park, Mourey, Subramanian, Anthony, & Jackson, 2008; Smith et al., 2012). The disadvantage of these methods is that they are not compatible with large-area manufacturing, and therefore they have a low potential for upscaling to industrial scale. New methods have emerged that meet the requirements for large-area manufacturing and at the same time maintain the cost-efficient capability for this technology. These methods include inkjet, gravure, and screen printing, doctor blading, and they can deliver fast deposition over large areas. The large-area manufacturing instrumentation consists of modular roll-to-roll (r2r) process line in which the flexible polymer substrate starts from the unwinding roll (starting roll), passes from the individual process steps (e.g., pretreatment, printing, curing, patterning, encapsulation), and ends at the winding roll (end roll) (Galagan et al., 2011; Kumar & Chand, 2011).

One of the most crucial steps of r2r production processes is the *in situ* quality control that will provide robust information on the printed film quality and will ensure the process stability and reproducibility (Heymann, Mirschel, Scherzer, & Buchmeiser, 2009; Logothetidis, Georgiou, Laskarakis, Koidis, & Kalfagiannis, 2013a; Madsen et al., 2011; Schmidt-Hansberg et al., 2009). That is, since the functionality of the printed films is significantly affected by their composition and thickness. These are controlled by the r2r process experimental parameters such as rolling speed, the curing temperature, and the material viscosity. The nonoptimal process optimization leads to fluctuations in microstructure and thickness during the printing process, and consequently to devices with nonreproducible functionality.

The major factors that affect the functionality of the printed films are the uniformity of composition and thickness (Logothetidis & Laskarakis, 2009a). These are controlled by the r2r process experimental parameters such as rolling speed, the curing temperature, and the material viscosity (Koidis, Logothetidis, Ioakeimidis, Laskarakis, & Kapnopoulos, 2013; Koidis et al., 2013b). The nonoptimal process optimization leads to fluctuations in microstructure and thickness during the printing process, and consequently to devices with nonreproducible functionality. Therefore, one of the most crucial steps of r2r production processes is the *in situ* quality control that will provide robust information on the printed film quality and will ensure the process stability and reproducibility (Logothetidis et al., 2013a).

In this chapter, we will discuss the latest advances of the implementation of in-line optical technique (spectroscopic ellipsometry) for the optical characterization of state-of-the-art nanomaterials (inorganic and organic barrier layers, transparent electrodes,

and organic semiconductors) by r2r gravure printing onto flexible polymer substrates. Gravure is a typical rotary printing method where ink is transferred from a physical printing form in a high-speed and high-throughput process; it is considered to be one of the most reliable techniques for the low-cost formation of patterned nanolayers suitable for a successful high-volume manufacturing of flexible OE devices, such as OPVs (Cheng, Yang, & Hsu, 2009; Galagan et al., 2011; Koidis et al., 2013; Lo et al., 2009; Noh et al., 2010). These will prove the potentiality of SE for implementation to (1) laboratory-scale processes as an important research tool that will contribute to the understanding and the optimization of the materials properties, and (2) industrial-scale processes as a powerful quality control tool for the r2r fabrication of flexible organic electronic devices.

10.2 Fundamentals of spectroscopic ellipsometry

10.2.1 Basic principles

Spectroscopic ellipsometry (SE) is a powerful, nondestructive and surface sensitive optical technique that has been extensively used for the investigation of optical vibrational, structural, and morphological properties; the composition and the growth mechanisms of inorganic and organic bulk materials; and thin films (Azzam & Bashara, 1977; Irene & Tompkins, 2005; Logothetidis, 2001). Its capabilities for *in situ* and real-time monitoring have been proved by the several published works that report on its combination with vacuum deposition processes for the *in situ* and real-time investigation of the optical properties, thickness, and growth mechanisms of vacuum-deposited thin films (An, 1998; Collins et al., 2000; Gioti et al., 2000; Kechagias, Gioti, Logothetidis, Benferhat, & Teer, 2000; Laskarakis, Kassavetis, Gravalidis, & Logothetidis, 2010; Logothetidis, 2001; Logothetidis, Laskarakis, Gika, & Patsalas, 2002). SE determines the optical and electronic properties of bulk materials and thin films as a function of the photon energy ω. The measured properties are the complex refractive index $\tilde{n}(\omega)$ and the complex dielectric function $\tilde{\varepsilon}(\omega)$ given by the following relations (Azzam & Bashara, 1977; Irene & Tompkins, 2005; Logothetidis, 2001):

$$\tilde{n}(\omega) = n(\omega) + ik(\omega) \tag{10.1}$$

$$\tilde{\varepsilon}(\omega) = \varepsilon_1(\omega) + i\varepsilon_2(\omega) \equiv n^2(\omega) = (n + ik)^2 \Rightarrow \begin{cases} \varepsilon_1 = n^2 - k^2 \\ \varepsilon_2 = 2nk \end{cases} \tag{10.2}$$

When the electromagnetic wave is reflected by the material smooth surface (see Figure 10.1), the polarization of the outgoing wave can be represented as:

$$\overrightarrow{E}_r = \left(\tilde{r}_p \overrightarrow{E}_{0x}\hat{x} + \tilde{r}_s \overrightarrow{E}_{0y}\hat{y} \right) \tag{10.3}$$
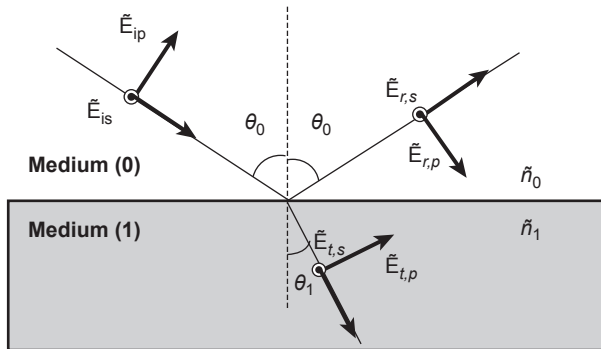
Figure 10.1 Oblique reflection and transmission of a plane electromagnetic wave at the sharp interface between two media (0) and (1) with refractive indexes n_0 and n_1, respectively. The electric field components E_p and E_s parallel -p and perpendicular -s to the plane of incidence, and the wave vector for the incident (i), reflected (r), and transmitted (t) waves are shown. θ_0 and θ_1 are the angles of incidence and refraction.

By using this formulation, the interaction of the electromagnetic wave with the material is described by the two complex Fresnel reflection coefficients $\tilde{r}_p$ and $\tilde{r}_s$. These reflection coefficients describe the influence of the material on the electric field components; the p- and s- refer to the plane of incidence and characterize the interface between two media (e.g., the ambient−medium 0, and the material studied−medium 1), and are given by the expressions (Azzam & Bashara, 1977; Irene and Tompkins, 2005):

$$\tilde{r}_p = \frac{\tilde{E}_{r,p}}{\tilde{E}_{i,p}} = \frac{|\tilde{E}_{r,p}|e^{i\theta_{r,p}}}{|\tilde{E}_{i,p}|e^{i\theta_{i,p}}} = \frac{|\tilde{E}_{r,p}|}{|\tilde{E}_{i,p}|}e^{i(\theta_{r,p}-\theta_{i,p})} = |\tilde{r}_p|e^{i\delta_p} \tag{10.4}$$

$$\tilde{r}_s = \frac{\tilde{E}_{r,s}}{\tilde{E}_{i,s}} = \frac{|\tilde{E}_{r,s}|e^{i\theta_{r,s}}}{|\tilde{E}_{i,s}|e^{i\theta_{i,s}}} = \frac{|\tilde{E}_{r,s}|}{|\tilde{E}_{i,s}|}e^{i(\theta_{r,s}-\theta_{i,s})} = |\tilde{r}_s|e^{i\delta_s} \tag{10.5}$$

The Fresnel reflection coefficients in the interface between two media, e.g., medium (0) and medium (1) in Figure 10.1, with refractive index $\tilde{n}_0$ and $\tilde{n}_1$, respectively, are given by the following expressions (Azzam & Bashara, 1977; Irene & Tompkins, 2005):

$$\tilde{r}_{01,p} = \frac{\tilde{n}_1 \cos\theta_0 - \tilde{n}_0 \cos\theta_1}{\tilde{n}_1 \cos\theta_0 + \tilde{n}_0 \cos\theta_1} \tag{10.6}$$

$$\tilde{r}_{01,s} = \frac{\tilde{n}_0 \cos\theta_0 - \tilde{n}_1 \cos\theta_1}{\tilde{n}_0 \cos\theta_0 + \tilde{n}_1 \cos\theta_1} \tag{10.7}$$

where the incident θ_0 and refracted θ_1 angles are related by the Snell law $\tilde{n}_1 \sin\theta_0 = \tilde{n}_1 \sin\theta_1$. When the light beam does not penetrate the medium (1), either

due to its high absorption coefficient or its infinite thickness, as shown in Figure 10.1, we are referred to a two-phase (ambient-substrate) system or a bulk material surrounding by medium (0). In this case the ratio of the $-p$ to $-s$ Fresnel reflection coefficients, namely the complex reflection ratio, is the quantity measured directly by SE, and it is given by the following expression that characterizes any bulk material (Azzam & Bashara, 1977; Irene and Tompkins, 2005):

$$\tilde{\rho} = \frac{\tilde{r}_p}{\tilde{r}_s} = \left|\frac{\tilde{r}_p}{\tilde{r}_s}\right| e^{i(\delta_p - \delta_s)} = \tan \Psi e^{i\Delta} \tag{10.8}$$

In this expression Ψ and Δ are the ellipsometric angles, and for a bulk material take values $0° < \Psi < 45$ and $0° < \Delta < 180°$. From an SE measurement the complex reflection ratio $\tilde{\rho}$ is estimated, through the calculation of amplitude ratio $\tan \Psi$ and the phase difference Δ. From these two quantities one can extract all the other optical constants of the material. For example, the complex dielectric function of a bulk material with smooth surfaces is directly calculated by the following expression (Azzam & Bashara, 1977; Irene and Tompkins, 2005):

$$\tilde{\varepsilon}(\omega) = \varepsilon_1 + i\varepsilon_2 = \tilde{\varepsilon}_0 \sin^2 \theta \left\{ 1 + \left[\frac{1 - \rho}{1 + \rho}\right]^2 \tan^2 \theta \right\} \tag{10.9}$$

where θ is the angle of incidence of the beam and $\tilde{\varepsilon}_0$ is the dielectric constant of the ambient medium (for the case of air $\tilde{\varepsilon}_0 = \tilde{n}_0 = 1$).

Although some information on the optical properties can be deduced directly from the SE measurements, quantitative data can be derived from theoretical modeling. This procedure includes the formulation of a theoretical model (which approximates the film architecture and structure of the studied material) and the fitting of the measured $< \tilde{\varepsilon}(\omega) >$ to this model by using the desired parameters as variables in the numerical analysis. The optical and electronic response of the thin films can be deduced by the parameterization of the measured $<\varepsilon(\omega)>$ by the use of appropriate theoretical models. These models include, for example, the damped harmonic oscillator (Lorenz model) and the Tauc−Lorentz (TL) model, which calculates the fundamental optical gap ω_g. This model is described by the following expressions (Jellison, 1998; Jellison & Modine, 1996):

$$\varepsilon_2(\omega) = \frac{A\omega_o C(\omega - \omega_g)^2}{(\omega^2 - \omega_o^2)^2 + C\omega^2} \frac{1}{\omega}, \quad \omega > \omega_g$$

$$\varepsilon_2(\omega) = 0, \quad \omega \leq \omega_g \tag{10.10}$$

$$\varepsilon_1(\omega) = \varepsilon_\infty + \frac{2}{\pi} P \int_{\omega_g}^{\infty} \frac{\xi \varepsilon_2(\xi)}{\xi^2 - \omega^2} d\xi \tag{10.11}$$

In the TL model, the imaginary part $\varepsilon_2(\omega)$ of the dielectric function is determined by multiplying the Tauc joint density of states by $\varepsilon_2(\omega)$ obtained from the Lorentz oscillator model. The $\varepsilon_1(\omega)$ is determined by the $\varepsilon_2(\omega)$ through the Kramers−Kronig integration. Thus, the TL model provides the ability to determine the energy position of the fundamental gap ω_g, the electronic transition energy ω_0, the broadening C, and the strength A of each oscillator. The energy position ω_0 of the TL model corresponds to the Penn gap where the strong absorption in a material takes place. The $\varepsilon_1(\infty)$ parameter is a constant term that accounts for the existence of electronic transitions above the measured energy region. Although the expressions of $\varepsilon_1(\omega)$ and $\varepsilon_2(\omega)$ in the TL model are empirical, this model can describe and predict the dielectric response and the optical properties of amorphous and crystalline films, since it satisfies the major criteria for models of dielectric functions and it is consistent with known physical phenomena. Finally, the extraction of the best-fit parameter from the analysis of the above described model has been performed using a regression process by the application of a nonlinear Levenberg−Marquardt minimization algorithm (Irene & Tompkins, 2005; Logothetidis, 2001).

10.2.2   Latest advances of in-line SE

Several published studies (Georgiou, Laskarakis, Koidis, Goktsis, & Logothetidis, 2008; Georgiou, Logothetidis, Koidis, & Laskarakis, 2008; Gravalidis, Gioti, Laskarakis, & Logothetidis, 2004; Koidis, Logothetidis, Georgiou, & Laskarakis, 2008; Laskarakis, Kassavetis, et al., 2010; Laskarakis, Georgiou, & Logothetidis, 2010) have reported the adaptation of SE units onto vacuum chambers for the *in situ* and real-time investigation of the optical properties of different inorganic and organic nanomaterials during their deposition by magnetron sputtering or evaporation methods. This methodology can provide information on the growth mechanisms and the deposition rate of the studied nanomaterials and the effect of the experimental parameters on the nanomaterials structure. Figure 10.2 shows a representative experimental setup of an ultra-high vacuum (UHV) deposition chamber with adapted two SE units by suitable optical ports. This specific experimental setup includes a Fourier transform infrared spectroscopic ellipsometer working in the wave number region of 900−4000/cm that can provide information on the bonding structure, and an ultrafast phase modulated multiwavelength spectroscopic ellipsometer working at the 1.5−6.5 eV that measures the thickness, optical and electronic properties of the deposited nanomaterials.

In this type of adaptation, the components of the SE units (which include the modulator and analyzer heads) are connected on the chamber wall through the optical ports that are sealed by transparent optical windows (such as BaF_2 windows) in order to maintain the pressure difference between the chamber and the outside environment and to allow the transmittance of the light beam inside and outside of the chamber (Laskarakis, Logothetidis, & Gioti, 2001). This type of adaptation ensures the minimization of possible vibrations of the optical elements, allowing the accurate measurement of the optical properties from the sample surface.
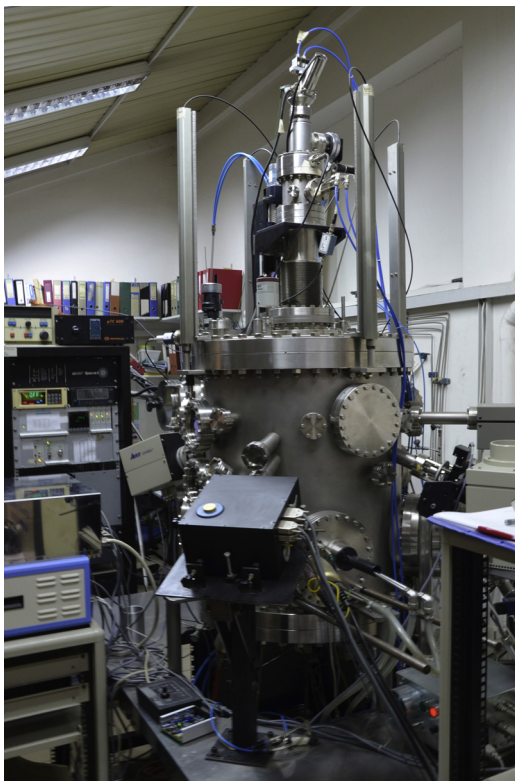
Figure 10.2 Experimental setup of an UHV deposition chamber equipped with two SE units for the *in situ* and real-time investigation of the optical properties of the deposited nanomaterials.

In order to demonstrate the capability of *in situ* and real-time SE for the robust investigation of the nanomaterials properties during their processing, we show in Figure 10.3 the ellipsometric optical density D of a polycarbonate substrate during its surface modification by a N_2 plasma treatment process inside the UHV deposition chamber. The ellipsometric optical density D can provide accurate results on the change of the bonding structure of a nanomaterial by measuring the ellipsometric ratio ρ, which refers to the studied nanomaterial (thin film on top of the substrate) and ρ_s that refers to the nanomaterial before its processing (e.g., bare substrate, or non-processed sample). This is defined by the relation (Laskarakis, Kassavetis, et al., 2010; Drevillon, 1998):

$$D = \ln\left(\frac{\rho_s}{\rho}\right) = \mathrm{id}_{ov}4\pi\omega\varepsilon_0^{1/2}\tan\theta_0\sin\theta_0\frac{\varepsilon_s(1-\varepsilon_0/\varepsilon_{ov})(\varepsilon_s-\varepsilon_{ov})}{(\varepsilon_s-\varepsilon_0)(\varepsilon_s-\varepsilon_0\tan\theta_0)} \qquad (10.12)$$

where d_{ov} is the overlayer thickness, ω is the wave number, θ_0 is the angle of incidence, and ε_0, ε_{ov}, and ε_s are the dielectric functions of ambient, overlayer, substrate. Using this formulation, a new chemical bond in the overlayer can be identified by a maximum of ReD together with a "negative" inflection point (negative slope) in ImD,
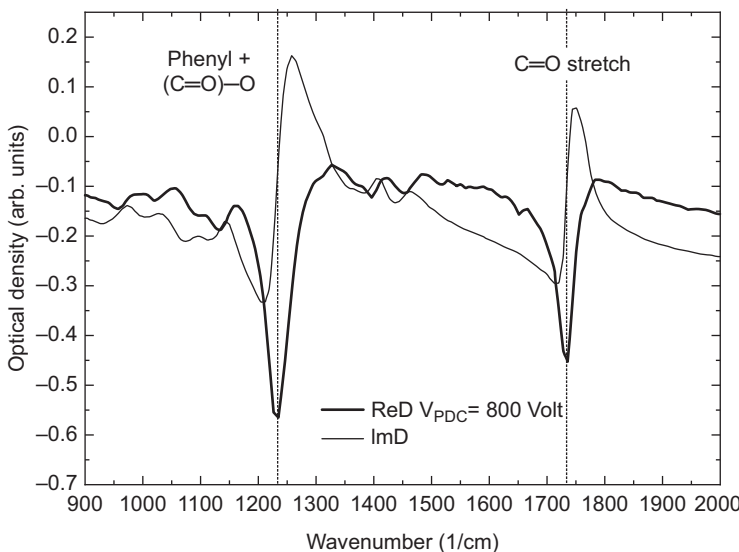
Figure 10.3 Real (ReD) and imaginary (ImD) part of the ellipsometric optical density D of PC that has been subjected to N$_2$ plasma treatment with a pulsed dc voltage of 800 V. Modified after Laskarakis et al. (2010a).

whereas a chemical bond of the polymer disappearing (even partially) from the surface will result in a minimum in ReD and a "positive" inflection point (positive slope) in ImD (Laskarakis, Kassavetis, et al., 2010; Drevillon, 1998).

Figure 10.3 shows the real (ReD) and imaginary (ImD) part of the ellipsometric optical density D of a PC sample during its surface treatment of a N$_2$ plasma by applying a pulsed dc voltage of 800 V. This has been calculated by the *in situ* and real-time optical measurements of the pseudodielectric function $\langle\varepsilon(\omega)\rangle$ of the PC during its processing. We observe that there are significant changes at the bonding structure of the PC. The major changes are the bond break of phenyl $+$ (C=O)$-$ at 1234/cm (attributed to macromolecular chain scissoring) and of C=O of the carbonyl group at 1720/cm. (Laskarakis, Kassavetis, et al., 2010).

However, the adaptation of the modulator and analyzer heads of the SE unit onto a r2r fabrication equipment, which has moving parts (unwinding and winding rolls) and a moving transparent substrate with thickness between 10 and 150 μm, is a challenging task. The main requirement for the achievement of successful optical measurements from the polymer web rolls is the fulfillment of the necessary optical geometry between the optical elements before and after the light reflection on the sample surface and the sample itself. This can only be fulfilled if there are no vibrations from the r2r equipment, and the flexible polymer substrate remains flat and stable during its rolling from the unwinding to the winding roll (independently of the roll speed). In the case that the flexible polymer rolls that are used as substrates are not stretched appropriately, they show a nonplanar surface that wrinkles, resulting from the defocusing of the reflected light beam away from the detection head (Logothetidis et al., 2013b).
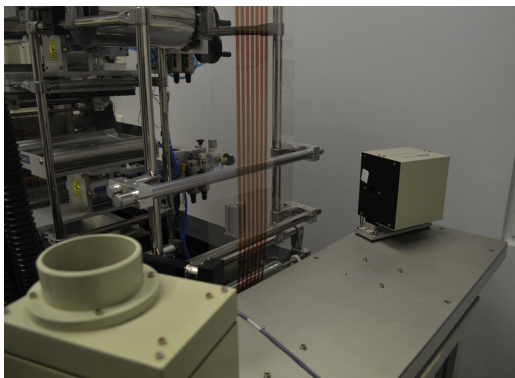
Figure 10.4 Experimental setup of the r2r printing unit onto which the in-line SE unit has been adapted. The plane of incidence of light at the measurement position is perpendicular to the plane of incidence of the polymer substrate roll (Logothetidis et al., 2013b; Logothetidis, 2010; Logothetidis, 2011).

Figure 10.4 shows a representative r2r system on which an in-line SE unit has been adapted. The measurement position is located on a vertical path of the roll direction, between two directional rolls. Between these rolls, the polymer substrate stays absolutely flat and stable, without any wrinkles and tilting vibrations. The SE unit is equipped with an array detector that consists of 32 fiber optics for the simultaneous measurement of $<\varepsilon(\omega)>$ at 32 specific photon energies at the spectral region 3.0−6.5 eV. The integration time (IT), which is the time for the completion of one multiwavelength (MWE) spectrum, can be adjusted at 100 ms. The corresponding sampling time (ST), which is the total time for the recording of one spectrum after the integration of several measurements in order to calculate the final $<\varepsilon(\omega)>$ spectra, should be higher than 100 ms. The foil has been stabilized in order to minimize the measurement artifacts and at the same time to assure the quality of the measurements.

In order to assure that the surface of the moving roll remains flat, stable, and without wrinkles during the rolling, a measurement of the optical and electronic properties of the plain PET roll over its entire length must be performed. In this way, the stability of the measured $<\varepsilon(\omega)>$ as well as the values of the band gap energy and the characteristic electronic transitions of the substrate material will provide information on whether the conditions for accurate optical measurements are fulfilled.

10.3 Characterization of organic electronic nanomaterials

10.3.1 Organic semiconductors

The active organic semiconductors that are used as active layers for OE devices can be divided in two categories: small molecules and polymer materials. The fundamental properties of these materials are similar. However, this differentiation relates to the way these materials are prepared in thin films. Small molecules are typically thermally

evaporated in vacuum and polymers are processed from solution methods. Both material classes have in common the fact that most properties, such as energy gap, solubility, electron affinity, and stability in ambient air, can be tuned by changing their chemical composition. The large number of already available and newly synthesized materials have enabled the findings of some structure−property relationships that are needed for the understanding of conjugated organic materials, and how they can most efficiently be used in OE devices. The detailed knowledge of the optical properties of the organic semiconductors is of significant importance and will enable the optimization of the functionality and performance of the final OE devices.

In the case of the OPV applications, the most widely used photoactive material structures are the bulk heterojunction (BHJ) that is formed by a *p*-type semiconductor (electron donor) with an *n*-type semiconductor (electron acceptor). Polymers are used as electron donors, whereas fullerene derivatives are mainly used as electron acceptors. The most successful OPV active material system consists of the poly(3- hexylthiophene) (P3HT) electron donor and the methanofullerene derivatives (PCBM) as electron acceptor (van Bavel, Sourty, de With, Frolic, & Loos, 2009; Campoy-Quiles et al., 2008; Hoppe & Sariciftci, 2006; Pavlopoulou et al., 2013). A large interfacial area between these two organic semiconductors is required to achieve maximum charge generation. However, the morphology of a BHJ consisting of a binary blend cannot be easily controlled. The formation of the blend film structure is affected by several parameters, such as blend composition, viscosity, solvent evaporation rate, or substrate surface energy, providing difficulties to the achievement of the desired blend morphology for maximum charge generation and transport (Campoy-Quiles et al., 2008; Hoppe & Sariciftci, 2006; Karagiannidis, Georgiou, Pitsalidis, Laskarakis, & Logothetidis, 2011; Pavlopoulou et al., 2013).

The optical properties of P3HT:PCBM blends have been investigated by ex situ SE in a wide spectral region. These studies focused on the contribution of the optical response of the blend components as well as on their vertical distribution in the blend volume. Figure 10.5 shows the experimentally measured $<\varepsilon(\omega)>$ as a function of the photon energy ω of two representative samples: without annealing, and annealed at 140 °C for 30 min. The changes in the measured $<\varepsilon(\omega)>$ are attributed to the effect of the annealing process that modifies the blend morphology and the distribution of the P3HT and PCBM constituents in the blend structure.

In order to obtain quantitative information from the measured $<\varepsilon(\omega)>$ spectra, this has been analyzed by the use of a theoretical model consisting of a multilayer stack of air/P3HT:PCBM/PEDOT:PSS/ITO/glass. For the calculation of the optical response of the P3HT:PCBM blend films and the effect of the postdeposition thermal annealing to the electronic transitions of the P3HT and PCBM, the blend films have been approximated as homogeneous materials. The blend optical response has been modeled by the Tauc−Lorenz oscillator model using five TL oscillators.

Figure 10.6 shows the calculated extinction coefficient (k) of the P3HT:PCBM blend films (as grown and annealed at 140 °C for various annealing times from 3 to 30 min). As can be seen in Figure 10.6, the blends' optical response in the Vis−fUV spectral region includes the appearance of electronic transitions at photon energies of 2.05, 2.24, 3.95, 4.65, and 5.89 eV. The optical absorption at 2.05 eV is
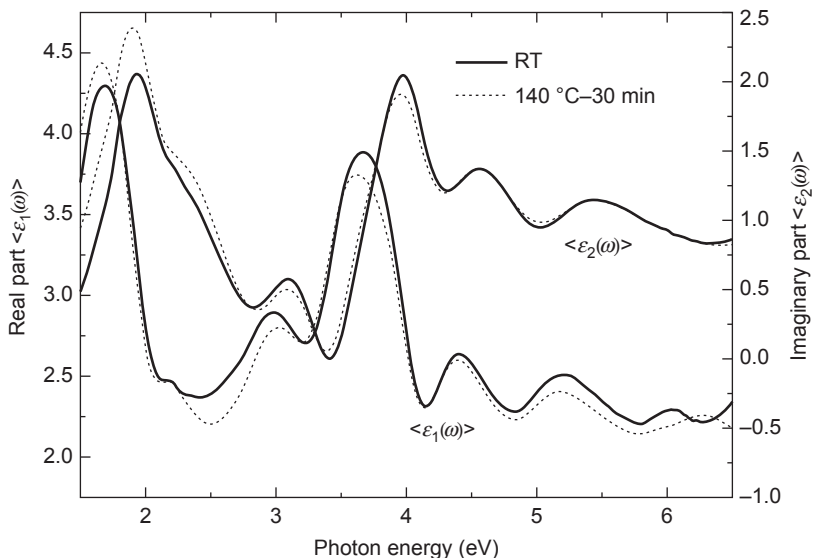
Figure 10.5 Measured pseudodielectric function $\langle\varepsilon(\omega)\rangle$ spectra of two representative P3HT: PCBM thin films; as grown (not annealed) and annealed at 140 °C for 30 min (Logothetidis et al., 2013a).
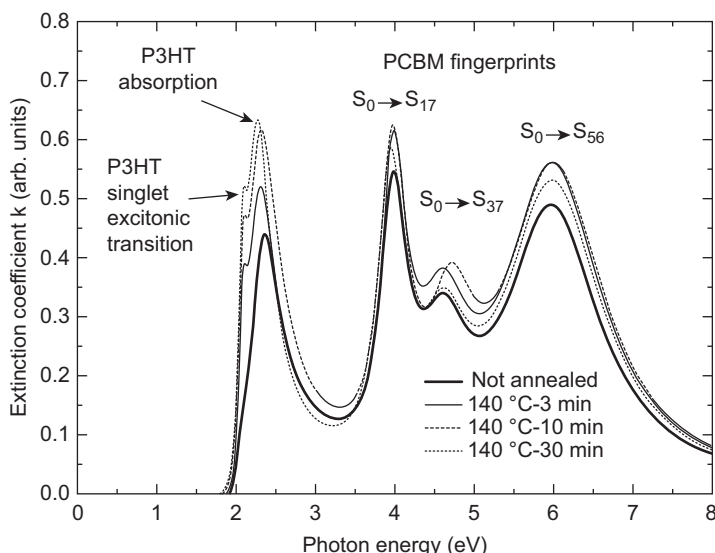
Figure 10.6 Extinction coefficient (k) of P3HT:PCBM after postdeposition thermal annealing at 140 °C for various periods of time based on the best-fit parameters from the analysis of $\langle\varepsilon(\omega)\rangle$ (Karagiannidis et al., 2011).

attributed to the singlet excitonic transition of P3HT, whereas the electronic transition at 2.24 eV corresponds to the formation of excitons with phonons. The electronic transitions at higher energies can be assigned to the electronic transitions $S_0 \rightarrow S_{17}$, $S_0 \rightarrow S_{37}$ and $S_0 \rightarrow S_{56}$, respectively, of PCBM. Another important result is the significant excitonic enhancement of the P3HT oscillator strengths that is observed at the annealed blends. This excitonic enhancement is related to the increase of the P3HT crystallization, which increases the interchain interactions. Indeed, a strong increase of the extinction coefficient from 0.08 to 0.38 at 2.05 eV and from 0.39 to 0.48 at 2.24 eV is observed at the first 3 min of annealing. This indicates that the crystallization process starts rapidly at the first stages of the thermal annealing process. As high-density P3HT crystals start to form, pathways between the polymer crystallites are created that facilitate the diffusion of PCBM molecules. On the other side, only minor changes in the strength of the PCBM absorption peaks are observed.

Besides the above results, there have been several works dealing with the investigation of the optical properties of organic semiconductor blends for different OE applications. However, the robust measurement of the optical properties during the r2r printing of the blend onto flexible polymer substrates can allow the optimization of the experimental conditions and the repeatability of the blend properties and functionality. The experimental parameters as printing speed and drying time are expected to have a remarkable influence on the properties and morphology of the printed P3HT: PCBM films in a continuous r2r gravure process. There have already been some reports on the morphology of sheet-to-sheet gravure printed P3HT:PCBM thin films and on the effect of the process parameters on the morphology, structure, and properties of r2r gravure printed photoactive blends.

Figure 10.7 shows the evolution of the P3HT:PCBM film thickness calculated during the passing of the roll in front of the in-line SE unit. The blend film thickness is ∼77 nm and it is stable over the whole length of the roll (above 9 m). Also, the calculated photon energies of the electronic transitions S_0-S_{37} and S_0-S_{56} at 4.59 and 5.76 eV, respectively, are found to be stable during the r2r printing process. This proves the stability of the gravure printing process and the thickness homogeneity of P3HT:PCBM at the different spots on the PET roll.

10.3.2 *Transparent electrodes*

The electrodes play a major role for the functionality and performance of the OE devices since their role is to collect and transport the charge carriers (electrons, holes) that were formed in the active layer of the device. In the conventional microelectronic devices based on Si technology, the electrodes consist only of metals, such as Al, Ca, etc. However, in the OE devices there are more strict requirements and properties that the electrode materials should fulfill, besides the sufficient electrical conductivity. A major requirement is that the used electrodes should be optically transparent in a wide spectral region. This is of considerable importance, since in the case of OPVs a large number of photons should penetrate the device to reach the photoactive layer in order to enable the generation of electron−hole excitons. Also, in the case of OLED displays
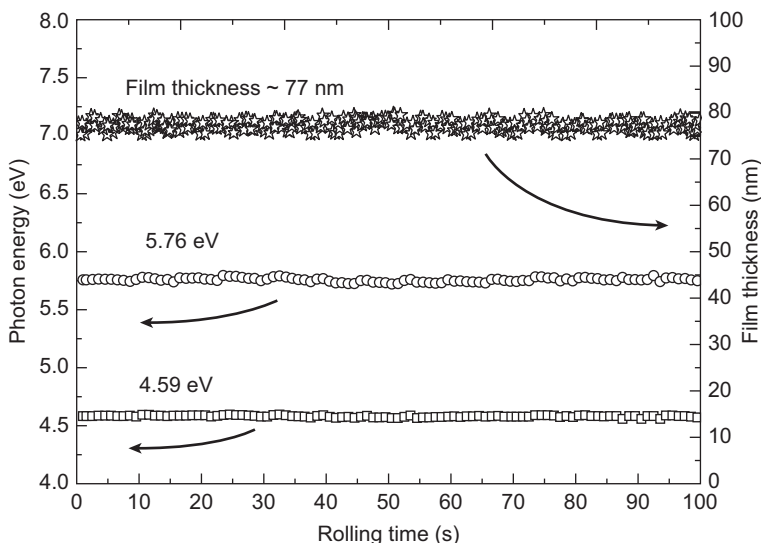
Figure 10.7 Evolution of blend thickness and electronic transitions of blend/PET with the rolling time. The length of the measured blend area is 9 m.
Modified after Logothetidis et al. (2013a).

for lighting and display, the generated photons should be transmitted outside of the device toward the human eye.

One of the most widely used materials as a transparent electrode is indium tin oxide (ITO), which has proven useful for the development of OE devices (Logothetidis & Laskarakis, 2009b). Its advantages include high electrical conductivity, piezoelectricity, easy fabrication, and nontoxicity. However, ITO is a brittle material that cannot be easily implemented as electrodes for flexible OE applications, whereas the low abundance of indium increases the cost of ITO and does not guarantee its commercially viable future. In addition, ITO is reported to diffuse in the photoactive layer and contribute to the degradation of the OPVs (Logothetidis & Laskarakis, 2009b).

There are several alternative materials to replace ITO, such as metal grids, carbon nanotubes, and graphene. One of the most promising materials is poly(3,4-ethylenedioxy-thiophene):poly(styrene-sulfonate) (PEDOT:PSS) that combines metallic-like behavior with sufficient solubility for printing onto large areas. PEDOT:PSS consists of a conducting part, PEDOT, a low-molecular weight polymer, which is insoluble and thus difficult to process, and an insulating polymer, PSS, that is a high-molecular weight polymer that gives the desirable flexibility and solubility in water solutions, making the polymer blend easy to process (Herrmann et al., 2012; Logothetidis & Laskarakis, 2009b; Nardes, Kemerink, & Janssen, 2007). The oligomer PEDOT segments are electrostatically attached on the PSS polymer chains.

The conductivity of PEDOT:PSS depends strongly on its structure and morphology. Pristine PEDOT:PSS yields a conductivity of below 10 S/cm, however,

the addition of solvents (such as ethylene glycol, sorbitol, glycerol, dimethyl-sulfoxide) and postdeposition processing (e.g., annealing) improves its electrical conductivity. Until now, conductivities above 800 S/cm have been reported (Herrmann et al., 2012; Logothetidis & Laskarakis, 2009b; Nardes et al., 2007).

The dielectric function of PEDOT:PSS consists of contributions from the conductive PEDOT and the nonconductive PSS part, at different photon energies. Its optical response in the Vis−UV spectral region includes two electronic absorptions at 5.37 and 6.38 eV that are attributed to the $\pi-\pi^*$ transitions of the benzene rings of the PSS part. Also, the absorbance of the conductive PEDOT part is reported to appear at lower energy values below 1.7 eV. Figure 10.8 shows the measured pseudodielectric function $<\varepsilon(\omega)>$ of PEDOT:PSS measured in-line during the film rolling (points) in comparison with a spectroscopic ex situ measurement (lines) in the energy range 1.5−6.5 eV(Logothetidis et al., 2013a). Although the available spectral region for the in-line measurements is limited to 3−6.5 eV, as can be seen from Figure 10.8, there is excellent agreement between the spectroscopically measured $<\varepsilon(\omega)>$.

The optical response of the PEDOT:PSS includes an absorption in the Vis−UV spectral region between 5.3 and 6.4 eV that can be attributed to the $\pi-\pi^*$ transitions of the benzene rings of the PSS part (Herrmann et al., 2012; Logothetidis & Laskarakis, 2009b; Nardes et al., 2007). Also, the absorbance of the more conductive PEDOT part is reported to appear at lower energy values below 1.7 eV (Koidis et al., 2013b; Koidis et al., 2011). Figure 10.9 shows the bulk dielectric function of PEDOT:PSS in the extended spectral region 0−7 eV that has been calculated by the analysis of the measured $<\varepsilon(\omega)>$.
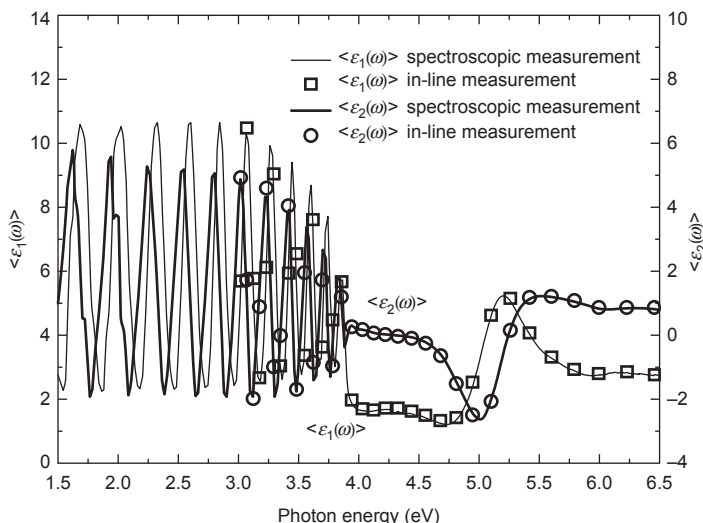
Figure 10.8 Pseudodielectric function of PEDOT:PSS measured in-line during the film rolling (points) in comparison with a spectroscopic ex situ measurement (lines) in the energy range 1.5−6.5 eV. The in-line SE measurement is limited to the spectral region 3−6.5 eV (Logothetidis et al., 2013a).
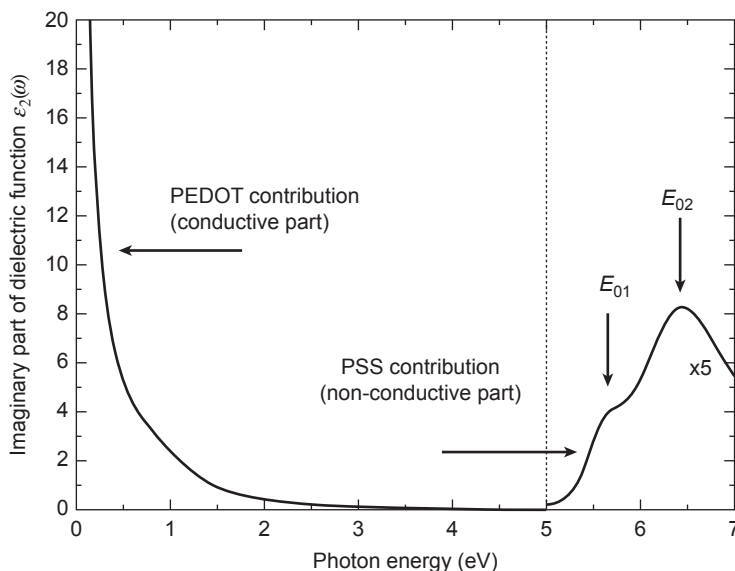
Figure 10.9 Representative bulk dielectric function $\varepsilon(\omega)$ of PEDOT:PSS. The conductive part contributes to the lower energy region, whereas the nonconductive PSS shows two electronic transitions at $\sim$5.5 and $\sim$6.3 eV.

It has to be noted that spin-coated PEDOT:PSS films are reported to show uniaxial optical anisotropy, with the ordinary complex refractive index in the plane of the film and the extraordinary complex refractive index normal to the film and parallel to the optical axis. This is the result of the film's structure that consists of PEDOT-rich flattened lamellas that are vertically segregated by PSS-rich layers. However, the printed PEDOT:PSS films that are described in this chapter are characterized by nondirectional structure, and their optical response can be modeled by the use of an isotropic optical model.

In the other case, the printed PEDOT:PSS films are characterized by an isotropic optical response. The thin film formation of PEDOT:PSS onto flexible polymer substrates by gravure printing is widely used in r2r processes (Kopola et al., 2011; Krebs, 2009b; Kumar & Chand, 2011; Voigt et al., 2011). The most common printing patterns include stripes parallel to the rolling direction in various sizes and distances. The determination of the thickness and the optical properties of the gravure-printed PEDOT:PSS thin films by in-line SE can provide significant insights into the film properties and how these are affected by the experimental parameters (e.g., speed, curing temperature). In addition, in-line SE can serve as a quality control tool that will ensure that the printed PEDOT:PSS films are homogeneous in the whole length of the roll.

For the determination of the optical response of the PEDOT:PSS films, a combination of the Lorentz−Drude model can be applied to provide accurate results. The Lorentz part can describe the electronic transitions at higher energies, whereas the
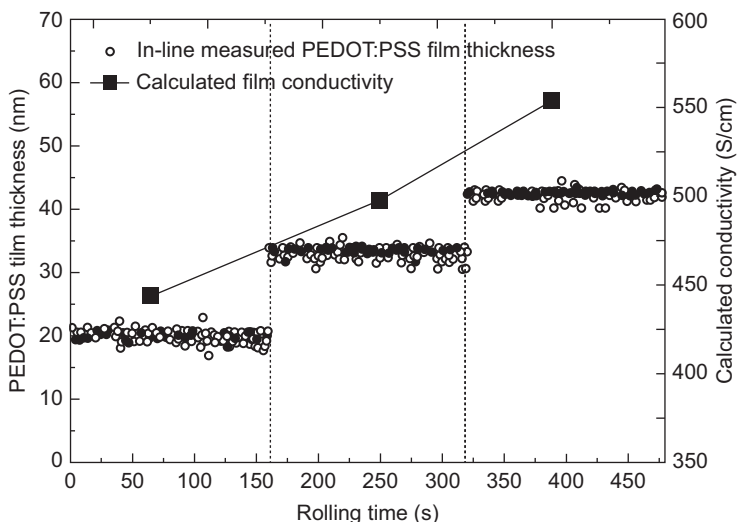
Figure 10.10 Calculated thickness of the PEDOT:PSS film measured in-line during the film gravure printing and calculated conductivity using the parameters from the optical modelling (Logothetidis, 2013a).

Drude model can successfully describe the metallic-like behavior of PEDOT:PSS at the low-photon energies. The optical model for the analysis consists of a multilayer stack of air/PEDOT:PSS/PET. The optical properties of the PEDOT:PSS layer were described by the use of two TL oscillators. These oscillators model the characteristic absorption peaks at ~5.5 and ~6.3 eV that originate from PSS. The reason for the modeling of only these two electronic transitions is that the optical absorptions of the more conductive PEDOT part are reported to appear at lower energy values below 1.7 eV, which is outside of the measured energy region. In addition, the resistivity ρ and the electrical conductivity σ of PEDOT:PSS can be calculated by the combination of the Drude model parameters (the plasma energy ω_p and Drude broadening Γ_D) that can be estimated from the analysis procedure of the measured $<\varepsilon(\omega)>$ (Herrmann et al., 2012; Humlicek et al., 1998; Irene & Tompkins, 2005; Laskarakis, Karagiannidis, Georgiou, Nikolaidou, & Logothetidis, 2013).

Figure 10.10 shows the in-line calculated thickness of the PEDOT:PSS film that has been gravure printed onto PET polymer substrate and its evolution with the rolling time. The PEDOT:PSS film was printed with various thicknesses by changing the web speed during the gravure printing processes. As can be seen, at specific times ($t = 160$ s, $t = 340$ s) the thickness increases from 20 to 34 nm and finally to 41 nm.

The capability for the robust determination of the thickness uniformity of the gravure printed stripes of PEDOT:PSS is shown in Figure 10.11, which shows the in-line calculated thickness of the PEDOT:PSS stripe. The printed stripe was extended onto the PET substrate over a total length of more than 3.5 m, and the rolling speed was 3 m/min. At some points of the strip, some areas were intentionally left uncoated
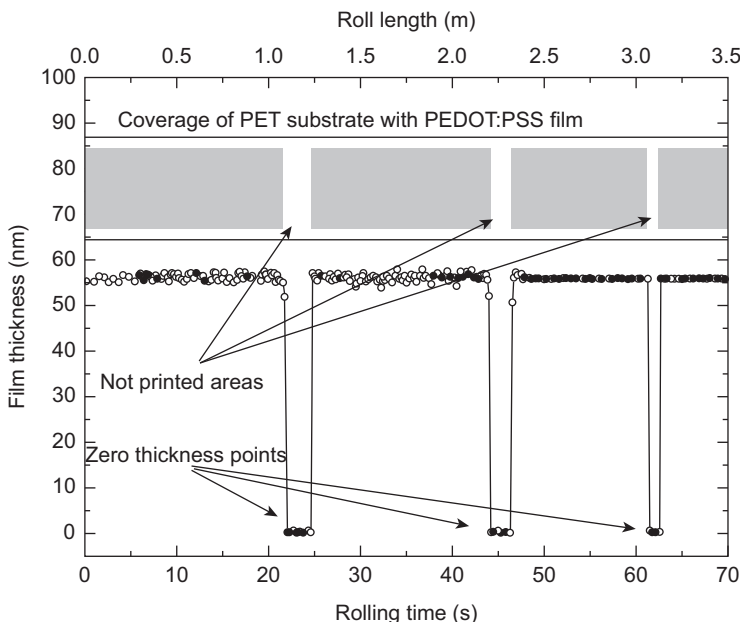
Figure 10.11 Thickness profile of a gravure-printed PEDOT:PSS stripe. The schematic shows the shape of the stripe and the three areas of different sizes where the PET substrate was left intentionally uncoated. The thickness profile immediately characterizes these areas at the zero thickness points (Logothetidis, 2013a).

in order to test the response of the in-line SE to abrupt changes of the thickness. The optical properties of the PEDOT:PSS were modeled by the use of a theoretical model that consists of a multilayer stack of air/PEDOT:PSS/PET. For the description of the film optical properties, we have used the TL oscillator model to approximate the characteristic absorption peaks at ~ 5.5 and ~ 6.3 eV (electronic transitions of PSS) that are included in the measured energy region. As can be seen from Figure 10.11, the PEDOT:PSS strip has a homogeneous film thickness of 55 nm over the entire printed area. On the unprinted areas, the in-line results indicate the zero thickness points, whereas immediately after the increase of the thickness, the calculated values are back to 55 nm.

10.3.3 High barrier nanomaterials for encapsulation

One of the main challenges for the fabrication of flexible OE devices is to achieve a sufficient protection of the active layers from the penetration of atmospheric gas molecules (O_2 and H_2O). This undesired phenomenon leads to the corrosion of the highly sensitive device active layers (small molecule and polymer organic semiconductors, organic conductors and electrodes, such as transparent conductive oxides, etc.) and their delamination from the substrate, limiting the device functionality, performance, and stability.

The commercial flexible polymer films used as flexible substrates (PET, PEN, etc.) exhibit permeability values for oxygen transmission rate (OTR) and for water vapor transmission rate (WVTR) of $10^{-1}-10^2$ cm^3/m^2 dbar (OTR), g/m^{2}d (WVTR), which are not sufficient except for applications in OE devices. The permeation requirements for OLED devices for display and lighting, flexible photovoltaic cells (OPVs), and flexible circuits and sensors, ask for values lower by another three orders of magnitude in the range below 10^{-5} cm^3/m^2 dbar (OTR) and g/m^{2}d (WVTR), which cannot be obtained by any of the currently used fabrication processes.

Some of the conventional encapsulation solutions involve the use of inorganic thin films, as SiO$_x$ and AlO$_x$ deposited onto the flexible polymeric substrate by vacuum methods (such as sputtering or evaporation). This reduces the O$_2$ and H$_2$O permeation rates just by two to three orders of magnitude from the permeation rate values of the uncoated plastic substrate. Another approach for the encapsulation of OE devices includes the use of hybrid polymers that have attracted great interest lately for their use as barrier materials. These are inorganic−organic nanocomposites that can be synthesized by sol−gel processes at relatively low temperatures. Moreover, the combination of hybrid polymers with inorganic layers can lead to a significant improvement of the barrier properties of the whole material structure. This is the result of the synergetic effect of the confinement of the permeation to the defect zones of the inorganic layer, and the formation of chemical bonds between the hybrid polymer and the inorganic layer (Amberg-Schwab, Katschorek, Weber, Hoffmann, & Burger, 2000; Charton et al., 2006; Fahlteich, Fahland, Schönberger, & Schiller, 2009).

The investigation of the optical properties of the hybrid polymers in the infrared (IR) to the visible and to the far ultraviolet (Vis−fUV) spectral region can provide valuable information on the understanding of their bonding and electronic structure and microstructure, as well as on their optical transparency. Moreover, it is more important to study the hybrid polymers' structure when these are deposited onto inorganic materials such as SiO$_x$, which are used as barriers as well as the bonding on the hybrid−inorganic interface and its effect on their functionality.

Figure 10.12 shows the pseudodielectric function $<\varepsilon(\omega)>$ in the Vis−fUV energy region (1.5−6.5 eV) of a representative hybrid polymer deposited onto SiO$_x$/PET. In the lower energy region the $<\varepsilon(\omega)>$ is dominated by interference fringes that are attributed to the multiple light reflections at the interfaces between the hybrid layer and the SiO$_x$ intermediate layer, as the result of their optical transparency in this energy region. At higher energies, the optical absorption of the hybrid polymer takes place. Since the back surface of the PET substrates has been roughened before the measurements, the multiple reflections of light between the PET substrate top and bottom surface have been diminished.

The $<\varepsilon(\omega)>$ in the Vis−fUV spectral region has been analyzed by the use of a four-phase geometrical model, which consists of a hybrid polymer layer (with thickness d) on top of an inorganic nanolayer that is grown on a PET (bulk) substrate. For the ambient medium, air has been used in which $\varepsilon_1(\omega) = 1$ and $\varepsilon_2(\omega) = 0$ for all energy values ω. The optical response of the inorganic and organic parts have been modelled by the use of the TL dispersion model. The hybrid polymers are characterized by high optical transparency at the visible spectral region and by electronic transition energies
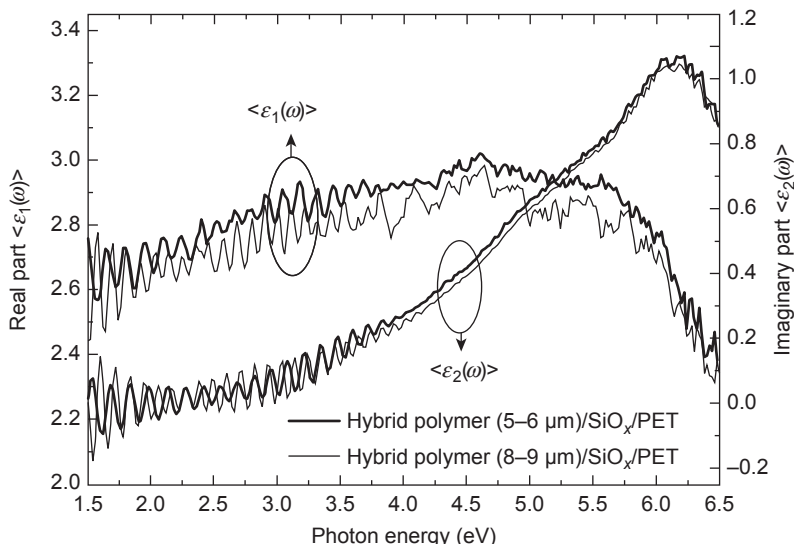
Figure 10.12 Measured pseudodielectric function $<\varepsilon(\omega)>$ of a representative hybrid polymer deposited onto SiO_x/PET substrates. All measurements were performed with the plane of incidence parallel to the MD, while the back surface of the PET substrates has been roughened in order to avoid the multiple reflections of light.
Modified after Georgiou et al. (2009).

at higher energy values. The energy band gap and electronic transition energy of the specific hybrid polymer of Figure 10.12 is calculated by the above mentioned model, at 2.41 and 7.56 eV (Georgiou et al., 2009).

In-line SE can be an important tool for the robust determination of the optical properties and thickness of the inorganic and hybrid polymer barrier layers deposited onto flexible polymer substrates with the form of rolls. The reference optical properties can be deduced from ex situ measurements by laboratory-scale equipment. These references can be used for the in-line calculation of the optical properties during the web rolling by in-line SE. This can provide information on the film homogeneity, uniformity of the printing, as well as the final (optical, barrier) properties. In addition, in-line SE can provide quality control in order to optimize the experimental conditions (e.g., rolling speed, curing temperature) (Heymann et al., 2009; Logothetidis et al., 2013a).

This can be shown in Figures 10.13 and 10.14, which show the evolution of the hybrid polymer film thickness that has been gravure printed onto a PET roll, with the roll speed and the curing temperature. The latter procedure is an important part of the printing process; its aim is to remove the residual solvent from the hybrid polymer structure and to form a cohesive inorganic—organic network. From Figure 10.13 it can be seen that the increase of the rolling speed from 1 to 6 m/min leads to the reduction of the film thickness of the hybrid polymer from 875 to 642 nm (Logothetidis, 2014b). The reduction of the film thickness is instantly calculated as the result of
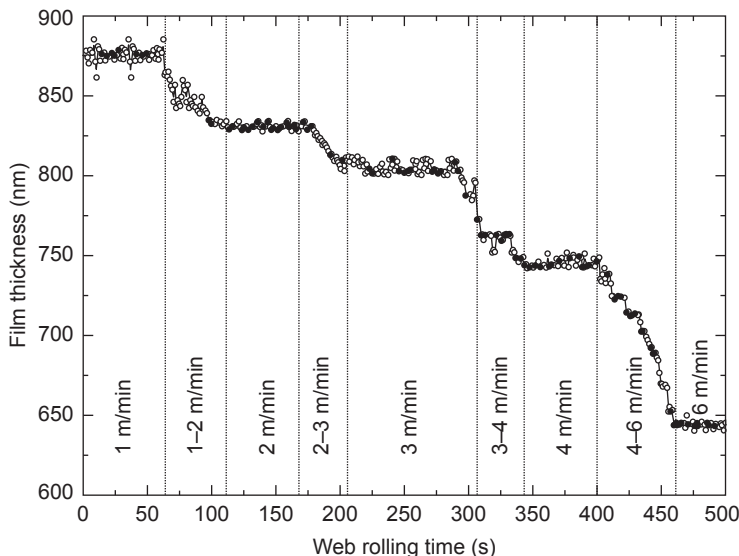
Figure 10.13 Evolution of the film thickness of the hybrid polymer barrier layer that has been gravure printed onto PET flexible substrate with the rolling speed. The thickness values were calculated in-line during the passing of the roll from the measurement point from the SE unit (Logothetidis, 2014b).
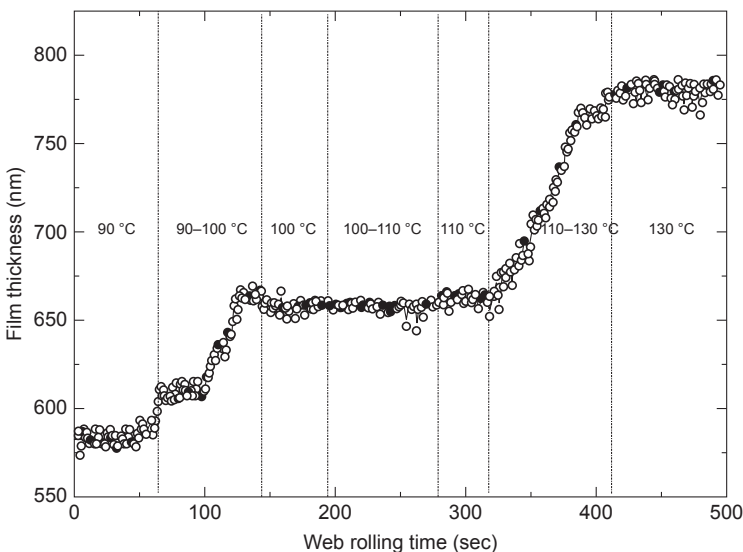
Figure 10.14 Evolution of the film thickness of the hybrid polymer barrier layer that has been gravure printed onto PET flexible substrate with the curing temperature. The thickness values were calculated in-line during the passing of the roll from the measurement point from the SE unit (Logothetidis, 2014b).

the higher rolling speed. In this way, the optimum rolling speed that will lead to the desired hybrid polymer film thickness can be finalized.

In the case of the curing temperature applied, we can observe from Figure 10.14 that the increase of the temperature from 90 °C to 130 °C results in an increase of the film thickness from 580 to 780 nm. This increase of the film thickness is attributed to the more intense cross-linking of the hybrid polymer as a result of the higher curing temperature (Logothetidis, 2014b).

10.4   Conclusions and future trends

In this chapter, we have discussed the latest advances in the implementation of in-line SE on r2r printing process for the real-time measurement and analysis of the thickness and optical properties of nanomaterials that will be used for the large-scale fabrication of OE devices. The in-line measurement and modeling of the optical and electronic properties, thickness, and quality control of the r2r gravure-printed nanomaterials plays an important role on the optimization of their functionality as well as on the stability and property repeatability of the printed layers. This is expected to have a positive impact on the achievement of the desired performance of the OE devices.

We have described the application of in-line SE for the monitoring of a number of different material systems, from organic semiconductors to barrier layers and transparent electrodes with thicknesses of several nanometers. The measurement scans at the lateral and transverse directions of the rolls and in combination with the real-time analysis of the $<\varepsilon(\omega)>$ have provided the thickness profiles as well as the characteristic electronic transition energies. The above emphasize the significance of nondestructive in-line optical characterization for r2r fabrication processes of single and/or multilayer structures deposited on flexible polymer substrates in the form of web rolls.

The implementation of in-line SE in the OE processing technology presents a series of challenges. The upcoming subjects to be addressed and challenges to be overcome include the use of multilayered materials with more complex structures, optical and electronic properties. The printing of complicated film patterns, such as in the case of OLEDs, OTFTs, and sensors, is also expected to set some difficulties on the robust quality control by in-line SE. Finally, the ultimate goal will be to apply in-line SE for the film quality control and for the feedback to the deposition instrument for the achievement of predefined material recipes. However, the continuous advancements in the instrumentation that will enhance the speed and accuracy of the measured spectra, along with the rapid development of computational algorithms, strongly suggest that in-line SE will become an essential part of the r2r fabrication of flexible OE devices.

Acknowledgements

References

Amberg-Schwab, S., Katschorek, H., Weber, U., Hoffmann, M., & Burger, A. (2000). Barrier properties of inorganic-organic polymers. *Journal of Sol-gel Science and Technology, 19*, 125−129.

An, I. (1998). Simultaneous determination of reflectance spectra along with {ψ(E), Δ(E)} in multichannel ellipsometry: applications to instrument calibration and reduction of real-time data. *Thin Solid Films, 313−314*, 79−84.

Azarova, N. A., Owen, J. W., McLellan, C. A., Grimminger, M. A., Chapman, E. K., Anthony, J. E., et al. (2010). Fabrication of organic thin-film transistors by spray-deposition for low-cost, large-area electronics. *Organic Electronics, 11*, 1960−1965.

Azzam, R. M. A., & Bashara, N. M. (1977). *Ellipsometry and polarized light*. Amsterdam: North Holland.

van Bavel, S., Sourty, E., de With, G., Frolic, K., & Loos, J. (2009). Relation between photo-active layer thickness, 3D morphology, and device performance in P3HT/PCBM bulk-heterojunction solar cells. *Macromolecules, 42*, 7396−7403.

Campoy-Quiles, M., Ferenczi, T., Agostinelli, T., Etchegoin, P. G., Kim, Y., Anthopoulos, T. D., et al. (2008). Morphology evolution via self-organization and lateral and vertical diffusion in polymer:fullerene solar cell blends. *Nature Materials, 7*, 158−164.

Cavallini, M., Facchini, M., Massi, M., & Biscarini, F. (2004). Bottom-up nanofabrication of materials for organic electronics. *Synthetic Metals, 146*, 283−286.

Charton, C., Schiller, N., Fahland, M., Hollander, A., Wedel, A., & Noller, K. (2006). Development of high barrier films on flexible polymer substrates. *Thin Solid Films, 502*, 99−103.

Cheng, Y.-J., Yang, S.-H., & Hsu, C.-S. (2009). Synthesis of conjugated polymers for organic solar cell applications. *Chemical Reviews, 109*, 5868−5923.

Collins, R. W., Koh, J., Fujiwara, H., Rovira, P. I., Ferlauto, A. S., Zapien, J. A., et al. (2000). Recent progress in thin film growth analysis by multichannel spectroscopic ellipsometry. *Applied Surface Science, 154−155*, 217−228.

Drevillon, B. (1998). Spectroscopic ellipsometry in the infrared range. *Thin Solid Films*, 625−630.

Fahlteich, J., Fahland, M., Schönberger, W., & Schiller, N. (2009). Permeation barrier properties of thin oxide films on flexible polymer substrates. *Thin Solid Films, 517*, 3075−3080.

Galagan, Y., de Vries, I. G., Langen, A. P., Andriessen, R., Verhees, W. J. H., Veenstra, S. C., et al. (2011). Technology development for roll-to-roll production of organic photovoltaics. *Chemical Engineering and Processing: Process Intensification, 50*, 454−461.

Georgiou, D., Laskarakis, A., Koidis, C., Goktsis, N., & Logothetidis, S. (2008). Growth mechanisms of silicon oxide nano-layers grown onto polymeric substrates for flexible electronics applications. *Physica Status Solidi (C), 5*, 3387−3391.

Georgiou, D., Laskarakis, A., Logothetidis, S., Amberg-Scwhab, S., Weber, U., Schmidt, M., et al. (2009). Optical properties of hybrid polymers as barrier materials. *Applied Surface Science, 255*, 8023−8029.

Georgiou, D., Logothetidis, S., Koidis, C., & Laskarakis, A. (2008). In-situ and real-time monitoring of high barrier layers growth onto polymeric substrates. *Physica Status Solidi (C), 5*, 1300−1303.

Gioti, M., Logothetidis, S., Patsalas, P., Laskarakis, A., Panayiotatos, Y., & Kechagias, V. (2000). Magnetron sputtered carbon nitride: composition and chemical bonding of as-grown and post-annealed films studied with real-time and in situ diagnostic techniques. *Surface and Coatings Technology, 125*, 289−294.

Gravalidis, C., Gioti, M., Laskarakis, A., & Logothetidis, S. (2004). Real-time monitoring of silicon oxide deposition processes. *Surface and Coatings Technology, 181*, 655−658.

Herrmann, F., Engmann, S., Presselt, M., Hoppe, H., Shokhovets, S., & Gobsch, G. (2012). Correlation between near infrared-visible absorption, intrinsic local and global sheet resistance of poly(3,4-ethylenedioxy-thiophene) poly(styrene sulfonate) thin films. *Applied Physics Letters, 100*, 153301.

Heymann, K., Mirschel, G., Scherzer, T., & Buchmeiser, M. (2009). In-line determination of the thickness of UV-cured coatings on polymer films by NIR spectroscopy. *Vibrational Spectroscopy, 51*, 152−155.

Hoppe, H., & Sariciftci, N. S. (2006). Morphology of polymer/fullerene bulk heterojunction solar cells. *Journal of Materials Chemistry, 16*, 45.

Humlicek, J., Nebojsa, A., Hora, J., Stransky, M., Spousta, J., & Sikola, T. (1998). Ellipsometry and transport studies of thin-film metal nitrides. *Thin Solid Films, 332*, 25−29.

Irene, G. E., & Tompkins, H. G. (Eds.). (2005). *Handbook of ellipsometry*. Norwich, NY: William Andrew Publishing.

Jellison, G. E. (1998). Spectroscopic ellipsometry data analysis: measured versus calculated quantities. *Thin Solid Films, 313−314*, 33−39.

Jellison, G. E., & Modine, F. A. (1996). Parameterization of the optical functions of amorphous materials in the interband region. *Applied Physics Letters, 69*, 371−373.

Karagiannidis, P. G., Georgiou, D., Pitsalidis, C., Laskarakis, A., & Logothetidis, S. (2011). Evolution of vertical phase separation in P3HT: PCBM thin films induced by thermal annealing. *Materials Chemistry and Physics, 129*, 1207−1213.

Kechagias, V. G., Gioti, M., Logothetidis, S., Benferhat, R., & Teer, D. (2000). 'Real-time' multiwavelength ellipsometry diagnostics for monitoring dry etching of Si and TiN$_x$ deposition. *Thin Solid Films, 364*, 213−219.

Koidis, C., Logothetidis, S., Georgiou, D., & Laskarakis, A. (2008). In-situ and real-time investigation of ZnO thin films growth onto rigid and flexible substrates. *Physica Status Solidi (C), 5*, 1366−1369.

Koidis, C., Logothetidis, S., Ioakeimidis, A., Laskarakis, A., & Kapnopoulos, C. (2013). Key factors to improve the efficiency of roll-to-roll printed organic photovoltaics. *Organic Electronics, 14*, 1744−1748.

Koidis, C., Logothetidis, S., Kapnopoulos, C., Karagiannidis, P. G., Laskarakis, A., & Hastas, N. A. (2011). Substrate treatment and drying conditions effect on the properties of roll-to-roll gravure printed PEDOT: PSS thin films. *Materials Science and Engineering: B, 176*, 1556−1561.

Koidis, C., Logothetidis, S., Kassavetis, S., Kapnopoulos, C., Karagiannidis, P. G., Georgiou, D., et al. (2013). Effect of process parameters on the morphology and nano-structure of roll-to-roll printed P3HT:PCBM thin films for organic photovoltaics. *Solar Energy Materials and Solar Cells, 112*, 36−46.

Kopola, P., Aernouts, T., Sliz, R., Guillerez, S., Ylikunnari, M., Cheyns, D., et al. (2011). Gravure printed flexible organic photovoltaic modules. *Solar Energy Materials and Solar Cells, 95*, 1344−1347.

Krebs, F. C. (2009). All solution roll-to-roll processed polymer solar cells free from indium-tin-oxide and vacuum coating steps. *Organic Electronics, 10*, 761−768.

Krebs, F. C. (2009). Fabrication and processing of polymer solar cells: a review of printing and coating techniques. *Solar Energy Materials and Solar Cells, 93*, 394−412.

Kumar, P., & Chand, S. (2011). Recent progress and future aspects of organic solar cells. *Progress in Photovoltaics: Research and Applications, 20*, 377−415.

Laskarakis, A., Georgiou, D., & Logothetidis, S. (2010). Real-time optical modelling and investigation of inorganic nano-layer growth onto flexible polymeric substrates. *Materials Science and Engineering B, 166*, 7−13.

Laskarakis, A., Karagiannidis, P. G., Georgiou, D., Nikolaidou, D. M., & Logothetidis, S. (2013). Optical investigations of the effect of solvent and thermal annealing on the opto-electronic properties of Poly(3,4-ethylenedioxythiophene):poly(styrenesulfonate) films. *Thin Solid Films, 541*, 102−106.

Laskarakis, A., Kassavetis, S., Gravalidis, C., & Logothetidis, S. (2010). In situ and real-time optical investigation of nitrogen plasma treatment of polycarbonate. *Nuclear Instruments and Methods in Physics Research Section B: Beam Interactions with Materials and Atoms, 268*, 460−465.

Laskarakis, A., & Logothetidis, S. (2006). On the optical anisotropy of poly(ethylene terephthalate) and poly(ethylene naphthalate) polymeric films by spectroscopic ellipsometry from visible-far ultraviolet to infrared spectral regions. *Journal of Applied Physics, 99*, 066101.

Laskarakis, A., & Logothetidis, S. (2007). Study of the electronic and vibrational properties of poly(ethylene terephthalate) and poly(ethylene naphthalate) films. *Journal of Applied Physics, 101*, 1−9.

Laskarakis, A., Logothetidis, S., & Gioti, M. (2001). Bonding structure of carbon nitride films by infrared ellipsometry. *Physical Review B, 64*, 1−15.

Laskarakis, A., Logothetidis, S., Kassavetis, S., & Papaioannou, E. (2008). Surface modification of poly(ethylene terephthalate) polymeric films for flexible electronics applications. *Thin Solid Films, 516*, 1443−1448.

de Leeuw, D. M., & Cantatore, E. (2008). Organic electronics: materials, technology and circuit design developments enabling new applications. *Materials Science in Semiconductor Processing, 11*, 199−204.

Logothetidis, S. (2001). In-situ and real-time spectroscopic ellipsometry studies: carbon based and metallic TiN_x thin films growth. In H. S. Nalwa (Ed.), *Thin films handbook*. Academic Press.

Logothetidis, S. (2010). *Method for the in-situ and real-time determination of the thickness, optical properties and quality of transparent coatings during their growth onto polymeric substrates and determination of the modification, activation and the modification depth of polymeric materials surfaces*. Patent US 7777882, 17 August 2010.

Logothetidis, S. (2011). *Method for in-line determination of film thickness and quality during printing processes for the production of organic electronics*. Patent WO 2012143742 A1, 26 October 2012.

Logothetidis, S. (2014a). *Robust optical investigations of nanomaterials for organic and printed electronics applications*. In preparation.

Logothetidis, S. (2014b). *Roll-to-roll printing of ultra high barrier nanomaterials for encapsulation of organic electronic devices*. In preparation.

Logothetidis, S., Georgiou, D., Laskarakis, A., Koidis, C., & Kalfagiannis, N. (2013). In-line spectroscopic ellipsometry for the monitoring of the optical properties and quality of roll-

to-roll printed nanolayers for organic photovoltaics. *Solar Energy Materials & Solar Cells, 112*, 144−156.

Logothetidis, S., Georgiou, D., Laskarakis, A., Koidis, C., & Kalfagiannis, N. (2013). Spectroscopic Ellipsometry for the optical properties and the quality control of roll-to-roll printed organic nanomaterials. *Solar Energy Materials & Solar Cells, 112*, 144−156.

Logothetidis, S., & Laskarakis, A. (2009). Towards the optimization of materials and processes for flexible organic electronics devices. *The European Physical Journal Applied Physics, 46*, 12502.

Logothetidis, S., & Laskarakis, A. (2009). Organic against inorganic electrodes grown onto polymer substrates for flexible organic electronics applications. *Thin Solid Films, 518*, 1245−1249.

Logothetidis, S., Laskarakis, A., Gika, A., & Patsalas, P. (2002). In situ and real-time ellipsometry diagnostic techniques towards the monitoring of the bonding structure and growth kinetics: silicon oxide coatings. *Surface and Coatings Technology, 152*, 204−208.

Lo, C.-Y., Hiitola-Keinänen, J., Huttunen, O.-H., Petäjä, J., Hast, J., Maaninen, A., et al. (2009). Novel roll-to-roll lift-off patterned active-matrix display on flexible polymer substrate. *Microelectronic Engineering, 86*, 979−983.

Madsen, M. V., Sylvester-hvid, K. O., Dastmalchi, B., Hingerl, K., Norrman, K., Tromholt, T., et al. (2011). Ellipsometry as a nondestructive depth profiling tool for roll-to-roll manufactured flexible solar cells. *The Journal of Physical Chemistry C, 115*, 10817−10822.

Nardes, A. M., Kemerink, M., & Janssen, R. A. J. (2007). Anisotropic hopping conduction in spin-coated PEDOT: PSS thin films. *Physical Review B, 76*, 085208.

Noh, J., Yeom, D., Lim, C., Cha, H., Han, J., Kim, J., et al. (2010). Scalability of roll-to-roll gravure-printed electrodes on plastic foils. *IEEE Transactions on Electronics Packaging Manufacturing, 33*, 275−283.

Park, S. K., Mourey, D. A., Subramanian, S., Anthony, J. E., & Jackson, T. N. (2008). High-mobility spin-cast organic thin film transistors. *Applied Physics Letters, 93*, 043301.

Pavlopoulou, E., Fleury, G., Deribew, D., Cousin, F., Geoghegan, M., & Hadziioannou, G. (2013). Phase separation-driven stratification in conventional and inverted P3HT: PCBM organic solar cells. *Organic Electronics, 14*, 1249−1254.

Schmidt-Hansberg, B., Klein, M. F. G., Peters, K., Buss, F., Pfeifer, J., Walheim, S., et al. (2009). In situ monitoring the drying kinetics of knife coated polymer-fullerene films for organic solar cells. *Journal of Applied Physics, 106*, 124501.

Smith, J., Zhang, W., Sougrat, R., Zhao, K., Li, R., Cha, D., et al. (2012). Solution-processed small molecule-polymer blend organic thin-film transistors with hole mobility greater than 5 cm^2/V s. *Advanced Materials, 24*, 2441−2446.

Voigt, M. M., Mackenzie, R. C. I., Yau, C. P., Atienzar, P., Dane, J., Keivanidis, P. E., et al. (2011). Gravure printing for three subsequent solar cell layers of inverted structures on flexible substrates. *Solar Energy Materials and Solar Cells, 95*, 731−734.

White Paper OE-A Roadmap (2011).

This page intentionally left blank

Optimization of active nanomaterials and transparent electrodes using printing and vacuum processes

11

C. Koidis[1], S. Logothetidis[2]
[1]Organic Electronic Technologies P.C. (OET), Thessaloniki, Greece; [2]Aristotle University of Thessaloniki, Thessaloniki, Greece

11.1   Introduction

The need for high precision and throughput processing of solution-based nanomaterials and vacuum-deposited thin films has become a key factor in the large-scale manufacturing of organic and printed electronics (OEs) such as organic photovoltaics (OPVs). For example, spin-coating is among the most popular techniques for the processing of various solution-based nanomaterials in lab-scale processes, because it is easy to use and it is fairly cheap to acquire the necessary equipment (Søndergaard, Hösel, & Krebs, 2013). However, it is not compatible with large-scale processes that include roll-to-roll (r2r) continuous procedures and too much material is wasted during processing, which imply that cost-efficiency is not fulfilled.

Various technologies have been developed for solution-based r2r processes including coating such as slot-die, and printing such as screen and gravure (Manceau et al., 2011; Kim, Jo, & Lee, 2012; Koidis et al., 2013a). One of the main differences between coating and printing techniques is that the latter ones are contact processes and enable the patterned deposition of the functional ink (with the exception of inkjet printing). Coating methods can either be contact based or contact free and in general are used for large-scale full-layer deposition of thin films, where patterning is in fact limited to stripes (Søndergaard et al., 2013). Large-scale r2r vacuum processing based on sputtering and/or thermal evaporation is also believed to significantly reduce manufacturing costs. High throughput and the use of relatively cheap metal foils and plastic webs as substrates will be the major cost reducing step for the production of flexible organic light emitting diodes (OLEDs). In addition, r2r vacuum technologies are used for the deposition of inorganic barrier materials, the efficiency of which strongly affects the lifetime and stability of the device. The combination of r2r printed hybrid (organic-inorganic) and r2r vacuum deposited inorganic multilayers fulfills the important requirement of impenetrability to water and oxygen (Laskarakis, Georgiou, et al., 2009; Laskarakis, Logothetidis, et al., 2009).

Furthermore, technologies like organic vapor phase deposition (OVPD) have been proven useful for the deposition of organic semiconductors and capable of the patterned

growth with μm resolution. OVPD enables the effective mass manufacturing of OLEDs for both display and lighting applications as well as other OE devices requiring functional stacks formed by organic small molecules (e.g., OPVs, OTFTs) (Kreis et al., 2013).

The high performance of devices such as OPVs is achieved through the best combination between the processing method and parameters, the solvents, the additives, the drying/treatment processes, the materials, and the substrate. Of course, when trying to up scale the OEs' fabrication by implementing r2r processes, it is difficult to achieve results similar to lab-scale device efficiencies. The limitations that arise come from the large number of parameters that need to be optimized in a r2r process. Some of the considerations in determining the printing/coating technique for each layer in the case of solution-based technologies include processing speed (typical range of 1−20 m/min or higher in the case of industrial systems), drying conditions/temperature, processing of multilayered structures, solvents, materials, substrates, various substrates' and films' treatments, etc.

In the case of OPVs, there are many parameters that affect their efficiency such as the morphology of the photoactive layer, usually poly(3-hexylthiophene): (6,6)-phenyl C61 butyric acid methyl ester (P3HT:PCBM) (Kim et al., 2006), and the vulnerability of the constituent layers, such as that of the conductive poly(3,4-ethylenedioxythiophene):poly(styrenesulfonate) (PEDOT:PSS), to air, contaminations, and impurities (Norrman et al., 2010). The combination of fabrication steps by printing/wet and vacuum techniques can enable the fabrication of OEs with alternative capabilities such as semitransparent OPVs (Franklin et al., 2014). For example, the metal cathode can be replaced by transparent conductive oxide (TCO) structures (e.g., TCO/metal/TCO multilayers) that would enable the semitransparency of the device (Guillén & Herrero, 2011).

On the other hand, characterization is a very important part of the optimization process for the production of OEs. Note the importance of the feedback that we can get from the analysis of the measurements taken on the printed and/or vacuum-deposited layers. The whole optimization process is based on those data that reflect the effect of the process parameters (e.g., printing speed, drying temperature, deposition time) on the properties of the materials and the efficiency of the whole device. Techniques such as spectroscopic ellipsometry (SE) can give important insights into the properties of the materials during their printing and/or vacuum deposition, which enables the cost-efficient optimization and quality control of the materials and processes (Logothetidis et al., 2013).

11.2   Optimization of r2r printed active nanomaterials and electrodes

The main objective in OEs is to achieve high performance, stability, and low cost. The cost reduction can be achieved using cost-efficient materials in combination with fast and continuous r2r processes. Indeed, compared to conventional silicon photovoltaics, OPVs are expected to be less expensive and easier to manufacture, due to the lower

energy consumption and the use of continuous large-scale r2r processes. However, compared with sputtering or evaporation processes in vacuum, the use of materials in solution involves several difficulties in terms of the need for removal of solvents contained in the solution and simultaneous control of phase separation for the preparation of thin films with the optimum morphology (Koidis et al., 2013a).

Many different r2r printing and coating techniques can be applied for the development of thin films of organic and inorganic materials such as slot-die, inkjet, screen, gravure, etc. (Krebs, 2009). Each technique has advantages and disadvantages depending on the application. For example, inkjet can print any design, but when it is integrated into r2r processes, it is not particularly fast.

On the contrary, gravure is a high speed r2r printing technique widely used in the graphic arts industry for long prints, where uniformity, stability, and accuracy of printing are essential. The products printed with gravure span a wide range of applications such as bank notes, gift wrappers, magazines, stamps, etc. The technology is based on engraving, which means that the design to be printed is engraved into a cylinder and transferred through pressure to the substrate. Of course, apart from printing, r2r processing includes several other very important steps such as heating, drying, UV treatment, encapsulation (lamination), etc.

11.2.1 Insights on the properties of r2r printed transparent electrodes

In material systems like PEDOT:PSS, charge carriers such as polarons and bipolarons mainly determine the mechanism of conductivity. The polaron corresponds to a positive charge at a monomer, while the bipolaron corresponds to two positive charges that are located along some monomers. Therefore, the transition from the polarons to bipolarons is due to configuration change of PEDOT chains coil (benzoid) to a linear or expanded coil (quinoid) where the charge carriers are freer to move along the PEDOT chains. Bipolarons are present even in the PEDOT:PSS without the addition of the commonly used solvent dimethyl sulfoxide (DMSO), where some of the polymer chains have a linear configuration or the extended coil conformation (Ouyang et al., 2004).

SE enables the investigation of the thickness, optical and structural properties as well as the growth mechanisms of thin films and multilayers (Gioti, Laskarakis, & Logothetidis, 2004; Koidis et al., 2010; Laskarakis, Gravalidis, & Logothetidis, 2004; Laskarakis & Logothetidis, 2006; Logothetidis et al., 1999; Logothetidis et al., 2013). For the analysis of the SE measurements taken on the PEDOT:PSS thin films, the Drude−Tauc−Lorentz model is used (Laskarakis et al., 2013). The contribution of the conductive PEDOT is given through the Drude model, which describes the dielectric response of free charge carriers, while the response of the insulating PSS is described through the Tauc−Lorentz model.

The value of the plasma energy E_p exported by the Drude model through the SE analysis can be used for the calculation of the optical conductivity of the films through Eqns (11.1) and (11.2):

$$E_p = \hbar\omega_p, \tag{11.1}$$

and

$$\omega_p = \sqrt{\frac{4\pi n e^2}{m^*}}, \tag{11.2}$$

where n is the density of charge carriers (in $1/cm^3$) with charge e and effective mass m^*.

In addition, the damping factor Γ_D, which includes the scattering of charge carriers associated with the electrical resistance and is approximately inversely proportional to the average time between collisions of charge carriers, is given by Eqn (11.3):

$$\Gamma_D = \frac{\hbar e}{m^* \mu}, \tag{11.3}$$

where μ is the charge carrier mobility. Through Drude modeling analysis, the parameters E_p and Γ_D can be derived, so according to the above equations, the optical conductivity σ_D of thin films can be determined by Eqn (11.4):

$$\sigma_D(E) = 134.49 \frac{E_p^2}{\Gamma_D}. \tag{11.4}$$

Coming to r2r processing, during the drying stage the wet film passes through (usually) hot air dryers so that solvent evaporates, resulting in the formation of the final film. In the case of PEDOT:PSS, the basic solvent to be removed is water. Figure 11.1 shows the pseudodielectric $<\varepsilon(\omega)> = (<\varepsilon_1(\omega)> + i<\varepsilon_2(\omega)>)$ and bulk dielectric $\varepsilon(\omega) = (\varepsilon_1(\omega) + i\varepsilon_2(\omega))$ functions of the PEDOT:PSS thin films that are r2r printed on polyethylene terephthalate (PET) substrate and dried at different temperatures (T_{r2r}) between 40 °C and 160 °C for 19 s. The Drude−Tauc−Lorentz model is used for the analysis in combination with a geometrical model consisting of the layer sequence: PET/PEDOT:PSS layer/PEDOT:PSS surface layer/air. The surface layer consists of PEDOT:PSS and voids. PEDOT:PSS Clevios™ FET used for the trials shows a main absorption peak at 5.3 eV due to π−π* intraband electronic transition in the benzene ring of the PSS. The broad band that appears to be centered at about 4.3 eV is due to an overlap of the transition from the ground state (S_0) to the first excited state (S_1) for PEDOT (which is supposed to appear at 4.98 eV) and of the excitation of the PSS molecule from its ground state (S_0) to the first excited state (S_1) due to the transfer of electron from HOMO to LUMO (which is supposed to appear at 4.85 eV). The oscillator strength of the PEDOT transition is greater than the oscillator strength of the PSS transition, and therefore this band can be considered to be almost completely due to the PEDOT transition (Agalya et al., 2005). In the low energies region (below about 2 eV), an increase of the $<\varepsilon_2(\omega)>$ and $\varepsilon(\omega)$ with decreasing energy is due to light absorption from the polymer due to intraband transitions because of the free carriers plasma resonance (due to the presence of bipolarons), which is a characteristic of metallic polymers in general (Agalya et al., 2005; Chang et al., 1999).
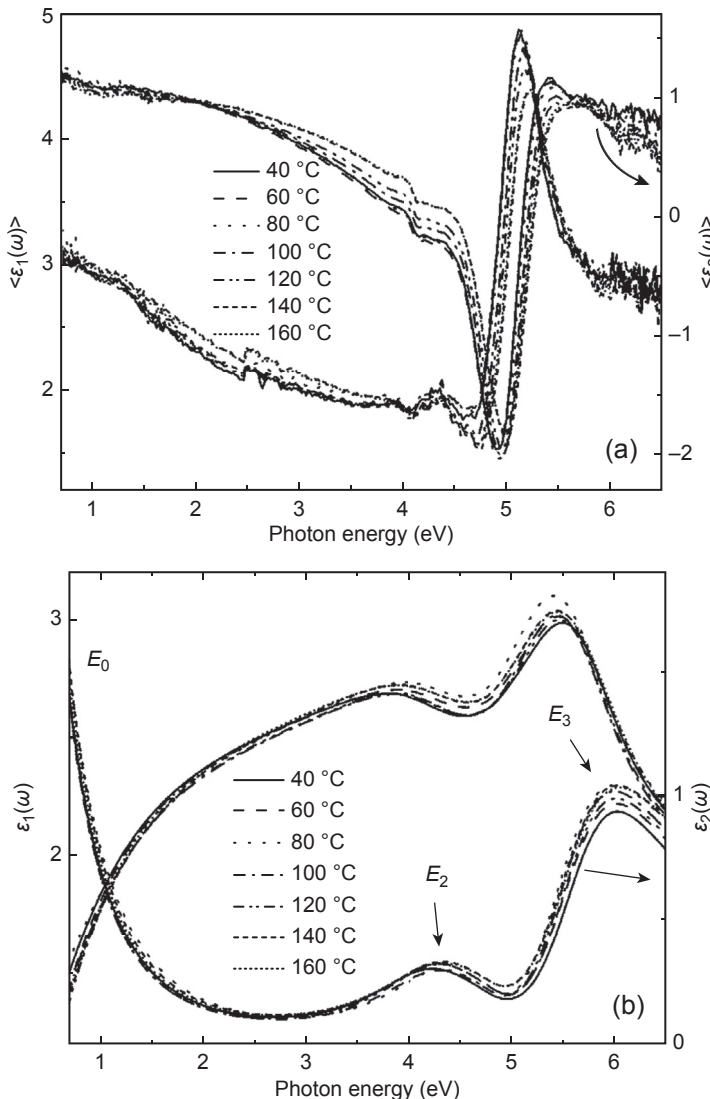
Figure 11.1 (a) The real $<\varepsilon_1(\omega)>$ and imaginary $<\varepsilon_2(\omega)>$ parts of the pseudodielectric functions $<\varepsilon(\omega)>$ of PEDOT:PSS/PET dried at 40, 60, 80, 100, 120, 140, and 160 °C. (b) The real $\varepsilon_1(\omega)$ and imaginary $\varepsilon_2(\omega)$ parts of the bulk dielectric functions $\varepsilon(\omega)$ of PEDOT:PSS thin films. The arrows indicate the absorption peaks E_2, E_3 and the Drude peak E_0.

Some of the optical parameters derived from the SE analysis (E_p, Γ_D, and σ_D) as well as the Van der Pauw−measured conductivity σ are summarized in Figure 11.2.

The plasma energy E_p of PEDOT:PSS thin films remains relatively constant up to 120 °C, while at 140 °C and 160 °C the value slightly increases, which indicates the
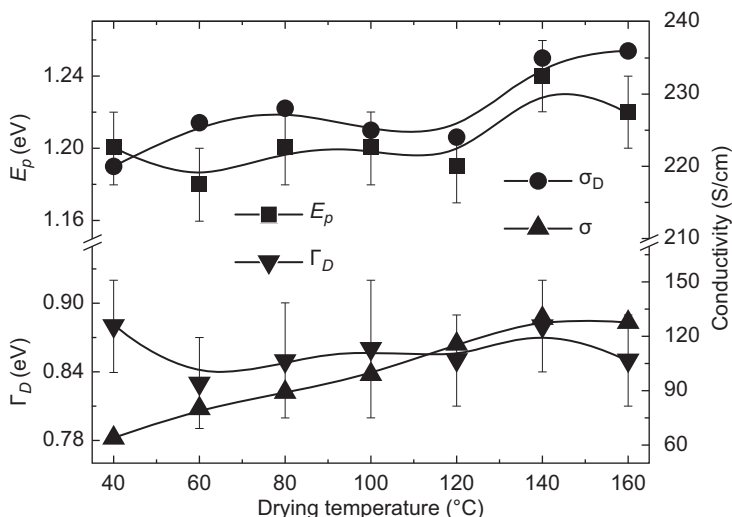
Figure 11.2 The variation of E_p, Γ_D, σ_D, and σ in relation to the drying temperature of the PEDOT:PSS thin films.

increase of the density of charge carriers n, which is attributed to the reduced amount of water in the film due to drying at temperatures sufficiently above the boiling point of water (100 °C). The value of Γ_D remains relatively constant, indicating similar mean time between collisions. The calculated conductivity σ_D is overestimated in relation to the measured one σ (taken through the Van der Pauw method), nevertheless the σ_D follows the trend of σ. Therefore, the main reason that limits the conductivity in the case of applying low temperature during drying is the reduction of the density of free charge carriers n due to the presence of water in the swollen particles and the corresponding morphology formed.

These results are in conjunction with the thickness and the morphological characteristics (corresponding images taken by Atomic Force Microscopy; AFM) of the printed films shown in Figures 11.3 and 11.4.

Removal of water allows a degree of rearrangement of the PEDOT chains to form the extended coil configuration (or even linear), which enables the enhancement of n, which is reflected by the increase in E_p at higher temperatures. On the other hand, the damping factor Γ_D remains constant with increasing drying temperature, which is attributed to the thickness reduction and the limited paths for the movement of the charge carriers between the PEDOT-rich particles (Sakkopoulos et al., 2010).

It is well known that PEDOT:PSS is a hygroscopic material. Figure 11.5 shows the real and imaginary parts of the pseudodielectric functions $<\varepsilon(\omega)>$ and the bulk dielectric functions $\varepsilon(\omega)$ of the PEDOT:PSS thin film r2r printed on PET and dried for 19 s at 140 °C, which are derived through analysis of the SE measurements using the Drude–Tauc–Lorentz model combined with the geometric model consisting of the layer sequence: PET/PEDOT:PSS layer/PEDOT:PSS surface layer/air. The measurements
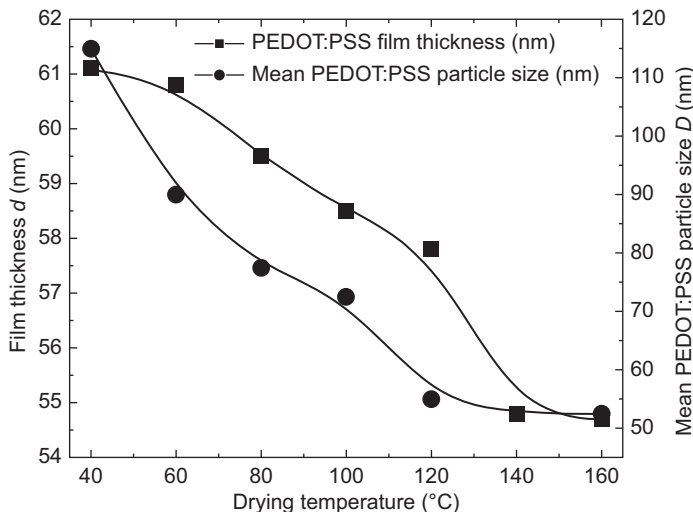
Figure 11.3 The thickness d of the PEDOT:PSS thin films and their average particle size D (according to the analysis of the AFM images) for each drying temperature.
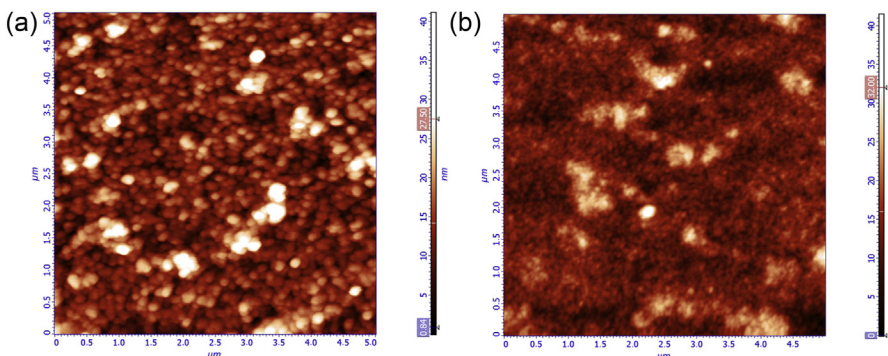
Figure 11.4 The AFM nanotopographies of the PEDOT:PSS thin films dried for 19 s at 40 °C (a) and 160 °C (b). Scanning area of 5×5 μm.

and the analysis data correspond to time $t = 0$ min, 30 min, 1, 3, 24, and 72 h after r2r printing process. According to Figure 11.6, the exposure of the film to air leads to a gradual reduction in the value of E_p, suggesting the influence of humidity on the density of charge carriers. Simultaneously, the value of Γ_D appears relatively stable since the morphological changes due to the humidity effect takes place mainly on the surface of the PEDOT:PSS film. The degradation of conductivity is indicated by the reduced slope of the $<\varepsilon_2(\omega)>$ and $\varepsilon_2(\omega)$ absorption spectra for $t > 0$ min, below about 2 eV (Figure 11.5).

Figure 11.7 shows the nanotopographies and phase images of the printed PEDOT:PSS thin film immediately after printing ($t = 0$ min) and for $t = 24$ h. The bright
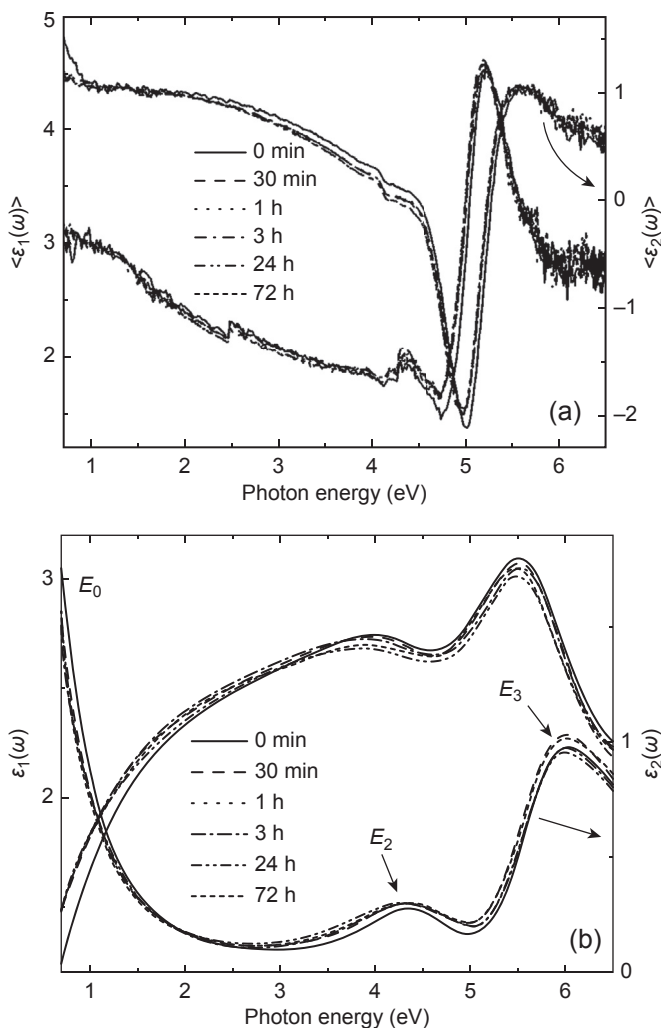
Figure 11.5 The real and imaginary parts of the pseudodielectric functions $<\varepsilon(\omega)>$ (a) and the bulk dielectric functions $\varepsilon(\omega)$ (b) of the PEDOT:PSS on PET at time $t = 0$ min, 30 min, 1 h, 3 h, 24 h, and 72 h after printing. The arrows indicate the absorption peaks E_2, E_3 and the Drude peak E_0.

(positive phase value) and dark (negative phase value) regions in the AFM phase images of Figure 11.7(b) and (d) correspond to PEDOT-rich and PSS-rich regions, respectively (Kim et al., 2011). The phase image of Figure 11.7(b) that corresponds to the surface of the PEDOT:PSS film for $t = 0$ min exhibits more bright areas in relation to the phase image of Figure 11.7(d), which corresponds to the surface of the
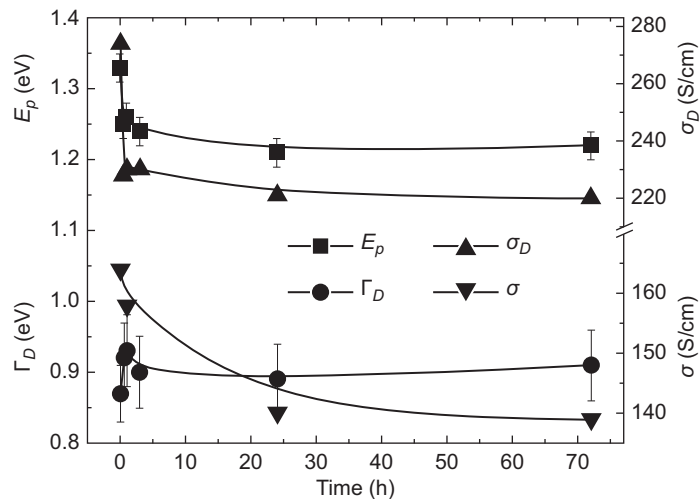
Figure 11.6 The variation of E_p, Γ_D, σ_D, and σ in relation to the time of exposure to air of the printed PEDOT:PSS film.
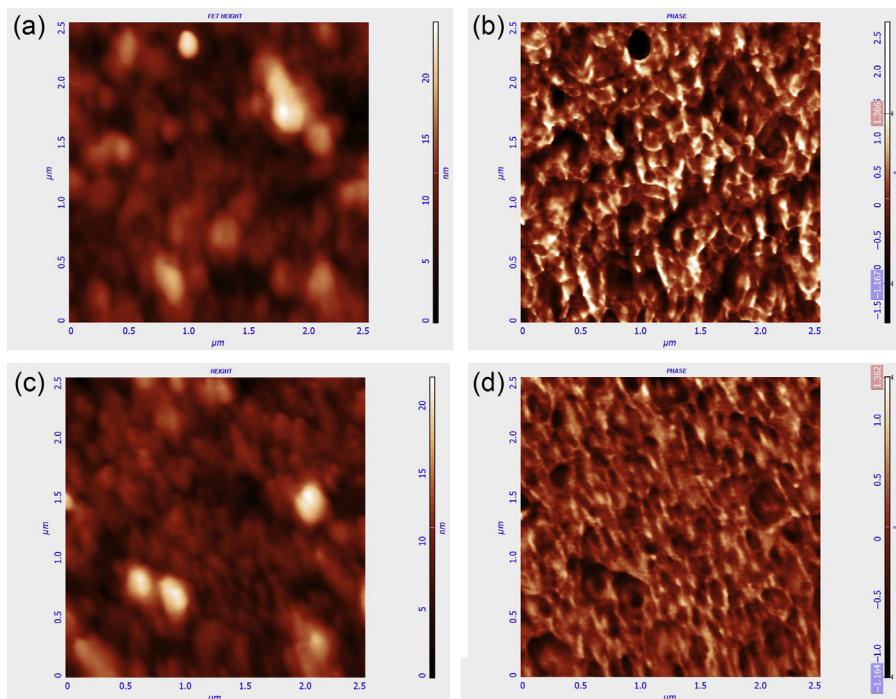
Figure 11.7 AFM nanotopographies and phase images of the PEDOT:PSS film right after printing ($t = 0$) (a and b, respectively) and for $t = 24$ h (c and d, respectively). Scanning area of 2.5×2.5 μm.

film for $t = 24$ h, indicating that immediately after printing the conductive areas are more than in the same surface after 24 h. Thus, as it is derived by the evolution of σ shown in Figure 11.6, the conductivity is limited by time, and the phenomenon tends to saturate, in conjunction with the trend of the E_p value. Additionally, the phase separation between the PEDOT and PSS for $t = 0$ min is much more distinct in relation to the case of $t = 24$ h, showing a morphology of increased conductivity and the formation of conductive pathways necessary for the efficient charge carriers transfer. Conversely, for $t = 24$ h, the reorganization of the molecules under the influence of the air leads to a homogenization of morphology, with the result that phase separation is no longer distinct.

According to the surface free energy calculations through the contact angle measurements of the printed PEDOT:PSS during its exposure to air, surface free energy value is reduced from about 58 mN/m for $t = 0$ min to about 53 mN/m for $t = 1$ h, and then remains almost constant. Indeed, the most pronounced value drop is observed during the first 30 min after printing, indicating that an immediate change in the morphological characteristics of the film under the influence of the air takes place. Another parameter that changes by time is the surface roughness. The root-mean-square (RMS) value of the surface roughness is reduced from 3.5 nm for $t = 0$ min to 2.9 nm for $t = 24$ h (corresponding peak-to-valley roughness values of 24.5 and 22 nm), in accordance with the observed decrease in the calculated SE thickness of the PEDOT:PSS surface layer, which simulates the surface roughness (Figure 11.8). The protection of PEDOT:PSS after printing leads to r2r printed OPVs with even doubled power conversion efficiency (PCE) (Koidis et al., 2013b).
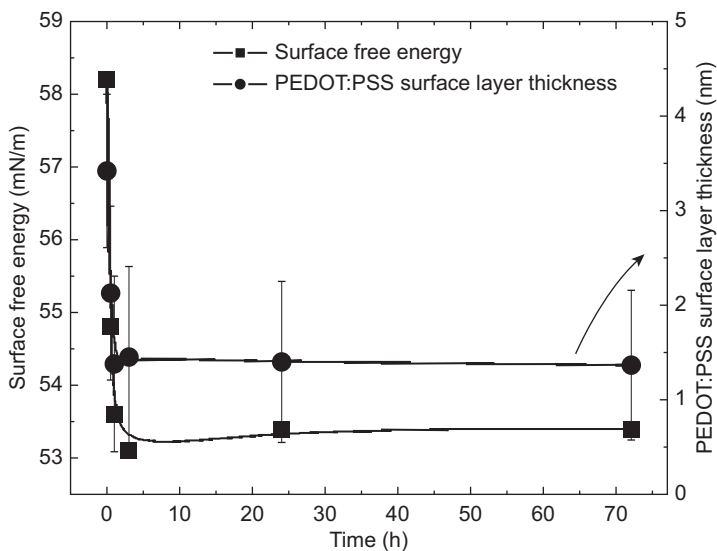
Figure 11.8 The variation of the surface free energy of the printed PEDOT:PSS film and the SE-calculated PEDOT:PSS surface layer thickness with the time of exposure in air.

11.2.2 Effect of process parameters on the properties of r2r printed photoactive thin films

During r2r processing and optimization of OEs such as OPVs, parameters such as the printing speed, drying time, and the concentration of solids in the solutions like P3HT: PCBM blend are expected to have a significant effect on the morphology and properties of the printed photoactive thin films (Noh et al., 2010; Schmidt-Hansberg et al., 2009; Moule, Bonekamp, & Meerholz, 2006). The following results and analysis are provided by the r2r printing of P3HT:PCBM (1:0.8) solutions of 50 mg/ml and 100 mg/ml in ortho-dichlorobenzene (o-DCB) under printing speeds of 3.7, 6, and 8.7 m/min on PEDOT:PSS/PET substrates.

By using SE, the optical parameters of the printed P3HT:PCBM films are extracted. In Figure 11.9, the pseudodielectric $<\varepsilon(\omega)>$ and the bulk dielectric functions $\varepsilon(\omega)$ of the P3HT:PCBM films of 50 mg/ml are shown, respectively. The analysis is performed by the use of the Tauc−Lorentz model in combination with the geometrical model consisting of the layer sequence: PET/PEDOT:PSS layer/P3HT:PCBM layer/P3HT: PCBM surface layer/air. Generally, the optical response of the P3HT:PCBM thin films in the spectral region of the visible to far ultraviolet (Vis-fUV) includes five optical absorptions at about 2.1, 2.4, 3.4, 4.5, and 5.3 eV (Karagiannidis et al., 2011). The first optical absorption is attributed to the transition to the single excitonic level in P3HT (Lioudakis et al., 2007b), while the peak at about 2.4 eV corresponds to the formation of excitons with phonons (Lioudakis et al., 2007a). The remaining three electronic transitions at higher energies (above about 3 eV) are attributed to PCBM and correspond to electronic transitions $S_0 \rightarrow S_{17}$, $S_0 \rightarrow S_{37}$ and $S_0 \rightarrow S_{56}$, respectively (Karagiannidis et al., 2011).

One characteristic optical parameter extracted by the SE analysis is the fundamental energy gap E_g of the P3HT:PCBM thin films. E_g gradually decreases from 1.95 eV to 1.70 eV with the increase of the (100) P3HT crystallite mean size in the bulk of the films (D_{P3HT}) from 14.1 nm to 20.9 nm (as it is derived by the grazing incident X-ray diffraction-GIXRD analysis), and the enhancement of the phase separation between P3HT and PCBM induced by the slow-drying process. The reduction of E_g is attributed to the increase of the conjugation length (π-conjugation) of the P3HT chains during the slow drying of the o-DCB solvent (that remains after the drying stage), as it is also observed during thermal annealing (Kanai et al., 2010; Xue et al., 2010). The conjugation length in crystallites becomes larger because the polymer molecules within such crystallites are perfectly oriented due to the slow-drying process, and there are no structural defects like chain kinks that limit the conjugation length.

There are m π-electrons in each monomer, so their total number in the polymer chain is $N \cdot m$. According to the exclusion principle of Pauli, in each energy level there can be up to two electrons and hence the number of occupied states is $(N \cdot m)/2$. Based on the above mentioned, E_g of the polymer is calculated from Eqn (11.5):

$$\Delta E = E_g = \frac{\hbar \pi^2}{2m_e a^2} \left(\frac{m}{N} + \frac{1}{N^2} \right), \tag{11.5}$$
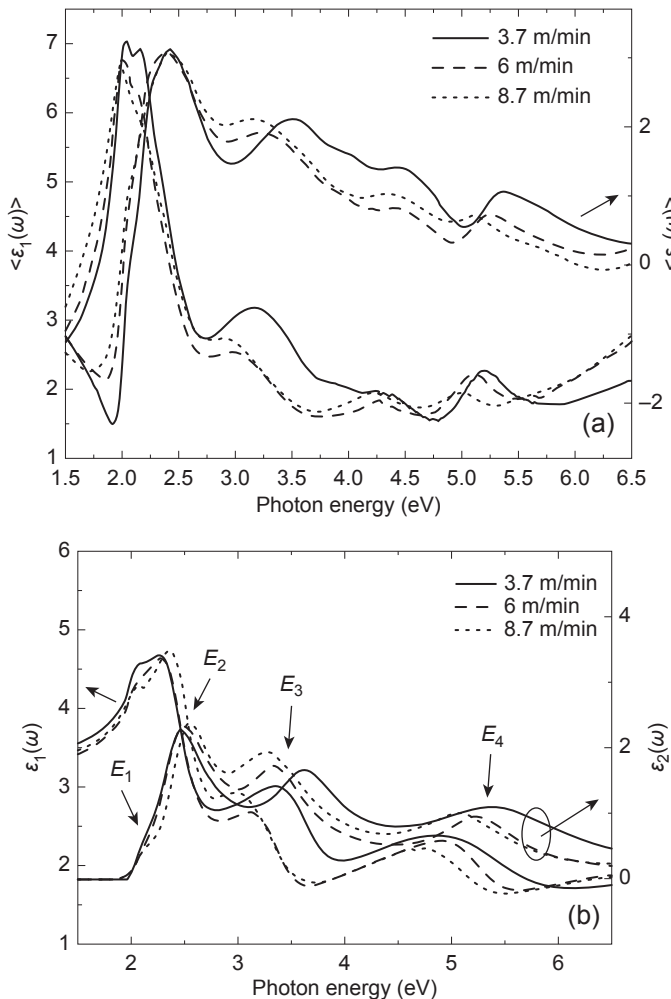
Figure 11.9 The real and imaginary parts of the pseudodielectric $\langle\varepsilon(\omega)\rangle$ (a) and bulk dielectric functions $\varepsilon(\omega)$ (b) of the printed P3HT:PCBM thin films from solution of 50 mg/ml. The arrows indicate the absorption peaks E_1, E_2, E_3, and E_4.

wherein $\hbar$ is the constant Planck, m_e is the electron mass, m the number of π-electrons per monomer, α is the monomer length and N the number of monomers.

Specifically, it is considered a polymer that has nonlocalized electrons along N repeating units (monomers). If the monomer has a length of α then the total length of the π-conjugation is given by Eqn (11.6):

$$L = Na. \tag{11.6}$$

From Eqn (11.6), for monomer length of $\alpha = 3.9$ Å for P3HT, according to first principle calculations (ab initio) (Kresse & Furthmüller, 1996) and taking into account
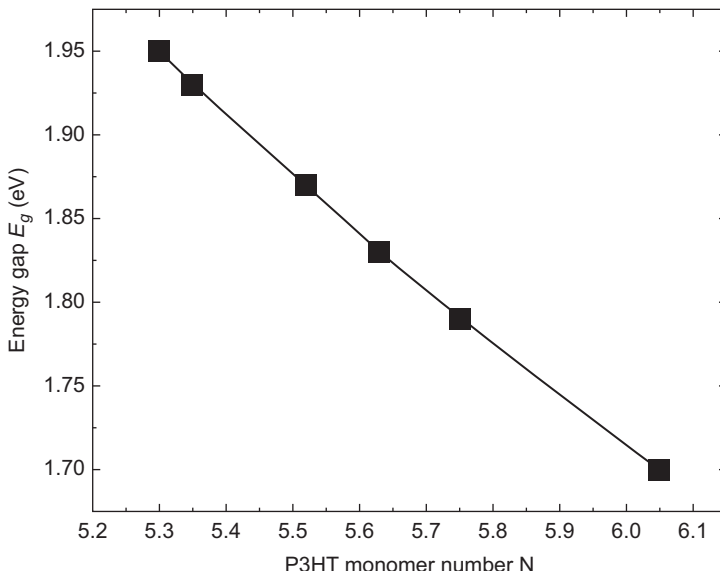
Figure 11.10 The variation of the fundamental energy band gap E_g with the number of monomers N of the P3HT conjugation length.

the E_g values calculated by SE analysis, the number of monomers per conjugation length can be calculated, as depicted in Figure 11.10. The reduction of E_g is accompanied by the increase of N and thus the increase of the conjugation length from 2.07 nm to 2.36 nm.

The kinetics of the molecular rearrangement in the blend films can be understood by the investigation of the vertical distribution of the volume fractions of the P3HT and PCBM constituents (Karagiannidis et al., 2012; Logothetidis et al., 2013; Madsen et al., 2011), and their dependence on printing and drying conditions. This information can be provided by SE through modeling the measured $\langle\varepsilon(\omega)\rangle$ spectra using the Bruggeman effective medium approximation (BEMA). In the gradient layer of the model that simulates the photoactive layer, the volume fractions of P3HT and PCBM are approximated to change exponentially from the bottom to the top of the blend film. The optical responses of the pristine P3HT and PCBM constituents are calculated by using the Tauc−Lorentz model and are fixed during the analysis of the $\langle\varepsilon(\omega)\rangle$ spectra, while the fitted parameters are the % volume fraction of the P3HT and PCBM at the top (P3HT$_{top}$, PCBM$_{top}$) and bottom (P3HT$_{bottom}$, PCBM$_{bottom}$) parts of the films, and the thickness (Koidis et al., 2013a; Karagiannidis et al., 2011). The extraction of the best-fit parameter from the analysis of the above described model is performed using a regression process by the application of a nonlinear Levenberg−Marquardt minimization algorithm.

In general, the slow-drying process has a similar effect to the thermal annealing (Campoy-Quiles et al., 2008). During the slow-drying process, the PCBM molecules diffuse out to the top part of the P3HT:PCBM film, where it forms aggregates, and

toward the interface with the PEDOT:PSS layer (normal OPV architecture), where PCBM domains are already present. Therefore, donor-enriched top regions (high P3HT content) and acceptor-enriched bottom regions (high PCBM content) are formed. This separation is attributed to the differences in the surface free energy of P3HT (24 mN/m) and PCBM (38 mN/m) and the induced dipole−dipole interactions between PCBM and the PEDOT:PSS. According to the SE analysis, the vertical phase separation is more pronounced in the 100 mg/ml films due to the larger amount of the remaining solvent and the enhanced slow-drying process (Figure 11.11(b)). The low PCBM percentage at the top part of the 100 mg/ml films is combined with the formation of PCBM nanocrystals that can be seen in the AFM images of Figure 11.12(b). The PCBM nanocrystals exhibit a diameter of 30−70 nm and height of 10−15 nm as shown in the AFM cross-section diagrams of Figure 11.12(e) and (f). In the case of the 50 mg/ml films, there are very few or no PCBM nanocrystals as shown in the AFM images of Figure 11.12(a). This is attributed to the weaker slow-drying process that takes place in those films. The larger domains of the 100 mg/ml films
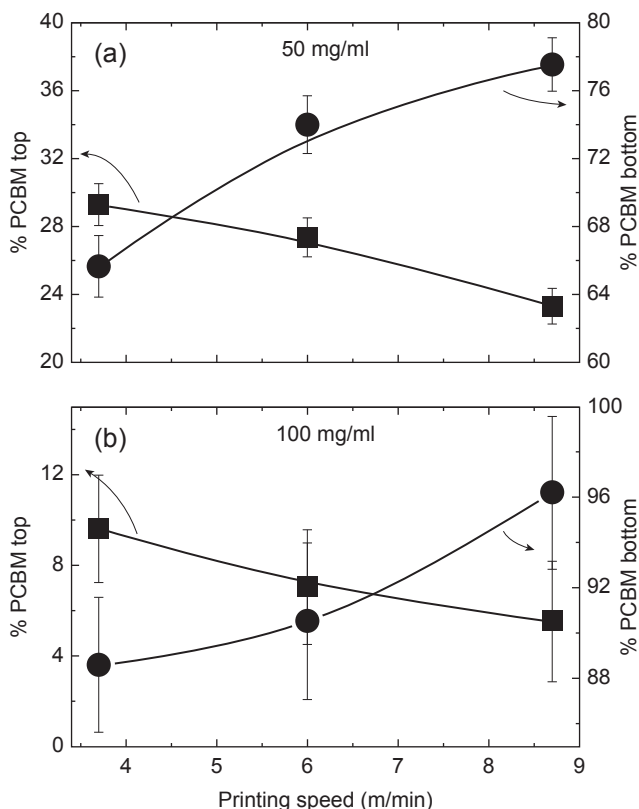
Figure 11.11 The SE-calculated % volume fraction of the PCBM at the top (PCBM$_{top}$) (squares) and bottom (PCBM$_{bottom}$) (circles) parts of the 50 (a) and 100 mg/ml (b) P3HT:PCBM thin films in relation to the printing speed.
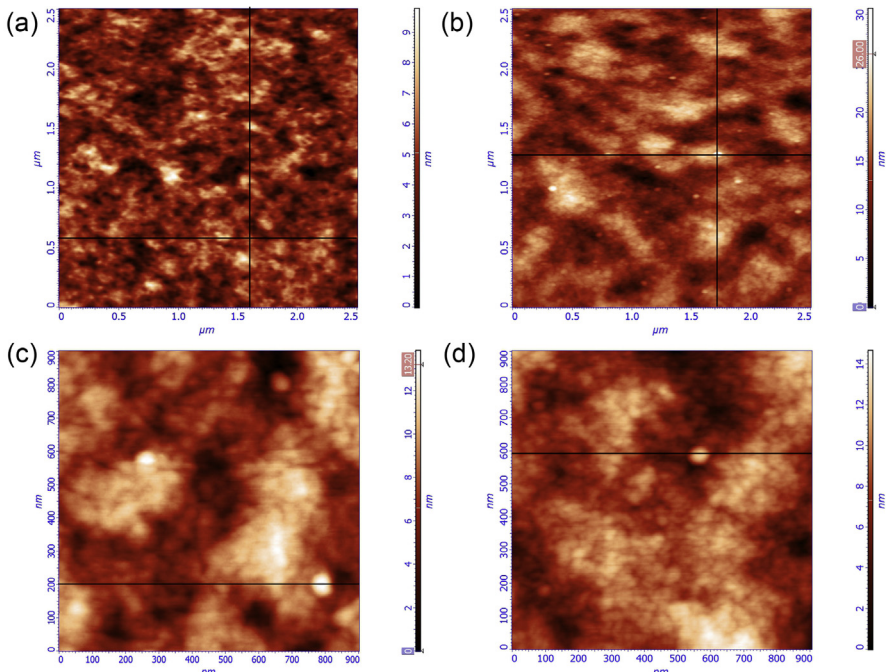
Figure 11.12 The AFM nanotopographies of the P3HT:PCBM thin films of 50 mg/ml printed at 3.7 m/min (a) and 100 mg/ml printed at 8.7 m/min (b). Scanning area of 2.5 × 2.5 μm. The AFM nanotopographies of the 100 mg/ml films printed at 3.7 (c) and 8.7 m/min (d). Scanning area of 900 × 900 nm. Comparative cross-section analysis at the *x*- and *y*-axis of the surface of the 50 mg/ml film printed at 3.7 m/min and that of the 100 mg/ml film printed at 8.7 m/min (e). Scanning area of 2.5 × 2.5 μm. Comparative cross-section analysis at the *x*-axis of the surface of the 100 mg/ml films printed at 3.7 and 8.7 m/min (f). Scanning area of 900 × 900 nm. The cross-sections are indicated by the black lines in images (a), (b), (c), and (d).

are attributed to the higher lateral phase separation between the P3HT and PCBM in combination with the enhanced vertical phase separation as presented in Figure 11.11(b).

As it is shown in the AFM images of the 100 mg/ml films printed at 3.7 m/min and 8.7 m/min with scan size of 0.9 × 0.9 μm² (Figure 11.12(c) and (d), respectively), a nodule-like structure is observed. The nodules formed in the film printed at 8.7 m/min (20−30 nm) are smaller compared to those formed in the film printed at 3.7 m/min (30−40 nm), also indicated in the cross-section analysis of Figure 11.12(f), which implies a reduction in the order of about 30%. This is in accordance with the reduction trend observed in the (100) P3HT crystallites mean size in the surface of the 100 mg/ml films, from about 19 nm (3.7 m/min) to 14 nm (8.7 m/min), that is also a reduction of about 30%, attributed to the effect of the hot air impingement on the surface of the films, which enhances the local surface crystallization. In view of
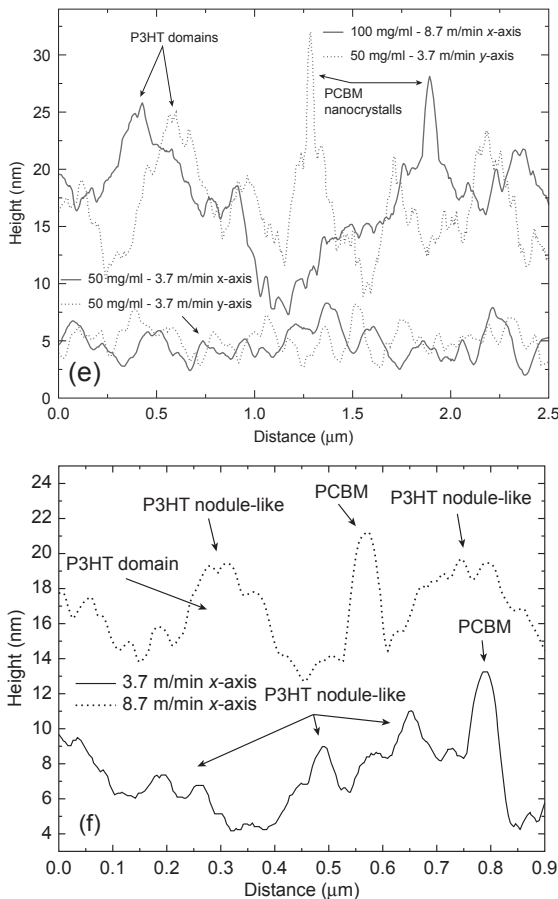
Figure 11.12 Cont'd

these, the nodule-like features are attributed to the crystalline P3HT. Therefore, the crystallization of the P3HT in the surface is defined by the hot air during the drying stage and not by the induced slow-drying process that controls the crystallites' size in the bulk of the films, where the more enhanced the slow-drying process the larger the P3HT crystallites.

The increase of the $PCBM_{top}$ drives to increase the surface free energy toward that of the pure PCBM (38 mN/m) (area II in Figure 11.13). On the contrary, at the low $PCBM_{top}$ regime (area I) the surface free energy approaches that of the pure P3HT (24 mN/m). In particular, the high $PCBM_{top}$ of the 50 mg/ml film printed at 3.7 m/min and the well-mixing morphology between P3HT and PCBM according to Figure 11.12(a) lead to a surface free energy value of 35 mN/m, close to that of the pure PCBM. On the other hand, in the 100 mg/ml films, the phase separation is
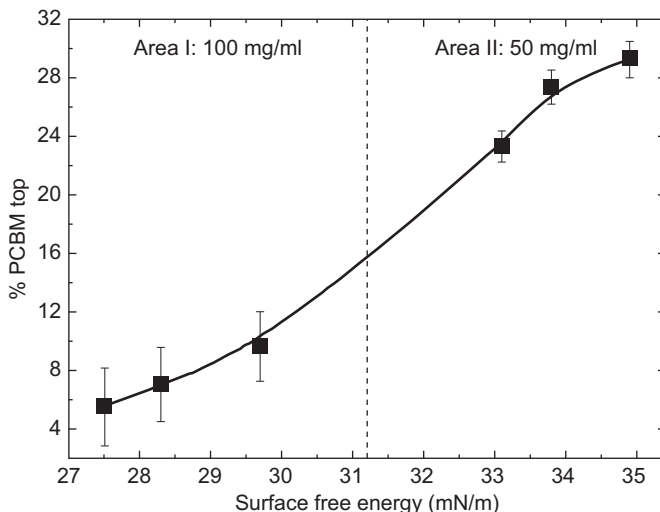
Figure 11.13 The SE-calculated % volume fraction of PCBM at the top part of the P3HT: PCBM thin films (PCBM$_{top}$) in relation to the calculated, through contact angle measurements, surface free energy.

strongly enhanced in relation to 50 mg/ml. The surface free energy of 27.5 mN/m of the film printed at 8.7 m/min approaches that of the pure P3HT since only about 5% PCBM is located on the surface in the form of nanocrystals, and P3HT domains of 200−300 nm are observed. Therefore, the lateral characteristic features that are observed in the AFM images are the result of the growing polymer aggregates the size of which depends on the extent of the slow-drying process and the PCBM diffusion.

11.2.3 Analyzing key parameters to improve the cost-efficiency of r2r processes

Both the protection of materials like PEDOT:PSS from the air immediately after their printing, and the efficient r2r drying and/or postannealing of the P3HT:PCBM, result in the change of morphology and the increase of the device efficiency (Koidis et al., 2013b). In particular, in order to suppress the vertical phase separation in the layer of P3HT:PCBM during r2r processing, the increase of drying time and the efficient evaporation of the solvent are necessary. Comparing the characteristics of P3HT: PCBM thin films dried during the r2r process for a time period of $t_{r2r} = 19$ and 60 s, there are significant differences in their morphology. In particular, for $t = 60$ s, the vertical phase separation between P3HT and PCBM is limited, so the PCBM$_{top}$ increases significantly, i.e., PCBM$_{top} = 23\%$, in contrast with the case of drying for 19 s where PCBM$_{top} = 11\%$ (Figure 11.14). As it is shown in the AFM images of Figure 11.15(a) and (b) that correspond to $t_{r2r} = 19$ s and 60 s,
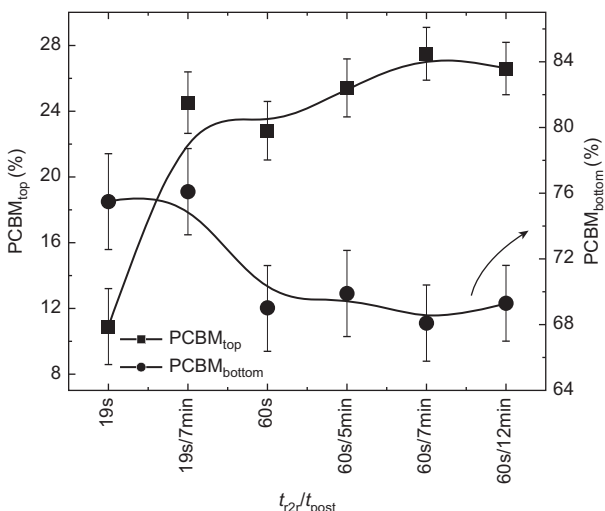
Figure 11.14 The % volume fractions of PCBM at the top (PCBM$_{top}$) and bottom (PCBM$_{bottom}$) parts of the P3HT:PCBM films in relation to the thermal treatment conditions (r2r drying−t_{r2r} and posttreatment−t_{post}).
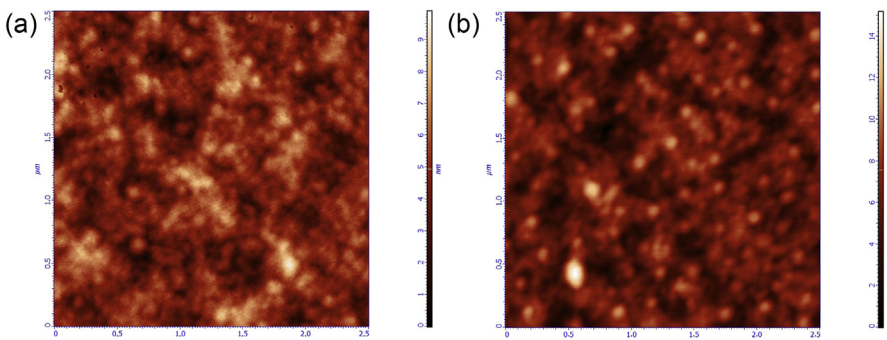
Figure 11.15 The AFM nanotopographies of the P3HT:PCBM printed on PET/ITO/PEDOT: PSS substrates and dried for $t_{r2r} = 19$ s (a) and 60 s (b) (in both cases $t_{post} = 0$ min).

respectively, the presence of a greater volume fraction of PCBM near the surface in the latter case, along with the lowest PCBM$_{bottom}$ (69% vs 76% for $t_{r2r} = 19$ s), leads to a more desired morphology characterized by interpenetrating networks of P3HT and PCBM at the nanoscale. Also, there is an increase in the roughness due to the formation of many more and larger PCBM nanocrystals. Furthermore, with increasing t_{r2r} (and/or thermal posttreatment time; t_{post}) the crystallinity of the films is significantly enhanced (Figure 11.16) in conjunction with the greater D_{P3HT} in the bulk of the films (Figure 11.17), which enable the more efficient transport of holes. According to the values of the (100) P3HT crystallite mean size in the surface of the films, shown in Figure 11.17, the crystallinity in the surface is not particularly
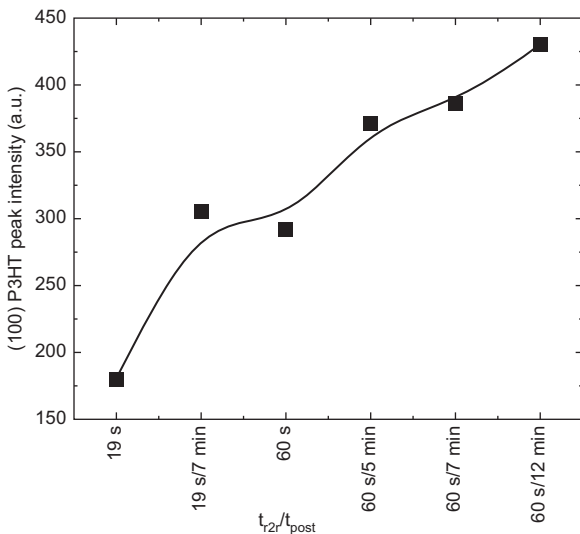
Figure 11.16 The GIXRD-measured (100) P3HT peak intensity of the P3HT:PCBM thin films in relation to the thermal treatment conditions (r2r drying$-t_{r2r}$ and posttreatment$-t_{post}$).
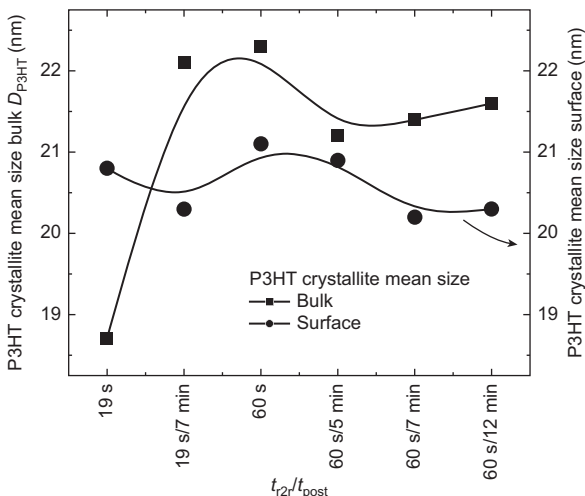
Figure 11.17 The mean P3HT crystallite size in the bulk (D_{P3HT}) and the surface of the P3HT: PCBM thin films in relation to the thermal treatment conditions (r2r drying$-t_{r2r}$ and posttreatment$-t_{post}$).

influenced by the increased drying time, which means that the incidence of hot air to the surface with a speed of about 3 m/s and the formation of a thin layer of residual hot air over the surface during the movement of the substrate is a proficient factor for defining the surface crystallinity, regardless of the drying time. To that, it may also
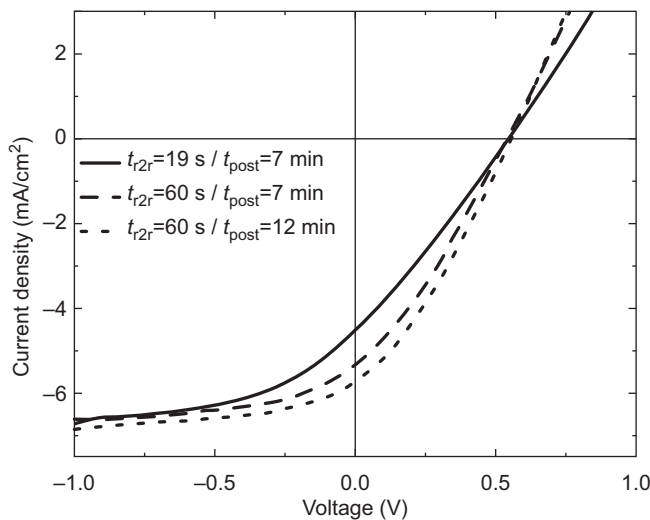
Figure 11.18 The J-V curves of the r2r printed organic photovoltaics.

contribute the fact that in the film dried for 60 s the PCBM accumulation at the surface and the formation of nanocrystals can block the increase of P3HT crystallite size (Ding et al., 2009).

Figure 11.18 shows the J-V characteristics of the r2r printed OPVs and Table 11.1 displays their electrical characteristics resulting from the analysis. As it can be seen, the increase of t_{r2r} from 19 to 60 s leads to doubling the PCE from 0.43% to 0.88% ($t_{post} = 7$ min in both cases), due to the improved morphology and crystallinity, the strengthening of the nanophase separation, and the increased interfacial area between P3HT and PCBM. This consequently enables the remarkable increase of short circuit current density (J_{sc}) and fill factor (FF) from 3.10 mA/cm^2 to 5.28 mA/cm^2 and from 25% to 31%, respectively.

For $t_{post} = 12$ min, there is an enhancement of the crystalline phase in the film (see Figure 11.16) in combination with the increase of the FF and the improvement of the contact between the photoactive layer and the cathode. These allow the increase of the PCE.

Table 11.1 The electrical characteristics of the r2r printed organic photovoltaics

t_{r2r} (s)	t_{post} (min)	J_{sc} (mA/cm^2)	V_{oc} (V)	FF (%)	R_s (Ω cm^2)	R_{sh} (Ω cm^2)	PCE (%)
19	7	3.10	0.55	25	254	216	0.43
60	7	5.28	0.54	31	78	168	0.88
60	12	5.68	0.55	32	71	183	1.00

In summary, we stress the great importance of the drying step in the r2r printing process, which determines the morphology and performance of the OPV. The morphology of the photoactive layer is characterized by intense vertical phase separation between P3HT and PCBM, which is induced during the printing process. The extensive phase separation during r2r processing without the controlled drying of the printed layers can theoretically favor the inverted OPV architecture but also leads to the deterioration of the morphology and restricts the formation of efficient charge carrier pathways. Therefore, in both normal and inverted OPV architecture, the optimization of the drying step during the r2r printing is classified as a very critical parameter for increasing the efficiency of the printed OPVs and other OEs. Furthermore, SE can be used as a robust tool for the calculation of the thickness, optical properties, and morphology of the functional layers of the OEs. In particular, in-line SE can become a very useful quality control system with unique capabilities that can be integrated in r2r and vacuum processes and enable the cost-efficient, large-scale manufacturing of OEs (Logothetidis et al., 2013; Koidis et al., 2010; Koidis et al., 2013b; Georgiou et al., 2008).

Process optimization data given above form the basis for the fabrication of printed OPV modules of both normal and inverted architectures. Figure 11.19 shows the I-V characteristics of indicative printed OPV modules with normal (structure of PET/ITO/PEDOT:PSS/P3HT:PCBM/Ca/Ag) and inverted (structure of PET/ITO/ZnO nanoparticles ink/P3HT:PCBM/PEDOT:PSS/Ag ink) architectures, and Table 11.2 shows the collected electrical characteristics resulting from the analysis.

The OPV modules can be available to product developers and system integrators for various applications such as for portable power. OPV modules can be produced in custom shapes and sizes, therefore they can fit into many product categories. In the
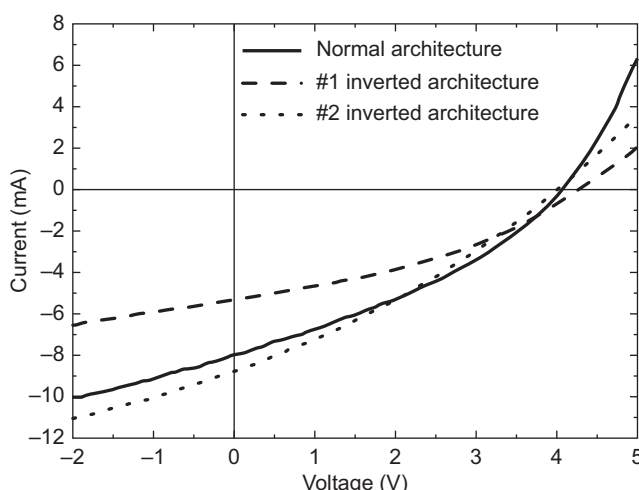
Figure 11.19 The I-V curves of the printed organic photovoltaic modules of both normal and inverted architectures.

Table 11.2 The electrical characteristics of the printed organic photovoltaic (OPV) modules

OPV module architecture	I_{sc} (mA)	V_{oc} (V)	FF (%)	Maximum power (mW)	R_s (Ω)	R_{sh} (Ω)	PCE (%)
Normal	7.95	4.05	34	11.02	259	769	1.10
Inverted#1	5.27	4.25	37	8.28	405	1676	1.23
Inverted#2	8.71	4.00	31	10.69	318	623	1.59

short term, OPV modules will provide supplementary power to portable electronics and to people who are off grid. OPVs are more versatile than most conventional photovoltaic technologies, working under both solar and indoor levels of illumination, and with direct as well as diffuse scattered light, making them especially suited to indoor energy harvesting. For example, sensors can be powered that will monitor the indoor air quality. In the long term, as the efficiency and lifetime of OPV modules improve, they will be the primary source of power for outdoors, off grid, and building integrated photovoltaic (BIPV) applications.

11.3 Combination of wet and vacuum techniques for OEs

The deposition of low sheet resistance TCO electrodes ($R_s < 100\ \Omega$/sq) on polymer substrates such as PET has been demonstrated mainly using sputtering techniques (Minami, Miyata, & Ohtani, 2007; Guillén & Herrero, 2011; Koidis, Logothetidis, Georgiou & Laskarakis 2008). In that case some sputter damage occurs on such substrates (Koidis, Logothetidis, Georgiou, Laskarakis, et al., 2008; Koidis et al., 2009) which, however, is acceptable taking into account the functionality that these layers provide. The majority of OE devices are fabricated with the TCO deposited directly on a substrate, and then the rest of the functional layers are deposited on top of that. The ability to directly deposit a TCO as a top contact is desirable as it enables device fabrication using metallic bottom contacts, introduces the possibility of TCOs acting as an encapsulant to protect the organic active layers from UV, moisture, and oxygen (Fahlteich et al., 2009; Hintz et al., 2011), and enables the fabrication of semitransparent OE devices (Franklin et al., 2014; Guillén & Herrero, 2011). Aluminum-doped zinc oxide (AZO) is attractive as a TCO and alternative to ITO showing lower material and processing costs (Logothetidis, 2008).

During the optimization of AZO thin films deposited by sputtering on PET substrates, the increase of the applied power on the sputtering target P_t leads to films with lower value of resistivity and higher carrier density, according to Figure 11.20. The thinnest AZO film exhibits the highest resistivity ascribed to the lowest carrier
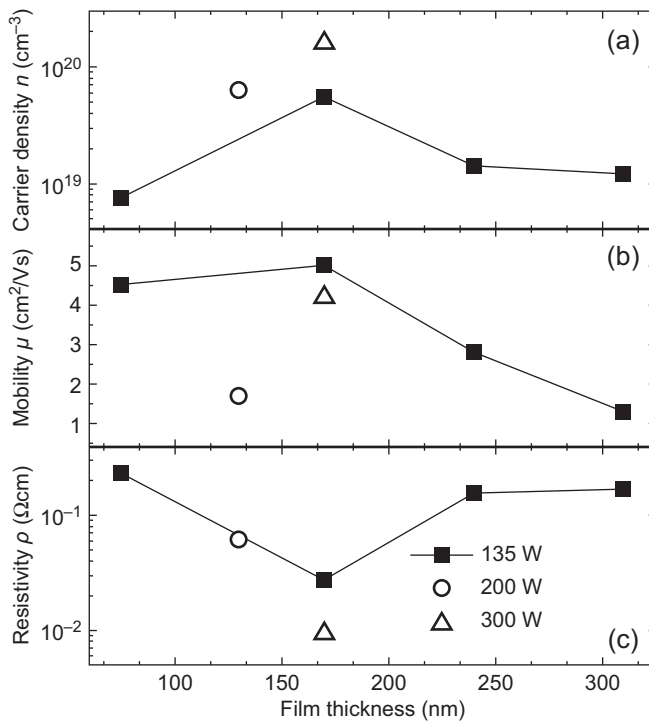
Figure 11.20 The charge carrier density n (a), the mobility μ (b), and the resistivity ρ (c) of the AZO thin films in relation to their thickness.

density, despite its relatively high mobility. This is attributed to the fact that in the AZO films with smaller values of thickness, the remained stress is higher than in the case of thicker samples, and the film contains many defects (samples grown under $P_t = 135$ W). As a result, many free electrons can be caught by a large number of traps formed by the defects, leading to higher resistivity values. In general, the increase of P_t leads to the increase of the carrier density and decrease of mobility due to both the formation of defects and dislocations, which probably act as electron traps and donors (Lebedev et al., 2006), respectively. The electrical properties of the AZO film deposited at 300 W are improved in comparison to that deposited at 200 W. In particular, the higher value of P_t results in film characterized by increased carrier density. Despite the lower mobility of the film deposited at 300 W, there is a significant increase of its carrier density compared to that deposited at 135 W (films having the same thickness), which gives lower resistivity. By applying 135 W on target leads to the domination of homogeneous AZO growth according to ZnO results (Koidis et al., 2008). For $P_t = 300$ W stresses are induced that favor the island growth, as the SE real-time results indicate in Figure 11.21. The evolution of the AZO film thickness during its deposition at 300 W comes from the analysis of the real-time measured $<\varepsilon(\omega)>$ spectra by using the Tauc−Lorentz model in combination with the geometrical model
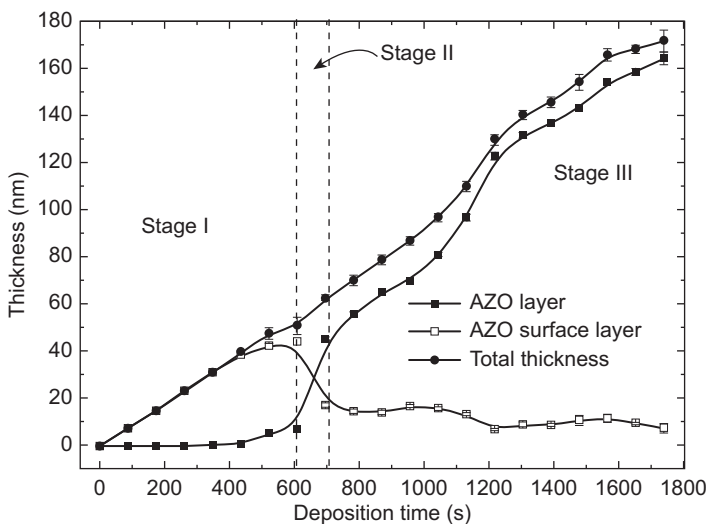
Figure 11.21 The evolution of the thickness of the layers of the geometrical model used for the analysis of the real-time SE spectra during the deposition of AZO film on PET under $P_t = 300$ W.

consisting of the layer sequence: PET/AZO layer/AZO surface layer/air. The specific growth mechanism can induce charges at grain barriers or extended defects leading to additional electron scattering and less mobility. According to Figure 11.21, during stage I the nucleation and growth of islands take place, which finally become about 45 nm in height indicated by the thickness of the AZO surface layer. The coalescence of the islands follows (stage II) denoted by the abrupt decrease of the AZO surface layer and simultaneous increase of the bottom layer (AZO layer). Stage III is dominated by the homogeneous growth of the AZO film.

The increase of the AZO film thickness and grain size can lead to lower resistivity and higher mobility and carrier density values (Lee, 2008). Contrarily, the increase of the thickness (above 170 nm) and grain size lead to the increase of resistivity and decrease of mobility and carrier density despite quality improvement of the crystallites. In polycrystalline TCOs with carrier density $<10^{20}$ $1/cm^3$, the resistivity model of Seto (Seto, 1975) and Bruneaux et al. (1991) are applicable, and the resistivity is mostly due to the grain barrier electron trapping. Therefore, the resistivity could be assumed to be determined by carrier trapping and grain boundary potential barrier, neglecting the bulk resistance of the grains, in accordance with the model of Seto. Hence, according to the grain boundary model, in order for the resistivity to grow with the grain size, the area density of traps on the grain boundary should also grow, as well as the density of the defects (David, Goldsmith, & Boxman, 2005).

Multilayer transparent systems, which include thin metal layers (thickness of a few nm), such as AZO/Ag/AZO, can be used to develop semitransparent OPVs substituting the opaque metal cathode, i.e., Al or Ag, which usually have a thickness of about

100 nm. In addition, AZO being at the outer surface of the OPV provides oxygen and humidity barrier properties, protecting both the metal layer and the internal organic layers. OPVs with Ca/AZO/Ag/AZO as cathode (AZO layers are sputtered and Ca, Ag are thermally evaporated) instead of Ca/Al or Ca/Ag, are nonfunctional since the high kinetic energy of the sputtered particles that impinge on the P3HT:PCBM/Ca system seems to destroy the integrity of the interfaces, resulting in the inoperability of the electrode.

This problem can be overcome by skipping the deposition of the first AZO layer, i.e., the cathode can consist of the layer sequence: Ca/Ag/AZO (thickness of 10 nm/12 nm/40 nm, respectively). For the deposition of AZO layer, P_t of 300 W is applied on the target that gives better quality films characterized by higher conductivity (Koidis et al., 2010). The presence of Ca is important: being a metal with a low work function, it determines, in conjunction with the high work function layer over ITO (i.e., PEDOT:PSS), the movement of the charge carriers toward the corresponding electrodes. According to Figure 11.22, the surface of the deposited AZO layer has a relatively low RMS (3.3 nm) and peak-to-valley (28.6 nm) roughness.

Figure 11.23 shows the J-V characteristic curves of the reference OPV having a structure of glass/ITO/PEDOT:PSS/P3HT:PCBM/Ca/Al and the semitransparent OPV with the structure of glass/ITO/PEDOT:PSS/P3HT:PCBM/Ca/Ag/AZO, while in Table 11.3 the electrical characteristics of the OPVs are collected, as derived from the analysis of the curves. There is a significant difference in the FF, which in the case of the reference OPV is 52%, whereas in the semitransparent OPV is 31%.

The difference in FF indicates the more difficult movement of the charge carriers in the semitransparent device because the Ag/AZO interface is involved, as well as the fact that the thin thickness of the Ag and AZO layers limit the conductivity. Additionally, the semitransparent device shows larger series (R_s) and lower parallel (R_{sh}) resistance in relation to the reference device.

On the other side, the semitransparent device shows much higher J_{sc} value (10.83 mA/cm^2 instead of 7.11 mA/cm^2 for the reference device), which is attributed to the reflectivity of Ag and the antireflective properties of AZO. In general, the increase
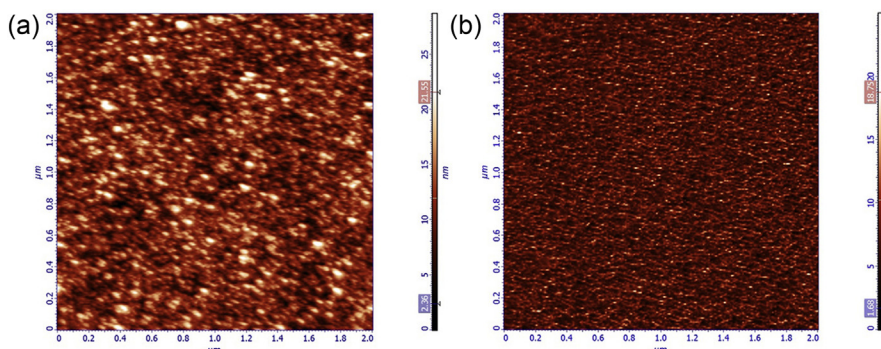
Figure 11.22 AFM nanotopography (a) and phase image (b) of the AZO film deposited under $P_t = 300$ W on glass/ITO/PEDOT:PSS/P3HT:PCBM/Ca/Ag system. Scanning area of 2×2 μm.
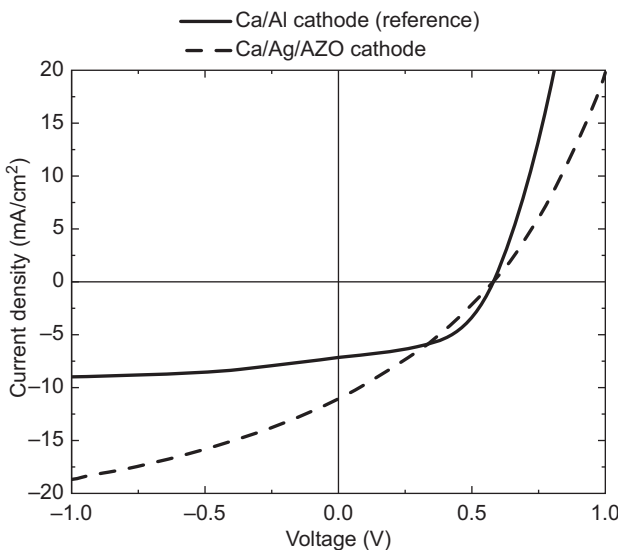
Figure 11.23 The J-V curves of the reference and semitransparent organic photovoltaic.

Table 11.3 The electrical characteristics of the reference and semitransparent organic photovoltaics (OPVs)

OPV	J_{sc} (mA/cm^2)	V_{oc} (V)	FF (%)	R_s ($\Omega \cdot$cm^2)	R_{sh} ($\Omega \cdot$cm^2)	PCE (%)
Reference	7.11	0.57	52	21	321	2.10
Semi-transparent	10.83	0.57	31	36	74	1.93

of the thickness of the Ag layer enhances the reflectivity and the absorption of the light (by the photoactive layer) that comes through the anode. On the other hand, the antireflective properties of AZO and the semitransparency of Ag due to its thin thickness allow the passing of the light from the side of the cathode, thus enhancing the absorption of the photoactive layer (although some percentage of the transmitted light from the cathode is reflected from the Ag layer). Therefore, due to the higher value of J_{sc} in the semitransparent device, its efficiency is quite similar to that of the reference device.

11.4   Future trends

There is a lot of research work focused on the development of new thin film materials and processes for the manufacturing of OEs. For example, the addition of additives and solvents (Liao et al., 2013; Hong et al., 2014; Kim et al., 2013; Vongsaysy et al., 2013), the introduction of new material systems such as ternary blends

(Goubard & Wantz, 2013; Ameri et al., 2013; Chen et al., 2013), new soluble buffer layers in OPVs (Li et al., 2013), and printable small-molecule materials in OLEDs (Tekoglu et al., 2013) or the combination of advanced materials and device architectures (You et al., 2013). In addition, ITO-free OEs such as OPVs (Angmo, Gevorgyan, et al., 2013; van de Wiel et al., 2013; Angmo & Krebs, 2013) with advanced architectures (Angmo, Gonzalez-Valls et al., 2013) and electrochromic devices (Jensen et al., 2013) are optimized, and graphene-based materials are fabricated for OEs (Iwan & Chuchmała, 2012; Han et al., 2013; He et al., 2012; Lee, Rana, & Ahn, 2013). In terms of manufacturing technologies, except for the well-known r2r techniques used for the printing/coating of the layers, advanced production techniques such as inkjet for the precise printing of thin films (Angmo, Larsen-Olsen et al., 2013; Angmo, Sweelssen et al., 2013; Hösel et al., 2013), laser processing tools for the patterning/scribing of them (Semaltianos et al., 2011), and monitoring systems for the quality control of the materials and processes (Logothetidis et al., 2013) are integrated in r2r processes toward the cost-efficient, large-scale manufacturing of OEs. Also, new processes are developed, for example, for the lamination of the devices (Kaduwal, Zimmermann, & Würfel, 2014). On the other side, particular attention is paid on practicality properties and functionality of the OE systems such as the semitransparency of the OPVs, which gives them new application capabilities (Guo et al., 2013).

To achieve the goal of manufacturing low-cost and large-scale OEs requires the optimization of materials and r2r processes to increase efficiency and lifetime of the manufactured systems. First of all, in the case of the solution-based processes, the solutions used should meet certain standards (such as viscosity) compatible with the technique to be used. Moreover, in the context of optimization process, it is necessary to identify those parameters that determine the properties of the developed films, e.g., printing speed in a r2r system or drying conditions of wet films that have just been printed. Another important consideration is the design and architecture of the device to be manufactured. It is therefore concluded that the optimization of r2r processes includes a plurality of parameters that should be related to each other in order to find the optimal conditions for the production of OEs. In addition to all of the above, the enhancement of the OEs' manufacturing cost-efficiency is expected to come through the smart implementation of all the available technologies such as the combination of printing, laser, vacuum, quality control processes, or the utilization of inert atmosphere facilities that would enable the improvement of the devices' performance toward mass production. Finally, the development of novel printable materials that are formulated using nonchlorinated solvents is targeted. The use of environmentally compatible solvents is a major prerequisite for cost reduction, as complex safety measures on an industrial scale will no longer be required.

Acknowledgements

References

Agalya, G., Lv, C., Wang, X., Koyama, M., Kubo, M., & Miyamoto, A. (2005). Theoretical study on the electronic and molecular properties of ground and excited states of ethylenedioxythiophene and styrenesulphonic acid. *Applied Surface Science, 244*(1−4), 195−198.

Ameri, T., Khoram, P., Min, J., & Brabec, C. J. (2013). Organic ternary solar cells: a review. *Advanced Materials, 25*(31), 4245−4266.

Angmo, D., Gevorgyan, S., Larsen-Olsen, T. T., Søndergaard, R. R., Hösel, M., Jørgensen, M., et al. (2013). Scalability and stability of very thin, roll-to-roll processed, large area, indium-tin-oxide free polymer solar cell modules. *Organic Electronics, 14*(3), 984−994.

Angmo, D., Gonzalez-Valls, I, Veenstra, S., Verhees, W., Sapkota, S., Schiefer, S., et al. (2013). Low-cost upscaling compatibility of five different ITO-free architectures for polymer solar cells. *Journal of Applied Polymer Science, 130*(2), 944−954.

Angmo, D., & Krebs, F. C. (2013). Flexible ITO-free polymer solar cells. *Journal of Applied Polymer Science, 129*(1), 1−14.

Angmo, D., Larsen-Olsen, T. T., Jørgensen, M., Søndergaard, R. R., & Krebs, F. C. (2013). Roll-to-roll inkjet printing and photonic sintering of electrodes for ITO free polymer solar cell modules and facile product integration. *Advanced Energy Materials, 3*(2), 172−175.

Angmo, D., Sweelssen, J., Andriessen, R., Galagan, Y., & Krebs, F. C. (2013). Inkjet printing of back electrodes for inverted polymer solar cells. *Advanced Energy Materials, 3*(9), 1230−1237.

Bruneaux, J., Cachet, H., Froment, M., & Messad, A. (1991). Correlation between structural and electrical properties of sprayed ton oxide films with and without fluorine doping. *Thin Solid Films, 197*, 129−142.

Campoy-Quiles, M., Ferenczi, T., Agostinelli, T., Etchegoin, P. G., Kim, Y., Anthopoulos, T. D., et al. (2008). Morphology evolution via self-organization and lateral and vertical diffusion in polymer:fullerene solar cell blends. *Nature Materials, 7*(2), 158−164.

Chang, Y., Lee, K., Kiebooms, R., & Aleshin, A. (1999). Reflectance of conducting poly(3,4-ethylenedioxythiophene). *Synthetic Metals, 105*, 203−206.

Chen, Y.-C., Hsu, C.-Y., Lin, R. Y.-Y., Ho, K.-C., & Lin, J. T. (2013). Materials for the active layer of organic photovoltaics: ternary solar cell approach. *ChemSusChem, 6*(1), 20−35.

David, T., Goldsmith, S., & Boxman, R. L. (2005). Dependence of zinc oxide thin film properties on filtered vacuum arc deposition parameters. *Journal of Physics D: Applied Physics, 38*(14), 2407−2416.

Ding, J. M., de la Fuente Vornbrock, A., Ting, C., & Subramanian, V. (2009). Patternable polymer bulk heterojunction photovoltaic cells on plastic by rotogravure printing. *Solar Energy Materials and Solar Cells, 93*(4), 459−464.

Fahlteich, J., Fahland, M., Schönberger, W., & Schiller, N. (2009). Permeation barrier properties of thin oxide films on flexible polymer substrates. *Thin Solid Films, 517*(10), 3075−3080.

Franklin, J. B., Gilchrist, J. B., Downing, J. M., Roy, K. A., & McLachlan, M. A. (2014). Transparent conducting oxide top contacts for organic electronics. *Journal of Materials Chemistry C, 2*(1), 84.

Georgiou, D., Logothetidis, S., Koidis, C., & Laskarakis, A. (2008). In-situ and real-time monitoring of high barrier layers growth onto polymeric substrates. *Physica Status Solidi (C), 5*(5), 1300−1303.

Gioti, M., Laskarakis, A., & Logothetidis, S. (2004). IR−FUV ellipsometry studies on the optical, electronic and vibrational properties of polymeric membranes. *Thin Solid Films, 455−456*, 283−287.

Goubard, F., & Wantz, G. (2013). Ternary blends for polymer bulk heterojunction solar cells. *Polymer International, 63*(8), 1362−1367.

Guillén, C., & Herrero, J. (2011). TCO/metal/TCO structures for energy and flexible electronics. *Thin Solid Films, 520*(1), 1−17.

Guo, F., Zhu, X., Forberich, K., Krantz, J., Stubhan, T., Salinas, M., et al. (2013). ITO-free and fully solution-processed semitransparent organic solar cells with high fill factors. *Advanced Energy Materials, 3*(8), 1062−1067.

Han, X., Chen, Y., Zhu, H., Preston, C., Wan, J., Fang, Z., et al. (2013). Scalable, printable, surfactant-free graphene ink directly from graphite. *Nanotechnology, 24*(20), 205304.

He, M., Jung, J., Qiu, F., & Lin, Z. (2012). Graphene-based transparent flexible electrodes for polymer solar cells. *Journal of Materials Chemistry, 22*(46), 24254.

Hintz, H., Egelhaaf, H.-J., Lüer, L., Hauch, J., Peisert, H., & Chassé, T. (2011). Photo-degradation of P3HT−A systematic study of environmental factors. *Chemistry of Materials, 23*(2), 145−154.

Hong, Y.-R., Chen, P.-K., Wang, J.-C., Lee, M.-K., Horng, S.-F., & Meng, H.-F. (2014). Simultaneous enhancement in both large-area coatability and photovoltaic performance of inverted organic solar cells with co-solvent. *Solar Energy Materials and Solar Cells, 120*, 197−203.

Hösel, M., Søndergaard, R. R., Angmo, D., & Krebs, F. C. (2013). Comparison of fast roll-to-roll flexographic, inkjet, flatbed, and rotary screen printing of metal back electrodes for polymer solar cells. *Advanced Engineering Materials, 15*(10), 995−1001.

Iwan, A., & Chuchmała, A. (2012). Perspectives of applied graphene: polymer solar cells. *Progress in Polymer Science, 37*(12), 1805−1828.

Jensen, J., Hösel, M., Kim, I., Yu, J.-S., Jo, J., & Krebs, F. C. (2013). Fast switching ITO free electrochromic devices. *Advanced Functional Materials, 24*(9), 1228−1233.

Kaduwal, D., Zimmermann, B., & Würfel, U. (2014). ITO-free laminated concept for flexible organic solar cells. *Solar Energy Materials and Solar Cells, 120*, 449−453.

Kanai, K., Miyazaki, T., Suzuki, H., Inaba, M., Ouchi, Y., & Seki, K. (2010). Effect of annealing on the electronic structure of poly(3-hexylthiophene) thin film. *Physical Chemistry Chemical Physics, 12*(1), 273−282.

Karagiannidis, P. G., Georgiou, D., Pitsalidis, C., Laskarakis, A., & Logothetidis, S. (2011). Evolution of vertical phase separation in P3HT: PCBM thin films induced by thermal annealing. *Materials Chemistry and Physics, 129*(3), 1207−1213.

Karagiannidis, P. G., Kalfagiannis, N., Georgiou, D., Laskarakis, A., Hastas, N. A., Pitsalidis, C., et al. (2012). Effects of buffer layer properties and annealing process on bulk heterojunction morphology and organic solar cell performance. *Journal of Materials Chemistry, 22*, 14624−14629.

Kim, J. Y., Kim, S. H., Lee, H.-H., Lee, K., Ma, W., Gong, X., et al. (2006). New architecture for high-efficiency polymer photovoltaic cells using solution-based titanium oxide as an optical spacer. *Advanced Materials, 18*(5), 572−576.

Kim, Y. H., Sachse, C., Machala, M. L., May, C., Müller-Meskamp, L., & Leo, K. (2011). Highly conductive PEDOT: PSS electrode with optimized solvent and thermal post-treatment for ITO-free organic solar cells. *Advanced Functional Materials, 21*(6), 1076−1081.

Kim, M., Kim, J.-H., Choi, H. H., Park, J. H., Jo, S. B., Sim, M., et al. (2013). Electrical performance of organic solar cells with additive-assisted vertical phase separation in the photoactive layer. *Advanced Energy Materials, 4*(2), 1300612.

Kim, C. H., Jo, J., & Lee, S.-H. (2012). Design of roll-to-roll printing equipment with multiple printing methods for multi-layer printing. *The Review of Scientific Instruments, 83*(6), 065001.

Koidis, C., Logothetidis, S., Laskarakis, A., Tsiaoussis, I., & Frangis, N. (2009). Thin film and interface properties during ZnO deposition onto high-barrier hybrid/PET flexible substrates. *Micron, 40*(1), 130−134.

Koidis, C., Logothetidis, S., Kassavetis, S., Laskarakis, A., Hastas, N. A., & Valassiades, O. (2010). Growth mechanisms and thickness effect on the properties of Al-doped ZnO thin films grown on polymeric substrates. *Physica Status Solidi (A), 207*(7), 1581−1585.

Koidis, C., Logothetidis, S., Kassavetis, S., Kapnopoulos, C., Karagiannidis, P. G., Georgiou, D., et al. (2013a). Effect of process parameters on the morphology and nanostructure of roll-to-roll printed P3HT: PCBM thin films for organic photovoltaics. *Solar Energy Materials and Solar Cells, 112*, 36−46.

Koidis, C., Logothetidis, S., Ioakeimidis, A., Laskarakis, A., & Kapnopoulos, C. (2013b). Key factors to improve the efficiency of roll-to-roll printed organic photovoltaics. *Organic Electronics, 14*(7), 1744−1748.

Koidis, C., Logothetidis, S., Georgiou, D., & Laskarakis, A. (2008). In-situ and real-time investigation of ZnO thin films growth onto rigid and flexible substrates. *Physica Status Solidi (C), 5*(5), 1366−1369.

Koidis, C., Logothetidis, S., Georgiou, D., Laskarakis, A., Lousinian, S., Tsiaoussis, et al. (2008). Growth, optical and nanostructural properties of magnetron sputtered ZnO thin films deposited on polymeric substrates. *Physica Status Solidi (A), 205*(8), 1988−1992.

Krebs, F. C. (2009). Fabrication and processing of polymer solar cells: a review of printing and coating techniques. *Solar Energy Materials and Solar Cells, 93*(4), 394−412.

Kreis, J., Schwambera, M., Keiper, D., Gersdorff, M., Long, M., & Heuken, M. (2013). Carrier-gas enhanced vapor phase deposition for organic thin films: addressing mass manufacturing requirements for OLED devices, and overcoming existing challenges with OVPD®. *Proceedings of SPIE - The International Society for Optical Engineering, 8829*, 88291C.

Kresse, G., & Furthmüller, J. (1996). Efficient iterative schemes for ab initio total-energy calculations using a plane-wave basis set. *Physical Review B - Condensed Matter and Materials Physics, 54*(16), 11169−11186.

Laskarakis, A., Karagiannidis, P. G., Georgiou, D., Nikolaidou, D. M., & Logothetidis, S. (2013). Optical investigations of the effect of solvent and thermal annealing on the optoelectronic properties of poly(3,4-ethylenedioxythiophene):poly(styrenesulfonate) films. *Thin Solid Films, 541*, 102−106.

Laskarakis, A., Georgiou, D., Logothetidis, S., Amberg-Scwhab, S., & Weber, U. (2009). Study of the optical response of hybrid polymers with embedded inorganic nanoparticles for encapsulation of flexible organic electronics. *Materials Chemistry and Physics, 115*(1), 269−274.

Laskarakis, A., Gravalidis, C., & Logothetidis, S. (2004). FTIR and Vis−FUV real time spectroscopic ellipsometry studies of polymer surface modifications during ion beam bombardment. *Nuclear Instruments and Methods in Physics Research Section B: Beam Interactions with Materials and Atoms, 216*, 131−136.

Laskarakis, A., & Logothetidis, S. (2006). On the optical anisotropy of poly(ethylene terephthalate) and poly(ethylene naphthalate) polymeric films by spectroscopic

ellipsometry from visible-far ultraviolet to infrared spectral regions. *Journal of Applied Physics, 99*(6), 066101.

Laskarakis, A., Logothetidis, S., Georgiou, D., Amberg-Schwab, S., & Weber, U. (2009). On the influence of silicon oxide nanoparticles on the optical and surface properties of hybrid (inorganic–organic) barrier materials. *Thin Solid Films, 517*(23), 6275–6279.

Lebedev, V., Morales, F. M., Cimalla, V., Lozano, J. G., González, D., Himmerlich, M., et al. (2006). Correlation between structural and electrical properties of InN thin films prepared by molecular beam epitaxy. *Superlattices and Microstructures, 40*(4–6), 289–294.

Lee, J.-H. (2008). Effects of sputtering pressure and thickness on properties of ZnO: al films deposited on polymer substrates. *Journal of Electroceramics, 23*(2–4), 512–518.

Lee, S., Rana, K., & Ahn, J. (2013). Graphene films for flexible organic and energy storage devices. *Journal of Physical Chemistry Letters, 4*(5), 831–841.

Liao, H.-C., Ho, C.-C., Chang, C.-Y., Jao, M.-H., Darling, S. B., & Su, W.-F. (2013). Additives for morphology control in high-efficiency organic solar cells. *Materials Today, 16*(9), 326–336.

Li, X., Zhang, W., Wu, Y., Min, C., & Fang, J. (2013). Solution-processed MoSx as an efficient anode buffer layer in organic solar cells. *ACS Applied Materials and Interfaces, 5*(18), 8823–8827.

Lioudakis, E., Othonos, A., Alexandrou, I., & Hayashi, Y. (2007a). Optical properties of conjugated poly(3-hexylthiophene)/[6,6]-phenylC[sub 61]-butyric acid methyl ester composites. *Journal of Applied Physics, 102*(8), 083104.

Lioudakis, E., Othonos, A., Alexandrou, I., & Hayashi, Y. (2007b). Ultrafast carrier dynamics on conjugated poly(3-hexylthiophene)/[6,6]-phenylC[sub 61]-butyric acid methyl ester composites. *Applied Physics Letters, 91*(11), 111117.

Logothetidis, S. (2008). Flexible organic electronic devices: materials, process and applications. *Materials Science and Engineering: B, 152*(1–3), 96–104.

Logothetidis, S., Gioti, M., Patsalas, P., & Charitidis, C. (1999). Insights on the deposition mechanism of sputtered amorphous carbon films. *Carbon, 37*(5), 765–769.

Logothetidis, S., Georgiou, D., Laskarakis, A., Koidis, C., & Kalfagiannis, N. (2013). In-line spectroscopic ellipsometry for the monitoring of the optical properties and quality of roll-to-roll printed nanolayers for organic photovoltaics. *Solar Energy Materials and Solar Cells, 112*, 144–156.

Madsen, M. V., Sylvester-Hvid, K. O., Dastmalchi, B., Hingerl, K., Norrman, K., Tromholt, T., et al. (2011). Ellipsometry as a nondestructive depth profiling tool for roll-to-roll manufactured flexible solar cells. *The Journal of Physical Chemistry C, 115*(21), 10817–10822.

Manceau, M., Angmo, D., Jørgensen, M., & Krebs, F. C. (2011). ITO-free flexible polymer solar cells: from small model devices to roll-to-roll processed large modules. *Organic Electronics, 12*(4), 566–574.

Minami, T., Miyata, T., & Ohtani, Y. (2007). Optimization of aluminum-doped ZnO thin-film deposition by magnetron sputtering for liquid crystal display applications. *Physica Status Solidi (A), 204*(9), 3145–3151.

Moule, A. J., Bonekamp, J. B., & Meerholz, K. (2006). The effect of active layer thickness and composition on the performance of bulk-heterojunction solar cells. *Journal of Applied Physics, 100*(9), 094503.

Noh, J., Yeom, D., Lim, C., Cha, H., Han, J., Kim, J., et al. (2010). Scalability of roll-to-roll gravure-printed electrodes on plastic foils. *IEEE Transactions on Electronics Packaging Manufacturing, 33*(4), 275–283.

Norrman, K., Madsen, M. V., Gevorgyan, S. A., & Krebs, F. C. (2010). Degradation patterns in water and oxygen of an inverted polymer solar cell. *Journal of the American Chemical Society, 132*(47), 16883−16892.

Ouyang, J., Xu, Q., Chu, C.-W., Yang, Y., Li, G., & Shinar, J. (2004). On the mechanism of conductivity enhancement in poly(3,4-ethylenedioxythiophene):poly(styrene sulfonate) film through solvent treatment. *Polymer, 45*(25), 8443−8450.

Sakkopoulos, V. S., Dalas, E., Paliatsas, N., Emmanouil, K., Malkaj, P., & Choulis, S. A. (2010). Correlation between thickness, conductivity and thermal degradation mechanisms of PEDOT:PSS films. *AIP Conference Proceedings, 1203*, 178−181.

Schmidt-Hansberg, B., Klein, M. F. G., Peters, K., Buss, F., Pfeifer, J., Walheim, et al. (2009). In situ monitoring the drying kinetics of knife coated polymer-fullerene films for organic solar cells. *Journal of Applied Physics, 106*(12), 124501.

Semaltianos, N. G., Koidis, C., Pitsalidis, C., Karagiannidis, P., Logothetidis, S., Perrie, W., et al. (2011). Picosecond laser patterning of PEDOT: PSS thin films. *Synthetic Metals, 161*(5−6), 431−439.

Seto, J. Y. W. (1975). The electrical properties of polycrystalline silicon films. *Journal of Applied Physics, 46*(12), 5247.

Søndergaard, R. R., Hösel, M., & Krebs, F. C. (2013). Roll-to-roll fabrication of large area functional organic materials. *Journal of Polymer Science Part B: Polymer Physics, 51*(1), 16−34.

Tekoglu, S., Hernandez-Sosa, G., Kluge, E., Lemmer, U., & Mechau, N. (2013). Gravure printed flexible small-molecule organic light emitting diodes. *Organic Electronics, 14*(12), 3493−3499.

Van de Wiel, H. J., Galagan, Y., van Lammeren, T. J., de Riet, J. F. J., Gilot, J., Nagelkerke, M. G. M., et al. (2013). Roll-to-roll embedded conductive structures integrated into organic photovoltaic devices. *Nanotechnology, 24*(48), 484014.

Vongsaysy, U., Pavageau, B., Wantz, G., Bassani, D. M., Servant, L., & Aziz, H. (2013). Guiding the selection of processing additives for increasing the efficiency of bulk heterojunction polymeric solar cells. *Advanced Energy Materials, 4*(3), 1300752.

Xue, B., Vaughan, B., Poh, C.-H., Burke, K. B., Thomsen, L., Stapleton, A., et al. (2010). Vertical stratification and interfacial structure in P3HT: PCBM organic solar cells. *The Journal of Physical Chemistry C, 114*(37), 15797−15805.

You, J., Dou, L., Yoshimura, K., Kato, T., Ohya, K., Moriarty, et al. (2013). A polymer tandem solar cell with 10.6% power conversion efficiency. *Nature Communications, 4*, 1446.

Laser processing of flexible organic electronic materials

12

P. Delaporte[1], D. Karnakis[2], I. Zergioti[3]
[1]Aix-Marseille University, CNRS, Marseille, France; [2]Oxford Lasers Ltd, Didcot, UK;
[3]National Technical University of Athens, Athens, Greece

12.1 Introduction

Lasers are unique tools for locally modifying with very high precision the morphological, physical, or chemical properties of surfaces without any mechanical contact. They represent one of the key technologies of the manufacturing processes of the next decades. They can deposit a well-controlled amount of energy in volumes as small as one cubic micrometer. The standard spot size is of a few micrometers square and the energy can be deposited within a few tens of nanometers in depth. The use of ultrashort pulse duration, picosecond and femtosecond, prevents any modification of the material surrounding the irradiated volume. These characteristics make lasers appear as a highly suitable tool for the development of processes in the field of flexible organic electronics. Indeed, organic electronic devices are made of stacks of very thin layers, and the processing of a specific layer must be done without degradation of the others. A resolution of a few micrometers is the target for manufacturing organic electronic devices on flexible substrates, and that is currently achieved by most laser systems. Moreover, lasers are nowadays very reliable and can offer high output power and high repetition rate compatible with the requirements of industrial manufacturing with high throughput and even roll-to-roll (r2r) production thanks to sophisticated ultrafast scanning systems. Laser is a generic acronym that includes a large set of systems providing high tunability to the processes. A smart selection of the wavelength, pulse duration, repetition rate, fluence (energy density per surface unit), beam shaping, and other parameters allows addressing most of the challenges encountered in the manufacturing of organic electronic products on flexible substrates.

In this chapter, we first provide very basic concepts of laser–matter interaction, with a focus on materials and systems of interest for flexible organic electronics. These inputs are mandatory to understand the potential and the limitations of laser processes and to have an initial idea of which source is suitable for a specific application. Then, the main industrial laser sources available for surface processing are introduced, and their specific performances are linked with some applications. Beam shaping and beam manipulation are clearly of prime importance to reach high resolution and high quality processing, and the main approaches to optimize these parameters are presented. The main part of this chapter is then dedicated to the description of the most important laser processes that can be used for manufacturing flexible organic

electronics. The ability of laser processes to tune the surface properties and to pattern surfaces at the microscale level by material removal or laser printing is presented.

12.2   The physics of laser interaction with thin films

The purpose of this section is to provide some general knowledge on the deposition and relaxation of laser energy in matter with some specific inputs for thin films and organic material. Many books and papers have been published on laser matter interaction, and for a reader who wants a deeper understanding of the physical mechanisms involved in these processes the following references are available, Bauerle (2011), and Fogarassy and Lazare (1992). It is important to mention that only short pulse lasers, from nanosecond to femtosecond, are of interest for surface processing in flexible organic electronics; the physics discussed hereafter deals only with pulsed laser interactions.

12.2.1   Absorption of laser energy

The first step in any laser matter interaction process is the absorption of the laser energy by the irradiated substrates. When a laser beam reaches the surface of a substrate, its energy is divided in three parts: the first one is reflected; the second one is transmitted if the substrate is transparent enough; and the last one is absorbed by the material. The percentage of energy absorbed by the substrate depends first on the reflectivity of the surface and then on the linear absorption coefficient α of the material, and for thin film, it also depends on the film thickness. The profile of the energy deposition as a function of the material depth is given in first approximation by the Beer−Lambert law: $I(z) = I_0 e^{-\alpha z}$, where I_0 is the total intensity of the laser that is not reflected. This absorption coefficient itself depends on the laser wavelength. The spectral range of the laser systems available for material processing extends from ultraviolet (UV from 193 nm) to near infrared (NIR up to 1064 nm), with a single point in infrared with CO_2 lasers emitting around 10 μm. As the energy of the photons is absorbed by the free electrons of the material, most of the conductive inorganic compounds, like metals, have a high absorption coefficient from UV to NIR, while dielectric materials exhibit a very weak linear absorption. The organic layers have a more complex behavior, and their absorption coefficients usually vary with wavelength from UV to NIR. Most of these materials strongly absorb wavelengths shorter than 300 nm, and the use of UV laser guarantees the deposition of the energy within a thin layer of the material, and hence a high degree of control of the process.

The second parameter that must be taken into account for energy absorption, besides laser wavelength, is pulse duration. Indeed, all previous considerations are based on linear absorption. However, for pulse durations shorter than a few picoseconds, multiphoton absorption mechanisms must be considered. In this situation, where the energy of a single photon is not sufficient to transfer an electron from its ground state to an excited state (or from valence band to conductive band), this multiphoton absorption process is achieved by several photons transferring simultaneously (time

scale shorter than 1 ps depending on the material) their energies to the same electron. So, when using lasers with pulse duration shorter than a few picoseconds, most of the materials can be considered highly absorbing.

12.2.2 Ablation processes

After the deposition of the laser energy inside the material, its modification is controlled by the way this energy is dissipated. The main processes of energy diffusion are thermal, mechanical, electrical, and chemical.

12.2.2.1 Thermal process

After the absorption of the energy, a significant part of the electrons of the irradiated volume are in an excited state. Then, they transfer their energy to the lattice in a few tens of picoseconds. This leads to an excitation of the ions and molecules and then to an increase of the temperature of the irradiated volume, and to the surrounding volume due to the thermal diffusion. The highest temperature is reached at the surface where most of the laser energy has been absorbed. The temperature decreases when moving away from the surface and from the irradiated area. When the vaporization temperature is reached, the material is removed and ejected, and a plasma expands perpendicularly to the surface. At lower temperature, melting zones can be observed, and the fast heating and cooling of the remaining material can induce some modifications of its properties, like stress generation. This points out the interest of using ultrashort pulses to limit the thermal diffusion and the volume of the heat-affected zone.

The ablation threshold is defined as the minimum fluence required for material removal. It usually depends only on laser parameters (wavelength and pulse duration) and on the material properties. However, in the particular case of thin films, it also depends on film thickness and on the material on which the thin film is deposited. Indeed, the ablation process is governed by the temperature of the material, and for thin film the thermal diffusion depends on the thermal conductivity of both the film and the substrate on which the film is deposited. If the latter is high, the thermal energy will dissipate in the substrate and lower the film temperature. On the contrary, a low thermal conductivity of the substrate will confine the thermal energy in the film, increase its temperature, and lower the ablation threshold.

12.2.2.2 Photochemical process

Organic materials are particularly sensitive to photochemical processes. During these mechanisms, the laser energy is absorbed by the electrons involved in the binding of the molecules, and if the deposited energy is high enough, the chemical bonds are broken and low mass products are desorbed. UV wavelength strongly favors the photochemical processes because of the high energy of the incident photons that directly excites the electronic levels higher than the dissociation limits of the bonds. This mechanism allows material removal without any deleterious thermal effect. However, to be purely photochemical, the ablation requires using laser with wavelength shorter than 300 nm (typically 266 nm or best 193 nm). Figure 12.1 illustrates
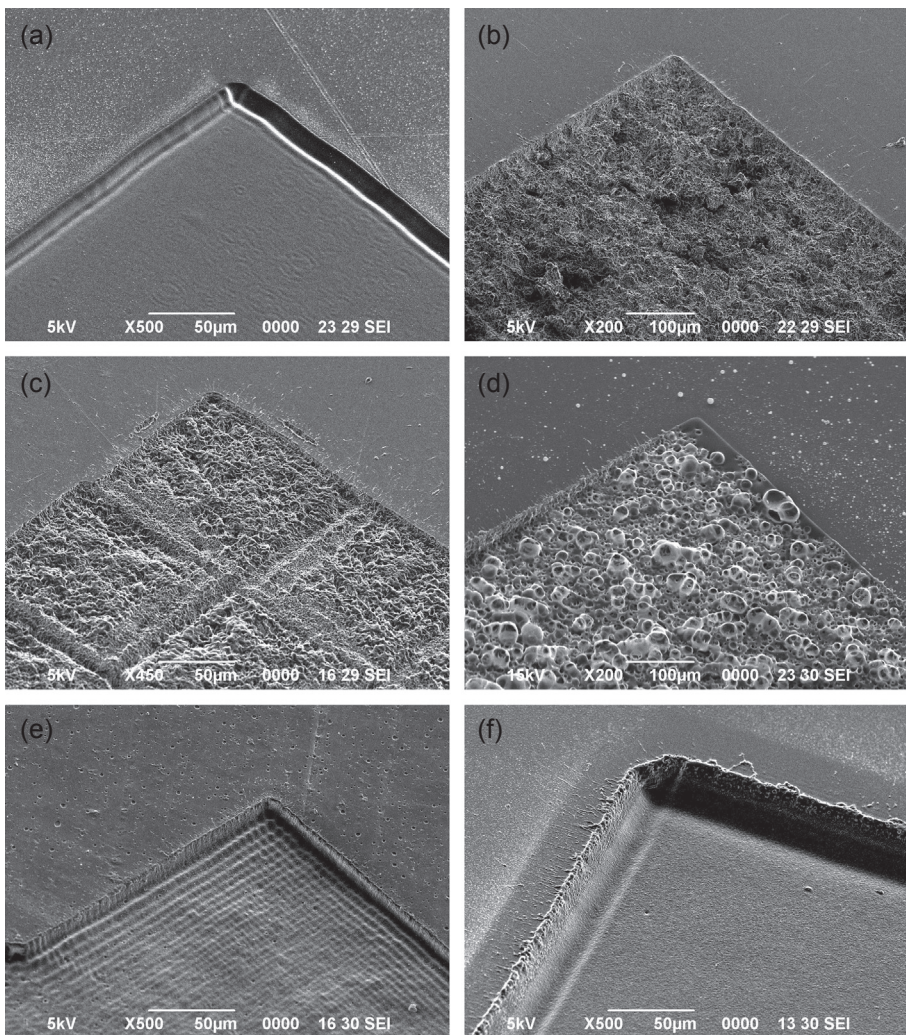
Figure 12.1 (a)−(d) Cavities realized by laser ablation in PMMA substrate, (e) and (f) PMMA doped with pyrene. The laser characteristics are the following: ArF (193 nm, 15 ns) for (a); Yb: YAG (343 nm, 40 ps) for (b); Nd:YAG (266 nm, 40 ps) for (c) and (e); and KrF (248 nm, 30 ns) for (d) and (f).

this mechanism. PMMA substrate has been irradiated at three different UV wavelengths. We can observe the very smooth ablation obtained when using laser at 193 nm (Figure 12.1(a)) for which photochemical processes are responsible for the ablation compared to strong thermal effects induced for irradiation performed at longer wavelengths as 355 nm (Figure 12.1(b)), 266 nm (Figure 12.1(c)), and 248 nm (Figure 12.1(d)). In order to favor the laser ablation of polymers, doping of these materials is performed (Lippert, Yabe, & Wokaun, 1997). Figure 12.1(e) (resp.

12.1f) shows the improvement of the surface quality after laser ablation at 226 nm (resp. 248 nm) of PMMA doped with pyrene.

12.2.2.3 Photomechanical process

The ablation of thin films based on photomechanical process is very attractive because it potentially allows removal of any material modification in the surrounding volumes; it is well suited for selective ablation of thin films. To favor this process, two important criteria must be fulfilled in the irradiated film (Paltauf & Dyer, 2003): "thermal confinement" and "stress confinement." This requires first, a maximum energy load in the irradiated film attained from high energy absorption and minimum thermal conduction losses away from the irradiated area and second, a high transient thermo-elastic stress, due to rapid thermal heating, that exceeds the film fracture limit before any thermal expansion allows for stress relaxation (Karnakis, Van Steenberge, Gielen, De Baets, & van den Brand, 2010). The choice of both laser wavelength and laser pulse duration are critical as the former controls laser absorption and the latter directly compares with the material's relaxation timescales. The only drawback of this approach is the risk of edge detachment when the film adherence is not high enough.

12.3 Laser systems and sources

A detailed description of various laser technologies used in organic electronics is outside the scope of this section, and readers are advised to review details in other text-books (Silfvast, 2008; Hooker & Webb, 2010). Instead we (1) offer a short practical guide outlining the most relevant laser microprocessing/optics technologies including recent technical specifications, (2) compare the merits of such technologies for indus-trial production highlighting advantages/limitations, and (3) discuss their use in certain applications. A few comments on the future direction of laser technology in general are also made. The lasers described below can be used for both *subtractive* and *additive* manufacturing.

Several commercial laser sources are available that can be divided according to laser emission wavelength, laser output power, laser pulse duration and output frequency in pulsed lasers, etc. Table 12.1 summarizes their main characteristics, advantages, limitations, and most useful processing applications.

Continuous wave (CW) lasers (diode, CO_2, CW fiber) provide high average power, and depending on their spatial coherence, they allow for tight beam focusing on target. Due to their low cost of ownership, usually poor beam quality (high M2), and low peak power, they are widely used in low quality marking, cutting, drilling, and welding of metals, plastics, etc. Commercial sources of high average power up to several tens kW are available. They can be integrated with optical scanners (polygon, galvanometer, etc.) and high speed modulators for varying process speed and laser frequency on target.

Pulsed lasers are mostly used when ablative etching is desirable with well-controlled localized energy input into the substrate (Bauerle, 2011). Laser

Table 12.1 Description of the main laser sources and their applications

Laser technology	Key characteristics	Merits (+)/Limitations (−)	Useful for
Diode	Direct-write, low quality beams, CW or pulsed operation, UV, visible and IR wavelengths	High average power (+), very low CAPEX, COO (+), mature technology (+)	Cutting, welding, curing/sintering
CO_2	Direct-write, diffraction limited beams	High average power (+), low CAPEX, COO (+), mature technology (+), high process speed (+)	Cutting, welding, via drilling, surface modification
Excimer	Low coherence, projection mask imaging, UV wavelengths only (157, 193, 222, 248, 308, 351 nm), nanosecond pulsed duration	High resolution (+), homogenous beam profile (+), moderate pulse energy (+), mature technology (+), low output frequency (−), slow process speed (−), limited etch selectivity (−), low energy utilization (−), unsuitable for r2r integration (−), high CAPEX and maintenance costs (−)	Large area processing, surface patterning, high density swallow via drilling
QS-DPSS	Direct-write, highly coherent, diffraction limited beams, mid-IR/ IR and higher harmonics, μs or ns pulsed duration	High resolution (+), high output frequency (+), high process speed (+), r2r compatible (+), medium CAPEX and maintenance costs (+), mature technology (+), low pulse energy (−)	Large area processing, surface patterning, high aspect ratio processing (via drilling, wafer cutting/dicing)
Fiber	Direct-write, mostly IR wavelengths (1, 1.55, 2−3 μm), very recently SHG and THG available	Small/compact size (+), ideal for r2r operation (+), low CAPEX and maintenance costs (+), low pulse energy (−)	Large area processing, drilling, cutting, surface patterning, high density via drilling
Ultrafast DPSS	Direct-write	Low pulse energy (−)	

CAPEX, capital expenditure; COO, cost of ownership.

wavelength, pulse duration, output power, output frequency, and laser beam quality (M2) are the most important characteristics. As they have the highest potential for application in flexible organic electronics, they are detailed in the following sections.

12.3.1 Transversed excited atmospheric CO_2 lasers

Pulsed transversed excited atmospheric (TEA) pressure carbon dioxide CO_2 lasers are common laser sources in laser processing due to their high conversion efficiency, simplicity, industrial reliability, and low cost of ownership and operation. They emit in the range 9.4−10.6 μm and can provide pulse spikes of 100−200 ns followed by long tails of several microseconds. CO_2 laser architecture and associated material processing have been widely discussed in the literature (Duley, 1976; Siegman, 1986; Steen, 2003). CO_2 lasers emitting at 9.4 μm are widely used for via drilling in polymer on metal for the manufacturing of Plastic Board Circuits (PCB).

12.3.2 Excimer lasers

Excimer gas lasers (Basting & Marowsky, 2010) provide a unique approach to achieve high power in the ultraviolet (UV) spectral range. The wavelength can be tuned by changing the gas mixture, including Fluorine F_2 (157 nm) and other rare gas halides (RGHs) like ArF (193 nm), KrCl (222 nm), KrF (248 nm), XeBr (282 nm), XeCl (308 nm), and XeF (351 nm). They are ideal UV sources for precision micromachining especially of organic materials due to their high photon energies, which allows strong optical absorption and direct bond photodissociation; short pulse duration (typically 10−40 ns), which limits thermal damage to heat sensitive or multilayered structures; and ironically, their relatively poor coherence that limits interference related problems in projection mask imaging. Modern commercial excimer lasers can be operated with pulse repetition rates of several kHz and average powers up to several hundreds of watts. High prices, the toxic nature of the halogen gases, and the limited gas lifetime due to gas impurities accumulation in the cavity are the key limiting factors restricting wider industrial adoption (Grigoropoulos, 2009).

12.3.3 Q-switched diode-pumped solid state lasers (DPSS)

This is a very attractive reliable class of industrial solid state lasers in various host rod or thin disc crystal architectures (YAG, YLF, Vanadate, etc.). They emit high average and high peak power at fundamental infrared or mid IR wavelengths depending on dopant (Nd, Yb, etc.) between 1 and 2 μm. Higher wavelength conversion harmonics (2nd, 3rd, 4th) from nonlinear crystals in the visible, near UV, and deep UV have nowadays also reached industrial level robustness. Typical pulse durations range from sub-ns to several hundred nanoseconds at output frequencies from single shot to hundreds of kHz (Koechner, 2010). They are mainly used for thin film scribing, patterning, trimming, cutting, and vial drilling.

12.3.4   Picosecond and femtosecond ultrafast DPSS lasers

This is a unique subcategory of DPSS lasers that has rapidly developed over the last 20 years due mainly to technological developments in diode pumping, passive mode-locking (SESAM, Kerr-lens, etc.), and chirped pulse amplification (CPA). They can be found in rod, disc, and fiber laser architecture, each one with its own merits, and are already used in industrial applications (photovoltaic solar, transparent conductive oxide patterning, display processing, etc.).

Picosecond lasers emit optical pulses with very short pulse duration between 1 ps and typically a few tens of picoseconds. They can be actively or passively modelocked resulting in pulse trains of low pulse energy (nano to microjoule) but very high repetition rates (several tens MHz or GHz). Pulse pickers can be used to select lower pulse frequencies or single shot mode operation. The most common gain media include neodymium doped (Nd) or ytterbium Yb doped ones. The typical output power from commercial amplifier sources can be found at infrared wavelengths of around 1 μm in the range 100 W, with pulse duration at full width half maximum (FWHM) of 5−20 ps and up to about 4 MHz. Lower power oscillator only units and shorter wavelengths from higher harmonics (SHG, THG, FHG, etc.) are also commercially available. They are particularly useful for direct-write applications such as selective thin film patterning of very thin layers and laser printing due to their precisely controlled heat input into the layers.

Femtosecond lasers are based on picosecond passive modelocked oscillators (bulk or fiber) which after one or more free space or fiber-based amplification stages are pulse compressed to yield ultrashort pulse durations typically in the range of a few fs to 700 fs. The most common types are the titanium sapphire (780−820 nm), Nd based (1064 nm) or Yb based (1030 nm) and their harmonics. Commercial amplifiers can reach output powers up to >30 W in TEM00 mode and repetition rates of several MHz. The reliability of these ultrafast lasers is improving rapidly, and they represent a very promising source for the development of applications in flexible organic electronics in the future.

12.3.5   Pulsed fiber lasers

Fiber lasers use optical fibers as gain media (resonators or amplifiers). These are usually doped with rare earth ions such as Erbium (Er^{3+}), Neodymium (Nd^{3+}), Ytterbium (Yb^{3+}), or Thulium (Tm^{3+}) and are typically diode laser pumped. They operate similarly to bulk DPSS lasers, but due to the waveguiding effect and the small effective mode area usually lead to substantially different properties of the lasers. They can be q-switched or modelocked, offering a variety of pulse durations in the ns and ps region. Rare earth−doped specialty fibers such as photonic crystal fibers (PCF) have relatively recently been successfully introduced, resulting in high power laser devices, supercontinuum generation, and other niche applications. Picosecond or femtosecond fiber lasers are also available and are particularly advantageous in power scaling and mode stability.

Fiber lasers have achieved tremendous growth over the last decade, and it is expected that they will one day replace conventional DPSS lasers as they will surpass

their performance characteristics offering lower costs, compactness, flexibility, and high electrical efficiency. They offer superb mode quality without changes with power scaling.

However, fiber lasers also suffer from important limitations, mainly due to high peak self-focusing damage thresholds that restrict short pulse generation, optical nonlinearities due to the long cavity length and small effective mode area, high resonator losses, temperature, and bending-related birefringence issues that affect polarization state (linear becomes elliptical). Another common limitation is related to their master oscillator power amplifier (MOPA) architecture that can amplify back-reflected laser light and end up damaging the seed fiber laser. Fiber laser designers take all these limitations into account to counteract them. Fiber laser components cannot be easily replaced in the field, as compared to DPSS units, ending up replacing the entire laser unit.

12.4   Beam delivery assembly

A very important component of every laser processing system is the optical beam delivery assembly. It dictates the overall optical system resolution (spatial, but also temporal in the case of burst pulse processing) and system performances. Depending on the available laser intensity or process speed requirements, a system can use one or more laser beams incident on target, such configurations termed here "single-beam" or "multiple-beam" processing. There are several options available, briefly described in the following sections.

12.4.1   Single-beam processing

Two simple approaches can be used to perform laser processing with a single beam: projection mask imaging and maskless direct writing.

12.4.1.1   Projection mask imaging

Projection mask imaging involves uniform laser illumination of a mask that is subsequently projection imaged onto the target by an appropriate objective lens system. This setup is suitable mostly for multimode lasers (high M2 DPSS, excimers). Depending on the object-to-image distance ratio from the lens, a certain (de)magnification can be achieved. The technique is very well established and limited only by the quality of the mask, projection optics, and the illuminating laser wavelength. Various extensions of the technique have been developed employing gray-scale masks, mask dragging synchronized with laser pulsing, and computer numerical control (CNC) motion to realize 3D structures.

12.4.1.2   Maskless direct writing

Maskless direct writing is the simplest, most common laser processing configuration. The laser beam is directly focused without a mask to a suitably small spot size on the substrate surface using an objective lens or mirror at normal or angled incidence.

Typically, either the part is translated with respect to a fixed laser beam or vice versa following a preprogrammed toolpath trajectory. The key figure of merit is the lens f# number (lens focal length/input laser beam diameter at lens) or numerical aperture NA of the system (NA = 0.5/f#). These dictate the working distance and the minimum laser spot size achievable on target, i.e., the optical system resolution, limited mainly by diffraction or lens aberrations. Low M2 laser beams are best suited for fine resolution direct writing. Such beam shapings offer Gaussian spatial irradiance profiles on target.

12.4.2   Multiple beam processing

For some applications the generation of multiple beams with a well-controlled repartition of the energy is of great interest to process a large area with high throughput. The techniques to produce these multiple beams are described hereafter.

12.4.2.1   Diffractive optic elements

Diffractive optic elements (DOE) used as beam splitters are periodic phase optical flats that divide a single input beam into multiple diffracted orders while usually retaining the divergence angle, diameter, and polarization of the input beam. Almost any 1D- or 2D-multibeam symmetrical or arbitrary patterns can be generated upon customization with no limitations on the available number of sub-beamlets. These devices are very useful for maximum energy beam utilization on target and by implication throughput optimization. Combined with focusing lenses they can create high density feature processing at very high speed. The main drawback is the low diffraction efficiency if binary or low level DOE is used with presence of zero order. Moreover, output beam balancing is impractical, and device performance depends heavily on input beam properties.

12.4.2.2   Particle lens arrays

High resolution large area nanotexturing below the diffraction limit can be achieved by 2D scanning of a focused laser beam over a layer of optically transparent microspheres dispensed on a target surface to form self-assembled particle lens arrays (PLAs) (Li et al., 2009; Pereira et al., 2008). PLA can simultaneously produce a very high density of identical nanofeatures (tens of millions over mm^2) by exploiting high energy localization below each microparticle from near-field enhancement of the incident wave. This technique is unique to realize 2D structures with sub-100-nm-scale resolution at low cost. Moreover, it avoids any optical contamination issues or swallow working distance engineering complexities. However, only single pulse exposure is allowed as particles are easily damaged or removed from the surface from various forces exceeding particle adhesion that are generated during the irradiation process. Also, a uniform patterning requires using particles with low variation in diameter and a uniform laser beam profile. Figure 12.2 shows a patterned surface (90 nm SiO_2 film on Si) at the nanoscale level realized with a single laser illumination of a SiO_2 particle array deposited on the surface.
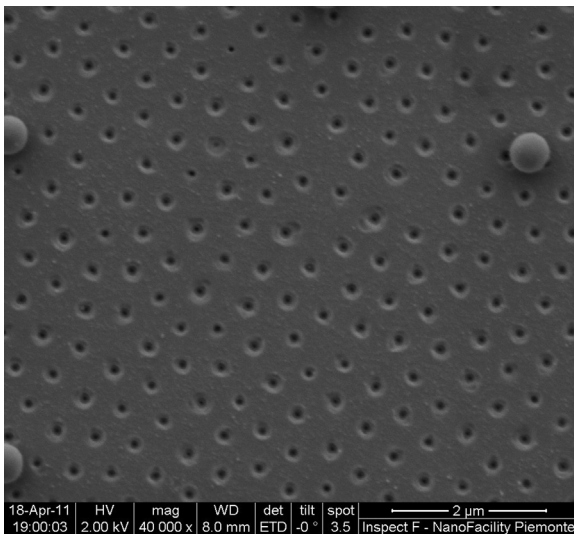
Figure 12.2 SEM image of periodic drilling of a 90 nm oxide film (SiO_2) formed on silicon substrate. This nanostructuration has been achieved by a single laser irradiation (λ las = 193 nm, τ las = 15 ns) of self-assembly monolayer of SiO_2 nanoparticles ($d = 550$ nm) deposited on the surface.

12.4.2.3 Multiple beam interference

Laser patterning with multiple beam interference on target (up to six beams reported) can produce subwavelength features (Voisiat, Gedvilas, Indrisiunas, & Raciukaitis, 2011). This is a very effective method of forming 2D high density nanostructures over a certain area (Steger, Hartmann, Beckemper, Holtkamp, & Gillner, 2013). The periodic structure characteristics can be controlled by the incidence beams angle, laser wavelength, phase difference between the beams, polarization, and intensity. Typical applications include surface wettability tuning in automotive, biomedical, and photonics industries; frequency selective surfaces (antennas, filters) for THZ, IR, or visible EM waves; OLED (Bai et al., 2011) for light outcoupling; or OPV solar cell efficiency improvement (Lasagni, 2011), and others.

12.4.3 Beam manipulation

To draw 1D, 2D, or 3D patterns on a surface with a single beam, systems must be implemented to move either the substrate or the laser beam, and in some cases a combination of both.

The first approach consists of using fixed optics and moving substrate. It is typically used in batch processing applications requiring fine resolution laser micromachining over a large area. A xyz CNC table is commonly employed to translate the substrate with respect to a laser beam. The main advantages are the high positioning accuracy (up to submicrometer) and the large process area up to a few square meters. The key disadvantages are that the CNC stage load slows down the process relative to competing technology, and the cost.

The second option is to keep the substrate fixed while the laser beam is moved on its surface. Optical laser beam scanning involves the controlled deflection of a single laser beam scanned rapidly over the target area (HOLS, 2004). Galvanometric, resonant, polygon mirror, acousto-optic or electro-optic scanners are typically used with or without focusing optics for 1D or 2D scanning. Preobjective scanning combined with flat field f-theta optics is the most common optical configuration. Postobjective scanning is best suited to large area cover applications demanding high process speed but not critical on precision. A z-axis optics translator is often used in combination for dynamic focus compensation in such cases. Optical trepanning heads (see www.oxfordlasers.com) create circular or spiraling beam paths on target, mainly used for microhole drilling of substrates. Of all of the above technologies, the 2D galvometer optical scanner is the most commonly encountered owing to its popularity because of the combination of speed, accuracy, ease of integration, and cost of ownership. All these scanning technologies offer very high process speed (typically several $10-100$ m/s) making them well suited to multi-kHz output frequency laser sources. Disadvantages: Expensive telecentric $f =$ theta optics are needed requiring optical distortion corrections, and the absence of encoded beam positioning feedback in most devices compromises precision.

12.4.4 Beam shaping

Some applications require more sophisticated spatial beam shaping than mask imaging or direct focusing. Beam shaping is the process of redistributing the irradiance and phase of a beam of optical radiation (LBSA, 2006). There is no single beam shaping method that addresses all situations well. The simplest, most primitive but quite useful spatial beam shaping method is "beam aperturing." In this case, the beam is expanded and an aperture is used to select a suitably flat portion of the beam. The resulting irradiance pattern can be imaged with magnification to control the size of the output beam. As it is rather lossy, it is seldom used in production setups where other more sophisticated methods are employed. Some of them are described below.

Field mapping refractive or diffractive (DOE) optics can be used to transform a Gaussian input beam profile to a super Gaussian near top hat irradiance profile at the target plane. Perceived benefits of this technology are the higher laser energy utilization, the higher process speed/throughout, and the better overall feature quality. Refractive beam shaping optics offer high transmission, ease of use, lower cost, and lack of zero order effects but are limited to input beam geometries. Diffractive beam shapers offer comprehensive design flexibility in output beam shapes (square, lines, multispots, etc.) but are more sensitive to exact input laser beam parameters.

Line focusing with long/short axis aspect ratio of 10^4 (for example, 100 mm/10 μm) can be achieved by cylindrical or anamorphic optics depending on desired beam homogeneity. Such setups are typically combined with high speed optical scanning for annealing, crystalization and cutting applications.

Beam integrator homogenizers (biprism, fly's eye lenslet arrays) are used with multimode lasers (excimers, high M2) essentially to divide an incoming beam into several subsections that are then superimposed to provide uniform intensity at a given

working plane downstream. By placing a mask at this beam homogenized plane and reimaging it to the workpiece, one can get rid of various unwanted beam edges and produce truly uniform sharp-edged illuminated features. The key disadvantages include the presence of diffraction, coherence length effects, as well as a dependence on optical manufacturing tolerances and alignment sensitivities. These can be mitigated to some degree by coherence scrambling measures and other design aspects.

The spatial light modulators (SLMs) are electrically addressable computer controlled pixelated devices essentially used as "dynamic programmable masks or gratings." They can vary the amplitude, phase, and polarization of an incoming laser beam, splitting it into several sub-beams in transmission or reflection. The two common 2D SLM technologies are MEMS-based micromirror arrays or liquid crystal spatial light modulators. Their key advantages are their ability to achieve beam modulation without mechanical moving parts associated with maximum laser energy utilization and high throughput potential. However, diffraction related and damage threshold limitations apply. MEMS-based devices offer higher switching speeds at multi-kHz frequencies compared to a few tens of Hz in the LC-SLM technology.

12.5   Laser modification of materials and C surfaces

Besides the well-known applications of drilling, scribing, cutting, or printing that correspond to removing or adding material and will be discussed in the following sections, the laser processes also allow modification of the physical and chemical properties of materials and surfaces. In this first part, we present some examples of laser-induced modifications of material properties that are relevant for flexible organic electronics.

12.5.1   Tuning surface properties

12.5.1.1   Laser cleaning

The implementation of many industrial processes requires precise control of the different surfaces involved in the processes. Cleaning is one of the major steps of preparation of these surfaces. Today, most of the cleaning techniques are based on mechanical or chemical techniques. These techniques are not suitable for flexible organic electronics, and new processes need to be implemented. Photonic techniques, like laser or plasma, are very attractive for this application. They are contact-free processes that do not generate any secondary wastes and can be remotely operated for the treatment of flexible substrate (not sensitive to distance variations), even in roll-to-roll mode.

The laser cleaning process has previously demonstrated its effectiveness (Delaporte & Oltra, 2006) in many fields of applications like microelectronics (Grojo, Cros, Delaporte, & Sentis, 2007; Tam, Park, & Grigoropoulos, 1998) or nuclear decontamination (Delaporte et al., 2003), and for different substrates like polymers (Fourrier et al., 2001) and optical surfaces (Pleasants & Kane, 2003). Photoacoustic stress waves (Soltani & Ahmadi, 1994), photothermal vaporization, and near-field enhancement (Grojo et al., 2012; Mosbacher et al., 2001) are the main processes for the removal

of particles and thin films of liquid (Grojo, Delaporte, Sentis, Pakarinen, & Foster, 2008; Vatry et al., 2011). Photochemical effects induced by UV laser irradiation are also efficient for organic contamination removal, like fingerprints (Lu, Komuro, & Aoyagi, 1994).

In flexible organic electronics cleanliness is less critical than in the silicon microelectronic industry because the typical sizes are larger and the manufacturing less sensitive to smaller contamination. Nevertheless, the surfaces need to be free of contamination to ensure good electrical contact and good adhesion between the successive layers. It is also important to get rid of any particles from light emitting surfaces (OLED) to avoid black, or even bright, spot effect on the display. After etching or via drilling steps, some debris also has to be removed. Laser processes can be successfully used for these cleaning applications with a good choice of the irradiation parameters.

12.5.1.2   Adhesion

Polymers are the standard substrates in flexible electronics, but they are also widely used for other industrial applications, especially in aeronautics and aerospace. In order to use these materials, one of the most important points that must be addressed is the adherence properties of polymer surfaces to improve the adhesion between polymer and polymer or metal. Plasma processes are often used very efficiently to perform these treatments. However, they are generally carried out at low pressure in specific mixtures (Chan, Ko, & Hiraoka, 1996) and this can generate some technical problems for the treatment of large surface areas: Laser treatment in ambient conditions has been successfully tested in the aeronautics industry, especially to improve polymer−polymer adhesion. Studies have investigated the effects of excimer laser irradiation characteristics on surface modifications (Ardelean, Petit, Laurens, Marcus, & Arefi-Khonsari, 2005; Laurens, Ould Bouali, Meducin, & Sadraset, 2000). The treatments were achieved in air below the polymer ablation threshold fluence (typically 20 mJ/cm^2), and X-ray photoelectron spectroscopy (XPS) analysis showed the formation of polar-oxygenated functional groups (C=O, O−C=O). Peel tests realized after the deposition of an aluminum film on the polymer surface exhibited a significant enhancement of polymer metal adhesion. This improvement is attributed to an increasing number of Al−O−C stable and cohesive complexes formed at the interface polymer-metal. Laser treatment of polymer in air is then a simple process to improve the surface adherence properties without any modification of the bulk. The irradiation conditions (low fluence and small number of shots) open the way to large surface area treatments. These results could be easily extended to flexible organic electronics where the adhesion between polymer and organic materials or metal inks is a daily concern.

12.5.1.3   Wettability

As mentioned previously the irradiation of polymer surface with UV light modifies the chemical bonds and then the properties of the surface. Among them, the wettability can be tuned by varying the irradiation conditions. Plasma treatments are currently used for this application (Beake, Ling, & Leggett, 1998) and they are very efficient for the

preparation of large surfaces. Laser processes can perform a similar treatment but with a resolution of a few micrometers. In particular, this approach allows the accurate control of the width of inkjet-printed lines. Laser treatment of the areas on which the lines will be printed or of the borders of these areas avoids the spreading of the inks. One can also mention the use of ultrashort pulse lasers for the generation of microspikes at the surface of the polymer. A functional coating of these microstructured surfaces can then be used to control their pH and provide an accurate tuning of their wettability properties, from superhydrophilic to superhydrophobic (Anastasiadis, 2013). This new approach has not yet been used in flexible organic electronics, but it appears very attractive to control the material deposition (Wang, Zheng, Li, Huck, & Sirringhaus, 2004).

12.5.2   Synthesis of nanomaterials

Laser ablation of metal induces the formation of dense plasma with electrons, ions, and atoms. In this plasma, aggregation occurs that can lead to the growth of nanoparticles whose composition depends on the surrounding atmosphere (Kabashin et al., 2010; Pereira et al., 2004). When ablation occurs in liquid ambience, the process leads to the release of nanoclusters into the liquid and the formation of a colloidal nanoparticle solution (Kabashin & Meunier, 2006). In contrast to conventional chemical reduction methods, this method enables avoidance of the use of toxic chemical reduction agents to control the growth of the nanoparticles. As an example, the laser ablation-based synthesis can be implemented in pure deionized water. The independence of laser-based synthesis on dirty colloidal chemistry makes it unique for the fabrication of markers of bioanalytes for sensing and imaging applications. In pure water, however, or any other aqueous solution exempted of additional chemically active components, the size of nanoparticles produced tends to be relatively large, since a natural coalescence of hot ablated nanoclusters cannot be easily overcome.

This approach, which has been extended to other materials than metals, has great potential for the preparation of nanoparticle inks with ultrapure materials and well-controlled size. Such inks are used, for instance, to print conductive patterns and for enhanced organic photovoltaics with plasmonic effects.

12.5.3   Laser sintering

Laser sintering is an additive layer technique used in rapid manufacturing and rapid prototyping technologies for the improvement of the electrical and structural properties of the sintered material. It involves the selective melting of powders or inks by incorporating continuous wave or pulsed lasers (Kumpulainen et al., 2011), which heats the powder to a specific temperature at which the particles sinter together. Laser sintering offers several advantages as it enables short sintering times and selectivity, regarding the area to be sintered, and it has been introduced as an alternative approach compared to conventional thermal sintering processes (oven, microwave), which are time-consuming and with low-heating rates.

Among the parameters that influence the effects of laser sintering are the laser output power, the sintering time and sintering velocity, and the heat affected zone (HAZ) of the sintered material. Pulsed lasers exhibit better penetration to the sintered material compared to continuous wave lasers, while on the other hand CW lasers enable more homogenous heating. In addition, laser sintering with pulsed lasers enables faster heating of the material to high temperatures and produces a smaller heat load; however, since spot overlapping is required in pulsed laser sintering, this means that the sintering speed is limited. Moreover, in case of low spot overlapping, the line will have nonsintered or partially sintered areas, thus increasing the resistivity of the final feature.

In this context, Bieri, Chung, Haferl, Poulikakos, and Grigoropoulos (2003) and Ko, Chung, Pan, Grigoropoulos, and Poulikakos (2007) have investigated the laser curing of gold nanoparticles, where a CW argon ion laser has been employed. In these studies, it was shown that the laser sintering process resulted in the coalescence of the Au NPs so as to form a continuous line. Electrical measurements of the final sintered lines showed a significant decrease in resistivity to $\sim 5.4\ \mu\Omega\cdot cm$. To date, laser sintering has been used for the sintering of silver nanoparticle thin films (Peng, Hu, & Zhou, 2012), polymers (Goodridge, Hague, & Tuck, 2010), and composites (Goodridge et al., 2011). Zhu et al. (2007) reported the laser sintering of ZnO thick films for gas sensing applications. In this study, it was shown that laser sintered ZnO thick films have lower resistance values compared to the nonsintered films and show improved sensitivity to the targeted analytes by controlling the laser energy and sintering time. This behavior can be attributed to changes in the stoichiometry of ZnO and the microstructure of films, caused by the laser sintering process. In other work, Goodridge (2011), has presented the laser sintering of a polyamide-12/carbon nano-fiber composite in order to improve the mechanical and physical properties of the polymeric matrix. Characterization with SEM and dynamic mechanical testing of the laser sintered polymer composite showed an increase of 22% of the storage modulus compared to the matrix material.

12.6   Laser ablation processes

Laser ablation is a "subtractive" etching technique, i.e., removes unwanted material from a specified location on a target to create different geometries such as via holes (laser drilling), through or blind channels (laser cutting), or from unpatterned deposited thin films (OE-A, 2013) to create finely patterned 2D structures. Laser ablation is acknowledged as a digital, noncontact, maskless (in the case of direct writing), dry and environmentally friendly, scalable, fast (depending on desirable resolution), and r2r compatible production process but remains largely a niche technique in flexible organic electronics.

The choice of laser in each case depends on a number of technical and operational metrics such as the desirable optical resolution or minimum feature size needed, the material's absorptivity and reflectivity, production throughput target, process speed, layer selectivity restrictions, equipment interfacing/compatibility, servicing cycles, laser

safety, etc. Pulsed lasers are more common than continuous wave as they offer better temporal resolution and can be easily synchronized with moving webs. Each individual laser pulse incident on target forms a crater and can remove as much as several tens of μm or as little as a few nm of material depending on laser intensity. In most cases, a suitable motion control device accompanies laser beam delivery on the target in the form of either (1) laser beam scanning (galvanometer scanners, polygon mirrors, trepanning heads, etc.) over a typically stationary target or (2) more traditionally CNC tables carrying a mounted target along a predetermined geometrical toolpath with respect to a fixed laser beam in order to machine an arbitrary-shaped geometry. Typically, the higher the desired resolution, the slower the production throughput might be.

12.6.1   Laser drilling

Laser drilling is typically used for packaging interconnects and is characterized by the via hole size, via number density and its aspect ratio (hole diameter/material thickness). It is the most common micromachining process and is divided into two subcategories: (1) *percussion* drilling, where holes are drilled stationary with one or more repetitive laser pulses arriving in the same target location, opening an orifice with dimensions similar to laser spot size dimensions/shape and (2) *trepanning* drilling, where a small focused laser spot is used to open up CNC programmed via hole size, shapes, and eccentricity directions. Variations of the exact toolpath on target might include *spiral trepanning*, *concentric circle trepanning*, or *helical trepanning drilling*, where the focused beam is moved perpendicularly along the hole axis. CO_2 and DPSS (YAG, etc.) laser drilling can nowadays achieve sub-100 μm via hole diameters for interconnection. Figure 12.3 presents an array of square holes drilled in VESPEL polyimide, and Figure 12.4 shows an array of circular holes drilled in fused silica. These examples demonstrate the ability of laser processes to pattern surfaces of a large set of materials with complex designs and high resolution.
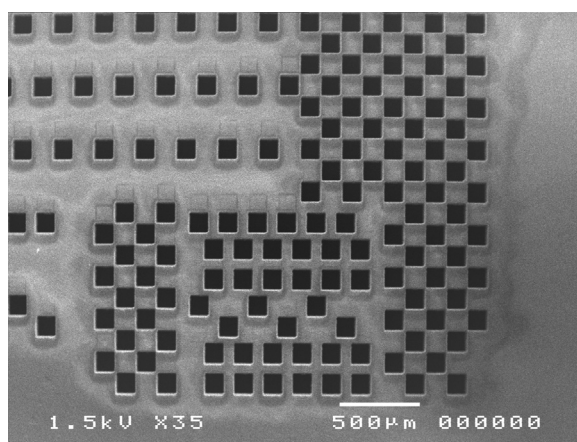
Figure 12.3 UV laser drilling of square holes in 0.2-mm-thick VESPEL polyimide.
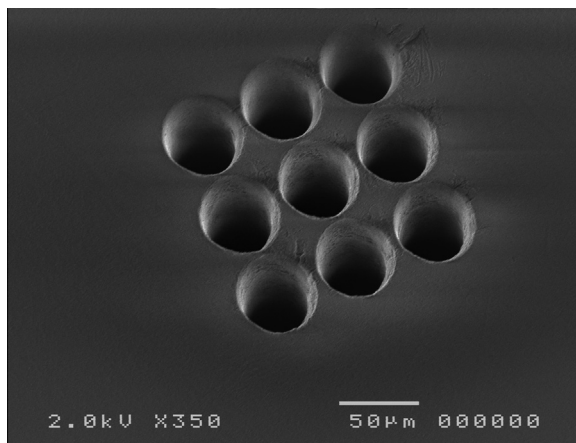
Figure 12.4 UV picosecond laser drilling of 0.05-mm-diameter holes with 0.06-mm-pitch distance in fused silica.

12.6.2   Laser cutting

Lasers can be used to cut a wide variety of materials. By cutting, we mean either ablative vaporization along any shape toolpath line to separate the workpiece material into separate parts or scribing and fracturing along straight lines. Laser cutting advantages include: ease of fixturing, fast setup and rapid design change, small kerf width, capability to cut complex shapes easily in addition to very high reliability, low maintenance requirements, high electrical efficiency, and a small footprint. Cutting speeds depend mainly on available average laser power and material thickness, and optical absorption/reflection properties. The CO_2 laser (CW modulated or q-switched) is the most commonly employed laser for ablative cutting of nonmetallic materials as such materials practically exhibit high absorption in the range 9.2−10.6 μm, whereas they are transparent at the fundamental Nd:YAG laser wavelength (Ready, 1997). Because it requires relatively low energy per unit volume to vaporize most organic materials such as the flexible device stacks, the cutting rates can be high and the thermal load low, resulting in good overall cut quality. For example CO_2 laser cutting of PET, polypropylene, polyethylene, etc. can be at approximately 0.5 m/s speed (125 μm thickness) but much faster (5 m/s) for thinner (50 μm) substrates (Lee, 2002).

Laser cutting of chemically strengthened glass or sapphire for scratch-resistant smartphone displays, tablet covers, etc. is another industrial application where lasers have found a niche as opposed to diamond wheel cutting, chemical etching, mechanical milling, or scribe/break processes. Such thin and brittle materials tend to break and build microcracks when exposed to thermal stresses. Hence, ultrashort-pulsed lasers, in particular picosecond (Heckl, Weiler, Luzius, Zawischa, & Sutter, 2013), have provided a breakthrough for mass production of mobile displays, offering not only advantages in terms of high strength edge quality but also flexibility in cutting shape geometries and cost reduction by eliminating lengthy postprocessing (grinding etc.). For thicker glass (>0.3 mm) applications such as contact wiring or solar panel glass cutting, other lasers are more productive (nanosecond q-switched DPSS, CO_2).

12.6.3   Laser surface patterning (dry etching)

Several applications exist using laser surface dry etch. This section does not aim to exhaustively detail those but merely indicate possibilities. Laser surface patterning is typically used in combination with full-area solution coating/printing techniques to dry etch thin films and multilayered stacks at high resolution. Maskless direct-write or projection imaging beam delivery can be used to structure sub-100-nm-thick films with typically down to a few μm lateral resolution. Selective layer patterning, i.e., the removal of one or more thin films on a transparent (glass, plastic) or metal substrate, is particularly common. OLED (Karnakis et al., 2010), OPV (Gebhardt, Hanel, Claire, & Scholz, 2011), thin film batteries, RFID circuits, sensors, and several other flexible electronics devices can be laser patterned this way. The film optical absorption, film thickness, as well as substrate optical and thermal properties are critical for optimum performance. Important laser parameters include the irradiating wavelength, focused spot size, pulse duration, intensity, spatial intensity distribution, and incident pulse number per area. Nanosecond or ultrafast (picosecond/femtosecond) duration lasers are mostly used. As a rule of thumb, the thinner the film to remove, the shorter the laser pulse is needed for optimum removal. For more details, see references in Bauerle (2011).

Another application, "self-aligned printing," involves tightly focused laser beams (<10 μm spot size) to direct write a pattern into a hydrophobic or lyophobic layer to expose in certain regions the surface of the underlying hydrophilic (or lyophilic) substrate, and hence define a surface energy pattern to enhance the resolution of inkjet printing (Klauk, 2006). In this way the spreading of the ink on the substrate is confined by the surface energy pattern, enabling source-drain electrodes for printed OTFTs to be defined with a channel length of only a few μm (Burns, Cain, Mills, Wang, & Sirringhaus, 2003) and even submicrometer dimensions (Wang et al., 2004).

Recent advances have been made in direct laser interference patterning for fabrication of repetitive 1D or 2D periodic arrays on macroscopic areas simultaneously in one ablation step (Lasagni, 2011). Fabrication of micro and submicrometer patterns on metals, ceramics, photoresists, conducting polymers, and carbon nanotubes has been demonstrated envisaged for mass production of actuators, sensors, solar cells, batteries, cell growth templates, or LEDs. The technique employs several focused laser beams combining on target to an interference pattern. If the energy density at the interference maxima within the irradiated volume is sufficiently high, local melting, ablation, and vaporization can occur on the irradiated substrate. The technique is not limited to laser wavelength or pulse duration, and by controlling the incident fluence, number of laser pulses, angle, and polarization of each input beamlet, the morphology and direction of nanostructures can be controlled (ripples or bumps).

Large-scale precision laser microstructuring of gravure print forms for the printing industry is a novel digital fabrication method. Direct laser engraving into the metallic print form surface is a fast and versatile process for gravure cylinder imaging (ablation rate up to 1 cm^3/min, area rate up to 0.1 m^2/min). High power Q-switch Nd:YAG and fiber lasers with multi-kHz repetition rates are typically used. A pulsed laser beam generates a complete ink cell with each single laser pulse. A fast modulation of the laser

beam profile for each single pulse allows for optimization of the cell shape to get the best ink transfer interaction on a specific print substrate. The entire cylinder surface is engraved in rotation by writing one single continuous helical track of precisely defined cells. Highest screen resolutions are made with single mode CW fiber lasers with output power greater than 100 W (Hennig, Selbmann, & Bruning, 2008). This method replaces traditional electromechanical and chemical etching techniques for gravure print form fabrication.

12.7 Laser printing

Laser forward and backward transfer techniques have shown significant advancements in recent years for the direct printing of materials, as an alternative approach to lithographic processes, for the deposition of high resolution and complex patterns. Laser induced forward transfer (LIFT) is a direct-write technique that was first reported by Bohandy, Kim, and Adrian (1986) for the deposition of Cu patterns on Si and fused silica substrates under high vacuum conditions. In this technique, a pulsed laser is used to induce the transfer of the material from a donor substrate to a receiver substrate, usually placed at a short distance or in contact with each other. Donor substrates are usually laser transparent and coated with a thin film of the material of interest. As the laser beam passes through the transparent substrate, it is being absorbed by the film, which is subsequently propelled toward the receiver substrate, above a certain laser energy threshold. LIFT has been used for the deposition of a wide range of materials such as metals (Willis & Grosu, 2005), polymers (Tsouti et al., 2010), biomaterials (Tsekenis et al., 2012), semiconductors (Rapp et al., 2012a,b), oxides (Zergioti et al., 1998) and carbon nanomaterials (Boutopoulos, Pandis, Giannakopoulos, Pissis, & Zergioti, 2010) for sensors (Di Pietrantonio et al., 2012), and organic electronic applications (Fardel, Nagel, Nüesch, Lippert, & Wokaun, 2007; Rapp et al., 2009). Figure 12.5 shows the carbon nanotubes printed with this technique. Among the advantages of laser printing compared to nozzle-based methods, such as inkjet printing, that face the problems of ink viscosity (high viscosity inks are required) and nozzle clogging, is that LIFT is a noncontact and nondestructive approach of material deposition that can be conducted in ambient conditions.

In addition, the dynamics of the LIFT technique have been investigated by several groups through time-resolved shadowgraphic studies on solid (Fardel, Nagel, Nüesch, Lippert, & Wokaun, 2009; Feinaeugle, Alloncle, Delaporte, Sones, & Eason, 2012) and liquid (Boutopoulos et al., 2013b; Duocastella, Fernández-Pradas, Morenza, & Serra, 2009) printed materials. These studies showed that the hydrodynamic mechanisms involved in the liquid printing depend not only on the thickness and the viscosity of the liquid but also on the laser parameters such as the energy and the spot size.

As an alternative approach to the LIFT technique, laser induced backward transfer (LIBT) has also been adopted for the direct printing of materials such as gold nano-droplets (Kuznetsov, Koch, & Chichkov, 2009). In this approach, the transfer is performed in the backward direction with respect to the incident laser beam direction. Another direct-write approach is the matrix-assisted pulsed laser evaporation-direct
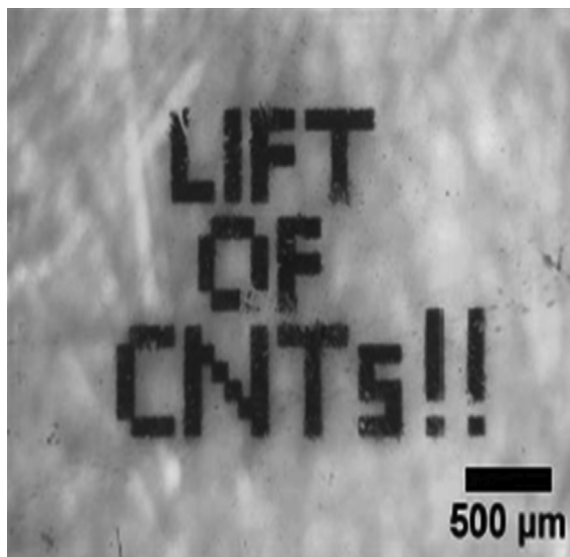
Figure 12.5 LIFT-printing of carbon nanotubes.

write (MAPLE-DW) technique (Piqué et al., 1999), in which a sacrificial matrix is used for the absorption of the laser beam and is removed after completion of the deposition. MAPLE-DW has been used for the deposition of ferroelectric (BaTiO$_3$ and SrTiO$_3$) and ferrite (Y$_3$Fe$_5$O$_{12}$) micron-sized powders (Piqué et al., 1999) and polymer thin films for sensor applications (Piqué et al., 2003). Recently, Patrascioiu, Duocastella, Fernandez-Pradas, Morenza, and Serra (2011) presented a novel film-free FS laser-based printing technique, where no donor substrate was used. More specifically, a tank filled with the solution to be printed is placed below a transparent receiver substrate and as the laser beam is passing through it focuses inside the liquid. In this way, by translating the receiver substrate along the *x*- or *y*-axis, biomolecule microarrays were printed (Duocastella, Fernandez-Pradas, Morenza, Zafra, & Serra, 2010).

In the frame of the e-LIFT European project (FP7- ICT-2009.3.3), Tri color (RGB) PLED pixels have been LIFT-printed without degradation of their characteristics (see www.e-LIFT-project.eu). They can be smaller than $20 \times 20 \ \mu m^2$ and exhibit luminance as high as 280 cd/m^2 (Shaw-Stewart et al., 2013). Organic thin film transistors have also been laser printed and exhibit mobilities of few 10^{-2} cm^2/V s, with I$_{on}$/I$_{off}$ of few 10^5 (Rapp, Biver, Alloncle, & Delaporte, 2013). A great interest in laser printing for the fabrication of sensors and biosensors has also been demonstrated (see Figure 12.6). The selectivity of sensors (resp. biosensors) has been increased by transferring, with a unique process, arrays of different sensitive polymers (resp. proteins) for the detection of volatile organic compounds (resp. chemical vapors) (Cannata et al., 2012). The sensitivity of SnO$_2$-based gas sensors printed with LIFT process has also been increased by a factor of four compared to similar industrial sensors currently manufactured by means of inkjet printing (Mattle, Hintennach, Lippert, & Wokaun,
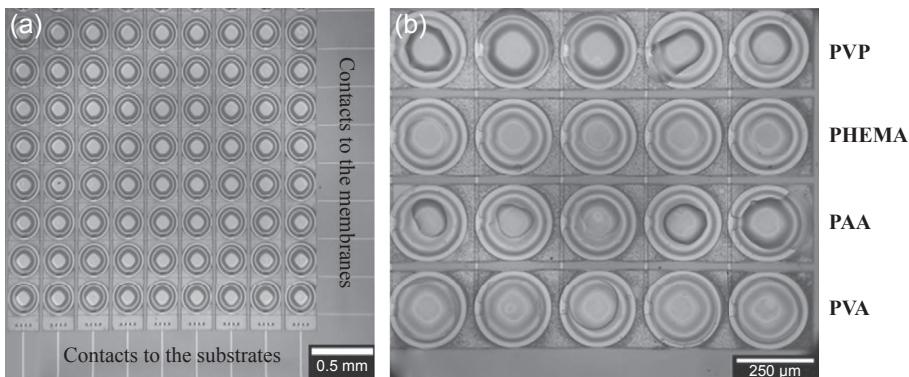
Figure 12.6 Optical microscopy images of a laser-printed chemical sensor array. (a) The Al contacts and (b) the sensors covered with various sensitive polymer layers by means of LIFT can be identified.

2013). In addition, thanks to the high impact pressure of the laser-transferred proteins onto the SPEs sensors (Boutopoulos et al., 2013a), the direct immobilization of this photosynthetic material (thylakoids) is preformed without the use of any chemical linkers. Moreover, this simpler fabrication process leads to a lowering of the detection limit of herbicides (Touloupakis, Boutopoulos, Buonasera, Zergioti, & Giardi, 2012). These few examples demonstrate the great interest in using laser printing for the heterogeneous integration of sensitive materials for the realization of sensors and biosensors on flexible substrates.

Another very promising application of LIFT for flexible organic electronics is the printing of conductive lines or 3D structures for interconnection purposes (see Figure 12.7). The laser printing of silver nanoparticle inks allows the realization of thin lines, down to few micrometers, with very high resolution and velocity as fast as 4 m/s (Rapp et al., 2013). Figure 12.8 shows a laser-printed structure of silver ink lines with various thicknesses and pitches. Moreover, inks with a wide range of viscosities can be printed, providing a better control of line morphologies (Rapp, Ailuno, Alloncle, & Delaporte, 2011). High viscosity silver pastes have been laser printed for the realization of 3D structures (Wang, Auyeung, Kim, Charipar, & Piqué, 2010), passive components, and conductive lines for high current applications. Laser printing represents a real alternative to inkjet for this application.

12.8   Conclusions and future trends

Laser processes have demonstrated their ability to become the best manufacturing technique in many very diverse fields of applications, such as automotive, aerospace, microelectronics, or art restoration. As described in this chapter, applications have already been developed to realize some of the manufacturing steps of flexible organic electronic components thanks to the unique properties of lasers. However, there is not
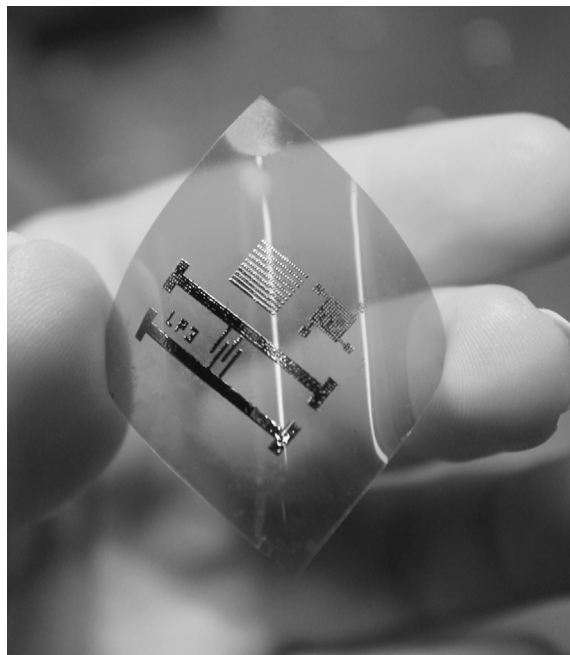
Figure 12.7 Interdigitated electrodes and contact pad printed on PET by laser transfer of silver nanoparticle inks.
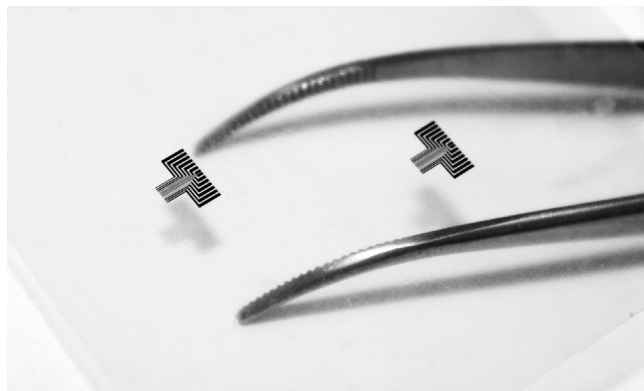
Figure 12.8 Set of laser-printed silver lines from nanoparticle ink on PET flexible substrate. On one side, thin lines (40 µm wide) are used for connection to the small pads of a device, and the larger lines on the other side allow connection with an inkjet-printed circuit.

just one laser source, and not just one way to use it. We have presented some specifics of the laser−matter interaction and a good understanding of the physics involved is required to select the appropriate laser source for a specific application. The beam shaping and handling is also of prime importance to get the full benefit of laser potential in terms of resolution, reliability, and throughput.

When all these considerations are taken into account, the laser becomes the right tool to fulfill all the requirements to develop a relevant manufacturing process. It is especially well adapted for all the applications related to high resolution microfabrication (drilling, scribbing, selective ablation, etc.), modification of surface properties and printing sensitive materials and conductive inks.

We conclude with a few sentences from the report "Photonics − Our vision for a key enabling technology in Europe" published by the European Technology Platform Photonics21 (Photonics21, 2011). The general key advantages of the laser processes that are underlined hereafter are fully relevant for the manufacturing of flexible organic electronics:

> *Photonics will be a strategic element and a key enabling technology in future manufacturing processes, even more so than it already is today. With tools using light in the form of a laser, processes can be handled automatically and flexibly, producing components and products with extraordinary quality. The trend towards customization and the growing importance of industrial design, as observed most notably in consumer electronics, will require novel methods to enable new product shapes and lot-size-one production capabilities. The inherent flexibility of the laser tool makes it the ideal choice for meeting these requirements. Furthermore, the advantages of the wearless working laser tool and of integrated monitoring and control systems based on intelligent photonic sensing techniques, will allow zero-fault production to be achieved, leading to higher product quality and reduced wastage. The laser is a key element for a future sustainable economy in Europe.*

Acknowledgements

References

Anastasiadis, S. H. (2013). Development of functional polymer surfaces with controlled wettability. *Langmuir, 29*, 9277−9290.

Ardelean, H., Petit, S., Laurens, P., Marcus, P., & Arefi-Khonsari, F. (2005). Effects of different laser and plasma treatments on the interface and adherence between evaporated aluminium and polyethylene terephthalate films: X-ray photoemission, and adhesion studies. *Applied Surface Science, 243*, 304−318.

Bai, Y., Feng, J., Liu, Y.-F., Song, J.-F., Simonen, J., Jin, Y., et al. (2011). Outcoupling of trapped optical modes in organic light-emitting devices with one-step fabricated periodic corrugation by laser ablation. *Organic Electronics, 12*, 1927−1935.

Basting, D., & Marowsky, G. (2010). *Excimer laser technology*. Berlin: Springer.

Bauerle, D. (2011). *Laser processing and chemistry* (4th ed.). Berlin: Springer.

Beake, B., Ling, J., & Leggett, G. (1998). Correlation of friction, adhesion, wettability and surface chemistry after argon plasma treatment of poly(ethylene terephthalate). *Journal of Materials Chemistry, 8*(12), 2845−2854.

Bieri, N., Chung, J., Haferl, S., Poulikakos, D., & Grigoropoulos, C. (2003). Microstructuring by printing and laser curing of nanoparticle solutions. *Applied Physics Letters, 82*(20), 3529−3531.

Bohandy, J., Kim, B. F., & Adrian, F. J. (1986). Metal deposition from a supported metal film using an excimer laser. *Journal of Applied Physics, 60*, 1538.

Boutopoulos, C., Alloncle, A.-P., Zergioti, I., & Delaporte, P. (2013b). A time-resolved shadowgraphic study of laser transfer of silver nanoparticle ink. *Applied Surface Science, 278*, 71−76.

Boutopoulos, C., Pandis, C., Giannakopoulos, K., Pissis, P., & Zergioti, I. (2010). Polymer/carbon nanotube composite patterns via laser induced forward transfer. *Applied Physics Letters, 96*, 041104.

Boutopoulos, C., Papageorgiou, D. P., Zergioti, I., & Papathanasiou, A. G. (2013a). Sticking of droplets on slippery superhydrophobic surfaces by Laser Induced Forward Transfer. *Applied Physics Letters, 103*, 024104.

Burns, S. E., Cain, P., Mills, J., Wang, J., & Sirringhaus, H. (2003). Inkjet printing of polymer thin-film transistor circuits. *MRS Bulletin, 28*(11), 829−834.

Cannata, D., Benetti, M., Di Pietrantonio, F., Verona, E., Palla-Papavlu, A., Dinca, V., et al. (2012). Nerve agent simulant detection by solidly mounted resonators (SMRs) polymer coated using laser induced forward transfer (LIFT) technique. *Sensors and Actuators B, 173*, 32−39.

Chan, C.-M., Ko, T.-M., & Hiraoka, H. (1996). Polymer surface modification by plasmas and photons. *Surface Science Reports, 24*, 1−54.

Delaporte, Ph, Gastaud, M., Marine, W., Sentis, M., Uteza, O., Thouvenot, P., et al. (2003). Dry excimer laser cleaning applied to nuclear decontamination. *Applied Surface Science, 208−209*, 298−305.

Delaporte, Ph, & Oltra, R. (2006). Laser cleaning: state of the art. In J. Perriere, E. Millon, & E. Fogarassy (Eds.), *Recent advances in laser processing of materials* (pp. 411−440). Elsevier press.

Di Pietrantonio, F., Benetti, M., Cannatà, D., Verona, E., Palla Papavlu, A., Dinca, V., et al. (2012). Volatile toxic compound detection by surface acoustic wave sensor arrays coated with chemoselective polymers deposited by laser induced forward transfer: application to sarin. *Sensors and Actuators B: Chemical, 174*, 158−167.

Duley, W. W. (1976). *CO_2 lasers − Effects and applications*. London: Academic Press.

Duocastella, M., Fernández-Pradas, J. M., Morenza, J. L., & Serra, P. (2009). Time-resolved imaging of the laser forward transfer of liquids. *Journal of Applied Physics, 106*, 084907.

Duocastella, M., Fernandez-Pradas, J. M., Morenza, J. L., Zafra, D., & Serra, P. (2010). Novel laser printing technique for miniaturized biosensors preparation. *Sensors and Actuators B, 145*, 596−600.

Fardel, R., Nagel, M., Nüesch, F., Lippert, T., & Wokaun, A. (2007). Fabrication of organic light-emitting diode pixels by laser-assisted forward transfer. *Applied Physics Letters, 91*, 061103.

Fardel, R., Nagel, M., Nüesch, F., Lippert, T., & Wokaun, A. (2009). Shadowgraphy investigation of laser-induced forward transfer: Front side and back side ablation of the triazene polymer sacrificial layer. *Applied Surface Science, 255*, 5430−5434.

Feinaeugle, M., Alloncle, A. P., Delaporte, Ph, Sones, C. L., & Eason, R. W. (2012). Time-resolved shadowgraph imaging of femtosecond laser-induced forward transfer of solid materials. *Applied Surface Science, 258*, 8475−8483.

Fogarassy, E., & Lazare, S. (1992). *Laser ablation of electronic materials*. North Holland Pub.

Fourrier, T., Schrems, G., Mühlberger, T., Heitz, J., Arnold, N., Bäuerle, D., et al. (2001). Laser cleaning of polymer surfaces. *Applied Physics A, 72*, 1−6.

Gebhardt, M., Hanel, J., Claire, M., & Scholz, C. (2011). Reel-to-reel machining with ultra short pulsed lasers. *Laser Technik Journal*, (1), 29−32.

Goodridge, R., Hague, R., & Tuck, C. (2010). An empirical study into laser sintering of ultra-high molecular weight polyethylene (UHMWPE). *Journal of Materials Processing Technology, 210*, 72−80.

Goodridge, R., Shofner, M., Hague, R., McClelland, M., Schlea, M., Johnson, R., et al. (2011). Processing of a Polyamide-12/carbon nanofibre composite by laser sintering. *Polymer Testing, 30*, 94−100.

Grigoropoulos, C. (2009). *Transport in laser microfabrication: Fundamentals and applications*. New York: Cambridge University Press.

Grojo, D., Boarino, L., De Leo, N., Rocci, R., Panzarasa, G., Delaporte, Ph, et al. (2012). Size scaling of mesoporous silica membranes produced by nanosphere mediated laser ablation. *Nanotechnology, 23*, 485305.

Grojo, D., Cros, A., Delaporte, Ph, & Sentis, M. (2007). Experimental analyses of ablation mechanisms involved in dry laser cleaning. *Applied Surface Science, 253*, 8309−8315.

Grojo, D., Delaporte, Ph, Sentis, M., Pakarinen, O., & Foster, A. (2008). The so-called dry laser cleaning governed by humidity at the nanometer scale. *Appied Physics Letters, 92*, 033108.

Heckl, O., Weiler, S., Luzius, S., Zawischa, I., & Sutter, D. (2013). Ultrafast disk technology enables next generation micromachining laser sources. In *Proceedings of SPIE* (vol. 8603), 86030B−86030B−7.

Hennig, G., Selbmann, K. H., & Bruning, S. (2008). Large scale laser microstructuring in the printing Industry. *Laser Technik Journal, 3*, 52−56.

HOLS. (2004). In Gerald F. Marshall (Ed.), *Handbook of optical and laser scanning*. New York: Marcel Dekker.

Hooker, S., & Webb, C. (2010). *Laser physics (Oxford master series in physics)*. Oxford University Press.

Kabashin, A. V., Delaporte, Ph, Pereira, A., Grojo, D., Torres, R., Sarnet, T., et al. (2010). Nanofabrication with pulsed lasers. *Nanoscale Research Letters, 5*, 454−463.

Kabashin, A. V., & Meunier, M. (2006). Laser ablation-based synthesis of nanomaterials. In J. Perriere, E. Millon, & E. Fogarassy (Eds.), *Recent advances in laser processing of materials* (pp. 1−36). Elsevier press.

Karnakis, D., Van Steenberge, G., Gielen, A., De Baets, J., & van den Brand, J. (2010). Mechanistic aspects of selective laser patterning of multilayered thin-film structures in OLED fabrication. In *Proceedings of LOPE-C conference*. Frankfurt am Main, Germany: Organic Electronics Association (OE-A), ISBN 978-3-00-029955-1. OE-A 2010, 143.

Klauk, H. (2006). *Organic electronics materials, manufacturing and applications*. WILEY-VCH Verlag GmbH.

Ko, S., Chung, J., Pan, H., Grigoropoulos, C., & Poulikakos, D. (2007). Fabrication of multi-layer passive and active electric components on polymer using inkjet printing and low temperature laser processing. *Sensors and Actuators A, 134*, 161−168.

Koechner, W. (2010). *Solid-state laser engineering* (6th ed.). Springer Series in Optical Sciences.

Kumpulainen, T., Pekkanen, J., Valkama, J., Laakso, J., Tuokko, R., & Mantysalo, M. (2011). Low temperature nanoparticle sintering with continuous wave and pulse lasers. *Optics and Laser Technology, 43*, 570−576.

Kuznetsov, A. I., Koch, J., & Chichkov, B. N. (2009). Laser-induced backward transfer of gold nanodroplets. *Optics Express, 17*(21), 18820−18825.

Lasagni, A. (2011). Exploring the possibilities of laser interference patterning for the rapid fabrication of periodic arrays on macroscopic areas. In *Fabrication and characterization in the micro-nano range new trends for two and three dimensional structures*. Berlin: Springer.

Laurens, P., Ould Bouali, M., Meducin, F., & Sadraset, B. (2000). Characterization of modifications of polymer surfaces after excimer laser treatments below the ablation threshold. *Applied Surface Science, 154−155*, 211−216.

LBSA. (2006). In F. Dickey, S. Holswade, & D. Shealy (Eds.), *Laser beam shaping applications*. New York: CRC Press.

Lee, S. (2002). *CO_2 processing at 9 microns*. Industrial laser solutions. http://www.coherent.com/Applications.

Li, L., Guo, W., Wang, Z. B., Liu, Z., Whitehead, D., & Luk'yanchuk, B. (2009). Large-area laser nano-texturing with user-defined patterns. *Journal of Micromechanics and Micro-engineering, 19*, 054002.

Lippert, T., Yabe, A., & Wokaun, A. (1997). Laser ablation of doped polymer systems. *Advanced Materials, 9*(2), 105−119.

Lu, Y., Komuro, S., & Aoyagi, Y. (1994). Laser-induced removal of fingerprints from glass and Quartz surfaces. *Japanese Journal of Applied Physics, 33*, 4691−4696.

Mattle, T., Hintennach, A., Lippert, T., & Wokaun, A. (2013). Laser induced forward transfer of SnO_2 for sensing applications using different precursors systems. *Applied Physics A, 110*, 309.

Mosbacher, M., Münzer, H.-J., Zimmermann, J., Solis, J., Boneberg, J., & Leiderer, P. (2001). Optical field enhancement effects in laser-assisted particle removal. *Applied Physics A, 72*, 41−44.

OE-A. (2013). *Organic and printed electronics applications, technologies and suppliers* (5th ed.). VDMA.

Paltauf, G., & Dyer, P. E. (2003). Photomechanical processes and effects in ablation. *Chemical Reviews, 103*, 487−518.

Patrascioiu, A., Duocastella, M., Fernandez-Pradas, J. M., Morenza, J. L., & Serra, P. (2011). Liquids microprinting through a novel film-free femtosecond laser based technique. *Applied Surface Science, 257*, 5190−5194.

Peng, P., Hu, A., & Zhou, Y. (2012). Laser sintering of silver nanoparticle thin films: micro-structure and optica properties. *Applied Physics A, 108*, 685−691.

Pereira, A., Cros, A., Delaporte, Ph, Georgiou, S., Manousaki, A., Marine, W., et al. (2004). Surface nanostructuring of metals by laser irradiation: effects of pulse duration, wavelength and gas atmosphere. *Applied Physics A, 79*(4−6), 1433−1437.

Pereira, A., Grojo, D., Chaker, M., Delaporte, Ph, Guay, D., & Sentis, M. (2008). Laser-fabricated porous alumina membrane (LF-PAM) for the preparation of metal nanodot arrays. *Small, 4*, 572−575.

Photonics21. (2011). *Photonics − Our vision for a key enabling technology in europe*. European Technology Platform Photonics21. www.photonics21.org.

Piqué, A., Auyeung, R. C. Y., Stepnowski, J. L., Weir, D. W., Arnold, C. B., McGill, R. A., et al. (2003). Laser processing of polymer thin films for chemical sensor applications. *Surface and Coatings Technology, 163−164*, 293−299.

Piqué, A., Chrisey, D. B., Auyeung, R. C. Y., Fitz-Gerald, J., Wu, H. D., McGill, R. A., et al. (1999). A novel laser transfer process for direct writing of electronic and sensor materials. *Applied Physics A, 69*, 279−284.

Pleasants, S., & Kane, D. (2003). Laser cleaning of alumina particles on glass and silica substrates: Experiment and quasistatic model. *Journal of Applied Physics, 93*(11), 8862−8866.

Rapp, L., Ailuno, J., Alloncle, A.-P., & Delaporte, P. (2011). Pulsed-laser printing of silver nanoparticles ink: control of morphological properties. *Optics Express, 19*(22), 21563−21574.

Rapp, L., Biver, E., Alloncle, A. P., & Delaporte, P. (2013). High-speed laser printing of silver nanoparticles ink. In *Proceedings of LAMP 2013, SP L2, # 13−004*. Toki Messe, Niigata, Japan: Japan Laser Processing Society. Available from: http://www.jlps.gr.jp/en/proc/lamp/13/.

Rapp, L., Diallo, A. K., Alloncle, A. P., Videlot-Ackermann, C., Fages, F., & Delaporte, Ph. (2009). Pulsed-laser printing of organic thin film transistors. *Applied Physics Letters, 95*, 171109.

Rapp, L., Diallo, A. K., Nenon, S., Alloncle, A. P., Videlot-Ackermann, C., Fages, F., et al. (2012b). Laser printing of a semiconducting oligomer as active layer in organic thin film transistors: impact of a protecting triazene layer. *Thin Solid Films, 520*, 3043−3047.

Rapp, L., Serein-Spirau, F., Lere-Porte, J.-P., Alloncle, A.-P., Delaporte, P., Fages, F., et al. (2012a). Laser printing of air-stable high performing organic thin film transistors. *Organic Electronics, 13*, 2035−2041.

Ready, J. (1997). *Industrial applications of lasers*. San Diego CA: Academic Press, 397.

Shaw-Stewart, J., Mattle, T., Lippert, T., Nagel, M., Nüesch, F., & Wokaun, A. (2013). The fabrication of small molecule organic light-emitting diode pixels by laser-induced forward transfer. *Journal of Applied Physics, 113*(4). art no 043104.

Siegman, A. E. (1986). *Lasers*. Mill Valley, CA: University Science Books.

Silfvast, W. T. (2008). *Laser fundamentals*. Cambridge University Press.

Soltani, M., & Ahmadi, G. (1994). On particle removal mechanisms under base acceleration. *Journal of Adhesion, 44*, 161−175.

Steen, W. M. (2003). *Laser material processing* (3rd ed.). Berlin, Heidelberg: Springer.

Steger, M., Hartmann, C., Beckemper, S., Holtkamp, J., & Gillner, A. (2013). Fabrication of hierarchical structures by direct laser writing and multi-beam-interference. In *Proc. LAMP2013−6th Int. Cong. On laser Advanced materials processing*. Toki Messe, Niigata, Japan: Japan Laser Processing Society.

Tam, A., Park, H., & Grigoropoulos, C. (1998). Laser cleaning of surface contaminants. *Applied Surface Science, 127−129*, 721−725.

Touloupakis, E., Boutopoulos, C., Buonasera, K., Zergioti, I., & Giardi, M. T. (2012). A photosynthetic biosensor with enhanced electron transfer generation realized by laser printing technology. *Analytical and Bioanalytical Chemistry, 402*(10), 3237−3244.

Tsekenis, G., Chatzipetrou, M., Tanner, J., Chatzandroulis, S., Thanos, D., Tsoukalas, D., et al. (2012). Surface functionalization studies and direct laser printing of oligonucleotides toward the fabrication of a micromembrane DNA capacitive biosensor. *Sensors and Actuators B, 175*, 123−131.

Tsouti, V., Boutopoulos, C., Goustouridis, D., Zergioti, I., Normand, P., Tsoukalas, D., et al. (2010). A chemical sensor microarray realized by laser printing of polymers. *Sensors and Actuators B, 150*, 148−153.

Vatry, A., Marchand, A., Delaporte, Ph, Grojo, D., Grisolia, C., & Sentis, M. (2011). Studies of laser-induced removal mechanisms for Tokamak-like particles. *Applied Surface Science, 257*, 5384−5388.

Voisiat, B., Gedvilas, M., Indrisiunas, S., & Raciukaitis, G. (2011). Flexible microstructuring of thin films using multi-beam interference ablation with ultrashort lasers. *Journal of Laser Micro/Nanoengineering, 6*(3), 185−190.

Wang, J., Auyeung, R. C., Kim, H., Charipar, N., & Piqué, A. (2010). Three-dimensional printing of interconnects by laser direct-write of silver Nanopastes. *Advanced Materials, 22*, 4462−4466.

Wang, J. Z., Zheng, Z. H., Li, H. W., Huck, W. T. S., & Sirringhaus, H. (2004). Dewetting of conducting polymer droplets − polymer FETs. *Nature Materials, 3*, 171−176.

Willis, D. A., & Grosu, V. (2005). Microdroplet deposition by laser-induced forward transfer. *Applied Physics Letters, 86*, 244103.

Zergioti, I., Mailis, S., Vainos, N., Papakonstantinou, P., Kalpouzos, C., Grigoropoulos, C., et al. (1998). Microdeposition of metal and oxide structures using ultrashort laser pulses. *Applied Physics A, 66*, 579.

Zhu, B. L., Xie, C. S., Wang, A. H., Wu, J., Wu, R., & Liu, J. (2007). Laser sintering ZnO thick films for gas sensor application. *Journal of Materials Science, 42*, 5416−5420.

This page intentionally left blank

Flexible organic electronic devices on metal foil substrates for lighting, photovoltaic, and other applications

13

B.W. D'Andrade[1], A.Z. Kattamis[2], P.F. Murphy[2]
[1]Exponent, Inc., Washington, DC, USA; [2]Exponent, Inc., New York, NY, USA

13.1   Introduction

Flexible consumer electronics for applications such as displays, lighting, and photovoltaics have garnered interest over the last decade because of their unique properties, including being lightweight, bendable, conformable, rugged, and nonbrittle (Zardetto, Brown, Reale, & Di Carlo, 2011). The interest in electronics on flexible substrates may be traced to research on flexible solar panels for space missions in the 1960s (Crabb & Treble, 1967; Ray, 1967). During that time, the availability of reliable, compact, and lightweight power sources capable of providing power in the 1- to 50-kW range was an issue, and a large area of solar cells on flexible substrates was studied as a means to address the issue.

During the 1960s, researchers at the Radio Corporation of America (RCA) pioneered the development of thin-film-transistors (TFTs) and liquid crystals. In 1973, 4 years after RCA demonstrated the first liquid-crystal display (LCD) digital clock, Sharp Corporation announced the first liquid-crystal pocket calculator, which was the first commercially successful LCD product. The interest in large displays is one factor that drove the development of TFT-LCDs, such that by the late 1980s, 10-in TFT-LCDs in laptop computers were introduced and then by 2006, LG Philips had a 100-in TFT-LCD for high-definition television (Cristaldi, Pennisi, & Pulvirenti, 2009).

The increase in flat-panel display size over a short time and the market consisting of billions of mobile displays (Li, Bhowmik, & Bos, 2008) were not immediately obvious in the 1960s. Hence, a new opportunity arose out of the need to have a portable, large display in a small-form factor. A means to transport a large-area electronic device (solar panel or display) is desirable such that it is compact until it is deployed for operation. In the case of solar panels for space, the panels have to be launched into space in a well-defined, small-area payload whereas in the case of displays, a user may carry a display in a shirt pocket and then deploy the display on their desk or on a wall.

In addition to the widespread consumer desire for smart mobile displays, display media researchers have searched for an electronic analog of paper since the 1970s (Comiskey, Albert, Yoshizawa, & Jacobson, 1998). Electrophoretic ink (Comiskey et al., 1998), used in E-readers, is one example of a display technology that is arguably

organic-based. E-readers have been clearly demonstrated with the ability to enable large-area, flexible displays such as the 19-in flexible E-reader having 0.3 mm thickness, weighing 130 g, and TFTs on an ultra-thin transparent metal foil backing produced by LG (2010a, 2010b, Shah, 2010). Flexible LCDs have also been demonstrated since 2005 (Kanellos, 2005), and liquid crystals in LCDs are organic materials.

However, the focus of this chapter is on organic electronics, in which organic material conducts charge and/or produces light, which is different from organic materials that mechanically respond to electric fields, such as liquid crystals and electrophoretic inks. One reason for interest in organic electronics is the ability to deposit organic films on various very-low-cost substrates such as plastic or metal foils and the relative ease of processing the organic compounds (Forrest, 2004). For example, the clear user applications for flexible displays and solar cells, coupled with the processing properties of organic films, have created the vision for the future of organic electronics on metal foil and have encouraged research in this area.

Gustafsson et al. (1992) showed that an organic light-emitting diode (OLED), used in OLED displays, could be fabricated on a flexible substrate. The work of Gustafsson et al. would be followed by efforts to produce a display on a flexible substrate. Gustafsson et al. noted that polymers were amenable to simple deposition processes such as spin casting or dip coating; therefore, they were suitable for fabricating large-area devices on flexible substrates.

Constant et al. (1995) demonstrated TFTs on flexible polyimide substrate, and in 1996, Theiss and Wagner (1996) integrated OLEDs with amorphous-Si TFTs on metal foil substrates. Given those developments, the 1990s was a decade in which the basic building blocks and proof of concept for organic electronics on flexible materials stoked interest in an endeavor to commercialize flexible displays.

Thin steel foils are attractive for use as flexible substrates for organic electronics because of their low oxygen and water permeation rates, tolerance to high-temperature processing ($\sim 1000\ ^\circ$C), dimensional stability, chemical resistance, relatively low coefficient of thermal expansion, and higher thermal conductivity (compared with glass), and they could provide a common voltage terminal (for ground or shielding). For OLED top-emitting-based displays, metal substrates can provide an excellent oxygen and moisture barrier that is critical for extended OLED lifetimes (Park, Chae, Chung, & Lee, 2011). A top-emitting OLED architecture (TOLED) refers to the feature of the OLED design that enables light to be directed away from the opaque steel substrate through transparent electrodes deposited onto the OLED (Hofmann, Thomschke, Lussem, & Leo, 2011); see Figure 13.1 for a graphical illustration of a top-emitting and bottom-emitting device.

The need for a moisture and oxygen barrier is because OLED performance degrades on exposure to water or oxygen. The degradation is exhibited as dark spots within the emissive area of the OLED (Burrows et al., 1994). For an OLED to have an operational lifetime of greater than 10,000 h, the water vapor transmission rate (WVTR) and oxygen transmission rates through any protective layer is $\sim 1 \times 10^{-6}$ g/m^2/day and 10^{-5}–10^{-6} g/m^2/day, respectively (Lewis & Weaver, 2004), but those rates may be high given the lifetime requirements of the state of the art in OLED displays and lighting.
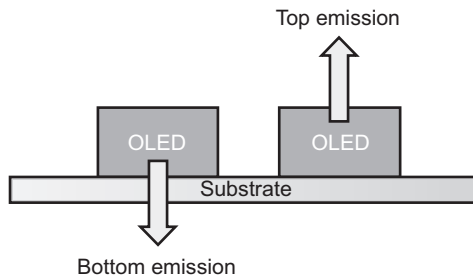
Figure 13.1 A top- and bottom-emission OLEDs on a substrate are pictorialized.

Defects in SiO_2, silicon nitride (SiN_x), or Al_2O_3 limit the effective permeation rates through single layers of those materials to an unsatisfactory level. Multilayer structures consisting of alternating layers of inorganic and polymer materials have been more successful (Chwang et al., 2003; Weaver et al., 2002). In addition, novel inorganic-polymer hybrid materials have also been demonstrated to provide laboratory-scale usefulness as permeation barriers (Gartside et al., 2008).

In addition to consumer electronic applications, manufacturing processes of electronics on flexible substrates is a long-term goal of researchers because there is the potential to substantially reduce manufacturing costs toward the costs associated with newspapers, food packaging, and other printed media (Momtaz, 2009; So, Kido, & Burrows, 2008). For example, white OLED (WOLED) manufacturing costs for illumination applications are a formidable challenge. An estimate for WOLED costs is $\sim$ \$10/lm (So et al., 2008), compared with the manufacturing costs for an incandescent lamp, which is less than \$0.03/lm. WOLEDs in 55-in flat-panel displays have been produced using vacuum sublimation and under very strict quality requirements that exceed those necessary for illumination products; therefore, the cost to manufacture WOLEDs, using vacuum deposition processes, is cost-prohibitive at this time. Therefore, new manufacturing technologies such as roll-to-roll processes (So et al., 2008) are pursued as methods to manufacture WOLEDs.

The current state of the art of organic electronics on flexible substrates ranges from a 55-in curved television product (Display, 2012) to prototype flexible displays on plastic for smartphones (Poor, 2012) and commercially available smartphone displays made on plastic (Display, 2013). As mobile display usage continues to grow, new form factors to provide information to consumers and to distinguish smartphones are attractive to manufacturers. Consumers also gain a device that is much less susceptible to the damage that is common with brittle glass displays.

This chapter examines the steps involved in building organic electronics on metal foil. The selection of substrates with characteristics that are appropriate for processing conditions and how a substrate is processed are discussed in Sections 13.2 and 13.3, respectively. A review of TFTs on metal foil, focused on silicon-based active materials, is provided in Section 13.4, and a review of the state of organic devices on metal foil is given in Section 13.5. Finally, Section 13.6 is a general outlook, including a discussion on what needs to be accomplished.

13.2   Substrate selection

Metal foils can be a good alternative to other flexible substrates such as plastic because of several characteristics, including lower chemical sensitivity, lower air and moisture permeability, and the ability to withstand higher process temperatures. When selecting a metal foil substrate, the following primary properties should be considered: the coefficient of thermal expansion (CTE), surface roughness, chemical sensitivity, and maximum process temperature. These properties should be compatible with the materials that comprise the devices built on the substrate. A summary of various properties for several metal foil substrates is provided in Table 13.1 together with properties of glass and several plastic substrate materials for comparison.

When thin, rigid films such as amorphous silicon, polysilicon, and silicon nitride are deposited onto flexible substrates, mechanical strains are induced in the deposited layers. The total mismatch strain (ε_M) for a thin film is the sum of three components: the built-in strain (ε_B), the thermal mismatch strain (ε_{TH}), and the moisture mismatch strain (ε_{CH}) (Cheng, Kattamis, Long, Sturm, & Wagner, 2005; Crawford, 2005).

The built-in strain is a response to the built-in stress that arises when atoms are deposited in nonequilibrium positions, and it is a function of the material system and deposition conditions (Floro, Chason, Cammarata, & Srolovitz, 2002). The thermal strain is independent of film thickness, and it is caused by the CTE mismatch between the film and the substrate according to

$$\varepsilon_{TH} = \left(CTE_s - CTE_f\right) \times \left(T_{room} - T_{deposition}\right) \tag{13.1}$$

where CTE_s is the CTE of the substrate and CTE_f is the CTE of the thin film.

For example, stainless steel has a CTE_S of ∼10−17 ppm/K (Ohring, 1992) that is significantly different from the CTE_f of SiN_x, which is ∼2.7 ppm/K (Maeda & Ikeda, 1998). By convention, a negative sign is often used for a compressive strain in Eqn (13.1).

Depositions of thin films are performed at elevated temperatures; hence, a stainless steel substrate shrinks more than a SiN_x deposited film when the sample cools to room temperature. This mismatch places a compressive strain on the thin film as the sample cools. The moisture mismatch strain is due to the difference in moisture uptake between a thin film and the substrate. This tends to be very small for metal foil substrates that do not easily absorb moisture as compared with plastic substrates.

The next consideration for selecting substrates is surface roughness. Ultra-smooth electronic-grade metal foils are generally not readily available because of the increased costs associated with manufacturing specialized substrates for displays. For cold rolled materials, striations form on the surface of the metal foils from defects in the rollers during the sheet rolling process. Point defects are also often encountered. Figure 13.2 shows a surface profile measurement (a) and an optical micrograph (b) of a sample of 304 stainless steel in which the unidirectional striations are evident. For example, the roughness of the sample in Figure 13.3 was approximately 1 μm RMS. (For comparison, indium-tin-oxide on glass substrates with <10 nm surface roughness are commercially available from Thin Film Devices, Inc.)

Table 13.1 **Selected properties of flexible substrate materials**

Substrate	T_{max} (°C)	CTE (ppm/K)	Optical transmission visible	Chemical sensitivity	Moisture uptake (%)	Surface roughness (as received)
Stainless steel (430)	900	10	Opaque	OK	∼0	∼1 μm
Stainless steel (304)		17	Opaque	OK	∼0	∼1 μm
Kovar (nickel-cobalt ferrous alloy)	800	5−6	Opaque	High	∼0	∼10 nm
Copper		17	Opaque	High	∼0	
Aluminum		24	Opaque	High	∼0	
Glass	600	2	>95%	High	∼0	∼1 nm
Polyimide (PI)	300	16	Semitransparent	High	2−3	∼10 nm
PEN (polyethylene naphthalate)	150	20−60	Transparent	High	2−3	∼10 nm
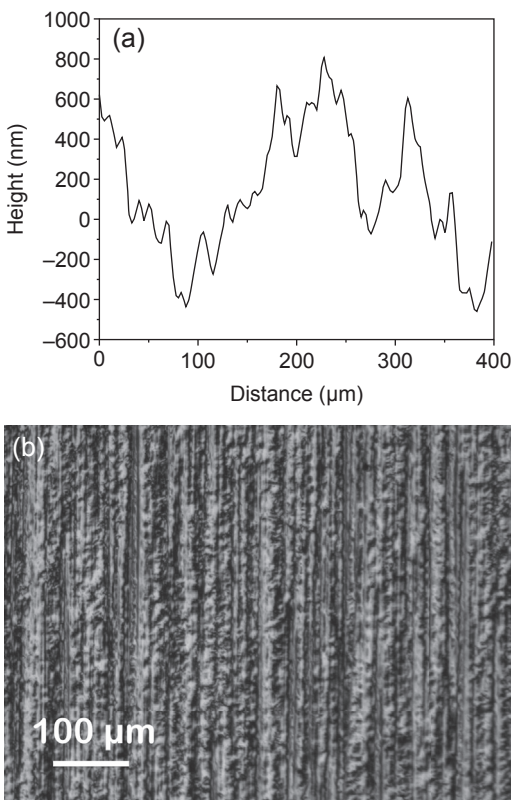
Figure 13.2 (a) Surface profile measurement and (b) optical micrograph of a sample of 304 stainless steel.
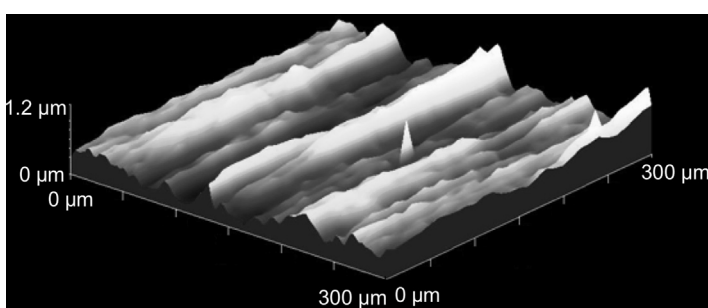
Figure 13.3 Three-dimensional surface profile measurement of 304 stainless steel.

Surface roughness can have a detrimental effect on the properties of TFTs, especially long-term gate bias stress stability. Furthermore, point defects, if large enough, can penetrate the TFT stack (which may be only ~ 2 μm thick) and penetrate thin OLED layers (which may be ~ 1 μm thick) causing shorts, "dead" pixels, and reduced
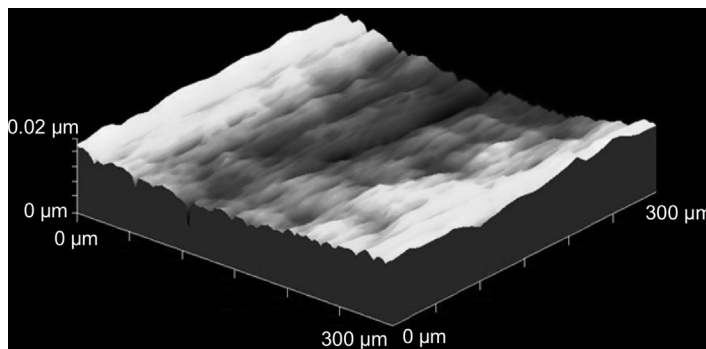
Figure 13.4 Three-dimensional surface profile of ultra-smooth stainless steel.

yields. If during manufacturing the metal rollers are kept free of dust particles, then the steel foils can be made ultra-smooth. A three-dimensional (3D) profile of one such example substrate is shown in Figure 13.4.

Nickel substrates are also an option for a flexible metal foil substrate (Khan, Ma, Choi, & Hatalis, 2011). These substrates are very sensitive to chemical attack and have to be properly encapsulated. Nickel is softer than stainless steel, and it can be found with very low surface roughness. In addition, nickel is easily polished. For example, the nickel substrate surface roughness can be less than 6 nm over similar sized areas as stainless steel substrates. Figure 13.5 shows a profile measurement (a) and an optical micrograph (b) of a sample of nickel.

Stainless steel is perhaps the best option for a metal foil substrate, primarily because of its insensitivity to chemicals used in TFT processing and its ability to withstand high processing temperatures. Although TFTs have been demonstrated on nickel, copper, and aluminum substrates, as discussed in more detail below, these materials are more highly reactive; therefore, they would require effective substrate encapsulation for many types of processing.

13.3 Substrate preparation

Substrate preparation typically includes planarization to reduce surface roughness and electrical passivation to reduce capacitive coupling between the devices and the conductive metal foil substrate. Most stainless steel substrates available have an average roughness that would prevent high-yield fabrication of OLED displays; therefore, planarization of the steel substrate is a necessary step. Stainless steel foils can be made smoother by using chemical-mechanical polishing (CMP) (Jun Hyuk et al., 2006); by electrolytic polishing (Li, Yu, Xue, & Leng, 2007); or by using the planarization materials available, ranging from spin-on glasses (SOGs) to polymers such as benzocyclobutene (BCB) and polyimide. SOGs (Theiss & Wagner, 1996) and polyimide (Chwang et al., 2006) have been used to planarize metal foils for TFT fabrication.
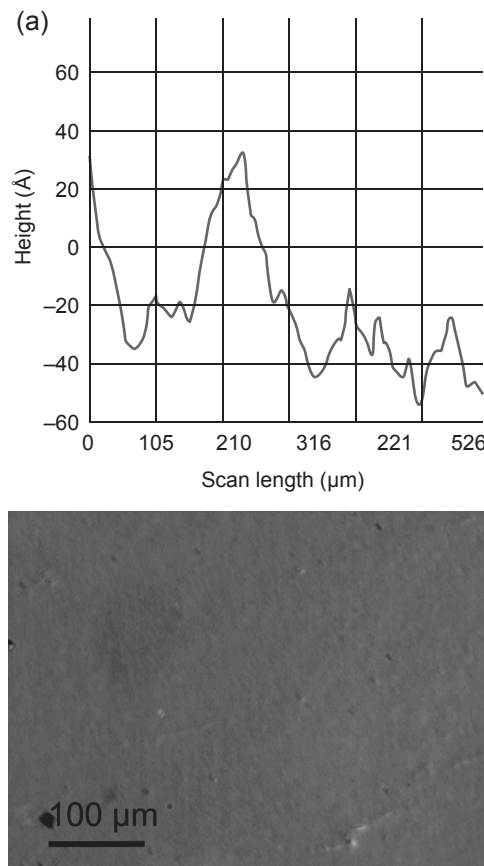
Figure 13.5 (a) Surface profile measurement and (b) optical micrograph of a sample of nickel.

CMP is a process in which the surface of the metal foil substrate is polished using a rotating pad and an abrasive and/or corrosive slurry. The pad rotates in a nonconcentric manner. CMP is a technique commonly used in the microelectronics industry for planarizing insulating layers between active materials and interconnects. The goal of CMP optimization is to improve the material removal rate while maintaining a smooth surface.

CMP use in planarizing stainless steel foil substrates has a short history. In the case of metal foil substrates, colloidal silica or alumina-based slurries are often used. Improved removal rates have been shown to be dependent on the oxidant content and pH of the slurry. Typical CMP results on stainless steel yield a surface roughness of $\sim 1-3$ nm (Dong-Jin, Sang-Hoon, Tae-Woo, & Shi-Woo, 2009; Jae Kyeong et al., 2007; Jun Hyuk et al., 2006). The pressure and rotation rate may also be adjusted to achieve a root-mean-squared roughness of 0.7 nm, equal to that of glass (Xiaokai et al., 2012).

Electrolytic polishing uses an anode electrolytic etching process on stainless steel. The steel foil is used as the anode, metal atoms dissolve to form metal ions, and a metal

oxide layer forms on the surface of the steel foil. This technique has been shown to reduce surface roughness from 0.12 μm to 44 nm (Li et al., 2007).

A SOG is a solution of colloidal silica particles suspended in a solvent. The solvent is driven out during a curing process to leave a gel, which further heating converts to a SiO_2 film with dielectric constant, $\varepsilon \sim 3-5$ (Brinker & Scherer, 1990). There are various SOG materials available, and process optimization is required to achieve desired surface roughness.

For example, SOG 20B, a silicate SOG, with an ε of ~ 5 and a nominal thickness of 300 nm can reduce surface roughness from ~ 1.2 μm to ~ 0.7 μm; however, this is not an adequate reduction in the surface roughness, primarily because of cracking when multiple layers of SOG are coated on each other (Kattamis et al., 2007). Figure 13.6 shows a profile measurement (a) and an optical micrograph (b) of a sample of stainless steel planarized with 300 nm of SOG 20B.
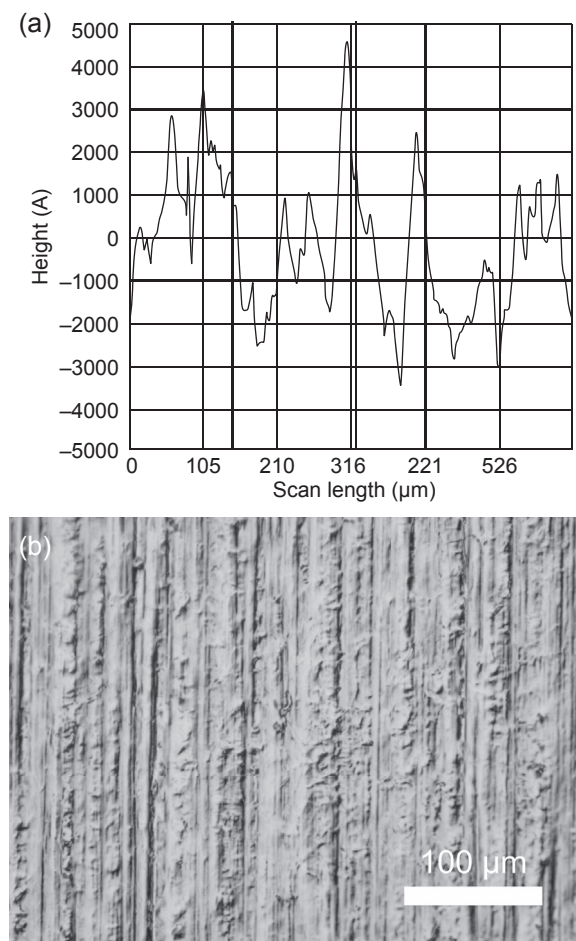
Figure 13.6 (a) Surface profile measurement and (b) optical micrograph of a sample of 304 stainless steel planarized with SOG 20B.
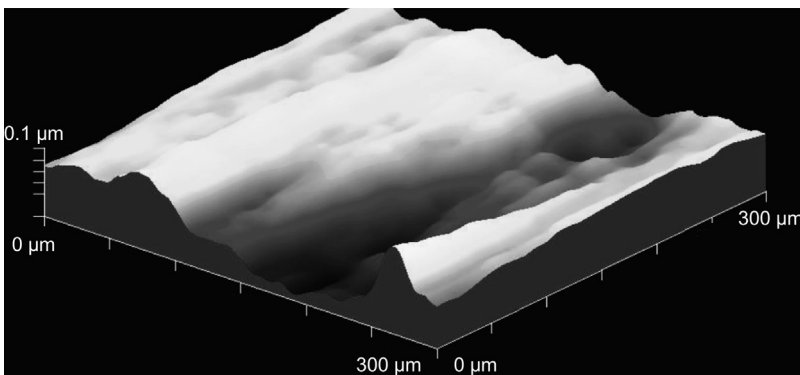
Figure 13.7 Three-dimensional surface profile of 304 stainless steel planarized with SOG 500F.

Alternatively, SOG 500F, available from Filmtronics, Inc., has an ε of ~ 3 and is amenable to double and triple coats. SOG 500F is a methylsiloxane glass. A triple coat of SOG 500F allows for a much thicker layer of ~ 1.6 µm and hence a smoother surface with ~ 0.3 µm peak-to-peak roughness on steel foils. This technique of multiple coats of SOG 500F also removes the short wavelength roughness. Figure 13.7 shows a 3D profile of a sample planarized with 1.6 mm of SOG 500F.

BCB, available from Dow Chemical, is a low-κ dielectric ($\varepsilon = 2.6$) resin that can be spun on and cured at low temperature ($\sim 250\,^{\circ}$C). It has been previously used in LCD displays as a planarization layer for the TFT backplanes (Lan & Kanicki, 1998). A BCB film thickness of 1.3 µm can be achieved such that the surface roughness of steel foil is reduced to ~ 0.1 µm peak to peak. Figure 13.8 shows a profile measurement (a) and an optical micrograph (b) of a sample of stainless steel planarized with 1.3 µm of BCB.

The surface roughness of available nickel foils can be less than ~ 30 nm. Such foils do not need planarization; however, electrical passivation is still required to reduce capacitive coupling and substrate current. An additional passivation (i.e., an insulating layer) is typically necessary for electrical insulation to reduce leakage currents and capacitive coupling between the display array and the metal foil substrate. Excessive leakage current to the substrate causes pixels to lose their charge within the frame time, and capacitive coupling to the substrate limits the size and frame rate of the display. These challenges require improved electrical insulation that may be obtained by depositing silicon dioxide and/or silicon nitride by plasma-enhanced chemical vapor deposition (PECVD) onto the SOG passivation layer.

For example, a 32-in OLED HDTV (1920×1080) can tolerate a maximum data line capacitance and therefore passivation capacitance of $C_{\mathrm{p}} < 2$ nF/cm^2 (Hong et al., 2006). The passivation leakage current (I_{P}) must be less than the value of the TFT off current. Assuming a 100×300 µm^2 pixel with a TFT gate footprint of 10% and a gate voltage of 20 V, a maximum allowable I_{P} is approximately 6 nA/cm^2.

The effectiveness of several types of electrical passivation of steel foil substrates were compared by forming a capacitor between the substrate and a 1 mm diameter circular Al top contact. For a 300-nm SOG 20B passivation layer, an initially high
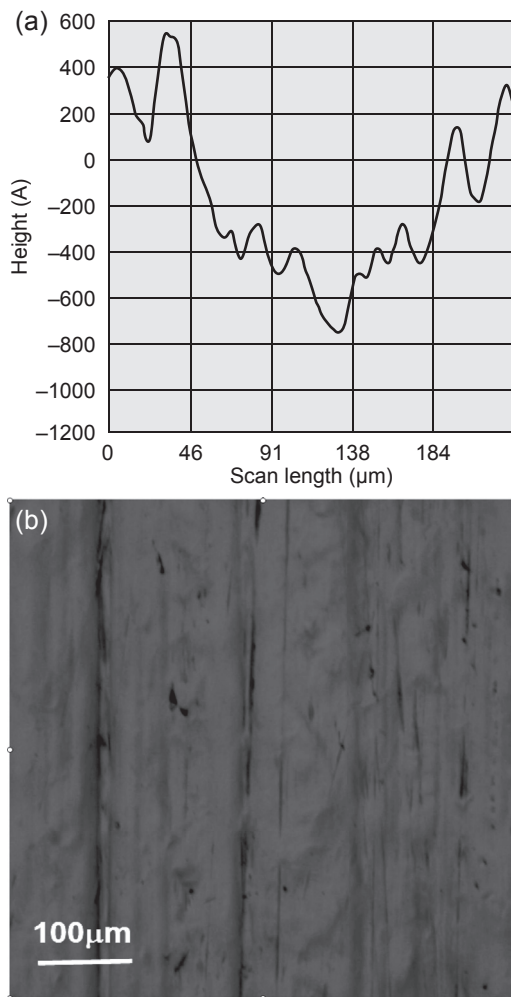
Figure 13.8 (a) Surface profile measurement and (b) optical micrograph of a sample of 304 stainless steel planarized with BCB.

leakage current of $I_P = 8 \ \mu\text{A/cm}^2$ was reduced by over one order of magnitude to $I_p = 0.1 \ \mu\text{A/cm}^2$ by adding the high-temperature cure cycle at 600 °C for 1 h. The 200-nm layer of PECVD SiO_2 lowered the leakage further to $I_P < 5 \ \text{nA/cm}^2$. The capacitance values have a similar trend. The increased cure temperature decreases the capacitance from $C_P = 40 \ \text{nF/cm}^2$ down to $C_P = 27 \ \text{nF/cm}^2$, and the addition of a PECVD SiO_2 insulator layer further decreased it to $C_P = 9.1 \ \text{nF/cm}^2$. The SOG 500F, which allowed for crack-free double and triple coats, was tested with an added insulation layer of 600-nm PECVD SiN_x. An $I < 5 \ \text{nA/cm}^2$ and $C_P = 3 \ \text{nF/cm}^2$ were measured, which meet the QVGA requirement. A thick planarization coating such as BCB may not need an additional electrical insulation layer for capacitance and

leakage current reduction because of its low dielectric constant. In this case, a single-coat, 1.3-μm-thick film produced $I_P < 5$ nA/cm^2 and $C_P = 2$ nF/cm^2. Smooth Ni substrates may be electrically passivated with either 1.3 μm BCB or 1 μm SiO$_2$. Both exhibited similar leakage currents, although, as expected, the BCB film had a lower capacitance because of its lower dielectric constant. Results indicate that BCB provided the best electrical passivation (Kattamis, 2007).

13.4 TFTs for displays on metal foil

This section will generally discuss the operation and fabrication TFTs and TFT backplanes with specific attention to requirements for OLED displays on metal foil. Most of the discussion will focus on a-Si:H (amorphous hydrogenated silicon) TFTs and backplanes because most work in this field has been reported for this materials system. A shorter discussion on metal oxide TFTs and organic TFTs (OTFTs) will follow.

13.4.1 TFTs on metal foil

Development of TFTs occurred in parallel to the development of the metal-oxide-semiconductor field-effect transistor (MOSFET). The first TFTs were made using compound semiconductors in the early 1970s. In 1979, the first amorphous silicon-based TFT was demonstrated. Although CdS TFTs exhibited better performance, it was the amorphous silicon device that became the workhorse of the display industry because of the ease of manufacturing as compared with CdS devices. The semiconducting materials most currently under development for TFTs on flexible substrates are amorphous and polycrystalline Si, amorphous and polycrystalline metal oxides based on ZnO, and semiconducting organic materials including small molecules and polymers (Kuo, 2013).

TFTs are field-effect transistors; therefore, they have a similar functional structure as crystalline silicon MOSFETs. Whereas MOSFETs are typically operated as inversion mode devices, TFTs are generally operated in accumulation mode. During inversion, a voltage applied to the gate attracts minority carriers to form an inversion channel. During accumulation, a voltage is applied to the gate, attracting majority carriers to form a conducting channel.

A typical n-channel MOSFET, shown in Figure 13.9, has n^+-doped S/D regions, a p-type body, and a SiO$_2$ gate dielectric insulator between the metal gate and the silicon
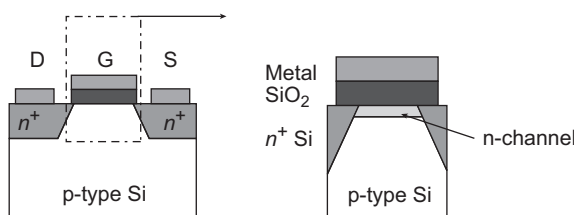
Figure 13.9 General structure of an n-channel MOSFET transistor is pictorialized.
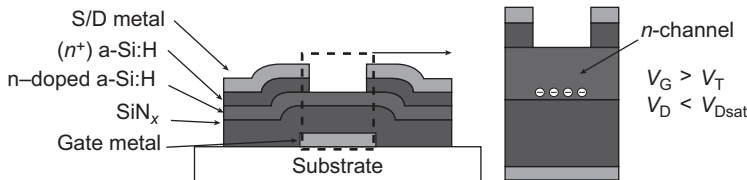
Figure 13.10 General structure of an amorphous silicon TFT is pictorialized.

body. When the device is off, there are two p–n junctions: one between the body and S region and a second between the body and D region. When the device is on, an n-channel (inversion layer) forms that allows the current to flow between the S/D regions.

TFTs are composed of a gate dielectric (typically SiN_x or SiO_x), a channel layer, an S/D layer, and gate contacts. Figure 13.10 shows a typical a-Si:H TFT structure and materials. The active layer in an a-Si:H TFT is made of undoped a-Si:H. The channel material is intrinsic, and the off current is dependent on the conductance of the channel. In the on state, a gate voltage attracts majority carriers that form a conducting path in the channel material at the dielectric interface. Polycrystalline silicon (poly-Si) and hydrogenated nanocrystalline silicon (nc-Si:H) TFTs are composed of the same active layers and have the same basic structure.

In a MOSFET, two pn-junctions exist along the channel as shown in Figure 13.9. Because there is no similar pn-junction in a TFT, the OFF current can be significantly larger for TFTs than MOSFETs. The off current of a TFT is set by the intrinsic resistivity of the channel-forming film. The goal for both OLED applications is to minimize the OFF current to ensure that the voltage on the pixel OLED remains constant over an entire frame period. A cross-section of an a-Si:H TFT is shown in Figure 13.10. The gate dielectric is SiN_x in this case and an n-channel forms when the gate voltage (V_G) is greater than the threshold voltage (V_T).

Three types of silicon thin-film materials for TFTs exist: a-Si:H, nc-Si:H, and poly-Si. These three comprise a continuum of material types from a-Si:H, which has no long range atomic order and an H content of up to 30 at/%, to nc-Si:H which is composed of 10–100 nm crystallite grains, to poly-Si which can have grains up to 1–10 μm. Charge mobility within an accumulation channel increases with increasing grain size.

13.4.2 TFT display backplanes on metal foil

Flat-panel display technologies generally require switching matrices to address and power a two-dimensional array of individual pixels, which in combination form the display image. The two major backplane schemes are passive-matrix and active-matrix. In passive-matrix, driving the display requires supplying the full operating "ON" voltage across all address lines along one axis on the display panel, one by one. The display must rapidly and continuously scan the panel to maintain a clear and legible image. Active-matrix displays involve a direct driving circuit at each pixel (Tsukada, 1999). An active-matrix pixel is generally composed of one or more TFTs and storage capacitors. Each pixel will maintain a charge by means of this capacitor

and each is controlled dynamically by display electronics. A basic pixel circuit shown in Figure 13.11 uses one a-Si:H TFT and one storage capacitor per active-matrix pixel.

The basic active-matrix driving scheme involves writing a voltage to the V_{DATA} line and then addressing individual TFTs via V_{SELECT}. When V_{SELECT} is greater than the threshold voltage (V_T) of the transistor, a conductive channel is formed and V_{DATA} is written to the storage capacitor and the liquid-crystal element.

A two-TFT pixel circuit, such as that shown in Figure 13.12, is used to provide a current source independent of the pixel address voltages (Zhiguo & Man, 2002). Setting the data and select voltages to high on a particular pixel turns transistor T1 on, which causes transistor T2 to turn on and conduct current from the power
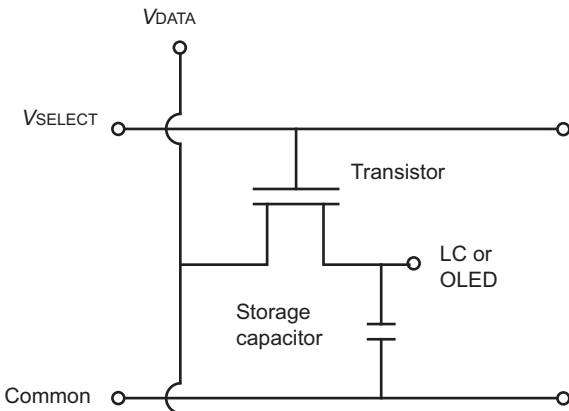
Figure 13.11 This is an illustration of a basic active-matrix pixel circuit layout.
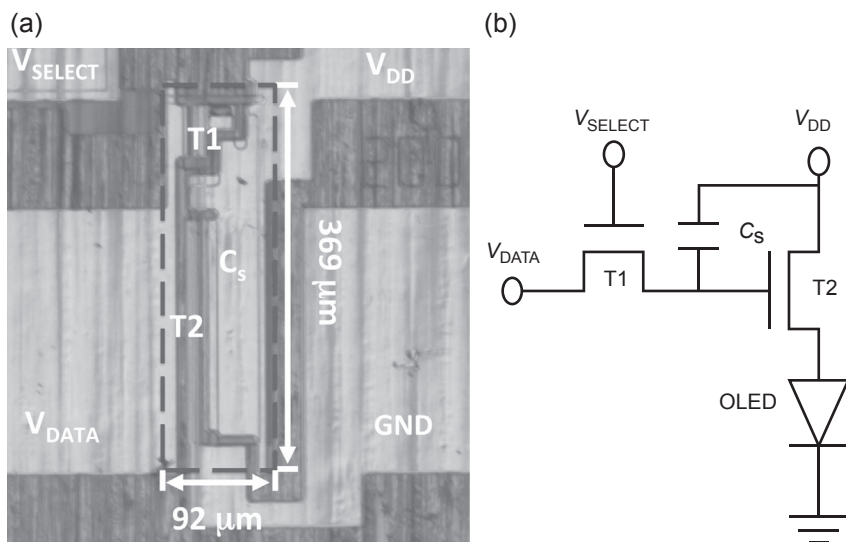
Figure 13.12 (a) Optical micrograph of a pixel circuit, with test pads. The dashed square designates the OLED area and (b) circuit schematic of the two-TFT circuit.

supply line (V_{DD}) through the OLED to ground. T1 is used as a switching transistor; therefore, it should have an adequate on/off ratio. T2 is used as a driving transistor; therefore, it should be capable of delivering adequate and stable current density. The comparative sizes of T1 and T2 are apparent in Figure 13.12(a).

Other active-matrix pixel circuits using three or four transistors have been proposed to improve the gray-level control of individual pixels and to deal with the threshold voltage shift (discussed below) in a-Si:H TFTs (Ashtiani, Servati, Striakhilev, & Nathan, 2005; Joon-Chul, Jin, Kyu-Sik, & Choong-Ki, 2003; Kumar et al., 2003; Yi, Hattori, & Kanicki, 2001). A four-transistor complementary metal-oxide semiconductor driving circuit has been proposed for an OLED display on metal foil with polysilicon TFTs (Afentakis, Hatalis, Voutsas, & Hartzell, 2003).

More sophisticated digital circuitry suitable for integration with the backplane circuitry discussed previously has also been demonstrated on metal substrates. For example, a 3-bit analog-to-digital converter was demonstrated on a steel foil substrate using laser-crystallized polysilicon TFT technology (Jamshidi-Roudbari, Po-Chin, & Hatalis, 2010).

13.4.3 Stability issues for OLED TFT display backplanes on metal foil

OLED TFT displays on metal foil face several issues that tend to degrade the display performance over time. The TFT and OLED devices of a display can be affected by external environmental factors (i.e., exposure to oxygen, moisture, and light), electrical stress, and mechanical stress from substrate bending in addition to the built-in strain in the constituent thin films (discussed previously). Because metal substrates reduce to some degree the influence of environmental factors, only electrical and mechanical stress will be discussed here.

Voltage-induced metastability is a major problem for a-Si:H TFTs. During operation, the characteristics of the a-Si:H TFT shift because of gate-bias stressing. Figure 13.13 shows an example of an a-Si:H TFT that is biased at $V_G = 30$ V
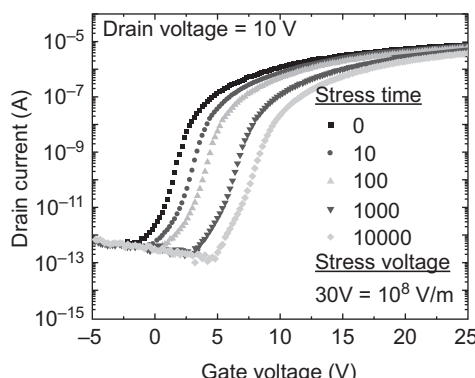
Figure 13.13 Transfer characteristic of an a-Si:H TFT for a series of stress times using a stress voltage of 30 V (10^8 V/m).
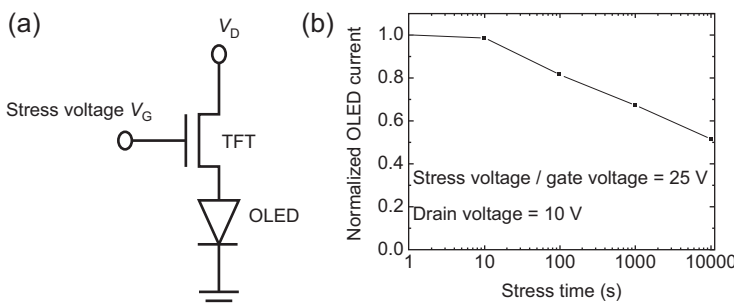
Figure 13.14 (a) Schematic of a simple TFT/OLED circuit. (b) Theoretical normalized OLED current versus the stress time (circuit ON time).

for periods of time up to 10,000 s. Between each bias-stress step, V_G is swept and the transfer curve is plotted. The V_T is clearly increasing (shifting toward the right).

This metastability can be problematic for TFT backplanes because gate voltages are applied for long durations over the lifetime of a display. V_T drifts to more positive values under constant gate bias, which decreases the drain current for a given bias. This can be seen by drawing a vertical line at a given V_G and measuring I_D for the different stress times. For $V_G = 25$ V, I_D drops from 1×10^{-5} A to 5×10^{-6} A after 10,000 s. Figure 13.14(a) shows a simple TFT/OLED circuit and Figure 13.14(b) shows the theoretical drop in OLED current versus time for a $V_G = 25$ V and $V_D = 10$ V. This gate voltage is higher than what would normally be used to accelerate the test, but it serves to illustrate the point.

In this case, if the display were to operate at these voltages within a few hours, then the OLED current would be cut in half. This decrease in current will lead to a decrease in display brightness. To compound the issue, each individual pixel will be biased differently to display images and video; therefore, not only will the brightness decrease, but uniformity will also suffer. Results have shown that increasing the deposition temperature of the SiN_x gate dielectric reduces this effect (Kattamis, 2007). In active-matrix OLEDs, this threshold shift is generally compensated for by using multiple TFT pixel circuits (as discussed previously). This increase in the number of TFTs increases the complexity of the fabrication process. However, OLEDs are deposited over TFTs, so the complexity of TFT fabrication has little effect on display characteristics such as aperture ratio (Kattamis et al., 2007).

OLED displays must also exhibit stable operation as the substrate undergoes bending and flexing. Figure 13.15 shows a completed a-Si:H backplane, test areas at the top and corners, and the pixel matrix centered on the substrate (Kattamis, 2007). To evaluate the functionality of a completed OLED display on metal foil, simple bending tests can be performed, as shown in Figure 13.16 and discussed below. This figure depicts a test display with all address lines electrically connected when flat and when bent to a radius of approximately 50 cm (Kattamis, 2007; Kattamis et al., 2007).
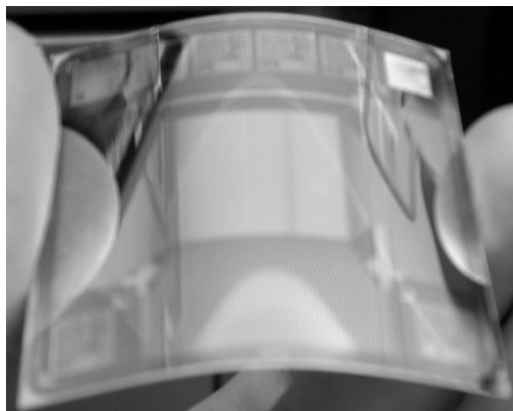
Figure 13.15 This is a picture of a completed amorphous silicon backplane on steel.
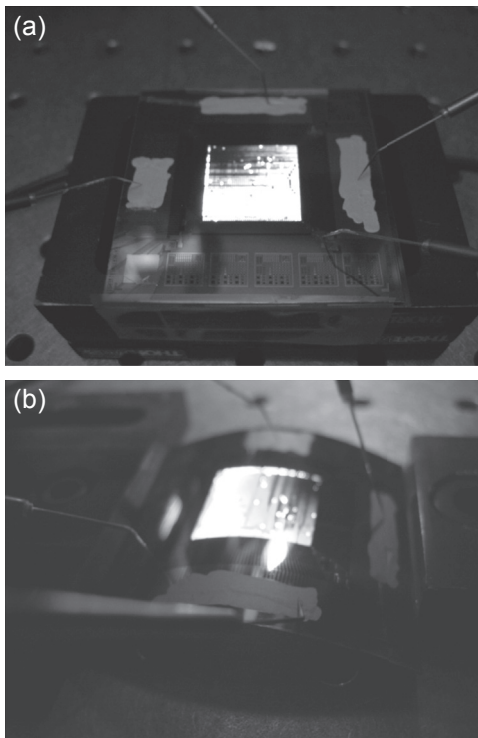
Figure 13.16 Completed active-matrix OLED array, driven by a-Si TFT backplane on steel (a) flat and (b) bent, with all pixels illuminated.

Several types of tests are used to characterize the durability of the constituent films and completed devices on flexible substrates. Such tests include tensile, bulge, and indentation tests as well as bending tests that may progressively decrease the bending radius of the substrate (i.e., increase the bending angle) or adopt an accelerated life
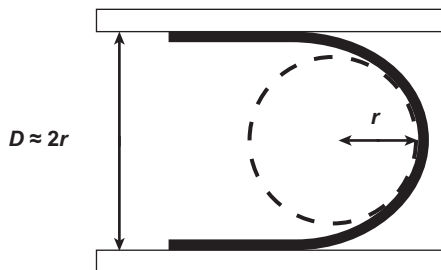
Figure 13.17 Schematic of bending test apparatus.
Source: After Schwamb et al. (2013).

testing methodology, such as cycling repeatedly between bent and unbent states (Lewis, 2006). In one typical bending test setup, shown schematically in Figure 13.17, opposite edges of a flexible substrate are fixed to respective parallel plates. Bringing the parallel plates closer together decreases the radius of curvature. The distance between the parallel plates is approximately twice the bending radius of curvature at the center of the substrate.

The device under test may be microscopically examined for evidence of cracking or delamination of conductors, permeation barriers, and active layers and to evaluate the effects of failures on adjacent layers and devices. The electrical, optical, or optoelectronic performance of electrical contacts, TFTs, or OLEDs are often characterized before, during, and after bending tests, as the test apparatus allows.

For example, using an apparatus similar to that shown in Figure 13.17, OLEDs on steel substrates were subjected to convex and concave bending. The resistances of the top contact were monitored during the tests, and the bending radius at which any OLEDs failed (i.e., ceased emitting light) was recorded. The sites of failed OLEDs were examined microscopically after the bending test. Under convex bending, samples were able to withstand as low as approximately 1.2 cm bending radius before failing, and failure was due to cracks in the encapsulation and top contact layer. Under concave bending, samples were able to withstand as low as approximately 0.6 cm bending radius before failure, and failure was due to the top contact delaminating and then cracking (Schwamb, Reusch, & Brabec, 2013).

As another example, a nonencapsulated organic photovoltaic (PV) device on stainless steel was subjected to a cyclic bending test at a radius of 0.8 cm in ambient and characterized after every 50 cycles. Two values of merit, the short circuit current density and power conversion efficiency, declined by less than 3% after 450 cycles (Fang-Chung et al., 2009).

13.4.4 Oxide semiconductor TFTs for OLED displays on flexible metal substrates

As with a-Si:H TFTs, OTFTs and metal oxide TFTs also generally work in accumulation mode. Oxide semiconductor TFTs are of interest for flexible displays because they can be deposited at relatively low temperatures via vacuum processing

(e.g., puttering or pulsed laser deposition) or via solution processing techniques, and they can be suitable for transparent electronics. In particular, In−Ga−Zn−O (IGZO) appears to be a prime candidate to replace amorphous silicon for high-resolution mobile displays and large-format high-definition LCD and OLED televisions. LG has reported a 3.5 in, 176×220 pixel, AMOLED display driven by amorphous IGZO TFTs on stainless steel foil (Lee et al., 2008; Sung et al., 2007).

Several amorphous or polycrystalline oxide semiconducting materials for TFTs based on ZnO are under investigations, including IGZO, Hf−In−Zn−O, Al−Sn−Zn−In−O, and others. A bottom-gate structure is generally preferred for oxide TFTs, and gate insulator materials have included materials such as SiO_x, SiN_x, SiO_xN_x, HfO_x, and other high-κ dielectrics (e.g., Al_2O_3, Y_2O_3, and others). Much work in terms of materials selection and processing parameters remains to produce oxide TFTs that exhibit long-term stability under bias in the presence of thermal fluctuations and under exposure to light (Jae Kyeong, 2011; Jin-Seong, 2013; Joon Seok, Wan-Joo, Hyun-Suk, & Jin-Seong, 2012).

13.5   OLED lighting and photovoltaics on metal foil

In addition to displays, illumination and PV devices are applications in which metal foils may be useful as substrates (Antoniadis & Pichler, 2001; Galagan, Moet, Hermes, Blom, & Andriessen, 2012). Flexible metal foils generally offer the potential to manufacture devices using roll-to-roll processes, which are desirable for low-cost production. In addition, a significant reason for choosing metal foil over plastic is the natural moisture barrier offered by metals versus plastic.

13.5.1   OLEDs for display pixels

OLED materials can be classified as small-molecule or polymer OLEDs. Polymer OLEDs may particularly find use in inkjet printing for flexible displays (Burroughes et al., 1990). Small-molecule OLEDs are generally fabricated by vacuum processing, and evaporation at pressures of $\sim 10^{-7}$ Torr is used to deposit the organic material and any metal electrodes (anode or cathode). Sputtering is generally used for deposition of the indium-tin oxide transparent conductor, which can be either an anode or cathode depending on OLED geometry. The most basic OLED is made up of an anode, hole and electron transport layers, an emissive layer, and a transparent cathode. TOLEDs are used for opaque substrates such as metal and require a transparent top contact. OLEDs for display pixels are optimized to produce red, green, or blue whereas OLEDs for lighting (discussed below) focus on producing white light.

13.5.2   OLED displays on metal foil

OLED displays have been demonstrated on metal foil with TFT backplanes based on silicon, metal oxide, and organic TFTs. To date, OLED displays using amorphous silicon and poly-Si TFTs have been fabricated on various metal foil substrates

including stainless steel (Howell, Stewart, Kamik, Saha, & Hatalis, 2000; Serikawa & Omata, 1999; Theiss & Wagner, 1996; Wu et al., 1997), Kovar (nickel alloy) (Afentakis, Hatalis, Voutsas, & Hartzell, 2006; Khan et al., 2011), copper (Yu-Sheng et al., 2010), and aluminum (Freitag, 2010).

13.5.3 OTFTs on flexible metal substrates

OTFTs have been demonstrated that meet basic suitability requirements for use in displays: on current higher than 1 µA and a ratio of on current to off current higher than 10^6. However, further work is required to establish the manufacturable OTFTs that are sufficiently durable and stable (Jang, 2006).

OFTFs on stainless steel foil were demonstrated to have high stability under mechanical bending tests. These TFTs used a layer of photoresist to planarize the substrate and a polyimide layer to promote adhesion, an evaporated bottom gate of aluminum, a spin-coated poly(vinyl cinnamate) gate dielectric, a thermally deposited pentacene semiconducting layer, and an evaporated gold source and drain contacts (Fang-Chung, Tzung-Da, Bing-Ruei, & Ya-Wei, 2011). Another group has reported the use of a CMP-treated stainless steel substrate that doubles at the gate electrode to compare pentacene OTFT characteristics with various gate dielectrics, surface treatments, growth parameters, and source/drain electrode materials (Yun, Lee, Yong, & Rhee, 2012; Dong-Jin et al., 2009).

13.5.4 OLED lighting on metal foil

The commercial and institutional lighting market segments are long-term opportunities for white OLEDs because those segments account for 40% of the entire lighting market (Ngai, 2010). Target white OLED device efficacy may have to be above 70 lm/W at luminances above 2000 cd/m^2 and product lifetimes may have to exceed 50,000 h (Ngai, 2010). These are challenging targets even for OLEDs on traditional glass substrates and are even more challenging with plastic substrates that need to be hermetically sealed; however, flexible illumination devices offer new form factors that lend themselves to new ways to use light sources as decorative fixtures or signage.

Work on large-area white OLEDs on metal foils has been ongoing but is mainly performed by companies. Some examples of the work include the following. In 2011, ArcelorMittal developed a surface treatment for metal foils that was suitable for roll-to-roll production. They demonstrated a white OLED with >22 lm/W and a large-area 60 × 60 cm white OLED on a metal foil (Guaino et al., 2011).

Also in 2011, Universal Display Corporation demonstrated a flexible white OLED lighting concept called the OLED "Swirl" that was built on flexible metal foil using the company's technology and materials and proprietary encapsulation technology (Universal Display Corporation, 2011). In 2013, Fraunhofer COMEDD and Tridonic Dresden completed a joint project called R2Flex with the overall aim that included developing a highly efficient white OLED processed using a roll-to-roll technology on cost-effective substrates, especially on metal foil (Cruickshank, 2013). They demonstrated their white OLED on a flexible metal foil at the Printed Electronics

conference in 2013. In 2011, Osram reported 11×3 cm size flexible white OLED panels on 100 μm thick steel substrate, with an efficiency of 32 lm/W (Cruickshank, 2014).

As with TFTs (see discussion above), the substrate surface roughness was found to have effects on OLED luminance uniformity and efficiency. High surface roughness was found to correlate with nonuniformity of the emissive layer thickness and suppression of light emission at large viewing angles, which reduced the angle dependence of the emission but decreased the device efficiency (Rooms et al., 2011). When substrate roughness is controlled by the addition of a planarization layer, the substrate material itself (whether steel, copper, or aluminum) was found to have an insignificant effect on the bending durability of OLEDs as compared with the substrate thickness (thinner substrates permit a tighter bending radius before device failure, as theoretically predicted) (Schwamb et al., 2013). A flexible copper substrate was found to provide a longer device lifetime as compared with glass substrate, which was attributed to the measured reduction in OLED device temperature because of the significantly higher thermal conductivity of copper (410 W/m*K) as compared with glass (1 W/m K). It is less clear if the relatively low thermal conductivity of stainless steel (16 W/m K) will outweigh its other properties for high-volume manufacturing of OLED lighting (Yu-Sheng et al., 2010). OLEDs fabricated on aluminum substrates with a SiO_x nanocomposite layer were found to have a shorter lifetime than similar devices fabricated on glass and could be bent to a radius of ~ 1 cm before fracture of the SiO_x layer damaged the device (Freitag, 2010).

13.5.5 OLED photovoltaics on metal foil

Organic bulk heterojunction PV cells have the potential to have lower module cost per peak watt than inorganic PV cells. This potential also heavily depends on the ability to fabricate devices with high-throughput processing techniques such as roll-to-roll coating on low-cost substrates such as metal foils. Metal foils are attractive for similar reasons as those for illumination and displays, and those reasons include the intrinsic barrier characteristics against moisture and oxygen and low cost (Gaynor, Jung-Yong, & Peumans, 2009).

One substantial challenge is that roll-to-roll processing on a large scale is a nontrivial issue and significant investment does not necessarily guarantee commercial success as in the case of Konarka Technologies (Hatcher, 2012). The collapse of the price of silicon eroded the argument that flexible low-cost PV cells have a cost advantage over more efficient silicon devices; however, very niche-flexible organic PV products are still being considered by companies such as Belectric (2012).

13.6 Future trends

IDTechEx estimates that the total market for printed, flexible, and organic electronics will grow from $16.04 billion in 2013 to $76.79 billion in 2023 (Das & Harrop, 2013). A significant portion of that market is flexible OLED displays, which are presently

available in consumer smartphones. The market for other flexible electronics, including logic and memory, bistable displays, thin-film batteries, photovoltaics, textiles, sensors, and conductors, is also expected to increase over the next decade. For example, complementary logic and chemical and biological sensors have been demonstrated (Dodabalapur, 2006). In addition, materials under research for future TFTs include carbon nanotubes and graphene, semiconductor nanowires, molybdenum sulfide, and other inorganic nanostructures or composite thin films (Chunlan, Rui, Lei, & Xiangfeng, 2013).

One interesting potential application area of flexible electronic devices is in health care because flexibility is a necessity for successful integration of electronics in biological systems (Nathan et al., 2012). Applications include a bionic ear and artificial eyes, noses, and tongues. Furthermore, there is the potential for flexible electronics to be used as diagnostic and monitoring tools (Nathan et al., 2012), which may include examples such as blood glucose monitoring systems. The market for blood glucose monitoring products is well into the billions of dollars (Hughes, 2009), and diabetes affects millions of people worldwide; therefore, there seems to be opportunities to use flexible electronics in such cases.

The development of flexible organic electronics is steadily progressing. There are many potential applications and novel device form factors that keep interests buoyant. The pace of the development of flexible OLED displays on plastic has seemingly picked up in 2013, and there are numerous entities in this field, including major consumer electronics manufacturers such as LG Chem, Samsung, and Semiconductor Energy Laboratory as well as research centers such as Holst Centre, Arizona University Flexible Electronics Center, and IMEC. There are frequent updates at SPIE and SID meetings occurring across the globe and daily updates on LinkedIn.com groups and oled-info.com.

References

Afentakis, T., Hatalis, M. K., Voutsas, A. T., & Hartzell, J. W. (2003). Polysilicon TFT AM-OLED on thin flexible metal substrates. In *Poly-silicon thin film transistor technology and applications in displays and other novel technology areas, 21−22 Jan. 2003*. USA. SPIE-International Society for Optical Engineering, 187−191.

Afentakis, T., Hatalis, M., Voutsas, A. T., & Hartzell, J. (2006). Design and fabrication of high-performance polycrystalline silicon thin-film transistor circuits on flexible steel foils. *IEEE Transactions on Electron Devices, 53*, 815−822.

Antoniadis, H., & Pichler, K. (2001). *Organic light emitting diode light source*. United States Patent No. 6,680,578.

Ashtiani, S. J., Servati, P., Striakhilev, D., & Nathan, A. (2005). A 3-TFT current-programmed pixel circuit for AMOLEDs. *IEEE Transactions on Electron Devices, 52*, 1514−1518.

Belectric. (2012). *BELECTRIC setting new standards with organic photovoltaics*. Available from http://www.belectric.com/fileadmin/MASTER/pdf/press_releases/pm_BEL_2012_1022_BELECTRIC_OPV_EN.pdf Accessed 4.11.13.

Brinker, C. J., & Scherer, G. W. (1990). *Sol-gel science: The physics and chemistry of sol-gel processing*. Elsevier Science.

Burroughes, J. H., Bradley, D. D. C., Brown, A. R., Marks, R. N., Mackay, K., Friend, R. H., et al. (1990). Light-emitting diodes based on conjugated polymers. *Nature, 347*, 539−541.

Burrows, P. E., Bulovic, V., Forrest, S. R., Sapochak, L. S., Mccarty, D. M., & Thompson, M. E. (1994). Reliability and degradation of organic light emitting devices. *Applied Physics Letters, 65*, 2922−2924.

Cheng, I. C., Kattamis, A., Long, K., Sturm, J. C., & Wagner, S. (2005). Stress control for overlay registration in a-Si:H TFTs on flexible organic-polymer-foil substrates. *Journal of the Society for Information Display, 13*, 563−568.

Chunlan, W., Rui, C., Lei, L., & Xiangfeng, D. (2013). High performance thin film electronics based on inorganic nanostructures and composites. *Nano Today, 8*, 514−530.

Chwang, A., Hewitt, R., Urbanik, K., Silvernail, J., Rajan, K., Hack, M., et al. (2006). Full color 100 dpi AMOLED displays on flexible stainless steel substrates. *44th international symposium, seminar, and exhibition, SID 2006, June 4, 2006−June 9, 2006*. San Francisco, CA, United states. Society for Information Display, 1833−1836.

Chwang, A. B., Rothman, M. A., Mao, S. Y., Hewitt, R. H., Weaver, M. S., Silvernail, J. A., et al. (2003). Thin film encapsulated flexible organic electroluminescent displays. *Applied Physics Letters, 83*, 413−415.

Comiskey, B., Albert, J. D., Yoshizawa, H., & Jacobson, J. (1998). An electrophoretic ink for all-printed reflective electronic displays. *Nature, 394*, 253−255.

Constant, A., Burns, G., Shanks, H., Gruber, C., Landin, A., Schmidt, D., et al. (1995). Development of thin film transistor based circuits on flexible polyimide substrates. In *Proceedings of second international symposium thin film transistor technologies, 10−14 October 1994*. Pennington, NJ, USA. Electrochem. Soc, 392−400.

Crabb, R. L., & Treble, F. C. (1967). Thin silicon solar cells for large flexible arrays. *Nature, 213*, 1223.

Crawford, G. P. (2005). Flexible flat-panel displays. *Information Display, 21*, 10−16.

Cristaldi, D. J. R., Pennisi, S., & Pulvirenti, F. (2009). *Liquid crystal display drivers*. Springer.

Cruickshank, C. (2013). *R2Flex successfully concludes and showcases flexible OLED luminaires*. The OSADIRECT Newsletter. Cintelliq Limited.

Cruickshank, C. (2014). *Osram announces a flexible OLED on steel substrates with efficiency of 32 lm/W*. The OSADirect Newsletter. cintelliq Limited.

Das, R., & Harrop, P. (2013). *Printed, organic & flexible electronics: forecasts, players & opportunities*. IDTechEx.

Dodabalapur, A. (2006). Organic and polymer transistors for electronics. *Materials Today, 9*, 24−30.

Dong-Jin, Y., Sang-Hoon, L., Tae-Woo, L., & Shi-Woo, R. (2009). Fabrication of the flexible pentacene thin-film transistors on 304 and 430 stainless steel (SS) substrate. *Organic Electronics, 10*, 970−977.

Fang-Chung, C., Jyh-Lih, W., Chia-Ling, L., Wen-Che, H., Chen, H. M. P., & Wen-Chang, C. (2009). Flexible polymer photovoltaic devices prepared with inverted structures on metal foils. *IEEE Electron Device Letters, 30*, 727−729.

Fang-Chung, C., Tzung-Da, C., Bing-Ruei, Z., & Ya-Wei, C. (2011). Influence of mechanical strain on the electrical properties of flexible organic thin-film transistors. *Semiconductor Science and Technology, 26*(034005), 5.

Floro, J. A., Chason, E., Cammarata, R. C., & Srolovitz, D. J. (2002). Physical origins of intrinsic stresses in Volmer-Weber thin films. *MRS Bulletin, 27*, 19−25.

Forrest, S. R. (2004). The path to ubiquitous and low-cost organic electronic appliances on plastic. *Nature, 428*, 911−918.

Freitag, P. (2010). White top-emitting OLEDs on metal substrates (Ph.D. thesis). Dresden Technical University.

Galagan, Y., Moet, D. J. D., Hermes, D. C., Blom, P. W. M., & Andriessen, R. (2012). Large area ITO-free organic solar cells on steel substrate. *Organic Electronics: Physics, Materials, Applications, 13*, 3310−3314.

Gartside, J., Mandlik, P., Wagner, S., Zhou, T., Silvernail, J., & Hack, M. (2008). Material characterisation of a novel permeation barrier for flexible organic displays. *Organic/Inorganic hybrid materials − 2007, 9−13 April 2007*. Warrendale, PA, USA. Materials Research Society, 123−128.

Gaynor, W., Jung-Yong, L., & Peumans, P. (2009). Fully solution-processed organic solar cells on metal foil substrates. In *Organic photovoltaics x, 3 August 2009*. USA SPIE − The International Society for Optical Engineering, 741614 (7 pp.).

Guaino, P., Maseri, F., Schutz, R., Hofmann, M., Birnstock, J., Avril, L., et al. (2011). Large white organic light-emitting diode lighting panel on metal foils. *Journal of Photonics for Energy, 1*(1), 011015.

Gustafsson, G., Cao, Y., Treacy, G. M., Klavetter, F., Colaneri, N., & Heeger, A. J. (1992). Flexible light-emitting diodes made from soluble conducting polymers. *Nature, 357*, 477−479.

Hatcher, Mike (Ed.). (2012). *Investors burned as Konarka enters liquidation*. optics.org. Available from http://optics.org/news/3/6/10 Accessed 4.11.13.

Hofmann, S., Thomschke, M., Lussem, B., & Leo, K. (2011). Top-emitting organic light-emitting diodes. *Optics Express, 19*, 1250−1264.

Hong, Y., Heiler, G., Kerr, R., Kattamis, A. Z., Cheng, I. C., & Wagner, S. (2006). Amorphous silicon thin-film transistor backplane on stainless steel foil substrates for AMOLEDs. In *44th international symposium, seminar, and exhibition, SID 2006, June 4, 2006−June 9, 2006*. San Francisco, CA, United states. Society for Information Display, 1837−1840.

Howell, R. S., Stewart, M., Kamik, S. V., Saha, S. K., & Hatalis, M. K. (2000). Poly-Si thin-film transistors on steel substrates. *IEEE Electron Device Letters, 21*, 70−72.

Hughes, M. D. (2009). The business of self-monitoring of blood glucose: a market profile. *Journal of Diabetes Science and Technology, 3*, 1219−1223.

Jae Kyeong, J. (2011). The status and perspectives of metal oxide thin-film transistors for active matrix flexible displays. *Semiconductor Science and Technology, 26*(034008), 10.

Jae Kyeong, J., Dong Un, J., Hyun Soo, S., Hun Jung, L., Minkyu, K., Tae Kyung, A., et al. (2007). Flexible full-color AMOLED on ultrathin metal foil. *IEEE Electron Device Letters, 28*, 389−391.

Jamshidi-Roudbari, A., Po-Chin, K., & Hatalis, M. K. (2010). A flash analog to digital converter on stainless steel foil substrate. *Solid-state Electronics, 54*, 410−416.

Jang, J. (2006). Displays develop a new flexibility. *Materials Today, 9*, 46−52.

Jin-Seong, P. (2013). Oxide TFTs for AMOLED TVs. *Information Display, 29*, 16−19.

Joon-Chul, G., Jin, J., Kyu-Sik, C., & Choong-Ki, K. (2003). A new a-Si:H thin-film transistor pixel circuit for active-matrix organic light-emitting diodes. *IEEE Electron Device Letters, 24*, 583−585.

Joon Seok, P., Wan-Joo, M., Hyun-Suk, K., & Jin-Seong, P. (2012). Review of recent developments in amorphous oxide semiconductor thin-film transistor devices. *Thin Solid Films, 520*, 1679−1693.

Jun Hyuk, C., Jong Hyun, C., Ji Ho, H., Jang, J., Hyun Soo, S., Jae Kyeong, J., et al. (2006). Active-matrix OLED on bendable metal foil. *IEEE Transactions on Electron Devices, 53*, 1273−1276.

Kanellos, M. (2005). *Samsung unveils largest flexible LCD*. CNET News.

Kattamis, A.Z. (2007). Silicon thin-film transistor backplanes on flexible substrates. 3286122 (Ph.D. thesis). Princeton University.

Kattamis, A. Z., Giebink, N., Cheng, I. C., Wagner, S., Forrest, S. R., Hong, Y., et al. (2007). Active-matrix organic light-emitting displays employing two thin-film-transistor a-Si:H pixels on flexible stainless-steel foil. *Journal of the Society for Information Display, 15*, 433–437.

Khan, S. A., Ma, X., Choi, N. B., & Hatalis, M. (2011). Amorphous IGZO TFTs and circuits on highly flexible and dimensionally stable kovar (Ni-Fe alloy) metal foils. *2010 MRS fall meeting, November 29, 2010–December 3, 2010*. Boston, MA, United states. Materials Research Society, 63–68.

Kumar, A., Sakariya, K., Servati, P., Alexander, S., Striakhilev, D., Karim, K. S., et al. (2003). Design considerations for active matrix organic light emitting diode arrays. *IEEE Proceedings-circuits, Devices and Systems, 150*, 322–328.

Kuo, Y. (2013). Thin film transistor technology-Past, present, and future. *Electrochemical Society Interface, 22*, 55–61.

Lan, J. H., & Kanicki, J. (1998). Planarized copper gate hydrogenated amorphous-silicon thin-film transistors for AM-LCDs. In *56th annual device research conference digest, 22–24 June 1998*. New York, NY, USA. IEEE, 130–131.

Lee, H.-N., Kyung, J., Sung, M.-C., Kim, D. Y., Kang, S. K., Kim, S.-J., et al. (2008). Oxide TFT with multilayer gate insulator for backplane of AMOLED device. *Journal of the Society for Information Display, 16*, 265–272.

Lewis, J. (2006). Material challenge for flexible organic devices. *Materials Today, 9*, 38–45.

Lewis, J. S., & Weaver, M. S. (2004). Thin-film permeation-barrier technology for flexible organic light-emitting devices. *IEEE Journal of Selected Topics in Quantum Electronics, 10*, 45–57.

LG Display. (2010a). *Form 6-K. Securities and exchange commission*.

LG Display. (2010b). *LG unveils world's largest flexible e-paper*. HighTech Review. Available from http://www.hitechreview.com/it-products/lg-unveils-worlds-largest-flexible-e-paper/21388/ Accessed 30.10.13.

LG Display. (2012). OLED technology prepares for landing in the commercial TV market. *Information Display*, 1475 S Bascom Avenue Ste 114, Campbell, CA 95112–4006, United States: Society for Information Display. Vol. 28, 33–36.

LG unveils World's first "Real" curved smartphone. (2013). LG Newsroom. Available from http://www.lgnewsroom.com/newsroom/contents/63988 Accessed 30.10.13.

Li, Y., Yu, Z.-N., Xue, W., & Leng, J. (2007). The electrolytic polishing study of the stainless steel foil (SUS 304). *International symposium on photoelectronic detection and imaging 2007: Laser, ultraviolet, and terahertz technology, 9–12 September 2007*. USA. SPIE – The International Society for Optical Engineering, 662222–662231.

Li, Z., Bhowmik, A. K., & Bos, P. J. (2008). *Mobile displays technology and applications*. Hoboken, NJ: John Wiley & Sons Inc.

Maeda, M., & Ikeda, K. (1998). Stress evaluation of radio-frequency-biased plasma-enhanced chemical vapor deposited silicon nitride films. *Journal of Applied Physics, 83*, 3865.

Momtaz, A. (2009). Opportunities for polymeric materials in organic electronic technologies. La place des materiaux polymeres "passifs" dans les applications en electronique organique. *Materiaux et Techniques, 97*, 247–252.

Nathan, A., Ahnood, A., Cole, M. T., Sungsik, L., Suzuki, Y., Hiralal, P., et al. (2012). Flexible electronics: the next ubiquitous platform. *Proceedings of the IEEE, 100*, 1486–1517.

Ngai, P. Y. (2010). On the lighting design aspect of OLED lighting. In *San Francisco, CA, United States. SPIE, the society of photo-optical instrumentation engineers (SPIE)*.

Ohring, M. (1992). *The materials science of thin films*. New York: Academic Press.

Park, J.-S., Chae, H., Chung, H. K., & Lee, S. I. (2011). Thin film encapsulation for flexible AM-OLED: a review. *Semiconductor Science and Technology, 26*.

Poor, A. (2012). Reformulating displays. *IEEE Spectrum, 49*, 28−29.

Ray, K. A. (1967). Flexible solar cell arrays for increased space power. *Aerospace and Electronic Systems, IEEE Transactions on, AES-3*, 107−115.

Rooms, H., Hermes, D., Harkema, S., Tanase, C., Mol, T. V., Blom, P. W. M., & Wilson, J. (2011). Optimization of the efficacy and angle dependence of emission of top-emissive organic light-emitting diodes on metal foils. *Journal of Photonics for Energy, 1*.

Schwamb, P., Reusch, T. C., & Brabec, C. J. (2013). Flexible top-emitting OLEDs for lighting: bending limits. In *Organic light emitting materials and devices XVII, 25−28 August 2013*. USA. SPIE − The International Society for Optical Engineering, 88291E (10 pp.).

Serikawa, T., & Omata, F. (1999). High-mobility poly-Si TFT's fabricated on flexible stainless-steel substrates. *IEEE Electron Device Letters, 20*, 574−576.

Shah, A. (2010). *LG to make E-paper for new generation of devices*. PCWorld. IDG Consumer & SMB.

So, F., Kido, J., & Burrows, P. (2008). Organic light-emitting devices for solid-state lighting. *MRS Bulletin, 33*, 663−669.

Sung, M.-C., Lee, H.-N., Kim, C. N., Kang, S. K., Kim, D. Y., Kim, S.-J., & Kim, S.-T. (2007). Novel backplane for AM-oled device. In *IMID symposium digest*. Korean Information Display Society, 133−136.

Theiss, S. D., & Wagner, S. (1996). Amorphous silicon thin-film transistors on steel foil substrates. *IEEE Electron Device Letters, 17*, 578−580.

Tsukada, T. (1999). Active-matrix liquid-crystal displays. In R. A. Street (Ed.), *Technology and applications of amorphous silicon*. Springer Verlag.

Universal Display Corporation. (2011). *Universal display exhibits next-generation oled technologyplatforms for high-performance, cost-effective flexible organic electronics*. Business Wire. Available from http://www.businesswire.com/news/home/20110517005285/en Accessed 30.10.13.

Weaver, M. S., Michalski, L. A., Rajan, K., Rothman, M. A., Silvernail, J. A., Brown, J. J., et al. (2002). Organic light-emitting devices with extended operating lifetimes on plastic substrates. *Applied Physics Letters, 81*, 2929.

Wu, C. C., Theiss, S. D., Gu, G., Lu, M. H., Sturm, J. C., Wagner, S., et al. (1997). Integration of organic LED's and amorphous Si TFT's onto flexible and lightweight metal foil substrates. *IEEE Electron Device Letters, 18*, 609−612.

Xiaokai, H., Zhitang, S., Weili, L., Fei, Q., Zefang, Z., & Haibo, W. (2012). Chemical mechanical polishing of stainless steel foil as flexible substrate. *Applied Surface Science, 258*, 5798−5802.

Yi, H., Hattori, R., & Kanicki, J. (2001). Improved a-Si:H TFT pixel electrode circuits for active-matrix organic light emitting displays. *IEEE Transactions on Electron Devices, 48*, 1322−1325.

Yu-Sheng, T., Shun-Hsi, W., Fuh-Shyang, J., Shu-Wei, C., Chuan-Hung, C., Ming-Hua, C., et al. (2010). Easy process and performance improvement for top-emission organic light-emitting diodes by using UV glue as the insulation layer on copper substrate. *Journal of Display Technology, 6*, 279−283.

Yun, D.-J., Lee, S., Yong, K., & Rhee, S.-W. (2012). Low-voltage bendable pentacene thin-film transistor with stainless steel substrate and polystyrene-coated hafnium silicate dielectric. *ACS Applied Materials and Interfaces, 4*, 2025−2032.

Zardetto, V., Brown, T. M., Reale, A., & Di Carlo, A. (2011). Substrates for flexible electronics: a practical investigation on the electrical, film flexibility, optical, temperature, and solvent resistance properties. *Journal of Polymer Science, Part B: Polymer Physics, 49*, 638−648.

Zhiguo, M., & Man, W. (2002). Active-matrix organic light-emitting diode displays realized using metal-induced unilaterally crystallized polycrystalline silicon thin-film transistors. *IEEE Transactions on Electron Devices, 49*, 991−996.

This page intentionally left blank

Part Three

Applications

This page intentionally left blank

Smart integrated systems and circuits using flexible organic electronics: automotive applications

14

N. Li Pira
Centro Ricerche Fiat, Strada Torino, Orbassano, TO, Italy

14.1　Introduction

During the last decade, microsystem technology has not only focused on the size of the components but on their flexibility. Cheap, mass-produced smart systems built around organic, flexible and large-area electronics will create many new business opportunities exploiting the use of electronics and digital processors. The future smart systems will be intelligent with several integrated functionalities; energy autonomous with energy scavenging, storage and management capabilities and interactive with users and/or other smart networked units. Secondly, they take advantage from new designs and performance opportunities, being flexible, printed, large-area, bendable and conformal with three-dimensional (3D) surfaces and integrated structures. Thirdly, they gain from the high-volume manufacturing capabilities such as cost-efficiency with continuous manufacturing, high yield with online optical process control systems and time-to-market with optimal use of flexible hybrid/heterogeneous manufacturing. Integrated smart systems (ISS) provide novel enabling functionalities and as such are currently a driving force behind disruptive product innovation. Because these devices are more shock-resistant, are cost-effectively manufactured and can be flexed or bent, they have the capability of being integrated into portable devices and packaging materials. The new products that did not exist before on the market will satisfy demands in terms of comfort, safety and usability. This opens up several market opportunities and various totally new values (Flexible Electronics, 2009; Towards Green Electronis, 2009).

Electronics and optoelectronics are not the only components of a microsystem. It needs to integrate power source and storage, sensors, actuators, lightings and input and output devices to communicate, display and transfer data. All such functions are examples of building blocks for effective integration within systems and devices. This chapter provides an overview of the main challenging aspects for production of ISS on the basis of flexible electronic building blocks. All of the manufacturing value chain needed for successful integration will be described concerning material, design, craft and processes. As an example of an application of system integration, the automotive sector will be presented, keeping attention to a reduction of complexity and lightweight and improved perceived quality.

14.2   Materials for integrated systems

Integrated electronic components and systems are increasingly based on flexible organic foils. The technologies enable electronic systems to be rolled, stretched, washed and worn and thereby conform to various architectural features. However, to be able to focus on new applications with new demands, attention on compatibility between the components and materials has to be paid. That is why the focus is on:

- Conductive structures on flexible electronic substrates
- Printable conductive, semi-conductive and insulating materials to wire up the flexible electronic boards and to prepare printable electronic devices
- New technologies to connect electronic devices on the flexible substrates
- Functional coatings such as hard-coating, antireflective or antiglare and able to be formed in different shapes.

14.2.1   Polymer laminates

Basically, the materials used for integrated systems are polymers for substrates, adhesives, packaging and body, and metal for the electrical conductors such as inks and pastes. The base material of a flexible substrate is a polymer film that provides the foundation for the laminate. This material provides most primary physical and electrical properties of the flexible circuits. In the case of non-adhesive circuit constructions, the base material provides all of the characteristic properties. However, polymer substrates that are to serve as drop-in replacements for plate glass substrates must meet many requirements:

1. Optical properties: Transmissive or bottom-emitting displays need optically clear substrates. In addition, substrate for liquid-crystal displays (LCDs) must have low birefringence.
2. Surface roughness: The thinner the device films, the more sensitive their electrical function is to surface roughness.
3. Thermal and thermomechanical properties: The working temperature of the substrate, for example the glass transition temperature (T_g) of a polymer, must be compatible with the maximum fabrication process temperature (T_{max}).
4. Chemical properties: The substrate should not release contaminants and should be inert against process chemicals. For example, within organic light-emitting diode (OLED) applications, the water vapour permeation rate should lie below 10^{-6} g/m^2/day and the oxygen permeation below 10^{-3} to 10^{-5} g/m^2/day.
5. Mechanical properties: A high elastic modulus makes the substrate stiff and a hard surface supports the device layers under impact.
6. Electrical and magnetic properties: A conductive substrate may serve as a common node and as an electromagnetic shield. Electrically insulating substrates minimize coupling capacitances. A magnetic substrate can be used for the temporary mounting of the substrate during fabrication or for affixing the finished product (Flexible Electronics, 2009).

A singular benefit of flexible-circuit substrates is that, unlike their counterparts within the rigid-circuit world, they are not restricted to processing in sheet form. Many manufacturing processes for flexible circuits take advantage of the nature of

the materials used in their construction to manufacture circuits in a continuous roll-to-roll (R2R) fashion. Although a wide range of thicknesses is possible, most flexible films are provided in a narrow range of relatively thin dimension (from 12 to 275 μm). With most materials, stiffness is proportional to the cube of thickness, which means that if the thickness is doubled, the material becomes 8 times stiffer and will only deflect one eighth as much under the same load. Many different materials have been used as base films or substrates for flexible circuit manufacture. Materials that have been widely used for various flexible plastic circuit applications include polyimide, polycarbonate, polyester, fluorocarbon films, Aramid papers and composites (Gilleo, 1992). However, the first two are the most used because of a combination of economic, end-product applications and assembly processing parameters of the final manufactured component.

Polymer laminates have been basically divided into low- and high-cost materials. Within low-cost materials, polyester (PS) is largely used. Several different types of PS films are available. The typical value of glass transition temperature for these polymers can exceed 185−220 °C. They are resistant to almost all kinds of solvents and chemicals. The two very common copolyesters are poly(ethylene) terephthalate (PET) and poly(ethylene) naphthalate (PEN). Because PET is thermoplastic, it can thus be heat-formed if desired. Because of low price, it is generally used for smart labels and cards. Because of its crystalline structure, copolyesters can form strong fibres. Common trade names for PS include Mylar®, Melinex® and Celanarand®. PET is tear-resistant, showing high flexibility, low moisture absorption, good electrical properties, good chemical resistance, limited suitability for soldering and maximum process temperature (120 °C). However, PS is unsuitable for extreme low temperature, becoming brittle when cold, and it supports combustion at atmospheric oxygen levels. Thermal-stabilized PET gives good chemical resistance with higher process temperature (150 °C). PEN is a new kind of PS as compared with PET. PEN has a higher glass transition temperature than PET. The chemical structure of PEN is just like PET except in place of one there are two benzene rings attached together. The presence of one extra benzene ring makes the PEN more resistant to heat than PET. PEN shows good chemical resistance and maximum process temperature (160 °C), and it is relatively low priced. However, all materials of the category have relatively low thermal stability, improvable by special treatment ($T_g < 100$ °C) (Amin & Amin, 2011).

Polycarbonate (PC) and poly(vinylchloride) (PVC) are also included in low-cost materials. PC films are characterized by outstanding optical clarity and mechanical strength, consistent printability and ease of processing. PC also offers high-temperature resistance and superb workability for secondary processes such as die-cutting, embossing and thermoforming. PC film comes in various surface textures, including gloss, velvet, matte and suede. Several brands are on the market today. Product groups for the various key applications of Makrofol® PC film have been developed. These groups include DE (design extrusion), UV (ultraviolet resistant), FR (flame retardant), SR (scratch resistant), HS (standard hardcoat), HF (formable hardcoat), ID (identification/security), BL (light diffusing), LT (light scattering) and LM (light management) (http://www.bayerfilms.com/products/makrofol/). Lexan® PC films are the preferred brand of the worldwide graphics industry. Lexan®, Valox®,

Ultem® and HP polycarbonate films from SABIC Innovative Plastics deliver performance and versatility. These materials are characterized by outstanding optical clarity, mechanical strength and ease of processing. Top quality is available in a wide choice of standard and high-performance grades and various surface finishes and textures, and they can be top coated with scratch, abrasion and chemical-resistant hardcoats (http://www.tekra.com/tech_resources/general_lit/Polycarbonate_Films.pdf).

High-cost polymers are generally high-temperature-resistant substrates. Polyamides (PA) contain amide as their repeated unit, which is linked by different elastomers. PAs are amorphous and opaque polymers that have very high resistances to temperature and electrical stress, mechanical stress, flame and chemicals. The typical value of glass transition is 220−275 °C. PA is the standard material for flex boards, with good chemical resistance (except hot alkaline solutions), excellent flexibility at all temperatures, maximum process temperature of >280 °C, quite high moisture absorption and the highest tensile strength. PA films are most popular for high-reliability type (military, medical, etc.) and dynamic applications. Trade names include Kapton®, Apical® and Upilex®. The most widely used PAs are PA6, PA6.6 (also known as Nylon®), Kevlar® and PA4.6. PAs show low viscosity and high fluidity at elevated temperatures; therefore, they are very hard to mould in thin parts using injection moulding. The high-temperature performance is then limited by the adhesive system used, the absorption of moisture (up to 3% by weight, formulation dependent) and the high cost compared with PS foils, which limits application in integrated systems (Amin & Amin, 2011; http://www.goodfellow.com/E/P.html). Liquid crystalline polymer (LCP) could represent an alternative for high-frequency applications. In addition, it has several attractive physical and electrical properties. For example, LCP materials have inherently low moisture absorption properties (0.02−0.1%), which should preclude the need for the baking that is commonly part of the PA manufacturing process because of its more hygroscopic nature. The low moisture uptake is also an important factor in the creation of a low signal-loss environment. With a loss tangent of 0.003 and a dielectric constant of approximately 2.9, LCP is very attractive for high-speed applications. It shows very high chemical resistance and a maximum process temperature of 280 °C, but it also currently has a high price. Table 14.1 (http://www.goodfellow.com/E/P.html; Clark & Wagner, 2002; Rosato, 2011) reports the main properties of used polymer films.

Plastics foils are available in various forms such as monofilms, co-extruded films, laminates and multilayered of all shapes and sizes. Compatibility with materials for soldering, versatility during manufacturing phases, adaptability in applications and finally implications of costs have prompted wide usage of different plastic solutions in electronics. In some cases, laminates could be useful to overcome manufacturing issues. Figure 14.1 shows the relative cost comparison and consequently the implications of selected flex circuit laminates. The least expensive option is baseline as a factor of 1.0 (glass epoxy example). A combination of the performances and costs data drives the material choice for most flexible circuit applications. For example, consider the flexible circuit often found in a telecom pager. This is an inexpensive consumer product in which the most cost-effective material that will meet the design requirements should be chosen. In this case, it would be reasonable to assume that the service

Table 14.1 **Properties of some flexible substrate materials**

Property	Unit	Test method	OPP 25 μm	PET 50 μm	PEN 50 μm	PEI 25 μm	PC 50 μm	PPS 25 μm	PI 25 μm	LCP 50 μm
Mechanical										
Tensile strength at break (longitudinal/ transverse)	N/mm²	JIS C2151	140/280	250/270	220/ 220	110/110	70/50	300/ 250	180/ 180	40/32
Elongation at break	%	JIS C2151	160/55	100/100	60/65	100/100	140/ 140	60/80	70/70	12/16
Thermal										
Melt temperature	°C	DSC	135−160	255−265	262	— (non-crystalline)	150	285	—	280
Glass transition temperature	°C	DSC	0−20	69−78	121	216	—	92	—	—
Coefficient of thermal expansion	10^{-6} °C	TMA	—	17	—	49	70	30	20	20
Surface energy	dyn/cm	Contact angle	38	45	36	—	—	—	—	—
Shrinkage	%	150 °C/ 30 min	5−10	Stand.: >1.5[a]	<0.8	<0.7	<0.7	<0.8	0.1	<0.1
Water absorption	%		0.01−0.03	0.15	0.3	0.25	0.15	0.22	0.15−1	0.04

Continued

Table 14.1 **Properties of some flexible substrate materials – cont'd**

Property	Unit	Test method	OPP 25 μm	PET 50 μm	PEN 50 μm	PEI 25 μm	PC 50 μm	PPS 25 μm	PI 25 μm	LCP 50 μm
Electrical										
Breakdown voltage (DC)	kV/mm		20−30	20	—	20	15	17	16	22
Isolation	10^{16} $\Omega\,cm$		1	100	100	10	—	50	100	1
Dielectric constant 1 kHz, 25 °C			2.25	3.3	3.2	3.2	3.0	3.0	3.1	3.0
Cost										
Price	ca. €/m²		0.07	0.25	1.0	5.0	5.0	10.0	15.0	20.0

[a]Inline: 0.8, Offline: 0.2.
LCP, Liquid Crystal Polymer; OPP, o-phenylphenol; PC, Polycarbonate; PEI, Polyethylenimine; PEN, Polyethylene naphthalate; PET, Polyethylene terephthalate; PI, Polyimide; PPS, poly(styrenesulfonate).
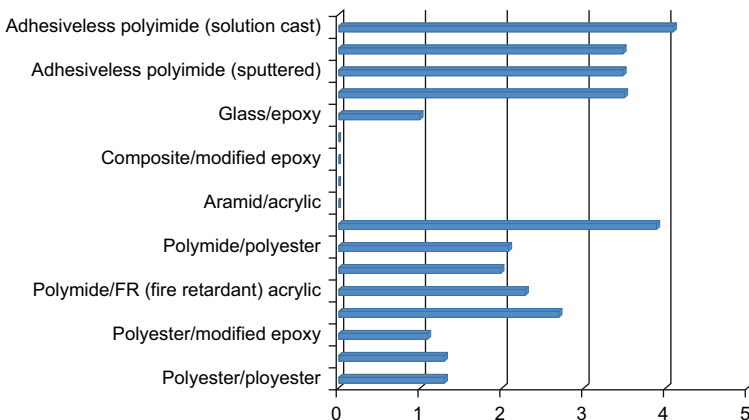
Figure 14.1 Approximate relative-cost comparison of selected flex circuit laminates.

temperature range would fall between −40 and +55 °C, that the electrical voltage and amperage requirements could be met by any of the materials listed, that the circuit would fit the non-demanding 'flex-to-install' criteria and that the risk of exposure to anything apart from humidity moisture would be low. PS is probably the best material for the application; however, great care must be taken when soldering PS with conventional tin/lead.

Alternative attachment techniques, such as lower temperature solder alloys or conductive adhesives, may be necessary to maintain acceptable process yields. If conventional solder processing is necessary but polyimide is cost prohibitive, hybrid materials have been developed to give properties somewhere between that of PS and polyimide (www.parlex.com/tech_library/BaseMAT.pdf).

Therefore, the material of choice for most flexible plastic circuits depends on a combination of performances, processing and costs. Because of the high cost of PA, it seems that lower-cost materials have to be used for the backplane. However, low-cost materials, such as PET or PEN, do not endure the conventional soldering temperatures; therefore, adhesives or low-temperature solders must be considered for attaching components. For such reason, hybrid solutions could be designed and manufactured. In such case, electronics components could be separately soldered onto smaller PA straps that are further attached to the main PS-based backplane.

14.2.2 Materials for printing

The attraction of printing technology for the fabrication of flexible electronics mainly results from the possibility of preparing stacks of microstructured layers in a much simpler and cost-effective way compared with conventional electronics (Blayo & Pineaux, 2005). The selection of the printing method is determined by requirements concerning printed layers, by the properties of printed materials and economic and technical considerations of the final printed products. Organic and inorganic materials are used for printed electronics. Ink materials must be available in liquid form for

solution, dispersion or suspension (Bao, 2000). They must function as conductors, semi-conductors, dielectrics or insulators.

14.2.2.1   Electrically conductive inks

The new lead-free solder alloys and inks, which have been used in the electronic industry and attracted extensive attention, need to meet various properties such as good wettability, low soldering temperature, low cost, environmental friendly, adequate strength, good thermal fatigue resistance and so on, which are superior to or even consistent with that of conventional Sn-Pb solders at least (Hu, Cao, Li, Ni, & Cui, 2011). Basically, electrically conductive and dielectric materials are needed for suitable electronics integration.

The most common types of electrically conductive inks are based on conductive nano- or microparticle components that have been dispersed into a polymer matrix (Electronics Manufacturing; Sankir, 2005). Such particle additives are metallic-based, such as silver, copper and gold as well as conductive oxides such as ITO or ZnO. In general, the basic physicochemical requirements for electrically conductive inks are similar to those of inks for graphic or paint purposes, but they should also provide good electrical conductivity of the printed pattern. The inks are usually cured by heat, which sinters the conductive particles into a continuous metal layer and decomposes all or part of the polymer vehicle. However, UV lighting or laser or microwave curing is also possible, gaining benefit by considerably reducing the sintering time. The conductivity is usually based on contact among each particle within the deposited layer. The ink is dried by heat, which removes binder and solvent, forming a conductive layer on the substrate. The required curing temperatures obviously depend on processing speed, substrate and temperature. They are typically in the range of 80−500 °C. The requested curing times are usually from 5 to 60 min. However, the drying is much faster, in the range of tens of seconds. Manufacturing speed can be adjusted up to several metres per second. The nature of the substrates determines what curing procedure and speed can be used for sintering the metal particles together. UV light-curable inks have many advantages. Firstly, the drying times may be significantly reduced with consequent reduction in costs. Compared with the drying of solvent inks, UV curing can be virtually instant. This is particularly important in reel-to-reel applications, in which it is essential that the ink is dry before it is rewound. Because UV inks tend to be non-volatile and rely on solidification rather than drying, the consistency of the rheological properties is maintained at the faceplate (Electronics Manufacturing).

Metallic-based inks are the most diffused inks for manufacturing sectors (Kamyshny, Steinke, & Magdassi, 2011). At present, most conductive inks are based on silver nanoparticles because silver possesses the highest electrical conductivity among metals ($6.3 \cdot 10^7/\Omega/m$) and is resistant to oxidation. There are several commercial silver water- and solvent-based inkjet inks produced by several companies, including Cabot (United States), SunJet (England), InkTec (Korea), Cima NanoTech (Israel), Harima (Korea), Advanced Nano Products (Korea), Samsung ElectroMechanics (Korea), Genesink (France), Amepox (Poland) and

Novacentrix (United States). Silver particle inks for gravure and flexo printing are available as solvent- and water-based formulations. Figure 14.2 shows traditional thick-film applications of silver inks and pastes of the market conditions today and a forecast of the next 8 years (Silver Inks & Paste markets, 2011).

Copper- and carbon-based inks are also available, although their conductivity is only 6% lower than that of silver-based inks. This could lead to reduced costs because the price of copper is less than 1% that of silver. The main challenge is avoiding copper oxidation at ambient conditions, which significantly limits application of these nanoparticles. There are only a few reports on copper nanoparticle inks and even fewer commercial products (Kim, Moon, Jeong, Kim, & Park, 2007; Lee, Choi, Lee, Scott, & Kim, 2008). Recent experiments clearly demonstrated the possibility to fabricate concentrated dispersions of copper nanoparticles suitable for use as copper ink precursors (Magdassi, Grouchko, & Kamyshny, 2010; Woo, Kim, Kim, Lim, & Moon, 2009).

Nanoparticles can also be suspended in lower viscosity liquids, enabling them to be used in printing processes. Nanosized particles have the benefit of reduced sintering and melting temperatures. A polymer shell protects the individual metal particles, preventing aggregation and promoting adhesion to the substrate. A wide range of nanoparticles can be manufactured from materials such as pure metals, metal oxides, ferromagnets, paramagnetic particles and luminescent particles. Decreasing the particle size, which is typically between 5 and 500 nm, can dramatically reduce the sintering temperature of the metal particles. This is considerably lower than the melting point of the bulk metal, enabling printing on substrates such as paper that can only withstand temperatures of approximately 100 °C (Harrop, 2007).
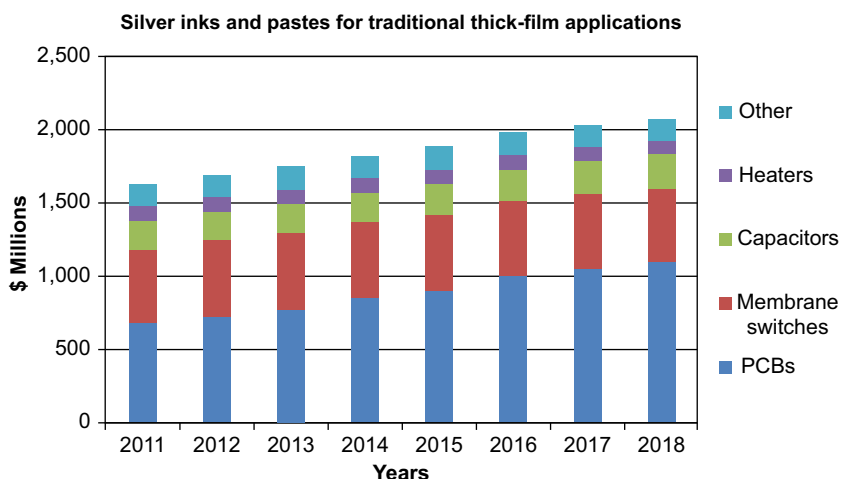
Figure 14.2 Silver inks and pastes for traditional thick-film applications.

14.2.2.2   UV-curable dielectric inks

Dielectric materials are important when electronic and optoelectronic systems are manufactured. Good electrical isolation between conductive layers avoids short circuits and reduces electromagnetic coupling that might interfere during operation of printed electronic circuitry. The compatibility with the substrates and other materials used in the flexible circuitry must be good. Viscosity of the dielectrics must be adjusted correctly so that, for example, in gravure printing the doctor blading is successful. The dielectric layer in a printed electronic circuit typically needs to be homogenous and thin. Its surface roughness must be as low as possible because it has to serve as a substrate for upper layers. The surface tension must be correct to avoid droplet formation so that the printed dielectric ink wets well. In many electrical applications, connections are needed through the dielectric layer. There must be holes in the dielectric layer. These holes are generated during the printing of the dielectric. If the wetting of the ink is too good, then these holes might be blocked. Sometimes additives are used to affect the printing properties of the dielectric ink, but these usually affect the electrical properties of the dielectric material, reducing its performance (Frost & Sullivan, 2006).

14.2.3   Adhesives

Adhesive and bonding materials have several expectations in terms of electrical bonding as well as chemical and mechanical resistance. The interconnections should typically withstand bending and other types of deformations during temperature cycles and humidity conditions of manufacturing processes, as well as in the course of the storage and usage lifetime. For such reasons, the interconnection materials must also be robust and at the same time compatible with the main raw used materials. Today, no commercialized electrically conductive adhesive (ECA) or tapes (ECTs) can replace tin-lead metal solders in all applications because of some challenging issues such as lower electrical conductivity, conductivity fatigue in reliability testing as decreased conductivity at elevated temperature and humidity aging or normal use condition, limited current-carrying capability and poor impact strength. Thus, electronics chips, bar dies and surface-mounted devices (SMDs) can be assembled by tin-lead metal soldering and adhesive bonding. However, to prevent the integrity of bonding pads from flux residues and oxidation, the attachment of the SMDs by soldering would be related to additional protection and cleaning steps. The use of conductive adhesives for the attachment of chips leads to the lowest possible number of process steps within the manufacturing chain. The manufacturing processes are compared in Table 14.2.

Depending on the conductive filler loading level, ECAs are divided into isotropically conductive adhesives (ICAs), anisotropically conductive adhesives (ACAs) and non-conductive adhesives (NCAs). For ICAs, the electrical conductivity in all x-, y-, and z-directions is provided because of the high filler content exceeding the percolation threshold. For ACAs or NCAs, the electrical conductivity is provided only in the z-direction between the electrodes of the assembly (Liu, 1999). Table 14.3

Table 14.2 Comparison of number of process steps for SMD assembling using either soldering (left column) or adhesive bonding (right column)

Printing the solder (stencil) for SMDs and the transistor chip	Printing the adhesive (stencil) for all components
Placing SMDs and transistor	Placing all components
Reflow soldering	Curing the adhesive
Cleaning (flux removing)	—
Dispensing the adhesive for the remaining chips	—
Placing the chips	—
Curing	—
Wire bonding	Wire bonding
Applying glob top	Applying glob top

Table 14.3 Conductive adhesives compared with soldering

Characteristic	Sn/Pb solder	ECA (ICA)
Volume resistivity	0.000015 Ωcm	0.00035 Ωcm
Typical junction R	10−15 mW	<25 mW
Thermal conductivity	30 W/m °K	3.5 W/m °K
Shear strength	2200 psi	2000 psi
Finest pitch	300 μm	<150−200 μm
Minimum processing temperature	215 °C	<150−170 °C
Environmental impact	Negative	Very minor
Thermal fatigue	Yes	Minimal

(Liu, 1999) gives a general comparison between the final characteristics of tin-lead solder and a generic commercial ECA.

ACAs are the usual materials for doing flex-to-flex interconnections. Commercial snap cure materials recommended for flip-chip interconnection but also suitable for strap interconnections are already on the market. A similar process could be used for connecting flexible substrates onto another flexible substrate. The adhesive should be dispensed onto all pad areas and possibly some non-conducting adhesive onto the other areas. The tool of the thermode could be designed to apply heat and pressure only on the places where connections are made. The sensitive areas of the assembled flex and substrate could then be left out of the high-temperature and high-pressure process
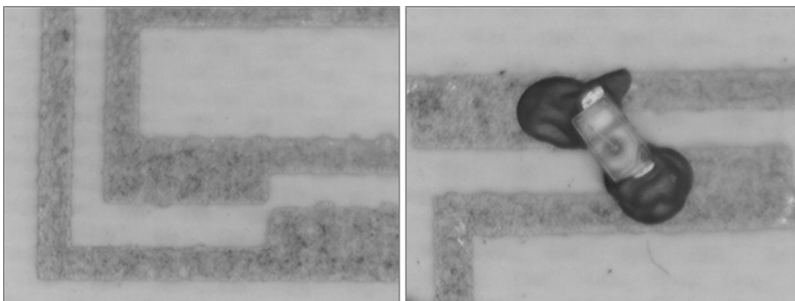
Figure 14.3 Left: Silver printed lines and pads on PC substrate (magnification ×2.5). Right: Bonded chip on pads with optically transparent glue on top (magnification ×2.5).

needed for the electrical interconnection. Figure 14.3 shows screen-printed pads on PC substrate before and after chip bonding. ACA has been used to get electrical conductivity between pads and chip electrodes through a flip-chip process. Optically transparent glue has been dispensed on top to avoid misalignment, damage or chip removal.

In ACA technology, the bonding pressure must be large enough to bring the pad surfaces to such a near contact that at least one conductive particle between the surfaces is able to make the electrical connection. Just as in bonding flexible substrate onto rigid substrate, the pad metallization should be elevated with respect to substrate level so that there is free volume between the conductors, which can act as a reservoir for the extra adhesive material. Anisotropically conducting adhesive film (ACT) has been alternatively used for flex-to-rigid applications, and it is also a potential technology for flex-to-flex applications. There are several commercially available materials suitable for strap interconnection such as those used in smart card module assemblies. These materials are claimed to form good adhesion to various substrates such as ABS (Acrylonitrile Butadiene Styrene), PVC (Poly(vinyl chloride)) and PET (PolyEthylene Terephthalate).

The most common adhesive interconnection technology uses ICAs, which contain electrically conducting particles in such a large concentration that the adhesive becomes electrically conducting after the curing procedure. Epoxies are the most common types of ICAs, but several materials are commercially available on the market. The advantage of ICA is that no pressure is needed during the curing and they are typically cheaper than ACAs; on the other hand, the curing times increase considerably when the curing temperatures are lowered. Therefore, ICA materials are the preferred interconnection materials when pitch is large enough so that there is no danger of short circuits. Certain ICA materials can also be cured using a die bonder or any other efficient method of rapid heat transfer. Therefore, the adhesive could be a potential candidate for local hot tool curing, which could have benefits in bonding thermally sensitive components, such as batteries, which cannot withstand the temperature of the curing process. The overall resistance of standard ICAs depends on several parameters. It is generally the sum of the resistance of fillers ($R_{fillers}$), the resistance between fillers ($R_{btw\ fillers}$) and the resistance between filler and pads ($R_{filler\ to\ bond\ pad}$).

$$R_{total} = R_{btw\ fillers} + R_{filler\ to\ bond\ pad} + R_{fillers} \tag{14.1}$$

To decrease the overall contact resistance, the reduction of the number of contact points between the particles may be obviously effective. Incorporation of nanofillers increases the contact resistance and reduces the electrical performance of the ICAs. The number of contacts between the small particles is larger than that between the large particles. If nanoparticles are sintered together, then the contact between fillers will be fewer. This will lead to smaller contact resistance. For example, by using effective surfactants for the dispersion and effective capping for conductive nanoparticles, the interdiffusion of silver atoms among nanosized particles could be facilitated and the resistivity of whole ICA could be reduced to 5×10^{-6} Ωcm (Wong, 2010).

NCAs have been used for bonding bumped chips onto rigid or flexible substrates. Here, the electrical connection is made by two touching conductive surfaces without any joining material and the NCA only produces the permanent stress, which keeps the surfaces in contact. For interconnections between two flexible substrates, NCA technology might not be suitable. However, the lamination process using adhesive between flexible substrates is fairly similar compared with the NCA curing process, in which heat and pressure are also applied. In principle, some electrically conducting rigid or flexible pieces that are thicker than adhesive layers could form electrical interconnection between flexes during the lamination process. However, more reliable connection could be obtained by using ICA paste in the interconnection points.

Finally, pressure-sensitive adhesives (PSA) are generally used to form a bond marrying adhesive with the adherent. No solvent, water or heat is needed to activate the adhesives that are self-adhesive and self-stick. They are used in pressure-sensitive tapes, labels, note pads, automobile trim and a wide variety of other products. PSAs are usually designed to form a bond and hold properly at room temperatures. PSAs typically reduce or lose their tack at cold temperatures and reduce their shear-holding ability at high temperatures.

14.3   Manufacturing processes

In future manufacturing scenarios, the experts have identified key technologies for the industry sectors such as improvement in reliability, control, measuring, precision and testing. In general, manufacturing technology can be expected to become multidisciplinary as boundaries between the sciences become blurred. Linking between plastic foil and plastic body technologies is needed for production of novel integrated systems.

Two main phases basically take place in the manufacturing chain. These are functional foil manufacturing such as R2R printing, bonding, curing, cutting, forming and packaging and over-moulding phases, including in-mould labelling (IML), in-mould decoration (IMD) or similar phases. However, a more complex process flow indicates a structured and multidisciplinary approach to integrated component production. Starting from raw plastic rolls, several manufacturing phases are basically needed to get the final embedded functional components. Each process step should be separately managed. In between the starting and final design steps, testing, fabrication, and inspection are expected; after completion, the flexible and stretchable circuit is moved
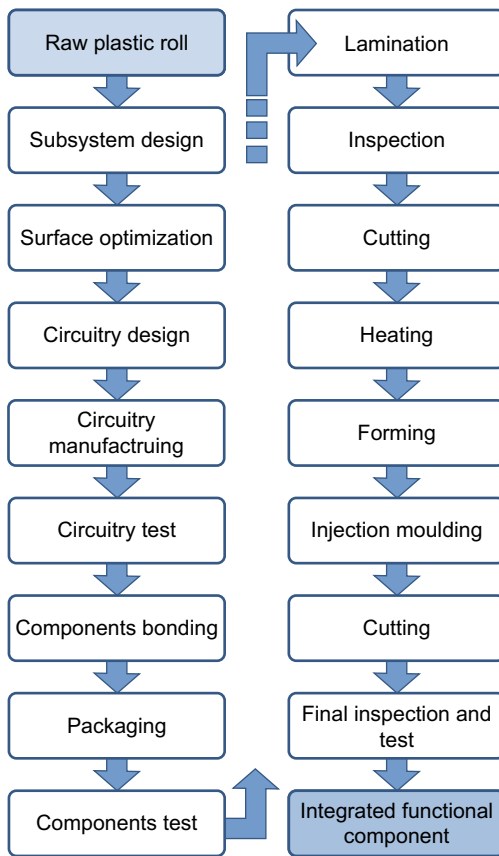
Figure 14.4 Example of manufacturing process flow, broken down in separate process steps.

to the polymer processing for forming and injection (Figure 14.4). Circuit bonding is generally expected at the end of back-injection phases, but in some cases it could occur before them. However, to achieve a high degree of integration, close cooperation among researcher, developer, producer and process engineers as soon as possible in the product design phase is rigorously requested.

14.3.1 Design

Today's aim of flexible circuit manufacturers is increasing the level of understanding at the outset of the design level to ensure fast and accurate design for manufacture. Implications on styles are the main drivers for the manufacturing of the final product. Factors on which design has an effect are:

1. Cost
2. Material choice and utilization
3. Physical shape, size and weight

4. Construction
5. Manufacturing process routes
6. Test and inspection
7. Electrical performance
8. Mechanical performance: Bend to install or dynamic
9. Physical performance: Dimensional stability, temperature/environmental resistance
10. Assembly technology

All of the above mentioned needs are to be considered within the product design cycle. The reverse can often be the case, with flexible circuits being an afterthought to solve other design problems. In either case, the use of design failure mode and effect analysis (FMEA) is extremely useful in eliminating potential issues (http://www.flexiblecircuits.co.uk/news/downloads/FlexibleManufacturing.pdf).

However, designers are not out of technicalities. For instance, material/process compatibility could strongly influence their choices. Thermal mismatch between device films and substrates may cause films to break during the thermal cycling associated with fabrication, failing finishing intentions. A rule of thumb for tolerable mismatch is $|\Delta CTE \cdot \Delta T| \leq 0.1-0.3\%$, in which ΔCTE is the difference in coefficients of thermal expansion (CTE) between substrate and the device film and ΔT is the temperature excursion during processing. Silicon-based circuits benefit from substrates with low CTE. High thermal conductivity may be important for cooling of current-load circuits. Dimensional stability during processing is a concern with plastic substrates (Flexible Electronics, 2009). To overcome compatibility issues at surfaces, industrial applications of atmospheric plasmas are key technologies for achieving stable material combinations and high-quality surface finishes with secure adhesion (Schüßler, 2008).

14.3.2   Printing for functional foil manufacturing

A great advantage of processable organic materials is a high combination between fabrication and patterning processes. Conventional photolithography is capable of generating very small feature sizes, but it is still relatively expensive for low-end devices. Recently, various printing techniques and non-conventional patterning methods involving imprinting lithography such as nano-imprinting lithography (NIL), stamping or microcontact printing (μCP) and micromoulding have shown promising results for organic optical and electronic devices (Bao, Rogers, & Katz, 1999). Although inkjet and screen printing have already been widely used for other applications, they are only capable of producing relatively large feature sizes, such as above 10 μm for inkjet and 50 μm for screen printing. Non-conventional μCP and NIL have been actively explored for patterning feature sizes down to 1 μm (Rogers, Bao, Makhija, & Braun, 1999). However, unevaluated issues, such as large-area printing capability and stamp deformation, may limit their applications.

Continuous deposition processes increase the manufacturing speed and throughput, decreasing the costs and amount of manufacturing steps in comparison with batch approaches. The main continuous compatible processes are based on the R2R concept, which enables deposition of the conductive and non-conductive layers on flexible

backplanes through printing and etching. Main R2R printing methods are flexography, gravure, offset, rotary screen, and inkjet. Typical advantages and disadvantages of printing methods are reported in Table 14.4.

The thickness of conductive layers should usually be in the range of 10−20 μm to obtain adequate conductivity. The 20-μm layer thickness can be obtained in one layer only by screen printing, which is the most widely used printing method in printed electronics. This method has been used in the electronics industry for decades in sheet and web processes, which is due to the large amount of commercially available inks and the good suitability of different substrates. A comparison among the principal printing processes is reported in Table 14.5 (Kipphan, 2001; Rigney, 2004).

14.3.3   Over-moulding techniques: IML and IMD

Several processes are available today using the concept of back injection. In these processes, a component of the moulding is inserted in the mould. The component comprises a carrier made of various non-thermoplastic materials, such as wood, fabric web, plastic film, rubber or metal (e.g. aluminium). The substrate usually provides a high-quality or specially designed surface into the plastic body by transferring (IMD). Likewise, further techniques can introduce reinforcements or insert into a plastic body (IML). The machines that can be used include standard injection moulding machines, various special machines and combinations of extruder and press (clamping station).

IML is a very robust method for decorating consumer and industrial products. IML gives product manufacturers the ability to have multiple colours, graphic effects and/or textures when the part comes out the mould. It is a cost-effective alternative to pad printing, hot stamping, paint and laser etching. IML has many advantages over pressure-sensitive labels such as its ability to eliminate secondary operations and problems typically seen with an adhesive application. It offers a 'no-label' look and is more durable. Some of the technical advantages of IML include:

- Complete decoration of the moulded part
- Durability of graphics: Inks are protected by film in second surface constructions
- Secondary operations associated with post-moulding decoration are eliminated
- Abolition of need for recessed label areas
- Multiple films and constructions available to meet customer requirements
- Easier to produce multi-colour applications
- Generally lower scrap rates
- More durable and tamper-proof
- Superior colour balancing
- No area where dirt can collect
- Unlimited colours available

Instead of decorating parts with a common pad printing or painting, IML is done during moulding. The label is loaded into the mould, where it is fused into the outer surface of the moulded part. Mould labelled graphics are impervious to chemicals and abrasion. A sealed construction with inks on the top (first surface) of the label that bonds to the moulding, or inks on the back (second surface) of a clear material that traps inks

Table 14.4 Typical advantages and disadvantages of printing methods

Printing method	Advantages	Disadvantages
Flexography	• Simple operation principle • Wide range of suitable substrates • Cheap, flexible and soft printing plates → better contact • Low nip pressure → no damage to underlying layers • Easily adjusted and controlled ink amount	• Poor print resolution and register • Low printing speed • Difficult to print solid tones and details via the same printing unit • Poor solvent resistance of the plates
Gravure	• Simple operation principle • High resolution, speed and throughput • Excellent solvent resistance • Precise ink application	• Expensive printing cylinders • Ink transfer problems → missing dots • Smooth and compressible substrate • Solvent recovery • Solid tones reproduced via ink spreading • High pressure
Offset	• High resolution and speed • Cheap printing plates • Versatile printing process • No excessive spreading • Waterless process possible	• Ink-water balance • Water limits the choice of materials • High surface strength of the substrate • Rough ink layer • Complex process • High pressure
Screen printing	• Wide range of substrates and inks • Large amount of applications • Adjustable ink layer thickness • Low printing pressure	• Low print quality and speed • Thick ink layers using pasty inks • Screen blocking
Inkjet	• High print quality • Noncontact method • No printing plates → direct imaging • No pressure • Curved substrates possible	• Low speed • Resolution decreases with higher speed • Expensive materials • Nozzle clogging • Free spreading of ink • Surface tension of ink affects print quality

Table 14.5 Comparison of principal printing processes

Printing method	Printing speed (m/s)	Nip pressure (MPa)	Ink viscosity (Pa s)	Layer thickness (μm)	Feature size (μm)	Registration (μm)	Typical application
Flexography	3−10	0.1−0.5	0.01−0.5	0.04−8	40−80	20−200	High volumes, packaging.
Gravure	10−16	1.5−5	0.01−0.2	0.1−12	20−75	>10	Very high volumes, packaging wide web.
Offset	8−15	0.8−2	1−100	0.5−3	25−50	>10	High volumes, papers, magazines, books etc. Wide web typically.
Screen printing	2−3	−	0.1−50	2−100	75−100	>25	Special applications; posters, graphics on fabrics. Narrow web or sheet.
Inkjet	0.01−5	−	0.001−0.04	0.05−0.5,20 (UV)	10−50	<10	Personalized printing, advertisement, often used for personalization for e.g. offset-printed material. Typically narrow web or partial coverage.

between the label and the moulding, makes IML highly durable. To facilitate handling during printing and in production, the film must be of a certain stiffness.

For an efficient production of IML articles, it is a must to optimally match the individual components of the system (i.e. moulding machine, mould and handling equipment). This is an absolute prerequisite to achieve a high availability and thereby productivity, and it is achieved by a high reproduction ability of the moulding machine, with precise closed loop control of the mould open position for the exact positioning of the labels by the shortest cycle times and by an increase of compatibility between materials. Use of the right film and correct printing as well as punching of the label are essential for a successful application of IML. In the interest of better adhesion and to avoid any peeling, the label material must be identical with the container's material. However, a combination between different plastics is also possible. Adhesion between different foils and over-moulding materials is reported in Table 14.6.

The demand for a one-substance packaging product is also satisfied in this way. Because of the plastic material's memory, the film's direction of extrusion or stretching must be kept in mind on printing and punching. However, because of the adhesion to the plastic substrate, the printed surface must not be too thick. An additional forming process could be needed to prepare the plastic sheet to its final shape, avoiding wraps and cracks of printed foil. With labels of this type, the printing and thereby the added functionalities are optimally protected. Table 14.7 reports specific features for different PS films with different functional layers printed on top.

On the other hand, IMD has become one of the main methods for plastic decoration in the world in place of traditional methods such as painting, silk-screen printing and pad printing. IMD is now widely known as the only method that can meet designers' high-level demands for beauty. During the process, a plastic carrier foil is placed inside of the opened mould. It carries the dried paint layers that are to be transferred to the main plastic part, with the paint facing the gate. After filling with plastic, the paint adheres to the plastic and is removed from the carrier when opening the mould. For the next cycle, the carrier foil is advanced, positioning the next area to be transferred. Some key features of the technology are the following:

- Considerable cost benefit for mass production.
- Because the process for moulding and decoration occur simultaneously, there is significant savings in floor space and processing time.
- Because the ink layer is thin, volatile organic compounds (VOCs) are not only significantly reduced, but reduction in wastes and the efficient utilization of energy also become possible because of excellent yield.
- Because the process occurs in a clean environment, there is no risk of environmental contamination such as you can get with organic solvents.
- The system can reproduce metallic effects, the luster of pearl, gloss, matte, wood grain, surface texture and other various artistic expressions with high-precision positioning accuracy.
- Complex 3D geometries can be decorated with high quality.
- The surface is protected by superior scratch-resistant hard-coating technology (http://www.nissha.co.jp/english/products/industrial_m/imd/index.html).

At first glance, IMD is a most cost-effective technique in comparison with IML because the thermoforming phase is not needed. However, IML provides more

Table 14.6 Adhesion between different foils and overmoulding materials

		Overmolded material															
		ABS	ASA	EVA	PA6	PA66	PBT	PC	PEHD	PELD	PET	PMMA	POM	PP	PS-HI	SAN	TPU
Foil mate-rial	**ABS**	++	+	+			+	+	−	−	+	+	−	−	*	+	+
	ASA	+	++	+			+	+	−	−	+	+	−	−	−	+	+
	EVA	+	+	++					+	+				+	+	+	
	PA6				++	+	*	*	*	*			−	*	−	+	+
	PA66				+	++	*	*	*	*			−	−	−	+	+
	PBT	+	+		*	*	++	+	−	−	+	−	−	−	−	+	+
	PC	+	+		*	*	+	++	−	−	+	+	−	−	−	+	+
	PEHD	−	−	+	*	*	−	−	++	+	−	*	*	−	−	−	−
	PELD	−	−	+	*	*	−	−	+	++	−	*	*	+	−	−	−
	PET	+	+				+	+	−	−	+	−	−		−		+
	PMMA	+	+				−	−	*	*	−	++		*	−	+	
	POM	−	−		−	−	−	−	*	*	−		++	−	−	−	−
	PP	−	−	+	*	−	−	−	−	+		*	−	++	−	−	−
	PS-HI	*	−	+	−	−	−	−	−	−	−	−	−	−	++	−	−
	SAN	+	+	+	+	+	+	+	−	−		+	−	−	−	++	+
	TPU	+	+		+	+	+	+	−	−	+			−	−	+	+

++ Excellent adhesion, + Good adhesion, * Weak adhesion, − No adhesion.

EVA, Ethylene vinyl acetate; PA6, Polyamide 6; PA66, Polyamide 66; PBT, Polybutylene terephthalate; PEHD, Polyethylene high density; PELD, Polyethylene low density; POM, Polyoxymethylene; PS-HI, Polystyrene High Impact; SAN, Styrene Acrylonitrile; TPU, Thermoplastic polyurethane.

Table 14.7 Different features for conductive layer on PS and LDS substrates

	PS films					LDS Cu film
	Printed Ag	ITO	Thin Cu < 1 μm	Thick Cu > 30 μm	PEDOT/ PSS	
Conductivity	+	~	+	++	−	+
Conductivity formed	~	−	+	−	+	n/a
Adhesion	~	+	++	++	~	++
Resolution	+	++	+	++	~	+
3D geometry	+	−	++	~	~	++
Transparency	−	++	−	−	+	−

++, excellent; +, good; ~, reasonable; −, bad; n/a, not applicable.
Ag, Silver; Cu, Copper; ITO, Indium Tin Oxide; LDS, Laser Direct Structuring; PEDOT/PSS, Poly(3,4-ethylenedioxythiophene) Polystyrene sulfonate; PS, Polyester.

complex 3D geometries with high curvature ranges. In between, several processes enable hybrid solutions that have the benefits and disadvantages of both. In terms of costs, if you consider one form of IML, a reduction of 40% is expected for IMD whereas the cost safety of hybrid solutions is approximately 25−30%.

14.4   Automotive applications

In today's automobiles, trucks and motorcycles, electronic components are essential to control movements and the entire range of chemical, mechanical and electrical processes involved. These electronic systems ensure safety, provide communication and are imperative for on-board entertainment. Whereas a strong increase of the electronic components' contribution to the total manufacturing expense is forecasted, revolutionary changes in the design and conceptualization of electronic devices are already afoot. In particular, benefits of lightweight, integration, complexity and perceived quality are to be taken into consideration. The current major transformations are occurring on several fronts that require a flexible workforce. These fronts include the following:

- Technology: The growing demand for greener technologies, coupled with a shift toward increased integration of mechanical, electrical and software engineering.
- Production: To reduce risks and costs, original equipment manufacturers (OEMs) and suppliers are shifting toward the closest low-cost production environments within trading zones.
- Research and development: To meet the needs of new customers in emerging markets, companies' research, development and design efforts are being centred in the markets they expect to serve.

A vision concerning the link between future trends and OEMs' domain is reported in Figure 14.5 (Vision of the Global, 2012).
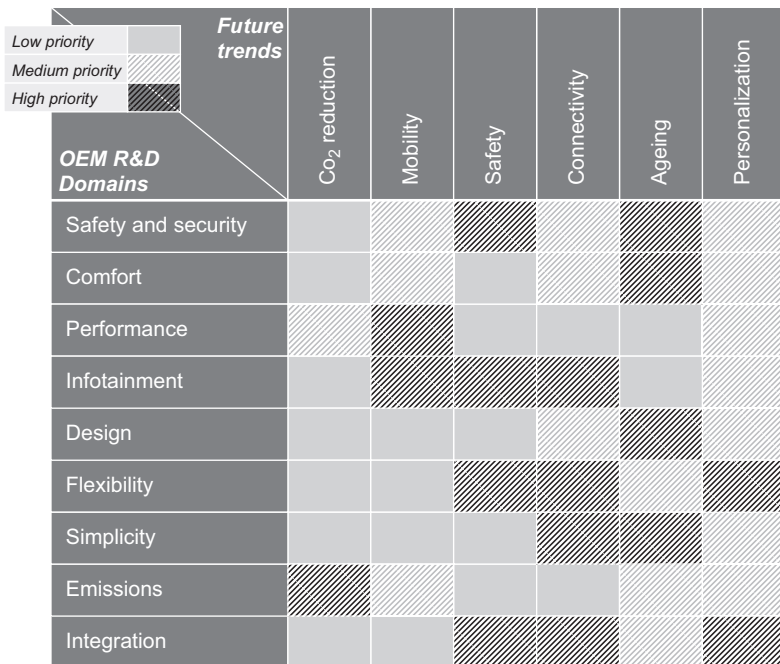
Figure 14.5 Automotive industry vision: global research and development trends, 2020.

With the growing number of electronically supported functions, vehicles are becoming more complex. Ensuring the functional reliability of electronic components has always been the major challenge for vehicle developers. Table 14.8 shows the average proportion of vehicle mass by type of materials for end-of-life vehicles for a Segment C vehicle (Automotive News, 2008).

Table 14.8 Average proportion of vehicle mass by type of material for end-of-life vehicles for a segment C vehicle

Material	1978	1995	2003	2010
Steel	59.5	55.1	54	47.6
Iron	14.3	12.4	10	7
Other metals (Cu, Zn, Mg…)	2.3	3	3.5	4.2
Polymers	9.7	13.6	13.6	15
Glass	4	2.9	2.9	2.6
Elastomers	4.1	4.2	4.4	4.5
Aluminium	3.2	5.8	8.3	12
Other materials	2.9	3	3.3	7.1

Thus, the increase in the use of plastic and the growth in electronic applications in vehicles result in greater use of electrical metals, such as copper, silver or aluminium, and in different usage of polymers. The road ahead to the automotive future is certainly the integration of materials and functions as in organic electronics systems. Therefore, printed films less than a millimetre thick are used as embedded displays and switches, including protective lamination and graphical overlays for crisp text and animated gauges, brightly coloured indicators and touch-operated switches. They might be fitted onto bent interior or exterior surfaces of the vehicle. Therefore, no screws are expected with a decisive gain of usable space and weight (Applications, 2007). Even if the growth in electronic and electrical parts plays against, the introduction of the massive use of plastic for interior and exterior applications brings great benefits in the overall proportion of the total body.

Printed electronics cover large areas while being less than a millimetre thick. In addition, facility in the integration improves the possibility of applications. Therefore, the automotive sector imposes no limits to the integration of flexible electronics: novel illumination systems, 'smart textile' seats, solar cell generators, integrated switches, embedded cabling and information and communication interfaces. The latter will bring revolutionary changes to the car's interior, interactively networking driver and vehicle with ambient traffic flows in a delicate balance of assistance and autonomy. Figure 14.6 shows the application in vehicles of flexible electronics for the integration of functional systems.

However, improvement in validation procedures and growth in accessibility of durable and high-quality plastic components is needed to meet automotive requirements. The car industry sets extreme conditions for application and assembly within vehicles. All of the devices must be tested and validated according to existing regulations in terms of efficiency, robustness and lifetime in harsh environments. With this purpose, novel procedures, settled for new integrated components in which electronics and plastics coexist together, are currently being assessed.

14.4.1   Lightweight

Weight reduction is a key issue for vehicle manufacturers as they look to meet targets for more fuel-efficient vehicles. A new paradigm in design and manufacture
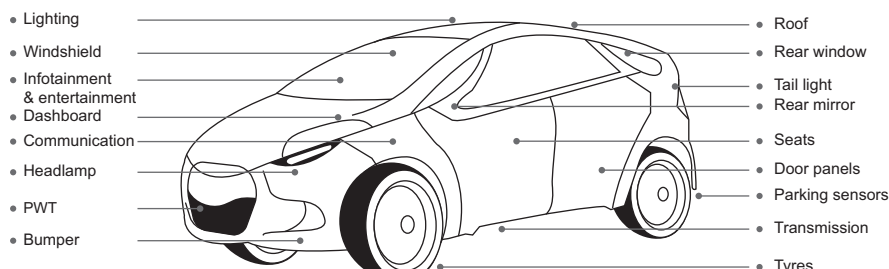
Figure 14.6 Flexible electronics applications in vehicles.

leads to weight saving for chassis, interiors and powertrains. Novel e-conductive materials enable the integration of functions within bulk components, as in the case of head front-lamp, central consoles, lighting inserts and intelligent seats. Generally, the number of e-connections trends increases while multiplexing technology aims to bring the weight of the wiring harness down. New materials are sought for conductivity and insulation in wiring. Aluminium instead of copper can save 4−7 kg on wiring per car, but it has drawbacks, including corrosion and it needs a bigger cross-section. Signal wires can be printed on foil to reduce weight and space. All of these types of designs will substitute for the standard copper-based cabling currently used in vehicle architecture. Today, the complete wiring harness of a car weighs approximately 40−50 kg, with an overall length from 4 to 6 km (http://www.acemr.eu/uploads/media/Trendstudy_ACEMR_Designmaterials_01.pdf). Studies indicate that 10% mass reduction relates to a 3−7% benefit in fuel consumption depending on the type of car and the drive cycle used. The effect is stronger with more fuel-efficient and downsized engines. On average, a weight reduction of 100 kg delivers −10 g CO_2/km. Weight reduction often comes with a penalty on cost. As a rule of thumb, the industry uses a target maximum of €5/kg gained. For high-volume cars in very price-sensitive segments, this target goes down to €2.5/kg.

The approach to interiors is generally dominated by several options, which include specific design to embed electronic into structural rigid components and to enhance material compatibility to tolerate plastic moulding. These can be up to 40% lighter, smaller and lower cost than previous systems such as overhead lighting and control clusters with rocker switches, spring contacts, filament bulbs and so on. They can be much more reliable because they are fully sealed and have no moving parts. T-Ink Ltd. and its partners pioneered this with the overhead lighting cluster of the Ford Fusion car in late 2012. Ink patterns capable of up to 500% stretch are used as electrodes, actuators, antennas and interconnect heaters in T-Ink's various structural components. In addition, such processes will be particularly valued for electric vehicles, whether on land, water or airborne (www.IDTechEx.com).

Development of smart textiles will also benefit lightweight characteristics. Automotive interiors are indeed a promising application area for smart textiles because cars already contain many different textile surfaces (e.g. in the seat cover, carpets, roof, door liners, tyres, hoses, safety belts, air bags etc.). Further developments also save weight in the interior and exterior. Thus far, automotive smart textiles include textiles providing external textile 'skins' replacing standard car exteriors as used in BMW's concept car 'Gina' (http://www.bmwusa.com/standard/content/allbmws/concept vehicles/gina/). Others 3D stretching possibilities are in various flexible photovoltaic sheets becoming available for the outside of vehicles. Stretching of sheets onto the roof of a sports car, cutting to shape is less attractive and robust than stretching, gripping and gluing to shape. However, flexible photovoltaic film currently bends in only one direction and includes flexible copper indium gallium diselenide (CIGS), dye-sensitized solar cells (DSSCs; titanium dioxide/ruthenium-based dye/iodine-based electrolyte), amorphous silicon and organic options relying on polythiophene inks (www.IDTechEx.com).

14.4.2 Complexity

Integration of functional elements at minimal space constraints, low energy consumption and simplified assembly has one priority more in forthcoming vehicles. The electronic component industry has succeeded in developing new generations of microprocessors based on ink-printed circuits for Systems-on-Chip solutions, advanced embedded software products and better sensors. The strong European automotive and industrial automation sectors have created a demand for innovative electronic components in the first place. They have been among the first users that replaced silicon semi-conductors for specific automotive applications. The flexible nature of organic polymers allows a higher degree of customization, higher reliability, reduced energy consumption and easier to recycle low-cost polymer substrates (Geyer, Scapolo, Boden, Döry, & Ducatel, 2003; http://www.acemr.eu/uploads/media/Trendstudy_ACEMR_Designmaterials_01.pdf). New conductive coatings are the base of the flexible technology as OLED and embedded switches (http://www.acemr.eu/uploads/media/Trendstudy_ACEMR_Designmaterials_01.pdf). Transparent conductive layers are also developed to create integrated components as ice-free, lighting and see-through glazing.

The main objective is the integration that allows a combination of several functionalities on the same components, reducing assembly issues, manufacturing steps, multiple designs and connections. Several research programmes have been initiated to tackle the challenges in manufacturing, encapsulation and performance of organic semi-conductors, which constitute the very basics of flexible electronics. Proactive printing companies are widening their horizons and expanding business to incorporate printing electronics on flexible substrates for integration. Several European projects, within 6 and 7 Research Framework Programme in Nanotechnologies, Advanced Materials and Production, Information Communication Technology as well as Transportation, developed smart integrated prototypes. As example integrated automotive components, as tail light or interior fascia, in which several functionalities such autonomy, bendability, lightweight and lighting joined into single devices have been designed and manufactured in the frame of Place-it (IST-0248048), Priam (ICT-2009-4) and Smart-EC (ICT-2009-3.9) projects (http://place-it-project.eu/Home/tabid/66/Default.aspx; http://www.smart-ec.eu/fe#, http://www.priam-project.eu/fe#).

Integration using two-component back-injection methods was optimized in November 2010 by Bayer Material Science for a PC tailgate with a backlight for automotive purposes. Unlike the conventional design involving a metal carrier and a glass window inserted in it, this part has a completely seamless outer skin consisting of coated PC. Non-transparent areas are either back-printed in a dark colour or back-injected with a black frame material using two-component injection moulding. Bayer estimates that a weight savings of approximately 30−40% is achieved with the Makrolon® part compared with the same vehicle part made of metal and glass. In addition, this reduces the number of parts for the lighting elements at least by the number of components formerly mounted on the outside. Tail lamps, indicators, brake lights, license plate lights, and the raised brake light are located behind the PC outer skin. The

Figure 14.7 Touch-sensitive intelligent surface that replaces mechanical switches, sliders and wheels with capacitive electronics.

same concept could obviously be adapted for several industrial applications (http://www.materialscience.bayer.com/en/Media/Photos-Films/Films.aspx).

Finally, fully integrated, smooth and aesthetically pleasing interiors with embedded displays and switches could be integrated as a surface, showing themselves only when needed and activated by slight touch. A special advantage of capacitive touch sensors is that they are proximity thoughtful switches. They can be activated by gestures, not to distract the driver's attention. With such purpose, active Touchskin® (http://www.touchskin.net/?p=575), or touch-sensitive surface, has been designed to shape the forthcoming interior design (see Figure 14.7). The surface completely replaces mechanical switches, sliders and wheels with capacitive electronics. In the dynamic console, an intuitive touch skin can control the board computer or recharge a mobile phone only through gently stroking.

Despite being differently based on laser direct structuring (LDS) technology (http://www.lpkf.com/_mediafiles/1797-lpkf-lds-process.pdf), MyWave-3D® focuses on similar targeted applications. It is essentially a combination of a decorated 3D plastic cover and 3D-shaped electronic interior. Developed by Helmbrechts, it generates a great deal of interest from readers and customers (http://www.helmbrechts.de/index.php?id=8). A more complete and visionary customizable solution has been developed by Harman. The DOCK + GO concept vehicle (http://www.harman.com) incorporates a customizable situational human machine interface adjusting to every driver's tastes and preferences, harnessing a universe of personalized entertainment and information from the web and finally making driving time easier, safer and more productive by learning driving routes and habits. All of these capabilities are available without the need to turn a dial, touch a screen, or even utter a word but only through a hand gesture.

14.4.3 Perceived quality

The 'car of the future' will show elegant and ergonomic cockpit designs with embedded illumination, displays and touch sensors. Thin, highly brilliant OLED

backlights will be glued directly to the car's body, making brilliantly coloured displays and capacitive touch sensors integrated in the curved trims of the car's interior, including the dashboard, central console, seats, ceiling, armrests, kick plates and more, positioned exactly where they provide touches of luxury and add ergonomic value. Flexible displays and sensors can easily functionalize the complicated geometries imposed by car designers. In 2003, BMW was the first European car maker to offer a head-up display that is based on laser projection onto the windshield, thus creating the first free-form display integration, making printed electronics a vast opportunity. The alternative drive control system, called 'Vision ConnectedDrive' is a free-form display embedded in a flat screen similar to a tablet Personal Computer, realizing novel design features (see Figure 14.8, http://www.bmwgroup.com/). As the main information monitor, it will emulate the car's drive-relevant instruments. Unfortunately, laser projectors are rather voluminous (Press Releases, 2011) and overall costs become prohibitive.

Multiple layers of transparent OLED films allow for displaying simultaneous information. This illumination system, realized as a free-form design, is one of the core applications of flexible plastic electronics. However, the quality of the OLED substances today significantly affects the lifetime and performance of OLED applications. This is a key area of interest for the use of OLED lighting, especially in automotive applications, where replacing light components could become expensive. Philips and Audi have recently worked together on an OLED concept car. For this purpose, the OLED manufacturing process, which was previously based on two-dimensional glass substrates, had to be adapted to the third dimension. This was related not only to the processes and technologies for manufacturing the glass substrates themselves, but also to vacuum-based OLED coating, encapsulation and electrical contacts (http://www.plusplasticelectronics.com/lighting/oleds-on-the-road-71130.aspx).

Figure 14.8 BMW ConnectedDrive concept (2011).

Display interface is an area of particular interest in the automotive industry. Today, the centre stack panel area has become the integration site for many occupant interface technologies, and it is being driven by consumer requirements influenced by today's personal electronic devices. Examples of integration are touch movement sensors for radio or navigator controls as well as driving assistance within a continuous curved surface that provides partial or complete hiding. This offers a high-craftsmanship appearance as a currently strong trend in automotive spaces. Further considerations include functional, aesthetic, performance and conformance categories. However, poke-through resistive touch displays recently yield a more modern touch lens in the integrated centre control panel (http://www. automotive-eetimes.com/en/modern-automotive-display-touch-lens-interface.html? cmp_id=71&news_id=222902655).

Thus, the bulky rims and knobs of the past are expiring, mutating to smooth operating surfaces for the highest functionally and perfect, futuristic cockpit designs. A forerunner of these ideas is the Porsche Cayenne. In 2008, automotive supplier Schreiner PrinTronics demonstrated its core competency of functional printing by fitting the show car's interior with blue light-emitting electroluminescent films, creating a distinctive ambient light experience. With their unconstrained geometric shape and multiple colours, they could open up new design options. It is conceivable that they will eventually be integrated within the seat covers that change colour at the press of a button. Then, the same technology could also be used to cover the whole of the roof lining with an array of LEDs to provide the interior lighting (Fihn, 2007).

Despite plastic films having relatively low durability, further research is certainly needed. It is hoped that flexible displays will succeed in breaking through into devices for the mass market, that the manufacturing costs will fall and their use in the automobile will as a result become more attractive to manufacturers. Although smart-material-based components are currently implemented by OEMs (Smart Materials, 2012), a real 'killer application' is still being sought.

14.5 Conclusions

Integrated systems with embedded electrical, optical and sensing functionalities will be developed to realize future conformable components for several purposes useful and applicable within several market sectors. In general, these offer greater freedom to create new types of products with attributes such as flexibility, lightweight, conformability, low costs, miniaturization and functional integration.

Integration of printing techniques and over-moulding processes as well as the resulting higher added manufacturing value require that a corresponding productivity is guaranteed only if some technical achievements have been performed. Because electronics and plastics coexist together in integrated components, improvement in validation procedures and growth in the accessibility of durable and high-quality products is needed to meet industry requirements and automotive necessities.

Next, the printed bendable electronics revolution will target the major megatrend of today as improved functionalities, manufacturability and cost/price reduction.

Addressing these issues, printed bendable electronics afford the most immediate opportunities within novel market sectors. At the systems levels, the short-to-medium opportunities concern flexible mobile displays, conformable lighting, powered smart cards, embedded switches and autonomous systems. To deliver more performing, less expensive and fashionable integrated systems with increasingly tighter time-to-market constraints imposed by worldwide competitiveness, the future development process for electronic systems must provide solutions to:

- Design complex functionality and distributed architectures consisting of several subsystems with constraints on non-functional metrics such as cost, power consumption, weight, position and reliability
- Overcome current limitations in materials compatibility, component miniaturization and active element manufacturability
- Integrating the functionality onto the components of a distributed architecture through reliable high-throughput manufacturing processes such as printing and over-moulding

So far, at the manufacturing level, these imply faster printing equipment, improved processing integration and materials compatibility.

References

Amin, S., & Amin, M. (2011). *Reviews on Advanced Materials Science, 29*, 15−30.

Applications of thin coatings in automotive industry (Vol. 24) (September 2007). Issue 1.

Automotive news. (2008). Automotive World Ltd.

Bao, Z., Rogers, J. A., & Katz, H. E. (1999). *Journal of Materials Chemistry, 9*, 1895.

Bao, Z. (2000). *Advanced Materials, 12*, 227.

Blayo, A., & Pineaux, B. (2005). *Joint sOC-EUSAI conference, Grenoble*.

Clark, T. A., & Wagner, J. R., Jr. (July 1, 2002). Film properties for good performance on vertical form-fill-seal packaging machines. *Journal of Plastic Film and Sheeting, 18*, 145−156.

Electronics manufacturing by inkjet printing, IPC printed circuit Expo, APEX & designer Summit Proceedings.

Fihn, M. (February 2007). Automakers are keeping a sharp eye on flexible displays. *Photonics Spectra*. Pittsfield MA, USA, 2007.

Flexible electronics: materials and applications. In Salleo, A., & Wong, W. S. (Eds.), *Electronic materials: Science & technology*, (2009).

Frost, & Sullivan. (31 March 2006). *Advances in plastics for electronic devices (Technical Insights)*. D624.

Geyer, A., Scapolo, F., Boden, M., Döry, T., & Ducatel, K. (March 2003). *Future of manufacturing in Europe 2015−2020*.

Gilleo, K. (Ed.). (1992). *Handbook of flexible circuits*. London: Chapman & Hall.

Harrop, P. (2007). *Developments in printed and thin film electronics*. Cambridge, UK: Printed Electronics. Europe 2007.

Hu, Y., Cao, F., Li, F., Ni, G., & Cui, X. (2011). *Reviews on Advanced Materials Science, 29*, 150−155.

Kamyshny, A., Steinke, J., & Magdassi, S. (2011). *Open Applied Physics Journal, 4*, 19−36.

Kim, J. S., Moon, J. H., Jeong, S. H., Kim, D. J., & Park, B. K. (August 9, 2007). *US20070180954A1*.

Kipphan, H. (2001). *Handbook of print media*. Heidelberg, Germany: Springer-Verlag.

Lee, Y., Choi, J.-R., Lee, K. J., Scott, N. E., & Kim, D. (2008). *Nanotechnology, 19*(415604), 1−7.

Liu, J. (1999). *Conductive adhesives for electronics packaging*. Port Erin, Isle of Man: Electrochemical Publications Ltd.

Magdassi, S., Grouchko, M., & Kamyshny, A. (2010). *Materials, 3*, 4626−4638.

Press releases LOPE-C, printed electronics Powers 'Car of the future' (Tuesday, February 22, 2011).

Rigney, J. (2004). Materials and processes for high speed printing for electronic components. proceedings of IS&T's NIP20. In *International Conference of digital printing technologies* (pp. 275−278).

Rogers, J. A., Bao, Z., Makhija, A., & Braun, P. (1999). *Advanced Materials, 11*, 741.

Rosato, D. V. (Ed.). (2011), *Plastics technology handbook* (Vol. 2). Momentum Press.

Sankir. N.D. Flexible electronics: Materials and device fabrication (dissertation thesis) Copyright 2005.

Schüßler, J. (2008). *In-line plasma treatment of plastics*. GAK, issue.

Silver inks and pastes markets − 2012, NanoMarket, December 12, 2011.

Technology map "Smart materials". (2012). Strategic Business Insights.

Towards green electronics in Europe, strategic research agenda organic & large area electronics. (2009).

M6A0. *2020 vision of the global automotive industry* (June 18, 2012). Frost & Sullivan.

Wong, C. P. (Ed.). (2010). *Nano-bio- electronic, photonic and MEMS packaging*. Springer Science & Business Media, LLC.

Woo, K., Kim, D., Kim, J. S., Lim, S., & Moon, J. (2009). *Langmuir, 25*, 429−433.

Chemical sensors using organic thin-film transistors (OTFTs)

15

M. Demelas, S. Lai, P. Cosseddu, A. Loi, M. Barbaro, A. Bonfiglio
University of Cagliari, Cagliari, Italy

15.1 Introduction

Organic electronics has attracted considerable attention over the past few decades because it offers the opportunity to produce electronic systems with multiple functionalities over large areas at low cost and possibly on flexible substrates (Braga & Horowitz, 2009; Kalyania & Dhobleb, 2012; Lin & Yan, 2012; Su, Lan, & Wei, 2012). After organic light-emitting diodes and displays based on organic devices, the era of another exciting application for this technology, namely sensors based on organic devices, is emerging. They may be fabricated at extremely low cost, with fast and cheap fabrication technologies over large areas, which allows ubiquitous distribution in the environment and implementation of the concept of ambient intelligence.

Through the point of view of sensing efficiency, efficient sensors may be fabricated starting from the concept of organic thin-film transistors (OTFT). One of the main advantages of employing these devices for sensing applications is that they are active devices; many different electronic parameters (mobility, threshold voltage, contact resistance, etc.), not just one as in chemo/piezoresistive sensors, for instance, can be extracted from their electrical characterization. Therefore, they are multiparametric sensors and offer the possibility of using a combination of variables to characterize their response to the parameter to be sensed. Moreover, active sensors combine in the same device both switching and sensing functions, and the electrical response of the device to a certain external stimulus can be locally amplified by the transistor itself, allowing the user to easily obtain sensing matrices of limited size and improved reliability.

Another important feature is that an OTFT is a multilayered structure dominated by the physical properties of several material interfaces, each of which can be employed to test different parameters; as a consequence, it is virtually possible to use a single device to achieve multimodal sensing ability.

Capacitive changes in the gate dielectric or conduction changes in the active layer can be employed to detect an external stimulus directly: for instance, a mechanical stimulus or even a chemical agent (gas or liquid) that can induce variations in the electrical response of the device when interacting with the material. In addition, these devices can be connected in series with a chemo/piezoresistive material to detect some sort of external stimulus indirectly. Moreover, the device electrodes may also be functionalized with specific self-assembled monolayers to achieve chemical sensing functionalities. In the following, a panoramic description of these different possibilities will be given.
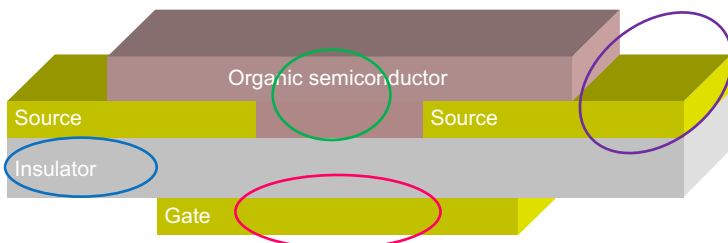
Figure 15.1 Bottom gate, bottom-contact organic thin-film transistors (OTFT) showing the different areas of the device that could be employed for sensing applications.

OTFT-based sensors are generally implemented using bottom-gate structures (see Figure 15.1), i.e., they are based on a thin film of an organic semiconductor deposited on top of a dielectric-coated conductor, acting as a gate. In these structures the organic semiconductor is exposed and works as a sensing layer and the sensing mechanism is based on direct interaction between the semiconductor and the analyte to be tested. Except for a few examples reported in the literature, OTFTs are not suitable in aqueous media: the high voltages needed to operate the device may cause electrochemical reactions and degradation processes that damage the device and affect reproducibility of the results. As a consequence, this structure was mainly used to create sensors operating in the dry state. The most important achievements obtained with OTFT-based sensors concern gas sensors and DNA sensors.

15.2   Gas and vapour sensors

Organic semiconductors and conducting polymers are suitable as sensing materials for gas sensors and e-noise fabrication because they may have a broad variety of interactions with gases and vapours.

Compared with vapour sensors based on metal-oxide−active layers, gas sensors based on organic semiconductors are usually characterized by higher chemical sensitivity and lower power consumption. Since 2000, development of low-cost fabrication techniques such as ink jet printing have boosted interest in this area.

As first reported in Torsi, Dodabalapur, Sabbatini, and Zambonin (2000), OTFT-based sensors allow the unambiguous identification of chemical species because they work as multiparameter sensors. In addition to semiconductor bulk conductivity, which is a specific property of organic thin film, two-dimensional field-induced conductivity, transistor field-effect mobility (μ), and transistor threshold voltage (V_{TH}) may separately measure the influence of the analyte. The authors created a bottom-contact OTFT based on 1,4,5,8-naphthalene tetracarboxylic dianhydride (NTCDA) as the active layer. In the off state the OTFT works as a chemoresistor; the variation in the conductivity of the active layer upon exposure to the chemical species under examination is derived from the drain current (see Figure 15.2).

When the gate is biased, the surface potential at the interface between the active layer and the gate causes highest occupied molecular orbital and lowest unoccupied
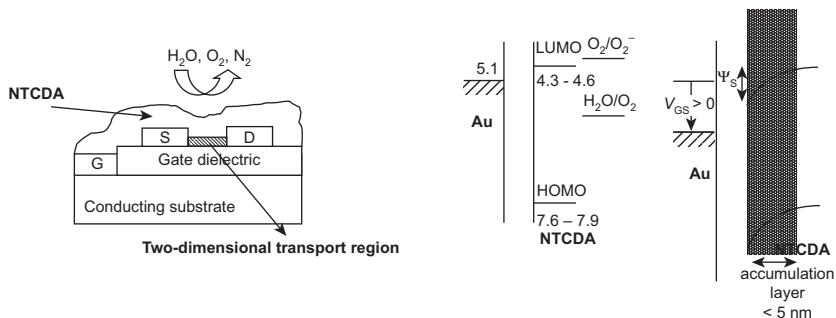
Figure 15.2 Structure of the NTCDA-based gas sensor (left) and energy band diagram for the *n*-type NTCDA-based transistor: at open circuit (left) side and at positive gate bias (right). *Source:* Reprinted from Torsi et al. (2000), Copyright (2003), with permission from Elsevier.

molecular orbital bending, which gives rise to a layer in which two-dimensional transport occurs. In general, threshold voltage and mobility depend on the volume density of the trapped charges and on the potential barrier at the contacts; because several chemical species cause charge trapping—detrapping processes, interaction of the transistor active layer with reactive molecules causes variations of V_{TH} and μ and changes in the corresponding drain currents. Therefore, molecular recognition is obtained by subtracting the device's response, obtained by exposing the semiconductor to the analyte, from the one obtained without the analyte application. The OTFT *trans*-characteristics are usually evaluated at a fixed drain potential, chosen in the saturation region.

The extent and nature of the response in an OTFT-based gas sensor depend on the mechanism associated with the semiconductor—analyte pair. As a consequence, combinatorial arrays of sensors able to respond differently to the components of an odour mixture can be achieved. In 2001, Crone et al. (2001) reported that OTFT sensors, based on different types of organic semiconductors, are sensitive to different types of primary alcohols, starting from butanol to nonanol, and that the degree of response to odour increases as the length of the semiconductor hydrocarbon end-group increases. Figure 15.3 summarizes the responses of 11 organic semiconductors to 16 vapours.

In many cases, the sensing mechanism in OTFTs results from the interaction between the gas molecules and the organic semiconductor: The larger the surface of interaction, the higher the potential for sensitivity of the device. Several investigations were carried out to elucidate the role of surface morphology in gas sensors. Someya, Katz, Gelperin, Lovinger, and Dodabalapur (2002) fabricated different sets of OTFTs based on α,ω-dihexylquarterthiophene (DHα4T) and modulated the active layers' morphological properties by changing the deposition parameters. In this way, they investigated the influence of the density of grain boundaries on the sensitivity of the fabricated sensors. Interestingly, a small response to vapour analyte was recorded in devices with no grain boundaries or with only a single grain boundary inside the active region, whereas higher current variations were measured in devices including polycrystalline films. These results demonstrated that the interaction between the organic semiconductor and the gaseous analyte mainly occurs at the grain boundaries. Further
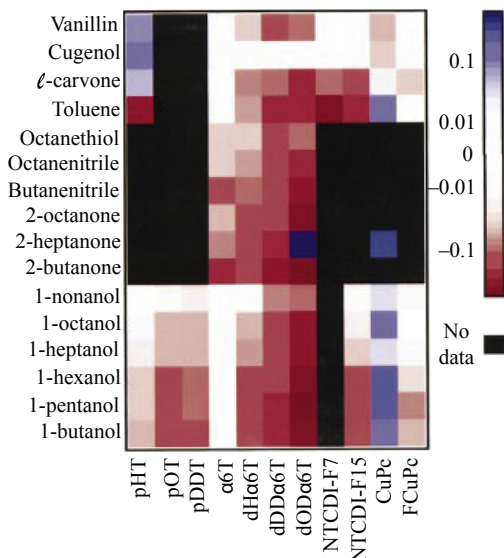
Figure 15.3 Effect of 16 analytes on 11 sensor materials. Black indicates that data are not available; white indicates a negligible response; blue shows positive changes in the sensor current; red shows decreases. Can be seen in Plate III (see colour section between pages 224 and 225). *Source:* Reprinted with permission from Crone et al. (2001), Copyright 2001, AIP Publishing LLC.

confirmation was obtained by Torsi et al. (2002), who investigated the roles of temperature and thickness of the active layer in determining the sensitivity of the device. Wang, Fine, and Dodabalapur (2004) demonstrated that the results obtained by Someya et al. (2002) and Torsi et al. (2002) could be extended to the nanoscale dimension.

Several strategies can be developed to improve the selectivity and sensitivity of OTFT gas sensors. To discriminate between vapours of small-molecule analytes, Sokolov et al. used calixarene as container molecules on the surface of an existing OTFT, so that the tunable nature of the container cavity served to trap desired molecular shapes and functionalities with typically high selectivity. Finally, Torsi et al. (2008) implemented a bilayer ultrasensitive OTFT able to combine field effect and chiral recognition properties. By means of this device, it was possible to discriminate with unprecedented sensitivity between two enantiomers in a mixture.

15.3 Humidity sensors

Pentacene is a commonly used *p*-type organic semiconductor because of its relatively high mobility. In 2002, Zhu, Mason, Dieckmann, and Malliaras (2002) demonstrated that it is sensitive to H_2O vapour. By exposing the OTFT to vacuum and N_2 gas with different levels of relative humidity (RH), a change in the saturation current by as much as 80% was recorded when the RH changed from 0% to 30%. The same was for the other OTFT-based gas sensors, in which the organic semiconductor works as

a sensitive layer; the sensing mechanism can be ascribed to diffusion of the vapour into crevices between the grains of the active layer.

Although the OTFT structure is by far the most used and tested method for gas and vapour detection, organic electrochemical transistors (OECTs) work for vapour detection as well. In OECTs the source and drain contacts are connected by a conductive polymer that acts as a channel; the gate electrode is separated from the active layer by the electrolyte, which in OECTs works as an ionic-conductive medium. When a proper bias is applied to the gate contact, ions from the electrolyte penetrate the polymer bulk. The interaction between the active layer and the analyte may induce changes in charge carrier density, charge carrier mobility, trap density, charge injection, and other parameters that can alter the measured source-drain current and sensor response. Therefore, the gate potential modulates electrochemical de-doping of the semiconductor.

Nilsson, Kugler, Svensson, and Berggren (2002) created a structure based on the working mechanism of OECTs to construct a humidity sensor. An OECT was fabricated by combining an OECT based on (3,4-ethylenedioxythiophene):poly(styrene sulfonate) (PEDOT:PSS) and Nafion, which is a proton conducting film. The OECT worked as a transducer whereas Nafion film worked as a receptor. (3,4-Ethylenedioxythiophene): poly(styrene sulfonate) was printed onto flexible polyester foils or thin papers, which were tested as substrates, to obtain flexible devices. Through an opening in a spacer, Nafion film was deposited on top of the transistor channel and the gate contact. Figure 15.4 shows a schematic representation of the device and experimental results.

The drain-source current drops two orders of magnitude when the relative air humidity changes from 40% to 90%. Therefore, the poly(3,4-ethylenedioxythiophene): poly(styrene sulfonate) (PEDOT:PSS) can be switched between different redox states by mobile ions in the electrolyte, addressed by the potential applied to the gate electrode, depending on the ionic conductivity of the Nafion film.
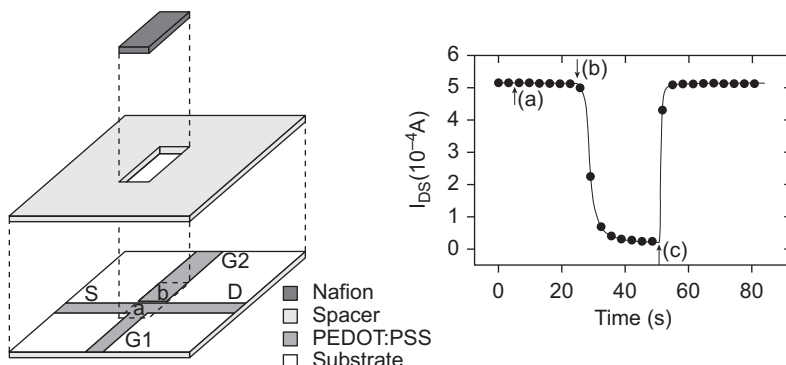
Figure 15.4 Schematic structure (left) and sensor response consecutively recorded under different gate bias and humidity conditions (right): 1.2 V and 30% in (a), 1.2 V and 80% in (b), and 0 V and 80% in (c).
Source: Reprinted from Nilsson et al. (2002), Copyright (2002), with permission from Elsevier.

15.4 pH detection

A wide range of chemical reactions depends on acid–base equilibrium. pH fluctuations can heavily influence the rates of biological reactions or even make them possible or impossible by activating or deactivating enzymes. As a consequence, pH detection may be considered interesting for other potential applications. Most of the reported sensors for pH detection are ion sensitive OFETs (ISOFETs); this refers to the chemical sensitivity of the device owing to exposure of the insulating layer (and not of the semiconductor) to the solution. This structure allows one to overcome the degradation phenomena of the semiconductor that generally occur in OTFTs operating in liquids. To expose the insulating layer to the electrolytic solution, the ISOFET is designed in a top-gate configuration and the gate is a reference electrode merged in the electrolyte. As a consequence, the organic semiconductor is not directly exposed to the measurement environment, thus preventing degradation. Because the reference electrode is characterized by a nonpolarizable interface, it guarantees a constant potential drop at the interface with the electrolyte. As a matter of fact, the electrolyte and the reference electrode form an ionic gate. The arrangement of the ions in solution determines the potential drop on the electrolyte–dielectric interface, which is measured through the field-enhanced conductivity of the organic semiconductor. In this way, as for OTFTs, the source-drain current is modulated by the charge variation at the electrolyte–insulator interface.

Bartic and Borghs (2006), Bartic, Palan, Campitelli, and Borghs (2002) developed the first charge transducer based on an ISOFET structure using silicon nitride (SiN$_4$) as a sensing layer. Depending on the pH of the solution, it causes the following reactions:

$$SiOH \rightleftharpoons SiO^- + H^+$$

$$SiOH + H^+ \rightleftharpoons SiOH_2^+ \tag{15.1}$$

$$SiNH_2 + H^+ \rightleftharpoons SiNH_3^+$$

By postulating charge neutrality for the whole electrolyte–insulator–semiconductor structure, the site-binding theory gives the relationship between the electrolyte–insulator interface potential and the charge that accumulates at the interface at a given pH of the electrolyte. Therefore, the gate voltage results from the sum of a constant term plus a further term associated with the chemistry-dependent potential drop at the solution–dielectric interface. When a pH change occurs in the electrolyte solution, the insulator surface changes; as a consequence, the channel conductance changes as well. Poly(3-hexiothiophene) (P3HT) was employed as the active layer of the device. Figure 15.5 schematically represents the device and the stability and reproducibility of the current response in time after successive immersions in different pH buffers (Bartic et al., 2002).

The structure described by Bartic et al. is not flexible and cheap enough to use for disposable devices. A few flexible ISOFETs for pH detection are reported in the literature. Gao, Zhu, Choi, and Ahn (2003) created a device meant to be integrated with
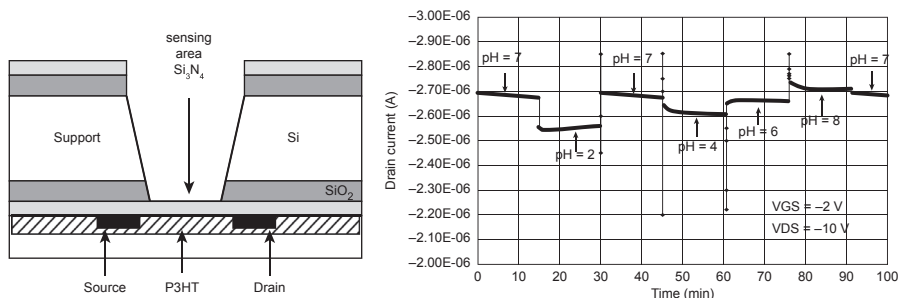
Figure 15.5 Device (left: with kind permission from Springer Science and Business Media (Bartic & Borghs, 2006) (Figure 15.4a)) and output characteristics recorded in different pH buffer solutions using the same biasing condition (right: reprinted from (Bartic et al., 2002), Copyright (2002), with permission from Elsevier)

disposable lab-on-a-chip and in vivo applications using tantalum pentoxide (Ta_2O_5) as a sensing layer. Loi, Manunza, and Bonfiglio, (2005) made a pH sensor using a 900-nm-thick Mylar sheet as both dielectric and substrate. Diallo, Lemiti, Tardy, Bessueille, and Jaffrezic-Renault (2008) created a flexible device using a thin hydrogenated silicon nitride layer (SiN:H) as a sensitive layer.

In more recent years, a novel structure for chemo- and biosensing in liquid environment was developed and tested. The device, named an organic charge-modulated field-effect transistor (OCMFET), is based on a floating gate field-effect transistor that acts as a charge sensor. Every chemical and biological reaction that can determine variations in the charge immobilized on the floating gate can be detected and transduced by modulating the output current of the device.

Compared with ISOFETs, the OCMFET has many advantages. First, it does not require a reference electrode. The operating point of the device is set by the effective voltage of the floating gate (V_F), which is determined by several contributions. The operating point is mainly set by the voltage (V_G) applied to a control capacitor (C_{CF}), but it also depends on the polarization of the source and drain electrodes through the parasitic capacitances of the transistor, C_{SF} and C_{DF}, respectively. Figure 15.6 shows an electrical model of the device.
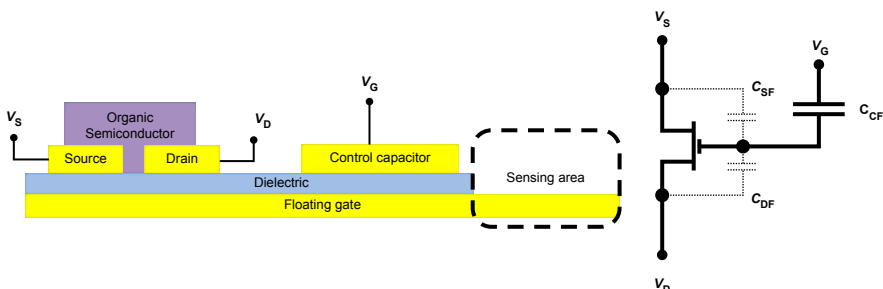
Figure 15.6 Organic charge-modulated field-effect transistor structure (left) and electrical model (right).

Charge sensitivity is obtained by immobilizing a charge Q_S onto the portion of the floating gate exposed to the environment (referred to here as the sensing area). From the Gaussian equation applied to the floating gate, an expression for the floating gate voltage can be easily derived:

$$V_F = \frac{C_{CF}}{C_{CF} + C_{SF} + C_{DF}} V_G + \frac{C_D}{C_{CF} + C_{SF} + C_{DF}} V_D + \frac{Q_S + Q_0}{C_{CF} + C_{SF} + C_{DF}}$$

(15.2)

where Q_0 is the native charge in the floating gate and a perfect induction of the charge to be sensed (Q_S) is supposed. The last equation shows that a variation in Q_S can modulate the actual voltage that drives the transistor, and thus determine the variation in its output current. By introducing the threshold voltage of the device, it is possible to describe the modulation of the operating point of the device with a shift in the threshold voltage, according to the equation

$$\Delta V_{TH} = \frac{Q_S}{C_{CF} + C_{SF} + C_{DF}}$$

(15.3)

The OCMFET approach was specifically conceived to overcome some of the problems of chemo- and biosensing based on organic transistors. A main innovation is that the sensing area does not coincide with the organic semiconductor, which prevents the degradation of performance of the transistor owing to the environment of the measurement. Moreover, the sensing mechanism does not rely on the choice of organic semiconductor and can be tailored to different applications by choosing the most appropriate sensing layer. Finally, the working mechanism does not depend on the choice of the materials employed in fabricating the device.

In Caboni, Orgiu, Barbaro, and Bonfiglio (2009) and Caboni, Orgiu, Scavetta, Barbaro, and Bonfiglio (2009), Caboni et al. demonstrated the feasibility of the OCMFET approach to pH monitoring in acid solutions. The device was fabricated using 1.5-μm-thick Mylar foil both as substrate and gate dielectric. The floating gate and sensing area were patterned on one side of the device whereas the transistor and control capacitor were fabricated on the other side, thus preventing any interaction between the liquid measurement environment and the organic semiconductor. The structure was completed with a PDMS flow cell and a capillary system, which allowed the inlet and outlet of the solutions onto the sensing areas. The pH sensitivity was obtained by functionalizing the gold surface of the sensing area with an amino-terminated self-assembled monolayer. In acid solutions, the aminic group of the molecules protonate according to the equation

$$NH_2 + H^+ \rightleftharpoons NH_3^+$$

(15.4)

As a result, the positive charge anchored onto the sensing area increased as the pH decreased, thus determining an absolute increase in the threshold voltage. Because pentacene (a p-type organic semiconductor) was employed as an organic
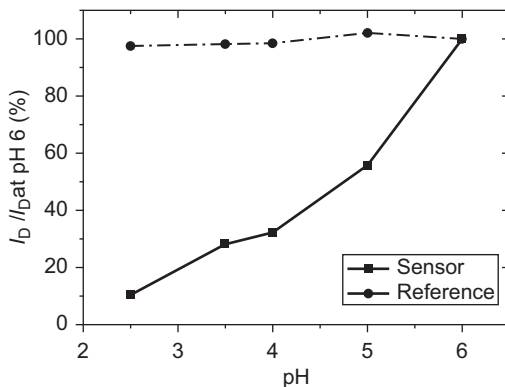
Figure 15.7 Trend of maximum drain currents with varying the pH. Current values are normalized with reference to current measured at pH 7 and are those recorded at $V_{SG} = 100$ V and VSD $= 100$ V.
Source: Reprinted with permission from Caboni, Orgiu, Scavetta, et al. (2009), Copyright 2009, AIP Publishing LLC.

semiconductor, the shift of the threshold voltage finally determined the decrease in the output current of the device.

To control the response of the device accurately during the experiment, two OCMETs were fabricated on the same substrate. The first acted as a sensor and was subjected to solutions with different pHs. The second acted as a reference and was maintained in a constant pH 7 solution. As shown in Figure 15.7, variation in the threshold voltage is obtained by varying the pH of the sensor, whereas that of the reference is almost constant in a pH 7 solution.

15.5 Glucose detection

Glucose level monitoring is vital for millions of people with diabetes mellitus. Much research has gone into glucose detection, and glucose sensors based on organic transistors have been created by using different architectures.

Bartic, Campitelli, and Borghs (2003) made an ISOFET based on P3HT as an organic semiconductor and tantalum pentoxide as a gate dielectric, They anchored the glucose oxidase (GOx) enzyme onto the dielectric surface. Sensitivity to glucose resulted from the catalytic properties of the enzyme and the sensitivity of the dielectric layer to pH. By catalyzing glucose, GOx converts glucose into gluconic acid and H_2O_2. Driven by the glucose concentration, local variation in pH is thus produced. An increase in gluconic acid causes a decrease in pH and a decrease in pH in the insulating layer affects the conducting channel properties of the channel. Figure 15.8 compares the drain-current values recorded in a buffer phosphate solution with those obtained in the glucose solution at two different biases of the reference electrode.

Liu, Agarwal, and Varahramyan (2008) created a glucose sensor based on an OTFT structure with PEDOT:PSS as a semiconductor channel and GOx as a sensitive layer.
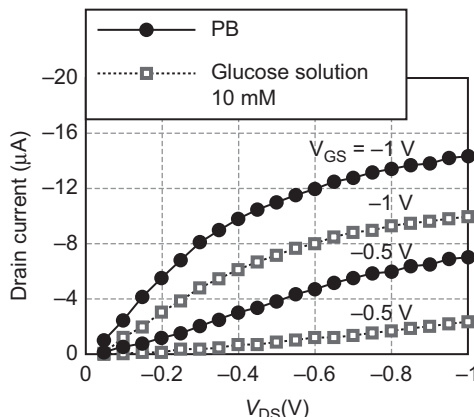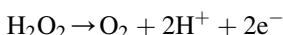
Figure 15.8 Characteristics at two different biases of the reference electrode.
Source: Reprinted with permission from Bartic et al. (2003), Copyright 2003, AIP Publishing LLC.

The sensor's working mechanism is based on the redox property of PEDOT:PSS and the oxidation of H_2O_2 produced by the chemical reaction catalyzed by the GOx. Poly(3,4-ethylenedioxythiophene):poly(styrene sulfonate) works as a semiconductor when it is oxidized whereas it behaves as an insulator when it is in the reduced state. H_2O_2 may work as a strong oxidant according to the following reaction

$$H_2O_2 \rightarrow O_2 + 2H^+ + 2e^-$$

When the hydrogen peroxide is produced next to the channel, it oxidizes, causing the reduction of PEDOT:PSS, which in turn becomes less conductive. The de-doping effect produced by the H_2O_2 can be removed by applying a negative bias to the gate contact as the electrons are pushed away from the channel. Poly(3,4-ethylenedioxythiophene):poly(styrene sulfonate) works as a *p*-type semiconductor, i.e., the transistor is switched on when the gate is negatively biased; in the presence of glucose, this behaviour is further enhanced because electrons are moved away from the channel (see Figure 15.9).

Zhu et al. (2004) demonstrated that an OECT based on a PEDOT:PSS channel and a Pt wire as a gate electrode can work for glucose detection with a limit of 0.1 mM L^{-1}. In its pristine state, PEDOT:PSS is doped by PSS and positively charged (PEDOT$^+$). By application of a negative bias to the gate electrode, positively charged ions penetrate into the channel from the solution (phosphate buffer solution (PBS), pH 7.14); they bind to the PSS and cause the reduction of PEDOT. This de-doping effect leads to a decrease in conductivity, as shown in Figure 15.10.

The current modulation did not change upon the addition of GOx to the electrolyte, whereas a dramatic current decrease (70%) was observed when glucose was added to the solution. Because GOx catalyzes the production of H_2O_2 and gluconic acid, the current change may be attributed to both of these products. Nevertheless, they proved
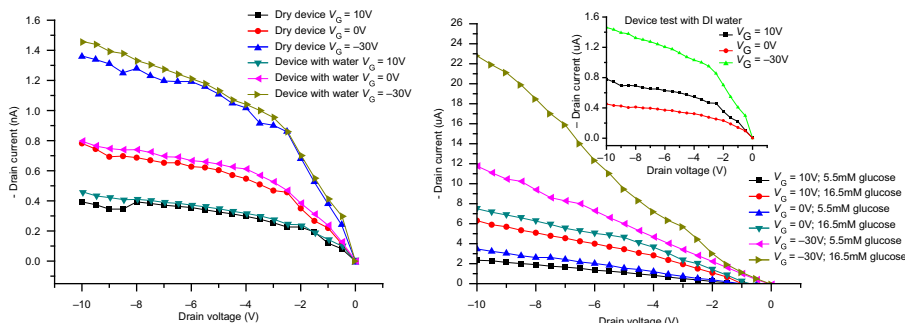
Figure 15.9 Drain current versus drain potential (left) and gate potential (right) showing sensor response recorded under different experimental conditions. Can be seen in Plate IV (see colour section between pages 224 and 225).
Source: Reprinted from Liu, Agarwal, and Varahramyan (2008), Copyright (2008), with permission from Elsevier.
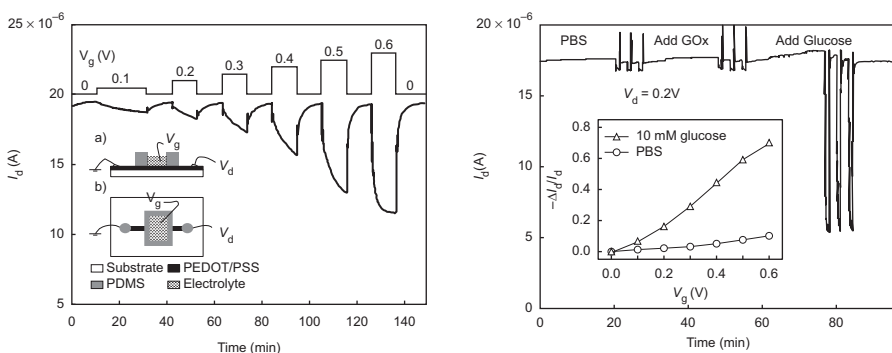
Figure 15.10 Current modulation in PBS of the device represented in the inset (left) and current changes obtained in the presence of GOx and glucose (right) (Zhu et al., 2004).
Source: Reproduced by permission of the Royal Society of Chemistry.

that the current modulation was pH-independent in standard buffer solutions with a pH ranging from 5 to 9. As a consequence, the sensing mechanism has to be attributed to the electrochemical mechanism of operation concerning H_2O_2. H_2O_2 oxidized at the Pt electrode whereas, to maintain charge balance, $PEDOT^+$ of the active channel was reduced (Nikolou & Malliaras, 2008). Compared with the glucose sensor based on an OTFT structure, the OECT structure allows the transducer to be decoupled from the recognition element, thus enabling simultaneous optimization of both. Moreover, the previous device had low detection times because glucose did not have to diffuse inside the polymer to find the enzyme.

Macaya et al. (2006) investigated detection times in this kind of sensor and which demonstrated that the lower and upper detection limits could be modulated by varying the gate voltage.
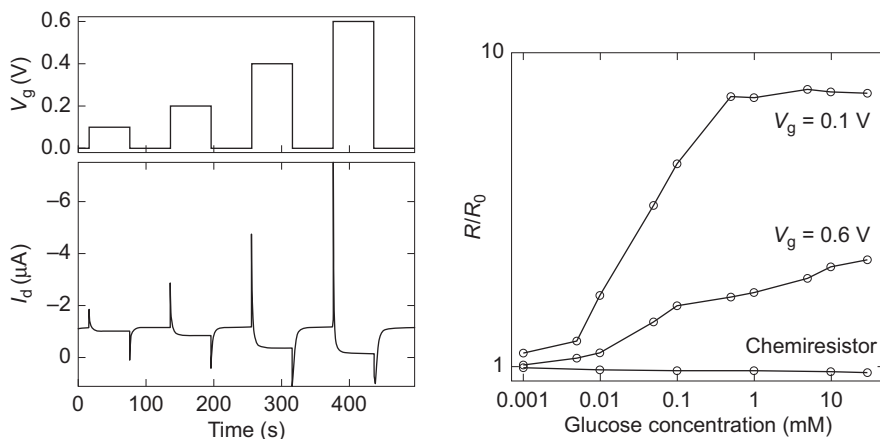
Figure 15.11 Temporal response of drain current as a function of the gate voltage (left) and normalized transistor response at different gate biases to different glucose levels (right). *Source:* Reprinted from Macaya et al. (2006), Copyright (2006), with permission from Elsevier.

Results in Figure 15.11 (left-hand side) show that the drain current saturates within 60 s and glucose detection is obtained ranging from 1 µM to 0.5 mM, depending on the gate potential. It is interesting that OECTs allows glucose detection with micromolar sensitivity for creating sensors for glucose detection in the range of the typical concentrations of glucose in human saliva, which varies between 0.008 and 0.21 mM (Yamaguchi, Mitsumori, & Kano, 1998). Figure 15.11 (right-hand side) shows the sensor response when it is used as a chemoresistor: that is, without applying a gate bias. The role of the gate is therefore confirmed by the fact that the sensor response is negligible with respect to that obtained with the device working as a transistor. Bernards et al. (2009) later obtained a universal curve that describes the operation of this device by detecting the transfer characteristics at various glucose concentrations; Yang et al. (2009) demonstrated that these sensors are promising candidates for system-on-a-chip applications.

Because the use of a Pt wire complicates fabrication of the device and increases costs, commercial glucose sensors sensitive to glucose levels comparable to those of human saliva need to use a different gate material. Shim et al. demonstrated that an OECT made entirely of PEDOT:PSS can work as a glucose sensor by using PEDOT:PSS together with the redox ferrocene [bis(5-cyclopentandienyl)iron] (Fc)/ferricenium ion couple. Because of its low redox potential, the ferrocene/ferrocenium couple can shuttle electrons from the reduced enzyme to the PEDOT:PSS electrode, as shown in the top image in Figure 15.12; the bottom image in Figure 15.12 reports the normalized response to glucose concentration.

Consistent with the results obtained by Macaya et al. when the transistor well is preloaded with a mixture that does not contain ferrocene, the normalized response is small; this result confirms that the redox couple is essential for a transistor working with a PEDOT:PSS gate. On the other hand, when using ferrocene as mediator, the normalized response starts at 0.13 for the 1 µM solution and increases to 0.57 for the 100 mM one.
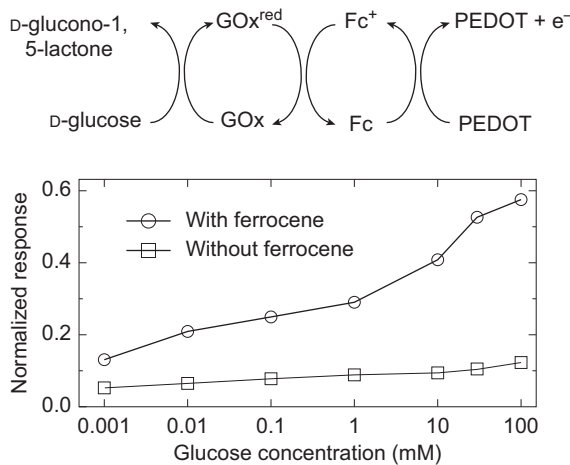
Figure 15.12 Reaction cycles for detection of glucose in devices with a PEDOT:PSS electrode and a ferrocene mediator (top); normalized response to glucose concentration for OECTs preloaded with a mixture with and without the ferrocene mediator (bottom).
Source: Reprinted from Shim et al. (2009), Copyright (2009), with permission from MDPI.

15.6 Deoxyribonucleic acid detection

Thanks to the peculiar characteristics of thin-film technology, deoxyribonucleic acid (DNA) sensing by means of organic transistors has been receiving increased interest. With respect to a standard silicon ISFET-based DNA sensor, field-effect modulation by means of the intrinsic negative charge of DNA backbones can be exploited without needing a reference electrode in solution to set the operating point of the device. Moreover, transduction mechanisms other than field-effect modulation can be employed for DNA sensing in both the dry and wet state.

The first DNA sensor based on an organic transistor was reported in 2007 by Zhang and Subramanian (2007). The DNA recognition occurred through electrical detection of DNA hybridization by measurements performed in the dry state. Different from the ISFET-based device, field-effect modulation was not used as a transduction mechanism; negatively charged DNA chains act as a dopant on the ultrathin (15 nm) pentacene semiconductor layer, attracting holes in the transistor channel and causing an increase in current and a positive shift of the threshold voltage. This working mechanism was further investigated by Stoliar et al. (2009).

Physical absorption of single-stranded (ss) and double-stranded (ds) DNA oligonucleotides was realized and statistically evaluated (Figure 15.13). The doping effect recorded after hybridization was lower than that measured after ssDNA immobilization. A possible explanation for this result was ascribed to the reduced immobilization efficiency of dsDNA with respect to ssDNA. According to the authors, differential sensitivity with respect to ssDNA and dsDNA doping would enable the unambiguous detection of DNA hybridization.
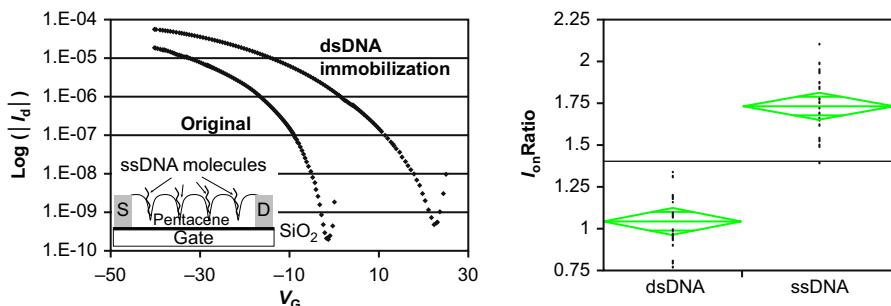
Figure 15.13 Organic thin-film transistor DNA sensor ($W/L = 10$) (left) and experimental results obtained by Zhang (Zhang & Subramanian, 2007): transfer curves obtained with drain voltages at -45 V (left) and differential sensitivity of ssDNA and dsDNA obtained as the ratio between the post−DNA-exposure drain saturation current and the original TFT one (right). *Source:* Reprinted from Zhang and Subramanian (2007), Copyright (2007), with permission from Elsevier.

In later work, Zhang, Jagannathan, and Subramanian (2010) further investigated the working mechanism of DNA sensors using several techniques including Kelvin probe microscopy, space charge limited current (SCLC), and time-of-flight secondary ion mass spectrometry analysis. Moreover, attempting to produce a sensor for label-free readout of on-chip DNA hybridization, they presented a novel photolithography-based method that allows building microfluidic systems on organic semiconductors to deliver the DNA solution automatically to the detection sites. They demonstrated that variation in the data is reduced when using the microfluidic system for DNA delivery and when obtaining regular active surfaces by depositing the semiconductor films at a low rate.

A similar structure was employed by Kim, Jha, Chand, Lee, and Kim (2011), but with a much thicker (70 nm) pentacene layer. In this way, effective field-effect modulation was obtained. Similar to Zhang and Subramanian (2007), physio-adsorption of DNA molecules on the pentacene surface was used, but in this case, because the DNA molecules were anchored atop a much thicker layer, DNA negative charges removed holes from the channel, causing a decrease in the transistor current (Figure 15.14).
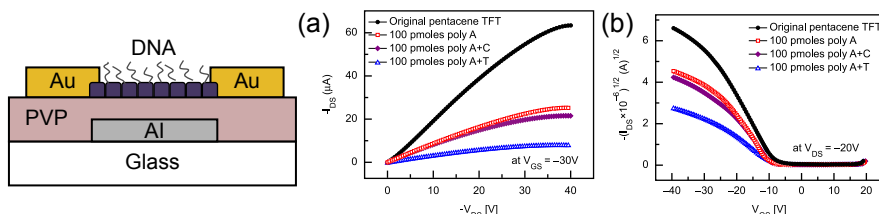
Figure 15.14 Sensor developed by Kim et al. (2011): schematic and sensing mechanism (left); (a) output and (b) transfer characteristics of the original device, after deposition of ssDNA (poly A), of a non-complementary (polyC) and complementary target (polyT). *Source:* Reprinted from Kim et al. (2011), Copyright (2011), with permission from Elsevier.

Approaches based on immobilization of DNA probes on the active layer surface present an important drawback. Organic semiconductors are generally sensitive to environmental conditions, and pentacene in particular is sensitive to exposure to ionic solution. Because the functionalization and hybridization procedures generally take place in liquid, they can compromise the device's stability and repeatability. Aiming to reduce semiconductor degradation, a different approach was proposed by Yan, Mok, Yu, Chan, and Yang (2009). The DNA recognition was achieved by comparing the electrical response of a group made up of three bottom-gate transistors (see Figure 15.15). According to the authors, DNA chains determine variation in the contact resistance of the semiconductor and electrodes; in particular, if hybridization occurs and dsDNA is formed, contact resistance results are higher than those obtained with functionalization with ssDNA. To compare variations in contact resistance, they functionalized one device with ssDNA and one with dsDNA; the third was left as a control.

Figure 15.14 show the output and transfer characteristics of three groups of devices: under the same bias, higher currents are recorded in the control device, intermediate currents are recorded in the device with ssDNA, and lower currents are noted in the device with dsDNA. To obtain a DNA hybridization sensor capable of operating in the wet state, Khan et al. (2010) deposited a protective layer (poly-maleic anhydride (pMA)) on the semiconductor, which prevented degradation. Similar to Zhang and Subramanian (2007), the working principle was based on the extraction of holes from the channel upon hybridization.

Amine-terminated peptide nucleic acid (PNA) was covalently attached to the pMA layer as a selective probe to target DNA. Compared with its DNA counterparts, which
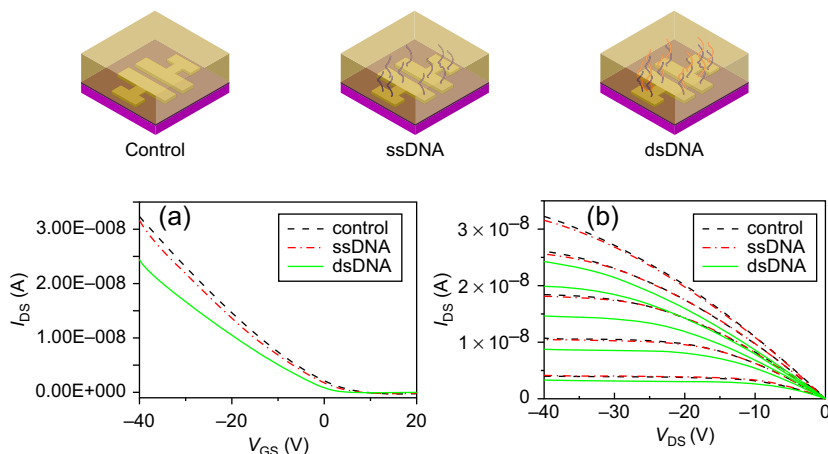
Figure 15.15 Organic thin-film transistor sensor fabrication incorporated with a DNA layer (top) and experimental results (bottom): output characteristics measured at different gate potentials ranging from −40 to 0 V (a) and transfer characteristics measured at a drain potential of −40 V (b).
Source: Reprinted from Yan et al. (2009), Copyright (2012), with permission from Elsevier.
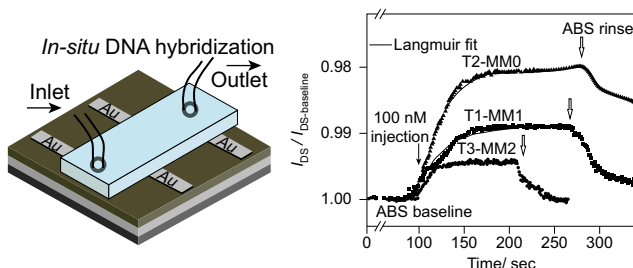
Figure 15.16 Organic thin-film transistor sensor fabrication (left) and experimental results (right): sensor response after hybridization of complement DNA at a minimum concentration (top) and the mismatch dependent PNA-DNA hybridization (bottom).
Source: Reproduced from Khan et al. (2010), Copyright © 2010 WILEY-VCH Verlag GmbH & Co. KGaA, Weinheim.

are negatively charged, PNA strands are neutral; this property allows hybridization with greater selectivity, affinity, and stability as it reduces electrostatic repulsion between two complementary strands. Figure 15.16(left) is a schematic representation of the sensor fabrication; the experimental results recorded highlighting the sensor's response to complement DNA-PNA and mismatch PNA-DNA hybridization are shown in Figure 15.16(right (top)) and (right (bottom)), respectively.

In particular, Figure 15.16(right (top)) compares the drain currents recorded in a sensor without target injection and the injection of 1 nM of DNA target. Figure 15.16(right (bottom)) shows the sensor response with time upon exposure to 1 nM of DNA sequences fully complementary to PNA (T2-MM0), with one mismatch (T1-MM1) and with three mismatches (T3-MM2) for an OTFT sensor operating at a constant bias. In this case, drain currents I_{DS} were normalized with respect to a baseline current $I_{DS\text{-baseline}}$ recorded after 100 s of constant bias before the analyte injection.

Because they operate in liquid media at low voltages, electrolyte-gated OFETs (EGOFETs) are especially suitable for sensors for biological applications. A DNA sensor with an EGOFET structure was created by Kergoat et al. (2012). Its special feature is that the device operates in pure water; for this reason, it works entirely in the field-effect mode. The authors called it water-gated OFET. The device, which has a bottom-contact top-gate structure, was built on a silicon wafer with 300 nm thermally grown oxide. A water droplet was deposited onto the semiconductor and a platinum wire was dipped into the droplet to obtain the gate electrode. Figure 15.17 shows a schematic representation of the device.

The bottom pictures in Figure 15.17 show the transfer characteristics recorded at gate voltages of −0.5 V; PBS was used during the measurements reported in (a) and (b), whereas 18 MΩ deionized water was used for tests shown in (c). Plots in 17(a) show that the probes' immobilization entails a decrease in current and a shift toward negative voltages of the threshold voltage.

This result is consistent with the fact that DNA molecules cause a shielding effect, which prevents the ions' penetration into the semiconductor. In fact, in an
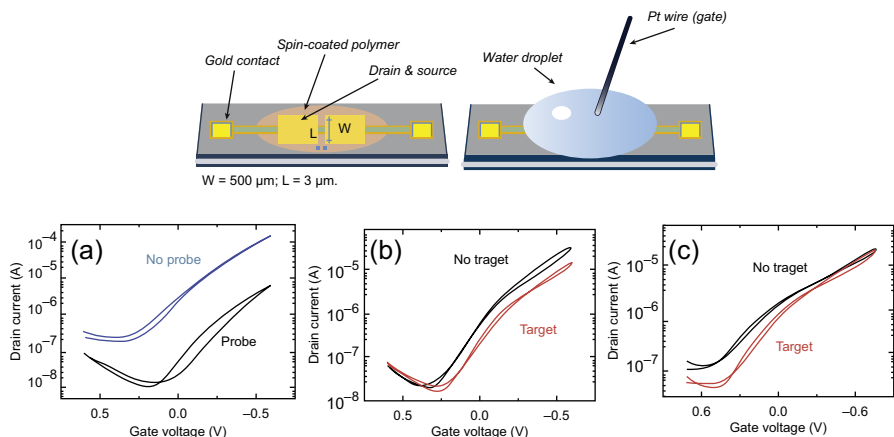
Figure 15.17 Organic thin-film transistor sensor (top); modification of transfer characteristics taken after probe immobilization (a) and hybridization in PBS (b) and after hybridization in pure water (c).

Source: Reprinted from Kergoat et al. (2012), Copyright (2012), with permission from Elsevier.

electrolytic-gated transistor, when the gate is positively biased, cations penetrate into the semiconductor bulk from the solution. The adsorbed ions change the concentration of positive charges at the electrolyte–semiconductor interface; within this condition, fewer holes have to be injected to switch the transistor on and the off current increases. The ion penetration is confirmed by the significant hysteresis observed in all measurements taken in PBS. Because DNA molecules are negatively charged, they form an electrostatic barrier that partially impedes diffusion of cations through the interface, reducing their doping effect. Figure 15.17(b) shows experimental results obtained after DNA hybridization. The DNA negative charge almost doubles after hybridization; nevertheless, the electrical screening is relatively weak with respect to the one recorded under probe immobilization. Upon hybridization, DNA strands form a rigid double helix, i.e., they unfold and assume a shape that makes the electrical screening phenomenon more effective because of the counterions contained in PBS. Only negative charges that lie within the Debye length can effectively be detected; therefore, the shift caused by DNA electrical screening after hybridization is relatively weak compared with the one observed under probe immobilization. Counterion screening can be reduced by using solutions with a lower ionic strength. Figure 15.17(b) reports the sensor response upon hybridization using pure water as a gate dielectric.

Application of the OCMFET for the detection of DNA hybridization was demonstrated by Demelas et al. (2012) and Lai et al. (2013), with interesting results. Deoxyribonucleic acid sensitivity is obtained by anchoring thiol-modified single-stranded DNA molecules onto the sensing areas, acting as probes. Because DNA strands are negatively charged, immobilization of the probes (functionalization) determines an absolute decrease in the threshold voltage, and thus an increase in the

output current of the device. If a solution hosting single-stranded DNA sequences complementary to the probes is sprayed into the sensing area, hybridization occurs and the immobilized negative charge increases, leading to a further increase in output current.

With respect to Caboni et al. (2009a) and Caboni et al. (2009b), several modifications to the layout of the device were implemented. As a main innovation, the device was assembled on 175-μm-thick polyethylene and insulating layers of different thickness were employed. Different dielectric materials were employed determining different working voltage ranges. In Demelas et al. (2012), a 1.5-μm-thick parylene C layer was deposited onto the floating gate; as a result, operating voltages of tens of volts were obtained. Figure 15.18 shows the shift in transfer characteristics of the device in response to functionalization and hybridization processes.

In the work of Lai et al. (2013), a novel implementation was presented. Employing an ultrathin, hybrid organic/inorganic dielectric, the authors obtained operating voltages in the range of 1 V (Cosseddu, Lai, Barbaro, & Bonfiglio, 2012; Demelas et al., 2013). This peculiar characteristic improved not only the portability of the device, but also the reliability of measurements in aqueous media with respect to implementation of high voltage. The left image of Figure 15.19 shows the sensitivity of the device to decreasing concentrations of target oligonucleotides in solution. Caboni, Orgiu, Scavetta, et al. (2009) and Caboni, Orgiu, Barbaro, et al. (2009) employed a nonfunctionalized reference device to compensate for the shift of the threshold voltage not specifically related to the hybridization process. From the net threshold voltage variation obtained by subtracting the threshold voltage shift of the reference device from that of the sensor, the effective charge of density was derived from Eqn (15.3). The results demonstrated that concentrations down to 100 pM could be detected. Besides being the best result obtained with an organic device, this level of sensitivity is the same as that for currently employed silicon-based devices. The
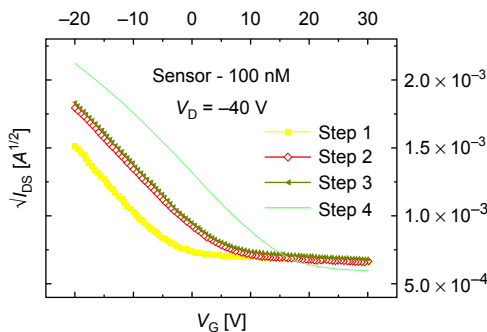
Figure 15.18 Square root of *trans*-characteristics of a sensor taken before (step 1) and after (step 2) immobilization of HS−ssDNA, and before (step 3) and after (step 4) deposition of fully complementary strands of HS−ssDNA; both probes and targets had a concentration of 100 nM. V_G varied from 30 V to −20 V (step −500 mV) whereas the V_D was kept constant at −40 V.
Source: Reprinted from Demelas et al. (2012), Copyright (2012), with permission from Elsevier.
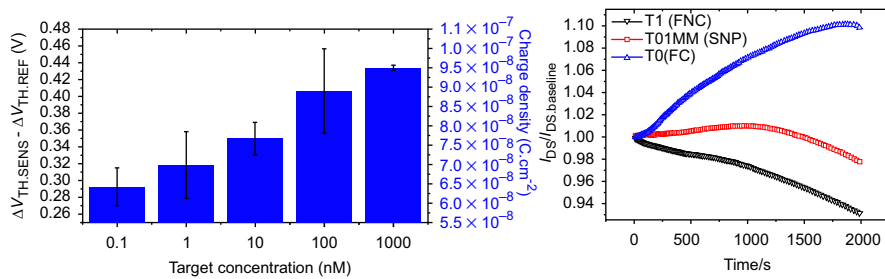
Figure 15.19 (Left) Average shift in net threshold voltage as a function of concentration of the target in solution; in the secondary axis, the correspondent net charge density is reported. (Right) Organic charge-modulated field-effect transistor output currents ($I_{DS}/I_{DS,BASELINE}$) during the hybridization process with fully noncomplementary (FNC), single-mismatched (SNP), and fully complementary (FC) sequences. The baseline current ($I_{DS,BASELINE}$) is the sensor output before injection of the target sequence (Lai et al., 2013).
Source: Reproduced from Lai et al. (2013), Copyright © 2013 WILEY-VCH Verlag GmbH & Co. KGaA, Weinheim.

right image of Figure 15.19 shows selectivity tests reporting unprecedented performances in correctly distinguishing between fully complementary, fully noncomplementary, and single-nucleotide mismatched sequences.

In Figure 15.20, the authors compared the performances of the devices and demonstrated that the relative variation in threshold voltage was higher in low-voltage implementation, characterized by narrow error bars as a consequence of the more reliable measurement process.
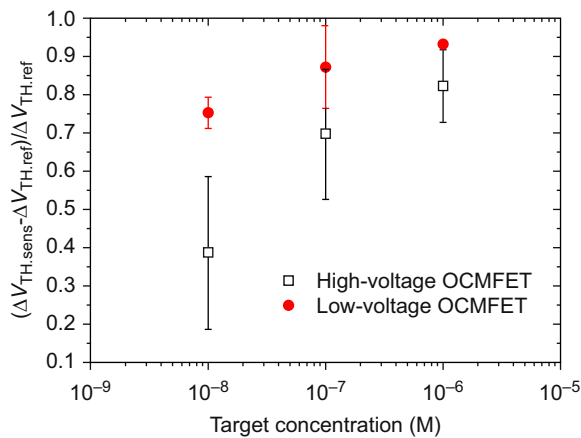
Figure 15.20 Sensitivity of OCMFET to different concentrations of target oligonucleotides in hybridization solution; responses of OCMFET in high-voltage implementation (square-dotted) and in low voltage (circle-dotted) are compared.
Source: Reproduced from Ref. Demelas et al. (2013) with permission from the Royal Society of Chemistry.

15.7 Conclusions

By exploiting the inherent ability of transistors to sense charge and/or of organic materials to interact with the external environment by modifying their properties, many examples of organic semiconductor-based devices have been developed for applications ranging from chemo- to biodetection. Different architectures and materials were employed in their fabrication, depending on requirements of the application. Successful results were obtained for gas detection as well as DNA detection, glucose, and pH monitoring in solution. Work is in progress toward the successful employment of these devices for multimodal monitoring, in an attempt to reach an acceptable tradeoff between the uniquely positive characteristics of organic semiconductors (chemical variety, bio-compatibility, and high sensitivity) and their possible drawbacks (environmental poor stability). Depending on the application, materials and layout can be carefully tailored to obtain the best performances. The future objective, which now appears possible with the proposed technology, is to create sensing systems able to monitor different parameters simultaneously and, thanks to mechanical flexibility and ease of processing, to adapt to a variety of innovative applications that fully exploit the possibility of large-area fabrication specific to the organic technology.

References

Bartic, C., & Borghs, G. (2006). Organic thin-film transistors as transducers for (bio)analytical applications. *Analytical and Bioanalytical Chemistry, 384*, 385 365.

Bartic, C., Campitelli, A., & Borghs, S. (2003). Field-effect detection of chemical species with hybrid organic/inorganic transistors. *Applied Physics Letters, 82*(3), 475−477.

Bartic, C., Palan, B., Campitelli, A., & Borghs, G. (2002). Monitoring pH with organic-based field-effect transistors. *Sensors and Actuators B: Chemical, 83*(1−3), 115−122.

Bernards, D. A., Macaya, D. J., Nikolou, M., DeFranco, J. A., Takamatsu, S., & Malliaras, G. G. (2009). All-Plastic electrochemical transistor for glucose sensing using a ferrocene mediator. *The Chemical Record, 9*(12), 9896−9902.

Braga, D., & Horowitz, G. (2009). High-performance organic field-effect transistors. *Advanced Materials, 21*, 1473−1486.

Caboni, A., Orgiu, E., Barbaro, M., & Bonfiglio, A. (2009). Flexible organic thin-film transistors for pH monitoring. *Sensors Journal, IEEE, 9*(2), 1963−1970.

Caboni, A., Orgiu, E., Scavetta, E., Barbaro, M., & Bonfiglio, A. (2009). Organic-based sensor for chemical detection in aqueous solution. *Applied Physics Letters, 2*(9), 123304.

Cosseddu, P., Lai, S., Barbaro, M., & Bonfiglio, A. (2012). Ultra-low voltage, organic thin film transistors fabricated on plastic substrates by a highly reproducible process. *Applied Physics Letters, 100*(9), 093305.

Crone, B., Dodabalapur, A., Gelperin, A., Torsi, L., Katz, H. E., Lovinger, A. J., et al. (2001). Electronic sensing of vapors with organic transistors. *Applied Physics Letters, 78*(15), 2229−2231.

Demelas, M., Lai, S., Casula, G., Scavetta, E., Barbaro, M., & Bonfiglio, A. (2012). An organic, charge-modulated field effect transistor for DNA detection. *Sensors and Actuators B: Chemical, 171−172*, 198−203.

Demelas, M., Lai, S., Spanu, A., Martinoia, S., Cosseddu, P., Barbaro, M., et al. (2013). Charge sensing by organic charge-modulated field effect transistors: application to the detection of bio-related effects. *Journal of Material Chemistry: B, 1*, 3811−3819.

Diallo, K., Lemiti, M., Tardy, J., Bessueille, F., & Jaffrezic-Renault, N. (2008). Flexible pentacene ion sensitive field effect transistor with a hydrogenated silicon nitride surface treated Parylene top gate insulator. *Applied Physics Letters, 93*, 183305−183311, 183305-3.

Gao, C., Zhu, X., Choi, J.-W., & Ahn, C. H. (2003). A disposable polymer field effect transistor (FET) for pH measurement. In *Transducers, solid-state sensors, actuators and microsystems, 12th international conference on 2003* (vol. 2, pp. 1172−1175).

Kalyania, N. T., & Dhobleb, S. J. (2012). Organic light emitting diodes: energy saving lighting technology—a review. *Renewable and Sustainable Energy Reviews, 16*, 2696−2723.

Kergoat, L., Piro, B., Berggren, M., Pham, M., Yassar, A., & Horowitz, G. (2012). DNA detection with a water-gated organic field-effect transistor. *Organic Electronics, 13*(1), 1−6.

Khan, H. U., Roberts, M. E., Johnson, O., Förch, R., Knoll, W., & Bao, Z. (2010). In situ, label-free DNA detection using organic transistor sensors. *Advanced Materials, 22*(40), 4452−4456.

Kim, J., Jha, S. K., Chand, R., Lee, D., & Kim, Y. (2011). DNA hybridization sensor based on Pentacene thin film transistor. *Biosensors & Bioelectronics, 26*(5), 2264−2269.

Lai, S., Demelas, M., Casula, G., Cosseddu, P., Barbaro, M., & Bonfiglio, A. (2013). Ultra-low voltage, OTFT-based sensor for label-free DNA detection. *Advanced Materials, 25*, 103−107.

Lin, P., & Yan, F. (2012). Organic thin-film transistors for chemical and biological sensing. *Advanced Materials, 24*, 34−51.

Liu, J., Agarwal, M., & Varahramyan, K. (2008). Glucose sensor based on organic thin film transistor using glucose oxidase and conducting polymer. *Sensors and Actuators B: Chemical, 135*(1), 195−199.

Loi, A., Manunza, I., & Bonfiglio, A. (2005). Flexible, organic, ion-sensitive field-effect transistor. *Applied Physics Letters, 86*, 103512−103521, 103512-3.

Macaya, D. J., Nikolou, M., Takamatsu, S., Mabeck, J. T., Owens, R. M., & Malliaras, G. G. (2006). Simple glucose sensors with micromolar sensitivity based on organic electrochemical transistors. *Sensors and Actuators B: Chemical, 123*(1), 374−378.

Nikolou, M., & Malliaras, G. G. (2008). Applications of poly(3,4-ethylenedioxythiophene) doped with poly(styrene sulfonic acid) transistors in chemical and biological sensors. *The Chemical Record, 8*(1), 13−22.

Nilsson, D., Kugler, T., Svensson, P.-O., & Berggren, M. (2002). An all-organic sensortransistor based on a novel electrochemical transducer concept printed electrochemical sensors on paper. *Sensors and Actuators B: Chemical, 86*(2−3), 193−197.

Shim, N. Y., Bernards, D. A., Macaya, D. J., DeFranco, J. A., Nikolou, M., Owens, R. M., et al. (2009). All-Plastic electrochemical transistor for glucose sensing using a ferrocene mediator. *Sensors, 9*(12), 9896−9902.

Someya, T., Katz, H. E., Gelperin, A., Lovinger, A. J., & Dodabalapur, A. (2002). Electronic sensing of vapors with organic transistors. *Applied Physics Letters, 81*(16), 3079−3081.

Stoliar, P., Bystrenova, E., Quiroga, S. D., Annibale, P., Facchini, M., Spijkman, M., et al. (2009). DNA adsorption measured with ultra-thin film organic field effect transistors. *Biosensors & Bioelectronics, 24*(9), 2935−2938.

Su, Y. W., Lan, S.-C., & Wei, K.-H. (2012). Organic photovoltaics-review article. *Materials Today, 15*, 554−562.

Torsi, L., Dodabalapur, A., Sabbatini, L., & Zambonin, P. G. (2000). Multi-parameter gas sensors based on organic thin-film transistors. *Sensors and Actuators B: Chemical, 67*(3), 312−316.

Torsi, L., Farinola, G. M., Marinelli, F., Tanese, M. C., Omar, O. H., Valli, L., et al. (2008). A sensitivity-enhanced field-effect chiral sensor. *Nature Materials, 7*, 412−417.

Torsi, L., Lovinger, A. J., Crone, B., Someya, T., Dodabalapur, A., Katz, H. E., et al. (2002). Correlation between Oligothiophene thin film transistor morphology and vapor responses. *Journal of Physical Chemistry B, 106*(48), 12563−12568.

Wang, L., Fine, D., & Dodabalapur, A. (2004). Nanoscale chemical sensor based on organic thin-film transistors. *Applied Physics Letters, 85*(26), 6386−6388.

Yamaguchi, M., Mitsumori, M., & Kano, Y. (1998). Noninvasively measuring blood glucose using saliva. *The Chemical Record, 17*(3), 59−63.

Yang, S. Y., DeFranco, J. A., Sylvester, Y. A., Gobert, T. J., Macaya, D. J., Owens, R. M., et al. (2009). Integration of a surface-directed microfluidic system with an organic electrochemical transistor array for multi-analyte biosensors. *Lab on a Chip, 9*(5), 704−708.

Yan, F., Mok, S. M., Yu, J., Chan, H. L. W., & Yang, M. (2009). Label-free DNA sensor based on organic thin film transistors. *Biosensors & Bioelectronics, 24*(5), 1241−1245.

Zhang, Q., Jagannathan, L., & Subramanian, V. (2010). Label-free low-cost disposable DNA hybridization detection systems using organic TFTs. *Biosensors & Bioelectronics, 25*(5), 972−977.

Zhang, Q., & Subramanian, V. (2007). DNA hybridization detection with organic thin-film transistors: toward fast and disposable DNA microarray chips. *Biosensors & Bioelectronics, 22*(12), 3182−3187.

Zhu, Z.-T., Mabeck, J. T., Zhu, C., Cady, N. C., Battb, C. A., & Malliaras, G. G. (2004). A simple poly(3,4-ethylene dioxythiophene)/poly(styrene sulfonic acid) transistor for glucose sensing at neutral pH. *Chemical Communications, 13*, 1556−1557.

Zhu, Z.-T., Mason, J. T., Dieckmann, R., & Malliaras, G. G. (2002). Humidity sensors based on Pentacene thin-film transistors. *Applied Physics Letters, 81*(24), 4643−4645.

Microfluidic devices using flexible organic electronic materials

16

Z.G. Wu
Uppsala University, Uppsala, Sweden

16.1 Introduction

In the past few decades, we have been witnessing the rapid development of micro (nano)-electronics (Cavin, Lugli, & Zhirnov, 2012). Although researchers have predicted that Moore's law will be invalidated, due to some physical constraints, it is still nearly a perfect reflection of this development in the past few decades (Vogel, 2007). As evidence, the history of CPU (central processing unit) development clearly fits the description of Moore's law (Moore, 1965). However, recently the continuous shrinkage of the market for personal computers (or the dilemma situation of Intel) gives us a warning signal. The traditional way of simply making a higher density of smaller components with higher density does not work well any longer in the highly competitive environment of today (Cavin et al., 2012). We need continuous innovation and development of radical new technology to satisfy the new demands from society. Hence, in recent years, people have focused on other technologies 'beyond Moore' (Cavin et al., 2012) or 'more than Moore' (Zhang & Roosmalen, 2009), for example, carbon materials-based (including carbon nanotubes, graphene and so on) electronics, organic electronics, printed electronics and so on.

One of the technologies regarded as 'beyond Moore', flexible electronics, was emphasized again recently (Song & Salleo, 2009). It is a technology that employs hybrid integration to assemble electronic devices on flexible substrates, especially in plastic foils such as polyimide (Kapton). It demonstrated high flexibility and bendability and obtained high acceptance in consumer products, such as in digital cameras. However, this mechanical flexibility is not sufficient when it comes to many other applications that are targeted onto complex surfaces such as the human body. Hence, a new concept, stretchable electronics, was coined recently (Rogers, Someya, & Huang, 2010). Differing from the traditional rigid and brittle silicon-based electronics, stretchable electronics mainly focuses on the soft and deformable format, which might have a dynamic shape instead of a static one. This is of particular interest for many devices which require ergonomic interfaces to enhance their user experience, e.g. a contact lens that intimately contacts/interacts with the human body, as demonstrated in the devices from the group from the University of Illinois, Figure 16.1. Ultimately it may reshape the concept and format of electronics.

16.2 Microfluidics and electronics

The birth of microfluidics is originally rooted in modern solid-state electronics, especially the large-scale, integrated circuits industry. Around half a century ago, scientists
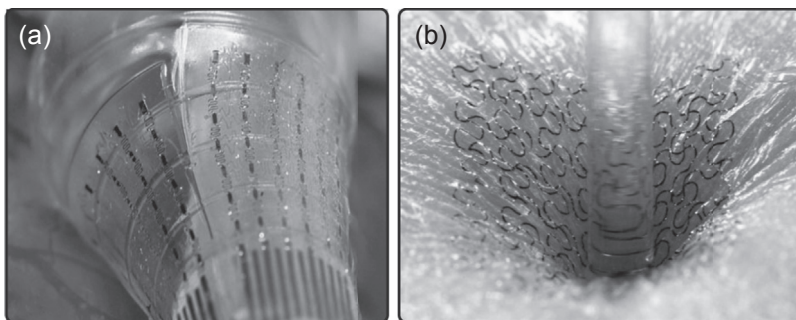
Figure 16.1 Two typical stretchable electronics: (a) a balloon catheter with various stretchable sensors *(Kim et al., 2011a, Courtesy of NPG)*; and (b) an epidermal sensor working on the skin *(Kim et al., 2011b, Courtesy of AAAS)*.

were trying to use the very advanced facilities from modern solid-state electronics to explore the 'bottom' world such as mechanics or chemistry (Feynman, 1959). This led to two new closely connected research areas: microsystems technology and microfluidics (Whitesides, 2006). The first demonstration of microfluidics was to use silicon-etched channels to replace the traditional fused silica capillaries in gas chromatography. Initially, microfluidics focused on analytical chemistry, and then it was found to be more suitable in biological and relevant fields. It offers many attractive merits such as less consumption on sample and reagent, less contamination, less energy, controllable reactions and, hence, high safety, full integration and automation and high throughput. After a shift from chemistry to biology applications, microfluidics has witnessed exploding development in the past few decades. It has become a very dynamic and innovative interdisciplinary research field, which offers a good common platform for scientists from various fields such as chemistry, physics, biology and engineering to discover the micro-nano world of tiny fluidics. Unfortunately, research directly coupled to electronics (instead of electrochemical perspectives) from microfluidic perspectives is rare, but it does offer a good possibility for a new generation of soft electronics (Cheng & Wu, 2012).

As a byproduct of World War II, polydimethylsiloxane (PDMS) was developed secretly in the United States. However, it was not widely used and was not recognized by academics due to various reasons. One partial reason is that PDMS was developed by commercial companies for military purposes for many years. It was introduced into the microfluidic community, together with so-called soft lithography by Whitesides et al. (Xia & Whitesides, 1998) at the end of the last century. In a short period after that, it became the most popular material in the prototyping of microfluidic devices. It has many merits, such as rapid processing, ease of fabrication, cost-effectiveness, gas permeability, optical transparency and so on. Researchers could explore a lot of interesting biological applications, which are difficult to explore with traditional biological techniques. From then, PDMS has nearly become a standard material in many microfluidic laboratories and is widely accepted by numerous academic laboratories. Besides the aforementioned advantages, PDMS also has other attractive characteristics: it has excellent

mechanical properties which are desired by soft electronics such as bendability, twistability, and stretchability, and it is a good electric insulator. This makes it attractive for use in stretchable electronics. Using appropriate fabrication processes, microfabricated PDMS could exhibit a favourable electrical performance and withstand severe twisting and stretching without any mechanical failure. The subsequent question is how to introduce it into conductive parts without hindering its super mechanical flexibility.

The pioneer work on this topic was to deposit a thin layer of solid metal such as gold, copper or silver, on the PDMS substrate using various deposition techniques such as thermal evaporation. Patterning PDMS surfaces with solid metals seems to be plausible (Bowden, Brittain, Evans, Hutchinson, & Whitesides, 1998). However, the well-known technical challenge in metalizing PDMS surfaces, the intrinsic mechanical and chemical mismatch, sets a limit for mechanical deformability and electrical reliability (Lacour, Wagner, Huang, & Suo, 2003). Generally, a moderate strain and limited stretching cycles work well. Further investigations of this approach indicated that pre-stretching PDMS would greatly enhance its stretchability and electrical and mechanical reliability. An approach using a very thin, inorganic material such as silicon foil to achieve this, regular wrinkles in an out-of-plane (or in-the-plane) form was developed at the University of Illinois, Urbana−Champaign (Kim et al., 2011b). Various attractive devices based on this approach have been demonstrated, for example, a high performance artificial eye sensor, surface mounted ergonomic biomedical sensors and epidermal electronics systems. However, the requirements of high-dedicated equipment on the processing hinders rapid diffusion of the technology.

To return to microfluidics, today, in the microfluidic laboratory, we are routinely patterning microfluidic channel networks on elastic PDMS substrates and manipulating tiny amounts of fluid of nearly unlimited mechanical deformability in the channel (if we do not consider the physical constraints of the vessel). Why can we not do the same for electronics? It would be an excellent combination to achieve high stretchability if we can find a proper conductive fluid as we usually handle any other liquids. Actually, a 'microfluidic' approach was used in electronics before the coining of the concept microfluidics. Looking back to the beginning of the computing era, tiny liquid mercury drops were used in punch card readers to read input information. This concept is still widely used in today's switches, relays and in similar applications with modern design. The major concern for this approach is the use of mercury, due to its high toxicity on humans and the environment. However, with the advance of material science, this approach using liquid conductance is coming alive again and is demonstrating new vitality.

16.3 Materials and fabrication techniques

Traditionally, electrolyte solutions are the most common liquid conductors we can find in daily life. In traditional microfluidics, we mostly deal with this kind of liquid. For example, capillary electrophoresis in many diagnosis applications deals with biological samples that are often conductive. However, it is still not a good electrical

conductor in active or passive electric or electronic components as we discuss further. These liquids are not discussed in detail in this chapter, as they have been well documented in other literature recently.

In the past few thousand years, mercury has been well-known as a conductive liquid metal and has been used widely in many applications. As a liquid metal, mercury has significantly higher surface tension than other common liquids. One consequence is that it is not easy to wet common surfaces such glass, and it tends to lead to non-discontinuity in the channel. This is one of the major reasons that it is used in drops in most applications. Another potential concern when it comes to mercury, is amalgamation. It tends to diffuse into the lattice of other metals to form a liquid alloy, and hence, changes or even destroys the original metal lattices. On contact with other components, this might be a potential drawback. Modern investigations indicate that it is extremely toxic to human health and the environment because it has a very low vapour pressure. Hence, it can be easily inhaled by the human body and can block many important physiological functions, severely weakening the body. Due to its high toxicity, the use of mercury is not allowed in many countries.

To find a suitable replacement for mercury, specialists shifted their focus from mercury to alloys, which could be liquid at room temperature. Some alloys were investigated, such as NaK alloy, Wood's metal and Field's metal and so on. Among these, gallium-based alloy attracted the most interest, since it has many advantages compared to the other alloys (including mercury). It is neither toxic nor reactive. More importantly, in its liquid form, it has quite a broad range compared to others. For example, a typical gallium-based alloy, galinstan (a eutectic alloy of gallium, indium and tin), is liquid from $-19\,°C$ to above $1500\,°C$. Hence, it can replace mercury for nearly every application. At the same time, from the perspective of microfluidic electronics, it has comparatively high electrical conductance, around a tenth of that of bulk silver.

Another new kind of liquid or liquid-similar conductor is a gel-like substance (or paste), which in most case is a composite. This kind of substance can normally be deformed to some extent. Traditionally, it suffers from low electrical conductivity, which is insufficient in most electrical applications, except those in electrochemical applications. However, owing to advances in material science and nanotechnology, remarkable progress has been made in the development of this kind of conductor. For instance, by mixing nano/micro silver particles (carbon particles/nanotubes) with PDMS matrices, flexible PDMS moulded electrode sensor devices were demonstrated which had very limited stretchability. Since their electrical conductivity is sensitive to the strain applied, they were normally used in developing a simple strain sensor, as shown in the following section. Another idea is to mix single-walled carbon nanotubes and ionic liquids with fluorinated copolymers. This demonstrated increased conductivity of approximately 5700 S/m (Sekitani et al., 2008). Compared with traditional carbon or metal particle composites with conductivities typically ranging from 0.1 to 1000 S/m, it is a remarkably big step. However, this is still roughly 10,000 times lower than that of good conductors such as copper and silver. Another recent work on highly conductive elastic materials is to dope double-sided carbon nanotubes with iodine

Table 16.1 List of physical properties of some conductive liquids

	Electrolyte solution (sea water)	Galinstan	Hg	Liquid/gel composite (Sekitani et al., 2008)
Melting point (°C)	−1	−19	−38.8	–
Boiling point (°C)	100.5	>1300	357	–
Density (kg/m^3)	1025	6440	1353	–
Electrical conductivity (S/m)	5	3.46×10^6	1.0×10^6	5700
Viscosity (Pa s)	1.08×10^{-3}	2.4×10^{-3}	1.5×10^{-3}	–
Surface tension (N/m)	0.074	0.718	0.487	–

(Zhao, Wei, Vajtai, Ajayan, & Barrera, 2011). They showed very impressive electrical conductivity, comparable to that of bulk copper. Although these works are still in the infancy stage, significant process will offer new opportunities for use in soft electronics. In Table 16.1, some of the physical properties of liquid-based conductors are listed.

Since liquid has very different mechanical characteristics, the fabrication techniques for microfluidic electronics are somewhat different from those of common solid materials. Currently, a few techniques are used to fabricate such kinds of electronic device. Roughly, they can be categorized into three, according to the way the fluid is handled: liquid filling or injection, liquid printing and casting/moulding. The first is often used for pure liquid handling, and the third is often used for paste/gel/polymer handling, while the printing could be used both for pure liquid or paste handling or patterning. In the following text, we introduce and discuss these three techniques individually.

The first technique comes directly from microfluidics, Figure 16.2, by combining traditional soft lithography and liquid filling or injecting. The soft lithography is used to make an elastic channel network, while the filling of the liquid conductor forms stretchable components or connects used in the electronic systems. Here is a typical process briefly. First, a negative photoresist (usually it is SU-8) was spun on a precleaned silicon wafer. Second, the pattern of the channel network was transferred into the photoresist by selectively high-energy exposure (normally UV) with an optical mask (either from chromium or plastics, which is dependent on resolution requirement), which serves as a master for the following step. Third, the pattern of channel network is obtained by pouring and curing the mixed PDMS mixture on the surface of the master on silicon. At the same time, another blank PDMS slab of a similar size was prepared, which can be bound to the pattern PDMS to form a close channel network. Finally, the channel network is filled by liquid either by injecting or sucking with a vacuum. Since inlets and outlets are necessary for injecting or filling, the holes for letting in the liquids should be punched before the two PDMS layers are bonded.

In addition, by making a porous PDMS, the stretchability can be significantly enhanced, Figure 16.3 (Park, Chen, & Wood, 2012).

By stacking a few layers of PDMS and microfluidic channels inside, this technique could be further extended for multilayer fabrication purposes. Principally, this approach could be used for any kind of liquid or liquid-similar substance filling. In particular, considering the huge surface energy difference between the liquid alloy and PDMS substrate, another approach using an intermediate layer was developed as well, Figure 16.4. In this approach, a thin layer of gold was deposited onto the PDMS channel, and then liquid alloy was filled with a Teflon squeegee (Kim, Maleki, Wei, & Ziaie, 2009). The advantage of this method is that it ensures high wetting between the channel and liquid
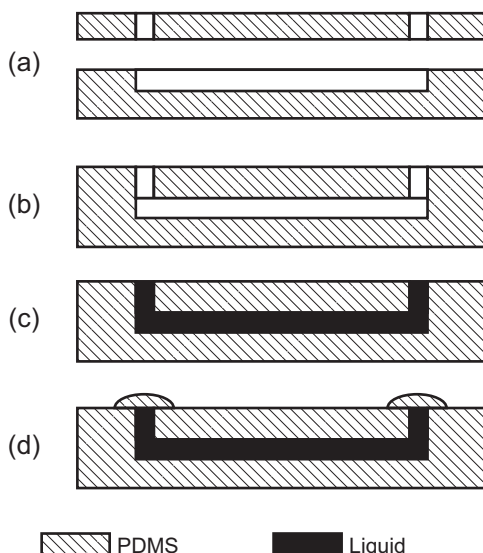
Figure 16.2 The schematic fabrication processing of microfluidic electronics with liquid conductor injection or filling. (a) Preparation of microchannels in PDMS and PDMS lid, (b) PDMS bonding, (c) conductor filling and (d) inlets/outlets sealing.
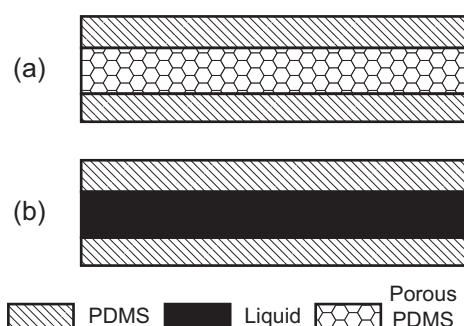
Figure 16.3 The schematic fabrication processing with porous PDMS for improved stretchability (Park et al., 2012).
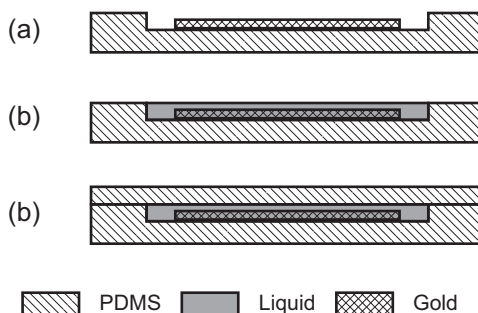
Figure 16.4 The schematic fabrication processing with an intermediate stick layer (Kim et al., 2009). (a) Deposition of intermediate stick layer, (b) liquid alloy filling and (c) liquid covering.

alloy. However, unnecessarily, it increases the complexity of the whole fabrication process significantly and, hence, reduces reliability.

In the aforementioned technique, microfluidic electronic devices were demonstrated by incorporating a liquid alloy into microfluidic channels. Since the conductive part is the liquid-alloy-filled channels, the preferred design is that all channels are connected together at a limited length. If the conductive parts of the components are isolated, then multiple liquid-alloy injection points are required, and the reliability of the process dramatically decreases. Furthermore, this approach is difficult to scale up for future mass scale or batch production. The reliability and yield would become a big obstacle when considering actual production. Another often used technique for liquid or similar material fabrication is printing, which can be scaled up for batch-based or large-scale production (Jeong et al., 2012). Traditionally, there are numerous techniques that can be used for printing, for instance, offset printing, flexography printing, screen printing, inkjet printing, transfer printing and so on. Among them, inkjet printing is suitable for low- viscosity liquid printing, while screen printing is suitable for high-viscosity liquid or paste printing and is widely used in flexible electronics fabrication. Gallium-based alloys have a very low viscosity and look very promising for inkjet printing. However, they have a very high surface energy, which makes them incompatible with most available inkjet printing equipment. Recently, with a metallic stencil mask, we successfully printed the liquid alloy onto elastic substrate, Figure 16.5. Furthermore, by introducing an adhesive transfer tape as a mask, the printing approach was significantly extended to include any kind of liquid shape patterning on substrates.

It is difficult to make semiconductor components such as transistors and integrated circuits (ICs), which are essential components for active electronics, by using current existed microfluidic technologies. This bottleneck hinders monolithic integration of fully functional microfluidic electronics with active components. However, a compromise solution, where semiconductor devices are sparsely distributed over large-area elastic substrates and connected with a liquid conductor on the substrate, could be used to solve this issue. With today's highly advanced semiconductor industry, extremely high integration densities can be achieved with power functionalities and very small footprints. Although some parts of the system are still rigid, the entire
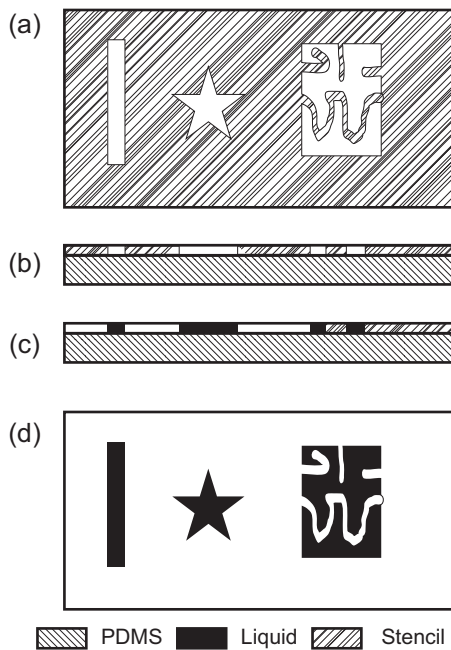
Figure 16.5 The schematic fabrication processing of microfluidic electronics with liquid conductor printing (Jeong et al., 2012). (a) Pattern design and transfer (into a stencil mask), (b) mask alignment of elastic substrate, (c) liquid alloy deposition and (d) mask removal.

device is stretchable to some degree. Using this strategy and intruding a so-called localized stiff cell, our group developed a hybrid approach for device integration (Cheng & Wu, 2010). In this technique, the active parts with semiconductor devices were first integrated onto a flexible circuit board and then encapsulated into a passive microfluidic electronics component to form a completely functional electronic system.

In addition, materials other than PDMS could be used as the elastic substrate or matrix, either for enhanced stretchability or compatibility to current industry manufacturing processes. For instance, a modified siloxane could offer much higher stretchability than common PDMS (Kubo et al., 2010). Elastic thermoplastic polyurethane (TPU) could be a potential material, though no microfluidic demonstrations are found in current existing literature.

16.4   Device examples

16.4.1   Components

Because of their good conductivity, liquid alloys were first investigated as various connectors either in the form of straight lines or in diamond shapes, with a reservoir as the traditional design. Thanks to the high liquidity, the fabricated devices demonstrated a high degree of bendability, foldability and twistability as well as stretchability.

Recently our tests showed that they have high reliability, too. In particular, because of its high wettability on PDMS, a post-structure was employed to obtain aligned electrodes as well. Other simple passive electronic components, such as microfluidic antenna operating at various frequency ranges, were also demonstrated (Cheng, Rydberg, Hjort, & Wu, 2009). Owing to the super electrical conductivity, such a kind of antenna offers a very high electrical performance in addition to a high degree of mechanical flexibility. Very recently, we used this technique on a three-dimensional electrically small antenna with a simple and low-cost planar fabrication technique. The demonstrated antenna had a high electrical performance compared to counterparts made by using previously very advanced fabrication techniques. And more importantly, by tuning the antenna pneumatically, it could cover a broad range of frequency band without a reduction of the antenna efficiency. The results indicated that our electrically small antenna could be tunable over a significantly large frequency range (12.4% of its centre frequency, and it was around 2% in the previous work) with high radiation efficiency (Jobs, Hjort, Rydberg, & Wu, 2013).

Noticing that there was an oxide layer on the liquid alloy, tunnelling junctions were made between the self-assembled organic molecules on silver and eutectic gallium and indium alloy (Chiechi, Weiss, Dickey, & Whitesides, 2008). These junctions could rectify current at a rectification ratio of 90−180. This semiconductor-like behaviour indicated the possibility of fabricating active components that are widely used in modern integrated circuits industry and further to achieve an electronic device or system in a monolithic way, although it is a long way ahead. Very recently, memristor-like behaviour was observed when a layer of electrolytes was inserted between two gallium-based alloy electrodes (Koo, So, Dickey, & Velev, 2011). Figure 16.6 shows some of the microfluidic electronic components.

16.4.2 E-ink display

Electrophoresis is one of the early intensively investigated fields in the microfluidic community. Transferring knowledge from traditional capillary fluidics, electrophoresis and electrokinetics developed rapidly and produced a lot of biological applications. At the end of the last century, an interesting display mechanism was proposed by Beni and Hackwood with electrowetting, which triggered the early investigation of today's digital microfluidics (Beni & Hackwood, 1981). Great efforts were intensively put on the relevant researches, e.g. electrochemical sensing, (die) electrophoresis-based analysis, and so on. Such kinds of work are central to today's microfluidic research. In this chapter, we do not intend to include this and repeat this technology. Here, E-ink (electrophoretic ink) technology is emphasized as a good example of how microfluidic electronics influence our daily life.

Electrophoretic ink is a typical microfluidic electronic device, which can be widely found in daily life, for instance, in the Amazon Kindle e-book reader. This technology was originally investigated in the MIT media laboratory (Comiskey, Albert, Yoshizawa, & Jacobson, 1998) and mainly commercialized in Taiwan. The working principle is shown in Figure 16.7. Basically, two types of charged pigments (usually white and black) are immersed in a transparent media (oil). With different kinds of charge on
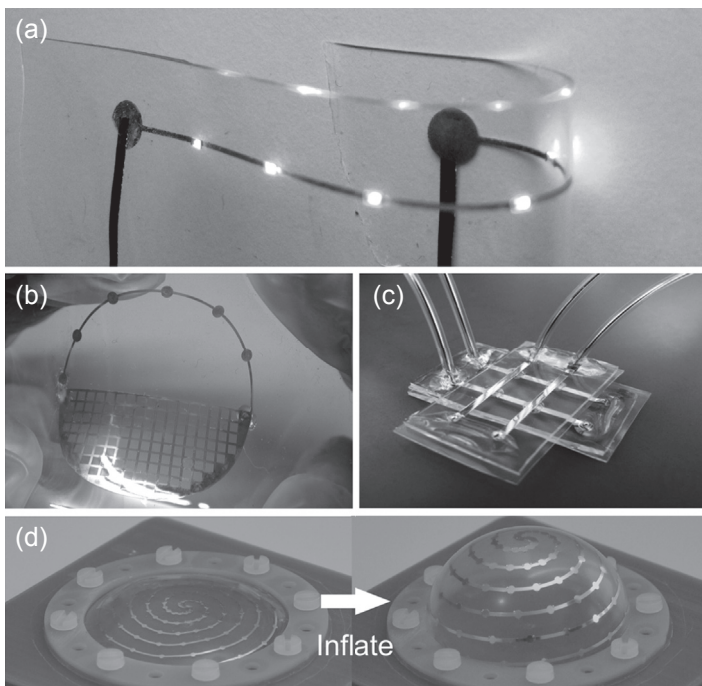
Figure 16.6 Some typical microfluidic electronic components. (a) DC interconnects (Jeong et al., 2012), (b) a loop antenna (Cheng et al., 2009), (c) a memristor *(Koo et al., 2011, Courtesy of Wiley)* and (d) a tunable 3D electrical small antenna *(Jobs et al., 2013, Courtesy of Wiley)*.
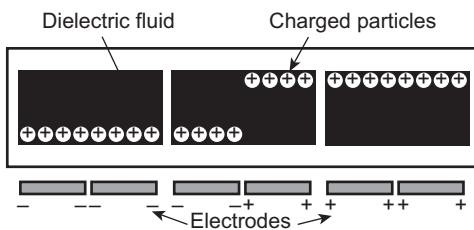
Figure 16.7 The schematic working principle of E-ink.

the pigments, they will response differently in an electric field. By controlling the electric field applied, the movement of pigments can be well-controlled via a control circuit. With millions of this kind of unit, it can display any kind of pattern, text or pictures. Similar to traditional ink, it is a reflective technology and is very friendly to the reader's eye. At the same time, since there is no active light part, it consumes very low energy. Compared to other display technologies for reading, it produces the most comfortable experience when reading for a long-time is needed. However, this technology suffers from long response time and low capability in colour reproduction; the main applications are very limited in e-readers and similar devices.

16.4.3 Radio frequency (RF)-related device

Due to high electrical conductivity, gallium-based microfluidic electronics have super electrical performance as well as high mechanical flexibility. As stated earlier, droplets are the earliest form of microfluidic electronics. Using a galinstan droplet in Teflon oil, a switchable liquid conductor was suspended in a microfludic channel (Chen & Peroulis, 2007). Adjusting the configuration of the liquid alloy over the metal electrodes, it can change the working state of high-frequency circuits. Applying this principle in a parallel way, a wideband RF switch was demonstrated, and recently, a tunable frequency selective surface was shown with a similar approach (Li, Yu, & Behdad, 2010).

As the first demonstrated integrated stand-alone microfluidic device, the RF radiation sensor device achieved an overall stretchability of up to 15% and could detect RF radiation at around 0.9 GHz over 5.0 m (Cheng & Wu, 2010). Equipped with an integrated LED, the results can be visualized in a simple way, Figure 16.8(a). As further development of this technology, a radio frequency identity (RFID) tag was fabricated using newly developed liquid alloy pattern technology, Figure 16.8(b). Compared to its rigid counterparts, it gave an excellent electric performance. It could be read at a distance of up to 13.95 m in ambient air and showed a good read speed compared to the reference samples. The initial mechanical tests indicated that it could be stretched up to 60% in one dimension at least 2000 times without any mechanical or electrical failure (Jeong et al., 2012).

16.4.4 Mechanical sensors

Mechanical sensors are typical devices used where high strains are often required. In the past decade, various mechanical sensors with different mechanisms have been demonstrated. Usually, the mechanical deformity will introduce a geometrical change of conductors. According to the relationship between the conductance and geometrical changes, the resistance changes could be tracked back to the strain applied. Hence, measurement of the resistance of the elastic conductor could be done as a strain sensor. For example, by encapsulating multiwalled carbon nanotubes (MWNT) into PDMS and a liquid alloy as interconnects, a strain senor was initially demonstrated
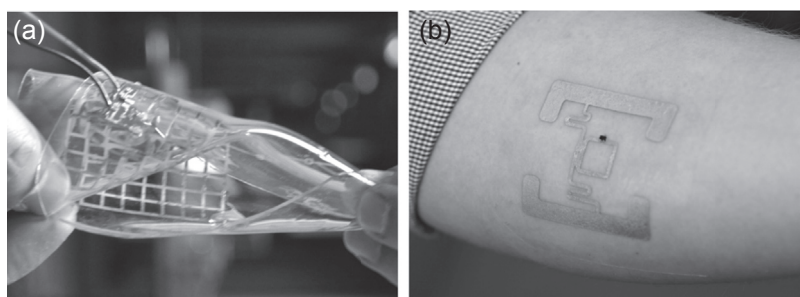
Figure 16.8 Microfluidic RF sensors. (a) Radiation sensor (Cheng & Wu, 2010) and (b) RFID (*Jeong et al., 2012, Courtesy of RSC*).

(Hu, Kashan, & Liu, 2007). Recently, this design was improved by moulding on an elastic conductor made from carbon black and PDMS (Lu, Lu, Yang, & Rogers, 2012). Another approach, based on carbon nanotubes, is to align the nanotubes in specially desired directions by periodically stretching and releasing the sensor. With this approach, the sensor could survive above 10,000 cycles stretching with a strain of up to 150% (Lipomi et al., 2011).

Using a stacked liquid alloy conductor in different layers, Wood's group developed an artificial skin sensor that could detect multiaxial strains and contact pressure at the same time. Since a highly stretchable silicone was introduced, it could survive a strain of up to 250% (Park et al., 2012). To enhance the sensitivity, ionic liquid was recently combined with this kind of sensor. However, this sensor cannot work stand-alone. A large number of supporting circuits outside the sensor are connected to it by wires, which makes it less attractive in the practical implementation. Adopting an unconventional approach, Wu's group demonstrated a strain sensor that could work stand-alone (Cheng & Wu, 2011). The major part of the sensor is a mechanically reconfigurable and reversibly deformable microfluidic antenna. A simplified RF transmitter with supportive circuits was assembled on a flexible substrate and then integrated into the microfluidic antenna heterogeneously. Since the electrical characteristics at operation frequency are highly sensitive to mechanical strains, its electrical signal could be used to identify the strain. Consequently, with an RF receiver working in the same frequency band, the strain could be measured remotely in real time. It could be potentially used in many situations in healthcare or fitness monitoring. Figure 16.9 gives some samples of these mechanical sensors.

16.4.5   Energy-handling devices

As an essential part of an electronic system, energy-handling devices are either energy conversion devices or storage devices, or both, and they are important for powering the system and keeping it working (Lipomi & Bao, 2011). However, in such a system the stored energy or conversed energy is often proportional to its volume or size. Traditional thin-foil technology used in flexile electronics strongly constricts the system
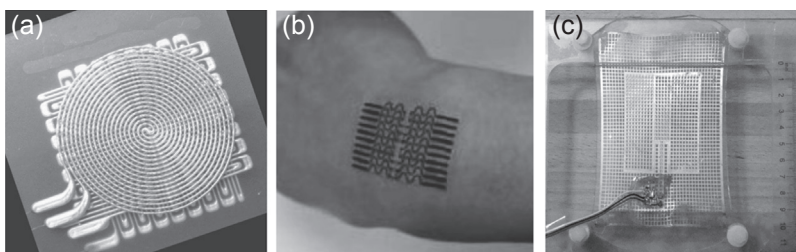
Figure 16.9 Microfluidic mechanical sensors with different designs. (a) A multiple parameter sensor with stacked liquid alloys *(Park et al., 2012, Courtesy of IEEE)*, (b) printable conductive PDMS *(Lu et al., 2012, Courtesy of Wiley)* and (c) a wireless strain sensor *(Cheng & Wu, 2011; Courtesy of Wiley)*.
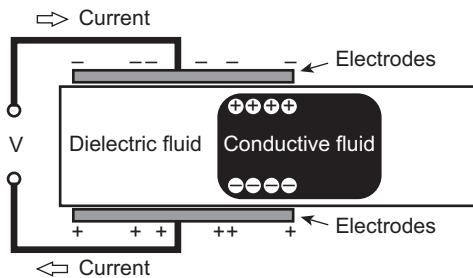
Figure 16.10 The schematic working principle of an energy harvester with reverse electrowetting (Krupenkin & Taylor, 2011).

design and development. Hence, it is very important to develop new techniques, which can either supply high energy densities or allow high volume active materials in a 'thick' (bulk) way. Here, the microfluidic way has a great advantage over the traditional way based on thin-film technology.

Simply by encapsulating the electrolyte pastes and gels into a microfluidic channel network, a dry primary cell was demonstrated. It can survive a strain up of to 100%, typically with a reasonable performance when the strain is below 50% (Kaltenbrunner, Kettlgruber, Siket, Schwodiauer, & Bauer, 2010). Microfluidic technology is also used to make a secondary battery, such as a lithium-ion battery (Yang, Jeong, Hu, Lee, & Cui, 2011). The fabrication process is very similar to the aforementioned primary cell. The slurry with active materials is injected into the microchannel network while the current-collecting gold electrodes are coated on the top and bottom wall of the channel network. Obviously, the fabrication technique is a serial-based process, which is not suitable for mass production. By modifying the active materials in electrodes with alumina particles, a joint research group made it possible to fabricate this stretchable lithium-ion battery in a parallel way (Kil et al., 2013). In addition, a new mechanism for energy-handling devices with microfluidics has been investigated by introducing a concept called reverse electrowetting (Krupenkin & Taylor, 2011). It has a configuration very similar to that of droplet switches, Figure 16.10. High conductive liquid droplets were suspended in the dielectric solution between two metal electrodes, which work as a capacitor with liquid metal droplets. When a pre-biased voltage was applied to the capacitor, the movement of the conductive liquid droplet changed the capacity. Consequently, it introduced the charge movement in the circuit and, hence, triggered the current inside it. The authors claim this approach could offer higher power density than other similar mechanical harvesters. However, the requirement of pre-biased voltage (power supply) might be a problem in a practical implementation.

16.5 Summary

Recalling the root of microfluidic electronics in liquid and soft materials, they are closely connected with their excellent mechanical flexibility. But the question is how high a degree of flexibility is required. Considering the flexible electronics (based on flexible

foils), they can survive around 2% strain normally. This means, flexible foiled base electronics could be used in many situations where rollability and bendability are required. As microfluidic electronics demonstrated a higher degree of mechanical flexibility, they could survive in situations where severe deformability is required, such as twistability and stretchability. The need for stretchability or flexibility is dependent on the technical requirements of the specific application. Considering that flexible electronics is a mature industry, fully exploiting the advantage of flexible electronics is very important when developing a new flexible or stretchable electronic system. In another sense, it is important for microfluidic electronics to discover new niche applications and demonstrate the great advantage of its high degree of mechanical flexibility.

Theoretically, high stretchability is one of the most attractive features of microfluidic electronics. Mechanical and electrical reliability are important in practical applications. However, there are very few reports on this (Cheng & Wu, 2012). A partial reason is that microfluidic electronics is in its infancy. There are very few groups working on this topic, and there is a shortage of personnel to dedicate to reliability studies. Another urgent issue is fabrication techniques. Most currently available fabrication techniques are still on the stage of handicraft. Although one batch-based fabrication technique was shown recently, it is far from a technique which could be used in future large-scale production. Great efforts should be put into the development of processing and repeatability. Otherwise, it will become a hindrance in the way of future development and commercialization of microfluidic electronics. Finally, energy conversion, storage and handing devices are still challenging issues for creating an integrated system.

16.6   Future trends

Thanks to its inherent fluidity, microfluidic electronics has demonstrated excellent performance in applications for stretchable electronics. It is anticipated that microfluidic electronics will strongly impact potential fields where complex surfaces with ergonomic design are desired, for example, sensor skins for robotics, sensors or devices used on the human body for healthcare or fitness monitoring and wearable communication/computing devices. In particular, microfluidic electronics based on gallium alloy show very good performance in RF applications. With much emphasis on user experience, there are huge opportunities for us to create a brand new user experience by exploiting the advantages of microfluidic electronics. However, there are still a lot of challenges ahead of us. It requires a lot of work for us to bridge the gap between traditional rigid electronics and microfluidic electronics, or even radically, find a brand new solution to build up a high performance monolithically soft electronic system.

Acknowledgements

References

Beni, G., & Hackwood, S. (1981). Electro-wetting displays. *Applied Physics Letters, 38*, 207−209.

Bowden, N., Brittain, S., Evans, A. G., Hutchinson, J. W., & Whitesides, G. M. (1998). Spontaneous formation of ordered structures in thin films of metals supported on an elastomeric polymer. *Nature, 393*, 146−149.

Cavin, R. K., Lugli, P., & Zhirnov, V. V. (2012). Science and engineering beyond Moore's law. *Proceedings of the IEEE, 100*, 1720−1749.

Cheng, S., Rydberg, A., Hjort, K., & Wu, Z. G. (2009). Liquid metal stretchable unbalanced loop antenna. *Applied Physics Letters, 94*, 144103.

Cheng, S., & Wu, Z. G. (2010). Microfluidic stretchable RF electronics. *Lab on a Chip, 10*, 3227−3234.

Cheng, S., & Wu, Z. G. (2011). A microfluidic, reversibly stretchable, large-area wireless strain sensor. *Advanced Functional Materials, 21*, 2282−2290.

Cheng, S., & Wu, Z. G. (2012). Microfluidic electronics. *Lab on a Chip, 12*, 2782−2791.

Chen, C.-H., & Peroulis, D. (2007). Liquid RF MEMS wideband reflective and absorptive switches. *IEEE Transactions on Microwave Theory and Techniques, 55*, 2919−2929.

Chiechi, R. C., Weiss, E. A., Dickey, M. D., & Whitesides, G. M. (2008). Eutectic Gallium−Indium (EGaIn): a moldable liquid metal for electrical characterization of self-assembled monolayers. *Angewandte Chemie International Edition, 47*, 142−144.

Comiskey, B., Albert, J. D., Yoshizawa, H., & Jacobson, J. (1998). An electrophoretic ink for all-printed reflective electronic displays. *Nature, 394*, 253−255.

Feynman, R. P. (1960). There's plenty of room at the bottom. *Caltech's Engineering and Science,* pp. 22−36.

Hu, H., Kashan, S., & Liu, C. (2007). Super flexible sensor skin using liquid metal as interconnect. In *Sensors, 2007 IEEE, Atlanta*. http://dx.doi.org/10.1109/ICSENS.2007.4388525.

Jeong, S. H., Hagman, A., Hjort, K., Jobs, M., Sundqvist, J., & Wu, Z. G. (2012). Liquid alloy printing of microfluidic stretchable electronics. *Lab on a Chip, 12*, 4657−4664.

Jobs, M., Hjort, K., Rydberg, A., & Wu, Z. G. (2013). A tunable spherical cap microfluidic electrically small antenna. *Small, 9*, 3230−3234.

Kaltenbrunner, M., Kettlgruber, G., Siket, C., Schwodiauer, R., & Bauer, S. (2010). Arrays of ultracompliant electrochemical dry gel cells for stretchable electronics. *Advanced Materials, 22*, 2065−2067.

Kil, E. H., Choi, K. H., Ha, H. J., Xu, S., Rogers, J. A., Kim, M. R., et al. (2013). Imprintable, bendable, and shape-conformable polymer electrolytes for versatile-shaped lithium-ion batteries. *Advanced Materials, 25*, 1395−1400.

Kim, D.-H., Lu, N., Ghaffari, R., Kim, Y.-S., Lee, S. P., Xu, L., et al. (2011a). Materials for multifunctional balloon catheters with capabilities in cardiac electrophysiological mapping and ablation therapy. *Nature Materials, 10*, 316−323.

Kim, D.-H., Lu, N., Ma, R., Kim, Y.-S., Kim, R.-H., Wang, S., et al. (2011b). Epidermal Electronics. *Science, 333*, 838−843.

Kim, H.-J., Maleki, T., Wei, P., & Ziaie, B. (2009). A biaxial stretchable interconnect with liquid-Alloy-Covered joints on elastomeric substrate. *Journal of Microelectromechanical System, 2009*(18), 138−146.

Koo, H.-J., So, J.-H., Dickey, M. D., & Velev, O. (2011). Towards all-soft matter circuits: prototypes of quasi-liquid devices with memristor characteristics. *Advanced Materials, 23*, 3559−3564.

Krupenkin, T., & Taylor, J. A. (2011). Reverse electrowetting as a new approach to high-power energy harvesting. *Nature Communicatios, 2*, 448.

Kubo, M., Li, X., Kim, C., Hashimoto, M., Wiley, B. J., Ham, D., et al. (2010). Stretchable microfluidic radiofrequency antennas. *Advanced Materials, 22*, 2749−2752.

Lacour, S. P., Wagner, S., Huang, Z. Y., & Suo, Z. G. (2003). Stretchable gold conductors on elastomeric substrates. *Applied Physics Letters, 82*, 2404−2406.

Lipomi, D. J., & Bao, Z. (2011). Stretchable, elastic materials and devices for solar energy conversion. *Energy and Environmental Science, 4*, 3314−3328.

Lipomi, D. J., Vosgueritchlan, M., Tee, B. C.-K., Hellstrom, S. L., Lee, J. A., Hox, C. H., et al. (2011). Skin-like pressure and strain sensors based on transparent elastic films of carbon nanotubes. *Nature Nanotechnology, 6*, 788−792.

Li, M., Yu, B., & Behdad, N. (2010). Liquid-tunable frequency selective surfaces. *IEEE Microwave and Wireless Components Letters, 8*, 423−425.

Lu, N., Lu, C., Yang, S., & Rogers, J. A. (2012). Highly sensitive skin-mountable strain gauges based entirely on elastomers. *Advanced Functional Materials, 22*, 4044−4050.

Moore, G. E. (1965). Cramming more components onto integrated circuits. *Electronics, 38*, 4−7.

Park, Y.-L., Chen, B.-R., & Wood, R. J. (2012). Design and fabrication of soft artificial skin using embedded microchannels and liquid conductors. *IEEE Sensors Journal, 12*, 2711−2718.

Park, J., Wang, S., Li, M., Ahn, C., Hyun, J. K., Kim, D. S., et al. (2012). Three-dimensional nanonetworks for giant stretchability in dielectrics and conductors. *Nature Communications, 3*, 916.

Rogers, J. A., Someya, T., & Huang, Y. (2010). Materials and mechanics for stretchable electronics. *Science, 327*, 1603−1605.

Sekitani, T., Noguchi, Y., Hata, K., Fukushima, T., Aida, T., & Someya, T. (2008). A rubberlike stretchable active matrix using elastic conductors. *Science, 321*, 1468−1472.

Song, W. S., & Salleo, A. (2009). *Flexible electronics: Materials and applications*. New York: Springer.

Vogel, E. (2007). Technology and metrology of new electronic materials and devices. *Nature Nanotechnology, 2*, 25−32.

Whitesides, G. M. (2006). The origins and the future of microfluidics. *Nature, 442*, 368−373.

Xia, Y., & Whitesides, G. M. (1998). Soft lithography. *Annual Review of Materials Science, 28*, 153−184.

Yang, Y., Jeong, S., Hu, L., Lee, S. W., & Cui, Y. (2011). Transparent lithium-ion batteries. *Proceeding of the National Academy of Sciences of the United States of America, 108*, 13013−13018.

Zhang, G. Q., & Roosmalen, A. (2009). *More than moore*. Dordrecht: Springer.

Zhao, Y., Wei, J., Vajtai, R., Ajayan, P. M., & Barrera, E. V. (2011). Iodine doped carbon nanotube cables exceeding specific electrical conductivity of metals. *Science Reports, 1*, 83.

Two-terminal organic nonvolatile memory (ONVM) devices

17

A. Sleiman[1], P.W. Sayers[1], D.A. Zeze[2], M.F. Mabrook[1]
[1] Bangor University, Bangor, UK; [2] Durham University, Durham, UK

17.1 Introduction

Organic materials have attracted a lot of attention recently in research due to their interesting features and potential applications in flexible electronics. Unlike most silicon-based devices, organic materials have an inherent flexibility, which make them viable for use on flexible substrates without developing stress fractures or losing their electronic characteristics. This has allowed for the development of a new generation of electronic devices called organic electronic devices. Such devices have attracted interest from both academic and industrial researchers due to their low cost, low temperature processing and mechanical flexibility. Applications such as organic solar cells (Gebeyehua et al., 2001; Har-Lavan, Ron, Thieblemont, & Cahen, 2009), light emitting displays (Müllen & Scherf, 2006; Zhou et al., 2006), organic field-effect transistors (Gelinck et al., 2004; Ball et al., 2009) and sensors (Someya et al., 2005) are all in rather advanced stages of research.

A major part of organic electronics research is targeted towards the fabrication of a reliable storage media to be used in flexible electronics applications. Organic nonvolatile memory (ONVM) emerges as the leading candidate for such applications, offering flexibility, printability, low fabrication cost and most importantly simple device architectures. The memory structure is said to be nonvolatile if its electrical state maintains itself after switching the power off on the device.

17.1.1 Two-terminal organic nonvolatile memory (ONVM) devices and the crossbar structure

Two-terminal ONVM (2T-ONVM) devices are composed of engineered organic structures sandwiched between two electrodes and exhibit two stable electrical states which can be controlled by an external electrical bias. The two stable electrical states (namely, ON and OFF states) may be resistive, ferroelectric or capacitive depending on the device structure. The performance of a 2T-ONVM device is tested by its retention characteristics, ON/OFF ratio, endurance upon ON/OFF cycling and switching speed. Retention characteristics measure the time a device can maintain its electrical state while the power is turned off, and retention characteristics of several years have been demonstrated for different 2T-ONVM (Cho et al., 2013; Son et al., 2010;

Yang, Ouyang, Ma, Tseng, & Chu, 2006). ON/OFF ratio is the ratio of the two measured electrical values in both states; high ON/OFF ratios were reported for certain 2T-ONVM structures (Cho et al., 2013). Endurance characteristics of the memory device are the number of times the device can operate, i.e. perform the write-read-erase-read cycle. Endurance characteristics vary in different 2T-ONVM structures and more than 10^5 cycles have been demonstrated for some devices (Son et al., 2010). Switching speed is the speed a 2T-ONVM can respond to the external electrical stimulus and switch from one state to another; a voltage pulse of several nanoseconds was reported to switch the devices in resistive type 2T-ONVM (Ouyang, Chu, Szmanda, Ma, & Yang, 2004).

2T-ONVM simple structures make it very easy to integrate in circuits; one of the simplest ways to integrate such structures in a circuit is using crossbar structure. In a crossbar structure, the bottom electrodes are deposited on the substrate, the active organic layer is engineered depending on the type of 2T-ONVM devices, and then the top electrodes are deposited to form an array as shown in Figure 17.1. Each cross-area between the bottom electrode and the top electrode is a storage memory cell. However, the external stimulus and control of each cell in the crossbar structure itself is not the simplest. The application of an external electrical stimulus on a top electrode affects the neighbouring and same row memory cells through leakage currents, the so-called crosstalk interference mechanism. But a simple solution of the addition of a diode or a transistor with the cell would improve the reading capability and reduce the effect of the crosstalk interference.

2T-ONVM devices also have the ability to be integrated with architectures which benefit from a third dimension in the memory stack. The third dimension, which benefits from the vertical stack of memory cells, is expected to increase the memory storage density. Depending on the type of 2T-ONVM, subsequent layers may be added on top of the first memory stack to end up in a larger number of memory devices in the same area of substrate. Song et al. (Song et al., 2010) demonstrated this on a resistive type ONVM with three consecutive stacks of memory devices in an 8×8 crossbar architecture.

17.1.2   Two-terminal memory technologies

In general, nonvolatile memory technologies can be divided into two types depending on the way we externally stimulate and control the device. The first type includes
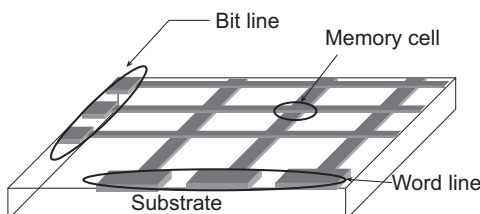
Figure 17.1 Crossbar structure and the resulting array of memory devices.
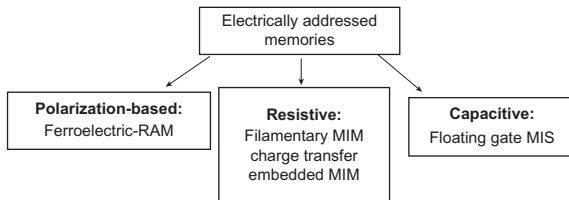
Figure 17.2 Electrically addressed two-terminal memory devices.

nonvolatile memories that can be mechanically addressed such as hard disks, optical disks, floppy disks or magnetic tapes; these types of technologies are not of particular interest in this chapter. The second type includes the nonvolatile memories that are electrically addressed, which again can be divided into many types depending on their structure, working mechanism and the electrical value that defines the ON and OFF states.

Electrically addressed organic nonvolatile memories can be polarization-based such as ferroelectric random-access-memory (FeRAM), resistive such as filamentary-based metal-insulator-metal (MIM), charge transfer-based MIM memory and embedded MIM structures, or capacitive such as floating gate embedded metal-insulator-semiconductor (MIS) structures (Figure 17.2).

17.1.2.1 Ferroelectric random-access-memory (FeRAM)

Ferroelectric RAMs (FeRAM) working mechanism is similar to that of the volatile dynamic-RAM (DRAM) except that the dielectric material of the DRAMs capacitor is replaced by ferroelectric material (Scott, 2013), which results in nonvolatile memory behaviour. In DRAMs, the memory structure consists of one transistor connected to a capacitor that gets charged or discharged to define the ON and OFF states. The capacitor loses the charges gradually. Thus, a continuous charging is needed to maintain the electrical state, which results in volatile memory. On the other hand, in FeRAM, the ferroelectric material in the capacitor has remnant polarization characteristics, and thus, it exhibits a hysteresis loop in the polarization−voltage (P−V) characteristics. This hysteresis results in two stable electrically addressed polarization states which may define the ON and OFF states and results in nonvolatile memory behaviour of the FeRAM.

17.1.2.2 Filamentary-based metal-insulator-metal (MIM)

A filamentary-based MIM memory device is an electrochemical cell that consists of an active electrode, an electrolyte and a counter electrode. The memory behaviour is represented by the switching behaviour of its current−voltage (I−V) characteristics between two stable resistance states, low and high resistance states (ON and OFF states). The switching occurs upon application of a positive bias on the active electrode which gets reduced to cations, migrates, and oxidizes on the counter electrode and forms a metallic filament that 'short-circuits' the electrolyte and switches the device to its low-resistance state. The application of a negative bias on the active electrode reverses the process, leads to the dissolution of the filament and turns the device

back to its OFF state. Organic filamentary-based MIM memories based on solid polymer electrolyte (Wu et al., 2011) and P3HTPCBM (Gao, Song, Chen, Zeng, & Pan, 2012) have been demonstrated.

17.1.2.3 Charge-transfer-based MIM memories

Charge-transfer memories consist of a combination of two materials; one is an electron donor and the other is an acceptor. The charge transfer that occurs from the donor to the acceptor upon the applied bias changes the resistivity of the acceptor material and the device between two different stable resistance states.

17.1.2.4 Embedded MIM

Organic MIM memories consist of an organic dielectric layer embedded with charge traps and sandwiched between two electrodes. The embedded MIM memories are another type of resistive switching memories where two stable resistance states define their ON and OFF states. The charging and discharging of the embedded traps switches the device between low and high resistance states. Organic, embedded MIM based on grapheme and different inorganic nanoparticles has been demonstrated (Son et al., 2010; Yang et al., 2006). The low-resistance state is achieved when the traps are filled with electrons, while the high resistance state is achieved when we discharge the embedded traps; a detailed explanation of the switching mechanism will be presented later in the chapter.

17.1.2.5 Embedded metal-insulator-semiconductor (MIS) structures

MIS structure is a widely used structure in many applications, such as capacitors, transistors and memories. Organic MIS structures are characterized by their capacitance−voltage (C−V) characteristics which exhibit three distinct regions: accumulation, depletion and deep depletion (inversion in inorganic MIS). Embedded MIS structures consist of charge traps added within the insulating layer of the structure; the charge traps behave as a floating gate. The addition of the floating gate results in a shift of the C−V curve and hysteresis in the double-sweep C−V characteristics. The hysteresis in the C−V characteristics may lead to the definition of two stable capacitance states, which may be controlled and read by an external bias stimulus and thus, exhibiting the expected memory behaviour. Embedded MIS structures using organic insulators and semiconductors have been previously reported (Mabrook, Yun, Pearson, Zeze, & Petty, 2009). Further details about the physics and mechanism of embedded MIS structures will be provided in the following sections.

17.1.3 Charge traps in 2T-ONVM devices

The most promising 2T-ONVM candidates are those that use charge traps inside a simple and well-known structure to induce the memory behaviour. The controlled
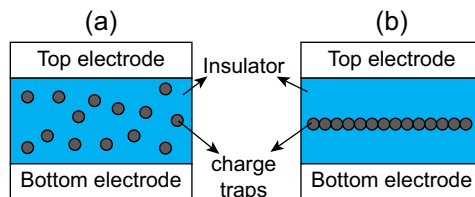
Figure 17.3 (a) Charge traps uniformly distributed inside the insulator, (b) Charge traps located in the middle of the insulator.

embedment of charge traps inside a simple MIM or MIS structure results in controlled memory behaviour and characteristics; this may be reflected in the number of charges that a memory can store which will be directly proportional to the amount of traps doped inside the structure.

As explained before, the embedded charge traps will result in a switching in the I−V characteristics between two different resistance states in the MIM structure, or a hysteresis in the organic MIS structure to define two capacitance states. The amount of charge stored is reflected by the ON/OFF ratio of the MIM memory and by the memory window at the flat band capacitance of the MIS memory. This amount of charge and the retention time inside the traps may be optimized by engineering the traps within the insulator. There are two ways to embed the traps inside the insulator. The first way is to blend the particles or traps in the insulator solution and spin the solution to create a thin, organic film, and the traps will be distributed almost uniformly throughout the organic film (Figure 17.3(a)). The second way is to position the traps in the middle of the insulating layer, which can be achieved as follows: spin coat a first insulating layer to form a surface where an assembly layer (matrix or thin film) of the traps are deposited on top. After the deposition of the traps, another insulating layer is spin coated on top of the traps to complete their confinement in the middle of two insulators (Figure 17.3(b)). Although the uniform distribution of the traps may result in a lower operating voltage while charging the storage nodes, the confinement of the traps in the middle of the insulator layer was reported to have the longest retention time (Jiao et al., 2010). This is attributed to the relatively thicker insulators confining the traps in the middle-trap-layer stack. Thus, whenever the charge is stored, it is trapped between two high and thick potential barriers, which minimizes the chances of charge leakage and thus optimizes the retention characteristics.

17.2   Carbon nanotube (CNT)-based 2T-ONVM structures

17.2.1   Layer-by-layer deposition of CNTs as charge traps embedded in 2T-ONVM

Carbon nanotubes (CNTs) have been used in different memory device structures. As charge storage nodes, CNTs have been used in silicon-based devices as a floating gate

in memory transistor structures (Lu & Dai, 2006; Ryu, Huang, & Choi, 2007). In 2T-ONVM, CNTs have been used as charge traps in embedded MIM memories; the CNTs were distributed uniformly throughout the insulator (similar to the structure shown in Figure 17.3(a)) and no retention characteristics were reported (Wei, Baral, Osterbacka, & Ivaska, 2008).

In this chapter, we will present the use of CNTs as charge storage nodes in organic MIS and MIM memories. The CNTs in our devices are deposited using layer-by-layer (LbL) technique which results in a CNT matrix or thin film and allows us to benefit from the middle-trap-layer structure similar to that shown in Figure 17.3(b). The CNT matrix confined between insulators optimizes the memory device's stability and retention characteristics.

LbL technique is a deposition technique based on a charge reversal to build up bilayer assemblies of oppositely charged (functionalized) molecules utilizing electrostatic attraction. The details of this technique and various film architectures built using CNTs are reported elsewhere (Jombert, Coleman, Wood, Petty, & Zeze, 2008; Palumbo et al., 2006). For the deposition of CNTs using LbL, three solutions were prepared: aqueous cationic Poly(ethyleneimine) (PEI) (Mw = 25,000) solution with pH = 8.5, aqueous anionic poly(acrylic acid) (PAA) (Mw = 4,000,000) solution with pH = 6.5 and an anionic CNTs solution (CNTs$_a$) functionalized and dispersed in sodium dodecyl sulphate (SDS) solution. Briefly, the deposition of CNTs using LbL is carried out as follows: functionalizing the substrate by seeds layers, which facilitates the adhesion of CNTs onto the substrate. This is performed by alternate immersion of the substrate in the PEI and PAA solutions for 15 min each. The substrate was then repeatedly immersed in PEI solution for 15 min, then in the CNTs$_a$ solution for 30 min. Each alternate immersion in PEI and CNTs$_a$ solution forms one bilayer. In the presented work in this chapter, the final CNTs matrix consists of three CNTs$_a$−PEI bilayers. A schematic diagram of the LbL deposition is presented in Figure 17.4(a) and an AFM image of deposited CNTs using LbL technique is shown in Figure 17.4(b).
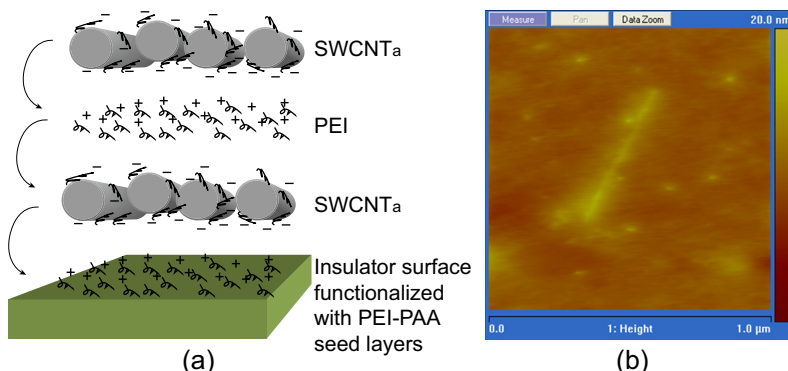
Figure 17.4 (a) Schematic diagram of the LbL technique, (b) AFM image of the deposited CNTs. Can be seen in Plate V (see colour section between pages 224 and 225).

17.2.2 CNTs as a floating gate in organic MIS memories

MIS memory devices are capacitive type memories where the two states (ON and OFF) are defined by two capacitive values. The simple organic MIS structure C−V characteristics may be divided into three regimes: accumulation, depletion and deep depletion as mentioned in Section 17.1.2.5. The C−V characteristic of a simple p-type MIS structure is shown in Figure 17.5(a); no hysteresis is observed upon the double bias sweep. On the other hand, in the embedded MIS memory devices, the C−V characteristics exhibit a clear hysteresis upon the double bias sweep (Figure 17.5(b)). If we define the accumulation capacitance by the ON state and the deep-depletion capacitance by the OFF state, the hysteresis enables us to read the state of the device at certain voltages and thus, use the device as a nonvolatile memory device.

In this section, we will present CNTs and pentacene-based ONVM devices consisting of MIS structure (entirely fabricated from materials compatible with flexible applications), which exhibited a relatively large memory window at low sweeping voltages and high charge retention. CNTs were sandwiched between SU8 photoresist and poly-methylmethacrylate (PMMA) insulators to serve as charge storage nodes. The device structure, shown in Figure 17.6, consists of Al/SU8/SWCNTs/PMMA/Pentacene/Au layers.

The device fabrication proceeded as follows: PEI, PAA, SDS, PMMA and pentacene were purchased from Sigma−Aldrich and SU8 was obtained from MicroChem Corp (MCC). These were combined with purified CNTs for the fabrication of the device shown in Figure 17.6 as described below.
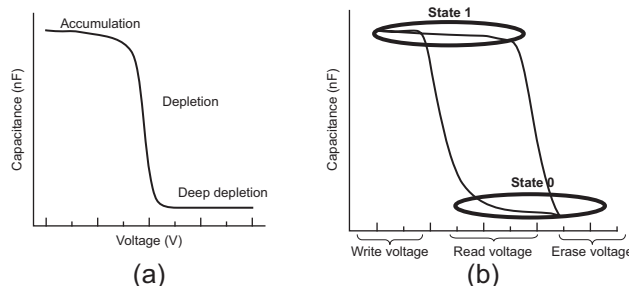
Figure 17.5 (a) Typical C−V characteristics of a simple p-type MIS structure (b) Hysteresis in the C−V characteristics of an embedded MIS structure.
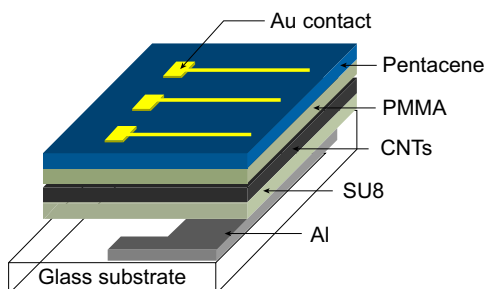
Figure 17.6 Schematic diagram of Al/SU8/CNTs/PMMA/pentacene/Au memory devices.

A glass substrate was cleaned using a piranha solution and a 100 nm-thick Al gate was thermally evaporated through a shadow mask. A 90 nm-thick layer of SU8 was spin coated (30 s at 3000 rpm, then baked for 5 min at 95 °C) and UV cross-linked to serve as a gate dielectric. CNTs were deposited using the LbL technique described in Section 17.2.1.

PMMA (20 wt% in chlorobenzene) was subsequently spin coated to a 40 nm thickness and baked for 25 min at 120 °C. Pentacene was thermally evaporated at a rate of 0.01−0.07 nm/s to a thickness of ∼30 nm. Finally, 30 nm of gold was deposited, through a shadow mask, to form Ohmic contacts. A PC-driven LCR Bridge (HP-4192) was used to record the capacitance−voltage (C−V) behaviour of the devices at 400 kHz with a 0.5 V/sec scan rate. Each test consisted of a double sweep (positive−negative) at room temperature in air.

A control device Al/SU8/PMMA/pentacene/Au was fabricated without CNTs, and its C−V characteristic is shown in Figure 17.7. The control device exhibited the usual characteristics of MIS structures based on p-type semiconductor, with flat band voltage of −2.5 V and full semiconductor depletion at 0 V. The double voltage sweep exhibited no hysteresis which is indicative of the absence of charge trapping in the bulk dielectrics and at the surface of the SU8 and PMMA layers. Assuming that the MIS structure consists of an insulator capacitance (C_{Ins}) connected in series with a semiconductor capacitance (C_S), the C−V characteristics of the control devices may be used to extract fabrication parameters.

Applying a positive DC bias to the gate of a p-type organic MIS capacitor causes majority carriers in the semiconductor to be repelled from the insulator interface. This is associated with a decrease in the capacitance as the depletion region expands. For a thin film, the capacitance is at its minimum when the organic semiconductor is fully depleted (the equivalent of the inversion regime for a conventional Si/SiO$_2$ MOS device). Thus, the minimum capacitance is determined by the insulator and semiconductor capacitances in series. The minimum capacitance (C_{min}) corresponding to full depletion is then given by (Yun, Pearson, & Petty, 2009):

$$C_{min} = A\frac{\varepsilon_{Ins}}{d_{Ins} + \frac{\varepsilon_{Ins}W_{Max}}{\varepsilon_S}} \tag{17.1}$$
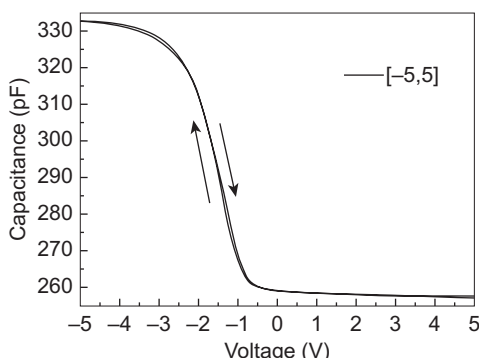
Figure 17.7 C−V characteristics of the control Al/SU8/PMMA/pentacene/Au device.

where ε_{Ins} is the dielectric constant of the SU8/PMMA insulator stack, d_{Ins} is the cumulative SU8 and PMMA thickness, A is the device area (1 mm^2) and ε_S is the dielectric constant of pentacene ($3 \times 8.85 \times 10^{-12}$ F/m) (Lee, Park, & Choi, 2003; Reddy, Das, Ray, & Dhar, 2007). Using the insulator stack thickness measured using AFM (130 nm), we obtained $\varepsilon_{Ins} = 43.18 \times 10^{-12}$ F/m, corresponding to an effective relative permittivity of 4.88. The maximum depletion width, $W_{Max} = 26$ nm, calculated from Eqn (17.1) is close to the estimated pentacene thickness.

On the other hand, the devices with added CNTs floating gate to form a Al/Su8/CNTs/PMMA/pentacene/Au structure exhibit clear hysteresis in their C−V and conductance−voltage (G−V) characteristics as shown in Figure 17.8. The memory devices exhibit a shift in the flat band voltage at the value of its flat band capacitance which was approximately 187 pF. The change in the capacitance of the memory devices as compared to the control devices is due to the fact that new material was added to the device, which induces trapping and de-trapping of electrons in a floating gate, i.e. it cannot be treated as simply the equivalent circuit of the control device.

However, the C−V curves indicate that after reaching accumulation in the first sweep more positive voltages are needed to reach the depletion of the pentacene and result in a shift in the flat band voltage towards more positive values. This shift induces a clockwise hysteresis which is a typical behaviour of floating-gate-MIS-based 2T-ONVM on p-type semiconductor where the carriers (electrons) are injected into the floating gate from the aluminium gate. This was attributed to the fact that the charging and discharging of the floating gate was easier through one Su8 layer as compared to the charging and discharging from the semiconductor layer where effectively a resistance of two layers exists − the semiconductor pentacene layer and the PMMA insulator layer. The shift in the flat band voltage (ΔV_{FB}) may be extracted from the shift in the peaks of the G−V characteristics between the positive and negative voltage sweeps. As shown in Figure 17.8, ΔV_{FB} increased as the voltage sweep range increased, which is expected in such memory devices, and at ± 30 V sweep range the ΔV_{FB} was estimated to be around 6 V. This shift multiplied by the capacitance usually defines the memory window of the devices, as such the charges
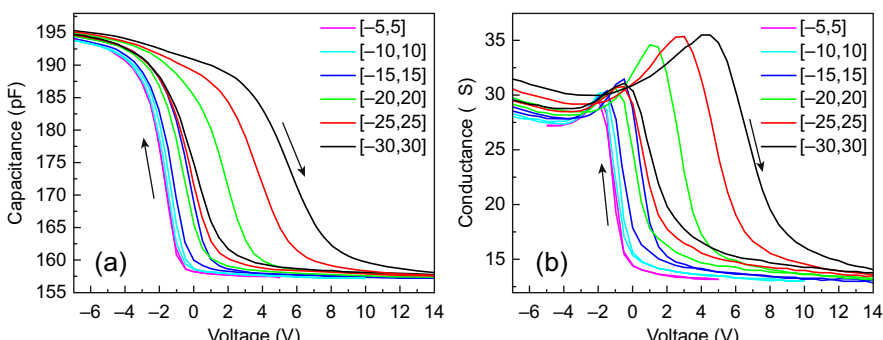
Figure 17.8 (a) C−V and (b) G−V characteristics of Al/SU8/CNTs/PMMA/pentacene/Au memory devices.

(Q) stored in the CNTs floating gate can be estimated by (Mabrook, Pearson, Kolb, Zeze, & Petty, 2008; Sleiman, Mabrook, et al., 2012; Sleiman, Rosamond, et al., 2012):

$$Q = C_{FB} \cdot \Delta V_{FB}$$

where C_{FB} is the flat band capacitance. For $C_{FB} = 187$ pF and $\Delta V_{FB} = 6$ V, a storage density of about 7.04×10^{10}/cm^2 was estimated to the memory devices at a sweep voltage of ± 30 V. An interesting feature of the presented devices is that the hysteresis is centered close to 0 V, which is favoured in memory applications as it indicates that the devices may operate at low voltages. For example, a reading voltage of 2 V is sufficient for present devices in order to distinguish between the low capacitance and high capacitance states.

The retention behaviour of the MIS-based memory structures was observed by monitoring the capacitance with time after charging the device for a few seconds and then applying a stress voltage (5 V in this study). Here, a two second 9 V pulse was applied to charge the memory device. Over 96% of the charge trapped in the CNTs remained confined in the floating gate over the measurement time of more than 400 min of continuous testing as shown in Figure 17.9. The relatively small change in the capacitance after 400 min of continuous testing indicates that the MIS memory structure has a very good retention capacity, and there is very little leakage current in the MIS structure, and this is due to the LbL deposited CNTs, which benefit from the middle-layer-traps (Figure 17.3 (b)) confined between two insulating layers.

17.2.2.1   CNTs as storage nodes in organic MIM memories

Embedded organic MIM memory devices are resistive type memories where the two states (ON and OFF) are defined by two resistive values. The memory behaviour of the device is shown by the switching in its I−V characteristics between two resistive states − low-resistance high-current ON state and high-resistance low-current OFF state. Upon sweeping the bias on the device, and if the device is initially in the OFF state, at a certain voltage the device current will increase abruptly and thus switch
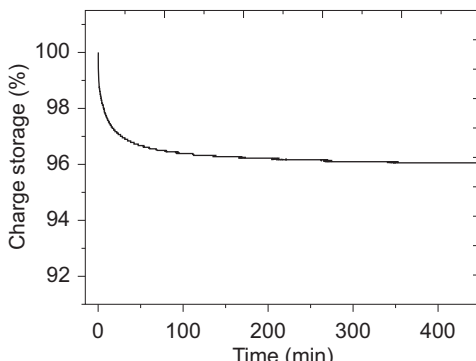
Figure 17.9 Retention characteristics of the fabricated MIS-based memory devices.

to ON state. That voltage is called the writing voltage. Similarly, upon sweeping in the opposite direction, at a certain voltage, the current will abruptly go back to its initial values (OFF state). This is called the erase voltage. At any voltage between the writing and the erase voltages, the device can exhibit both states ON or OFF (depending on the previously applied voltage) and thus, the range of voltages between the write and erase voltages may be used as the read voltage. Usually, the read voltage is chosen at the highest ON/OFF ratio to be able to easily distinguish between the different states.

In this section, we will present 2T-ONVMs based on CNTs as charge storage nodes embedded between two PMMA insulating layers to form the active layer of the Al/PMMA/CNTs/PMMA/Al devices (Figure 17.10(a)). CNTs were deposited using the LbL technique, which ensures that the CNTs form a 'thin-film' matrix. This technique will also ensure that the CNTs are confined between the bottom and top PMMA layers (similar to Figure 17.3(b)), allowing for switching behaviour and the out-of-plane charge transport within the memory layer to be investigated. As discussed in Section 17.1.3, the position of the charge traps in the middle of the insulating layer is believed to enhance the performance of the 2T-ONVMs in terms of stability and retention as the stored charges will be trapped between two potential barriers formed by the top and bottom PMMA layers.

For the fabrication of such devices, a 100 nm-thick Al bottom electrode was thermally evaporated on a glass substrate cleaned using the Piranha procedure. PMMA (20 wt% in chlorobenzene) was then spun coated to a thickness of 40 nm (6000 rpm for 50 s) and baked for 25 min at 120 °C. CNTs were deposited using the LbL technique. A second layer of 40 nm PMMA was then deposited on the device to complete the CNTs encapsulation. Finally, the top Al electrode was thermally evaporated to finalize the fabrication of the device in a crossbar structure similar to Figure 17.1, with a surface area of 1 mm^2.

The device area was masked while the excess organic thin film was etched using oxygen plasma dry etching to reveal the Al bottom contact. A PC-driven HP 4140 b pA Meter/DC voltage source was used to record the current−voltage (I−V) characteristics of the devices with a scan rate of 0.2 V/sec. Each test consisted of a double sweep (positive−negative) at room temperature in air.

Figure 17.11 shows the I−V characteristics for an Al/PMMA/SWCNTs/PMMA/Al memory device (inset of Figure 17.11 shows the I−V characteristics in log scale). The
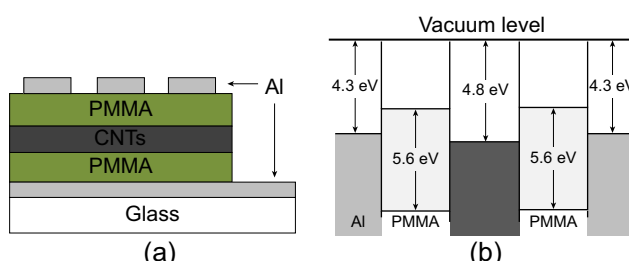
Figure 17.10 (a) Schematic diagram and (b) Band diagram of the Al/PMMA/CNTs/PMMA/Al memories.
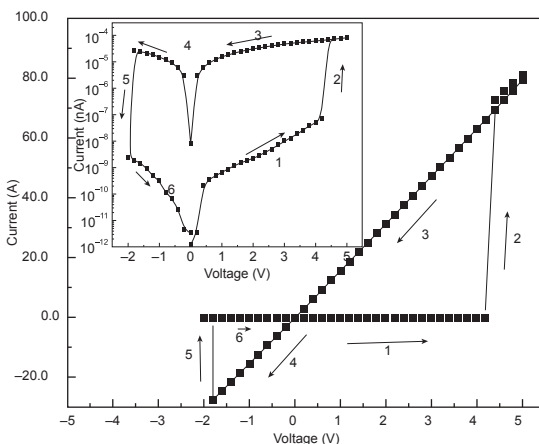
Figure 17.11 I—V characteristics of the fabricated memories. Inset: I—V characteristics in Log scale.

voltage applied to the device was split into two consecutive parts, a positive scan starting from 0 V towards 5 V and then back to 0 V, then a negative scan starting at 0 V towards −2.1 V and then back to 0 V. The I—V characteristics for the devices show clear electrical switching behaviour. Initially, the device was in the low conductivity state (OFF state) during the positive scan. The conductivity of the device switched from its low conductivity to high conductivity (ON state) when the voltage exceeded a threshold voltage of 4.4 V, which represents the writing voltage. The high conductivity state was sustained even when the power was turned off (after sweeping back to 0 V) as shown in Figure 17.11.

On the other hand, the negative scan causes the devices to switch from the ON to the OFF state; the transition to the OFF state was achieved by applying a reverse voltage of −2.1 V which represents the erase voltage. The maximum current ratio between the ON and OFF states for the tested devices is about 2×10^5 using a low reading voltage of 1 V.

The conduction mechanism in the fabricated devices can be described as follows: the conduction mechanism in the initial OFF state follows a thermionic emission mechanism at low voltages where the electrons pass through the potential barrier at the Al/PMMA interface and a trap-limited space-charge-limited-current (SCLC) at higher voltages, where the CNTs capture the electrons and trap them inside the PMMA layer. As the voltage is further increased to reach a threshold voltage where the CNTs traps are completely filled with electrons, the injected electrons flow independent of the traps influence and can easily reach the counter electrode and thus, the device is switched to its ON state. On the other hand, a negative bias sufficient to de-trap the electrons will cause the filled states to become empty again and thus switch the device back to its OFF state. Using the proposed switching mechanism, we are able to extract the density of traps inside the device at the trap-filled voltage (V_{TFL}), i.e. the switching voltage at which the traps are totally filled with electrons and the transition happens to the filled-traps conduction (4.4 V in our devices). The
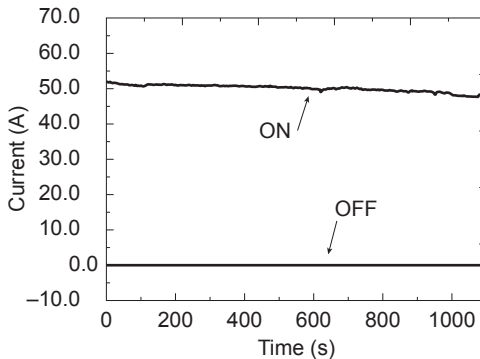
Figure 17.12 Retention of the ON and OFF states of the fabricated memories.

density of traps (N_t), is given by (Arif et al., 2007; Sleiman, Mabrook, et al., 2012; Sleiman, Rosamond, et al., 2012)

$$N_t = \frac{3}{2} \frac{\varepsilon \varepsilon_0 V_{TFL}}{q d^2} \qquad (17.2)$$

where ε is the dielectric constant, ε_0 is the free space permittivity, q is the electron charge and d is the thickness of the structure. using the dielectric constant of the PMMA to be between 2.89 and 3.66 (Yun et al., 2009), the density of traps inside the device was estimated to be between 2.19×10^{17}/cm^3 and 2.78×10^{17}/cm^3.

The stability and retention characteristics of the bistable memory devices were tested by monitoring the current in both ON and OFF states at a constant applied reading voltage of 3.5 V for more than 1000 s. The device was switched ON by applying a 1 s pulse of 4.5 V, then the retention of the ON state was recorded. The retention ability of the OFF state was also observed after switching the device back to the OFF state using a 1 s pulse of −2.1 V. The current-time characteristics of the ON and OFF states are shown in Figure 17.12 at a reading voltage of 3.5 V. The current maintained the original value of 40 µA in the ON state and 20 nA in the OFF state (representing a 2×10^3 ON/OFF ratio at reading voltage 3.5 V). Similar to the MIS structure in the previous section, the relatively small change in the current after continuous testing indicates that the MIM memory structure has a very good retention capacity, and there is very little leakage current in the MIM structure. This is due to the LbL-deposited CNTs which benefit from the middle-layer-traps (Figure 17.3(b)) confined between two insulating layers.

17.3 Conclusion

In this report, we presented the utilization of CNTs as charge storage nodes in two-terminal ONVM. Two-terminal ONVMs benefit from the crossbar structure and their ability to be used in three-dimensional memory stacks. CNTs were used as a floating gate in MIS memory and as charge traps in embedded MIM memory structures. The

CNTs were deposited by LbL technique, which results in a CNTs matrix, and allows us to confine the traps between two insulating layers, which optimizes the memory devices stability and retention characteristics.

In the MIS structure, CNTs served as the floating gate in a pentacene-based floating-gate memory device in the form of an Al/SU8/CNTs/PMMA/pentacene/Au structure. The structure showed enhanced memory effects at relatively low voltages and a high charge retention of 96%. The charge-trapping effect is attributed to the charges injected from the gate through the SU8 to the CNTs.

In the embedded MIM memory, an organic bistable device was fabricated, benefitting from CNTs between two PMMA insulating layers (Al/PMMA/CNTs/PMMA/Al). The devices exhibit an electrical bistability and nonvolatile memory characteristics in terms of switching between ON and OFF states due to application of positive and negative voltages, respectively. The retention characteristics showed two stable and distinct conduction states. The fabricated memory operates below 5 V in terms of writing, reading, and erasing and it has an ON/OFF ratio of $\sim 2 \times 10^5$ at a 1 V reading voltage. The electrical bistability of the device was attributed to the trapping and detrapping of electrons by CNTs.

The characteristics described in this work for two different memory structures clearly demonstrate the potential for CNTs to be used as storage elements in advanced nonvolatile organic memory devices for flexible electronics. And, it suggests the possibility for using simple and low-cost structures for memory devices. Further work is needed on the long-term stability and write-read-erase endurance cycles of the devices.

References

Arif, M., Yun, M., Gangopadhyay, S., Ghosh, K., Fadiga, L., Galbrecht, F., et al. (2007). Polyfluorene as a model system for space-charge-limited conduction. *Physical Review B, 75*(19), 195202. http://dx.doi.org/10.1103/PhysRevB.75.195202.

Ball, J. M., Wöbkenberg, P. H., Colléaux, F., Heeney, M., Anthony, J. E., McCulloch, I., et al. (2009). Solution processed low-voltage organic transistors and complementary invertors. *Applied Physics Letters, 95*(10), 103310. http://dx.doi.org/10.1063/1.3212736.

Cho, B., Song, S., Ji, Y., Choi, H., Ko, H. C., Lee, J., et al. (2013). Demonstration of addressable organic resistive memory utilizing a PC-interface memory cell tester. *IEEE Electron Device Letters, 34*(1), 51. http://dx.doi.org/10.1109/LED.2012.2226231.

Gao, S., Song, C., Chen, C., Zeng, F., & Pan, F. (2012). Dynamic processes of resistive switching in metallic filament-based organic memory devices. *The Journal of Physical Chemistry C, 116*(33), 17955. http://dx.doi.org/10.1021/jp305482c.

Gebeyehu, D., Brabec, C. J., Padinger, F., Fromherz, T., Hummelen, J. C., Badt, D., et al. (2001). The interplay of efficiency and morphology in photovoltaic devices based on interpenetrating networks of conjugated polymers with fullerenes. *Synthetic Metals, 118*(1−3), 1. http://dx.doi.org/10.1016/S0379-6779(00)00276-9.

Gelinck, G. H., Huitema, H. E. A., Veenendaal, E., Cantatore, E., Schrijnemakers, L., Putten, J. B. P. H., et al. (2004). Flexible active-matrix displays and shift registers based on solution-processed organic transistors. *Nature Materials, 3*(2), 106. http://dx.doi.org/10.1038/nmat1061.

Har-Lavan, R., Ron, I., Thieblemont, F., & Cahen, D. (2009). Toward metal-organic insulator-semiconductor solar cells, based on molecular monolayer self-assembly on n-Si. *Applied Physics Letters, 94*(4), 043308. http://dx.doi.org/10.1063/1.3076115.

Jiao, B., Wu, Z., He, Q., Tian, Y., Mao, G., & Hou, X. (2010). Dependence of the organic nonvolatile memory performance on the location of ultra-thin Ag film. *Journal of Physics D: Applied Physics, 43*(3), 035101. http://dx.doi.org/10.1088/0022−3727/43/3/035101.

Jombert, S., Coleman, K. S., Wood, D., Petty, M. C., & Zeze, D. A. (2008). Poole−Frenkel conduction in single wall carbon nanotube composite films built up by electrostatic layer-by-layer deposition. *Journal of Applied Physics, 104*(9), 094503. http://dx.doi.org/10.1063/1.3006015.

Lee, Y. S., Park, J. H., & Choi, J. S. (2003). Electrical characteristics of pentacene-based Schottky diodes. *Optical Materials, 21*(1−3), 433. http://dx.doi.org/10.1016/S0925-3467(02)00178-7.

Lu, X. B., & Dai, J. Y. (2006). Memory effects of carbon nanotubes as charge storage nodes for floating gate memory applications. *Applied Physics Letters, 88*(11), 113104. http://dx.doi.org/10.1063/1.2179374.

Mabrook, M. F., Pearson, C., Kolb, D., Zeze, D. A., & Petty, M. C. (2008). Memory effects in hybrid silicon-metallic nanoparticle-organic thin film structures. *Organic Electronics, 9*(5), 816. http://dx.doi.org/10.1016/j.orgel.2008.05.023.

Mabrook, M. F., Yun, Y., Pearson, C., Zeze, D. A., & Petty, M. C. (2009). Charge storage in Pentacene/Polymethylmethacrylate memory devices. *IEEE Electron Device Letters, 30*(6), 632. http://dx.doi.org/10.1109/LED.2009.2018128.

Müllen, K., & Scherf, U. (2006). *Organic light emitting devices*. Germany: Wiley-VCH.

Ouyang, J., Chu, C. W., Szmanda, C. R., Ma, L., & Yang, Y. (2004). Programmable polymer thin film and non-volatile memory device. *Nature Materials, 3*(12), 918. http://dx.doi.org/10.1038/nmat1269.

Palumbo, M., Lee, K. U., Ahn, B. T., Suri, A., Coleman, K. S., Zeze, D., et al. (2006). Electrical investigations of layer-by-layer films of carbon nanotubes. *Journal of Physics D: Applied Physics, 39*(14), 3077. http://dx.doi.org/10.1088/0022-3727/39/14/030.

Reddy, V. S., Das, S., Ray, S. K., & Dhar, A. (2007). Electrical characteristics of pentacene thin film junctions. International workshop on physics of semiconductor devices. *IWPSD 2007, 1*(1), 569.

Ryu, S. W., Huang, X. J., & Choi, Y. K. (2007). Vertically standing carbon nanotubes as charge storage nodes for an ultimately scaled nonvolatile memory application. *Applied Physical Letters, 91*(6), 063110. http://dx.doi.org/10.1063/1.2767211.

Scott, J. F. (2013). Prospects for ferroelectrics: 2012−2022. *ISRN Materials Science, 2013*(1), 187313. http://dx.doi.org/10.1155/2013/187313.

Sleiman, A., Rosamond, M. C., Alba Martin, M., Ayesh, A., Al Ghaferi, A., Gallant, A. J., et al. (2012). Pentacene-based metal-insulator-semiconductor memory structures utilizing single walled carbon nanotubes as a nanofloating gate. *Applied Physics Letters, 100*(2), 023302. http://dx.doi.org/10.1063/1.3675856.

Sleiman, A., Mabrook, M. F., Nejm, R. R., Ayesh, A., Al Ghaferi, A., Petty, M. C., et al. (2012). Organic bistable devices utilizing carbon nanotubes embedded in poly (methyl methacrylate). *Journal of Applied Physics, 112*(2), 024509. http://dx.doi.org/10.1063/1.4737599.

Someya, T., Kato, Y., Sekitani, T., Iba, S., Noguchi, Y., Murase, Y., et al. (2005). Conformable, flexible, large-area networks of pressure and thermal sensors with organic transistor active matrixes. *Proceedings of the National Academy of Sciences of the United States of America, 102*(35), 12321. http://dx.doi.org/10.1073/pnas.0502392102.

Son, D. I., Kim, T. W., Shim, J. H., Jung, J. H., Lee, D. U., Lee, J. M., et al. (2010). Flexible organic bistable devices based on graphene embedded in an insulating Poly(methyl methacrylate) polymer layer. *Nano Letters, 10*(7), 2441. http://dx.doi.org/10.1021/nl1006036.

Song, S., Cho, B., Kim, T.-W., Ji, Y., Jo, M., Wang, G., et al. (2010). Three-dimensional integration of organic resistive memory devices. *Advanced Materials, 22*(44), 5048. http://dx.doi.org/10.1002/adma.201002575.

Wei, D., Baral, J. K., Osterbacka, R., & Ivaska, A. (2008). Memory effect in an ionic liquid matrix containing single-walled carbon nanotubes and polystyrene. *Nanotechnology, 19*(5), 055203. http://dx.doi.org/10.1088/0957−4484/19/05/055203.

Wu, S., Tsuruoka, T., Terabe, K., Hasegawa, T., Hill, J. P., Ariga, K., et al. (2011). A polymer-electrolyte-based atomic switch. *Advanced Functional Materials, 21*(1), 93. http://dx.doi.org/10.1002/adfm.201001520.

Yang, Y., Ouyang, J., Ma, L., Tseng, R. J.-H., & Chu, C.-W. (2006). Electrical switching and bistability in Organic/Polymeric thin films and memory devices. *Advanced Functional Materials, 16*(8), 1001. http://dx.doi.org/10.1002/adfm.200500429.

Yun, Y., Pearson, C., & Petty, M. C. (2009). Pentacene thin film transistors with a poly (methyl methacrylate) gate dielectric: optimization of device performance. *Journal of Applied Physics, 105*(3), 034508. http://dx.doi.org/10.1063/1.3075616.

Zhou, L., Wanga, A., Wu, S.-C., Sun, J., Park, S., & Jackson, T. N. (2006). All-organic active matrix flexible display. *Applied Physics Letters, 88*(8), 083502. http://dx.doi.org/10.1063/1.2178213.

Printed, flexible thin-film-batteries and other power storage devices

18

G. Huebner[1], M. Krebs[2]
[1] Institute for Applied Research (IAF), Hochschule der Medien (HdM), Stuttgart, Germany;
[2] VARTA Microbattery GmbH, R&D, Ellwangen, Germany

18.1   Introduction

Batteries are very common in daily life, with a lot of daily articles (e.g., shaver, torches, mobile devices, laptops, cell phones) containing either rechargeable or non-rechargeable batteries, typically with battery cells of the size AA or AAA, custom sizes, or the smaller button cells. Basically, a battery consists of two electrochemical active materials, the so-called electrodes that are able to convert stored chemical energy into electrical energy. The battery has an anode, the positive terminal, and a cathode, the negative end. Between the electrodes is an electrolyte that allows ion transport. Nonrechargeable batteries are called primary batteries; they are only used once and have to be discarded and should be recycled. Rechargeable ones are called secondary batteries (in some countries called "accumulators") and can be used multiple times, if good care is taken they can be cycled (charged, discharged) several hundred times.

The basic combination of anode, cathode, and electrolyte is called a single battery cell. Each cell offers a characteristic nominal voltage (e.g., a lead-acid cell has 2.1 V). If higher voltages are required, cells can be connected in a series; thus, in a car six lead-acid cells are combined for a 12-V starter battery. For detailed information about battery technology, see Kiehne and Albert (2003) and Linden (1995).

There are many known electrochemical systems for conventional batteries. Each system has its own history and specific disadvantages and advantages. They are more or less toxic. For instance, the NiCd system vanished during the past two decades because of the poisonous cadmium. Mercury that formerly was an ingredient of a lot of batteries is no longer allowed. In most cases, the electrochemical systems are inseparably linked to specific standardized housings (e.g., AA, AAA cells). These housings typically are metallic cups where the cup often functions as the current collector of the negative pole. Inside the cell, a mechanical pressure is applied to establish a good contact between the electrodes and the separator/electrolyte. These standardized housings are produced in millions of products. A change in design causes enormous costs for new tools and dedicated production facilities.

A new type of cell was introduced in the mid-1990s, the so-called pouch cells. These are also called lithium-polymer batteries (i.e., lithium-ion with a polymeric

electrolyte). The electrodes are sheet type and laminated together with a separator. The whole cell is wrapped in a barrier foil. If a failure occurs, the cells inflate due to internal gases. These pouch cells paved the way to printed, flexible batteries.

The printing technologies promise a great flexibility in design and a change in the layout can easily be done without generating too much cost. It is just a matter of changing the printing forms. As usual in conventional multicolor printing, it is easy to print several layers on top of each other.

Considering the pros and cons of common electrochemical systems, the systems that are promising candidates to be printed are listed in Table 18.1. Therefore, it is necessary for the electrode materials to be available in printable paste form. The basic electrochemical reaction is shown in Table 18.1.

In conventional batteries, the housing is responsible for several tasks. First, it keeps the grainy electrode materials together to enable the electron and ion transport. In printed batteries, the cohesion of the grains of the electrode materials must be ensured by adding certain amounts of binder. Second, the housing functions as the current collector. When batteries are printed onto nonconductive flexible plastic substrates, conductive layers must be added to collect the current; they additionally function as the outside connectors. A third task of the housing is to provide an appropriate sealing. Metals typically are impermeable enough but for instance standard PET foil is not. The battery must be sealed against loss of humidity from inside to outside. If the electrolyte dries out completely, the battery does not function. On the other hand, some gases may not be able to get into the cell. As an example, carbon dioxide can react with alkaline electrolytes. The sealing must allow that the current collectors can lead to the outside of the cell.

Some of the electrochemical systems are quite easy to adapt to printing technologies; others are more challenging. Lithium-containing materials are complicated because they are humidity sensitive and therefore need inert (dry) atmospheres

Table 18.1 Possible chemical systems for printed batteries

Electrochemical systems	Voltage	Electrochemical reaction
Nonrechargeable		
Zinc/manganese-dioxide	1.5 V	$Zn + 2MnO_2 + H_2O \rightarrow ZnO + 2MnO(OH)$
Zinc/air	1.4 V	$2Zn + O_2 + 2H_2O \rightarrow 2Zn(OH)_2$
Zinc/silver oxide	1.5 V	$Zn + Ag_2O \rightarrow 2Ag + ZnO$
Lithium/manganese dioxide	3.0 V	$Li + MnO_2 \rightarrow MnOOLi$
Rechargeable		
Nickel/metal hydride	1.2 V	$Metal\text{-}H + 2NiOOH \rightarrow Metal + 2Ni(OH)_2$
Lithium-ion	3.7 V	$Li_{1-x}Mn_2O_4 + Li_xC_n \rightarrow LiMn_2O_4 + nC$
Zinc/air	1.45 V	$Zn + 1/2O_2 \rightarrow ZnO$
Post lithium	Different	Different systems using air, sulphur-cathode, or solid-state components

Table 18.2 **Applicability for printing**

Electrochemical systems	Voltage	Electrolyte	Applicability for printing
Nonrechargeable			
Zinc/manganese-dioxide	1.5 V	Zinc chloride	++
Zinc/air	1.4 V	Alkaline	−− Cathode complicated,
Zinc/silver oxide	1.5 V	Alkaline	o
Lithium/manganese dioxide	3.0 V	Organic (aprotic)	− Humidity/water sensitive
Rechargeable			
Nickel/metal hydride	1.2 V	Alkaline 25% KOH potassium hydroxide (caustic potash)	o
Lithium-ion	3.7 V	Organic	− Humidity/water sensitive
Zinc/air	1.45 V	Alkaline	−− Cathode complicated,
Post lithium	Different	Organic	not possible

++ very easy; + easy; o feasible; − difficult, inert (dry) atmospheres required; −− very complicated.

(e.g., appropriate glove boxes). Some of the chemical reactions take place in a very alkaline environment; see Table 18.2.

From Table 18.2 it can be derived that zinc/manganese systems are the easiest to be printed, but those that use alkaline electrolytes are not much more complicated to print at room temperature as long as the electrolyte handling is mastered.

18.2 The development of printed batteries

About 20 years ago, printed film type batteries were reported. Since then, a few companies have gone commercial with printed batteries. However, all commercially available printed batteries solely use the zinc/manganese-dioxide electrochemical system, which are not rechargeable and produce a nominal 1.5-V voltage. Since 1997, an Israeli company called "Power Paper" has offered printed batteries under the same brand name for medical and beauty applications (cosmetic patches; www.powerpaper.cn). Today they are based in China.

Other enterprises started to offer printed flexible batteries. The German based company KSW-Microtec no longer exists.

Figure 18.1 Thin, flexible batteries SoftBattery by Enfucell.
Source: © Enfucell Oy.
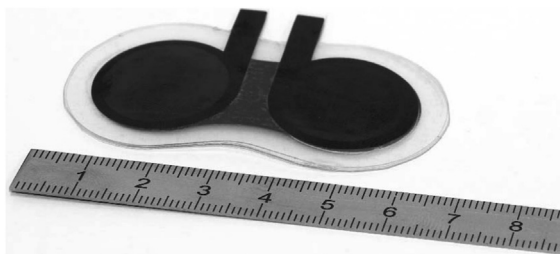
Figure 18.2 Screen-printed battery.
Source: Fraunhofer-Gesellschaft (http://www.fraunhofer.de/presse/presseinformationen/2009/juli/batterien-drucker.jsp).

Another vendor offering flexible batteries was Thin Battery Technologies, Inc., launched in 2003 based on knowledge of the company Eveready (now Energizer). Thin Battery Technologies has merged into the company Blue Spark Technologies and is located in Westlake, Ohio (see www.bluesparktechnologies.com).

Around 2007, the company Enfucell based in Vantaa, Finland, entered the market. Nowadays they offer three types of so-called "SoftBattery": a larger single-cell battery (Figure 18.1), a smaller one, and a series connection of two small cells. In July 2009, the Fraunhofer Research Institution for Electronic Nanosystems in Chemnitz, Germany, announced a screen-printed battery. This printed battery is also based on the zinc-manganese system and combines two cells in a series connection (Figure 18.2). On the web are more offerings on zinc/manganese-dioxide printable batteries. There is the Austrian company Prelonic (www.prelonic.com; Plastic Electronic) and the Thin Profile Technologies in Champlin, Minnesota (http://www.thinprofiletech.com/) and others.

Other types of electrochemical systems for printed batteries have only been shown in the laboratory stage, but so far, no commercial application is known to the authors. A project funded by the EU called GREENBAT with partners CEA Liten (Grenoble, France), the Imperial College (London, UK), VTT (Oulu, Finland), Plastic Electronic

Figure 18.3 Printed NiMH battery, as presented at the LOPE-C 2010 fair.
Source: www.hdm-stuttgart.de/iad.

(Linz, Austria), Norbert Schläfli (Zofingen, Switzerland), and VARTA Microbattery (Ellwangen, Germany) started in 2008 and aimed to develop environmentally friendly "green" batteries based on lithium ion. The project finished in 2011.

The University of Applied Science, Hochschule der Medien Stuttgart, Germany, started around 2007 based on a feasibility study (Vindus, 2006) together with VARTA Microbattery to investigate Ni/MH rechargeable batteries. Since then, several prototypes (e.g., Figure 18.3) have been developed, presentations given at conferences, and results published (Wendler, Krebs, & Huebner, 2011; Wendler, Krebs, & Huebner, 2010). The work is ongoing in a project called BatMat.

In the United States, Berkeley researchers founded an enterprise called Imprint Energy, Inc. (http://www.imprintenergy.com/), which works on zinc-polymeric electrolyte rechargeable printable batteries. They provide views of the stencil printing manufacturing process in a YouTube promotional video (http://www.youtube.com/watch?v=dEh7BFb9464).

Newer publications (3D Printing, 2013) report tiny batteries (lithium-ion) directly coming from three-dimensional printers. The US based company Solicore (www.solicore.com) just recently announced an inkjet-printed Lithium-polymer primary cell (3 V).

18.3 Basic design of printed batteries

The principal structure of a printed battery differs only marginally from that of a conventional battery. The basic concept is based on stacked layers (Figure 18.4) that comprise the anode, cathode, separator that is drenched in electrolyte, the corresponding current collectors, and the housing, which here is a flexible substrate.

The overall thickness of the thin, flexible batteries is around 0.5 mm. One very important feature is the sealing. Besides the barrier property of the substrate itself, the sealing between the bottom and the top substrate is crucial for the life of the battery. The final assembly could perhaps be compared with an Italian noodle specialty, ravioli.
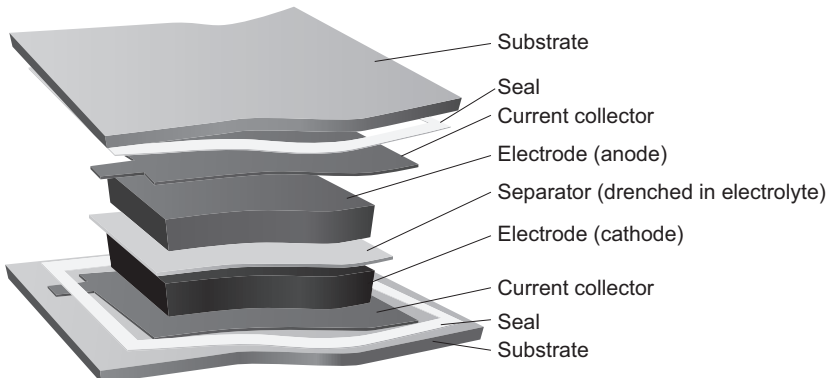
Figure 18.4 Basic printed battery "stack type" cell concept.
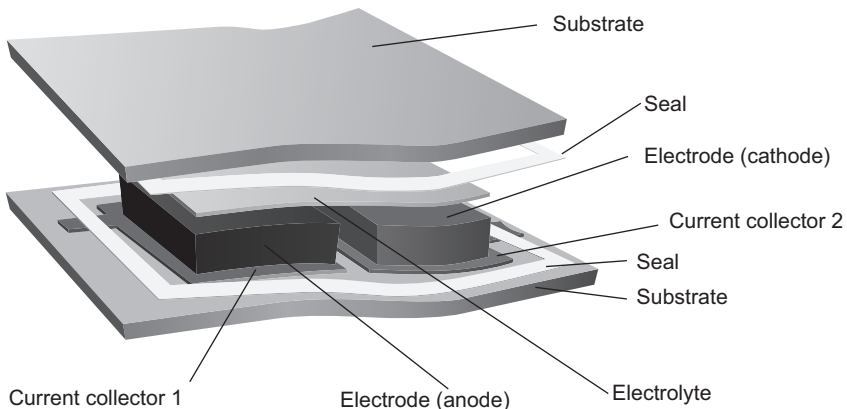
Figure 18.5 Battery design concept in coplanar type.

For printed batteries, besides the stack type concept another basic design concept exists, the coplanar-type or side-by-side design (Figure 18.5). The differences in design influence their performance as well as their complexity in manufacturing. The decisive advantage of the coplanar cell concept (Figure 18.5) is that no separator is needed in the cell because the electrodes are located side by side on the same layer. Further reduction of the manufacturing costs in comparison to the stack type is achieved because even with the same lateral dimensions of the cell, only about 50% of the collector material is needed.

The cells in the stack-type design (Figure 18.4) have lower internal resistance, and therefore allow lower charging times. They are able to deliver higher peak currents in a short period than the cells of the coplanar type design. Stack type cells have a higher capacity at the same lateral dimensions, because they comprise about twice the amount of active electrode material on the same base area. These cells could therefore be used for "demanding" applications. A major disadvantage of the stack concept, however, is

the need to bring a separator between the two electrodes to protect the cell against an electrical short circuit.

This additional separator is quite contradictory to the demand for the low-cost production principle of printed batteries. In conventional batteries, the separator often is a piece of fleece material soaked with electrolyte. In an in-line production process, the inlaying of the classical separator fleece would be a rather difficult "pick-and-place" step and may have to be done off-line before the encapsulation.

However, the internal resistance of a coplanar cell is significantly higher, because the ion flux is primarily within the small gap region and spreads rather slowly over the whole electrode surface unlike the stacked cell, in which the ion flux is distributed evenly over the entire electrode surface. The capacity is lower because, for the same size, only about half of the electrode material is incorporated in the cell.

18.4 Printing technologies and challenges

The layers shown in Figures 18.4 and 18.5 may be applied by different printing technologies. Table 18.3 lists the layers and discusses the pros and cons of thinkable printing techniques.

18.4.1 Electrodes

For conventional batteries, the electrode materials are available as powders or suspensions called "slurries." These slurries are not suitable for printing without further treatment and dispersion techniques. Because of the rather coarse particle sizes (grains sizes) of the electrode materials (20−70 µm) and the wide particle size distribution, it is evident that only screen-printing and no other printing process is able to handle this kind of material. Even in comparison to graphic screen printing, very coarse meshes for the screen printing forms have to be used. It must be guaranteed that the particles fit through the mesh openings.

The capacity of a printed battery is determined by the amount of electrochemically active material used. However, the specific electrochemical capacity of the anode and cathode materials are different. For optimum performance and no "useless" excess material, the amount of anode and cathode materials must match. Depending on the electrochemical system, gassing is sometimes possible. To avoid it, there should be little excess cathode material. The deposited amount of electrode material can easily be adjusted in screen-printing by choosing the appropriate mesh. The most important parameter is the theoretical ink volume, which is provided by the mesh manufacturer in cm^3/m^2. The numerical value directly corresponds to the expected printed layer thickness in µm. For calculating the final balance, the mechanical density of the materials must be considered as well.

When printing this kind of rather large solid tone areas in screen-printing, the mesh geometry plays the most important role whereas the influence of the stencil can be neglected. Fine-tuning the thickness can be achieved by adjusting other printing parameters such as squeegee material, pressure, and edge geometry.

Table 18.3 Possible printing technologies for the layers of printed batteries

Layer	Printing technology	Discussion
Current collector	Screen printing	Easy to use, provides a sufficient layer thickness, maybe even too high a thickness. A lot of commercial inks (silver and carbon) are available on the market. Printing speed may be a little too slow.
	Flexo	Common in label printing, commercially available conductive inks not well-developed. Fast printing speeds. Compatibility of polymer printing form with solvents must be checked.
	Gravure	Difficult printing form (cylinder) preparation, commercially available conductive inks not well developed. Very fast printing speeds
	Inkjet	Possible, but silver and carbon inks must be on nano scale to not block nozzles.
Anode	Screen printing	Easy to use, provides a sufficient layer thickness. Because of coarse grains and required large-layer thickness, no other printing process is suitable.
Cathode	Screen printing	Easy to use, provides a sufficient layer thickness. Because of coarse grains and required large-layer thickness, no other printing process suitable.
Separator/electrolyte	Screen printing	Some manufacturers of printed batteries use pick-and-place techniques to bring in a separator that is soaked in electrolyte. It is a great advantage to use printable, gum-like electrolytes that function as separators simultaneously. Such printable electrolytes preferably are printed using screen printing because of the required layer thickness. Inkjet is possible.

In principle, printing pastes for battery electrodes comprise four categories of material:

- Electroactive material (50−80 wt%)
- Binder
- Conductive agent
- Solvent

The electroactive materials are able to store an electrical charge according to the Faraday law. The most important point is that they can be either oxidized or reduced. Typical materials are:

Anode: zinc, metal hydride, or lithium
Cathode: MnO_2, $NiOH_2$, or lithium iron phosphate

The function of the binder is to build a kind of matrix around the grains of the electroactive materials to provide sufficient mechanical stability without interfering too much with the electrical conductivity. Binder materials typically are polyvinyl alcohol, carboxyl methyl cellulose, polyvinylidene fluoride, or poly(vinyl pyrrolidone). They may contain a thickener such as polyacrylate or carbopol.

Conductive agents are needed to boost the conductivity, especially if the electroactive materials rather have insulating properties (oxides). Conductive agents typically are carbon-based (e.g., carbon black). The solvents that are used to make the dispersion printable either can be water or liquids such as N-methyl pyrrolidone, ketone, or alcohol. Water-based dispersions are preferable for environmental reasons.

Because the electrochemical process is complicated and not easily predictable, it is of great importance to pay attention to the compatibility of the used materials. For instance, the high oxidation potential of cathode materials can oxidize organic components. Sometimes contamination of the electroactive materials can lead to complete failure. To achieve a good battery performance, a sufficient porosity is required in the electrodes so that the electrolyte will be soaked into them.

The layers of the printed battery are build-up one after the other; therefore, good adhesion of the electrodes upon the current collectors is required. The layers must be dried sufficiently before the next layers are applied. Therefore, the usual drying technologies - infrared or hot air - can be used. The duration of this process is comparable to those of standard printing inks.

If a batch process or a preprint technique is used in this state, this intermediate product can be stored. As soon as the electrolyte is added, the battery must be closed and sealed to prevent the exchange of gases with the environment and the loss of humidity.

18.4.2 Current collectors

One disadvantage of the stack concept, as shown in Figure 18.4, is that the lead-outs of the current collectors lie on the opposing substrates. During the "PrintAkku" research project at HdM, a special folding technique was developed so that the upper lead-out is folded together with the basic substrate and thus stretches out to the same side as the

lower one, as shown in Figure 18.6. The final result is shown in Figure 18.7. This is a major advantage if considering contacting to the appliance.

Because the inner resistivity of the battery plays a major part for the overall capacity performance, it should be as low as possible. There are not too many types of conductive printing inks available:

- Carbon-filled ink (carbon black) sheet resistance from 1000 to 10,000 Ohms per square
- Metal-filled inks (metals might infringe with the electrochemical reaction)
  - Silver 0.03 to 0.1 Ohms per square
  - Copper (a disadvantage is that copper particles tend to oxidize and loose conductivity)
  - Nickel (might be a good choice for Ni/MH-type but not presently commercially available)
  - Gold, platinum, palladium, etc. (too expensive)
- Conductive polymers (PEDOT:PSS) 100−10,000 Ohms per square
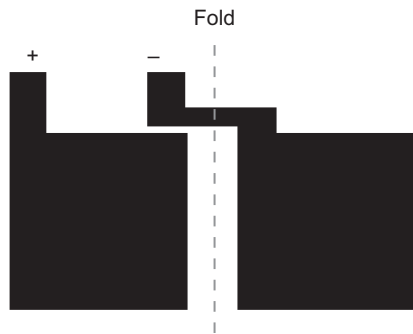
Figure 18.6 Schematic drawing of the fold (gray dotted line) that goes through the lead-out tracks of the current collectors.
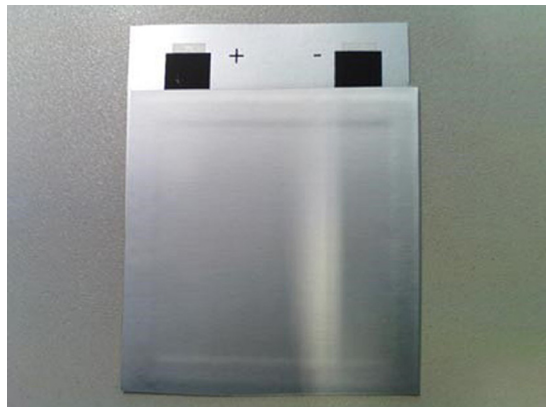
Figure 18.7 Cell after folding with both contacts on the same side of substrate.

The simplest and cheapest choice is carbon black ink because no infringement with the electrochemical processes must be feared. However, the resistivity is quite high, bringing the performance of the battery down. Thus, some research groups use a silver ink layer as the lowermost one and cover the silver layer ("booster layer") with a carbon black one for protective purposes. However, care must be taken when the electrolyte is filled in because it may migrate between the layers and can cause delamination between the silver layer and the substrate.

All of the conductive inks need a thermal treatment after printing. The percolation of the conductive filler grains typically is achieved after a few minutes at temperature around $120-150\,°C$. Difficulties arise if the substrate is not able to stand these temperatures. In particular, sheets of unsuitable substrates show pronounced curling, completely hindering further process steps. In roll-to-roll processes, the curling is not a major problem, but the necessary duration of the thermal treatment (several minutes) cannot be easily accomplished in standard roll-to-roll equipment. For ease of manufacturing, it is possible to preprint the current collectors in roll-to-roll processes. Figure 18.8 shows such a roll that can be refed into the presses for consecutive print runs.
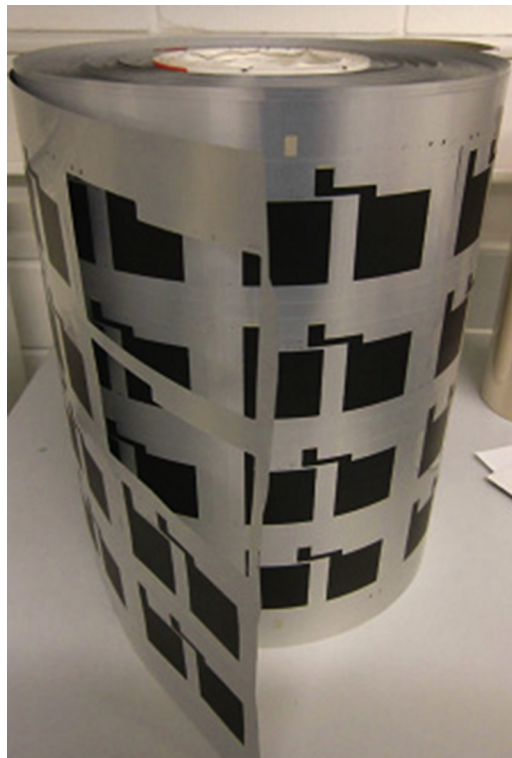
Figure 18.8 Roll of preprinted current collectors.

18.4.3 Sealing

As mentioned previously, one of the great challenges in manufacturing printed batteries is the leak tightness, especially because the sealing of the collector lead-throughs is very problematic. As shown in Figure 18.9 this problem could be solved by printing a sealing layer around the collectors and electrodes. The sealing layer is a polymer glue that can be activated by heat application. The cell is finalized after filling in the electrolyte/separator by flapping one side on top of the other and then apply heat to the sealing. Figure 18.10 depicts the principle of this process, which is quite common in manufacturing of graphical products.
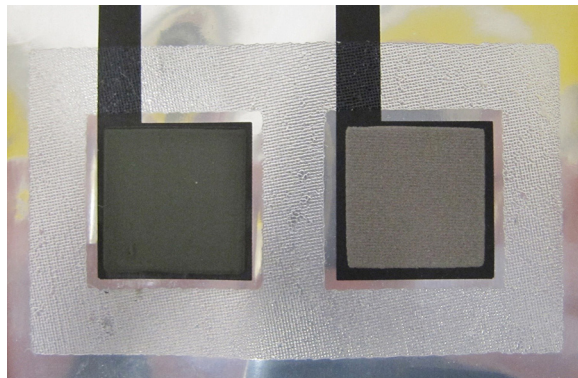
Figure 18.9 Sealing printed around the collectors and electrodes.
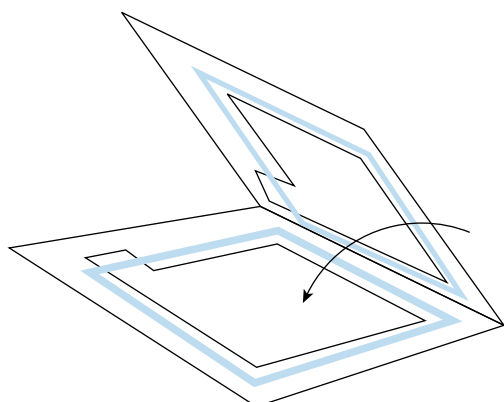
Figure 18.10 Flapping technique for finishing of the cell.

18.4.4   Electrolyte/separator

The greatest challenge in manufacturing thin, flexible, printed batteries is the handling of the electrolyte/separator. As mentioned previously, in conventional battery manufacturing, the separator is a fleece material soaked in electrolyte and then placed onto the electrodes. For manufacturing the batteries using printing processes solely, a printable electrolyte/separator layer (for stack type) or printable electrolyte (for coplanar) type is extremely desirable.

In a large-scale experimental design setup, described in the thesis of Hagedorn (Hagedorn, 2009), a combination of thickening agents and other additives was tested to bring the 25% caustic potash into a printable form without influencing the electrochemical properties. After numerous trials, a formulation was found that works quite well.

A group of researchers at the Imperial College London worked on printable electrolytes as well. These use PolyHIPE materials (Porous Polymers Synthesized within High Internal Phase Emulsions) that were developed during the Greenbat project.

18.4.5   Manufacturing and mass production

In the battery market, there is always the challenge of competing with low-cost button cells coming from the Far East. Although there are some advantages to printed batteries and the overall selling prices may not be too high. To open up a mass market for printed batteries, the prices should not exceed a few cents. To achieve that, fully integrated in-line manufacturing processes are needed. The area of label manufacturing already has roll-to-roll presses that provide enough printing stations (at least five) and finishing units for a complete in-line process. These presses use either rotary screen-printing or flatbed screen-printing units in which the web is halted briefly for the printing strokes or presses, like the Kamman K15 press, which uses a kind of Michael Jackson's "Moonwalk" movement.

Our next step in the BatMat project therefore is to design such a manufacturing process. For this process, some of the drying steps needed between the printing units require special considerations. Other topics that need to be investigated in the near future are the possibility of intermediate storing of the primary cells without electrolyte. Can they be finalized and activated by adding the electrolyte some weeks or months after printing? Other topics of the project are long-term tests and investigations about the shelf life time.

18.4.6   Series connection of battery cells

One of the major advantages of the printing technologies is the extremely flexible layout. An ambiguous number of cells can be added in a row. For primary cells, a series connection up to 15 cells have been demonstrated. As an example, the cross-section of the layout for a five-cell series connection is shown in Figure 18.11, whereas Figure 18.12 shows the top view of such a configuration. The assembly of the series connection of the cells can be completed by employing a similar flapping technique as for single cells as indicated in Figure 18.13. The resulting setup is shown in Figure 18.14.

Figure 18.11 Series connection of printed battery cells.
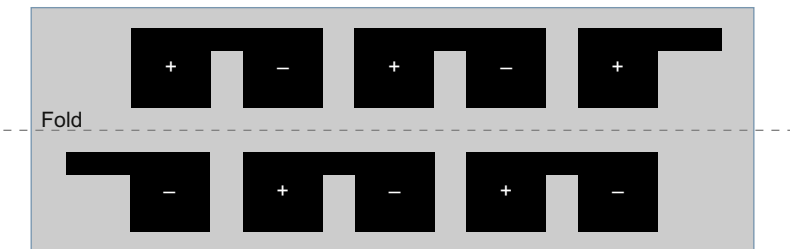
Figure 18.12 Top view on a current collector structure of a five-cell series connection. After adding the sealing, the electrodes and the separator/electrolyte the battery is finalized by folding along the folding line and activating the sealing.
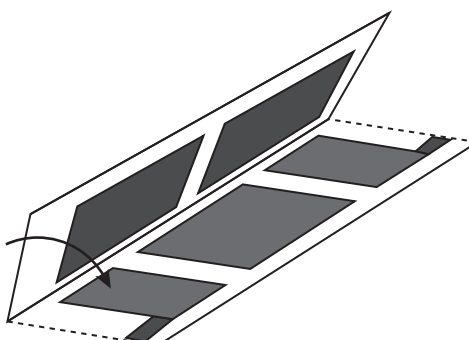
Figure 18.13 Assembly of the series connection of printed battery cells.

Figure 18.14 Five printed zinc-manganese dioxide cells in series connection.

18.5 Properties of printed batteries

The main electrical properties characterizing batteries are the cell voltage and the capacity. The basic electrical property of a nonrechargeable battery can be best summarized in a discharge curve as shown in Figure 18.15. The first results of electric properties of printed rechargeable batteries were published in a feasibility study by Vindus (Vindus, 2006). The separator of the cell that is shown in Figure 18.16 was a fleece soaked in potassium hydroxide (25%). Figures 18.17(a) and (b) show the
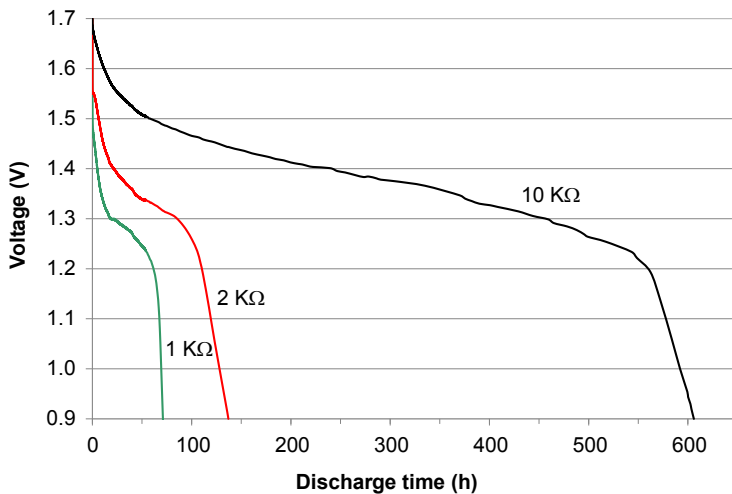
Figure 18.15 Discharge curves of SoftBattery® Reg 1.5 V with various loads at room temperature.
Source: © Enfucell Oy.
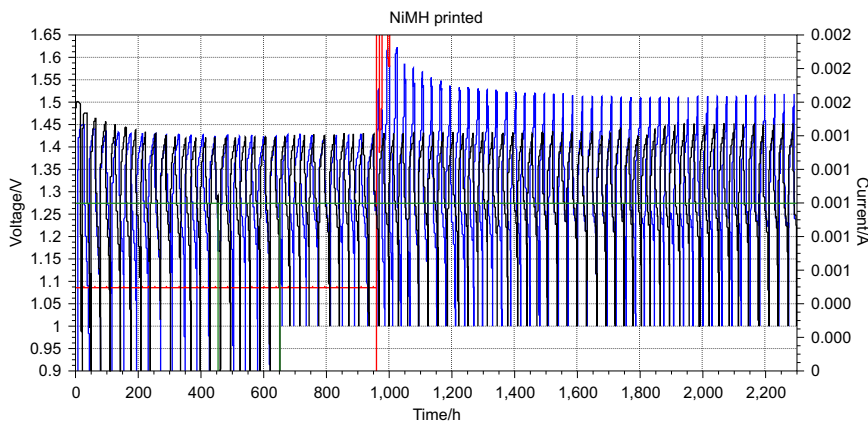
Figure 18.16 Voltage during cyclization.

electrical performance measurements of this first prototype cell. These measurements proved the concept that a secondary battery cell can be manufactured by screen-printing technology.

Rechargeable batteries have further properties such as the charge current and the end-of-charge voltage. Because there is little information available for printable batteries, all of these parameters must be investigated first. Figures 18.16 and 18.18 show the results of the battery cycling (using the cell from Figure 18.19) over 70 cycles (charge/discharge) for a sum 2300 h, in which the first 25 cycles were carried out at a charge current of 500 μA. Because the cell has a much higher capacity than expected in the first

(a)

(b)
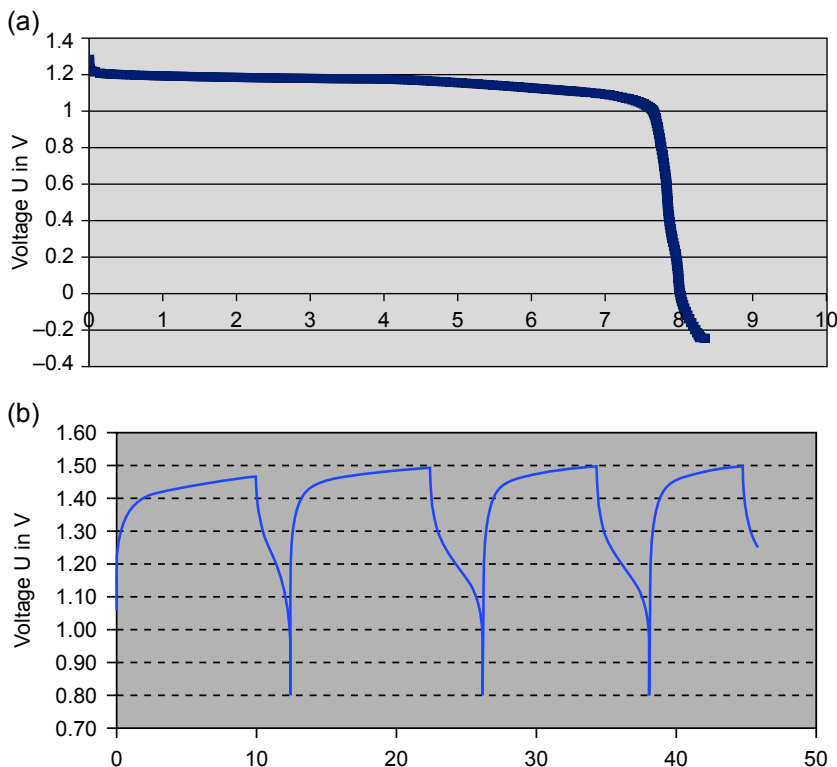
Figure 18.17 (a) Discharging curve of the first prototype of a printed NiMH cell (Vindus, 2006). (b) Charging and discharging curve (cycling) of a printed NiMH cell (Vindus, 2006).
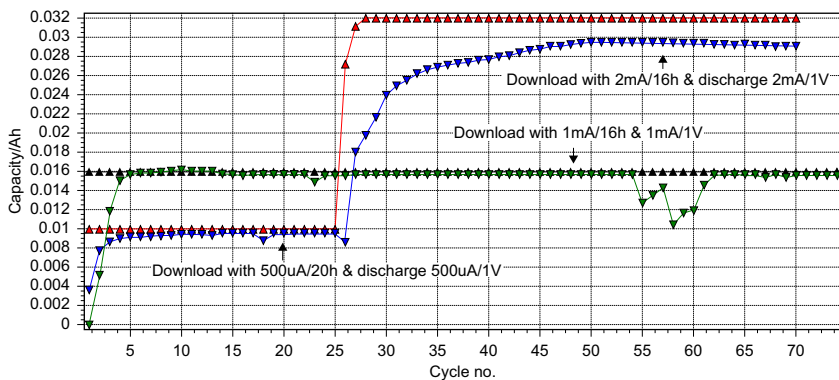
Figure 18.18 Battery capacity during the cyclization.

moment, the charge current was increased from 500 µA to 2 mA, starting with the 25th cycle. As shown in Figure 18.18, the cell provides from the 27th cycle on a constant capacity of about 31 mAh, which is quite close to the theoretical capacity of the electrode layers.
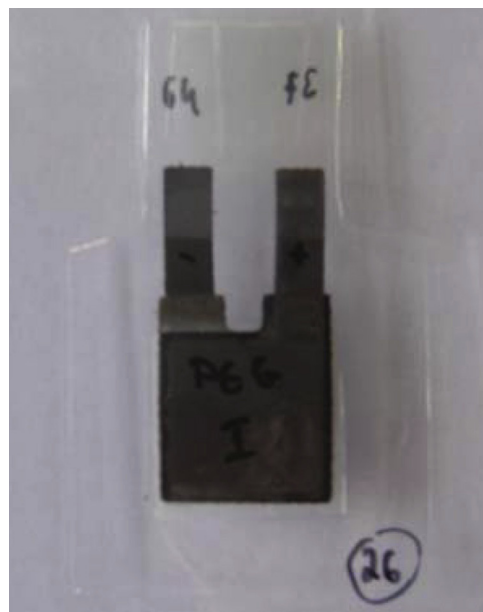
Figure 18.19 The first prototype of a secondary cell (in PET) (Vindus, 2006).

Other electrical properties of batteries are the internal resistance (impedance) and the pulse load capability. Electro impedance spectroscopy can be used to find out about these values. Figure 18.20 depicts the result of such a measurement represented in a so-called Nyquist plot. For different frequencies of alternating current load, the
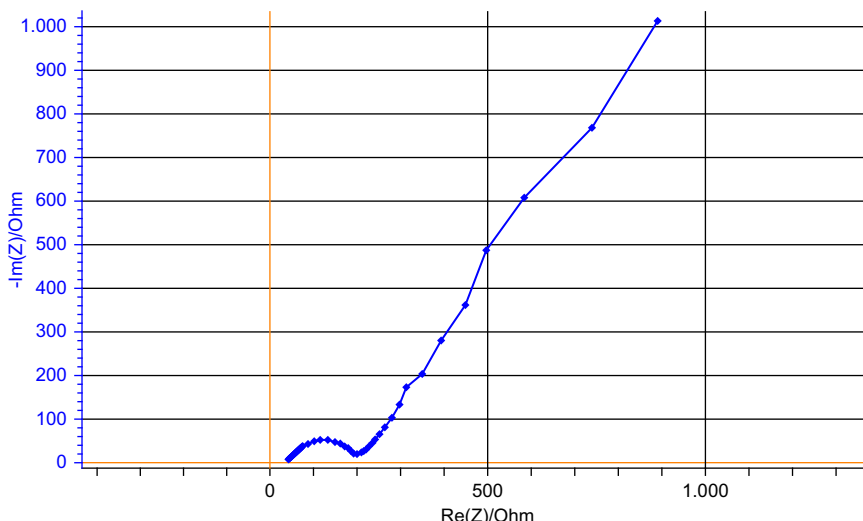
Figure 18.20 Nyquist plot of a printed rechargeable battery.

imaginary and real part of the impedance is plotted. The curve starts with low frequencies of about 10 mHz in the upper right corner of the plot. With increasing frequency, both the imaginary and real parts of the impedance decrease. The curve typically ends at a frequency of 10 kHz. There are several models for equivalent circuits of batteries. The commonly used model consists of a resistor in series with an R/C circuit and the Warburg resistance (diffusion circuit element). The half-circle shape at the left end of the curve represents the R/C circuit; the branch to the right of the circle is the so-called Warburg impedance.

Rechargeable batteries often require a formation process to reveal their full capacity. That means that, before the first full charging process, there are one or more charging/discharging processes with softer charging settings necessary.

18.6   Conclusions and future trends

For many years, it has now been proven that printing technologies can be used to produce thin film batteries. The design can easily be adjusted and customized to the demand of the product, device, or sensor that needs the power supply. Printable electrolytes are further pushing on the development. Besides zinc/manganese-dioxide, other (most of them rechargeable) chemical systems such as Ni/MH, Li-polymer, radical polymer, or zinc/air are presently under investigation and will bring other opportunities for smart objects, smart devices, and wearable electronics. According to forecasts (e.g., roadmaps given by the OE-A organization—www.oe-a.org—in the next five−20 years), there will be a tremendous increase in usage, sales, and performance of such electronic components containing printed and flexible batteries.

Appendix: Patent applications on printed batteries

Owner: Varta (M. Krebs Varta, M. Wendler HdM) druckbarer Separator DE102010018071 20.04.2010.

Owner: Varta (M. Krebs Varta, M. Wendler HdM) Kontaktlayout gedruckte Batterien DE102010023092 31.05.2010.

References

3D printing of interdigitated Li-ion microbattery architectures. *Advanced Materials, 25*(33), (September 6, 2013), 4539−4543.
Hagedorn, R. *Optimierung einer im Siebdruck hergestellten elektrochemischen Zelle* (Bachelor thesis) im Studiengang Druck- und Medientechnologie der HdM Stuttgart 08/2009.
Kiehne, & Albert, H. (5 Aufl. 2003). *Batterien Grundlagen und Theorie, aktueller technischer Stand und Entwicklungstendenzen*. Renningen: Expert Verlag, ISBN 3-8169-2275-9.
Linden, D. (1995). *Handbook of batteries. McGraw-Hill handbooks* (2nd ed.). New York: McGraw-Hill.

Vindus, B. *Feasibility Studie zum Drucken von NiMH-Akkumulatoren* (Diploma thesis) HdM Stuttgart 10/2006.

Wendler, M., Krebs, M., & Huebner, G. (December 2010). Screen printing of thin, flexible primary and secondary batteries. In *Advances in printing and media technology* (vol. 37, pp. 303−312). IARIGAI, ISBN 978-3-9812704-2-6.

Wendler, M., Krebs, M., & Huebner, G. (2011). Development of printed thin and flexible batteries. In *IC International Circular of Graphic Education and Research. The International Circle of Educational Institutes for Graphic Arts, Technology and Management* (pp. 32−41). No 4.

This page intentionally left blank

Index

Note: Page numbers followed by "f" and "t" indicate figures and tables, respectively.

This page intentionally left blank

Plate I (Chapter 2) Contour plot of E_{coh} along (a) the tetragonal and (b) the trigonal continuous path. Lighter (red) regions correspond to preferable structures (with higher E_{coh}), while darker (blue) regions are less favourable. BCC and FCC lattices correspond to $c/a = 1$ and $c/a = \sqrt{2}$ (dashed lines), respectively. White dots represent maxima of the E_{coh}, crossed regions have negative E_{coh}, and the interval between lines is 0.05 eV. Labels I, II, 1D, and 2D-T refer to corresponding stable structures.

Source: Adapted from Volonakis et al. (2013a); © IOP Publishing. Reproduced by permission of IOP Publishing. All rights reserved.

(a)

FC-module with pillars, V1

Bending test V1 with thermal pre-load
pressure & chuck removed + cooling from 200 C to RT
+ placement on roll
+ application stretching force

stress-xx (MPa)

	3.70+02
	2.61+02
	1.53+02
	4.38+01
	-6.50+01
	-1.74+02
	-2.83+02
	-3.91+02
	-5.00+02

def. 1x

(b)

FC-module with pillars, V1

pressure @ 200 C (on chuck)
pressure & chuck removed + cooling from 200 C to RT
+ cooling to -40 C and dwell
+ heating to 150 C and dwell
+ 2nd cooling to -40 C and dwell

max. principal stress (MPa)

	4.47+02
	3.58+02
	2.69+02
	1.81+02
	9.18+01
	2.90+00
	-8.60+01
	-1.75+02
	-2.64+02
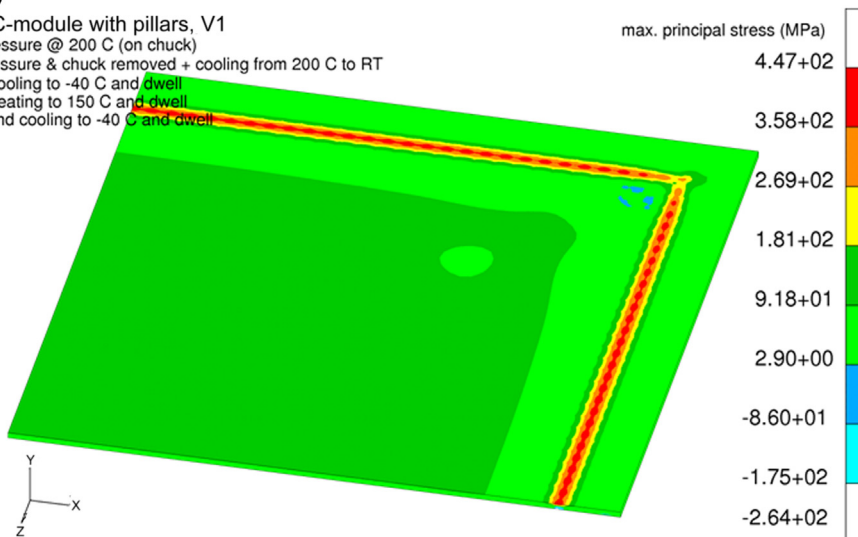
Plate II (Chapter 6) (a) Finite element analysis (FEA) of a flip chip module mounted on polyimide (PI) and bent to 20 mm bending radius; (b) FEA of the same flip chip module after processing at 240 °C and temperature cycled between −40 °C and 150 °C.
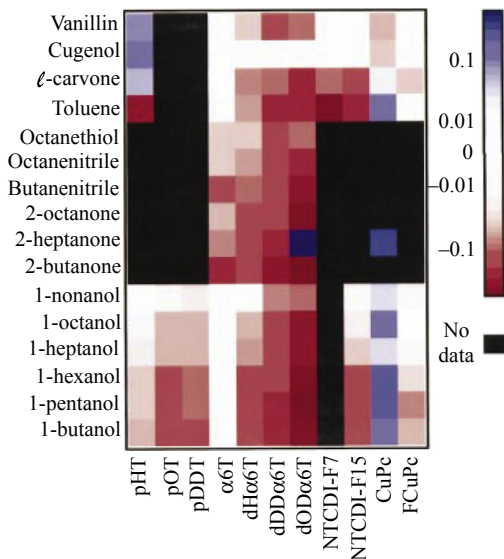
Plate III (Chapter 15) Effect of 16 analytes on 11 sensor materials. Black indicates that data are not available; white indicates a negligible response; blue shows positive changes in the sensor current; red shows decreases (b).
Source: Reprinted with permission from Crone et al. (2001), Copyright 2001, AIP Publishing LLC.
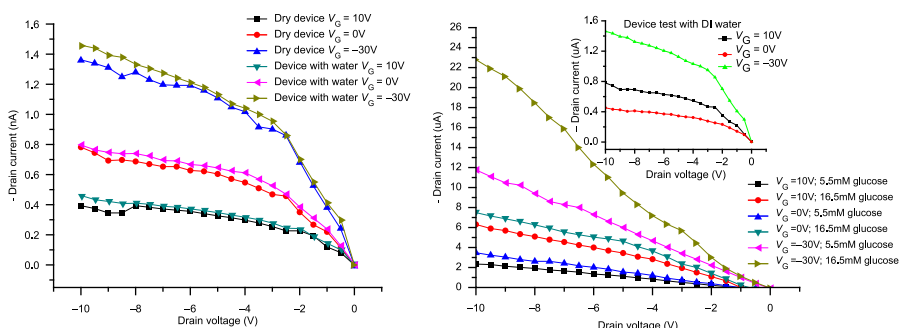

Plate IV (Chapter 15) Drain current versus drain potential (left) and gate potential (right) showing sensor response recorded under different experimental conditions.
Source: Reprinted from Liu, Agarwal, and Varahramyan (2008), Copyright (2008), with permission from Elsevier.
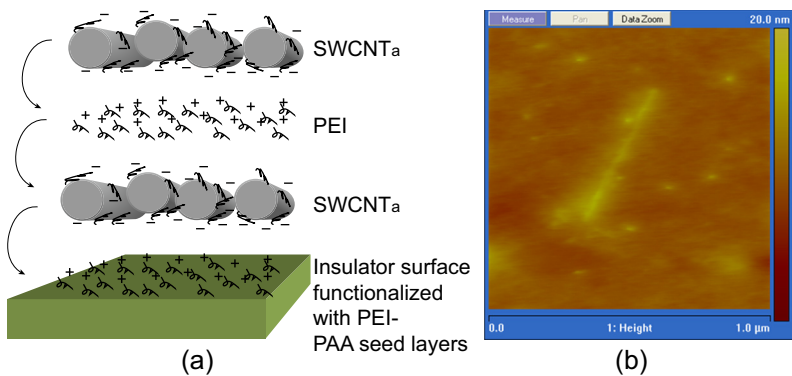
Plate V (Chapter 17) (a) Schematic diagram of the LbL technique, (b) AFM image of the deposited CNTs.